The physics of shape changes in biology

Habilitationschrift
zur Erlangung der Lehrbefähigung
für das Fach Physik

vorgelegt dem Fakultätsrat der
Mathematisch-Naturwissenschaftlichen Fakultät
der Universität Potsdam

von

John William Chapman Dunlop

Max Planck Institute of Colloids and Interfaces

Potsdam, October 2015

Published online at the
Institutional Repository of the University of Potsdam:
URN urn:nbn:de:kobv:517-opus4-96554
http://nbn-resolving.de/urn:nbn:de:kobv:517-opus4-96554

Abstract

Biological materials, in addition to having remarkable physical properties, can also change shape and volume. These shape and volume changes allow organisms to form new tissue during growth and morphogenesis, as well as to repair and remodel old tissues. In addition shape or volume changes in an existing tissue can lead to useful motion or force generation (actuation) that may even still function in the dead organism, such as in the well known example of the hygroscopic opening or closing behaviour of the pine cone. Both growth and actuation of tissues are mediated, in addition to biochemical factors, by the physical constraints of the surrounding environment and the architecture of the underlying tissue. This habilitation thesis describes biophysical studies carried out over the past years on growth and swelling mediated shape changes in biological systems. These studies use a combination of theoretical and experimental tools to attempt to elucidate the physical mechanisms governing geometry controlled tissue growth and geometry constrained tissue swelling. It is hoped that in addition to helping understand fundamental processes of growth and morphogenesis, ideas stemming from such studies can also be used to design new materials for medicine and robotics.

Zusammenfassung

Biologische Materialien verfügen nicht nur über außergewöhnliche physikalische Eigenschaften, sie können auch ihre Form und ihr Volumen verändern. Ermöglicht werden diese Anpassungen während der Morphogenese und des Wachstums sowohl durch die Bildung neuer Gewebe, als auch die Umformung und/oder Reparatur alter Gewebe. Zusätzlich führen Form- oder Volumenänderungen in Geweben häufig zur Generierung von Kräften (Aktuation) und daraus resultierenden Bewegungen. Ein bekanntes Beispiel dafür ist der feuchtigkeitsgetriebene Öffnungs- und Schließmechanismus der Schuppen von Kiefernzapfen, die ausschließlich aus totem Gewebe ohne aktiven Metabolismus bestehen. Bestimmend für Wachstum und Aktuation sind dabei nicht nur biochemische Faktoren sondern auch physikalische Randbedingung definiert durch die Umgebung und die Gewebearchitektur. Die vorliegende Habilitationsschrift basiert auf biophysikalischen Arbeiten der Gruppe „Biomimetic Actuation and Tissue Growth“ zu wachstums- und quellungsbedingten Formänderungen biologischer Systeme. Physikalische Mechanismen von Gewebewachstum und Quellprozessen unter dem kontrollierenden Einfluss von geometrischen Randbedingungen werden mit theoretischen und experimentellen Methoden untersucht und erklärt. Die gewonnenen Ergebnisse tragen nicht nur zum Verständnis grundlegender Wachstums- und Morphogeneseprozesse bei, sie könnten zukünftig auch für die Entwicklung neuer Materialien für die Medizin und Robotik von Nutzen sein.

Acknowledgements

This work spans almost ten years of activities at the Department of Biomaterials, at the Max Planck Institute of Colloids and Interfaces firstly as a postdoc and then as a group leader. As such there are an enormous number of people to thank for their support, friendship and guidance. If I miss anyone, my apologies, it is certainly not on purpose, but rather due to the limited amount of sleep that we have been getting in the last months…

I would firstly like to thank Peter Fratzl for giving me the opportunity to work with him on such interesting topics. When I first came for an interview at the Department, wrapped in bandages after a nasty accident with a gas stove, he offered me a position only on the proviso that I do theoretical work, and that I was to stay away from the lab until I get suitable fire training. I followed his advice, at least to start with, which enabled me to do theoretical work together with a wonderful group of experimentalists. Thank you Peter, for your trust, advice and most especially for the friendly supportive atmosphere that you have created in your department.

To my former "Maitre de thèse" Yves Bréchet, thank you for encouraging me on this journey to one of the bastions of the enlightenment, your continued support and collaboration in so-many projects, for the meetings in strange places, and the wild blue-light rides to the airport…

To all my group members, Cécile, Sébastien, Lorenzo, Leonardo, Vanessa, Francis, Paul, Jate, Sebastian, Alan, Livnat, Karen, Khashayar, Huynh, Philip and Krishna, I thank you for your support, hard work and enthusiasm that made the research in our group possible. You have all taught me so much, and hopefully have been at least been able to reciprocate in some small way in return. To all the technicians in the department, especially Petra and Christine, many thanks for your technical support, for your patience and unending help.

I also wish to thank all my collaboration partners especially: Leonid Ionov, Carsten Werner, Dieter Fischer, Ernst Gamsjäger, Gerald Zickler, Thomas Antretter, James Weaver, Fred Vermolen, Yael Abraham, Rivka Elbaum, Ron Shahar, Monika Rumpler, Ansgar Petersen, Pascal Joly, Georg Duda, Amaia Cipitria, Jiayin Yuan, Laura Hartmann, and Thomas Stach. These collaborations have been instrumental in moving the research forward, and it has been a pleasure to work with you all. I also wish to thank the funding agencies, especially the Max Planck Society, Bild Wissen Gestaltung, and the Humboldt Foundation for support during our research.

To the members of the Institute of Physics at Potsdam University, especially Svetlana Santer, and Carsten Beta, I thank you for the opportunity to first teach and then do my habilitation in the Institute. Before I left Australia, I would never have thought it possible that I would or could give lectures in Physics in German!

A big thanks to Markus, Davide, Ricci, Mason, Matt, Wolfgang for the great discussions and chats over coffee and beer. To all the other members and former members of the Department of Biomaterials that I have had the chance to spend time with over the last years, I thank you for your friendship, trust and advice, it has been a pleasure working with you all. To Ricci and Wolfgang especially I thank you both for the critical reading of this manuscript and a big thank you to Oskar, Jutta and Josef, for the chance to have our short Leobener Sabbatical which helped so much in making progress in the writing.

I would like to thank my now extended Austr(al)ian family for their love and support. To Mum and Dad thank you for encouraging me to travel and to follow my interests and yet still support me so strongly from afar.

Finally to Michi, my climbing partner, my fellow hunter gatherer and explorer, my friend and colleague, and our two wonderful daughters thank you all for keeping me on track, and keeping what is most important in life in focus.

Table of Contents

ABSTRACT I

ZUSAMMENFASSUNG III

ACKNOWLEDGEMENTS V

TABLE OF CONTENTS VII

1 INTRODUCTION 1

2 TISSUE GROWTH 11

2.1 BACKGROUND 11
2.2 RESULTS AND DISCUSSION 19
2.3 SUMMARY 32

3 ACTUATION 33

3.1 BACKGROUND 34
3.2 RESULTS AND DISCUSSION 45
3.3 SUMMARY 52

4 CONCLUSIONS AND OUTLOOK 53

5 LIST OF FIGURES AND PERMISSIONS 55

5.1 FIGURE LIST 55
5.2 PERMISSIONS 56

6 REFERENCES 59

6.1 MANUSCRIPTS FORMING THE BASIS OF THIS THESIS 59
6.2 FULL PUBLICATION LIST 60
6.3 REFERENCES CITED IN THIS THESIS 65

7 FULL PUBLICATIONS 77

1 Introduction

This short introduction should provide a background for the reader about research into shape changes in biology due to growth and swelling, the focus of this habilitation thesis. It turns out that even historically, research in this field has demonstrated the importance of physical principles on biological shape changes, especially through signalling via mechanical forces. By understanding such shape changes, one can not only learn about the formation of external structures and shape, but also the development of internal tissue microstructures, which has an important role on function.

The ability of biological tissues to grow and change shape has long fascinated us. Throughout the centuries, scientists such as Galileo, Trembley, Haeckel, Darwin and many others, have worked on understanding how new tissues in Nature form, as well as how they change shape, or actuate, after growth is complete. In his classic book, "*On Growth and Form*", D'Arcy Thompson (1942) argues that the development of form in biology, is controlled by the application of physical forces during growth, implying that an understanding of physical principals is necessary to understand morphogenesis (See also Gould (1971)). Amongst many examples linking physical laws and organic forms, he showed that simple geometric rules could describe the shape, and growth of shells (Figure 1–1a). With the advent of modern computing, these geometric ideas have been tested systematically (Raup 1962), compared to real shell geometries (Meinhardt 2009), and even linked to physical mechanisms behind shell growth (Chirat et al. 2013). Thompson's thesis, that as biological organisms grow and act in a physical world they therefore can be described by equations from physics, is perhaps too strong considering recent advances in evolutionary and molecular biology, however there is still much to learn about the link between physics, biology and geometry, as will be seen in the following.

Thompson's connection between physics and biology, although ground-breaking, was based on earlier work going back at least as far as Galileo (1638). An example is shown in Figure 1–1b, an image from Galileo's "*Dialogues concerning two new sciences*" (1638), that illustrates his argument of how the long bones of animals should scale with body size. If an animal's volume and hence mass scale to the cube of its linear dimension, but the ability of a bone to resist load scales only with the square of the linear dimension, then in order to withstand the increasing load with larger body size, the ratio of length to thickness of long bones should scale with a power of two thirds. It turns out this power law is largely supported when real bones are measured, e.g. (Currey 2002); see also (Gould 1966), (Schmidt-Nielsen 1984) or (Niklas 1994) for other applications of allometric methods in biology.

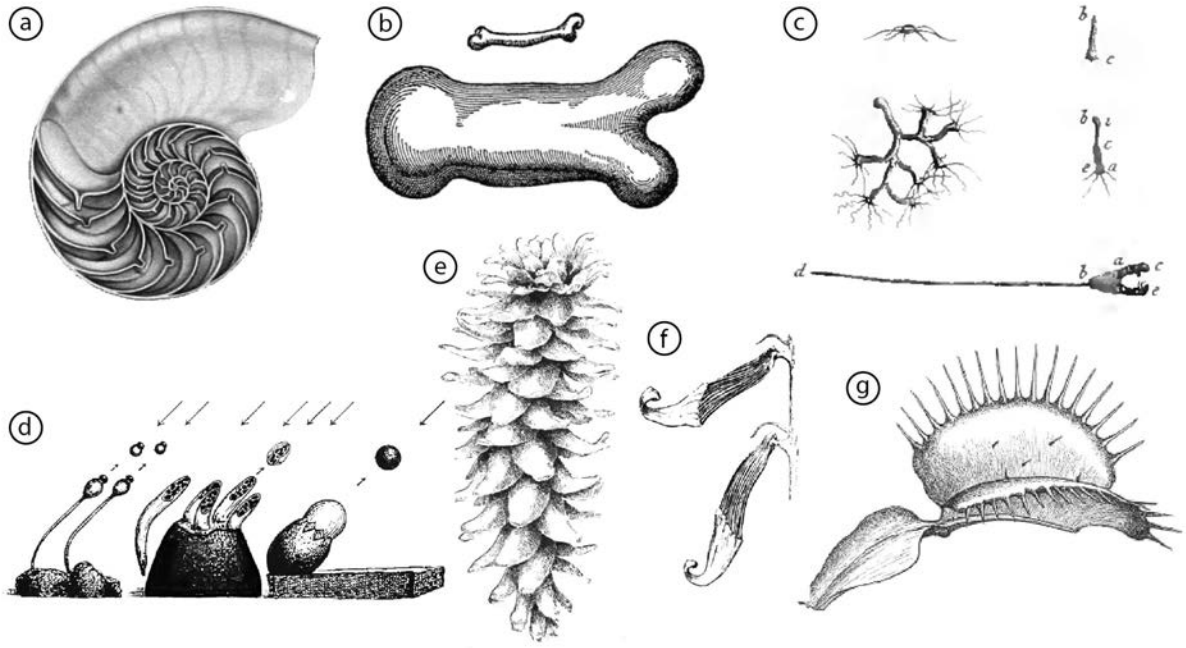

Figure 1–1: Some historical examples of studies of shape changes in biology
Tissue shape and its changes have been studied for centuries, with some illustrative examples given above. a) Thompson (1942) analysed the geometry of the shell of the chambered nautilus, *Nautilus pompilius*, , showing that the shell shape could be described by an equiangular spiral (image from Chenu (1842)), b) the role of mechanics on the unequal scaling of thickness and length in long bones was discussed by Galileo, (1638), in his Dialogues concerning two new sciences, c) the possibility of tissue and organ regeneration was discovered in hydra, the image shows different stages of regeneration in the species *Hydra vulgaris* as studied by Trembley (1744) d) projectile motion used for spore dispersal in the fruit bodies of some fungi (left, *Pilobolus longpipe,* middle, *Ascobolus immersus,* and right, *Sphaerobolus stellatus*) studied by Buller (1958), e) hygroscopic motion in pine cones as studied by Shaw, (1914), image shows an opened cone of *Pinus acayahuite,* f) dissected scale of the same species showing movement from wet (below) to dry (above), image also by Shaw, (1914), g) the snapping motion of the Venus fly trap, *Dionaea muscipula,* as studied by Darwin (1875).[1]

This link between loading and shape was observed prior to Thompson not only in the external shape of bone (due to development), but also inside it (due to adaptation), within the cancellous or trabecular bone present in vertebra or in the end of long bones. This porous structure was seen to be strongly anisotropic, with individual trabeculae oriented along the directions of principal stresses (Ward (1876), but see also (Lee and Taylor 1999) for a historical perspective). Upon observing these structures, Roux (1885) and Wolff (1892), came to the conclusion that bone adapts its architecture dynamically with respect to changes in the applied loading. This implies that bone cells can sense and respond to physical forces by specifically removing or producing new bone, thus modifying the local mechanical stress state. Research into bone remodelling, or the feed-back between physical loading and bone cell behaviour, has accelerated in recent years due to the use of modelling methods from physics, for some examples see e.g. (Frost 1987, Huiskes et al. 2000, Ruimerman et al. 2003, Tsubota and Adachi 2004, Weinkamer et al. 2004, van Oers et al. 2008, Dunlop et al. 2009, Hartmann et al. 2011). In addition to its application to bone, an understanding of the physical basis of morphogenesis is fundamental in the field of tissue regeneration. This field of research was pioneered by Trembley (1744), with the observation that damaged or even missing tissues and organs can regenerate in Hydra (Figure 1–1c) (Dinsmore 1991). In the last century it has become clear that in addition to biochemical and genetic factors physical forces also play an important role regeneration such as in wound healing (Gurtner et al. 2008), limb

[1] To improve the clarity of the figure captions all sources and permissions for images used are listed in detail at the end of this thesis in Section 5.2.

regeneration (Calve and Simon 2010), and bone healing (Vetter et al. 2011), to name only a few examples.

Of course cells and tissues not only can respond to force but can also generate it as exemplified in the spectacular spore dispersal mechanisms (Figure 1–1d) seen in the fruiting bodies of some fungi (Buller 1958) or in the closing mechanism of the Venus fly trap (Darwin 1875)(Figure 1–1g). Other examples of the utility of force generation in tissues, include the hygroscopic movements found in plants, as seen in the way a pine-cone opens to release its seeds (Figure 1–1e and f). Although these movements are perhaps not as spectacular as those of the fungi, they are more interesting from a bio-inspired materials perspective. As the responsive components of these tissues are dead, they operate without any complex metabolic machinery. This means that in principle if we can understand how the internal structure of such tissues controls motion, we can copy this in synthetic systems (Burgert and Fratzl 2009, Fratzl and Barth 2009, Martone et al. 2010). More examples of such work will be discussed in more detail in Chapter 3 of this habilitation thesis.

The main focus of interest of the research summarised in this thesis are dynamic shape changes due to growth or swelling of a tissue. Before going into more detail it is of course necessary to understand the microstructure of a static tissue. On one hand this tissue microstructure arises as a consequence of growth, but on the other hand, microstructure controls function as will be seen in examples in Chapter 3. Although a large range of types and forms of tissues can be found in Nature, it is somewhat surprising that the majority of structural tissues in biology are made of only a limited range of components, or "chemical building-blocks" (Fratzl 2007). This could potentially be related either to limitations in the availability of different chemical elements in the environment, or perhaps due to evolutionary restrictions. Interestingly these different building blocks can be observed throughout almost all kingdoms of life as illustrated in Figure 1–2. which shows a simple phylogenetic tree on which is marked the occurrence of major materials components in biological materials including fibrous polymers such as cellulose, chitin, collagen, and minerals such as calcite, calcium phosphate and silica (Knoll 2003).

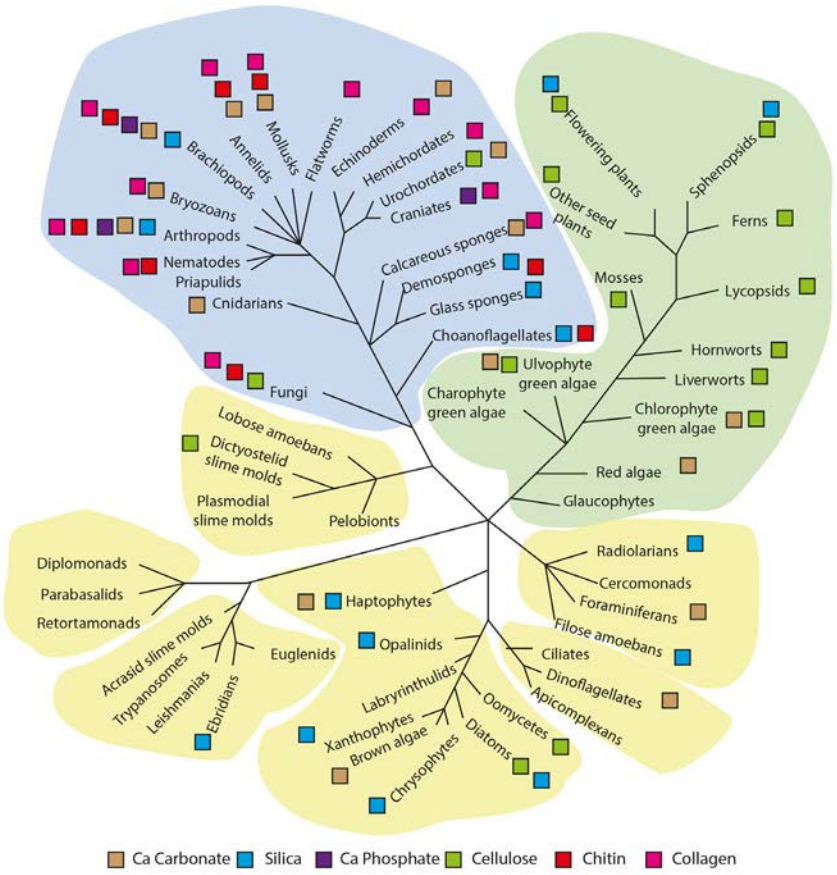

Figure 1–2 : Map of major constituents of biological tissues.
Phylogenetic tree with the occurrence of some major building blocks (Calcium Carbonate, Silica, Calcium Phosphate, Cellulose, Chitin and Collagen) highlighted. The spread of symbols highlights that basic materials building blocks can be found throughout almost all kingdoms. Modified with permission from (Knoll 2003).

Despite the apparent paucity in available of constituent materials, Nature is still capable of producing materials with a wide range of properties (Ashby et al. 1995, Wegst and Ashby 2004) as illustrated in the materials property chart for a selection of natural materials in Figure 1–3. This map shows that natural materials can span at least 3 orders of magnitude in strength and 5 orders in magnitude in Young's modulus.

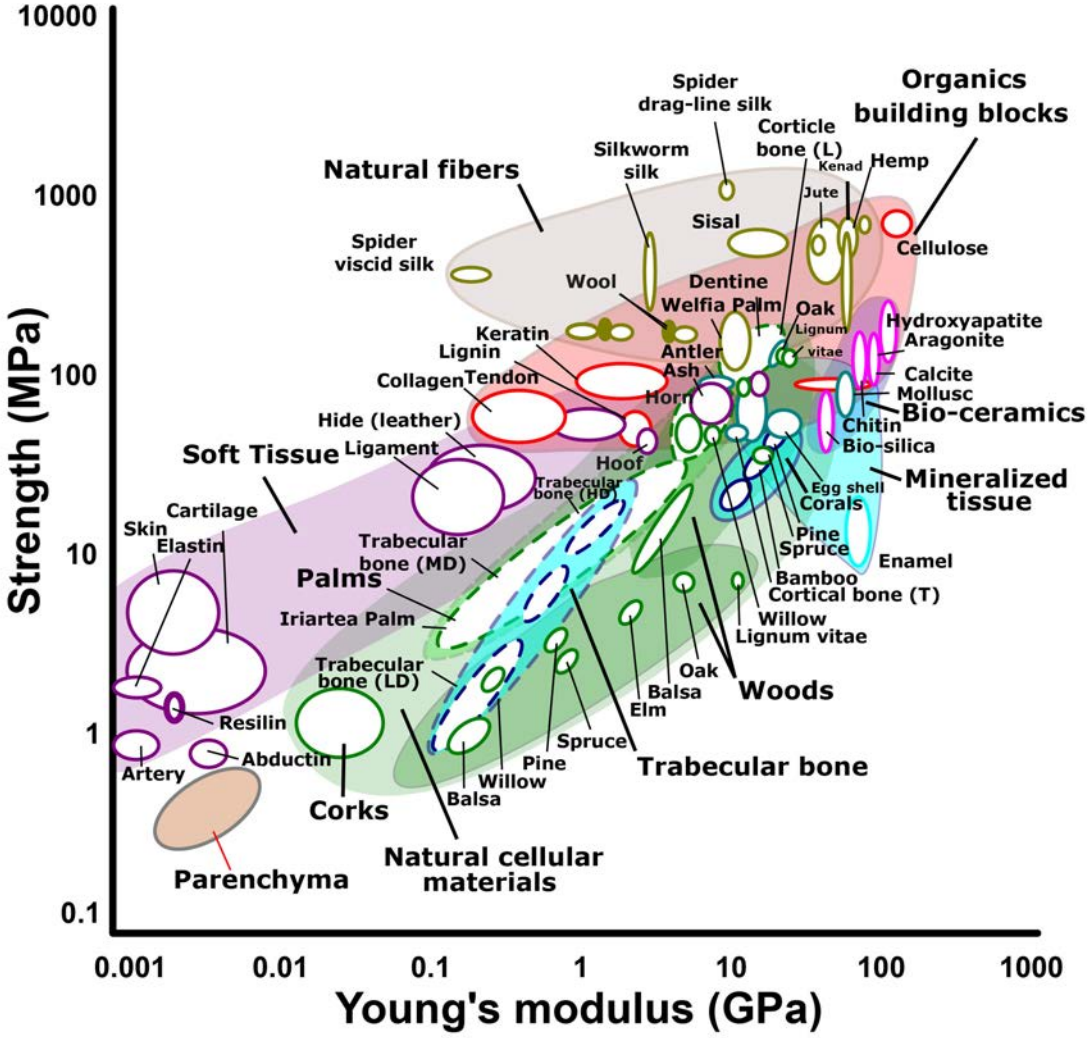

Figure 1–3 : Properties of a sample of biological materials.
A so-called Ashby map showing the strength and Young's modulus of a range of biological materials. Based on data in (Wegst and Ashby 2004).

This wide range of properties in biological tissues comes from the fact that they are composite materials (Neville 1993) combining different physical properties from each of the constituent building blocks (Fratzl and Weinkamer 2007, Dunlop and Fratzl 2010). By just controlling the architecture or microstructural arrangement of the constituents at different length scales (Dunlop and Fratzl 2013), as well as the composition and structure of internal interfaces (Dunlop et al. 2011) Nature can achieve a wide range of different properties with the same components and in addition may also achieve novel functionalities not possible in a single constituent. This concept of multi-scale tissue architectures is illustrated in Figure 1–4 with two examples: bone (left) or wood (right), although similar observations can be made in many other biological materials such as: the lobster cuticle (Fabritius et al. 2009), the skeleton of *Euplectella* (Aizenberg et al. 2005), or the abalone shell (Lin and Meyers 2005). See also (Wainwright et al. 1982, Vincent 1990, Niklas 1992, Currey 2002, Gibson et al. 2010) for more examples or the citations in the following review articles (Weiner and Wagner 1998, Fratzl and Weinkamer 2007, Meyers et al. 2008, Meyers et al. 2011, Speck and Burgert 2011, Wang and Gupta 2011, Meyers et al. 2013).

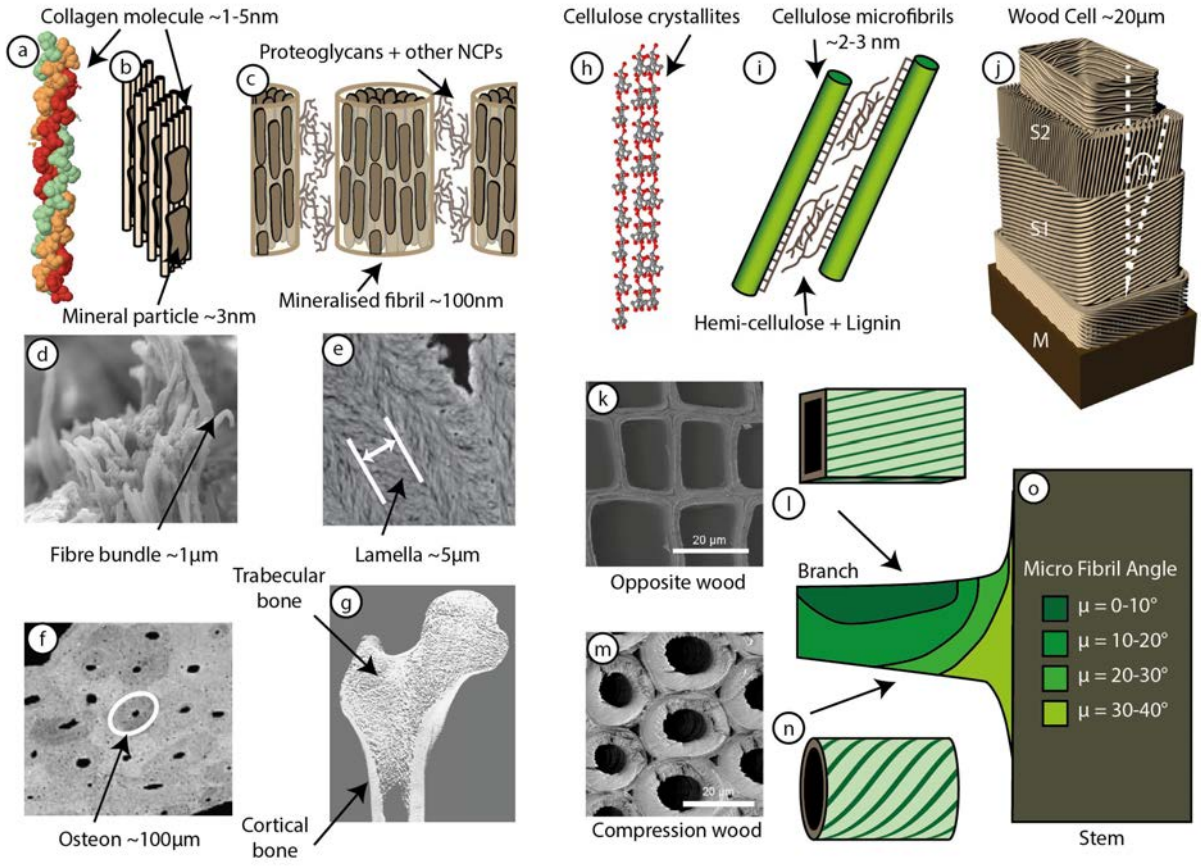

Figure 1–4: Multi-scale composite architectures in Bone and Wood
Both bone (left) and wood (right) can be viewed as fibre reinforced natural composites. **Bone (left: a-g)** consists of collagen molecules (a) in highly ordered arrays reinforced by plate-like mineral particles (b): Mineralised fibrils are held together by non-collagenous proteins (NCPs) (c) making up mineralised fibre bundles (d) arranged into lamellae (e). Cortical bone seen in the image of the human femoral head (g), consists of osteons (f) arranged in concentric layers of lamellae. The remaining bone (g) consists of porous trabecular bone (from (Fratzl et al. 2004) and (Fratzl and Weinkamer 2007), see also (Weiner and Wagner 1998)). **Wood (right h-o):** The wood cell wall is made of stiff crystalline cellulose fibrils (h) embedded in a softer matrix of hemicelluloses, pectins and lignin (i). A single wood cell consists of multiple layers of more or less ordered cellulose microfibrils spirally wound around the lumen (j). The thickest layer, the S2 layer is the major contributor to the mechanical properties of the cell, determined by the microfibril angle µ. At larger length scales, trees can control the microfibril angle (MFA) and the cell geometry, as seen in the SEM images (courtesy M. Eder) and sketch of opposite wood (k and l) and compression wood (m and n) in spruce. In a spruce branch (o) these angles are distributed to have stiff cells with low MFAs on the upper side and compression resistant cells on the lower side with larger MFAs (Farber et al. 2001). Schematics adapted from (Dunlop and Fratzl 2010) and (Dunlop and Fratzl 2013).

Bone (Figure 1–4a-g) is a particle reinforced fibre composite, consisting of collagen, hydroxyapatite, some non-collagenous proteins and water (Weiner and Wagner 1998). These components are arranged in complex ways over multiple length scales starting from mineral reinforced collagen fibrils at the nanometre scale being arranged into micron scale fibre bundles. These bundles in turn form sheets or lamellae, stacked in layers which make up osteons which are some of the major structural units inside the outer cortex of the macroscopic bone. The mechanical properties of the main components, collagen and hydroxyapatite are either too flexible or too brittle when used by themselves as structural materials, it is only through the multi-scale architecture shown in Figure 1–4a-g, that bone can be both stiff and tough enough to be used as skeletal elements.

Wood, also displays a hierarchical architecture (Figure 1–4h-o). At the length scale of the cell wall, it can be viewed as a fibre reinforced composite consisting of stiff cellulose microfibrils embedded in a soft matrix of hemi-celluloses and lignin (Figure 1–

4h-j). At intermediate length scales, within a growth ring (Figure 1–4k and m) it can be seen as a honeycomb like material and at the scale of the branch it can be viewed as a functionally graded composite (Figure 1–4l, m and o). It is interesting that although the components remain the same, by modifying architectural parameters, such as cellulose microfibril angle, cell size, at these different length scales during growth, mechanical properties can be optimised for changing conditions during a plants life (Burgert et al. 2007). One key architectural parameter, the microfibril angle, and its role on mechanical response of tissues will be described in more detail later in this thesis.

The concept illustrated by these two natural examples of "architectured" or hybrid materials, has been gaining more attention from materials scientists in recent years (see (Ashby and Bréchet 2003, Ashby 2005, Ashby 2011, Bréchet and Embury 2013)). This is motivated by the observation that by controlling the geometric arrangement of constituents in a material at different length scales it is not only possible to simply improve an existing property but it is possible even to gain novel ones not possible in the bulk material. One simple illustration of this, is the "fragmented" design of wire cables that allow for high tensile strength but a high flexibility that doesn't exist in the bulk (Ashby and Bréchet 2003). Due to the environmental and evolutionary constraints mentioned above, Nature has already explored many such architectures providing an interesting range of potential designs for the development of bio-inspired materials. As part of this process it is important not only to understand structure function relationships in such biological materials, it is also fundamental to understand how such structures are formed during the process of growth.

To do this it is important to define several key points illustrated schematically in Figure 1–5. Firstly we need to define what exactly is a "tissue". A simple collection of adherent cells are often considered to be "tissues" (Figure 1–5a), this describes well early stages in embryogenesis, but very soon extracellular matrix can be formed (Figure 1–5b), whose architecture plays an important role in further function. In the case of plants, and some components of animal organs (such as hair, feathers, bone, or nails), it is possible for the remaining extracellular matrix (and intracellular matrix in the case of keratin containing cells), to retain a particular function for the organism even after cell death. This question of how ECM is formed and oriented during growth is a fundamental one, and many research questions still remain open. Secondly it is useful to distinguish between two possible ways in which a tissue can grow, appositional growth or volumetric growth. During appositional growth (Figure 1–5d), the next layer of tissue is added on top of a previous static or non-growing layer. The simplest and perhaps the earliest example of such growth can be seen in the growth of the microbial mats known as stromatolites (Dunlop et al. 1978, Grotzinger and Rothman 1996, Cuerno et al. 2012). More complex examples include the formation of bark on trees (Federl and Prusinkiewicz 2002, Stiven 2013) the layer by layer growth of wood, and at certain length scales even the growth of new unmineralized bone within bone resorption lacunae during bone-remodelling may be viewed as appositional growth (Robling et al. 2006). Appositional growth need not be uniform and interesting feedback mechanisms can lead to branch formation as seen for example in the growth of corals (Merks et al. 2004, Dullo 2005, Kaandorp et al. 2005, Chindapol et al. 2013). The other way growth can occur is through volume changes in the bulk (Figure 1–5e) for examples in tumor growth (Roose et al. 2007, Ambrosi et al. 2012). Such bulk volume changes of course can become transport limited for large volumes when nutrients need to be transported from an external source. Another example of bulk growth would be in the swelling of tissues due to changes in water content (Burgert and Fratzl 2009). One subtle consequence of the nature of growth on modelling or rather on the mathematical description of growth

is that it is important to decide on an appropriate coordinate system (Figure 1–5f). This seems trivial, but there are intrinsic differences in the equations for growth whether one looks at it in a global Cartesian system attached to the laboratory coordinates, or whether one describes growth by the motion of materials points attached to the tissue itself. The second version has advantages in that many equations become simpler, however there is an issue related to bulk growth in that new materials points can appear inside the material. This is a subtle problem still under discussion by mathematical biologists today (Ambrosi et al. 2011, Prusinkiewicz and Runions 2012).

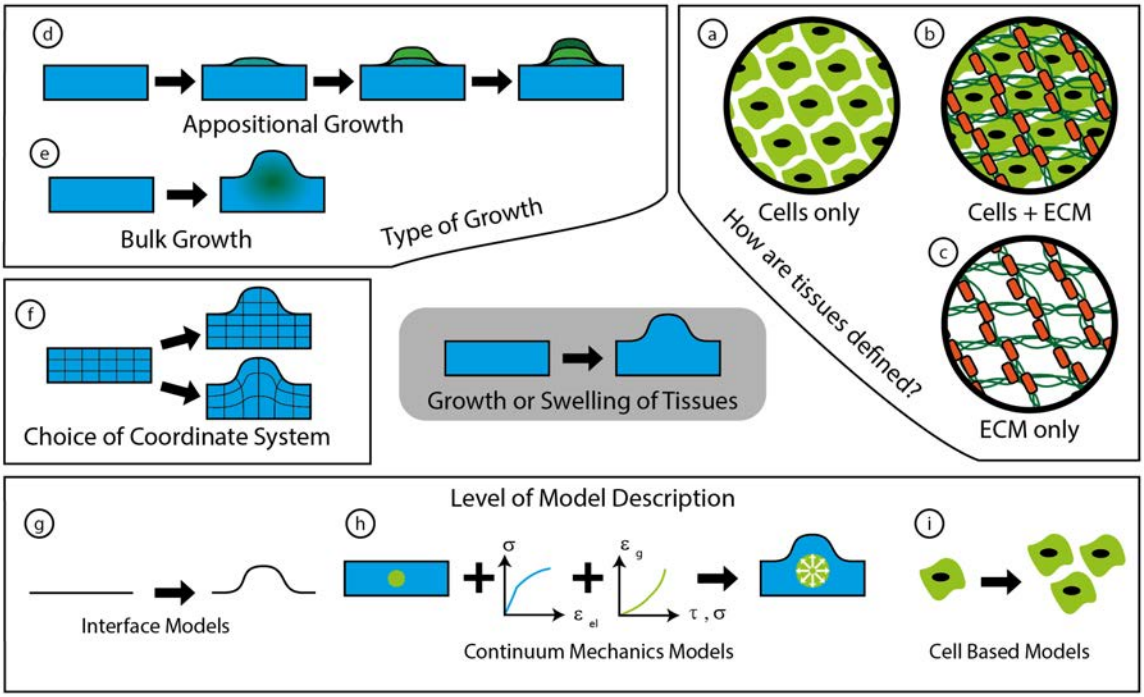

Figure 1–5: Describing shape changes of biological tissues
It is possible to view the growth of biological tissues from a variety of viewpoints. Firstly tissues can be defined in a variety of ways, as collections of cells (a), as a collection of cells surrounded by extracellular matrix (ECM) consisting of biopolymers and/or minerals (b) or as dead tissues (c) in which cells are no-longer living. Growth can occur (d) through apposition of new layers on an inert substrate or (e) via growth due to volume changes in the bulk of the tissue. This has consequences on the choice of coordinate system (f) used to describe growth mathematically with both Eulerian and Lagrangian viewpoints having advantages and disadvantages. The physical description of how tissues grow or swell can also be viewed in different ways, (g) as an interfacial process, (h) at a continuum level or (i) at the level of the single cell.

The final point to think about when dealing with processes of growth and swelling in tissues is at what length scale, or coarseness the processes will be modelled. It is possible for example to simplify the problems of growth and look only at the motion of the interface of a growing tissue (Figure 1–5g). Such an approach is equivalent to models of phase transformations in metal physics such as in crystal growth (Kardar et al. 1986) which has incidentally also been used to describe layer formation in stromatolites (Cuerno et al. 2012). Such descriptions have the advantage of being relatively simple to model, but unfortunately they lose all information about the structure of the bulk. Although these models allow macroscopic shape changes to be described their simplicity makes it very difficult to understand the development of the complex hierarchical structures (Figure 1–4). To get a deeper understanding of growth/swelling, especially the coupling between mechanics and growth, it is necessary to model tissues in more detail. One way is to have suitable constitutive laws describing the 3D stress strain response of tissues coupled with suitable laws of growth (Figure 1–

5h). These then need to be applied together with appropriate boundary conditions and then solved, analytically or using finite element techniques (Ambrosi et al. 2011). A third way to look at tissues, especially when tissues are considered as collections of cells is to develop cell-based or agent based models that describe the local behaviour of each of the cells (Figure 1–5i). Such cell based models, like the Cellular Potts model (Graner and Glazier 1992, Glazier and Graner 1993) have been very successful in describing problems of morphogenesis in a variety of systems see e.g. (Krieg et al. 2008).

Regardless from which point of view or length scale one views shape changes of tissues, one common feature is the importance of geometric constraints. The shapes of surfaces upon which tissues grow, or the spatial arrangement of swellable and non-swellable tissues all play a fundamental role on the macroscopic shape changes of a material or structure, and to understand this role of geometric constraints is the key research aim guiding the work that is described in this habilitation thesis.

This thesis is based on research done over the past years within the Department of Biomaterials, at the Max Planck Institute of Colloids and Interfaces, Potsdam, and most of it was performed while the author led the research group Biomimetic Actuation and Tissue Growth. As suggested by the name of the research group, there are two main research directions that we have been working on. Firstly we have been working on trying to understand growth processes in living systems and especially the role of geometric constrains upon growth (See Chapter-2). Secondly we have also been interested in researching the role of the geometric arrangement of active tissues on actuation or swelling induced shape changes such as those observed in seed structures in plant tissues (See Chapter-3). Despite the differences in focus, with one topic dealing with living and growing tissues through the "creation" of new matter, with the other dealing with volume changes in dead "static" matter, they both can be described using very similar mathematical tools and physical descriptions. Furthermore they both fit within the general framework of understanding the overriding role of geometric boundary conditions on macroscopic shape changes and eventually the internal organisation of tissues.

This thesis is presented as a cumulative thesis and the majority of research results presented have been already published (See Chapter 6.1 for a list of the papers which are reproduced in Section 7). The following two chapters will summarise firstly some of the results of the group on the topics of Tissue Growth (Chapter-2) and then Actuation (Chapter-3). The key outcomes of the groups work will be summarised in the final chapter, together with an outlook describing potential new directions of research arising from this thesis.

2 Tissue Growth

In order to understand how developmental/genetic disorders give rise to physical deformities, how healing of damage in wounds can be accelerated or is hindered, or how to engineer replacement tissues in the lab, it is of course necessary to gain a fundamental understanding of the biochemical and biophysical mechanisms that control the formation of new tissues. The research presented in this chapter uses a variety of experimental and theoretical model systems to learn about the role that physical boundary conditions have on the kinetics of tissue growth and eventually on the resultant structure of the tissues formed. The chapter starts with a short background, illustrating firstly the importance of mechanical signalling for cell and tissue behaviour. This is then followed by a discussion of the role of geometric boundary conditions on tissues and cells at different length scales both in-vitro and in-vivo. It turns out that cell collectives and tissues can display emergent behaviours, allowing them to be described by macroscopic physical parameters such as surface tension or liquid crystal ordering. These two examples will be followed with an overview of some selected research highlights coming from the group, described in full detail inside the publications attached at the end of this thesis (See Section 7).

2.1 Background

Cells not only have a sense of "smell/taste", in that they can monitor and respond to their biochemical environments, they are also able to "touch" and can sense physical features of their surroundings (Figure 2–1) see e.g. (Discher et al. 2005, Kollmannsberger et al. 2011). Cells can sense the mechanical properties of the substrate they are in contact with as well as the surface topology, and respond with modified cell behaviour in terms of differentiation, proliferation and the production of extracellular matrix.

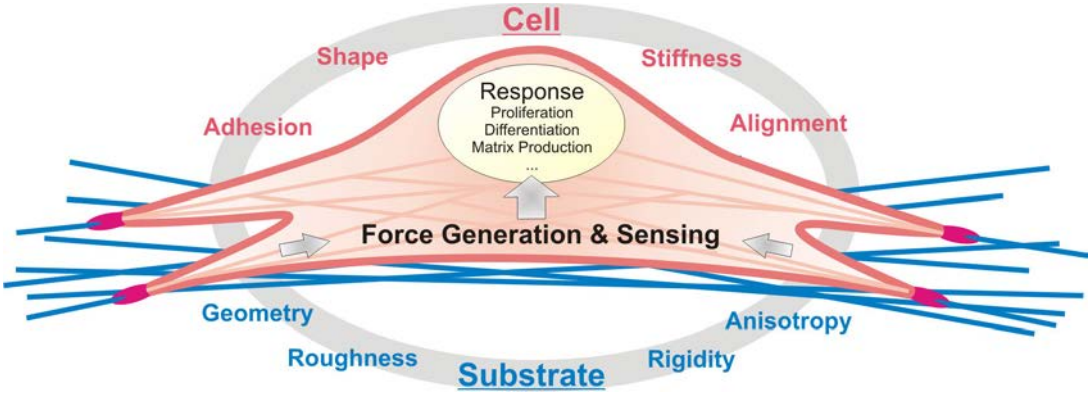

Figure 2–1: Physical interactions between a cell and its environment
Cells attached to a substrate respond to its physical properties via the generation of forces applied by the cytoskeleton to the focal adhesions. These mechanical signals give rise to responses in cell behaviour for example with changes in proliferation, differentiation and extracellular matrix production. From (Kollmannsberger et al. 2011).

Perhaps the most prominent example of such physical sensing is the ability of cells to sense the elastic properties of their substrates, see (Discher et al. 2005) for a review. Using polyacrylamide gels with different cross-linking densities, coated with type I collagen, Pelham and Wang (1997) produced substrates with similar chemical properties but varying stiffness. Epithelial and fibroblast cells cultured on these substrates showed a decreased ability to spread, coupled with an increased motility with increasing substrate stiffness. The same types of substrates were used by Engler et

al. (2006) who demonstrated that the fate of mesenchymal stem cells was modified with stiffness. On stiffer substrates cells tended to differentiate and express bone-like markers, but on softer substrates cells expressed markers indicating differentiation along the neuronal direction. The fact that cells can sense the mechanical properties of their environment arises because they can actively contract via actin-myosin complexes, thus applying forces on their surroundings.

In addition to being able to apply forces, cells can sense externally applied forces, as is illustrated by the process of bone remodelling (Robling et al. 2006). This process firstly allows for old damaged bone to be replaced by new defect free bone (Taylor et al. 2007), and also has the consequence that the structure of bone can adapt to changing external loads (Eriksen 1986, Currey 2002, Robling et al. 2006). Bone remodelling is mediated through the action of three cell-types; osteoclasts, which remove bone, osteoblasts that produce new un-mineralised bone, and osteocytes, which are former osteoblasts that become embedded inside the new bone matrix. The osteocytes are thought to act as mechanosensors (Bonewald and Johnson 2008), signalling osteoclasts and then osteoblasts to start removing or adding bone upon mechanical stimulation. The complex interplay between the cell-responses results in bone being produced where it is mechanically needed and removed where it is not see e.g. (Frost 1987). A striking example of the consequences of this can be seen in the asymmetry found in the bones of greyhounds arising from the different loading experiences as the dogs race and train in only one direction around the racing track (Johnson et al. 2000). Other examples include bone loss after extended bed rest (Thomsen et al. 2005) or after space flight (Carmeliet et al. 2001).

One of the consequences of the ability of cells to physically sense and probe their mechanical environment is that external boundary conditions become important, even if the physical boundaries are relatively speaking a long way from the cell. This means that the shape of the physical environment surrounding cells and tissues may have a strong influence on how mechanical signals are produced, transmitted and sensed. Indeed such observations have been made *in-vitro* on single cell and tissues (Figure 2–2) as well as *in-vivo* (Figure 2–3), hinting that the geometry of the environment around cells is an important factor. The role of the surrounding geometry on collective cell behaviour within tissues, is an important focus of the research group and will be outlined in section (2.2) and in the relevant publications from the group (Section 7).

Indeed much work has been done in the last years on the role of geometric features on cell and tissue behaviour. For two recent reviews see for example (Zadpoor 2015) which focuses on macro scale features and (Dalby et al. 2014) which focuses on the response of cells to nano-scale features. Due to the ease of visualisation, and the possibilities opened by soft lithography or micro-contact printing (Xia and Whitesides 1998, Alom Ruiz and Chen 2007) most work has been done on flat surfaces. Some examples from the literature that explore the role of 2D geometric features at different length scales on cell and tissue behaviour are illustrated in the top part of Figure 2–2. Cells have been shown to respond to geometric features at the nanoscale (Figure 2–2a), as illustrated using gold nano-dot arrays functionalised with integrin receptors (Selhuber-Unkel et al. 2010). Cell adhesion strength was shown for example to depend strongly on the receptor spacing at length scales in the order of 50-90nm. Numerous other studies show other size dependent cell responses at these length scales, one example being the observation that the spacing of nanotubes can control stem-cell differentiation (Oh et al. 2009). See also (Dalby et al. 2014) for a more detailed review. At length scales comparable to the size of a single cell, significant geometric effects have also been observed, mainly through the use of patterned adhesive fibronectin patches

(Alom Ruiz and Chen 2007). The shape of these patches has been shown to have a strong influence on the internal environment of the adhered cell, with both the arrangement of actin stress fibres (Figure 2–2b), and the resultant forces exerted by the cells being influenced by the geometric boundary conditions (Théry et al. 2006, Théry et al. 2006). The probability of cell death or apoptosis has also even been shown to depend on the size of these adhesive patches (Chen et al. 1997) (Figure 2–2c). Staying in 2D, but at length scales much larger than the size of a single cell, similar studies using adhesive patches with different shapes show that collections of many cells will also respond to geometric features in 2D (Figure 2–2d and e). When such patches are covered with a confluent layer of cells, cell-contractility leads to variations in the local stress states as a function of location on the patch. Such stress variations lead to differences in differentiation illustrated in (Figure 2–2d) with adipocytic differentiation being localised in concave regions of the patches (in red) (Ruiz and Chen 2008). Similar work has also demonstrated that high cell proliferation correlates with locally high stresses found on the external boundary of these patches (Nelson et al. 2005).

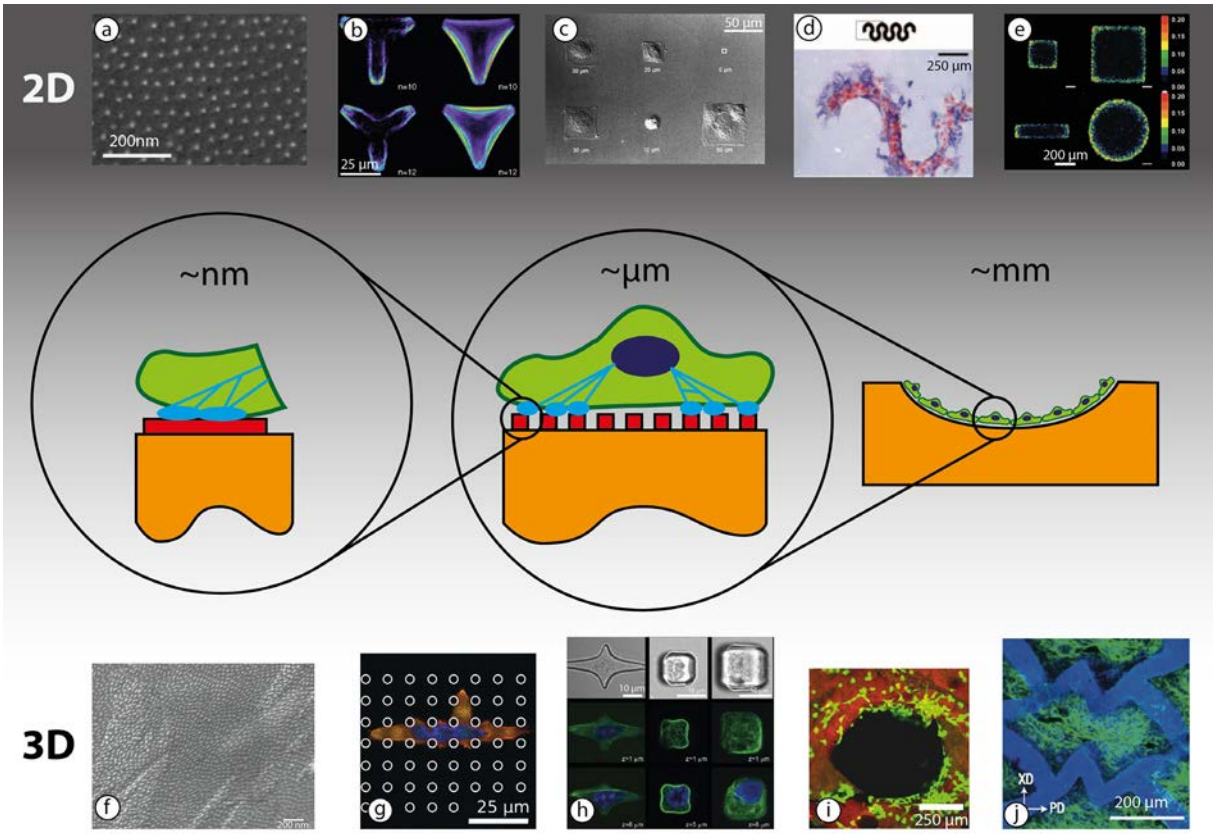

Figure 2–2: Cells interact and respond to geometric features in 2D and 3D over many length scales
The central cartoon illustrates how cells respond to topologies at different length scales ranging from the nanometre up to the millimetre scale in 2D (a-e) and 3D (f-j). On flat 2D surfaces single cells respond to a) the spacing of gold nano-dots (Selhuber-Unkel et al. 2010), b) the shapes of adherent fibronectin patches (Théry et al. 2006), and c) the size of fibronectin patches (Chen et al. 1997). The interaction of cells with 2D shapes also extends to collections of multiple cells which gives rise to d) spatially dependent differentiation (Ruiz and Chen 2008), and e) spatially dependent cell proliferation (Nelson et al. 2005). Attempts have been made to study such behaviour in 3D, for example by presenting nano-structures on curved surfaces f) (Sjostrom et al. 2013) , or g) the interaction of cells with micron sized posts (Hohmann and von Freymann 2014) and h) with holes of different 3D shapes (Ochsner et al. 2007). At the multicellular level controlled geometries have been investigated for example on 3D printed zero mean curvature surfaces i) (Rajagopalan and Robb 2006) or in complex deformable honeycomb structures to mimic the function of heart tissue j) (Engelmayr et al. 2008).

The ability to control shapes and geometry in 3D is perhaps less well studied than the work done in 2D, most likely due to the technical difficulties in visualising and following cell behaviour in 3D. This being said a variety of studies have been done looking at the role of geometric features on cells and tissues at multiple length scales in 3D as illustrated in the bottom half of Figure 2–2. Much effort is being focussed on creating controlled nano-structures on curved substrates (Figure 2–2f) with the goal of improved osteoinduction especially on titanium substrates (Sjostrom et al. 2013). At length scales comparable to a single cell, micropost arrays (Hohmann and von Freymann 2014) and 3D shaped holes (Ochsner et al. 2007) have been used for example to investigate cell behaviour with the aim of getting a better idea of how cells interact with a 3D environment that at least approaches structures found in *in-vivo* (Figure 2–2g and h). Recent advances in additive manufacturing or 3D printing technologies (Melchels et al. 2012) means that it is now possible in principle to design and print almost arbitrary structures in 3D however with length scales much larger than the single cell (Zadpoor 2015). Although this has been extensively studied, the focus of most studies is more on the potential applications in tissue engineering rather than on the detailed biophysics controlling the behaviour of cells. One example is the use of 3D printing to produce zero mean curvature surfaces (Figure 2–2i) for tissue engineering purposes as they mimic geometries seen in trabecular bone (see Figure 2–3 g and h), although interestingly they observed no significant tissue growth on these surfaces (Rajagopalan and Robb 2006). Other studies using less rigid materials, use geometric features to create a mechanically anisotropic environment for contractile cardiomyocytes, with the goal of providing functional scaffolds for heart regeneration (Figure 2–2j) (Engelmayr et al. 2008).

The previous discussion has focussed entirely on *in-vitro* studies on the role of geometric constraints on cell and tissue behaviour, but what happens in the living organism? Despite the difficulties in performing clean and controlled *in-vivo* experiments, an influence of geometric features on tissue behaviour can be found in a variety of examples as illustrated in Figure 2–3. All examples are taken from the field of bone regeneration which lends itself well to such studies, mainly due to the high stiffness of bone with respect to other tissues giving rise to a relatively stable geometric features. Early examples investigated the healing of circular defects drilled into the cortex of rabbit femurs (Figure 2–3a), and showed a strong correlation between the internal microstructure (i.e. collagen alignment) with the orientation of the walls of the hole (Shapiro 1988). More recent work on bone fracture healing shows that also here, tissue organisation is strongly correlated with geometry. When no geometric signals are present (at the start of healing) very porous disorganised bone is formed and it is only after this endogenous scaffold is formed that organised aligned bone will be produced (Kerschnitzki et al. 2011) (Figure 2–3b and c). Similar observations have also been observed during the growth of another somewhat exotic bone type, the antler of deer (Figure 2–3d) where organised bone is only formed after a fast porous scaffold is deposited (Krauss et al. 2011). In addition to just looking at the internal arrangement of tissues as a function of geometry, the amount of tissue growth has been shown to depend on the local curvature as illustrated in (Figure 2–3e and f) by the differences in the amount of tissue (brown) formed on the implants (black) with different shapes (van Eeden and Ripamonti 1994, Ripamonti et al. 2012). A final point coming from the field of bone is the observation that trabecular bone (Figure 2–3e and f) has close to a zero mean surface curvature indicating a strong control by cells of the surface geometry of bone (Jinnai et al. 2001, Jinnai et al. 2002). Despite the obvious interest in understanding the role of 3D geometries on tissue behaviour and structure much remains to be understood, especially in the context of evaluating and predicting cell responses to

surfaces with highly controlled 3D geometries, and especially to understand how cells can collectively sense geometries much larger than the size of the single cell.

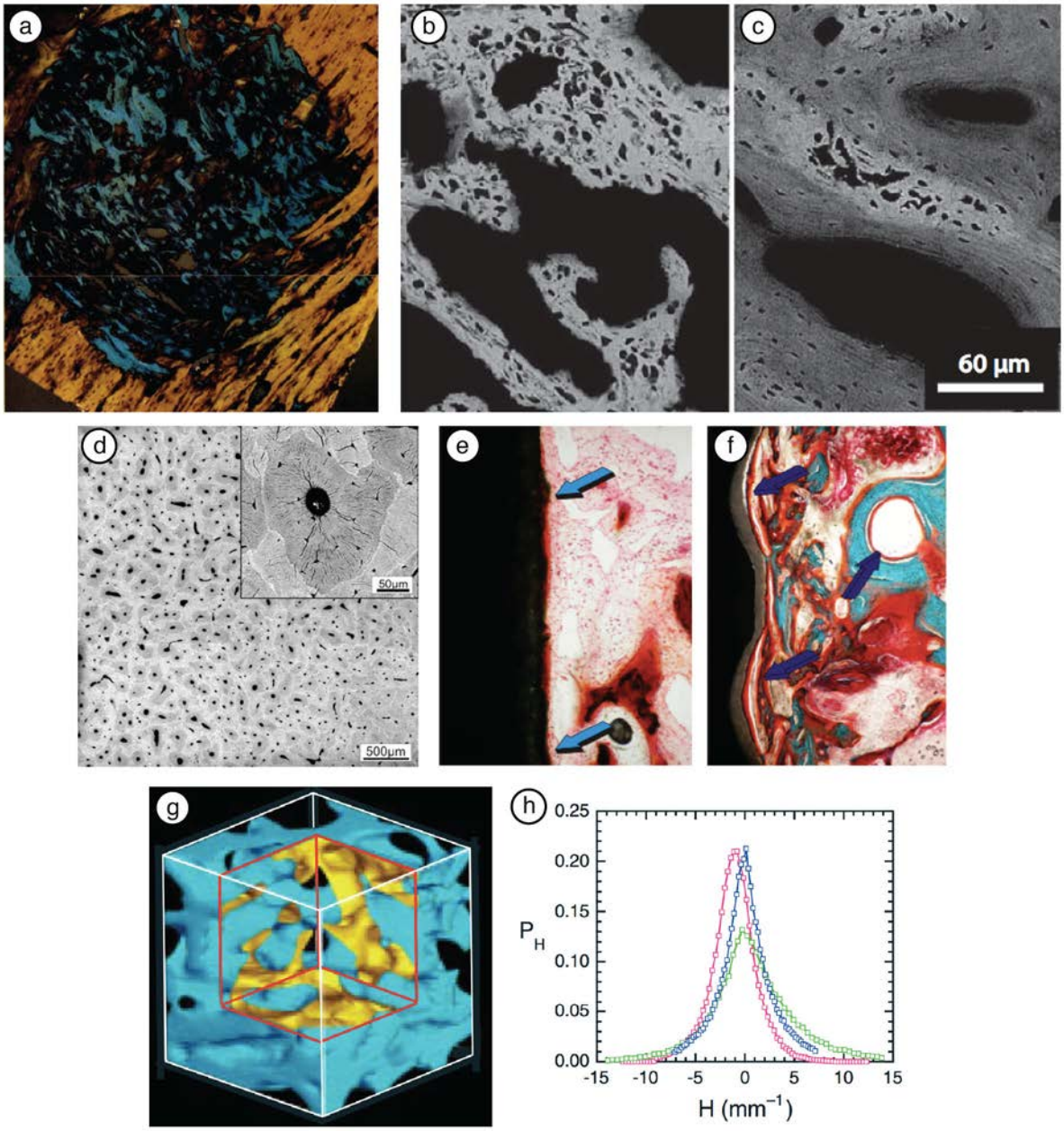

Figure 2–3: The geometry of substrates play an important role on *in-vivo* tissue behaviour
a) Polarised light microscopy image of disordered bone (blue) formed after 8 weeks healing in a 2.4mm defect drilled into the more aligned cortex (orange) of a rabbit femur (Shapiro 1988). b) Back scattered electron image of fast forming disordered bone (2 weeks after osteotomy) that is first formed in the fracture gap of the sheep femur (Kerschnitzki et al. 2011) c) This substrate then appears to act as a "scaffold" for further ordered tissue growth, here shown in a similar region 9 weeks after osteotomy (Kerschnitzki et al. 2011). d) Back scattered electron image of a cross section of mature antler showing darker regions of younger ordered bone being formed inside the tubular network of fast growing disordered bone (Krauss et al. 2011). Substrate geometry also influences bone growth (brown) seen in the 800 µm deep cavities (f) compared to none on smooth surfaces (e) on titanium implants implanted in the tibia of Chacma Baboons (Ripamonti et al. 2012). Analysis of the 3D tomographic images of trabecular bone, g) shows narrow mean curvature distributions, h) localised at zero mean curvature highlighting the ability of cells to also control geometric features of bone (Jinnai et al. 2002).

Although the mechanisms controlling the ability of tissues to sense large scale geometric features is not fully clear, the following example gives an illustration of one mechanism by which local interactions between many cells can give rise to a collective

response that can be described by simple physical laws. The fact that cells are motile, can be adherent to each other and also contract implies that cell collectives can display liquid like properties such as displaying an effective surface tension (Lecuit and Lenne 2007). The origins of tissue surface tension can be understood by comparing the molecular origins of surface tension in a liquid (Figure 2–4a) with that of a tissue (Figure 2–4b). Molecules (or cells) within the bulk of the fluid will experience maximal cohesive forces from the surrounding molecules. Compared to the bulk, those on the surface experience a net inward force giving rise to an energetic cost of producing extra surface area, appearing as a surface tension. Such surface tissue tensions are in fact measurable, as demonstrated by Foty and co-workers (Foty et al. 1994, Foty et al. 1996). Another consequence of the ability cells to adhere to each other and contract, is seen in the spontaneous phase separations observed in mixtures of two cell-types with differences in the amounts of the molecule N-Cadherin responsible for cell-cell adhesion (Figure 2–4c and d) (Foty et al. 1996, Foty and Steinberg 2005). The green-stained cells with the higher expression of N-Cadherin, cluster preferentially in the centre of the spheroid, expelling the red-stained cells to the exterior. Another similar observation can be made, when different cell types are mixed, with cells of the highest surface tension clustering in the inside of the spheroids (Foty et al. 1996) (Figure 2–4e). This view of tissues as liquids is of course simplistic and doesn't take into account the complex effects of the contractile cytoskeleton of cells, and the extracellular matrix, however has proved to be useful to describe some phenomena in living tissues. For more details on the discussion of surface tension on cell-sorting and morphogenesis see e.g. (Foty and Steinberg 2005, Steinberg 2007, Manning et al. 2010).

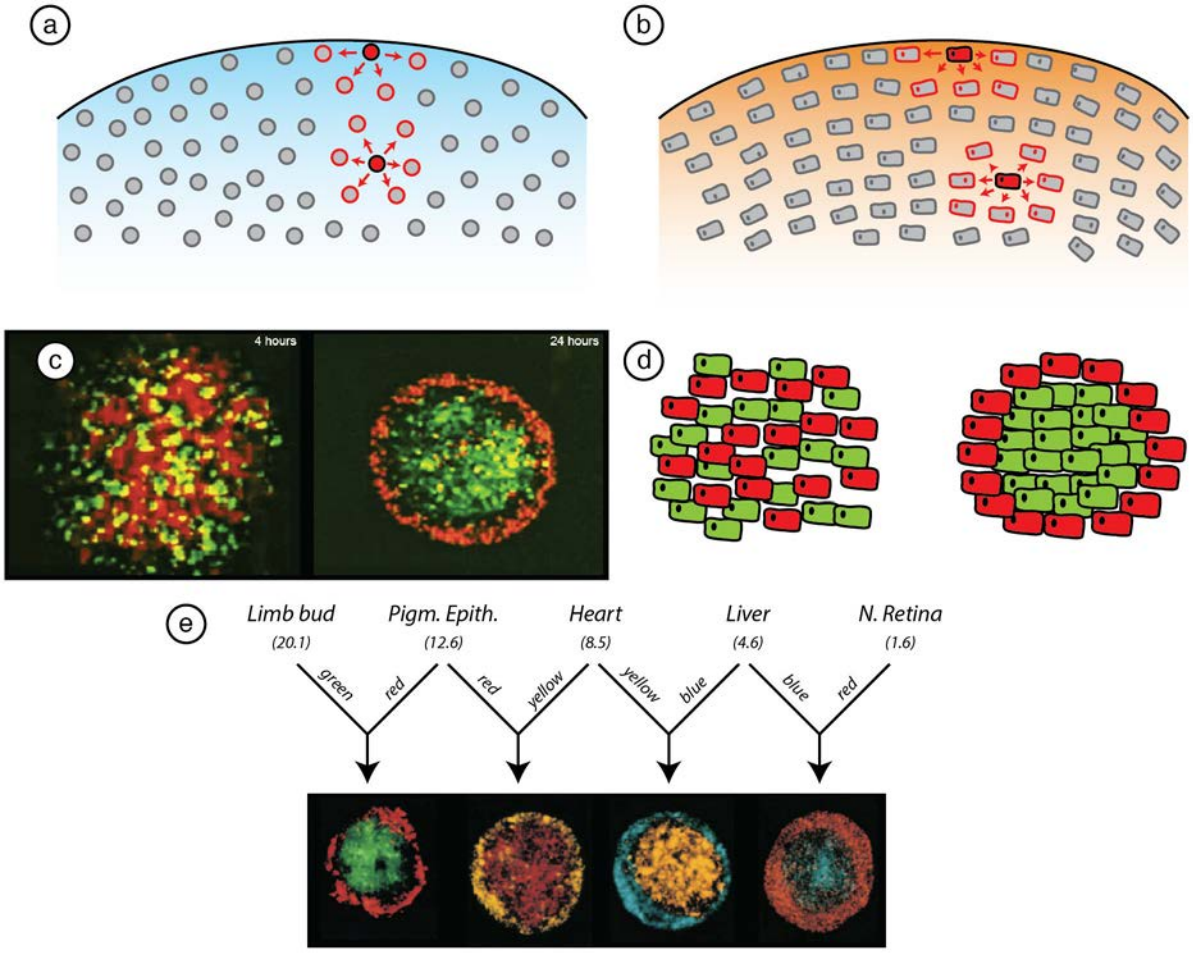

Figure 2–4: The collective interactions of cells leads to fluid like behaviour of tissues
A comparison of the "atomistic" model for the development of surface tension for a molecular fluid a) and a cell based fluid b) after (Lecuit and Lenne 2007). c) Phase separation seen in L-clones with differencing amounts of the molecule N-Cadherin vital for cell-adhesion (Foty and Steinberg 2005) d) Sketch of the phase separation seen in c) after (Lecuit and Lenne 2007). e) The final results of a series of different cell-sorting experiments using different cells with different surface tensions (Surface tension in dyne/cm in brackets). Image from (Foty et al. 1996)

As highlighted in the introduction (see Figure 1–4), the wide range of functionality achieved in biological materials stems from the way in which the component materials are combined together in complex ways (Weiner and Wagner 1998, Fratzl and Weinkamer 2007). The question arises how is this tissue architecture controlled during growth over such large length scales? One elegant model arising from the pioneering work by Bouligand (Bouligand 1972, Bouligand 2008), and Giraud-Guille (Giraud Guille 2001) stems from the observation that many tissues display structures that are reminiscent of cholesteric liquid crystal phases (Figure 2–5a-c) (see also (Neville 1993)). Banding patterns found for example in wood, bone or arthropod match cholesteric phases found in other materials. Furthermore when the fibrous bio-polymers of collagen or cellulose are properly treated *in-vitro* they can also spontaneously form such long range complex structures (Reis et al. 1991, Giraud Guille et al. 2003) (Figure 2–5d and e). Although liquid-crystal like ordering can explain some of the long-range organisation of the extracellular matrix components, the precise arrangement certainly requires some active control by cells. Much work is still needed to understand the mechanisms controlling this, although the fact that fibroblasts for example can use their contractile machinery to organise collagen (Harris et al. 1981) hints towards the important role of mechanics, and implicitly the role of the external boundary conditions on tissue organisation.

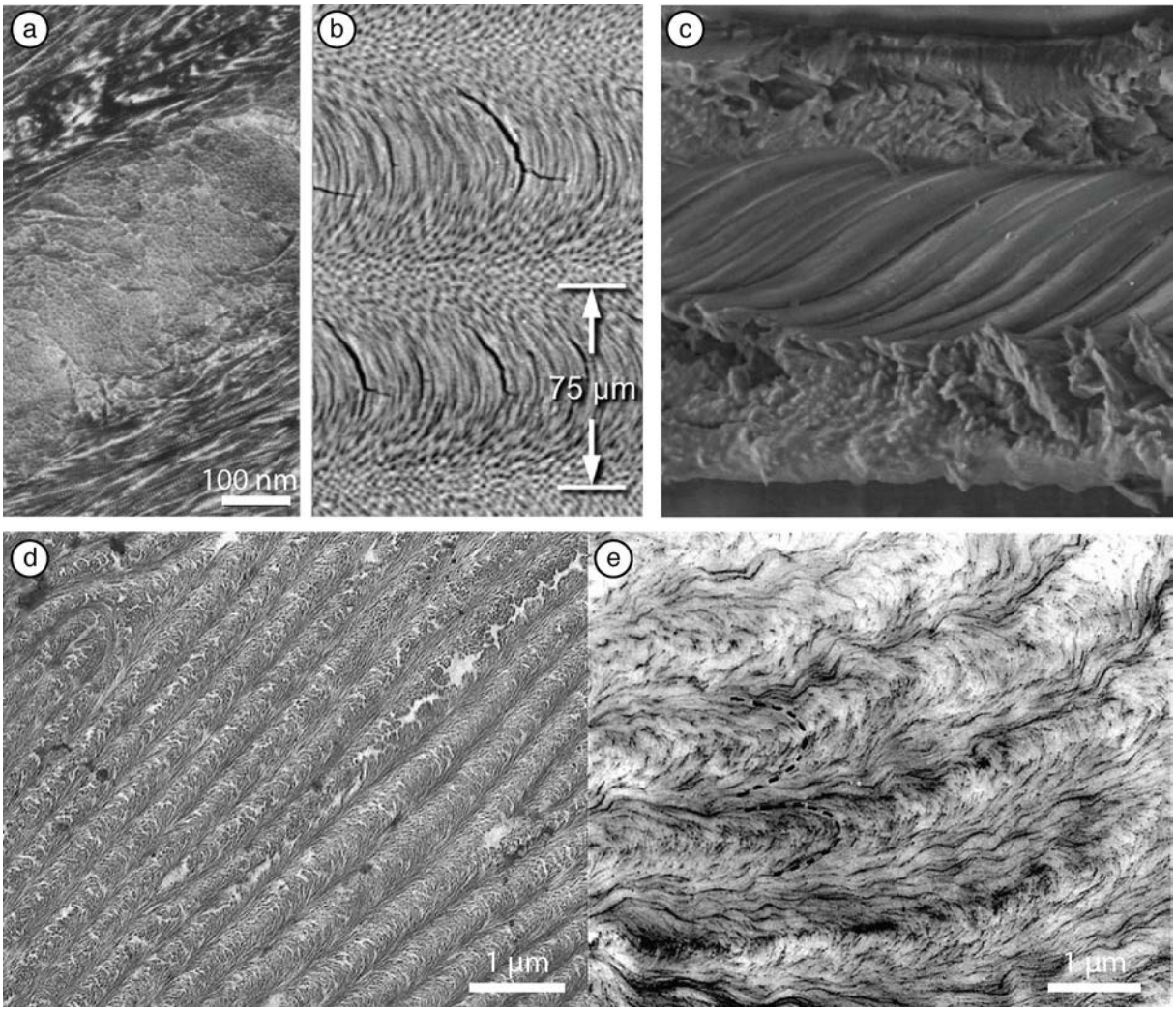

Figure 2–5: Liquid-crystal-like order in biological tissues and synthetic counterparts
Examples of liquid-crystal like ordering by; a) collagen in bone (Giraud Guille et al. 2003), b) the chitin in stomatopod cuticle (Weaver et al. 2012), and c) cellulose in the cell-wall of compression wood in spruce (lumen ~10µm wide) (image courtesy of Michaela Eder). In-vitro experiments show similar structures spontaneously forming in d) solutions of fibrillar collagen (Giraud Guille et al. 2008) and cellulose (Reis et al. 1991).

This brief introductory section has given a brief overview into some important concepts necessary to understand the research presented in the following section. From this short discussion, it is clear that mechanical forces play an important role controlling a variety of processes in cells and tissue behaviour. As mechanical perturbations propagate at the speed of sound and over long distances, an understanding of mechanical signalling is fundamental to understand self-organising behaviour seen in tissues at length scales much larger than the size of cells themselves. As a consequence of these long range interactions, the shape of the external environment plays a fundamental role in tissue growth, something that will explored in more detail in the following.

2.2 Results and Discussion

The key results of the author's publications related to tissue growth are reproduced and discussed in the following section. A detailed publication list is given in Section 6.1, and each publication is indicated by its number, i.e. **[TG1]** or **[TG2]** and reproduced in Section 7.

It is clear that both single cells and tissues (cells and extracellular matrices) react to geometric features both in 2D and 3D (see Figure 2–2 and Figure 2–3), however till recently it was difficult to quantify and predict this behaviour. One of the major limitations of previous studies was the difficulty to produce 3D surfaces with controlled surface topologies. An initial advance was made through the development of rapid prototyping or 3D printing technology (Woesz et al. 2005, Zadpoor 2015) which could produce scaffolds with defined pore sizes and shapes in the range of hundreds of microns. Previous studies in the department perfected the technique and its application for producing hydroxyapatite scaffolds consisting of a regular lattice of large interconnected pores (Woesz et al. 2005, Rumpler et al. 2007). Despite demonstrating that tissue produced by pre-osteoblast cells could grow in-vitro inside these scaffolds it is difficult to follow the growth of tissue inside such complex structures. This led to the simplification used in (Rumpler et al. 2008) in which tissue growth inside individual pores was investigated. This paper was the first on Tissue Growth in which the author of this thesis made a contribution, specifically in the theoretical interpretation of the experimental results, and inspired the later work discussed in this section.

Observations of the role of pore-shape on the kinetics of tissue growth [TG1]

By observing tissue growth inside large well-defined pores with dimensions of several cubic millimetres, it was possible to quantify the role of pore geometry (shape and size) on the kinetics of tissue growth for the first time (Rumpler et al. 2008). These experiments are illustrated in Figure 2–6a which show phase contrast microscopy images as a function of cell-culture time of two pores in hydroxyapatite plates with circular (top) and square (bottom) cross-sections. MC3T3-E1 cells (known to produce collagen (Choi et al. 1996, Rumpler et al. 2007)), are seeded onto the scaffolds and images in transmission were taken at regular intervals during growth. Such images show that with time tissue (brown) forms on the HA scaffold (black) leading to curved, circular layers that get more and more circular with time. Tissue forms more readily in the corners than the flat surfaces of the square pores, but is uniformly distributed over the surface of circular pores. It can be seen that the amount of tissue measured from these images in the pores increases steadily with time, even though these 2D images are only a proxy for the total 3D tissue formed (NB: pores are 3mm deep). Such images can be quantified as seen in Figure 2–6b which shows the projected tissue area (the area of brown tissue in Figure 2–6a) as a function of time for a set of different pores with different sizes (blue, green and red symbols) and shapes. The shape of the symbols (triangular, square, hexagonal, and circular) corresponds to the 2D shape of the pore cross section. Pore size is given by the perimeter of the pore cross section meaning that each pore in the same size-class has the same available surface area for cells to colonise. For a given pore size (i.e. a given colour in the graph), the growth curves are linear, and there is no effect of the pore shape on the growth rate. Pore size seems to delay the onset of growth, although the rates, after the initial phase of growth are also the same. This is better illustrated in Figure 2–6d in which the data from in Figure 2–6b is shifted by subtracting a constant value of t_0 from the data for each size class. Once this is done the data all falls on one master curve.

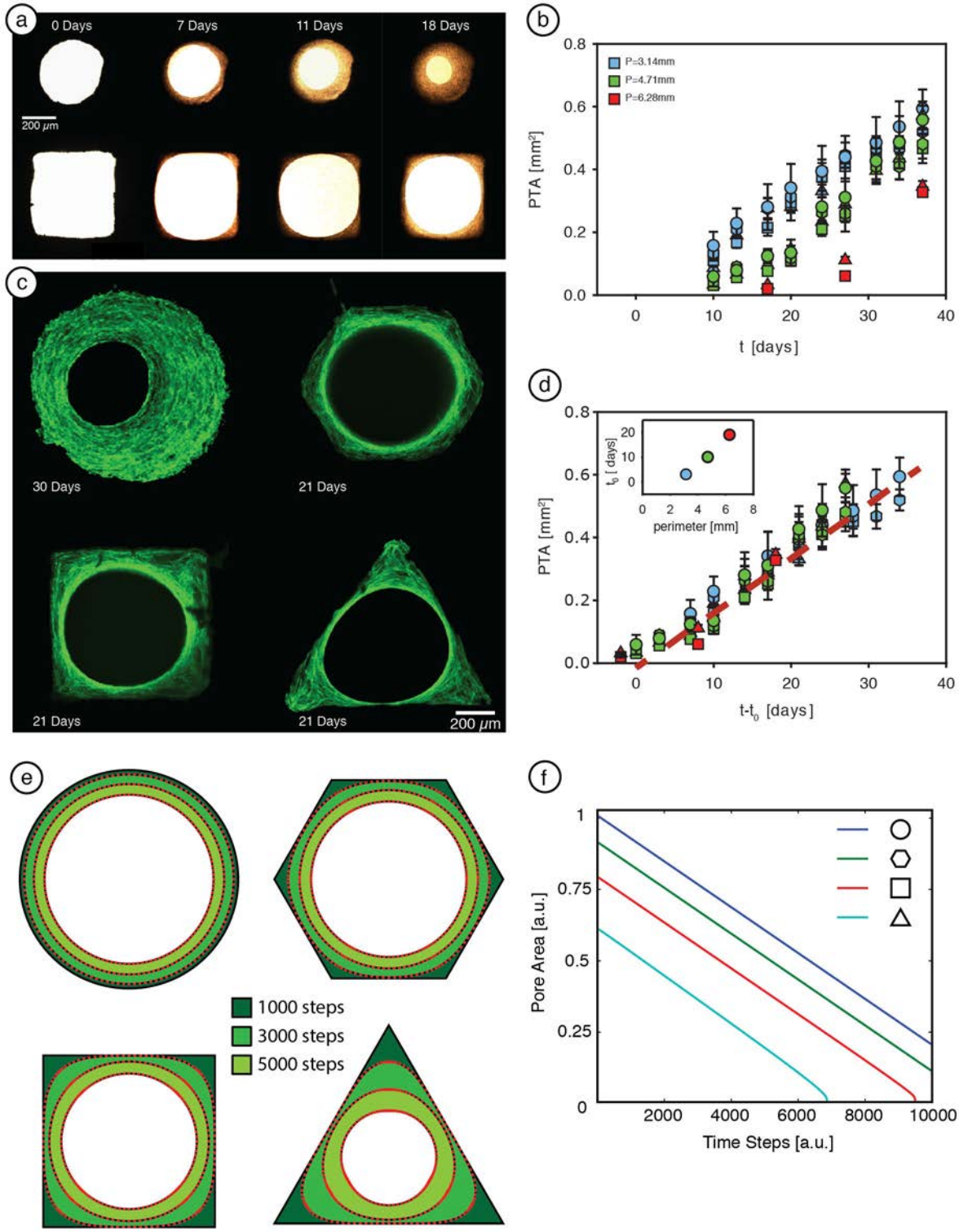

Figure 2–6: Experiments and simulations of tissue growth in convex pores

a) Phase contrast microscopy images of 2 pores within hydroxyapatite (HA) scaffolds, during MC3T3-E1 cell-culture experiments. Tissue appears brown, scaffold is black, and medium appears white (Images produced by C. Bidan). b) Projected tissue area as a function of culture time for four different pore cross-sections (circular, hexagonal, square and triangular) and 3 different pore perimeters (3.14, 4.71 and 6.28mm). Error bars indicated standard error (n=10). (Data from (Rumpler et al. 2008)). c) Laser scanning confocal microscopy images of four different HA pores containing tissue produced by MC3T3-E1 cells in which actin has been stained (green) with phalloidin-FITC. The image of the circular pore contains tissue grown for 30days the other pores show images after 21days of culture. d) The data from b) is re-plotted as a function of culture time minus lag time t_0, which is the time taken for linear growth to start. The red dotted line indicates the linear growth of tissues on hydroxyapatite scaffolds in convex shaped pores. e) Predicted tissue geometries according to the curvature driven growth model (Rumpler et al. 2008) at 3 different time points. Each shape has the same starting perimeter. f) Calculated remaining pore area (white) as a function of time for the simulations shown in e).

The increasing value of t_0 with increasing pore surface area, can be interpreted as the increasing time taken to colonise (through migration and proliferation) a larger area. This highlights that at least in the pores analysed the kinetics of tissue growth was independent of both the pore size and shape. Although the macroscopic rate of tissue growth is independent of pore geometry a closer look at the spatial distribution of tissue shows something else (Figure 2–6c). In these confocal stacks it appears that more tissue is formed in the corner of the pores than on the flat surfaces. Furthermore it seems like the amount of tissue formed is related to the angle (or curvature) of the corners with more tissue formed in the corners of the triangle vs the square vs the hexagon. This indicates that the local surface curvature controls the rate of growth.

2D modelling of the role of curvature on the kinetics of tissue growth [TG1]

To test the role of pore curvature on tissue growth we developed a simple 2D geometric model for curvature controlled growth. In this model the interface between tissue and medium is taken to move normal to the tissue surface at a rate proportional to the local curvature:

$$\frac{d\mathbf{r}}{dt} = -\lambda\kappa\mathbf{n} \qquad \text{Eq. 2.1}$$

where κ is the local 2D curvature, t is time, $\mathbf{n}$ is the normal vector to the tissue interface at position $\mathbf{r}$ and λ is a rate constant. The qualitative results of this model, that is the predicted shapes of the tissue-medium interfaces in the four different pores (Figure 2–6e), agree surprisingly well with the experimental tissue morphologies (Figure 2–6c). Furthermore the calculated projected tissue area as a function of simulation time shows no difference in the growth rates between the different pore shapes (Figure 2–6f) even though each of the pores start with different areas, which also is in agreement with the experimental observations. This linear macroscopic growth rate can be readily understood in terms of a microscopic curvature dependent growth rate by the following argument. Consider a circular pore, of radius r_0 with a tissue-medium interface located at radius, r. If the area of tissue, A, (equivalent to the projected tissue area) is given by:

$$A = \pi r_0^2 - \pi r^2, \qquad \text{Eq. 2.2}$$

then the rate of change of total tissue area is:

$$\frac{dA}{dt} = -2\pi r\frac{dr}{dt} \qquad \text{Eq. 2.3}$$

Combining (Eq. 2.3) with (Eq. 2.1) and introducing the surface curvature $\kappa = 1/r$, the macroscopic growth rate now becomes:

$$\frac{dA}{dt} = 2\pi\lambda, \qquad \text{Eq. 2.4}$$

which is linear in time and also independent of the starting pore size. A similar analysis can be made for polygons with rounded corners taking the limit as the radius of curvature at the corners tends to zero.

The next question about why the growth rate is independent of shape, at least for the pore cross sections chosen, can be understood through the work of the German mathematician Fenchel (Fenchel 1928). He demonstrated that for convex shapes in the plane, the curvature averaged over the length of the perimeter, P, is simply equal to

$\langle \kappa \rangle_P = \frac{2\pi}{P}$, (Fenchel 1928). If the local growth behaviour of a tissue can indeed be described by curvature driven growth, then the growth rate averaged over the perimeter will be simply proportional through (Eq. 2.1) to the average curvature over the perimeter. As all pore cross sections in this study had convex shapes and were chosen (within a given size class) to have the same perimeter it is clear that the growth rate would then be the same. Despite the simplicity of the model of curvature driven growth, being 2D and describing only geometric changes and nothing about the mechanisms responsible for growth, it is still remarkably successful in describing the experimental results both locally and macroscopically.

The role of substrate stiffness or chemistry on 3D tissue growth [TG2]

Arising from Figure 2–6d is the observation that regardless of the starting size and shape (at least for convex pores), the rate of growth is independent of geometric factors after the first period of growth has occurred (i.e. after the lag time t_0). Motivated by the observation that cells behave differently on surfaces with different stiffnesses (e.g. (Engler et al. 2006)), we performed a similar set of 3D tissue growth experiments to those shown in Figure 2–6d, however with transparent polyurethane scaffolds with differing stiffnesses rather than hydroxyapatite. In addition to varying the stiffness (and substrate material) we also tested the role of seeding on the kinetics of growth (Figure 2–7a). After the initial phase of growth, the growth rate was the same as that found for hydroxyapatite scaffolds (red-dashed line in Figure 2–7a), meaning that the material properties of the scaffold, at least in this stiffness range, do not affect the rate of growth once the first layer of tissue has formed. This being said, seeding methods and material properties play a strong role in the value of the lag time, t_0 (Figure 2–7b). One potential reason for the differences in lag-time could be related to the differences in the ability for cells to adhere and migrate along a surface. This idea was tested using the Cellular Potts model (Graner and Glazier 1992, Glazier and Graner 1993) as implemented in the computational framework CompuCell3D (Swat et al. 2012). The model has been tested extensively by other groups (See e.g. (Krieg et al. 2008, Marmottant et al. 2009)) and provides a useful tool to discuss the experimental results shown in Figure 2–7a and b. This work was performed in my group by Philip Kollmannsberger and the results are awaiting publication. The model essentially refers to a large number q Potts model on a discrete lattice in 2D, where sites with identical spins belong to the same cell (or region, i.e. medium or substrate). The substrate is constrained such that it cannot change, acting as a fixed geometric boundary on which cells can move and proliferate. The Hamiltonian function with the following form is used:

$$H = \sum_{\text{interfaces}} J_{ij} P_{ij} + \sum_{\text{cells}} \lambda_A \left(A_i - A_{0i} \right)^2 . \qquad \text{Eq. 2.5}$$

Here, the first term gives the sum of the energy over all the interfaces P_{ij}, between regions i and j, related to cell-cell adhesion and cell-substrate adhesion and cortical tension (the cell-medium interface), where J_{ij} is the energy per interface (Figure 2–7e). The second term gives the elastic energy of a cell due to a deviation in the actual cell area A_i to some target area A_{0i}, where λ_A is somewhat akin to a bulk modulus. Cell proliferation is driven by tension such that a given cell will divide when above a certain threshold. The dynamics of the system is modelled using the Metropolis Monte-Carlo algorithm.

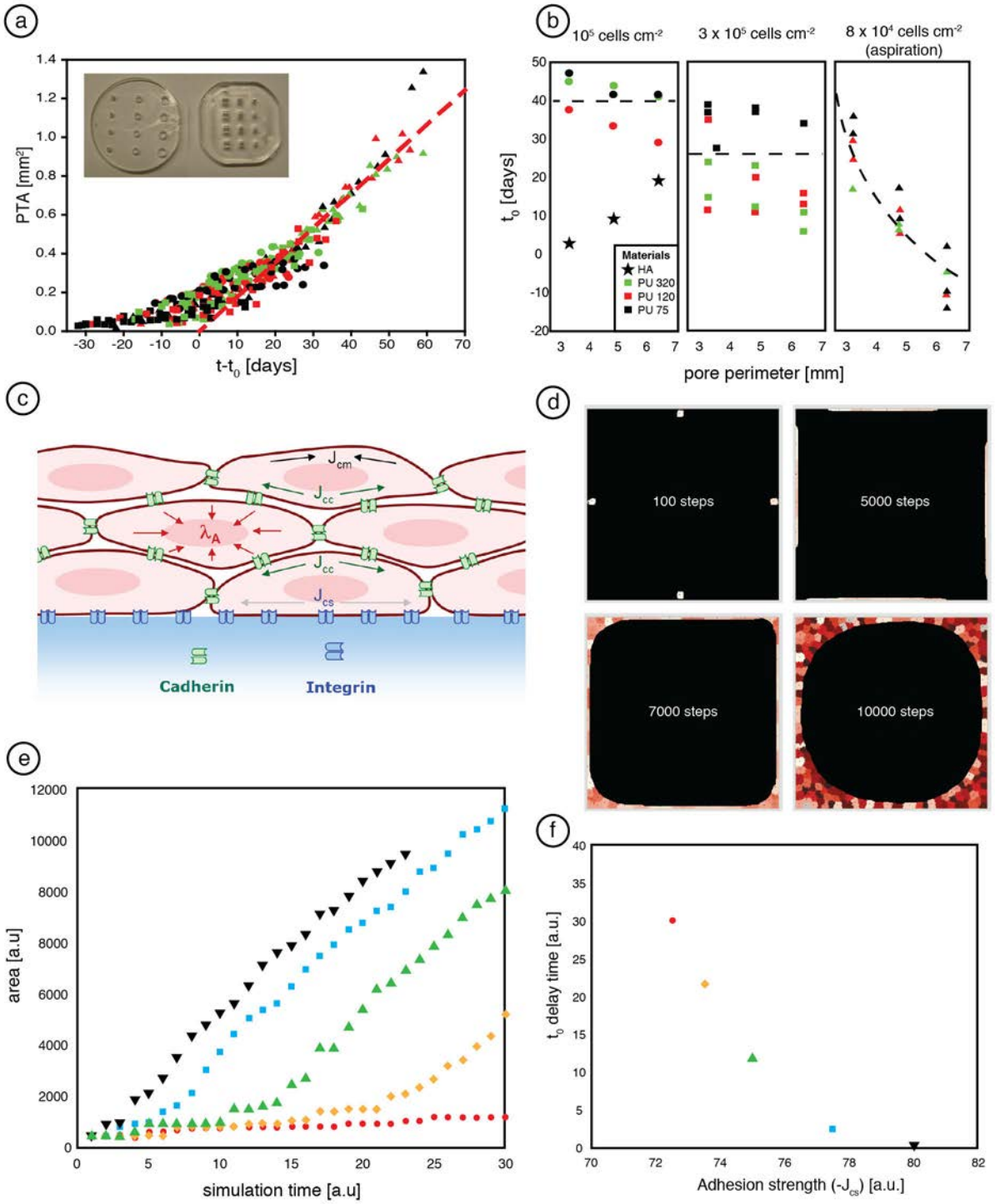

Figure 2–7: Effect of the substrate on experimental and simulated tissue growth
a) Projected tissue area as a function of culture minus lag time for MC3T3-E1 cells cultured in polyurethane scaffolds (inset) with different stiffnesses and different cell seeding methods, (data and image from (Kommareddy et al. 2010)). The symbol colour corresponds to stiffness, Green (320 MPa) Red (120 Mpa) and Black (75 MPa) and the symbol shape corresponds to the cell density used, circles – 10^5 cells cm^{-2}, square – 3 x 10^5 cells cm^{-2}, triangles 8 x 10^4 cells cm^{-2} with aspiration. The red line has the same slope as the red line for the hydroxyapatite data in Figure 2–6d. b) lag times for the data shown in a). c) Sketch of the important parameters in the Cellular Potts (CP) Model. d) results of the CP model simulated using the CompuCell software (Swat et al. 2012) e) Simulated growth curves for different adhesion energies.

Although the results are somewhat difficult to relate directly to the kinetics of the cell cycle, one can see that the surface tension mediated spreading leads to proliferation in the corners of square pores (Figure 2–7d), leading to similar geometries as predicted by Eq. 2.1. When the cell-substrate adhesion energy is varied, the shape of the simulated tissue growth curves (Figure 2–7e) remains the same but is shifted by a value t_0, that decreases with increasing adhesion energy (Figure 2–7f). This corresponds closely with the shapes of the experimental growth curves and highlights the important role of substrate adhesion on the initial parts of growth. This has an important implication the design of scaffolds for tissue engineering in that surface properties appear to be mainly important only in early stages of growth and colonisation of the surface by the cells, and less important at later stages in growth, where macroscopic geometric constraints become more important.

The role of convexity on tissue growth [TG3]

One important corollary of Fenchel's theorem (Fenchel 1928) is the observation that in general the curvature averaged over the perimeter for any closed planar curve is given by $\langle \kappa \rangle_P \geq \frac{2\pi}{P}$. This means that in principle by producing pores with non-convex shapes it may be possible to accelerate growth by playing with convexity and geometry of the pore cross-section (Figure 2–8). An indication of the possibilities of controlling growth by geometry is highlighted by the observation that tissue growing on a wave-like surface grows asymmetrically (Gamsjäger et al. 2013),with only a thin layer forming on the convex side of the waves and thick tissue growing on the concave portion (Figure 2–8a). This indicates that cells can sense the sign of curvature. To investigate the role of convexity pores with square and cross shaped cross-sections and the same surface area were seeded with pre-osteoblast cells and the tissue growth kinetics observed over 25 days (Figure 2–8b and c) (Bidan et al. 2013). At early stages only the concave regions of the pores filled with tissue, only a mono-layer of tissue was observed on the flat and convex surfaces. Tissue grew over the convex regions only when the concave regions in the arms of the pores became filled thus changing the local curvature. The curvature driven growth model was applied to the experimental images and gave excellent agreement to the experiments in terms of predicted tissue shape (Figure 2–8c), and curvature (Figure 2–8d and e), and this with only one fitting parameter (λ in Eg. 2.4). The predicted growth curves (Figure 2–8f and g) also agree with the experimental data in the first 14 days of growth. These results highlight that just by changing the pore geometry, for the same surface area, it is possible to double the rate of tissue growth inside a pore. At later stages however the measured growth slows down compared to the theoretical predictions. There are a variety of potential reasons for this, see (Bidan et al. 2013) for a more detailed discussion. One potential reason for the slow down in the rate of growth is that the MC3T3 pre-osteoblast cells studied are becoming more mature at later stages, as supported by the increased production of alkaline phosphatase, and hence do not proliferate as strongly. Another potential reason is that our curvature driven growth model is in 2D and doesn't take into account the changes in curvature within the depth of the pore. Due to growth the surface becomes more convex in the z-direction which implying that the mean curvature under certain circumstances could decrease with growth thus slowing down the growth rate. Our model has since been extended to 3D (Bidan et al. 2013) and indeed displays this slow down in predicted growth for certain geometries. Current work is underway to test the models predictions experimentally both *in-vitro* and *in-vivo*.

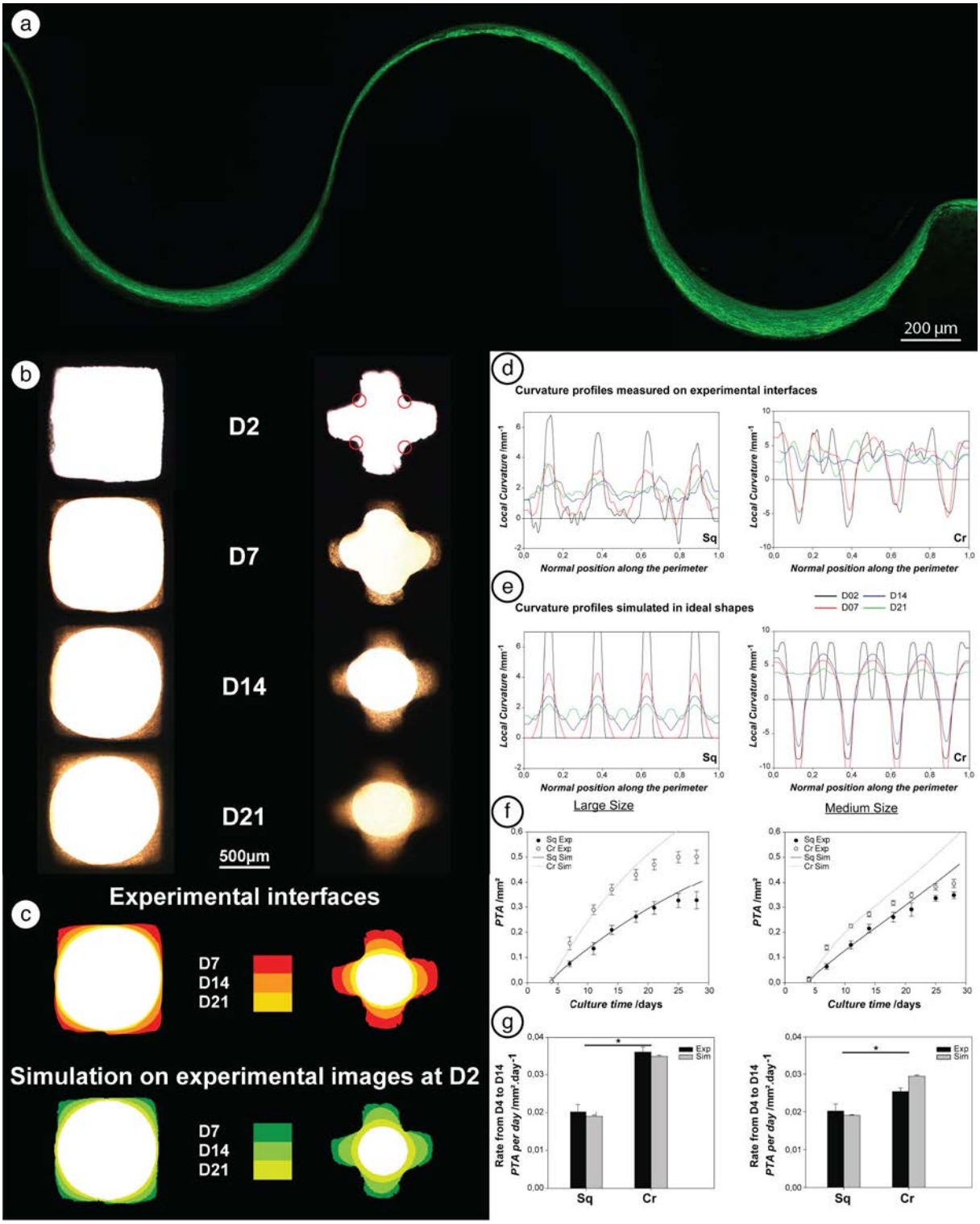

Figure 2–8: The role of pore convexity on tissue growth

a) An example of the growth of tissue by pre-osteoblasts on a wave like substrate (medium above, scaffold below), stained for actin (Gamsjäger et al. 2013). b) Phase contrast images of tissue grown in pores with convex (square) and non-convex (cross) geometries with the same surface area. c) A comparison of the measured tissue-medium interfaces from b) (above) to the simulated tissue-medium interfaces (below). d) measured curvature in square (left) and cross (right) pore geometries, and e) predicted curvatures in ideal square (left) and cross (right) pore geometries. f) comparison between experimental and simulated tissue growth kinetics between square and cross shaped pores of different sizes (large left and medium right). g) A comparison between simulated and experimental growth rates measured from day 4 to day 14 between square and cross shaped pores of different sizes (large left and medium right). Images (b-g) come from (Bidan et al. 2013).

The model of curvature controlled growth can also be used as a design tool to predict optimum scaffold geometries for tissue regeneration (Figure 2–9). Pore shapes can be defined by a combination of circularity, which defines how much a shape differs from a circle, and by the non-convexity which gives a measure for the average positive curvature over the perimeter of the pore (Figure 2–9a). This then can be used to plot design maps of the average growth rates as a function of pore size, and geometry for a given scaffold with defined porosity (Figure 2–9b).

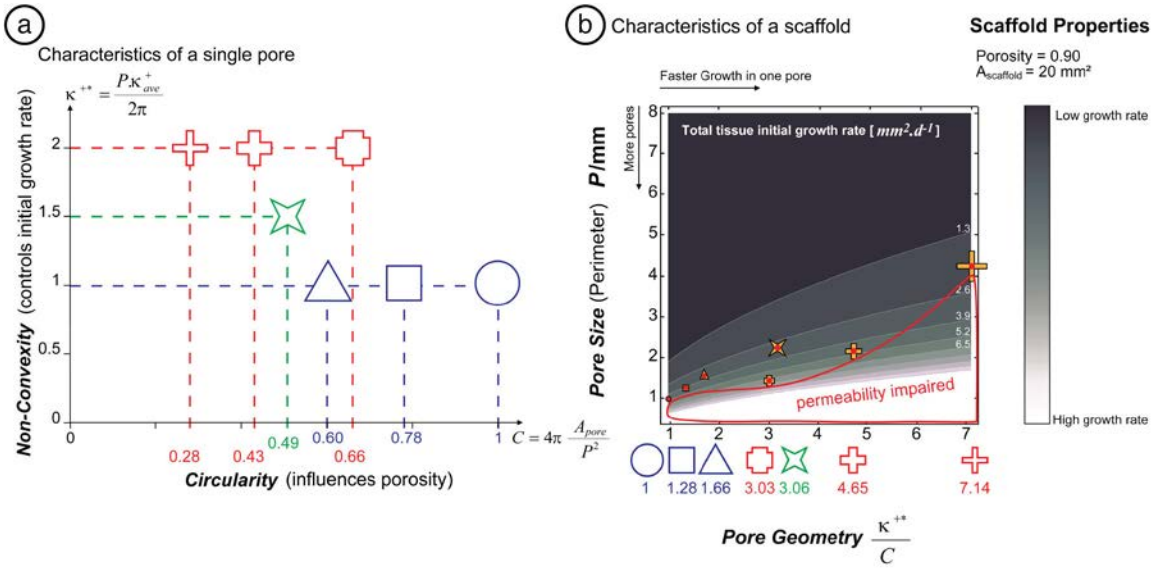

Figure 2–9: Curvature driven growth model as a scaffold design tool
a) The shapes of prismatic pores in a scaffold can be classified according to their circularity which is related to the ratio of the pore area to the area of a circle which has the same perimeter as the pore, and the non-convexity which is the positive curvature of a pore averaged over the perimeter. b) A map of predicted growth rates for a scaffold containing prismatic pores with a given porosity (0.90) as a function of pore size and pore geometry (defined by the ratio of non-convexity to circularity) (Bidan et al. 2013).

Possible role of geometry on bone-remodelling [TG4]

The ideas presented previously of the role of geometry on the behaviour of tissue forming cells may also have implications on the understanding of the process of bone remodelling (Robling et al. 2006). During bone remodelling, bone material is continuously renewed during an organisms lifetime, by the action of osteoclasts resorbing bone on its surface followed by the deposition of new bone on the new surface by osteoblasts. This process of resorption and deposition directly implies a local change in the bone surface geometry during remodelling, with the creation of concave regions on the surface by osteoclasts (Figure 2–10a and b). Two types of remodelling can be observed; osteonal remodelling (Figure 2–10a), which occurs in the dense cortical bone and hemi-osteonal remodelling which is found in trabecular bone (Figure 2–10b).These processes differ essentially in the topology of the resultant lacunae. Osteonal remodelling results in the formation of a cylindrical channel (Figure 2–10a) which then is filled by concentric layers of unmineralised new bone (and a blood vessel in the centre). Hemi-osteonal remodelling results in a hemi-cylindrical channel on the surface of trabecular bone which then slowly fills in with layers of osteoid. As an osteon fills in, it's surface curvature increases until growth is halted by the closure of the pore and the presence of the Haversian canal, however as a hemi-osteon fills in the surface curvature decreases with time.

Inspired by the *in-vivo* geometries of osteoclast resorption lacunae found in bone (Figure 2–10a and b), we investigated tissue growth in circular and semi-circular pores both of the same curvature (Figure 2–10c). No growth was observed on the convex corners of the semi-circular pores, with tissue appearing to be "pinned" on the corners. There was excellent agreement between the simulated tissue-medium interfaces and those measured experimentally (Figure 2–10d). Circular pores filled with tissue faster than in the semi-circular pores (Figure 2–10e and g) with the surface curvature increasing for circular pores and decreasing for hemi-circular pores as growth proceeds (Figure 2–10f). Again we see the general slow down in growth after about 15-20 days of culture which could be due to the development of convex curvature in 3D (see also the previous section).

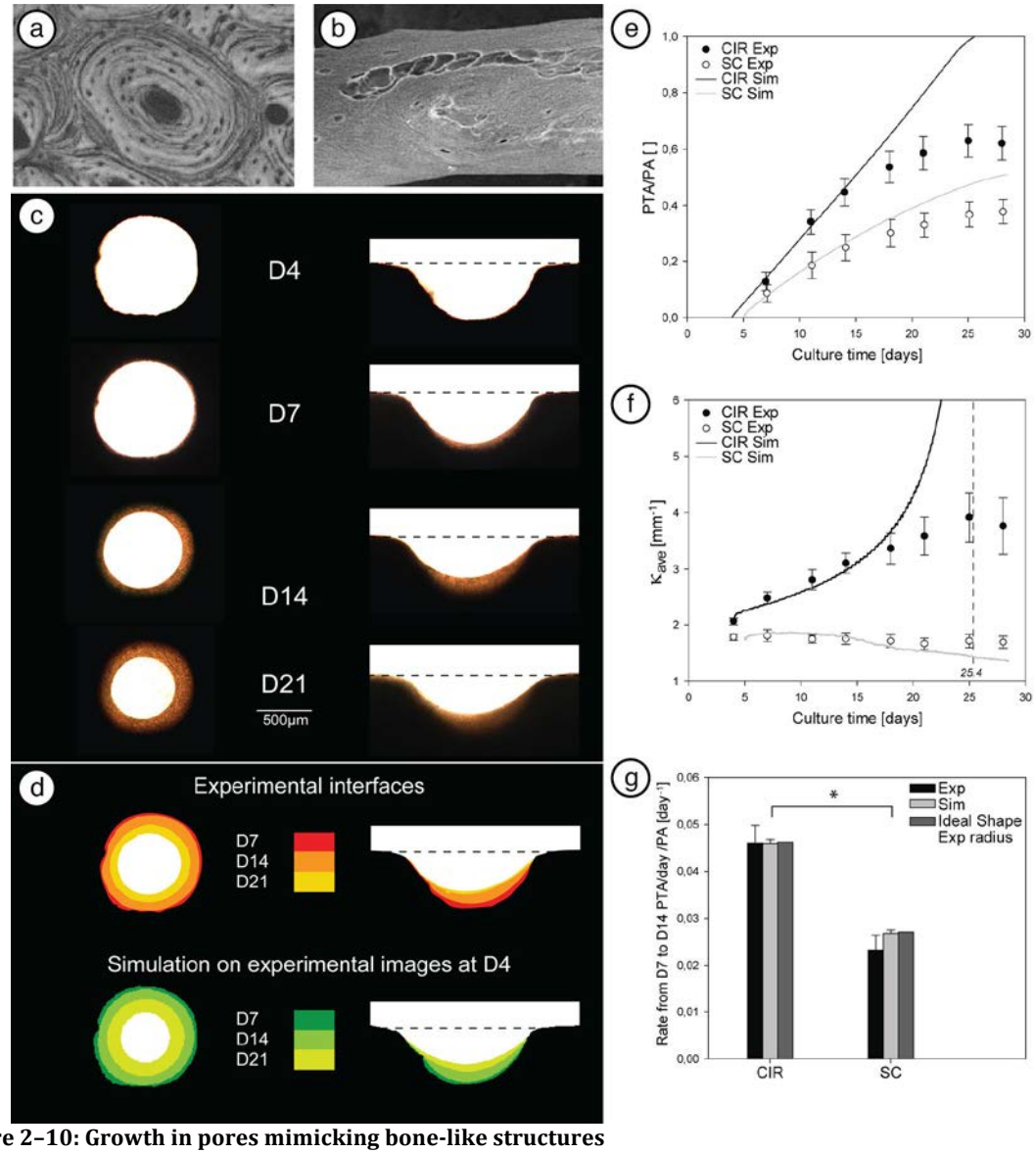

Figure 2–10: Growth in pores mimicking bone-like structures
a) An example of an osteon taken from a polished transverse cross-section of cortical bone in a horse radius, b) An scanning electron microscopy image of hemi-osteonal resorption lacunae in human trabecular bone (Gentzsch et al. 2004). c) Phase contrast images of MC3T3-E1 cells cultured on circular and semi-circular pores of the same curvature d) A comparison of the location and shape of experimental tissue-medium interfaces with those predicted using the curvature driven growth model. e) Experimentally measured and simulated growth kinetics for the circular and semi-circular pores in terms of projected tissue area vs pore area f) Simulated and experimentally measured curvatures as a function of culture time, g) Simulated and experimental growth rates from day 7 to day 14 for circular and semi-circular pores compared to predicted growth rates in pores of ideal geometry.

There may also be interesting consequences of our in-vitro experiments and simulations on the understanding of bone remodelling, where it has been observed that the rate of bone formation in trabecular bone (in hemi-osteons) is slower than that in cortical bone (osteons) (Agerbaek et al. 1991, Eriksen 2010). Based on our results the observed difference in in-vivo growth rates may not be due to an intrinsic difference between osteoblasts in trabecular bone versus osteoblasts in cortical bone, but rather just be due to fundamental differences in the geometry of the lacunae (closed versus open). Furthermore our results suggest a simple solution to the question of how osteoblasts in trabecular bone know when to stop filling the osteoclast lacunae. Instead of requiring complex signalling pathways between osteocytes (embedded in the bone matrix) and the bone forming osteoblasts, all that is necessary is that osteoblasts produce new bone on the surface at a rate proportional to the local curvature. This means that growth will stop when hemi-osteons become filled and the curvature tends towards zero. This would suggest that the steady state surface curvature of trabecular bone would be close to zero as is observed experimentally (Jinnai et al. 2001, Jinnai et al. 2002).

Substrate geometry controls the microstructures of tissues [TG4]

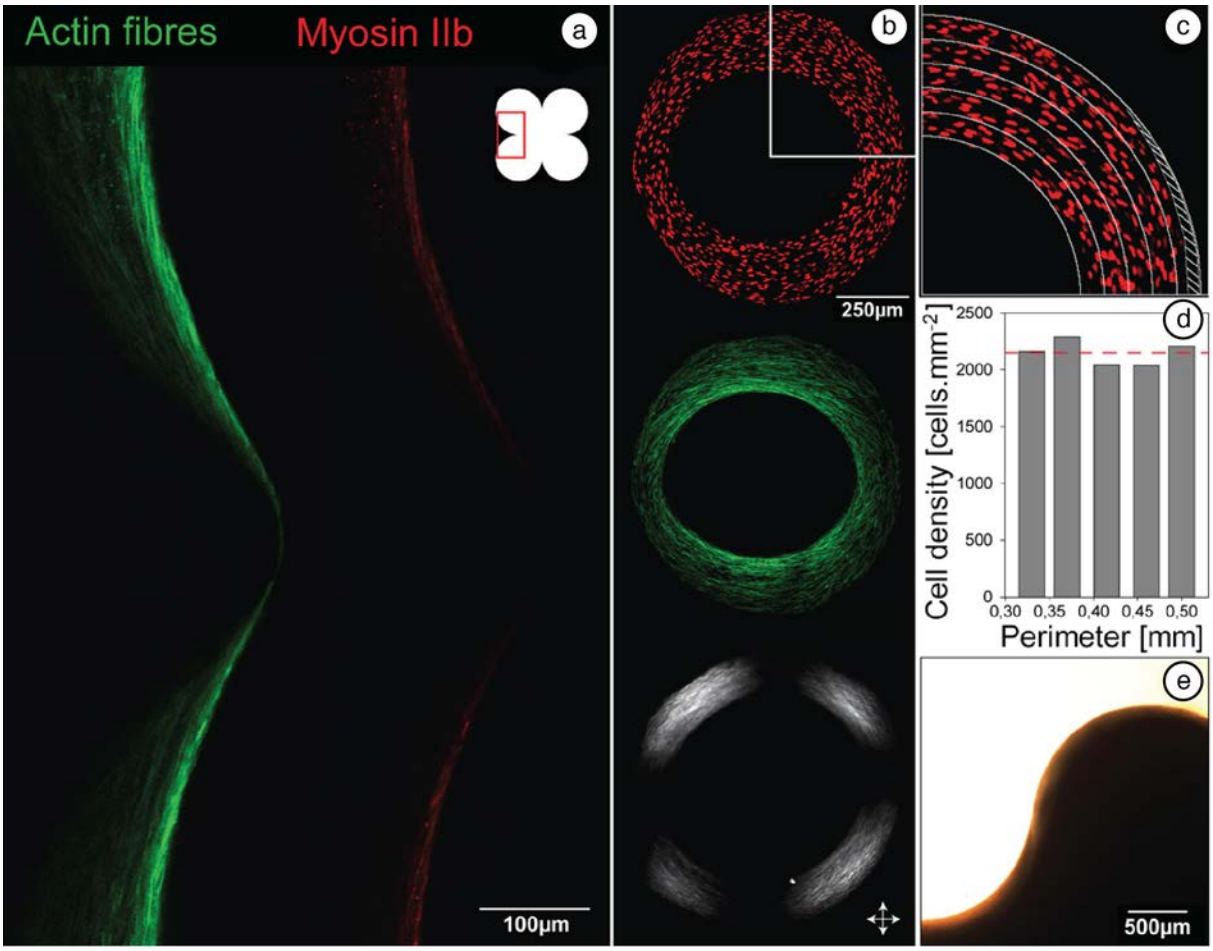

Figure 2–11: The microstructure of different tissue components as a function of geometry
a) Confocal images of a tissue produced by MC3T3-E1 cells, stained for actin (green) and myosin IIb (red) showing a co-localisation of actin and myosin at the tissue medium interface. b) (top) Confocal image of tissue in a circular pore stained for actin (green), (middle) nuclei staining (red) and (bottom) polarised transmitted light microscopy image of the same pore (crossed arrows indicates the polarisation direction). c) zoom of b-middle showing the uniform density of cells throughout the tissue, d) quantification of cell density as a function of distance. e) Phase contrast microscopy image of a convex region in a pore showing only limited growth on the surface.

The microstructure of tissue formed in the pores was studied using laser scanning confocal microscopy and polarised light microscopy (Figure 2–11). These measurements help to give some insight into the mechanisms that give rise to curvature driven growth. In all tissues a higher concentration of actin is observed at the tissue medium interface, with actin stress fibres aligned parallel to the interface (Figure 2–11a). Tissues stained for Myosin IIb, show a colocalisation with actin. This highlights the contractile nature of these surface regions, in many ways similar to the "purse-string" contractile structures observed in two-dimensional wound-healing. Cell-nuclei (Figure 2–11b top) are oriented along the direction of the actin fibres (Figure 2–11b middle). Interestingly the density of cell nuclei (Figure 2–11c and d) is independent of the position through the tissue thickness. Collagen fibrils produced in older tissue by the cells appear also to be aligned with the actin as seen in polarised light microscopy (Figure 2–11b bottom), and this has been confirmed by second harmonic generation microscopy (data not shown). This co-orientation of ECM and cells implies a fundamental role in the pre-organisation of cells on the later organisation of collagen and other ECM components. Recent studies indicate similar co-orientation of another ECM component, fibronectin, with cell and collagen organisation (data not shown).

Linking curvature driven growth to tissue structure [TG4]

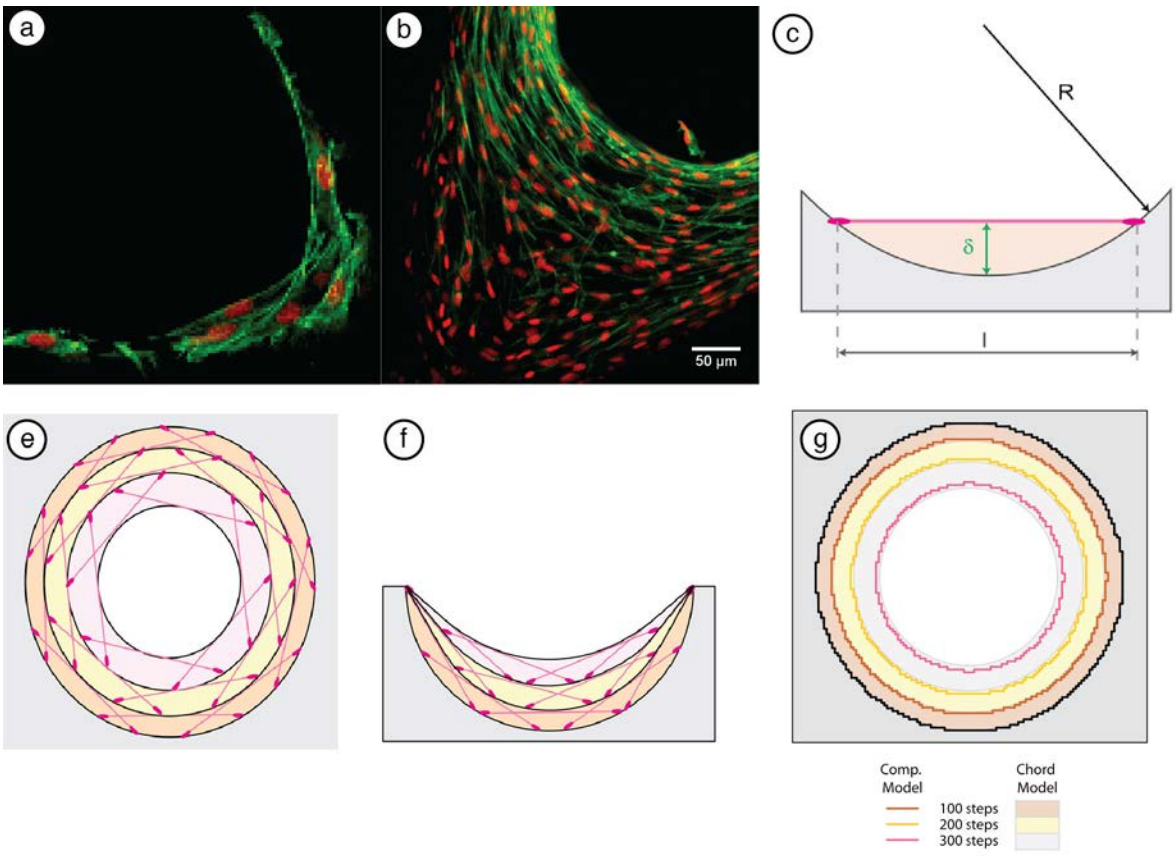

Figure 2–12: Tissues modelled as stacked "chord-like" elements
Confocal images of tissues stained for actin (green) and nuclei (red), after 2 days (a) and 35 days (b) of culture indicating cells stretched over large distances. These cells can be simplified as chords c) spanning a distance l giving rise to a tissue thickness δ which is a function of the radius of curvature R of the underlying surface. By stacking such elements over the surface similar tissue geometries can be formed as those observed in d) circular and e) semi-circular pores (see Figure 2–10) and in fact can be proven to be completely equivalent to the curvature driven growth model as seen in g).

Confocal images of the structure of tissues grown inside our pores indicate another way to understand and even model the growth of our in-vitro tissues. High magnification images of the pores indicate that cells are stretched over long distances and take on the appearance of elongated linear tensile elements, much like chords (Figure 2–12a and b). Such a stretched element when placed on a concave surface will enclose a region between it and the substrate (Figure 2–12c) which will be related to the radius of curvature of the underlying substrate. In (Bidan et al. 2012) we demonstrated that the layering of a collection of such chord-like elements onto a surface gives rise to tissue geometries identical to those predicted from the curvature driven growth model (Figure 2–12e and f) and furthermore we could show that with an appropriate calibration constant, our chord-model was mathematically identical to the curvature driven growth model. This highlights the importance of the tensile elements of cells and ECM in producing and organising tissues.

The role of mechanics on tissue growth [TG5, TG6 and TG7]

It is clear that mechanical signalling plays an important role in cell proliferation and may potentially be responsible for the macroscopic growth responses that we observe experimentally. In the three previously described modelling approaches (curvature driven growth, chord model and Potts model) none of them explicitly included the role of mechanics. It turns out however that there is an extensive theoretical framework developed by the continuum mechanics community to describe phase transformations (Fischer et al. 2008) that is ideally suited to describe mechanical problems coupled to growth, and has also been used by a variety of groups to describe biological growth, see e.g. (Garikipati 2009, Cowin 2010, Ciarletta et al. 2012). We thus extended the formulation of Ambrosi and co-workers (Ambrosi and Guana 2005, Ambrosi and Guillou 2007, Ambrosi et al. 2012), in collaboration with Dieter Fischer (Montan Universität Leoben), in order to understand the role of mechanics on the confined tissue growth observed in our experiments. This approach relies on the assumption that it is possible to decompose the deformation of a volume element of tissue into two independent components, the growth strain and the elastic strain applied to the tissue due to mechanical constraints. See also (Ambrosi et al. 2011) for a more detailed discussion. We first focussed on developing a thermodynamically consistent equation to describe growth based on energy and mass balance considerations see (Dunlop et al. 2010) for details. In a small strain setting this equation takes the form:

$$\dot{\mathbf{g}} = f\left(\boldsymbol{\sigma} - \mathbf{M}\right) \qquad \text{Eq. 2.6}$$

where $\dot{\mathbf{g}}$ is the growth strain rate, f is a mobility coefficient, $\boldsymbol{\sigma}$ is the stress tensor and $\mathbf{M}$ is the chemical potential tensor. This equation implies that growth stops when the local stress state of a volume element of tissue is equal to the biochemical driving force, equivalent to the concept of stress homeostasis used to describe cell responses in bone remodelling (Frost 1987, Huiskes et al. 2000, Robling et al. 2006). Assuming the mechanical properties of the tissue can be described by Hooke's Law we investigated the response of tissues growing on a cylindrical surface in two directions, inward growth (corresponding to a cylindrical pore with concave curvature) or outward growth (corresponding to a convex solid cylinder) (Figure 2–13a and b) (Gamsjäger et al. 2013). To account for the tension developed in the outer surface of our tissues (as observed experimentally in Figure 2–11), we applied a curvature dependent surface stress to the tissues according to the Laplace law. The consequences of this surface stress can be seen on the predicted growth curves (Figure 2–13c and d) which show that growth only

occurs on convex surfaces when the biochemical driving force $\tilde{\mu}$ can overcome the surface tension $\tilde{\gamma}$ (Figure 2–13e).

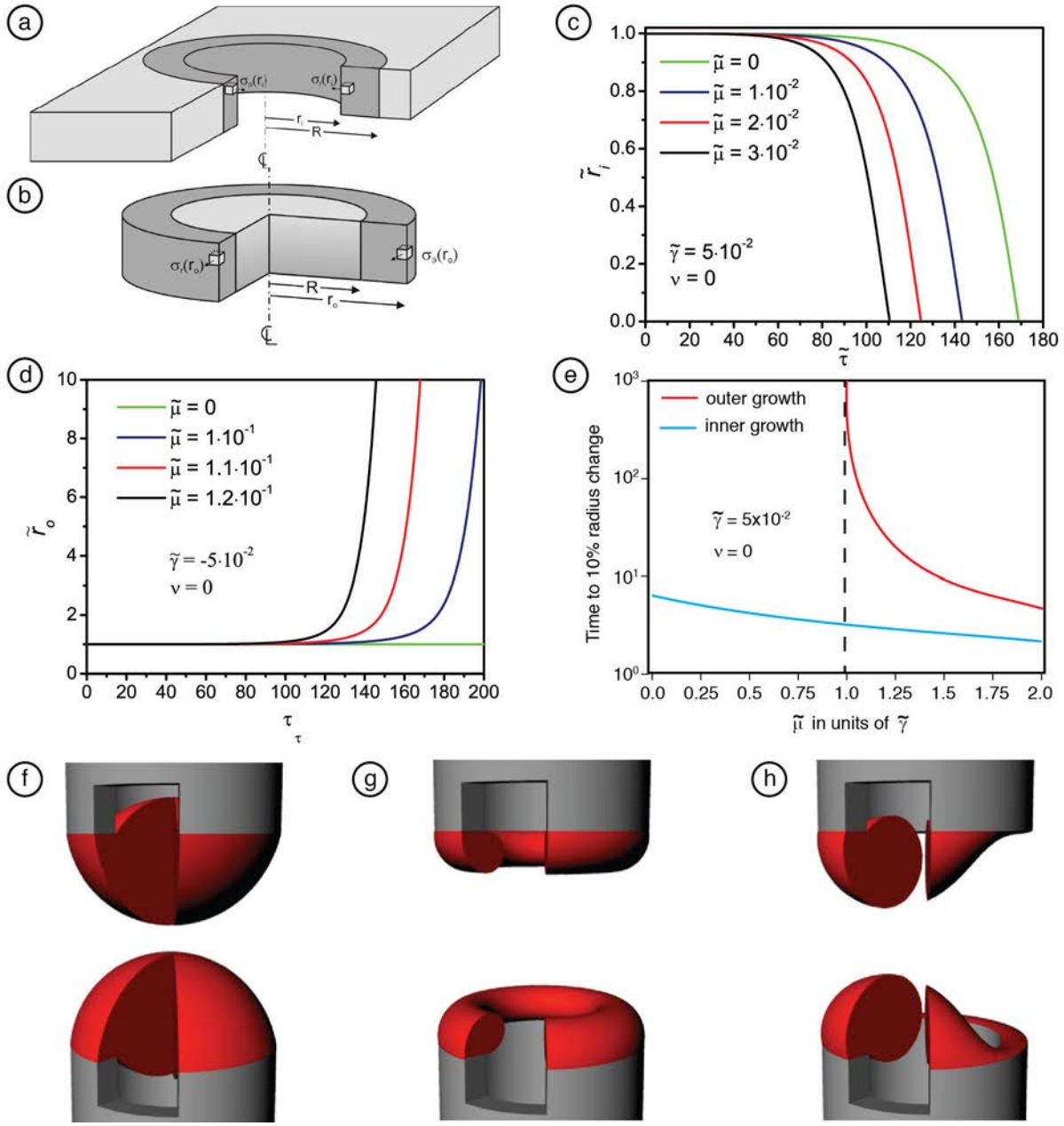

Figure 2–13: Continuum mechanics model of tissue growth
This growth model was applied in two axi-symmetric geometries, that of a) inward growth corresponding to the filling of a cylindrical pore, and b) outward growth corresponding to the growth of a tissue on the exterior of a cylinder. Predicted position of the tissue medium interface as a function of time for increasing values of the driving force for growth $\tilde{\mu}$ for inner growth c) and outer growth d). e) A comparison of the time for a 10% radius change for inner and outer growth for different values of the ratio of the driving force $\tilde{\mu}$ to the surface tension $\tilde{\gamma}$. f-h) three different configurations of predicted 3D growth on hollow cylindrical geometries that mimic the shape of a simulated bone fracture or osteotomy.

A further extension of the model was recently performed where we investigated the consequences of such a growth law in more realistic 3D geometries (Fischer et al. 2015) instead of the 2D geometries looked at previously. This allows us to test such models in geometries that become closer to the in-vivo situation. The model in its simplest form when applied to geometries reminiscent of fracture defects in bone healing, displays features also observed experimentally, and gives a biomechanical explanation for why there is a critical fracture gap size above which no bone healing can occur (Figure 2–13f-h).

2.3 Summary

In this chapter we have described some of the key results coming from work that has been done in our group towards understanding the process of tissue growth and the influence of geometric constraints on this growth. By using advanced 3D printing technology we can produce substrates of controlled geometries that can be seeded with tissue producing cells. A combination of different microscopy techniques leads us towards an understanding of the link between geometry and underlying tissue microstructure. Surprisingly simple geometric models (related to surface curvature) are remarkably successful in describing tissue shapes and kinetics of growth. Two other theoretical models have been developed: an agent based model based on the cellular Potts model, and a continuum mechanics model. Each of these models have different strengths and of course weaknesses. With appropriate descriptions of cell behaviour, agent based models have the advantage about being able the to describe self-organising behaviour of cells in developing large scale patterns within tissues, however cannot describe the mechanical state of the system as well as continuum mechanics approaches. One potential direction of future would be to couple such models as has been demonstrated in bone remodelling (see e.g. (van Oers et al. 2008)). Further work in the group is now focussed on trying to understand the behaviour of different tissue forming cell types, the role of cells on the organisation of ECM and to visualise the processes of growth in 3D.

Four key outcomes of our research with important implications for tissue engineering are:

- The observation that the rate of tissue growth in-vitro in osteoblast cell-culture is proportional to the local concave curvature meaning that by controlling the pore shape in scaffolds tissue growth can be accelerated.
- A model based on tissue geometry that helps us understand the difference in *in-vivo* bone remodelling rates in cortical versus trabecular bone.
- An understanding of the importance of geometry on cell arrangement inside a growing tissue which in turn controls the arrangement of the extracellular matrix.
- The development of a continuum mechanics model for growth that predicts the formation of a critical gap size as observed in bone fracture healing.

3 Actuation

The previous chapter has focused on the biophysics of how tissues change form and shape during growth. The chapter highlighted that the geometry of the external boundaries of a growing tissue has important consequences not only on the local rate of growth of a tissue but also upon its microstructure. As emphasized in the introduction of this thesis (Figure 1–4), the microstructure of a tissue controls function, with plants for example, being able to change the physical properties (stiffness and swellability) of their tissues simply by modifying the orientation of cellulose microfibrils within the cell wall. This localised microstructural control within a tissue in turn allows tissues to change shape in a controlled way through differential or localised swelling as a response to changes in the environment even after the tissue is no longer metabolically active, which leads to the second major research topic presented in this thesis.

The current chapter focuses on actuating structures (or materials) that change shape due to localised swelling. More specifically it describes investigations into how the geometric arrangement of swellable and non-swellable materials inside a structure controls macroscopic shape changes. This work is motivated by studies carried out within other research groups of the Department of Biomaterials (Together with Peter Fratzl, Ingo Burgert, Luca Bertinetti and Michaela Eder) on hygroscopic actuators from the plant world. In the first part of this chapter a short introduction into natural hygrosopic actuators is given, with examples coming from the literature as well as from some of the research the author has participated in within the Biomaterials Department. The second part of the chapter, gives an overview of a selection of the research results coming from the group on generalised concepts about actuation and their implementation in synthetic systems. These results are described in full detail inside the publications attached at the end of this thesis (See Section 7).

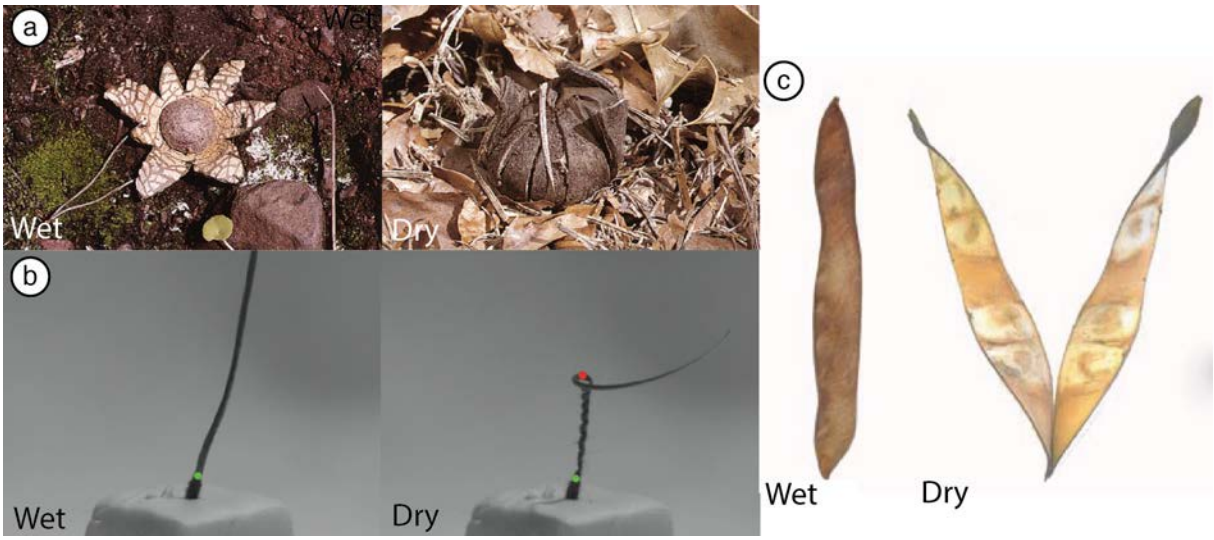

Figure 3–1: Examples of natural actuators powered by water
a) The fruiting body of the fungus *Astraeus hygrometricus* opens when wet and closes when dry (curiously another species *Gaestrum campestris* shows the opposite behaviour) (Brand and Finlay 1996) b) The filaree, *Erodium cicutarium*, coils upon drying (Evangelista et al. 2011), and c) the seed pod of *Bauhinia variegate* opens in a chiral fashion upon drying (Armon et al. 2011).

3.1 Background

Many examples of hygroscopic actuators exist in Nature, with examples ranging from the fruiting body of the fungus *Astraeus hygrometricus* (Brand and Finlay 1996), which closes upon drying and closes upon wetting (Figure 3–1a), to the twisting awns of *Erodium cicutarium* (Figure 3–1b) (Evangelista et al. 2011, Abraham et al. 2012, Abraham et al. 2012, Abraham and Elbaum 2013), to the chiral twisting seed capsules of *Bauhinia variegate* (Figure 3–1c) *(Armon et al. 2011)*. What all of these systems have in common is the presence of a controlled geometric arrangement of different tissues within an organ that swell in different amounts giving rise to macroscopic motion. Such movements have provided inspiration for the development of synthetic actuators and have been discussed in numerous reviews see e.g. (Fratzl et al. 2008, Fratzl and Barth 2009, Martone et al. 2010, Speck and Burgert 2011, Elbaum and Abraham 2014, Studart and Erb 2014). The following section gives a short introduction into the mechanics of the plant cell wall, and importantly the role of the cellulose microfibril angle (MFA or μ) on the mechanical properties and ability for the tissue to swell. This will be followed by several examples of different plant tissues that use materials architecture in the cell wall components to control hygroscopic actuation.

As highlighted in Figure 1–4 the plant cell wall consists of long stiff crystalline cellulose microfibrils wrapping around the axis of the cell embedded in a soft hydroscopic swellable matrix (Figure 3–2a). The average cellulose microfibril angle (MFA), with respect to the axis of the cell predominantly determined by the microfibrils in the secondary cell wall plays a fundamental role on the mechanical and swelling properties of the plant cell (Burgert et al. 2007, Fratzl et al. 2008, Gibson 2012). This can be seen in the measured tissue stiffness (Young's modulus) both in single wood fibres and thicker tissues containing many cells as a function of MFA (Figure 3–2b) (Cave 1969, Wimmer et al. 1997, Reiterer et al. 2001, Eder et al. 2013). The highest stiffness is achieved for cells with low MFAs, in which case the stiff microfibrils are loaded almost directly in tension, and the lowest stiffness for microfibrils oriented at larger angles to the cell axis. This has the consequence that just by controlling the simple architectural parameter of the MFA, plants can achieve a large range of mechanical properties, using the same cell wall components (Burgert and Fratzl 2009, Burgert and Dunlop 2011). The same principle also applies for the role of MFA on the swelling behaviour of plant tissues. This can be understood by a simple thought experiment illustrated in (Figure 3–2c) which displays 3 schematic cells or cylinders with different MFAs (Burgert et al. 2007, Burgert and Fratzl 2007). These cylinders can be virtually cut along their length and unfolded (second column) such that one microfibril (in red) spans the diagonal of the resultant rectangle. When the cylinders swell, i.e. the green region representing the soft swellable matrix increases in area, the presence of the stiff fibrils will constrain the resultant deformation. For low MFAs an increase in rectangle area for fixed length of the diagonal, means the rectangle will shorten and increase in width. The inverse occurs for high MFAs (Figure 3–2c bottom) which will lengthen upon swelling. For MFAs around 45° increase in area can only occur upon changes in the length of the diagonal. Such observations have been experimentally verified in swelling experiments of high and low MFA wood tissues (Burgert et al. 2007).

A more realistic model to describe the role of microfibril angle on the swelling of the cell-wall was developed by Fratzl and co-workers (Keckes et al. 2003, Fratzl et al. 2004, Burgert et al. 2007, Fratzl et al. 2008, Bertinetti et al. 2013), using theoretical tools from composite mechanics see e.g. (Chou 1992, Hull and Clyne 1996), for a full derivation and description of the model see (Fratzl et al. 2008)). The model can be briefly summarised as follows. Plant cells are approximated as perfect cylinders with a

cell-wall consisting of stiff non-swellable fibrils oriented at an angle μ to the cell axis (Figure 3–2a). These fibrils are assumed to be embedded in an isotropic soft matrix, with Young's Modulus E and Poisson ratio ν, that swells isotropically an amount η upon changes in moisture content. Assuming sufficiently thin cell-walls, the 3D problem can be simplified to 2D.

The equations for elastic equilibrium of the matrix can be readily formulated in a local coordinate system oriented along the fibril direction (direction 1 being along the fibrils, and direction 2 perpendicular to the fibrils) giving:

$$\begin{aligned}\sigma_1 - E_f\varepsilon_1 &= \frac{E}{1-\nu^2}(\varepsilon_1-\eta)+\frac{\nu E}{1-\nu^2}(\varepsilon_2-\eta)\\ \sigma_2 &= \frac{\nu E}{1-\nu^2}(\varepsilon_1-\eta)+\frac{E}{1-\nu^2}(\varepsilon_2-\eta)\\ \tau_{12} &= \frac{E}{2(1+\nu)}\gamma_{12}\end{aligned} \qquad \text{Eq. 3.1}$$

where σ_1, σ_2, and τ_{12} are the normal stresses and shear stress in the matrix and ε_1, ε_2, and γ_{12} are the normal strains and shear strain in the matrix in the 1 and 2 directions. The second term on the left hand side of the top equation, describes the role the stiff fibrils have in stress shielding the matrix, where the parameter E_f is equivalent to the Young's modulus of the fibril multiplied by the fibril volume fraction. By rotating the coordinate system by an angle μ it is straightforward to write the equations in a coordinate system oriented parallel to the cell-axis. By then summing the results over all fibril orientations (as described by the MFA orientation distribution function as given by $p(\mu)$) it is possible to derive:

1) the stress, $\bar{\sigma}_x$, exerted by a swelling cell when it is constrained along its axis,
2) the strain, $\bar{\varepsilon}_x$, produced by a swelling cell along its axis when it is free to expand, and
3) Y_{eff}, the effective modulus in the axial direction,

as a function of (i) microfibril angle μ and (ii) the ratio between microfibril stiffness and matrix stiffness $f = (1-\nu^2)E_f/E$.

The results of such an analysis for a unidirectionally oriented microfibril angle distribution are plotted in (Figure 3–2d-f) as a function of microfibril angle μ for different values of f in comparison to randomly oriented fibrils (for the full equations see (Fratzl et al. 2008)). What is intriguing is that by simply tuning the angle of the reinforcing fibres with respect to the cell axis, tissues can be turned into compressive or tensile stress generators, or can be used to achieve large deformation in expansion or contraction due to an isotropic matrix swelling strain, and this with the same chemical composition. For example in (Figure 3–2d-f) for the highest stiffness contrast of 100 (dark green line) gives maximal tensile stress for MFAs ~20°, maximal tensile strain for MFA ~40° and starts developing compressive stress/strains for MFAs above 45°.

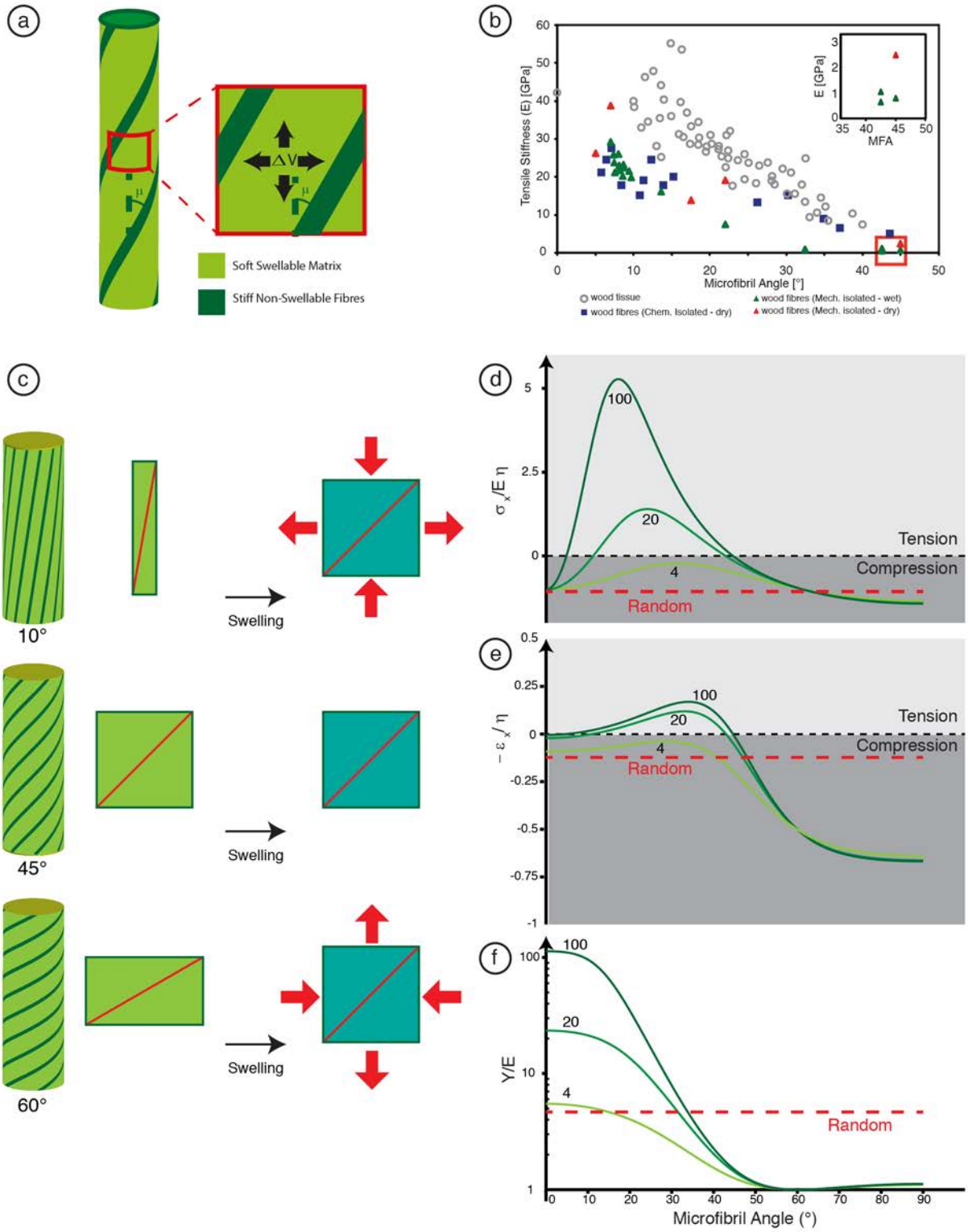

Figure 3–2: The cellulose microfibril angle controls the mechanics and swelling of the plant cell wall
a) Schematic of a simplified cell wall, consisting of a soft swellable matrix reinforced by stiff fibres wrapped at an angle μ around the cell b) A collection of literature data of the stiffness of different wood tissues and single fibres plotted as a function of the MFA (Eder et al. 2013) c) A schematic of how cells with different MFAs will respond to swelling of the soft matrix, when the stiff fibres are constrained from stretching, After (Burgert et al. 2007), How the model of Fratzl and co-workers predicts d) the axial stress produced by a cell swelling upon constraint e) the axial deformation developed upon swelling an amount and f) the Young's modulus as a function of microfibril angle for different values of the stiffness contrast of the cell-wall components. Note the graphs are normalised by the matrix modulus and the swelling strain. After (Fratzl et al. 2008)

These concepts of using the microfibril angle as a way to control tissue function are commonly used by plants in the context of seed dispersal. Two well-known examples in which plants use the MFA to control function are: the hygroscopic opening mechanism of the pine cone (Figure 3–3, See also Figure 1–1e and f) and the hygroscopic "swimming" motion of the wheat awn (Figure 3–4). In addition plants have two other mechanisms in which they can use cell wall architecture to modify mechanical function, by filling the lumen with a so-called g-layer as is found in the example of tension wood (Figure 3–5) or by modifying the cell cross section as seen in the tissues of the ice-plant seed capsules (Figure 3–6). These examples highlight how through the simple control of local tissue architecture (through the cellulose MFA), plants can develop highly complex functions that operate long after the tissue itself is dead.

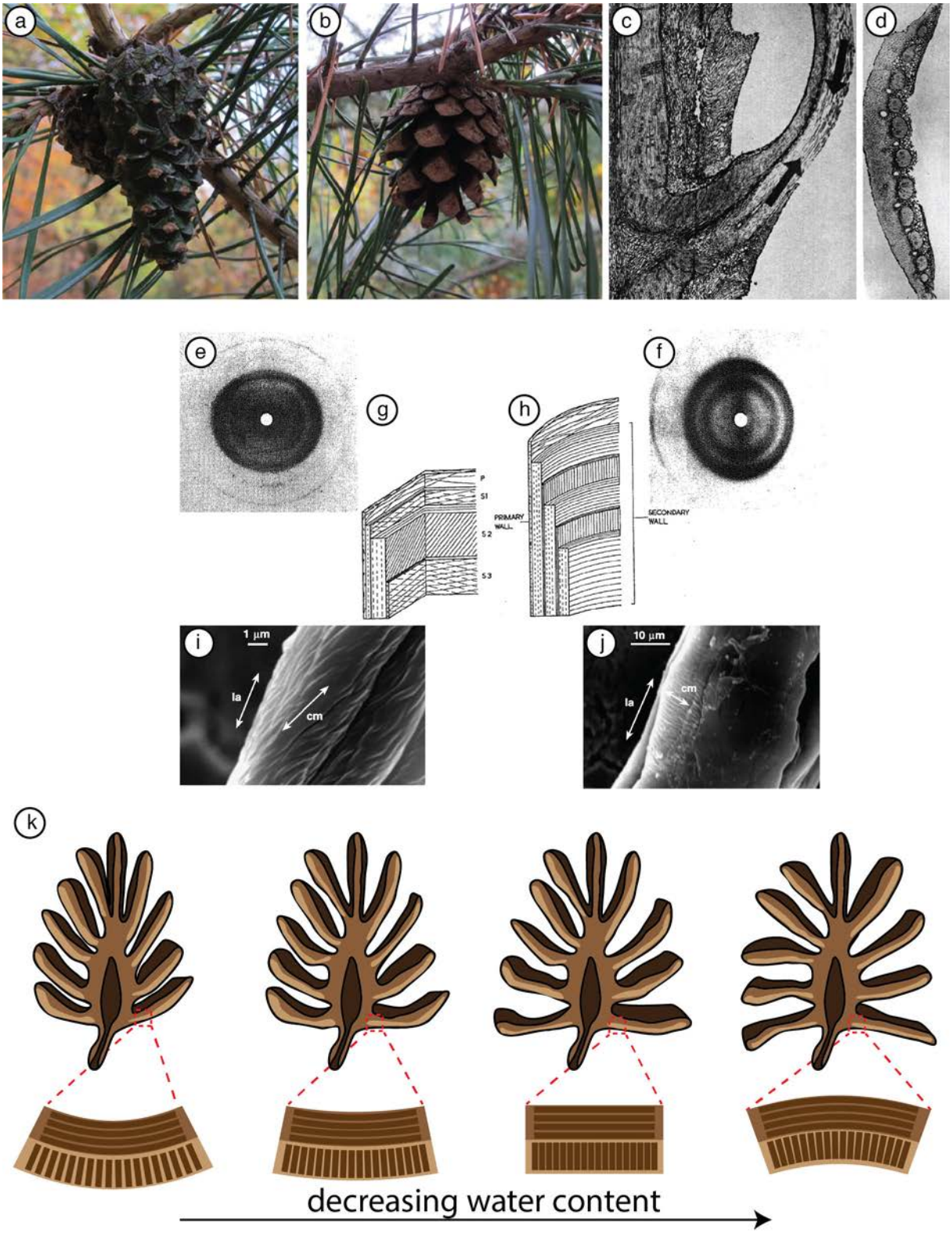

Figure 3–3: Hygroscopic opening of pine cones
Pine cones are well known examples of natural hygroscopic actuators whose scales are a) closed when wet b) and open when dry for seed release. c) Longitudinal section, and d) Transverse section of a scale illustrating the two tissue types found in the cross section (Harlow et al. 1964). These layers have different microfibril angles as illustrated by the X-ray scattering patterns in the upper e) and lower f) portions of the scales and the associated cell wall models (Allen and Wardrop 1964). SEM images of close ups of the scale tissues in the inner fibrous region i) and outer active j) portions of the scales show large differences in MFA (Dawson et al. 1998). The differences in MFA in the upper and lower portions results in a bi-layer giving rise to bending of the tissue upon drying as illustrated schematically in k) (Dunlop et al. 2011).

The opening mechanisms of pine cones have been well-studied, with some of the earliest research going back a century (Shaw 1914). Pine cones in the wet or green state have closed scales (Figure 3–3a), but upon drying (Figure 3–3b) the scales bend outwards opening the cone, allowing for seed release. Cross sections through scales in the longitudinal (Figure 3–3c) and transverse directions (Figure 3–3d), indicate the presence of at least two distinct tissue layers; one layer towards the innermost side of the scale consisting of thick fibrous or woody tissue and an outer layer consisting of shorter thick-walled cells (Harlow et al. 1964). This outer layer was found to change length considerably upon drying-wetting cycles, contracting almost 30% upon drying in some species (Harlow et al. 1964). Initial electron microscopy work (Harlow et al. 1964), and X-ray diffraction (Allen and Wardrop 1964) on the two tissues (Figure 3–3e and f) indicated the presence of very high MFAs in the outer tissue layer and much lower angles in the inner tissue. In more recent electron microscopy studies this difference in MFA can be clearly seen on the tissues (Figure 3–3i and j) (Dawson et al. 1998). The difference in cell-wall organisation between the two layers is well illustrated in the structural models of the cell walls developed by (Allen and Wardrop 1964) showing the organisation of inner (Figure 3–3g) and outer tissues (Figure 3–3h) respectively. From the previous discussion about the role of MFA on tissue contraction/expansion (see Figure 3–2e), the scales of the pine cones can be viewed as being essentially bi-layers, that change in curvature due to the differential strains developing in the two tissues with low and high-microfibril angles (Figure 3–3k). Such structures can be readily mimicked using paper and adhesive tape (Reyssat and Mahadevan 2009) and using advanced ceramic templating methods (Fritz-Popovski et al. 2012) it has even been possible to create active ceramic replicas of pine-cone scales (Zollfrank, pers. comm.).

Another example of hygroscopic actuation controlled by the microfibril angle of the cell walls, can be found in the hygroscopic motion of the awns of wild wheat, *Triticum turgidum* ssp*. Diccocoides* (Figure 3–4a) (Elbaum et al. 2007). Wheat seeds are attached to long "antenna-like" awns (Figure 3–4b and c) that move apart when dry and close when wet. In modern varieties, in which the wheat seed remains on the plant before harvest, these awns are much less-well pronounced. This hygroscopic motion comes about again due to the presence of two different tissue types in the cross section of the awn (Elbaum et al. 2007). Although no chemical difference between tissues in the cross-sections could be observed, these tissues become readily visible in acoustic microscopy images (Figure 3–4d) showing the presence of a layer of stiff tissue on the outside and softer tissues on the inside. This indicates local structural differences that become apparent from X-ray diffraction experiments of the two tissues (Figure 3–4e, f and g for the integrated images), which indicate very low microfibril angles for the outer tissue (Figure 3–4e) and a more random orientation for the inner tissue (Figure 3–4f). Although the outer tissue layer will not contract, the randomly oriented tissue will giving rise to differential swelling in the two layers and result in a hygroscopic bending of the awns (see Figure 3–2e). The awns also are covered on the outside by silica spikes (Figure 3–4h) that allow sliding of the awns with respect to a substrate only in one direction (see also (Kulić et al. 2009)). This has the consequence that upon cyclic humidity changes as found between day and night, wheat seeds will move their awns, with the silica spikes allowing them to "swim" away from the mother plant (Elbaum et al. 2007). A closer look at the cell-walls of the active tissue with randomly oriented MFAs (Figure 3–4i) indicates the presence of alternate high and low angle MFAs in the cell wall. Using simple FE models we showed that radial tensile stresses would develop at the interface between the layers upon swelling that could lead to crack opening and therefore faster water absorption (Zickler et al. 2012).

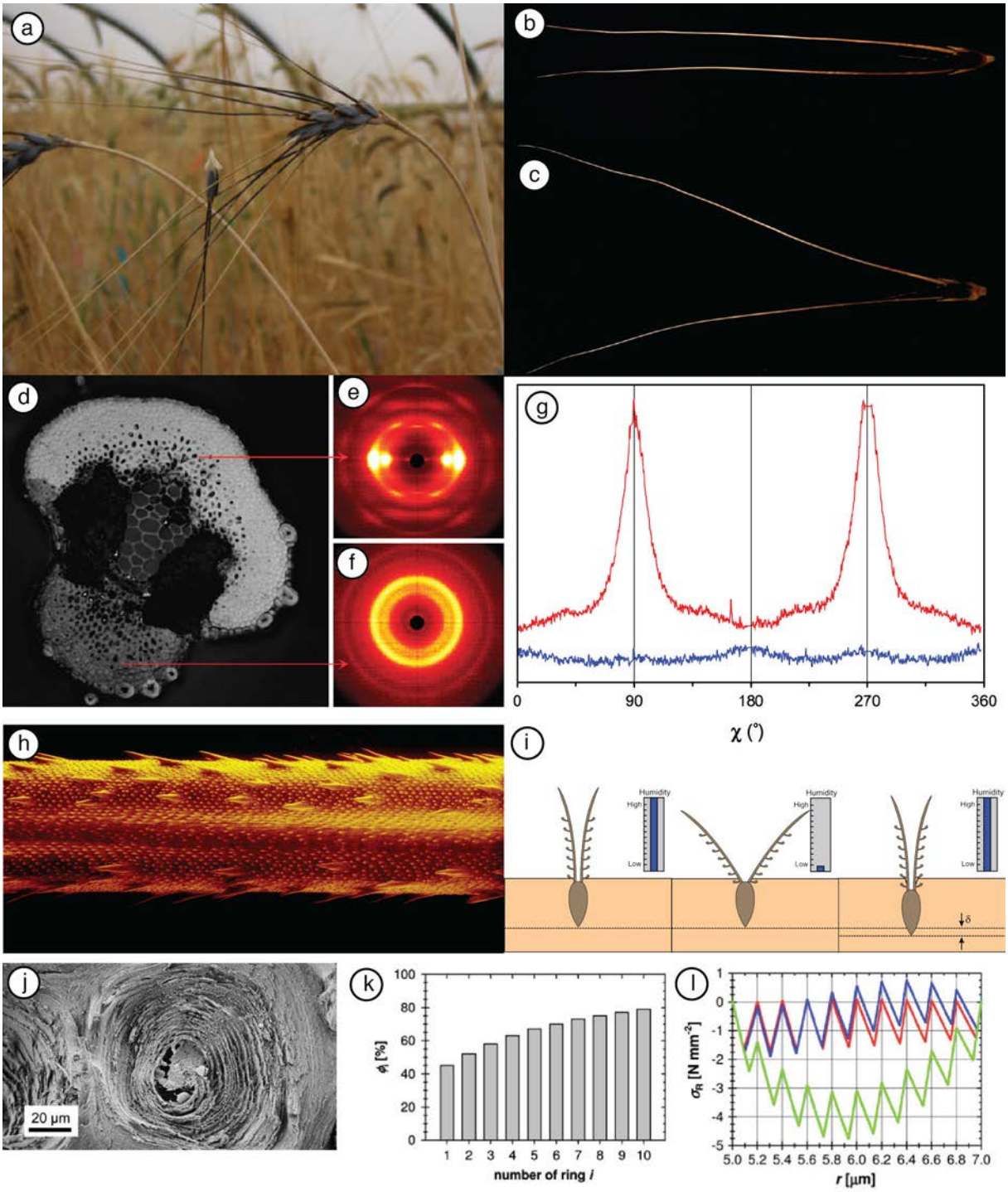

Figure 3–4: Hygroscopic motion in the awns of wheat

a) Image of wild wheat (*Triticum turgidum* ssp*. diccocoides*) (Elbaum et al. 2008), Image of the wheat awns when wet b) and dry c) (length of an awn ~10cm). (images courtesy of M. Eder) d) Acoustic microscopy image of a cross-section through a wheat awn. A lighter colour indicates a higher acoustic impedence (higher stiffness for the same density), which indicates different mechanical properties of the tissues (Elbaum et al. 2007). e) f) show X-ray scattering patterns of the two tissues (Elbaum et al. 2007), radially integrated in g) (the red curve being from e) and the blue curve from f) (Elbaum et al. 2008). h) False coloured SEM image of the siliceous hairs on the outside of the awns (image courtesy of M. Eder). that act to allow it only to be propelled in one direction upon changes in humidity as illustrated schematically in i) (Elbaum et al. 2007). j) SEM image of a cross section of one of the actuating cells showing multi-laminate structure (Zickler et al. 2012). A simple finite element model consisting of alternate layers of 0° and 90° MFAs with varying thickness (k), illustrates that upon swelling it is also possible to open up cracks between the layers as indicated by the tensile stresses shown in l) (Zickler et al. 2012).

Trees control the arrangement of cellulose microfibrils not only for purposes of actuation, but also to develop large active stresses in their tissues through the production of reaction wood (see e.g. (Wilson and Archer 1977)). These stresses are used to solve the problem that trees face of having branches that get heavier and heavier as they grow longer and longer (Figure 3–5a and b), and to change the orientation of leaning stems for example (Farber et al. 2001, Reiterer et al. 2004). Reaction wood is a specialised tissue grown by a tree that either pushes, in the case of compression wood, or pulls in the case of tension wood branches upright (Figure 3–5c). Compression wood can have large cellulose MFAs of around ~45° and it has been shown through swelling experiments of spruce tissues that these tissues indeed elongate significantly upon swelling, (Burgert et al. 2007), see also the previous discussion (Figure 3–2). In tension wood, a tissue found in about 50% of deciduous trees, an additional microstructural feature to the microfibril angle has evolved, that creates tensile stresses of up to 70 MPa (Okuyama et al. 1994) on the upper side of branches (Mellerowicz and Gorshkova 2012). In these tissues, the lumens of the wood cells (Figure 3–5d) are filled with a so called gelatinous layer (G-layer) consisting of cellulosic material that can be readily removed with enzymatic treatment (Figure 3–5e) (Goswami et al. 2008). X-ray scattering measurements before (Figure 3–5f) and after (Figure 3–5g) this treatment indicate that this G-layer has a very low cellulose MFA with the remaining cell-wall having a structure similar to normal wood (Goswami et al. 2008). From the previous discussion it is clear that a G-layer with longitudinally oriented cellulose microfibrils cannot change dimensions significantly in the longitudinal direction of the cells, but only transverse to the cell axis, i.e. within the plane of the image in Figure 3–5d. These observations led us to develop a simple model to describe the development of tensile stresses in the tissue (Figure 3–5h and i) (Goswami et al. 2008). Any swelling of the G-layer would impart a pressure p on the cell wall, giving rise to radial stresses $\sigma_r = pR/t$, where, R and t, are the cell radius and wall thickness respectively. For a cell-wall reinforced with stiff microfibril angles oriented at an angle μ, it is possible using the same composite mechanics models of Fratzl and co-workers (Fratzl et al. 2008), to predict the relationship between axial stress σ_a and radial stress σ_r:

$$\sigma_a = \frac{\nu + f\cos^2\mu\sin^2\mu}{1 + f\sin^2\mu}\sigma_r \qquad \text{Eq. 3.2}$$

where ν is the Poisson ratio, and $f = \frac{\left(1-\nu^2\right)E_f}{E}$ is the stiffness contrast between fibrils and matrix introduced in Eq. 3.1 (Goswami et al. 2008). This simple model predicts positive tensile stresses being developed for high stiffness contrasts (Figure 3–5j) for MFAs close to those found in the cell wall. Although this is just one hypothesis about the mechanism behind stress generation in tension wood, (see (Mellerowicz and Gorshkova 2012) for a recent critical review), it highlights again the importance of the geometric arrangement of tissues on cell function both inside the cell-wall and inside the lumen. In addition to being found in tension wood, G-layers are found in many other active plant tissues including tendrils (Bowling and Vaughn 2009, Gerbode et al. 2012) and roots (Schreiber et al. 2010) (Figure 3–5k,l). In *Trifolium pratense,* the observation of the formation of g-layers in the root is thought to be responsible for the mechanism by which roots contract pulling the plant into the ground (Figure 3–5m) (Schreiber et al. 2010).

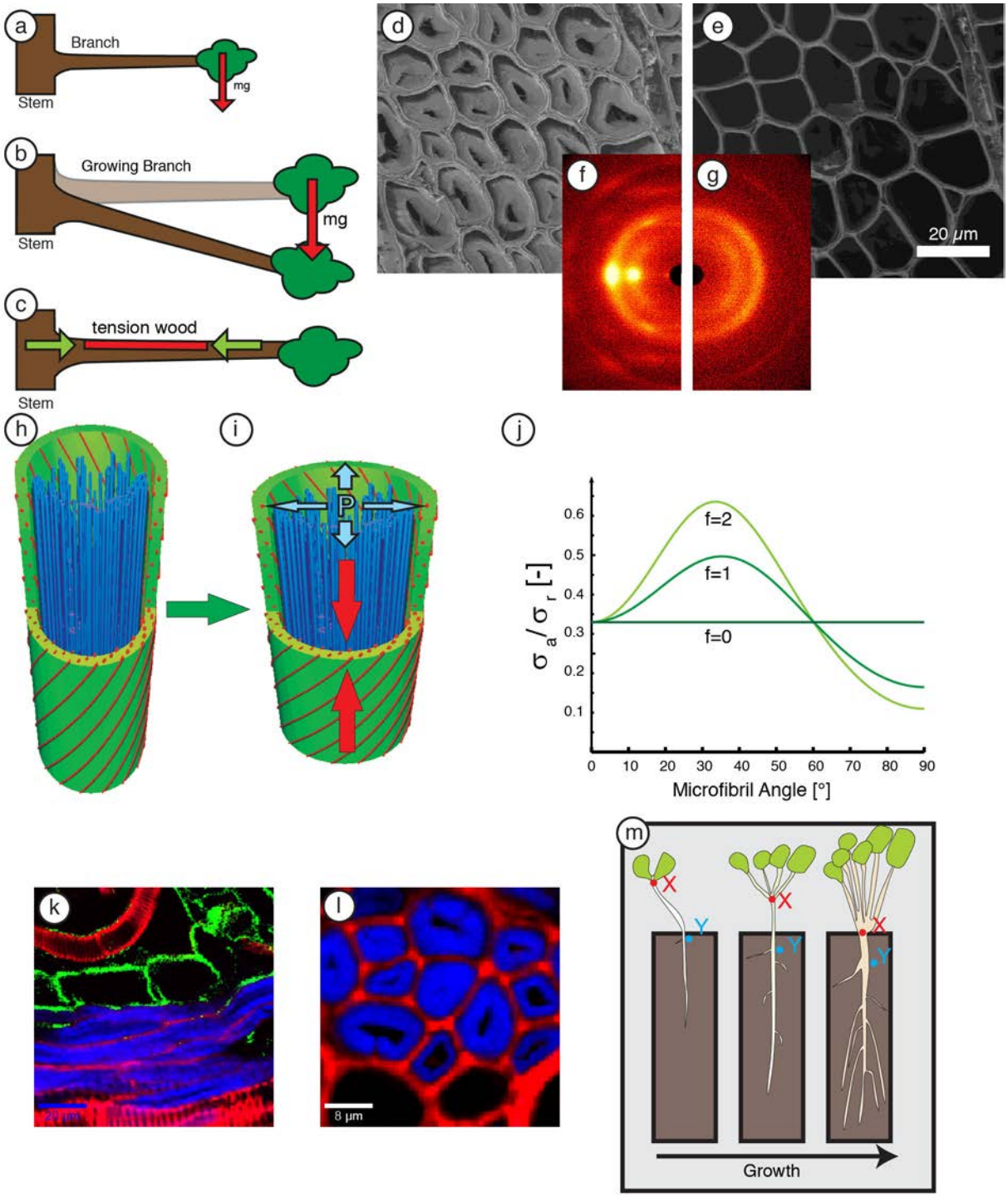

Figure 3–5: Gelatinous layers as alternative structures for stress generation in plant cells
A schematic of a growing tree branch: as a given branch a) grows it gets longer and thicker b). In order to compensate for the increasing bending moment, trees generate so-called reaction wood which can create active stresses to keep branches upright. An example of such tissue is given in d) which shows an SEM image of tension wood in poplar (note the filled lumens of the cells) e) the same tissue after cellulase treatment highlighting the g-layer is mainly cellulose. X-Ray scattering images before f) and after g) enzymatic treatment show that this g-layer consists of low MFA fibrils, whereas the cell-wall has a similar structure to normal wood (Goswami et al. 2008). This leads to a model (h and i) by which the g-layer upon hydration swells and applies a pressure on the cell-wall causing contraction due to the high MFA in the secondary cell wall (Goswami et al. 2008). j) Predicted tensile stress generation as a function of MFA of the secondary cell wall for different values of the stiffness contract parameter f (increasing values indicate higher cell wall anisotropy) (Goswami et al. 2008). In addition to tension wood, G-layers have also been found in the contractile roots of *Trifolium pratense,* as shown in the Raman-images (Schreiber et al. 2010). Upon growth these roots contract pulling the plant into the ground as illustrated schematically in m) (Dunlop et al. 2011).

In addition to controlling the microfibril angle within the cell-wall or the content of the cell-lumen, another geometric feature that plants can use to control function is the shape of the cell-cross section. One example of this mechanism can be found in a specialised tissue within the seed capsules of the ice-plant (*Delosperma nakurense*) (Harrington et al. 2011, Razghandi et al. 2014) (Figure 3–6). These plants occur near coastlines around the world in typically quite arid areas. After flowering, a protective seed capsule is formed (Figure 3–6a) which holds seeds back only opening when the capsule comes in contact with sufficient rain (Figure 3–6b and c). Upon contact with further raindrops these seeds can then be splashed out into the surroundings (Parolin 2006). Interestingly these capsules are not responsive to changes in humidity, common in the regions where they are found, meaning seeds are only released into a wet environment suitable for germination.

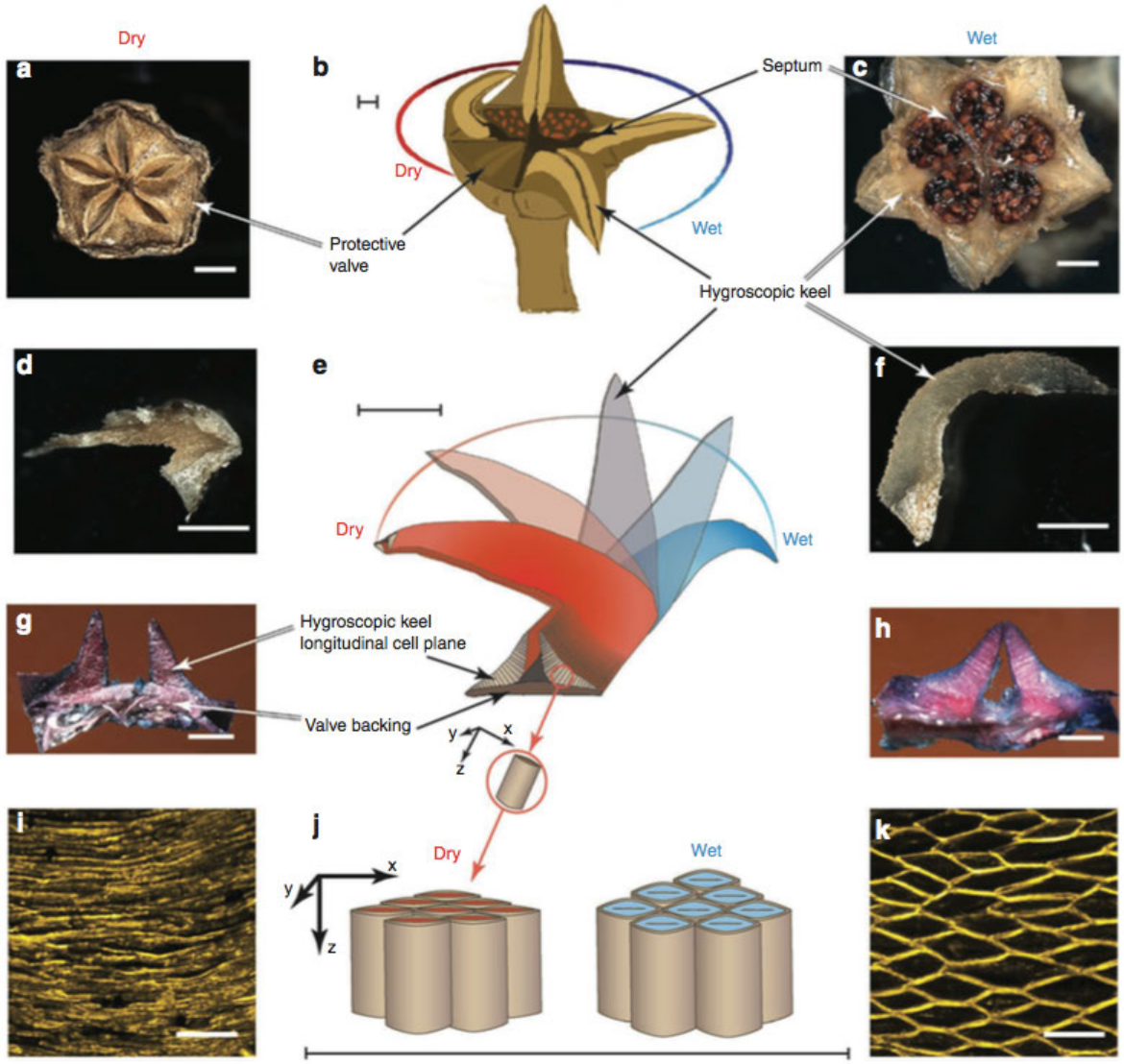

Figure 3–6: Hygroscopic opening of the ice-plant seed capsule is controlled by tissue microstructure
Illustration of the different levels of architectural complexity in the ice-plant seed capsule at different length scales (a-k). On the left hand side, images show the different tissue structures in the dry state and on the right hand side in the wet state. The central column gives schematic illustrations of the different tissues. Scale bars are defined as: a and c = 2 mm; b, e and j≈1 mm; d and f=1mm; g and h=0.5mm; i and k=0.1mm. (Harrington et al. 2011)

The protective valves holding the seeds back inside the seed capsules are actuated by a tissue called the hygroscopic keel, which when dissected away from the backing shows large displacements upon wetting (Figure 3–6d, e and f). The backing itself is passive, although it changes curvature slightly upon wetting of the keel tissue

(Figure 3–6g, and h). The microstructural features of the plant cells responsible for the large swelling of the keel tissue are illustrated in (Figure 3–6 i, j and k), which show keel cross sections in the dry and wet state respectively. In the dry state cells are collapsed, making it somewhat difficult to visualise their shape, but when swollen an array of cells with diamond shaped cross-sections can be seen. The lumens of these cells are filled with a cellulose-like material, akin to a G-layer, that swells upon wetting as demonstrated by enzymatic treatments (Harrington et al. 2011). The mechanics of such honeycomb-like structures is well known (Gibson 2005, Gibson et al. 2010), and from this it is intuitive that such a structure will swell along the short or soft direction of the honeycomb (vertical direction in(Figure 3–6 I and k). This being said it is curious that despite the huge amount of literature available on the mechanics of cellular solids, there is still a lot to be learnt about these structures their behaviour under pressure.

This brief overview has given an insight into some of the design principles controlling hygroscopic actuation in the plant world. In particular we have focussed on the concept of the microfibril angle, as this allows plants to modify greatly the mechanical and actuation response by just changing one simple geometric parameter, while keeping the chemistry of the cell-wall essentially constant. Actuation responses can be also amplified through the presence of a swellable medium inside the lumens of plant tissues as well through the tight control of cell-shape. All of this highlights the important role that the geometric arrangement of swellable and non-swellable tissues has on resultant tissue deformations, something that will be explored in more detail in the following.

3.2 Results and Discussion

The key results of the author's research related to actuation are reproduced and discussed in the following section. A detailed publication list is given in Section 6.1, and each publication in this list is indicated in the text by it's number, i.e. **[AC1]** or **[AC2]** and is reproduced in Section 7.

From the previous discussion of the mechanics of natural actuators, it is clear that the geometric arrangement of swellable and non-swellable components in a tissue controls the macroscopic shape change observed. In some situations, such as the simple bi-metallic beam used in thermostats (Timoshenko 1925), the macroscopic response is perhaps quite intuitive. If one side of a beam swells in the direction of the long axis of the beam and the other one doesn't then it is clear the beam will bend in order to minimise the elastic energy arising from the different strains on each side. This being said, great complexity in the resultant motion can arise due to the presence of free boundaries, or due to the actuating system having several (meta)stable minimal energy configurations that can be reached when swelling is non-uniform. In the following, several examples are presented of more general studies on the role of geometric constraints on actuation of 1D and 2D structures. Although our work here is mainly done from a theoretical perspective, collaborations with polymer chemists enabled us to compare simulations with experiments, allowing us on one hand to understand interesting phenomenon observed in polymeric actuators, but also to predict new behaviour not yet observed in these systems. The experimental work on patterned bi-layers was done in the group of Leonid Ionov (Leibniz Institute, Dresden) and the graded porous actuators was done in the group of Jiayin Yuan (Colloids Department, MPIKG, Potsdam). The 3D printing of the swellable honeycombs was done by James Weaver (Wyss Institute, Harvard) although the swelling experiments were performed in our group.

The role of symmetry on 1D actuators [AC1]

Inspired by work done that we did together with Rivka Elbaum on the awns of *Erodium* (Abraham et al. 2012), that twist and coil upon drying (Figure 3–1b), and the awns of wheat (Zickler et al. 2012) that bend, we started investigating the role of internal and external geometry on "pseudo" 1D actuators (Turcaud et al. 2011). The analysis is simplified by reduction to one dimension i.e. we focus on long beams that in principle could be manufactured by extrusion. We therefore assume that the shape of the cross section, and the arrangement of the swellable/non-swellable components within a cross section, is invariant along the beams length. Starting with perhaps the simplest section geometry of a square, at least with respect to the restrictions of the discrete nature of finite element simulations, we investigated how the symmetry of the arrangement of swellable (blue) and non-swellable (red) materials controlled actuation (Figure 3–7a). According to Curie's principle (Curie 1894) which states that the symmetry of the effects should at least have the same symmetry as the causes, we would expect that as long as we remain in a regime of linear elasticity then the resultant deformation of a beam should respect the symmetry of the distribution of the swellable and non-swellable components. This has the consequence that, of the cross sections illustrated in (Figure 3–7a), those that have mirror symmetries will bend in the mirror plane, and those with rotational symmetries will twist around the rotational axis. If combinations of symmetries occur then this results in "symmetric locking" as bending or twisting would break remaining symmetries. To test this we performed finite element simulations on beams consisting of these structures (Figure 3–7b and c), and indeed structures with cross sections such as the second line and fifth line of (Figure 3–7a),

twist and rotate respectively, although the twisting was minimal. In order to increase the twisting of these structures we also investigated the role of changing the external cross section (Figure 3–7d, e and f), and showed that by increasing the distance of the swelling contrast from the rotation axis we could achieve greater actuation. More recent experimental work using 3D printing supports these ideas and highlights the important role of internal material symmetry on actuation.

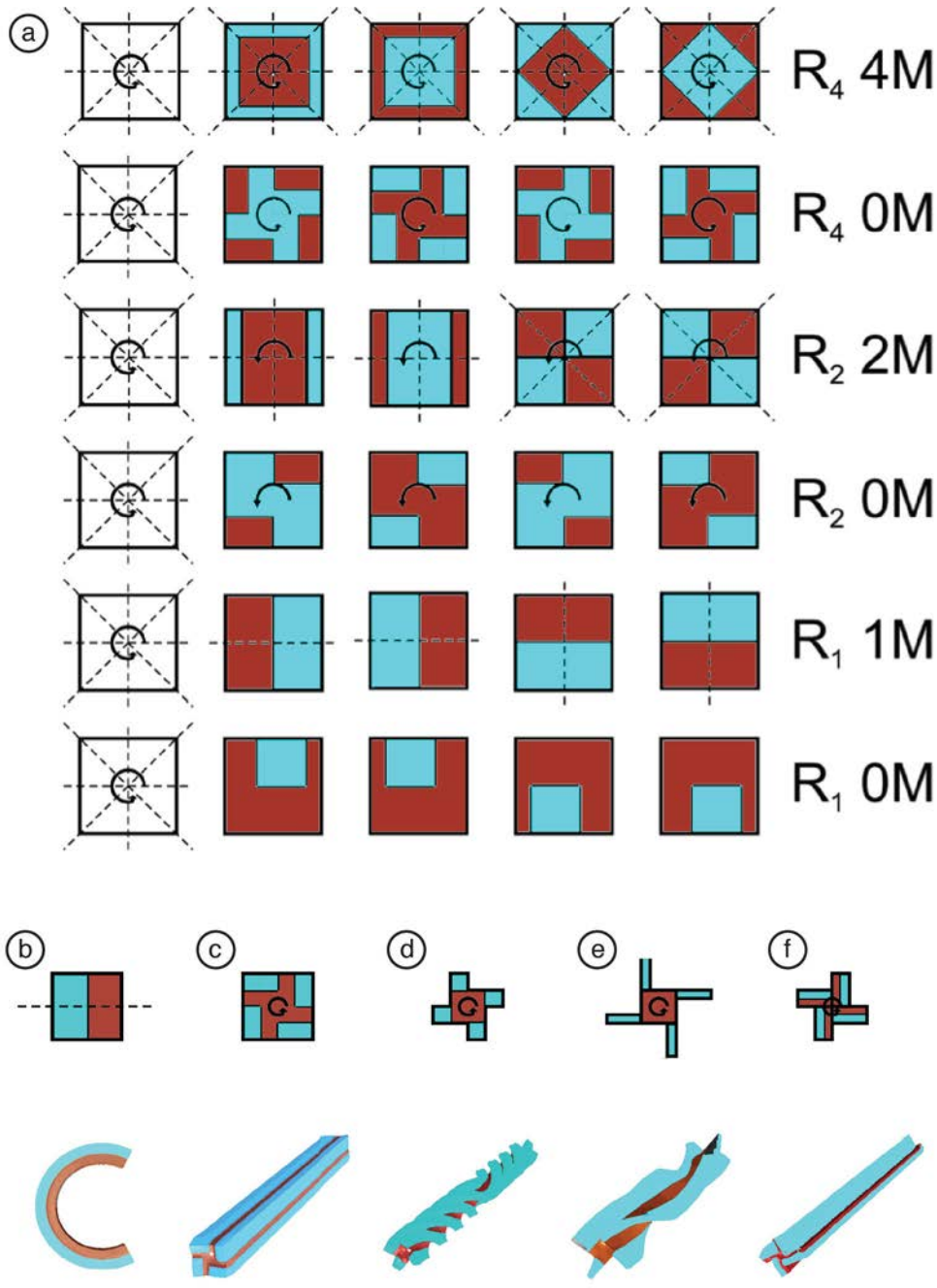

Figure 3–7: Extrudable bi-material actuators
a) Examples of cross sections of extrudable bi-material actuators with their respective rotational R and mirror M symmetries. From the Curie principle these symmetries will have a consequence on the resultant motions available. b) example images of finite element simulations of 1D extrudable actuators consisting of a swellable (blue) and non-swellable (red) phase giving rise to bending or even twisting. (Turcaud et al. 2011)

Spatio-temporal control of actuating bi-layers [AC2, AC3]

Leonid Ionov and co-workers had previously demonstrated the possibility of using bi-layer structures of PolyNIPAM and PMMA patterned on silicon wafers using photolithography to generate self-rolling structures that actuate upon changes in temperature (Zakharchenko et al. 2010, Stoychev et al. 2011). These structures can find potential application in the producing devices for the encapsulation of cells and drugs. Upon heating the PNIPAM layer absorbs water and swells, giving rise to local bending and therefore actuation. Although this sounds rather straightforward a certain amount of complexity can arise as the PNIPAM layer is attached to the substrate, which means swelling and therefore bending starts at the edge of the patterns (Figure 3–8a,b). Our group joined the project in order to help provide a theoretical understanding of the complex actuation behaviours observed. We investigated the rolling behaviour of rectangular bi-layers of different aspect ratios, using finite element simulations, where it was found that there was a change in rolling behaviour from diagonal to long side rolling (Figure 3–8c and d). (Stoychev et al. 2012). This behaviour was unusual, as free rectangular bi-layers are expected to roll along their short sides from energetic considerations (Alben et al. 2011), however we could demonstrate the importance of the spatial control of the kinetics of actuation (due to the diffusion front) in driving actuation into alternative minimum energy configurations. Further work with different patterns of circular, elliptical and star like patches, showed that upon edge actuation the boundary would start to wrinkle (Figure 3–8e). This is similar to what has been observed (and modelled) in the edge growth of leaves (Liang and Mahadevan 2009) or flowers (Liang and Mahadevan 2011) or in the patterns observed during tearing of polymer membranes (Audoly and Boudaoud 2002). Our simulations predicted that the number of wrinkles would be inversely proportional to the length of the diffusion front (or actuation depth) (Figure 3–8f) and this was confirmed experimentally (Figure 3–8g-j). Eventually as wrinkling progresses, tubes form on the sides of these membranes creating local stiffening elements that block the bi-layers from completely rolling forcing the bi-layer to fold in complex ways (Stoychev et al. 2013).

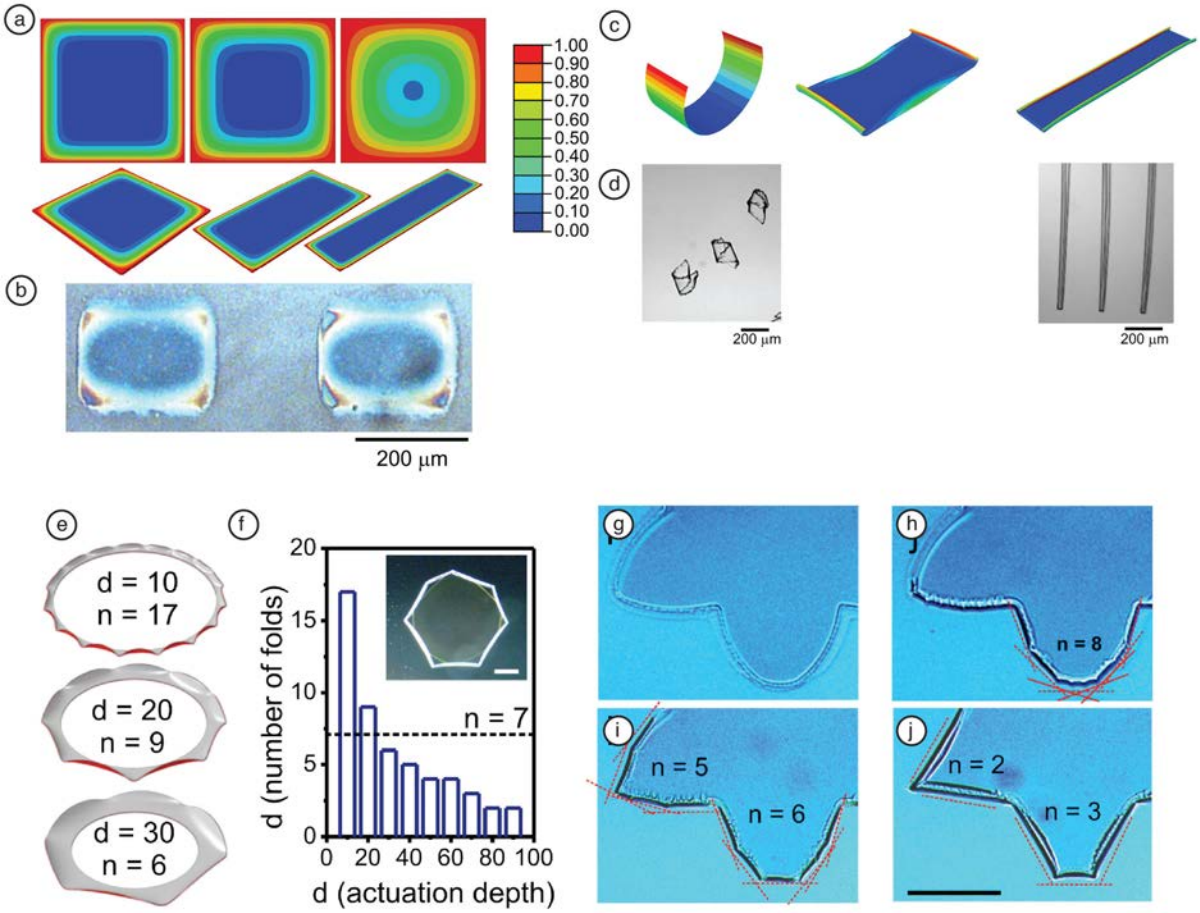

Figure 3–8: Spatial control of actuation fields in patterned bi-layers
a) Predicted concentration profiles due to edge diffusion patterns as a function of time (top) and for different shapes (bottom) b) Actual diffusion profiles observed in membranes c) Simulated actuation of the bi-layer due to swelling induced by the predicted concentration profiles d) Observed long-versus short rolling as a function of bi-layer geometry (Stoychev et al. 2012) e) Circular patches develop wrinkles with a number of wrinkles being inversely proportional to actuation depth f), Such wrinkling is indeed observed with the number of wrinkles decreasing as actuation proceeds (g-j) (Stoychev et al. 2013).

Ultrafast actuation of poly-ionic liquids [AC4, AC5]

One challenge in designing actuating devices that operate due to local swelling, is the inherently slow kinetics of the diffusion of solvents into the swellable material. In the example of the wheat awn (Elbaum et al. 2007, Elbaum et al. 2008, Zickler et al. 2012) this appears to be controlled by the plant by actively creating new porosity by controlled cracking during the swelling process itself (Figure 3–4). By developing poly-ionic liquid membranes with high porosity the group of Jiayin Yuan has have recently developed actuating membrane materials that respond almost instantaneously to changes in concentrations of a variety of different solvent vapours (Zhao et al. 2014, Zhao et al. 2015). Our group's role is to interpret the mechanical data in order to understand the role of the gradient in electrostatic complexation through the cross-section of the membranes upon actuation. This gradient is thought to result in a change in swellability and stiffness giving rise to bending upon contact with solvents, potentially minimising the development of large interfacial stresses. Current work is being done to control the orientation of bending, by incorporating stiff fibres in defined orientations into the membrane.

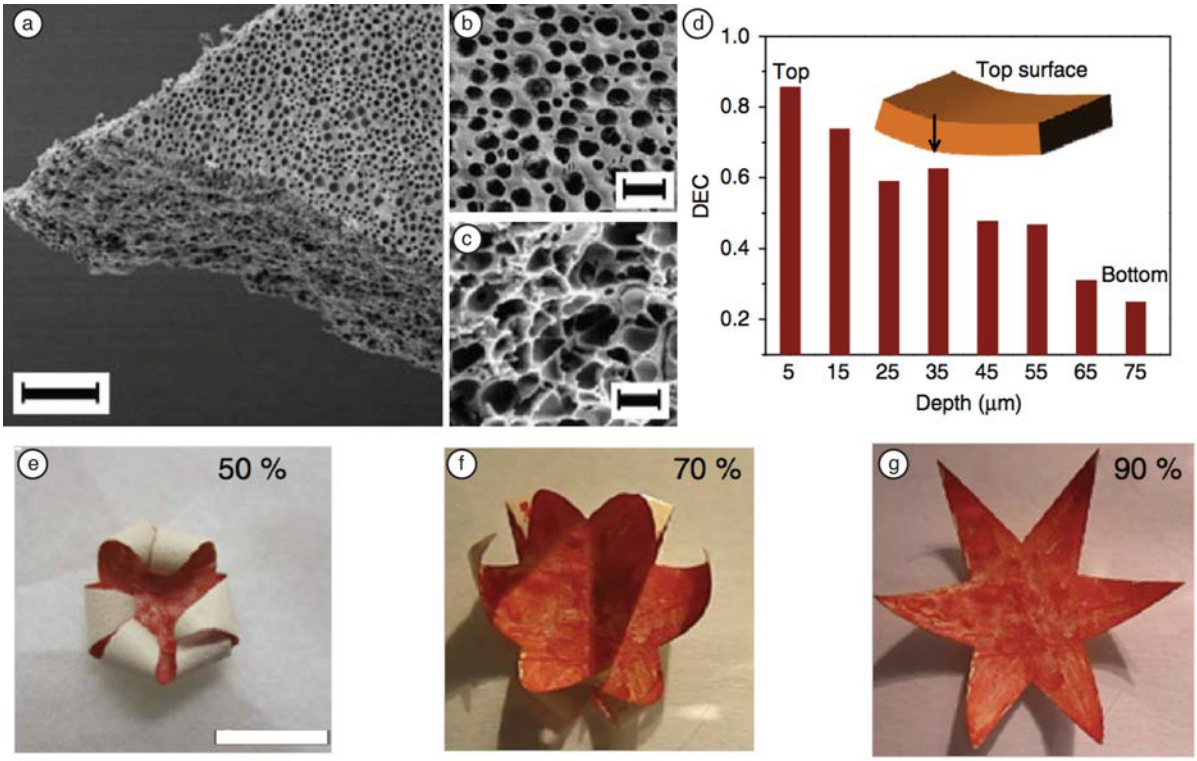

Figure 3–9: High speed porous actuators
a) SEM image of porous poly-ionic liquid actuator (scale bar 30 μm) close up of b) top surface (scale bar 3 μm) and c) bulk (scale bar 1μm). d) Measurement of the gradient in the degree of electrostatic complexation (DEC) throughout the thickness of the membrane. e-f) reversible actuation due to changes in humidity of a star-shaped membrane (Zhao et al. 2014)

The mechanic response of swellable honeycombs [AC6, AC7]

Inspired by the structures of the tissues found in the ice plant (Figure 3–6), we started investigating the mechanical response of swellable honeycombs using finite element (FE) simulations and simple micromechanical models (Guiducci et al. 2014). These 2D simulations were used to determine the role of internal pressure on the elastic deformation of the honeycomb as a function of wall stiffness and other geometric factors (Figure 3–10). Upon pressurization the honeycomb deforms first anisotropically, with large contraction in the short cell-direction, as observed in the ice-plant (Figure 3–10a, and b). After a certain pressure the cells are square and the swelling behaviour becomes isotropic (Figure 3–10c). Parametric simulations enabled maps of actuation strains and effective honeycomb modulus to be produced as a function of pressure and wall-stiffness (Figure 3–10d and e). Although FE simulations enable realistic swelling behaviour to be accurately modelled, it is difficult to extract the key architectural parameters that control the observed behaviour. It is known that the energy of stretching or bending of the cell-walls dominates the in-plane tensile and compressive response of honeycombs (Gibson 2005, Gibson et al. 2010). To test this we developed a simplified bead-spring model, that gave actuation behaviour matching well the FE simulations (Figure 3–10f and g). This bead-spring model highlights the importance of the ratio of the energies of wall-stretching to wall bending on the actuation behaviour of swellable honeycombs. Such structures can also be printed using advanced multi-material 3D printing, which allow for the printing of polymers with different cross-linking densities. Upon immersion in a suitable solvent the polymer with the lowest cross-linking density will swell the most allowing us to test actuation behaviour (Figure 3–10h). See also (Ge et al. 2013) for one of the first publications on this so-called "4D printing".

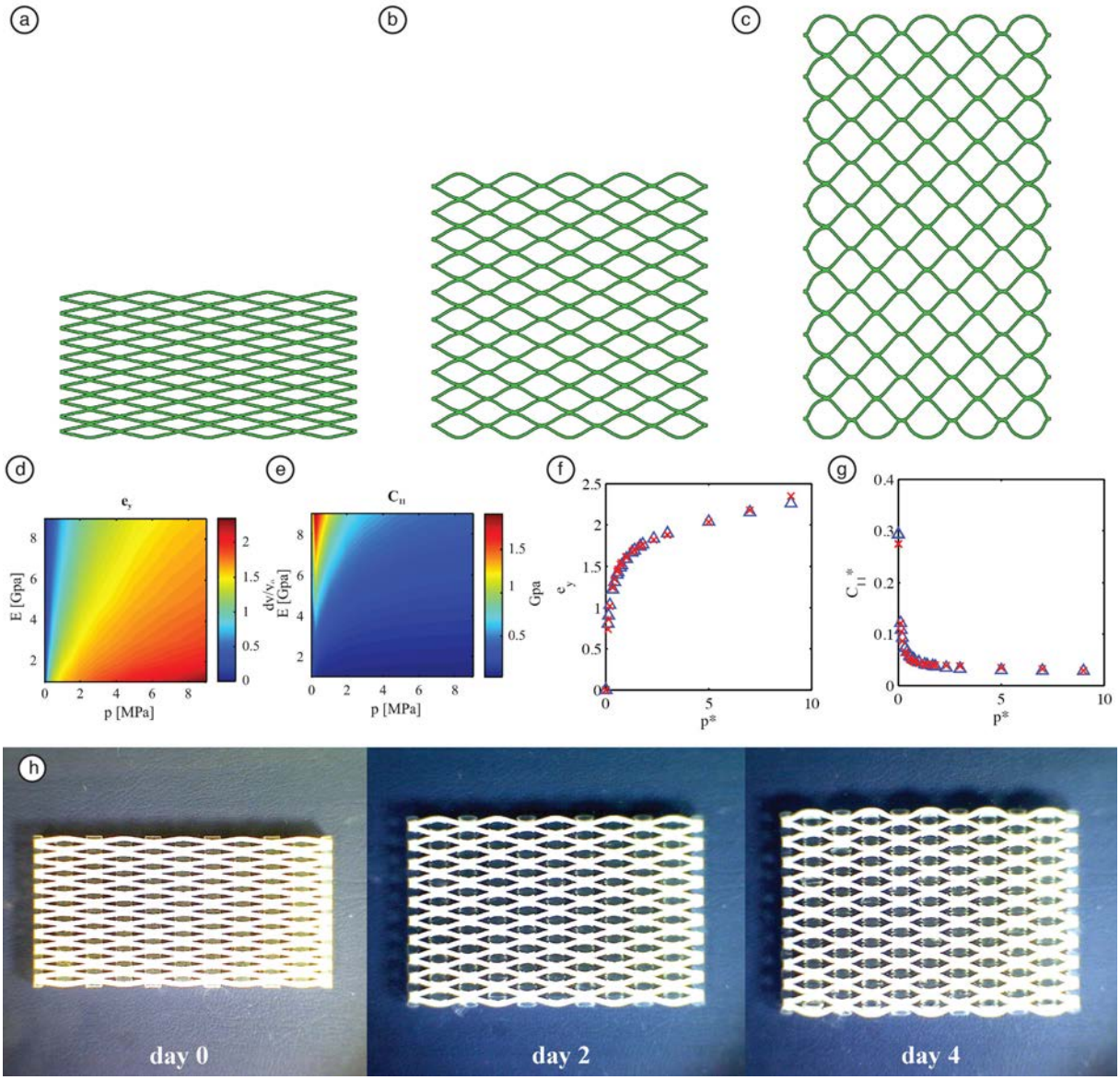

Figure 3–10: The mechanics of swellable diamond-cell honeycombs
Finite element simulations of diamond honeycombs with a wall-modulus of 1GPa for different actuation pressures a) 0 , b) 0.3 and c) 7.5 MPa. Maps of d) actuation strain and e) effective modulus in the vertical direction as a function of actuation pressure and wall stiffness. These maps can be collapsed to master curves f) and g) which match well to the results of a simplified bead-spring model (Guiducci et al. 2014). h) Rapid prototyped specimens of diamond honeycombs printed with a swellable (clear) and non-swellable (white) material as a function of swelling time.

One of the consequences of developing the bead-spring model is that we started wondering how one could change the effective wall stiffness (thus reducing the wall stretching energy) without making the walls too thin. Using similar approaches (FE-simulations and 3D printing) we came up with the idea of introducing kinks into the walls of the cells creating local flexible links in the structures (Guiducci et al. 2015) (Figure 3–11). What quickly became apparent is that by simply controlling the shape and the arrangement of the cells it was possible to generate a wide range of actuation behaviour, converting isotropic swelling in the pores to deformations ranging from uniaxial to shear deformations.

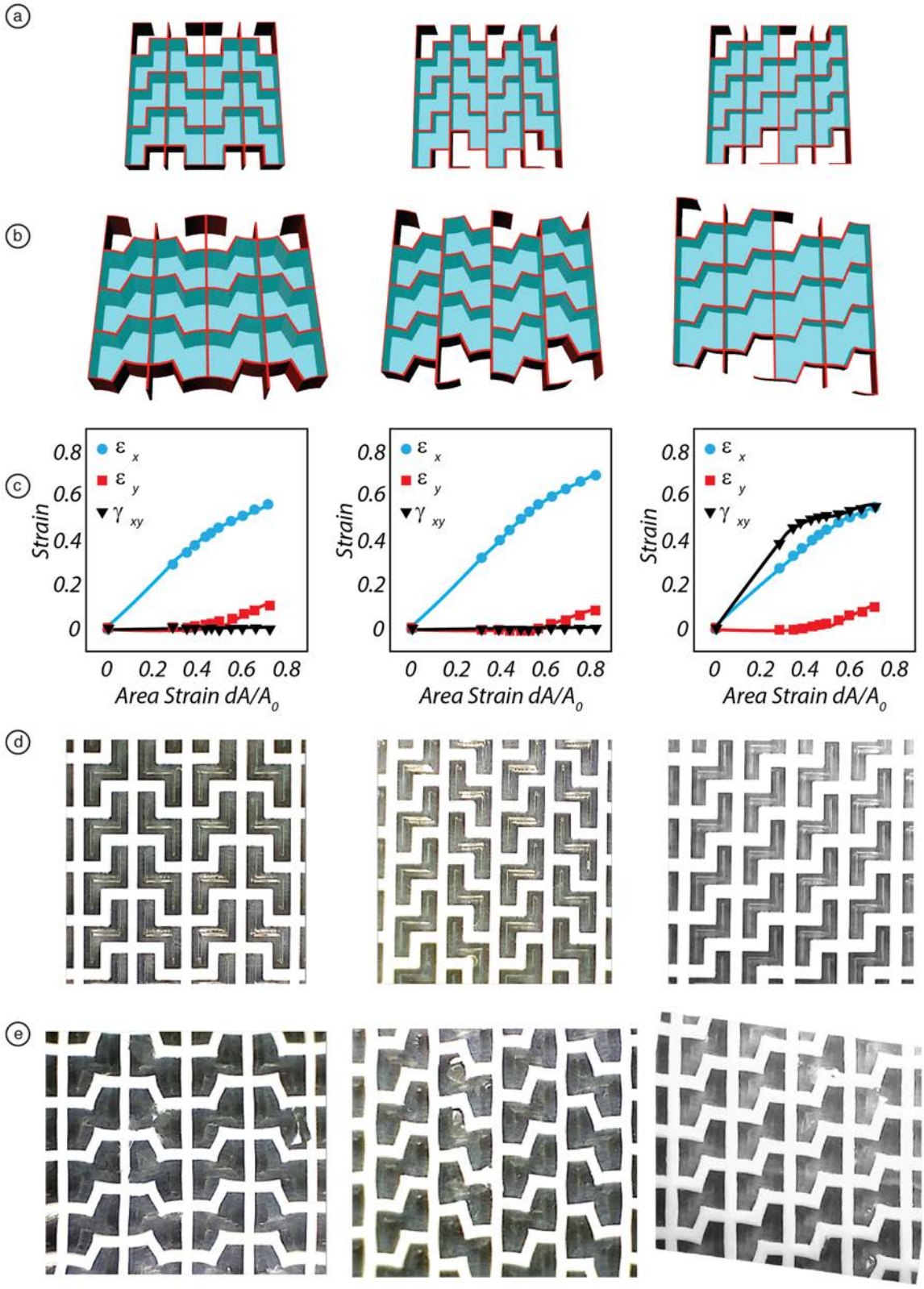

Figure 3–11: Complex honeycombs with more complex shapes
Finite element simulations of three different honeycombs a) before and b) after swelling. c) Normal and shear strains plotted as a function of the uniform swelling strain for the three different honeycombs (FE Simulations). D) 3D printed models of the honeycombs (cell size ~cm) consisting of swellable (clear) and non-swellable (white) polymers before swelling and e) after swelling in isopropanol (Guiducci et al. 2015).

3.3 Summary

In this chapter we have highlighted the importance of geometric constraints on actuation. Much of this work is inspired by observations of hygroscopic actuation from the plant world, where plants encode the ability to actuate in complex ways inside their tissues, and surprisingly keep this function long after the tissue is no longer metabolically active. In our work we have shown for 1D actuators the importance of the symmetry of the cross-sections.

Key outcomes of this combination of theoretical and experimental research are:

- The important role of the symmetry of the distribution of swellable components on the symmetry of deformation. This was observed in 1D actuators but also similar effects can be found in the tiling of pores in the honeycomb based actuators
- The possibility of controlling the time of actuation, for example due to the diffusion controlled swelling from the edges of bi-layers, in order to get systems to actuate into metastable intermediate states.
- The use of pore shape to modulate wall stretching energies, in order to control actuation behaviour in swellable honeycomb actuators.

In the group we have only started investigating synthetic and theoretical systems. However our results support the importance of understanding geometric boundary constraints in the design of novel actuating materials. A promising direction is that of investigating the mechanics of porous actuators, of which we have only scratched the surface and not yet even looked at 3D.

The following section will give an outlook of the sort of research that can be done next based on the outcomes of this thesis.

4 Conclusions and Outlook

This cumulative habilitation thesis has provided a short overview of selected research done inside the group "Biomimetic Actuation and Tissue Growth". This research is reported in more detail in the attached full papers (see Section 6.1 for a list and Chapter 7 for the manuscripts). The group has focussed on two different research topics, that of shape changes in biology due to the processes of growth and shape changes due to local swelling in response to changes in the external environment. In both research directions we have used a combination of theoretical approaches together with experiments supported by advanced 3D printing technologies. The use of 3D printing allows for accurate spatial control of structures for cell-culture or even to directly print actuators. Despite the differences in the two topics they both share important commonalities in that the outcome of localised growth and localised swelling is a macroscopic shape change. As such similar theoretical tools, especially those developed in the continuum mechanics community can be used to describe both processes. Our work has demonstrated clearly the importance of geometric constraints via mechanics on both growth and actuation, and although we have made progress in quantifying and modelling both processes, there is much still to be done. Some key directions that are promising are as follows:

- The role of 3D surface curvature on tissue growth. One perhaps glaring omission in the research presented in this thesis is that we have till now only investigated pores with straight sides (i.e. zero Gaussian curvature). Although we have shown that curvature in these pores controls growth, due to experimental limitations we have not been able to observe surfaces with arbitrary principle curvatures, to work out what curvature (mean, Gaussian or principle curvatures) truly controls growth.
- The role of mechanical signalling on growth. We are now getting much closer to understanding some of the biophysical mechanisms behind tissue growth. It is clear that mechanical signalling is fundamental to long-range cell communication and organisation, and likely to be responsible for some of the behaviours described in this thesis. To test this it would be useful to mechanically perturb a growing tissue locally, either by local application of a force or by biochemical methods.
- Influence of geometry on extra-cellular matrix organisation. Still unclear are biophysical principles behind the long-range organisation seen in the extra-cellular matrix. One problem is that although cell or agent based models can describe cell patterning, they are very limited when it comes to combining cell-behaviour with the formation of structured extracellular matrix. Such work also requires advanced 3D visualisation techniques for example light sheet microscopy to observe cell motion and ECM structure in large volumes in a time resolved way.
- The role of cell-type or state on geometry sensing. The data discussed in this thesis has mainly dealt with one single osteoblast cell line and it is unclear how general the observations are. In recent work we applied our experimental approach to a fibroblast cell line as well as mesenchymal stem cells in a collaboration with the group of Carsten Werner, Dresden (Herklotz et al. 2015). This early work suggests that the behaviour observed in our osteoblasts is generalizable, however a more systematic study is required to confirm this.
- How timing of actuation can be used to control shape changes. We have shown experimentally that by controlling the location and timing of the actuating field we

can force actuators to undergo metastable shape changes, that may not be the global elastic energy minimum. Currently we have no theoretical framework that can predict such behaviour ad-hoc, and further work is required to develop models to do this.

- Exploring the possibilities of actuating honeycombs. The honeycombs actuators we have looked at until now have been rather simple. Although our most recent paper highlights the role of cell shape and tiling on actuation, this has not yet been looked at in a systematic manner and it is still not clear what are the physical limitations in possible actuation behaviours observed in such structures.
- Exploring the possibilities of 3D porous actuators. The honeycomb actuators have an advantage as they can be readily modelled in 2D and visualised. The principles that control the behaviour of such structures are of course also valid in 3D. In order to solve this however one needs to overcome issues of visualising deformation in 3D, and ensuring that swelling is uniform throughout the interior of a swelling structure.
- Combining actuation and tissue growth. A final promising direction is to combine the work done on actuating structures with the work on tissue growth. As cells are contractile, it could be that they develop sufficient forces to be able to deform the substrate giving rise, potentially to large scale macroscopic shape changes.

The work presented in this thesis into the biophysics of shape changes in tissues and actuating structures is basic research, however its outcomes may have important implications to society in the fields of medicine and engineering. An understanding of the role of shape on tissue behaviour, for example, could help biomedical engineers design more efficient scaffolds for tissue repair. One point that is still not clear how much biology should a scaffold provide? Scaffolds with zero mean surface curvature certainly mimic the surface topology of trabecular bone, but they may not be a good solution as cells are not stimulated sufficiently to allow for growth. The development of extensive geometric design rules for actuators for example would have applications in the developing field of soft robotics, or in the development of low-energy sensors operating autonomously with changes in environmental conditions. Although interest in these research topics is not new, as highlighted by the many historical examples cited in the introduction, the combination of modern analytical techniques with advanced numerical modelling and the possibility of collaborating with people over many disciplines, suggests a richness in potential that will be keeping scientists excited and busy for many years to come.

5 List of Figures and Permissions

5.1 Figure List

Figure 1–1: Some historical examples of studies of shape changes in biology 2
Figure 1–2 : Map of major constituents of biological tissues. 4
Figure 1–3 : Properties of a sample of biological materials. 5
Figure 1–4: Multi-scale composite architectures in Bone and Wood 6
Figure 1–5: Describing shape changes of biological tissues 8
Figure 2–1: Physical interactions between a cell and its environment 11
Figure 2–2: Cells interact and respond to geometric features in 2D and 3D over many length scales 13
Figure 2–3: The geometry of substrates play an important role on *in-vivo* tissue behaviour 15
Figure 2–4: The collective interactions of cells leads to fluid like behaviour of tissues 17
Figure 2–5: Liquid-crystal-like order in biological tissues and synthetic counterparts 18
Figure 2–6: Experiments and simulations of tissue growth in convex pores 20
Figure 2–7: Effect of the substrate on experimental and simulated tissue growth 23
Figure 2–8: The role of pore convexity on tissue growth 25
Figure 2–9: Curvature driven growth model as a scaffold design tool 26
Figure 2–10: Growth in pores mimicking bone-like structures 27
Figure 2–11: The microstructure of different tissue components as a function of geometry 28
Figure 2–12: Tissues modelled as stacked “chord-like” elements 29
Figure 2–13: Continuum mechanics model of tissue growth 31
Figure 3–1: Examples of natural actuators powered by water 33
Figure 3–2: The cellulose microfibril angle controls the mechanics and swelling of the plant cell wall 36
Figure 3–3: Hygroscopic opening of pine cones 38
Figure 3–4: Hygroscopic motion in the awns of wheat 40
Figure 3–5: Gelatinous layers as alternative structures for stress generation in plant cells 42
Figure 3–6: Hygroscopic opening of the ice-plant seed capsule is controlled by tissue microstructure 43
Figure 3–7: Extrudable bi-material actuators 46
Figure 3–8: Spatial control of actuation fields in patterned bi-layers 48
Figure 3–9: High speed porous actuators 49
Figure 3–10: The mechanics of swellable diamond-cell honeycombs 50
Figure 3–11: Complex honeycombs with more complex shapes 51

5.2 Permissions

Figure 1–1 a) Image of *Nautilus pompilius* taken from Chenu (1842), (no longer under copyright). Scanned version was downloaded from the online resource: http://www.biolib.de. b) Image by Galileo (1638) on the role of mechanics on the scaling of bone with body size, from his Dialogues concerning two new sciences (no longer under copyright), taken from the online resource: https://ebooks.adelaide.edu.au/g/galileo/dialogues/complete.html c) Image from Trembley (1744), (no longer under copyright). Scanned version downloaded from the online resource, the Biodiversity Heritage Library: https://archive.org/details/mmoirespourservi01trem d) Image from Buller (1958), (no longer under copyright). Scanned version downloaded from the Biodiversity Heritage Library: https://archive.org/details/researchesonfung05bull e) Image from Shaw, (1914), (no longer under copyright). Scanned version downloaded from the internet archive: https://archive.org/details/genuspinus00shawuoft f) Image from Shaw, (1914), (no longer under copyright). Scanned version downloaded from the internet archive: https://archive.org/details/genuspinus00shawuoft, f) Image from Darwin (1875), (no longer under copyright). Scanned version downloaded from the online resource: http://darwin-online.org.uk/reproductions.html

Figure 1–2 Image modified with permission from (Knoll 2003).

Figure 1–3 Produced using the Cambridge Engineering Software with permission from Mike Ashby.

Figure 1–4 - Schematics were adapted from (Dunlop and Fratzl 2010) with permission and (Dunlop and Fratzl 2013) with permission from Elsevier. a) Was produced using Jmol: an open-source Java viewer for chemical structures in 3D. http://www.jmol.org/ with data downloaded from the protein data base, www.rcsb.org/pdb/, PDB ID: 1CAG, from the paper (Bella et al. 1994). b) Image adapted from (Fratzl et al. 2004), c) Image adapted from (Fratzl and Weinkamer 2007) with permission from Elsevier. d-g) Reproduced from (Fratzl et al. 2004) with permission from the Royal Society of Chemistry, h) Was produced using Jmol: an open-source Java viewer for chemical structures in 3D. http://www.jmol.org/ with data from (Nishiyama et al. 2003). i) Was based on (Keckes et al. 2003); j) Was drawn using Rhino software with assistance from Michaela Eder. k) SEM image was kindly provided by Michaela Eder, l) Was based on (Burgert et al. 2007), m) SEM image was kindly provided by Michaela Eder, n) Was based on (Burgert et al. 2007), o) Was based on data in (Farber et al. 2001).

Figure 2–1 Reproduced from (Kollmannsberger et al. 2011) with permission from The Royal Society of Chemistry. (For authors no formal request is required).

Figure 2–2 a) Image from (Selhuber-Unkel et al. 2010) with permission from Elsevier, b) Image from (Théry et al. 2006) with permission from Wiley and Sons, c) Image from (Chen et al. 1997) with permission of The American Association for the Advancement of Science, d) Image from (Ruiz and Chen 2008) with permission from Wiley and Sons, e) Image from (Nelson et al. 2005) copyright from the National Academy of Sciences (Images can be freely used for non-commercial educational use) ,f) Image from (Sjostrom et al. 2013) with permission from Wiley and Sons, g) Image from (Hohmann and von Freymann 2014)with permission from Wiley and Sons, h) Image from (Ochsner et al. 2007) with permission from the Royal Society of Chemistry, i) Image from (Rajagopalan and Robb 2006) with permission from Elsevier, j) Image from (Engelmayr et al. 2008) with permission from Nature Publishing

Figure 2–3 a) Image from (Shapiro 1988) with permission from the Journal of the Bone and Joint Surgery-American. b-c) Images from (Kerschnitzki et al. 2011) with permission from S. Karger AG Basel, d) Image from (Krauss et al. 2011) with permission

from Elsevier, e-f) Images from (Ripamonti et al. 2012) with permission from Elsevier, g- h) Images from (Jinnai et al. 2002) with permission from John Wiley and Sons.

Figure 2–4 a,b,d) Images based on (Lecuit and Lenne 2007) with permission from Nature Publishing, c) Image from (Foty and Steinberg 2005) with permission from Elsevier, e) Image from (Foty et al. 1996) with permission from the Company of Biologists.

Figure 2–5 a) Image reproduced from (Giraud Guille et al. 2003) with permission from Elsevier., b) Image reproduced from (Weaver et al. 2012) with permission from The American Association for the Advancement of Science, c) Image kindly provided by Michaela Eder, d) Image reproduced with permission from (Giraud Guille et al. 2008) Copyright, © 2008 French Academie des Sciences, published by Elsevier Masson SAS., e) Image reproduced from (Reis et al. 1991) with permission from John Wiley and sons.

Figure 2–6 b-f) Images based on data from (Rumpler et al. 2008) (Creative Commons licence)

Figure 2–7a-b) Images based on data from (Kommareddy et al. 2010), inset from (Kommareddy et al. 2010), (Creative Commons non-commercial licence), c) Image from data coming from the simulations performed by Philip Kollmannsberger, in a manuscript currently under preparation

Figure 2–8a) Image from (Gamsjäger et al. 2013) with permission from Elsevier, b-g) Images from (Bidan et al. 2013) with permission from John Wiley and Sons.

Figure 2–9a-b) Images from (Bidan et al. 2013) with permission from John Wiley and Sons.

Figure 2–10 a) Image courtesy of Ron Shahar see also (Shahar et al. 2011), b) Image from (Gentzsch et al. 2004) with permission from Springer, c-g) Images from (Bidan et al. 2012) (Creative Commons licence)

Figure 2–11a-e) Images from (Bidan et al. 2012) (Creative Commons licence)

Figure 2–12a-b) Images from Bidan et al, manuscript under preparation, c-g) Images from (Bidan et al. 2012) (Creative Commons licence)

Figure 2–13a-b) Images based on (Gamsjäger et al. 2013) with permission from Elsevier, c-e) Images based on data from (Dunlop et al. 2010) with permission from Elsevier, f-h) Images from (Fischer et al. 2015) with permission from the Royal Society

Figure 3–1 a-b) Image from (Brand and Finlay 1996) with permission from Elsevier**,** c-d) Image adapted from (Evangelista et al. 2011) with permission from the Journal of Experimental Biology, e-f) Image from (Armon et al. 2011) with permission from The American Association for the Advancement of Science

Figure 3–2a,c)Images based on (Burgert et al. 2007) with permission from Springer, Image reproduced from (Eder et al. 2013) (Creative Commons Attribution Licence), d-f) Image based on (Fratzl et al. 2008) with permission from the Royal Society of Chemistry.

Figure 3–3 a-b) Image was kindly provided by Michaela Eder, c-d) Image reproduced from (Harlow et al. 1964) with permission, e-h) Image reproduced from (Allen and Wardrop 1964) with permission from CSIRO publishing (http://www.publish.csiro.au/nid/65/paper/BT9640125.htm.), i-j) Image reproduced from (Dawson et al. 1998) with permission from Nature Publishing, k) Image based on (Dunlop et al. 2011) (Creative Commons Licence).

Figure 3–4 a-g) Images reproduced from (Elbaum et al. 2008) with permission from Elsevier**,** b-c,h) Images were kindly provided by Michaela Eder, d-f,i) Images reproduced from (Elbaum et al. 2007) with permission from The American Association for the Advancement of Science, g) Image reproduced from (Elbaum et al. 2008) with

permission from Elsevier, j-l) Images were reproduced from (Zickler et al. 2012) (Creative Commons Licence)

Figure 3–5 a-c) New images sketched by JWCD, d-g,j) Images reproduced from (Goswami et al. 2008) with permission from John Wiley and Sons, h,i,k,l,m) Images reproduced from (Dunlop et al. 2011) (Creative Commons Licence)

Figure 3–6 Panel reproduced from (Harrington et al. 2011) (no permission required, Nature Publishing Group)

Figure 3–7 Panel adapted from (Turcaud et al. 2011) with permission from Carl Hanser Verlag

Figure 3–8 a-d) Reprinted with permission from (Stoychev et al. 2012). Copyright American Chemical Society, e-j) Reprinted from (Stoychev et al. 2013) with permission from John Wiley and Sons

Figure 3–9 (a-g) are reproduced from (Zhao et al. 2014) with permission from Nature Publishing Group

Figure 3–10 Images (a-g) are reproduced from (Guiducci et al. 2014), with permission from the Royal Society Images h are reproduced from the PhD thesis of Lorenzo Guiducci, and the results form part of a publication currently in preparation.

Figure 3–11a) Reproduced from (Guiducci et al. 2015) with permission from John Wiley and Sons

6 References

6.1 Manuscripts forming the basis of this thesis

The following papers form the basis of the results section in this thesis, and are reproduced in the Chapter 7.

Tissue Growth

[TG1] - Rumpler, M., Woesz, A., Dunlop, J. W. C., van Dongen, J. T., Fratzl, P., *The effect of geometry on three-dimensional tissue growth,* **Journal of the Royal Society Interface**, 2008, 5, 1173-1180.

[TG2] - Kommareddy, K. P., Lange, C., Rumpler, M., Dunlop, J. W. C., Manjubala, I., Cui, J., Kratz, K., Lendlein, A., Fratzl, P., *Two stages in three-dimensional in vitro growth of tissue generated by osteoblast-like cells*, **Biointerphases**, 2010, 5, 45-52.

[TG3] - Bidan, C. M., Kommareddy, K. P., Rumpler, M., Kollmannsberger, P., Fratzl, P., Dunlop, J. W. C. *Geometry as a Factor for Tissue Growth: Towards Shape Optimization of Tissue Engineering Scaffolds.* **Advanced Healthcare Materials**, 2013, *2*, 186–194.

[TG4] - Bidan, C. M., Kommareddy, K. P., Rumpler, M., Kollmannsberger, P., Bréchet, Y. J. M., Fratzl, P., Dunlop, J. W. C. *How Linear Tension Converts to Curvature: Geometric Control of Bone Tissue Growth*. **PLoS ONE**, 2012, *7*(5), e36336.

[TG5] Dunlop, J. W. C., Fischer, F. D., Gamsjäger, E., Fratzl, P. (2010). *A theoretical model for tissue growth in confined geometries*. **Journal of the Mechanics and Physics of Solids**, 2010, *58*(8), 1073–1087.

[TG6] Gamsjäger, E., Bidan, C. M., Fischer, F. D., Fratzl, P., Dunlop, J. W. C. *Modelling the role of surface stress on the kinetics of tissue growth in confined geometries*. **Acta Biomaterialia**, 2013, *9*, 5531–5543.

[TG7] Fischer, F. D., Zickler, G., Dunlop, J. W. C., Fratzl, P. *Tissue growth controlled by geometric boundary conditions: a simple model recapitulating aspects of callus formation and bone healing,* **Journal of the Royal Society Interface**, 2015, 12, 20150108.

Actuation

[AC1] - Turcaud, S., Guiducci, L., Bréchet, Y. J. M., Fratzl, P., Dunlop, J. W. C. *An excursion into the design space of biomimetic architectured biphasic actuators.* **International Journal of Materials Research**, 2011, 102, 607–612.

[AC2] - Stoychev, G., Zakharchenko, S., Turcaud, S., Dunlop, J. W. C., Ionov, L. *Shape-Programmed Folding of Stimuli-Responsive Polymer Bilayers*. **ACS Nano**, 2012, 6(5), 3925–3934.

[AC3] - Stoychev, G., Turcaud, S., Dunlop, J. W. C., Ionov, L. *Hierarchical Multi-Step Folding of Polymer Bilayers*. **Advanced Functional Materials**, 2013 23, 2295–2300.

[AC4] - Zhao, Q., Dunlop, J. W. C., Qiu, X., Huang, F., Zhang, Z., Heyda, J., et al. (2014). *An instant multi-responsive porous polymer actuator driven by solvent molecule sorption*. **Nature Communications**, 5, 4293.

[AC5] - Zhao, Q., Heyda, J., Dzubiella, J., Täuber, T., Dunlop, J. W. C., Yuan, J., *Porous poly(ionic liquid) actuator with ultra-high sensitivity to solvents*, **Advanced Materials**, 2015, 27, 2913-2917.

[AC6] - Guiducci, L., Fratzl, P., Bréchet, Y. J. M., Dunlop, J. W. C. (2014). *Pressurized honeycombs as soft-actuators: a theoretical study*. **Journal of the Royal Society Interface**, 20140458.

[AC7] - Guiducci, L., Weaver, J. C., Bréchet, Y. J. M., Fratzl, P., Dunlop, J. W. C., *The Geometric Design and Fabrication of Actuating Cellular Structures,* **Advanced Materials Interfaces**, 2015, online DOI: 10.1002/admi.201500011

6.2 Full Publication List

Review Articles

- Weinkamer, R., Dunlop, J. W. C., Bréchet, Y. J. M., Fratzl. P., *All but diamonds – biological materials are not forever*, **Acta Materialia**, 2013, 61 ,880-889.
- Eder, M., Arnould, O., Dunlop, J. W. C., Hornatowska, J., Salmén, L., *Experimental micromechanical characterization of wood cell walls*, **Wood Science and Technology**. 2013, 47, 163-182.
- Dunlop, J. W. C., Fratzl, P., *Multilevel Architectures in Natural Materials*, **Scripta Materiala**, 2013. 68, 8 -12.
- Dunlop, J. W. C., Weinkamer, R., Fratzl, P., *Artful interfaces within biological materials*, **Materials Today**, 2011, 14, 70-78.
- Kollmannsberger, P., Bidan, C. M., Dunlop, J. W. C., Fratzl, P. *The physics of tissue patterning and extracellular matrix organisation: How cells join forces,* **Soft Matter**, 2011, 7, 9549-9560.
- Dunlop. J. W. C. and Fratzl, P., *Biological Composites*, **Annual Review of Materials Research**, 2010, 40, 1-24

Publications on tissue growth, bone remodelling and bone mechanics

- Habegger, M.L, Dean M.N, Dunlop, J. W. C., Mullins, G, Stokes, M, Huber, D.R, Winters, D and Motta, P.J, *Feeding in billfishes: inferring the role of the rostrum from a biomechanical standpoint*, **Journal of Experimental Biology**, 2015, 218, 824-836.
- Fischer, F. D., Zickler, G., Dunlop, J. W. C., Fratzl, P. *Tissue growth controlled by geometric boundary conditions: a simple model recapitulating aspects of callus formation and bone healing,* **Journal of the Royal Society Interface**, 2015, 12, 20150108.
- Herklotz, M., Prewitz, M. C., Bidan, C. M., Drichel, J., Scharnetzki, D., Dunlop, J. W. C., Fratzl, P., Werner, C., *Availability of extracellular matrix biopolymers determines space-filling growth of human mesenchymal stem cells in vitro*, **Biomaterials**, 2015, 60, 121-129.
- Bidan C.M., Kommareddy K.P., Rumpler M., Kollmannsberger P., Fratzl P., Dunlop J.W.C. *Geometry as a factor for tissue growth: Towards shape optimization of tissue engineering scaffolds,* **Advanced HealthCare Materials**, 2013, 2, 186-194.
- Tamjid, E., Simchi, A., Dunlop, J. W. C., Fratzl, P., Bagheri, R., Vossoughi, M., *Tissue growth into three-dimensional composite scaffolds with controlled micro-features and nanotopographical surfaces*, **Journal of Biomedical Materials Research A**, 2013, 101, 2796-2807.
- Gamsjäger, E., Bidan, C. M., Fischer, F.D., Fratzl P., Dunlop, J.W.C., Modelling the role of surface stress on the kinetics of tissue growth in confined geometries, **Acta Biomaterialia**, 2013, 9, 5531-5543.
- Bidan, C, M., Wang, F. M., Dunlop, J. W. C., *A three dimensional model for tissue deposition on complex surfaces*, **Computer Methods in Biomechanics and Biomedical Engineering**, 2013, 16, 1056-1070.

- Gupta, H. S., Krauß, S., Kerschnitzki, M., Karunaratne, A., Dunlop, J. W. C., Barber, A. H., Boesecke, P., Funari, S. S. Fratzl, P., *Intrafibrillar plasticity through mineral/collagen sliding is the dominant mechanism for the extreme toughness of antler bone*, **Journal of Mechanical Behaviour of Biomedical Materials**, 2013. 28, 366-382.
- Galvis, L, Masic, A., Dunlop, J. W. C., Duda, G. and Peter Fratzl– *Theoretical and experimental study of polarized Raman anisotropic response of collagen amide I band in tendon*, **PLoS ONE** 2013, 8(5): e63518
- Rusconi, M., Valleriani, A., Dunlop, J. W. C., Kurths, J., Weinkamer, R., *Quantitative approach to the stochastics of bone remodelling* **EPL**, 2012. 97, 28009.
- Vermolen, F. J., Gefen, A., and Dunlop, J. W. C., *Modeling of in–vitro 'wound' healing: some models and experimental validation*, **Advanced Biomaterials**, 2012, 14, B76-B88.
- Bidan C.M., Kommareddy K.P., Rumpler M., Kollmannsberger P., Bréchet Y., Fratzl P., Dunlop J.W.C., How Linear Tension Converts to Curvature: Geometric Control of Bone Tissue Growth, **PLoS ONE**, 2012, 7(5): e36336.
- Seto, J., Busse, B., Gupta, H. S., Schäfer, C., Krauss, S., Dunlop, J. W. C., Masic, A., Kerschnitzki, M., Zaslansky, P.,Boesecke, P.,Catalá-Lehnen, P., Schinke, T., Fratzl, P., Jahnen-Dechent, W. *Accelerated growth plate mineralization and foreshortened proximal limb bones in Fetuin-A knockout mice*. **PLoS ONE,** 2012, 7(10): e47338.
- Hartmann, M., Dunlop, J. W. C., Fratzl, P., Bréchet, Y., Weinkamer, R., *Trabecular bone remodelling simulated by a stochastic exchange of discrete bone packets from the surface*, **Journal of Mechanical Behaviour of Biomedical Materials**, 2011, 4, 879-887.
- Hoo, R.-P., Fratzl, P., Daniels, J., Dunlop, J. W. C., Honkimäki, V., Hoffman, M., *Cooperation of length scales and orientations in the deformation of bovine bone,* **Acta Biomaterialia**, 2011, 7, 2943-2951.
- Shahar, R., Lukas, C., Papo, S., Dunlop, J. W. C., Weinkamer, R., *Characterization of the spatial arrangement of secondary osteons in the diaphysis of equine and canine long bones*, **Anatomical Record**, 2011, 294, 1093-1102.
- Masic, A., Bertinetti, L., Schuetz, R., Galvis, L., Timofeeva, N., Dunlop, J. W. C., Seto, J., Hartmann, M. A., Fratzl, P., *Observations of Multi-scale, Stress-induced Changes of Collagen Orientation in Tendon by Polarized Raman Spectroscopy*, **Biomacromolecules**, 2011, 12, 3989-3996.
- Dunlop, J. W. C., Fischer F. D., Gamsjäger, E,. Fratzl, P., *A theoretical model for tissue growth in confined geometries*, **J. Mech. Phys. Solids**, 2010, 58, 1073-1087
- Gamsjäger, S., Masic, A., Roschger, P., Kazanci, M., Dunlop, J. W. C., Klaushofer, K., Paschalis, E. P., Fratzl, P., C*ortical bone orientation and composition as a function of bone maturation in a mouse animal model obtained by Raman spectroscopy,* **Bone**, 2010, 47, 392-399.
- Kommareddy, K. P., Lange, C., Rumpler, M., Dunlop, J. W. C., Manjubala, I., Cui, J., Kratz, K., Lendlein, A., and Fratzl, P., *Two stages in three-dimensional in vitro growth of tissue generated by osteoblast-like cells*, **Biointerphases**, 2010, 5, 45-52.
- Dunlop, J. W. C., Hartmann, M. A., Bréchet, Y. J. M., Fratzl, P., Weinkamer, R., *New suggestions for the mechanical control of bone remodeling*, **Calcified Tissue International**, 2009, 85, 45-54.
- Rumpler, M., Woesz, A., Dunlop, J. W. C., van Dongen, J. T., Fratzl, P., *The effect of geometry on three-dimensional tissue growth*, **Journal of the Royal Society Interface**, 2008, 5(27): 1173–1180.

Publications on actuation and plant biomechanics

- Zhao, Q., Heyda, J., Dzubiella, J., Täuber, T., Dunlop, J. W. C. Yuan, J., *Porous poly(ionic liquid) actuator with ultra-high sensitivity to solvents*, **Advanced Materials**, 2015, 27, 2913-2917.
- Guiducci, L., Weaver, J. C., Bréchet, Y. J. M., Fratzl, P., Dunlop, J. W. C., *The Geometric Design and Fabrication of Actuating Cellular Structures*, online **Advanced Materials Interfaces**, 2015 DOI: 10.1002/admi.201500011.
- Zhao, Q., Dunlop, J. W. C., Qiu, X., Huang, F., Zhang, Z., Heyda, J., Dzubiella, J., Antonietti, M., and Yuan, J., *An instant multi-responsive porous polymer actuator operating via solvent molecule sorption*, **Nature Communications**, 2014, 5, 4293.
- Razghandi, K., Bertinetti, L., Guiducci, L., Dunlop, J. W. C., Neinhuis, C., Fratzl P. Burgert, I., *Hydro-actuation of ice plant seed capsules powered by water uptake*, **Bioinspired, Biomimetic and Nanobiomaterials**, 2014, 3, 169-182.
- Guiducci, L., Fratzl, P., Bréchet, Y. J. M., Dunlop, J. W. C., *Pressurized honeycomb as soft-actuators: a theoretical study*, **Journal of the Royal Society Interface**, 2014, 11: 20140458.
- Stoychev, G., Turcaud, S., Dunlop, J. W. C., Ionov, L., Hierarchical multi-step folding of polymer bilayers, **Advanced Functional Materials**, 2013, 23, 2295-2300.
- Abraham, Y., Tamburu, C., Klein, E., Dunlop, J. W. C., Fratzl, P., Raviv, U., Elbaum, R., *Tilted cellulose arrangement as a novel mechanism for hygroscopic coiling in the stork's bill awn*, **Journal of the Royal Society Interface**, 2012, 9, 640-647.
- Stoychev, G., Zakharchenko, S., Turcaud, S., Dunlop, J. W. C., Ionov, L., *Shape programmed folding of stimuli-responsive polymer bilayers*, **ACS Nano**, 2012, 6, 3925-2934.
- Zickler, G. A., Ruffoni, D., Dunlop, J. W. C., Elbaum, R., Weinkamer, R., Fratzl, P., Antretter, T., *Finite element modeling of the cyclic wetting mechanism in the active part of wheat awns*, **Biointerphases**, 2012, 7:42, DOI/ 10.1007/s13758-012-0042-x
- Harrington, M. J., Razghandi, K., Ditsch, F., Guiducci, L., Rueggeberg, M., Dunlop J. W. C., Fratzl, P., Neinhuis, C., and Burgert, I., *Origami-like unfolding of hydro-actuated ice plant seed capsules,* **Nature Communications**, 2011, 2, 337.
- Turcaud, S., Guiducci, L., Fratzl, P., Y. J. M., Bréchet, Dunlop, J. W. C., *An excursion into the design space of biomimetic architectured biphasic actuators*, **International Journal of Materials Research**, 2011, 6, 607-612.
- Abasolo, W., Eder, M., Yamauchi, K., Obel, N., Reinecke, A., Neumetzler, L., Dunlop, J. W. C., Mouille, G., Pauly, M., Höfte, H., Burgert, I., *Pectin may hinder the unfolding of xyloglucan chains during cell deformation – implications of the mechanical performance of Arabidopsis hypocotyls with pectin alterations*, **Molecular Plant,** 2009, 2, p990-999.
- Goswami, L., Dunlop, J. W. C., Jungnikl, K, Eder, M., Gierlinger, N., Coutand, C., Jeronimidis, G., Fratzl, P., Burgert, I., *Stress generation in tension wood of poplar is based on the lateral swelling power of the G-layer,* **The Plant Journal**, 2008, 56, 531-538.

Publications on the mechanics of zirconium alloys (PhD Thesis).

- Dunlop, J., Bréchet, Y., Legras, L., and Estrin, Y., *Dislocation density based modelling of plastic deformation of Zircaloy-4.* **Materials Science and Engineering A**, 443, p77-86, 2007

- Dunlop, J., Bréchet, Y., Legras, L., and Zurob, H., *Modelling isothermal and non-isothermal recrystallisation kinetics. Application to Zircaloy-4.* **Journal of Nuclear Materials**, 2007, 266, 178-186.
- Zurob, H., Bréchet, Y. and Dunlop, J. *Quantitative criterion for nucleation of recrystallisation in solid solutions*, **Acta Materialia**, 2006, 54, p. 3983-3990.

Publications on coordination chemistry of thiacalixarenes (BSc Honours Thesis).

- Bilyk, A. Dunlop, J. W., Hall, A. K., Harrowfield, J. M., Wais Hosseini, M., Koutsantonis, G. A., Skelton, B. W., and White, A. H., *Systematic Structural Coordination Chemistry of p-tert-Butyltetrathiacalix[4]arene: Main Group Metal Complexes Other Than Those of Group 1*, **European Journal of Inorganic Chemistry**, 2010, 14, 2089-2105.
- Bilyk, A. Dunlop, J. W., Fuller, R. O., Hall, A. K., Harrowfield, J. M., Wais Hosseini, M., Koutsantonis, G. A., Murray, I. W., Skelton, B. W., Stamps, R. L., and White, A. H., *Systematic Structural Coordination Chemistry of p-tert-Butyltetrathiacalix[4]arene: Further Complexes of Transition-Metal Ions,* **European Journal of Inorganic Chemistry**, 2010, 14, 2106-2126.
- Bilyk, A. Dunlop, J. W., Fuller, R. O., Hall, A. K., Harrowfield, J. M., Wais Hosseini, M., Koutsantonis, G. A., Murray, I. W., Skelton, B. W., Sobolev, A. N., Stamps, R. L., and White, A. H., *Systematic Structural Coordination Chemistry of p-tert-Butyltetrathiacalix[4]arene: Further Complexes of Lanthanide Metal Ions***,** **European Journal of Inorganic Chemistry**, 2010, 14, 2127-2152.
- Asfari, Z., Bilyk, A., Dunlop, J., Hall, A., Harrowfield, J., Wais Hosseini, M., Skelton, B., and White, A., *Subtleties with Sulfur: Calixerenes as Uranophiles*, **Angewandte Chemie International Edition**, 2001, 40, 4, p. 721-723

Other Publications

- Bennet, M., McCarthy, A., Fix, D., Edwards, M. R., Repp, F., Vach, P., Dunlop, J. W. C., Sitti, M., Buller, G. S., Klumpp, S., Faivre, D., *Influence of Magnetic Fields on Magneto-Aerotaxis*, **PLoS One**, 2014, 9(7), e101150.
- Ruffoni D., Dunlop J. W. C., Fratzl P., and Weinkamer R., *Effect on minimal defects in periodic cellular solids* **Philosophical Magazine**, 2010, 90, 1807-1818.
- Muter, D., Jahnert S., Dunlop, J. W. C., Findenegg, G., Paris O., *Pore structure and fluid sorption in ordered mesoporous silica II: Modeling*, **Journal of Chemical Physics C.,** 2009, 113, 15211-15217.

6.3 References cited in this thesis

Abraham, Y. and Elbaum, R. (2013). "Hygroscopic movements in Geraniaceae: the structural variations that are responsible for coiling or bending." New Phytologist **199**(2): n/a-n/a.

Abraham, Y., Elbaum, R., Sharon, E. and Kupferman, R. (2012). "Emergence of Spontaneous Twist and Curvature in Non-Euclidean Rods: Application to Erodium Plant Cells." Physical Review Letters **108**(23): 238106.

Abraham, Y., Tamburu, C., Klein, E., Dunlop, J. W. C., Fratzl, P., Raviv, U. and Elbaum, R. (2012). "Tilted cellulose arrangement as a novel mechanism for hygroscopic coiling in the stork's bill awn." Journal of the Royal Society Interface **9**(69): 640-647.

Agerbaek, M. O., Eriksen, E. F., Kragstrup, J., Mosekilde, L. and Melsen, F. (1991). "A reconstruction of the remodelling cycle in normal human cortical iliac bone." Bone and mineral **12**(2): 101-112.

Aizenberg, J., Weaver, J. C., Thanawala, M. S., Sundar, V. C., Morse, D. E. and Fratzl, P. (2005). "Skeleton of Euplectella sp.: structural hierarchy from the nanoscale to the macroscale." Science **309**(5732): 275-278.

Alben, S., Balakrisnan, B. and Smela, E. (2011). "Edge Effects Determine the Direction of Bilayer Bending." Nano Letters **11**: 2280–2285.

Allen, R. and Wardrop, A. B. (1964). "The opening and shedding mechanism of the female cones of Pinus Radiata." Australian Journal of Botany **12**: 125-134.

Alom Ruiz, S. and Chen, C. S. (2007). "Microcontact printing: A tool to pattern." Soft Matter **3**(2): 168-177.

Ambrosi, D., Ateshian, G. A., Arruda, E. M., Cowin, S. C., Dumais, J., Goriely, A., Holzapfel, G. A., Humphrey, J. D., Kemkemer, R., Kuhl, E., Olberding, J. E., Taber, L. A. and Garikipati, K. (2011). "Perspectives on biological growth and remodeling." Journal of the Mechanics and Physics of Solids **59**(4): 863-883.

Ambrosi, D. and Guana, F. (2005). "Stress-Modulated Growth." Mathematics and Mechanics of Solids **12**(3): 319-342.

Ambrosi, D. and Guillou, A. (2007). "Growth and dissipation in biological tissues." Continuum Mechanics and Thermodynamics **19**(5): 245-251.

Ambrosi, D., Preziosi, L. and Vitale, G. (2012). "The interplay between stress and growth in solid tumors." Mechanics Research Communications **42**: 87-91.

Armon, S., Efrati, E., Kupferman, R. and Sharon, E. (2011). "Geometry and Mechanics in the Opening of Chiral Seed Pods." Science **333**(6050): 1726-1730.

Ashby, M. F. (2005). "Hybrids to fill holes in material property space." Philosophical Magazine **85**(26-27): 3235-3257.

Ashby, M. F. (2011). "Hybrid Materials to Expand the Boundaries of Material-Property Space." Journal of the American Ceramic Society **94**: s3-s14.

Ashby, M. F. and Bréchet, Y. J. M. (2003). "Designing hybrid materials." Acta Materialia **51**(19): 5801-5821.

Ashby, M. F., Gibson, L. J., Wegst, U. G. K. and Olive, R. (1995). "The Mechanical-Properties of Natural Materials .1. Material Property Charts." Proceedings of the Royal Society of London. Series A: Mathematical, Physical and Engineering Sciences **450**(1938): 123-140.

Audoly, B. and Boudaoud, A. (2002). "'Ruban a godets';: an elastic model for ripples in plant leaves." Comptes Rendus Mecanique **330**(12): 831-836.

Bella, J., Eaton, M., Brodsky, B. and Berman, H. M. (1994). "Crystal and molecular structure of a collagen-like peptide at 1.9 A resolution." Science **266**: 75-81.

Bertinetti, L., Fischer, F. D. and Fratzl, P. (2013). "Physicochemical Basis for Water-Actuated Movement and Stress Generation in Nonliving Plant Tissues." Physical Review Letters **111**(23): 238001.
Bidan, C. M., Kommareddy, K. P., Rumpler, M., Kollmannsberger, P., Bréchet, Y. J. M., Fratzl, P. and Dunlop, J. W. C. (2012). "How Linear Tension Converts to Curvature: Geometric Control of Bone Tissue Growth." PLoS ONE **7**(5): e36336.
Bidan, C. M., Kommareddy, K. P., Rumpler, M., Kollmannsberger, P., Fratzl, P. and Dunlop, J. W. C. (2013). "Geometry as a Factor for Tissue Growth: Towards Shape Optimization of Tissue Engineering Scaffolds." Advanced Healthcare Materials **2**: 186-194.
Bidan, C. M., Wang, F. M. and Dunlop, J. W. C. (2013). "A three-dimensional model for tissue deposition on complex surfaces." Computer Methods in Biomechanics and Biomedical Engineering **16**(10): 1056-1070.
Bonewald, L. F. and Johnson, M. L. (2008). "Osteocytes, mechanosensing and Wnt signaling." Bone **42**(4): 606-615.
Bouligand, Y. (1972). "Twisted fibrous arrangements in biological materials and cholesteric mesophases." Tissue & Cell **4**(2): 189-217.
Bouligand, Y. (2008). "Liquid crystals and biological morphogenesis: Ancient and new questions." Comptes Rendus Chimie **11**(3): 281-296.
Bowling, A. J. and Vaughn, K. C. (2009). "Gelatinous fibers are widespread in coiling tendrils and twining vines." American Journal of Botany **96**(4): 719-727.
Brand, A. W. and Finlay, J. (1996). "Astraeus hygrometricus, an uncommon earthstar." Mycologist **10**(3): 109.
Bréchet, Y. J. M. and Embury, J. D. (2013). "Architectured materials: Expanding materials space." Scripta Materialia **68**(1): 1-3.
Buller, A. H. R. (1958). Researches on Fungi, Hafner Publishing Co.
Burgert, I. and Dunlop, J. W. C. (2011). Micromechanics of Cell Walls. P. Wojtaszek. Berlin, Heidelberg, Springer Berlin Heidelberg. **9:** 27-52.
Burgert, I., Eder, M., Gierlinger, N. and Fratzl, P. (2007). "Tensile and compressive stresses in tracheids are induced by swelling based on geometrical constraints of the wood cell." Planta **226**(4): 981-987.
Burgert, I. and Fratzl, P. (2007). "Mechanics of the expanding cell wall." The Expanding Cell: 191-215.
Burgert, I. and Fratzl, P. (2009). "Actuation systems in plants as prototypes for bioinspired devices." Philosophical Transactions of the Royal Society A: Mathematical, Physical and Engineering Sciences **367**(1893): 1541-1557.
Calve, S. and Simon, H.-G. (2010). "Extracellular control of limb regeneration." 257-266.
Carmeliet, G., Vico, L. and Bouillon, R. (2001). "Space flight: a challenge for normal bone homeostasis." Critical reviews in eukaryotic gene expression **11**(1-3): 131-144.
Cave, I. D. (1969). "Longitudinal Youngs Modulus of Pinus Radiata." Wood Science and Technology **3**(1): 40-48.
Chen, C. S., Mrksich, M., Huang, S., Whitesides, G. M. and Ingber, D. E. (1997). "Geometric control of cell life and death." Science **276**(5317): 1425-1428.
Chenu, J.-C. (1842). Illustrations conchyliologiques ou description et figures de toutes les coquilles connues vivantes et fossiles, classées suivant le système de Lamarck modifié d'après les progrès de la science et comprenant les genres nouveaux et les espèces rècemment découvertes. Tome I. Paris, A. Franck, Libraire-Éditeur, rue Richelieu.
Chindapol, N., Kaandorp, J. A., Cronemberger, C., Mass, T. and Genin, A. (2013). "Modelling Growth and Form of the Scleractinian Coral Pocillopora verrucosa and the Influence of Hydrodynamics." PLOS Computational Biology **9**(1): e1002849.

Chirat, R., Moulton, D. E. and Goriely, A. (2013). "Mechanical basis of morphogenesis and convergent evolution of spiny seashells." Proceedings of the National Academy of Sciences of the United States of America **110**(15): 6015-6020.
Choi, J. Y., Lee, B. H., Song, K. B., Park, R. W., Kim, I. S., Sohn, K. Y., Jo, J. S. and Ryoo, H. M. (1996). "Expression patterns of bone-related proteins during osteoblastic differentiation in MC3T3-E1 cells." Journal of Cellular Biochemistry **61**(4): 609-618.
Chou, T.-W. (1992). Microstructural design of fiber composites. Cambridge, Cambridge University Press.
Ciarletta, P., Ambrosi, D. and Maugin, G. A. (2012). "Mass transport in morphogenetic processes A second gradient theory for volumetric growth and material remodeling." Journal of the Mechanics and Physics of Solids **60**(3): 432-450.
Cowin, S. C. (2010). "Continuum kinematical modeling of mass increasing biological growth." Internation Journal Of Engineering Science **48**(11): 1137-1145.
Cuerno, R., Escudero, C., Garcia-Ruiz, J. M. and Herrero, M. A. (2012). "Pattern formation in stromatolites: insights from mathematical modelling." Journal of the Royal Society, Interface / the Royal Society **9**(70): 1051-1062.
Curie, P. (1894). "Sur la symétrie dans les phénomènes physiques, symétrie d'un champ électrique et d'un champ magnétique." J. Phys. Theor. Appl. **3**(1): 393-415.
Currey, J. D. (2002). Bones - Structure and Mechanics. Princeton, Princeton University Press.
Dalby, M. J., Gadegaard, N. and Oreffo, R. O. C. (2014). "Harnessing nanotopography and integrin–matrix interactions to influence stem cell fate." Nature Nanotechnology **13**(6): 558-569.
Darwin, C. (1875). Insectivorous plants.
Dawson, C., Vincent, J. F. and Rocca, A.-M. (1998). "How pine cones open." Nature **390**(6661): 668-668.
Dinsmore, C. E. (1991). A history of regeneration research: Milestones in the evolution of a science. Cambridge, Cambridge University Press.
Discher, D. E., Janmey, P. A. and Wang, Y.-l. (2005). "Tissue cells feel and respond to the stiffness of their substrate." Science **310**(5751): 1139-1143.
Dullo, W.-C. (2005). "Coral growth and reef growth: a brief review." Facies **51**(1-4): 33-48.
Dunlop, J. S. R., Muir, M. D., Milne, V. A. and Groves, D. I. (1978). "A new microfossil assemblage from the Archaean of Western Australia." Nature **274**: 676-678.
Dunlop, J. W. C., Fischer, F. D., Gamsjäger, E. and Fratzl, P. (2010). "A theoretical model for tissue growth in confined geometries." Journal of the Mechanics and Physics of Solids **58**(8): 1073-1087.
Dunlop, J. W. C. and Fratzl, P. (2010). "Biological Composites." Annual Review of Materials Research **40**(1): 1-24.
Dunlop, J. W. C. and Fratzl, P. (2013). "Multilevel Architectures in Natural Materials." Scripta Materialia **68**: 8-12.
Dunlop, J. W. C., Hartmann, M. A., Bréchet, Y. J. M., Fratzl, P. and Weinkamer, R. (2009). "New suggestions for the mechanical control of bone remodeling." Calcified Tissue international **85**(1): 45-54.
Dunlop, J. W. C., Weinkamer, R. and Fratzl, P. (2011). "Artful interfaces within biological materials." Materials Today **14**(3): 70-78.
Eder, M., Arnould, O., Dunlop, J. W. C., Hornatowska, J. and Salmén, L. (2013). "Experimental micromechanical characterisation of wood cell walls." Wood Science and Technology **47**(1): 163-182.

Elbaum, R. and Abraham, Y. (2014). "Insights into the microstructures of hygroscopic movement in plant seed dispersal." Plant Science **223**: 124-133.
Elbaum, R., Gorb, S. N. and Fratzl, P. (2008). "Structures in the cell wall that enable hygroscopic movement of wheat awns." Journal of Structural Biology **164**(1): 101-107.
Elbaum, R., Zaltzman, L., Burgert, I. and Fratzl, P. (2007). "The role of wheat awns in the seed dispersal unit." Science **316**(5826): 884-886.
Engelmayr, G. C., Cheng, M., Bettinger, C. J., Borenstein, J. T., Langer, R. and Freed, L. E. (2008). "Accordion-like honeycombs for tissue engineering of cardiac anisotropy." Nature Materials **7**(12): 1003-1010.
Engler, A. J., Sen, S., Sweeney, H. L. and Discher, D. E. (2006). "Matrix Elasticity Directs Stem Cell Lineage Specification." Cell **126**(4): 677-689.
Eriksen, E. F. (1986). "Normal and pathological remodeling of human trabecular bone: three dimensional reconstruction of the remodeling sequence in normals and in metabolic bone disease." Endocrine Reviews **7**(4): 379-408.
Eriksen, E. F. (2010). "Cellular mechanisms of bone remodeling." Reviews in Endocrine & Metabolic Disorders **11**(4): 219-227.
Evangelista, D., Hotton, S. and Dumais, J. (2011). "The mechanics of explosive dispersal and self-burial in the seeds of the filaree, Erodium cicutarium (Geraniaceae)." Journal of Experimental Biology **214**(Pt 4): 521-529.
Fabritius, H.-O., Sachs, C. and Raabe, D. (2009). "Influence of Structural Principles on the Mechanics of a Biological Fiber-Based Composite Material with Hierarchical Organization: The Exoskeleton of the Lobster Homarus americanus." Advanced Materials **21**(4): 391-400.
Farber, J., Lichtenegger, H. C., Reiterer, A., Stanzl-Tschegg, S. E. and Fratzl, P. (2001). "Cellulose microfibril angles in a spruce branch and mechanical implications." Journal of Materials Science **36**(21): 5087-5092.
Federl, P. and Prusinkiewicz, P. (2002). Modelling fracture formation in bi-layered materials, with applications to tree bark and drying mud. Proceedings of the 13th Western Computer ….
Fenchel, W. (1928). "Über Krümmung und Windung geschlossener Raumkurven." Math Annalen: 238-252.
Fischer, F. D., Waitz, T., Vollath, D. and Simha, N. K. (2008). "On the role of surface energy and surface stress in phase-transforming nanoparticles." Progress in Materials Science **53**(3): 481-527.
Fischer, F. D., Zickler, G. A., Dunlop, J. W. and Fratzl, P. (2015). "Tissue growth controlled by geometric boundary conditions: a simple model recapitulating aspects of callus formation and bone healing." J R Soc Interface **12**(107).
Foty, R. A., Forgacs, G., Pfleger, C. M. and Steinberg, M. S. (1994). "Liquid properties of embryonic tissues: Measurement of interfacial tensions." Physical Review Letters **72**(14): 2298-2301.
Foty, R. A., Pfleger, C. M., Forgacs, G. and Steinberg, M. S. (1996). "Surface tensions of embryonic tissues predict their mutual envelopment behavior." Development **122**(5): 1611-1620.
Foty, R. A. and Steinberg, M. S. (2005). "The differential adhesion hypothesis: a direct evaluation." Developmental biology **278**(1): 255-263.
Fratzl, P. (2007). "Biomimetic materials research: what can we really learn from nature's structural materials?" Journal of the Royal Society Interface **4**(15): 637-642.
Fratzl, P. and Barth, F. G. (2009). "Biomaterial systems for mechanosensing and actuation." Nature **462**(7272): 442-448.

Fratzl, P., Burgert, I. and Keckes, J. (2004). "Mechanical model for the deformation of the wood cell wall." Zeitschrift Fur Metallkunde **95**(7): 579-584.
Fratzl, P., Elbaum, R. and Burgert, I. (2008). "Cellulose fibrils direct plant organ movements." Faraday Discussions **139**: 275.
Fratzl, P., Gupta, H. S., Paschalis, E. P. and Roschger, P. (2004). "Structure and mechanical quality of the collagen-mineral nano-composite in bone." Journal of Materials Chemistry **14**(14): 2115-2123.
Fratzl, P. and Weinkamer, R. (2007). "Nature's hierarchical materials." Progress in Materials Science **52**(8): 1263-1334.
Fritz-Popovski, G., Van Opdenbosch, D., Zollfrank, C., Aichmayer, B. and Paris, O. (2012). "Development of the Fibrillar and Microfibrillar Structure During Biomimetic Mineralization of Wood." Advanced Functional Materials: n/a-n/a.
Frost, H. M. (1987). "Bone "Mass" and the "Mechanostat": A Proposal." The Anatomical Record **219**: 1-9.
Galilei, G. (1638). Dialogues concerning two new sciences.
Gamsjäger, E., Bidan, C. M., Fischer, F. D., Fratzl, P. and Dunlop, J. W. C. (2013). "Modelling the role of surface stress on the kinetics of tissue growth in confined geometries." Acta Biomaterialia **9**: 5531-5543.
Garikipati, K. (2009). "The Kinematics of Biological Growth." Applied Mechanics Reviews **62**(3): 030801.
Ge, Q., Qi, H. J. and Dunn, M. L. (2013). "Active materials by four-dimension printing." Applied Physics Letters **103**(13): 131901.
Gentzsch, C., Pueschel, K., Deuretzbacher, G., Delling, G. and Kaiser, E. (2004). "First Inventory of Resorption Lacunae on Rods and Plates of Trabecular Bone as Observed by Scanning Electron Microscopy." Calcified Tissue international **76**(2): 154-162.
Gerbode, S. J., Puzey, J. R., McCormick, A. G. and Mahadevan, L. (2012). "How the Cucumber Tendril Coils and Overwinds." Science **337**(6098): 1087-1091.
Gibson, L. J. (2005). "Biomechanics of cellular solids." Journal of Biomechanics **38**(3): 377-399.
Gibson, L. J. (2012). "The hierarchical structure and mechanics of plant materials." Journal of the Royal Society Interface.
Gibson, L. J., Ashby, M. F. and Harley, B. A. C. (2010). Cellular Materials in Nature and Medicine. Cambridge, Cambridge University Press.
Giraud Guille, M. M. (2001). "Plywood structures in nature." Current Opinion in Solid State & Material Science **3**: 221-227.
Giraud Guille, M. M., Belamie, E., Mosser, G., Helary, C., Gobeaux, F. and Vigier, S. (2008). "Liquid crystalline properties of type I collagen: Perspectives in tissue morphogenesis." Comptes Rendus Chimie **11**(3): 245-252.
Giraud Guille, M. M., Besseau, L. and Martin, R. (2003). "Liquid crystalline assemblies of collagen in bone and in vitro systems." Journal of Biomechanics **36**(10): 1571-1579.
Glazier, J. A. and Graner, F. (1993). "Simulation of the differential adhesion driven rearrangement of biological cells." Physical Review. E **47**(3): 2128-2154.
Goswami, L., Dunlop, J. W. C., Jungnikl, K., Eder, M., Gierlinger, N., Coutand, C., Jeronimidis, G., Fratzl, P. and Burgert, I. (2008). "Stress generation in the tension wood of poplar is based on the lateral swelling power of the G-layer." The Plant Journal **56**(4): 531-538.
Gould, S. J. (1966). "Allometry and size in ontogeny and phylogeny." Biological reviews of the Cambridge Philosophical Society **41**(4): 587-640.
Gould, S. J. (1971). "D'Arcy Thompson and the Science of Form." New Literary History **2**: 229-258.

Graner, F. and Glazier, J. A. (1992). "Simulation of biological cell sorting using a two-dimensional extended Potts model." Physical Review Letters **69**(13): 2013-2016.
Grotzinger, J. P. and Rothman, D. H. (1996). "An abiotic model for stromatolite morphogenesis." Nature **383**(6599): 423-425.
Guiducci, L., Fratzl, P., Bréchet, Y. J. M. and Dunlop, J. W. C. (2014). "Pressurized honeycombs as soft-actuators: a theoretical study." Journal of the Royal Society Interface: 20140458.
Guiducci, L., Weaver, J. C., Bréchet, Y. J. M., Fratzl, P. and Dunlop, J. W. C. (2015). "The Geometric Design and Fabrication of Actuating Cellular Structures." Advanced Materials Interfaces: n/a-n/a.
Gurtner, G. C., Werner, S., Barrandon, Y. and Longaker, M. T. (2008). "Wound repair and regeneration." Nature **453**(7193): 314-321.
Harlow, W. M., Cote, W. A. and Day, A. C. (1964). "The opening mechanism of pine cone scales." Journal of Forestry **62**(8): 538-540.
Harrington, M. J., Razghandi, K., Ditsch, F., Guiducci, L., Rüggeberg, M., Dunlop, J. W. C., Fratzl, P., Neinhuis, C. and Burgert, I. (2011). "Origami-like unfolding of hydro-actuated ice plant seed capsules." Nature Communications **2**: 337-337.
Harris, A. K., Stopak, D. and Wild, P. (1981). "Fibroblast traction as a mechanism for collagen morphogenesis." Nature **290**(5803): 249-251.
Hartmann, M. A., Dunlop, J. W. C., Bréchet, Y. J. M., Fratzl, P. and Weinkamer, R. (2011). "Trabecular bone remodelling simulated by a stochastic exchange of discrete bone packets from the surface." Journal of the Mechanical Behavior of Biomedical Materials **4**(6): 879-887.
Herklotz, M., Prewitz, M. C., Bidan, C. M., Dunlop, J. W. C., Fratzl, P. and Werner, C. (2015). "Availability of extracellular matrix biopolymers and differentiation state of human mesenchymal stem cells determine tissue-like growth in vitro." Biomaterials **60**: 121-129.
Hohmann, J. K. and von Freymann, G. (2014). "Influence of Direct Laser Written 3D Topographies on Proliferation and Differentiation of Osteoblast-Like Cells: Towards Improved Implant Surfaces." Advanced Functional Materials: n/a-n/a.
Huiskes, R., Ruimerman, R., van Lenthe, G. H. and Janssen, J. D. (2000). "Effects of mechanical forces on maintenance and adaptation of form in trabecular bone." Nature **405**(6787): 704-706.
Hull, D. and Clyne, T. W. (1996). An Introduction to Composite Materials. Cambridge, Cambridge University Press.
Jinnai, H., Nishikawa, Y., Ito, M., Smith, S. D., Agard, D. A. and Spontak, R. J. (2002). "Topological similarity of sponge-like bicontinuous morphologies differing in length scale." Advanced Materials **14**(22): 1615-1618.
Jinnai, H., Watashiba, H., Kajihara, T., Nishikawa, Y., Takahashi, M. and Ito, M. (2001). "Surface curvatures of trabecular bone microarchitecture." Bone **30**(1): 191-194.
Johnson, K. A., Muir, P. and Nicoll, R. G. (2000). "Asymmetric adaptive modeling of central tarsal bones in racing greyhounds." Bone.
Kaandorp, J. A., Sloot, P. M. A., Merks, R. M. H., Bak, R. P. M., Vermeij, M. J. A. and Maier, C. (2005). "Morphogenesis of the branching reef coral Madracis mirabilis." Proceedings of the Royal Society B: Biological Sciences **272**(1559): 127-133.
Kardar, M., Parisi, G. and Zhang, Y.-C. (1986). "Dynamic Scaling of Growing Interfaces." Physical Review Letters **56**(9): 889-892.
Keckes, J., Burgert, I., Frühmann, K., Müller, M., Kölln, K., Hamilton, M., Burghammer, M., Roth, S. V., Stanzl-Tschegg, S. E. and Fratzl, P. (2003). "Cell-wall recovery after irreversible deformation of wood." Nature Materials **2**(12): 810-813.

Kerschnitzki, M., Wagermaier, W., Liu, Y., Roschger, P., Duda, G. N. and Fratzl, P. (2011). "Poorly ordered bone as an endogenous scaffold for the deposition of highly oriented lamellar tissue in rapidly growing ovine bone." Cells, tissues, organs **194**(2-4): 119-123.
Knoll, A. H. (2003). Biomineralization and evolutionary history. Biomineralization. **54:** 329-356.
Kollmannsberger, P., Bidan, C. M., Dunlop, J. W. C. and Fratzl, P. (2011). "The physics of tissue patterning and extracellular matrix organisation: how cells join forces." Soft Matter **7**: 9549–9560.
Kommareddy, K. P., Lange, C., Rumpler, M., Dunlop, J. W. C., Manjubala, I., Cui, J., Kratz, K., Lendlein, A. and Fratzl, P. (2010). "Two stages in three-dimensional in vitro growth of tissue generated by osteoblastlike cells." Biointerphases **5**(2): 45-52.
Krauss, S., Wagermaier, W., Estevez, J. A., Currey, J. D. and Fratzl, P. (2011). "Tubular frameworks guiding orderly bone formation in the antler of the red deer (Cervus elaphus)." Journal of Structural Biology **175**: 457–464.
Krieg, M., Arboleda-Estudillo, Y., Puech, P.-H., Käfer, J., Graner, F., Müller, D. J. and Heisenberg, C.-P. (2008). "Tensile forces govern germ-layer organization in zebrafish." Nature Cell Biology **10**(4): 429-436.
Kulić, I. M., Mani, M., Mohrbach, H., Thaokar, R. and Mahadevan, L. (2009). "Botanical ratchets." Proceedings of the Royal Society B: Biological Sciences **276**(1665): 2243-2247.
Lecuit, T. and Lenne, P.-F. (2007). "Cell surface mechanics and the control of cell shape, tissue patterns and morphogenesis." Nature Reviews Molecular Cell Biology **8**(8): 633-644.
Lee, T. C. and Taylor, D. (1999). "Bone remodelling: Should we cry wolff?" Irish journal of medical science **168**(2): 102-105.
Liang, H. and Mahadevan, L. (2009). "The shape of a long leaf." Proceedings of the National Academy of Sciences of the United States of America **106**(52): 22049-22054.
Liang, H. and Mahadevan, L. (2011). "Growth, geometry, and mechanics of a blooming lily." Proceedings of the National Academy of Sciences of the United States of America **108**(14): 5516-5521.
Lin, A. and Meyers, M. A. (2005). "Growth and structure in abalone shell." Materials Science and Engineering A **390**(1-2): 27-41.
Manning, M. L., Foty, R. A., Steinberg, M. S. and Schoetz, E.-M. (2010). "Coaction of intercellular adhesion and cortical tension specifies tissue surface tension." Proceedings of the National Academy of Sciences of the United States of America **107**(28): 12517-12522.
Marmottant, P., Mgharbel, A., Käfer, J., Audren, B., Rieu, J.-P., Vial, J.-C., van der Sanden, B., Maree, A. F. M., Graner, F. and Delanoë-Ayari, H. (2009). "The role of fluctuations and stress on the effective viscosity of cell aggregates." Proceedings of the National Academy of Sciences of the United States of America **106**(41): 17271-17275.
Martone, P. T., Boller, M., Burgert, I., Dumais, J., Edwards, J., Mach, K., Rowe, N. P., Rüggeberg, M., Seidel, R. and Speck, T. (2010). Mechanics without Muscle: Biomechanical Inspiration from the Plant World. Integrative and Comparative Biology. **50:** 888-907.
Meinhardt, H. (2009). The Algorithmic Beauty of Sea Shells. Dortrecht, Springer.
Melchels, F. P. W., Domingos, M. A. N., Klein, T. J., Malda, J., Bartolo, P. J. and Hutmacher, D. W. (2012). "Additive manufacturing of tissues and organs." Progress in Polymer Science **37**(8): 1079-1104.
Mellerowicz, E. J. and Gorshkova, T. A. (2012). "Tensional stress generation in gelatinous fibres: a review and possible mechanism based on cell-wall structure and composition." Journal of Experimental Botany **63**: 551–565.

Merks, R. M. H., Hoekstra, A. G., Kaandorp, J. A. and Sloot, P. M. A. (2004). "Polyp oriented modelling of coral growth." Journal of Theoretical Biology **228**(4): 559-576.
Meyers, M. A., Chen, P.-Y., Lin, A. Y.-M. and Seki, Y. (2008). "Biological materials: Structure and mechanical properties." Progress in Materials Science **53**(1): 1-206.
Meyers, M. A., Chen, P.-Y., Lopez, M. I., Seki, Y. and Lin, A. Y. M. (2011). "Biological materials: a materials science approach." Journal of the Mechanical Behavior of Biomedical Materials **4**(5): 626-657.
Meyers, M. A., McKittrick, J. and Chen, P.-Y. (2013). "Structural Biological Materials: Critical Mechanics-Materials Connections." Science **339**: 773-779.
Nelson, C. M., Jean, R. P., Tan, J. L., Liu, W. F., Sniadecki, N. J., Spector, A. A. and Chen, C. S. (2005). "Emergent patterns of growth controlled by multicellular form and mechanics." Proceedings of the National Academy of Sciences **102**(33): 11594-11599.
Neville, A. C. (1993). Biology of Fibrous Composites. Cambridge, Cambridge University Press.
Niklas, K. J. (1992). Plant Biomechanics: An Engineering Approach To Plant Form And Function, University of Chicago Press.
Niklas, K. J. (1994). Plant allometry: the scaling of form and process, University of Chicago Press.
Nishiyama, Y., Sugiyama, J., Chanzy, H. and Langan, P. (2003). "Crystal Structure and Hydrogen Bonding System in Cellulose I α from Synchrotron X-ray and Neutron Fiber Diffraction." Journal of the American Chemical Society **125**(47): 14300-14306.
Ochsner, M., Dusseiller, M. R., Grandin, H. M., Luna-Morris, S., Textor, M., Vogel, V. and Smith, M. L. (2007). "Micro-well arrays for 3D shape control and high resolution analysis of single cells." Lab on a chip **7**(8): 1074.
Oh, S., Brammer, K. S., Li, Y. S. J., Teng, D., Engler, A. J., Chien, S. and Jin, S. (2009). "Stem cell fate dictated solely by altered nanotube dimension." Proceedings of the National Academy of Sciences of the United States of America **106**(7): 2130-2135.
Okuyama, T., Yamamoto, H., Yoshida, M., Hattori, Y. and Archer, R. R. (1994). "Growth stresses in tension wood: role of microfibrils and lignification. ." Ann. Sci. For. **51**: 291-300.
Parolin, P. (2006). "Ombrohydrochory: rain-operated seed dispersal in plants—with special regard to jet-action dispersal in Aizoaceae." Flora **201**: 511–518.
Pelham, R. J. and Wang, Y.-l. (1997). "Cell locomotion and focal adhesions are regulated by substrate flexibility." Proceedings of the National Academy of Sciences of the United States of America **94**(25): 13661-13665.
Prusinkiewicz, P. and Runions, A. (2012). "Computational models of plant development and form." New Phytologist **193**(3): 549-569.
Rajagopalan, S. and Robb, R. A. (2006). "Schwarz meets Schwann: Design and fabrication of biomorphic and durataxic tissue engineering scaffolds." Medical Image Analysis **10**(5): 693-712.
Raup, D. M. (1962). "Computer as Aid in Describing Form in Gastropod Shells." Science **138**(3537): 150-152.
Razghandi, K., Bertinetti, L., Guiducci, L., Dunlop, J. W. C., Fratzl, P., Neinhuis, C. and Burgert, I. (2014). "Hydro-actuation of ice plant seed capsules powered by water uptake." Bioinspired, Biomimetic and Nanobiomaterials **3**: 169–182.
Reis, D., Vian, B., Chanzy, H. and Roland, J. C. (1991). "Liquid crystal-type assembly of native cellulose-glucuronoxylans extracted from plant cell wall." Biology of the Cell **73**(2-3): 173-178.
Reiterer, A., Lichtenegger, H. C., Farber, J., Stanzl-Tschegg, S. E. and Fratzl, P. (2004). Variability of Microfibril Angles in Softwood, Hardwood and Reaction Wood**:** 1-13.

Reiterer, A., Lichtenegger, H. C., Tschegg, S. and Fratzl, P. (2001). "Experimental evidence for a mechanical function of the cellulose microfibril angle in wood cell walls." Philosophical Magazine A **79**(9): 2173-2184.
Reyssat, E. and Mahadevan, L. (2009). "Hygromorphs: from pine cones to biomimetic bilayers." Journal of the Royal Society Interface **6**(39): 951-957.
Ripamonti, U., Roden, L. C. and Renton, L. F. (2012). "Osteoinductive hydroxyapatite-coated titanium implants." Biomaterials **33**(15): 3813-3823.
Robling, A. G., Castillo, A. B. and Turner, C. H. (2006). "Biomechanical and molecular regulation of bone remodeling." Annual Review of Biomedical Engineering **8**: 455-498.
Roose, T., Chapman, S. J. and Maini, P. K. (2007). "Mathematical Models of Avascular Tumor Growth." SIAM Review **49**(2): 179.
Roux, W. (1885). "Beitrage zur Morphologie der funktionnellen Anpassung." Arch Anat. Physiol. Anat. Abt. **9**: 130-158.
Ruimerman, R., van Rietbergen, B., Hilbers, P. A. J. and Huiskes, R. (2003). "A 3-dimensional computer model to simulate trabecular bone metabolism." Biorheology **40**(1-3): 315-320.
Ruiz, S. A. and Chen, C. S. (2008). "Emergence of Patterned Stem Cell Differentiation Within Multicellular Structures." Stem Cells **26**(11): 2921-2927.
Rumpler, M., Woesz, A., Dunlop, J. W. C., van Dongen, J. T. and Fratzl, P. (2008). "The effect of geometry on three-dimensional tissue growth." Journal of the Royal Society Interface **5**(27): 1173-1180.
Rumpler, M., Woesz, A., Varga, F., Manjubala, I., Klaushofer, K. and Fratzl, P. (2007). "Three-dimensional growth behavior of osteoblasts on biomimetic hydroxylapatite scaffolds." Journal of biomedical materials research. Part A **81**(1): 40-50.
Schmidt-Nielsen, K. (1984). Scaling. Why is Animal Size so Important. Cambridge, Cambridge University Press.
Schreiber, N., Gierlinger, N., Pütz, N., Fratzl, P., Neinhuis, C. and Burgert, I. (2010). "G-fibres in storage roots of Trifolium pratense(Fabaceae): tensile stress generators for contraction." The Plant Journal **61**(5): 854-861.
Selhuber-Unkel, C., Erdmann, T., López-GarcIa, M., Kessler, H., Schwarz, U. S. and Spatz, J. P. (2010). "Cell Adhesion Strength Is Controlled by Intermolecular Spacing of Adhesion Receptors." Biophysical Journal **98**(4): 543-551.
Shahar, R., Lukas, C., Papo, S., Dunlop, J. W. C. and Weinkamer, R. (2011). "Characterization of the Spatial Arrangement of Secondary Osteons in the Diaphysis of Equine and Canine Long Bones." The Anatomical Record **294**(7): 1093-1102.
Shapiro, F. (1988). "Cortical Bone Repair - the Relationship of the Lacunar-Canalicular System and Intercellular Gap-Junctions to the Repair Process." Journal of Bone and Joint Surgery-American Volume **70A**(7): 1067-1081.
Shaw, G. R. (1914). The Genus Pinus, Riverside Press.
Sjostrom, T., McNamara, L. E., Meek, R. M. D., Dalby, M. J. and Su, B. (2013). "2D and 3D Nanopatterning of Titanium for Enhancing Osteoinduction of Stem Cells at Implant Surfaces." Advanced Healthcare Materials **2**(9): 1285-1293.
Speck, T. and Burgert, I. (2011). "Plant Stems: Functional Design and Mechanics." Annual Review of Materials Research **41**(1): 169-193.
Steinberg, M. S. (2007). "Differential adhesion in morphogenesis: a modern view." Current Opinion in Genetics & Development **17**(4): 281-286.
Stiven, C. (2013). "Biomechanics of Bark Patterning in Grasstree." 1-3.
Stoychev, G., Puretskiy, N. and Ionov, L. (2011). "Self-folding all-polymer thermoresponsive microcapsules." Soft Matter **7**(7): 3277-3279.

Stoychev, G., Turcaud, S., Dunlop, J. W. C. and Ionov, L. (2013). "Hierarchical Multi‐Step Folding of Polymer Bilayers." Advanced Functional Materials **23**(18): 2295-2300.
Stoychev, G., Zakharchenko, S., Turcaud, S., Dunlop, J. W. C. and Ionov, L. (2012). "Shape-Programmed Folding of Stimuli-Responsive Polymer Bilayers." ACS Nano **6**(5): 3925-3934.
Studart, A. R. and Erb, R. M. (2014). "Bioinspired materials that self-shape through programmed microstructures." Soft Matter **10**(9): 1284.
Swat, M. H., Thomas, G. L., Belmonte, J. M., Shirinifard, A., Hmeljak, D. and Glazier, J. A. (2012). "Multi-Scale Modeling of Tissues Using CompuCell3D." Computational Methods in Cell Biology **110**: 325-366.
Taylor, D., Hazenberg, J. G. and Lee, T. C. (2007). "Living with cracks: Damage and repair in human bone." Nature Materials **6**(4): 263-268.
Théry, M., Pépin, A., Dressaire, E., Chen, Y. and Bornens, M. (2006). "Cell distribution of stress fibres in response to the geometry of the adhesive environment." Cell Motility and the Cytoskeleton **63**(6): 341-355.
Théry, M., Racine, V., Piel, M., Pepin, A., Dimitrov, A., Chen, Y., Sibarita, J. B. and Bornens, M. (2006). "Anisotropy of cell adhesive microenvironment governs cell internal organization and orientation of polarity." Proceedings of the National Academy of Sciences of the United States of America **103**(52): 19771-19776.
Thompson, D. A. W. (1942). On Growth and Form, Dover.
Thomsen, J. S., Morukov, B. V., Vico, L., Alexandre, C., Saparin, P. I. and Gowin, W. (2005). "Cancellous bone structure of iliac crest biopsies following 370 days of head-down bed rest." Aviation, space, and environmental medicine **76**(10): 915-922.
Timoshenko, S. P. (1925). "Analysis of bi-metal thermostats." J. Opt. Soc. Am **11**(3): 233-255.
Trembley, A. (1744). Mémoires pour servir à l'histoire d'un genre de polypes d'eau douce, à bras en forme de cornes, A Leide : Chez Jean & Herman Verbeek.
Tsubota, K.-i. and Adachi, T. (2004). "Changes in the Fabric and Compliance Tensors of Cancellous Bone due to Trabecular Surface Remodeling, Predicted by a Digital Image-based Model." Computer Methods in Biomechanics and Biomedical Engineering **7**(4): 187-192.
Turcaud, S., Guiducci, L., Bréchet, Y. J. M., Fratzl, P. and Dunlop, J. W. C. (2011). "An excursion into the design space of biomimetic architectured biphasic actuators." International Journal of Materials Research **102**: 607-612.
van Eeden, S. P. and Ripamonti, U. (1994). "Bone differentiation in porous hydroxyapatite in baboons is regulated by the geometry of the substratum: implications for reconstructive craniofacial surgery." Plastic and reconstructive surgery **93**(5): 959-966.
van Oers, R. F. M., Ruimerman, R., Tanck, E., Hilbers, P. A. J. and Huiskes, R. (2008). "A unified theory for osteonal and hemi-osteonal remodeling." Bone **42**(2): 250-259.
Vetter, A., Witt, F., Sander, O., Duda, G. N. and Weinkamer, R. (2011). "The spatio-temporal arrangement of different tissues during bone healing as a result of simple mechanobiological rules." Biomechanics and Modeling in Mechanobiology **11**(1-2): 147-160.
Vincent, J. F. (1990). Structural Biomaterials. Princeton, Princeton University Press.
Wainwright, S. A., Biggs, W., Currey, J. D. and Gosline, J. M. (1982). Mechanical Design in Organisms. Princeton, Princeton University Press.
Wang, R. and Gupta, H. S. (2011). "Deformation and Fracture Mechanisms of Bone and Nacre." Annual Review of Materials Research **41**(1): 41-73.
Ward, F. O. (1876). Outlines of Human Osteology. London, Renshaw.

Weaver, J. C., Milliron, G. W., Miserez, A., Evans-Lutterodt, K., Herrera, S., Gallana, I., Mershon, W. J., Swanson, B., Zavattieri, P. D., DiMasi, E. and Kisailus, D. (2012). "The Stomatopod Dactyl Club: A Formidable Damage-Tolerant Biological Hammer." Science **336**(6086): 1275-1280.
Wegst, U. G. K. and Ashby, M. F. (2004). "The mechanical efficiency of natural materials." Philosophical Magazine **84**(21): 2167-2186.
Weiner, S. and Wagner, H. D. (1998). "The material bone: Structure mechanical function relations." Annual Review of Materials Science **28**: 271-298.
Weinkamer, R., Hartmann, M. A., Bréchet, Y. J. M. and Fratzl, P. (2004). "Stochastic Lattice Model for Bone Remodeling and Aging." Physical Review Letters **93**(22): 228102.
Wilson, B. F. and Archer, R. R. (1977). "Reaction Wood: Induction and Mechanical Action." Annual Review of Plant Physiology **28**: 23-43.
Wimmer, R., Lucas, B. N., Tsui, T. Y. and Oliver, W. C. (1997). "Longitudinal hardness and Young's modulus of spruce tracheid secondary walls using nanoindentation technique." Wood Science and Technology **31**(2): 131-141.
Woesz, A., Rumpler, M., Stampfl, J., Varga, F., Fratzl-Zelman, N., Roschger, P., Klaushofer, K. and Fratzl, P. (2005). "Towards bone replacement materials from calcium phosphates via rapid prototyping and ceramic gelcasting." Materials Science & Engineering C **25**(2): 181-186.
Wolff, J. (1892). Das Gesetz der Transformation der Knochen. Berlin, Verlag von August. Hirschwald.
Xia, Y. and Whitesides, G. M. (1998). "Soft lithography." Annual Review of Materials Science **28**(1): 153-184.
Zadpoor, A. A. (2015). "Bone tissue regeneration: the role of scaffold geometry." Biomaterials Science **3**(2): 231-245.
Zakharchenko, S., Puretskiy, N., Stoychev, G., Stamm, M. and Ionov, L. (2010). "Temperature controlled encapsulation and release using partially biodegradable thermo-magneto-sensitive self-rolling tubes." Soft Matter **6**(12): 2633.
Zhao, Q., Dunlop, J. W. C., Qiu, X., Huang, F., Zhang, Z., Heyda, J., Dzubiella, J., Antonietti, M. and Yuan, J. (2014). "An instant multi-responsive porous polymer actuator driven by solvent molecule sorption." Nature Communications **5**.
Zhao, Q., Heyda, J., Dzubiella, J., Täuber, K., Dunlop, J. W. C. and Yuan, J. (2015). "Sensing Solvents with Ultrasensitive Porous Poly(ionic liquid) Actuators." Advanced Materials **27**: 2913-2917.
Zickler, G. A., Ruffoni, D., Dunlop, J. W. C., Elbaum, R., Weinkamer, R., Fratzl, P. and Antretter, T. (2012). "Finite element modeling of the cyclic wetting mechanism in the active part of wheat awns." Biointerphases **7**(1-4): 42.

7 Full Publications

Due to copyright restrictions in reprinting publications in the final published form, the following texts are the final accepted versions of the publications. As such there can be some minor changes in the publications during the review and proof process. For the final published version see the online version accessible via the DOI numbers.

7 Full Publications 77
7.1 [TG1] The effect of geometry on three-dimensional tissue growth 79
7.2 [TG2] Two stages in three-dimensional in vitro growth of tissue generated by osteoblast-like cells 87
7.3 [TG3] Geometry as a Factor for Tissue Growth: Towards Shape Optimization of Tissue Engineering Scaffolds. 95
7.4 [TG4] How Linear Tension Converts to Curvature: Geometric Control of Bone Tissue Growth. 105
7.5 [TG5] A theoretical model for tissue growth in confined geometries. 115
7.6 [TG6] Modelling the role of surface stress on the kinetics of tissue growth in confined geometries. 127
7.7 [TG7] Tissue growth controlled by geometric boundary conditions: a simple model recapitulating aspects of callus formation and bone healing 141
7.8 [AC1] An excursion into the design space of biomimetic architectured biphasic actuators. 149
7.9 [AC2] Shape-Programmed Folding of Stimuli-Responsive Polymer Bilayers. 155
7.10 [AC3] Hierarchical Multi‐Step Folding of Polymer Bilayers. 165
7.11 [AC4] An instant multi-responsive porous polymer actuator driven by solvent molecule sorption. 171
7.12 [AC5] Porous poly(ionic liquid) actuator with ultra-high sensitivity to solvents 179
7.13 [AC6] Pressurized honeycombs as soft-actuators: a theoretical study. 185
7.14 [AC7] The Geometric Design and Fabrication of Actuating Cellular Structures 197

7.1 [TG1] The effect of geometry on three-dimensional tissue growth

Rumpler, M., Woesz, A., Dunlop, J. W. C., van Dongen, J. T., Fratzl, P.
*Published in the **Journal of the Royal Society Interface**, 2008, 5, 1173-1180.*
doi:10.1098/rsif.2008.0064

Reprinted with permission from the Royal Society (Open Access CC licence)

Abstract: Tissue formation is determined by uncountable biochemical signals between cells, but also physical parameters have been shown to exhibit significant effects on the level of the single cell. Beyond the cell however there is still no quantitative understanding of how geometry affects tissue growth, which is of high significance for bone healing and tissue engineering. In this paper it is shown that the local growth rate of tissue formed by osteoblasts is strongly influenced by geometrical features of channels in an artificial three-dimensional matrix. Curvature driven effects and mechanical forces within the tissue may explain the growth patterns as demonstrated by numerical simulation and confocal laser scanning microscopy. This implies that cells within the tissue surface are able to sense and react to radii of curvature much larger than the size of the cells themselves. This has important implications for the understanding of bone remodelling and defect healing as well as for scaffold design in bone tissue engineering.

1. Introduction

Cells react to the chemistry, geometry (Chen et al., 1997) and mechanics (Discher et al., 2005) of their local environments. In addition to the well studied response of cells to biochemistry, the influence of mechanical parameters is well described for mesenchymal stem cells where it is possible to control the differentiation of these cells through substrate stiffness. Neuronal cells for example are formed on soft substrates, muscle cells on stiffer substrates and osteonal cells on more rigid matrices (Engler et al., 2006). Focal adhesion sites of cells become more stable and the cell cytoskeleton more organised with increasing substrate stiffness, enabling larger forces to be transmitted (Discher et al., 2005). Cells appear to probe their local environment through the transmission of forces from the environment via focal adhesion sites attached to the cytoskeleton (Balaban et al., 2001) and seem to be able to sense and transmit forces over long distances relative to their size (Bischofs and Schwarz, 2003). The geometric arrangement of the local environment is also a critical factor in determining cell behaviour. It has been shown, for example, that both the chemical composition and sub-cellular organization of focal adhesion molecules differs for cells grown in a three-dimensional matrix compared to those grown on a flat plate in two dimensions (Cukierman et al., 2001, Cavalcanti-Adam et al., 2007). On the micron scale, the geometry of adhesive regions controls cell shape and the spreading of cells across a substrate (Chen et al., 1997). Cells also respond to variations in geometry on the nano-scale, and substrates patterned with different densities of integrin coated nano-dots show differences in the dynamics of focal adhesion and cell motility (Cavalcanti-Adam et al., 2007).

The influence of surface geometry is well studied for the behaviour of single cells, but no data are available for the collective behaviour of groups of cells, namely at the tissue level. Such data are essential in tissue engineering to optimise the support for new tissue formation in artificial replacement materials. Scaffolds for tissue engineering act as a physical support structure to replace tissue removed after injury or cancer ablation, and ideally should regulate biological events such as cell proliferation, viability and intra-cellular signalling (Geiger and Bershadsky, 2002, Geiger et al., 2001). Bone replacement materials, for example should have an open porosity with channels in the order of a few hundred microns diameter. This not only allows for the migration of single cells into the scaffold but also provides sufficient space for the formation and growth of new tissue with a cellular and structural organisation similar to that seen in vivo (Rumpler et al., 2007, Woesz et al., 2005). Studies investigating the effect of pore size at the micrometer level have focused on cell attachment, migration and cell division with respect to biocompatibility (van Eeden and Ripamonti, 1994). Pore channels in scaffold materials can vary between round and irregular cross sections (Jin et al., 2000, Habibovic et al., 2005) but the effect of pore shape on tissue formation has not yet been systematically investigated. An understanding of the effect of geometry on tissue growth could assist in the optimisation of porous scaffolds for tissue engineering as well as help improve understanding of the processes of bone remodelling and healing.

This paper investigates a model system for tissue growth consisting of three-dimensional hydroxylapatite (HA) plates of controlled architecture placed within a culture of murine osteoblast-like cells. These cells are known to undergo differentiation from an immature pre-osteoblastic to a mature osteoblastic phenotype in vitro, accompanied by the expression of characteristic marker proteins at each stage of development (Quarles et al., 1992). Furthermore, they are capable of building an extracellular matrix consisting of densely packed and well organised collagen fibrils with representative non-collagenous matrix proteins known from bone tissue (Rumpler et al., 2007, Choi et al., 1996). The aim of this paper is to investigate the impact of geometrical features (channel shape and size) on new tissue formation in vitro.

2. Materials and Methods

Production of the hydroxylapatite (HA) plates. HA plates (2mm thick) containing four channel shapes (triangular, square, hexagonal and circular) and three channel sizes (perimeters P = 3.14, 4.71 and 6.28 mm) were produced by slurry casting. Casting moulds were designed with computer-aided-design (CAD) software

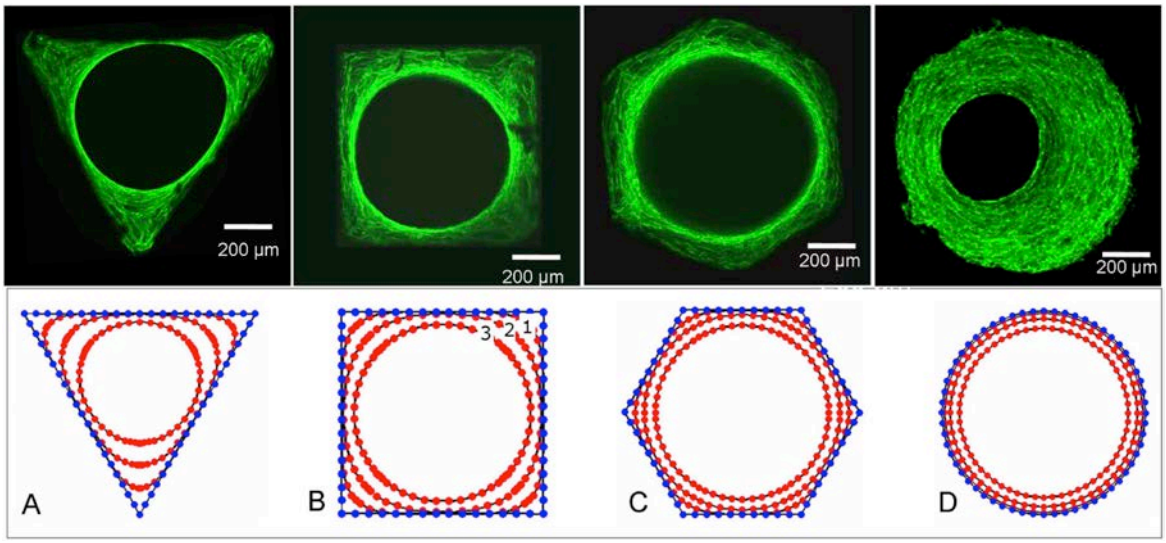

Figure 1. Upper images: New tissue formed in three-dimensional matrix channels. Actin stress fibres are stained with phalloidin-FITC and visualized under a confocal laser scanning microscope. Here the tissue formation is shown after 21 days (A – D) and after 30 days (D) of cell culture in the channels of a triangular (A), square (B), hexagonal (C) and round (D) shape introduced into a HA plate in vitro. Lower images: Numerical simulation of tissue formation within channels of various shapes. The lines (early time point 1, ongoing times 2 and 3) mark the simulated development of tissue formation due to ongoing culture time, which corresponds closely to the observed development of new tissue formation in vitro.

(Pro/Engineer PTC, USA) and produced using a 3D wax printer (Solidscape, Model Maker II) as described in Manjubala et al. (2005). The moulds were then filled with a slurry of hydroxylapatite particles, dried in air and then heated to 600°C to remove the wax moulds. A final sintering treatment was performed at 1300°C for 1 hour (Woesz et al., 2005).

Cell culture. Murine pre-osteoblastic cells, MC3T3-E1, were seeded with a density of 80,000 cells/cm^2 on the surface of the HA plates and cultured in α−MEM (SIGMA) supplemented with 10% FBS, 30 µg/ml ascorbic acid and 30 µg/ml gentamicin in a humidified atmosphere, 5% CO_2 at 37°C.

Visualisation of actin stress fibres. Cell cultures were washed with PBS, fixed with 4% paraformaldehyde, permeabilised with 0.1% Triton-X100 and incubated with 4x10^{-6} M phalloidin- fluoresceinisothiocyanate for 30 min at 4°C. Images of the stress fibres were obtained with a confocal laser scanning microscope (LEICA).

Quantification of the tissue area. The projected tissue area was determined by transmission light microscopy in combination with image analysis for each channel and time point.

pO_2 measurements. Oxygen concentrations were measured using a fibre optic oxygen micro-sensor with a tip diameter of approximately 30 µm (MicroxTX2, Presens, Regensburg, Germany) (van Dongen et al., 2003). The sensor tip was positioned within the channel closely against the growing tissue using a micro-manipulator (M3301, World Precision Instruments, Berlin Germany) and a stereo-microscope (MZ6, Leica Microsystems, Bensheim, Germany). Measurements were done in a clean-bench (Herasafe KS12, Heraeus, Germany) under sterile conditions and the same tissue was used for repeated oxygen measurements at a later time point. These values, expressed as a percentage of air-saturated buffer were plotted against the free area of the central channel.

Modelling curvature driven tissue growth in 2D. Tissue growth is modelled by the motion of the tissue-fluid interface in two dimensions. The initial tissue interface corresponded to the shape of the channel cross section, with all distances being normalised by the initial channel perimeter. The interfaces were discretized by a set of 90 equally spaced points on the channel surface. The local curvature κ_i, at a point i, is estimated from the inverse of the radius of curvature of the circle (circumcircle) that passes through this point and its two immediate neighbours, points $(i-1)$ and $(i+1)$. The tissue at point i on the interface is then taken to grow only if $\kappa_i \le 0$ (concave surface). It is assumed that no tissue can be lost, meaning that if $\kappa_i > 0$ (convex surface) at point i then the tissue is taken to be quiescent. The tissue at point i grows at a rate linearly proportional to the local curvature i.e. $ds_i / dt = -\lambda\kappa_i$ where λ is a constant giving the growth rate, with the direction of growth being towards the centre of curvature.

3. Results

The impact of three-dimensional geometrical features on new tissue formation in vitro was studied in HA plates perforated with channels of different shapes (triangular, square, hexagonal and round) and sizes. HA was chosen as the substrate material, since HA supports the formation of bone tissue rather than other tissue types (Kuboki et al., 1998).

3.1 Tissue formation in vitro

After seeding, the MC3T3-E1 murine osteoblasts adhered to the surface of the HA-plates, they started to proliferate, covering the surface of the HA plate and the inner surface of the channels. With ongoing culture time the multicellular network further amplified and formed new tissue within the channels of the artificial HA plate. The tissue consists of embedded cells and a collagen extracellular matrix. The advantage of the cell line used is that it is able to synthesize collagen fibrils and to build up a collagenous tissue matrix in the presence of ascorbic

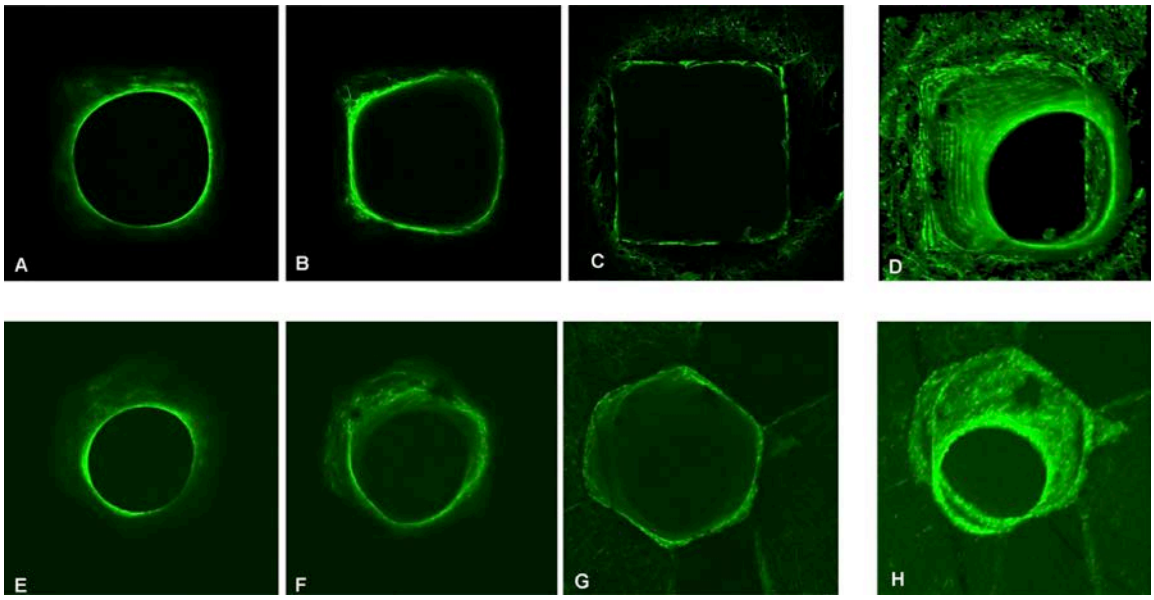

Figure 2. Three-dimensional fluorescence images. The cytoskeleton of the cells within the tissue is visualized by FITC staining and serial 2-dimensional sections were obtained with a confocal laser scanning microscope. Three-dimensional pictures were then stacked from all single pictures. In A to C three examples of the serial pictures obtained from the tissue formed in a squared channel are shown at depth 0 (C), -135 µm (B) and -470 µm (A), as well as the combination of all single pictures (D). In E to G three examples of the serial pictures obtained from the tissue formed in a hexagonal channel are shown at depth 0 (E), -260 µm (F) and -485 µm (G), as well as the combination of all single pictures (H).

acid completely autonomously (Rumpler et al., 2007). The formation of new tissue started in the corners of the polygonal channels, while cells on the faces were initially resting. Tissue grew uniformly on the surface of the round channels. The tissue thickness in the corners was greater in the triangular channel followed by the square and then the hexagonal channel, that is, in order of decreasing local curvature. Tissue amplification on the channel faces however was greater for the hexagonal channel than the square and then the triangular channel. This growth behaviour led to a rounding of the corners and the formation of a round central opening, regardless of the original shape (Fig. 1, upper images). The round opening of tissue is maintained even into the depth of the channels, as verified by confocal laser scanning microscopy (Fig. 2). With time the remaining space reduces in diameter, gradually becoming filled by tissue.

3.2 Tissue formation kinetics

Quantitative data on tissue formation kinetics were obtained from two cell culture experiments over more than 37 days with HA plates containing three channel sizes (perimeters P = 3.14, 4.71 and 6.28 mm) and four different cross-sectional shapes (triangle, square, hexagon, circle). Tissue formation as a function of culture time was estimated by measuring the projected tissue area A (Fig. 3) using transmission light microscopy. The amount of tissue within a given channel is roughly proportional to the project area, A, at any time point. An effect of pore size on tissue growth has been previously observed and was attributed to the increased surface area available to cells (O'Brien et al., 2005). This area dependence can be removed from the data by simply normalizing the projected tissue area A by the initial channel perimeter P, giving a mean layer thickness of tissue growing on the channel wall. The measured dependence of A/P on culture time is given in Fig. 4A. There is a significant difference between the mean layer-thickness due to channel size (perimeter), with more tissue being deposited at any time point in the smaller compared to the larger channels. However, as the mean layer thickness is normalized by the initial perimeter, accounting for the difference in initial surface areas, the effect of channel size implies that other geometric factors control the tissue growth, such as curvature. Although the local tissue formation was different in regions of different curvature (corners versus faces), no significant difference was seen in the total amount of tissue produced as a function of channel shape. This leads to the general effect that the mean layer thickness is similar in the different geometries despite the local variation in tissue distribution within the channels themselves.

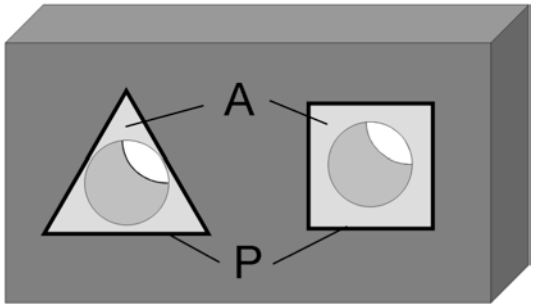

Figure 3. Sketch of two channels in a HA plate (dark grey). The figure illustrates the definition of the initial perimeter of the of channel cross-section P and of the projected tissue area A (light grey) with transmission light microscopy in each channel, which was used to calculate quantitative data for tissue formation kinetics.

3.3 Mechanisms of tissue growth

The observations made above illustrate that tissue growth depends on the geometry. One potential mechanism that would give such a behaviour is the generation of hypoxia due to respiratory activity of the cells. It is known for example, that an exogenous hypoxic state can induce proliferation in mammalian

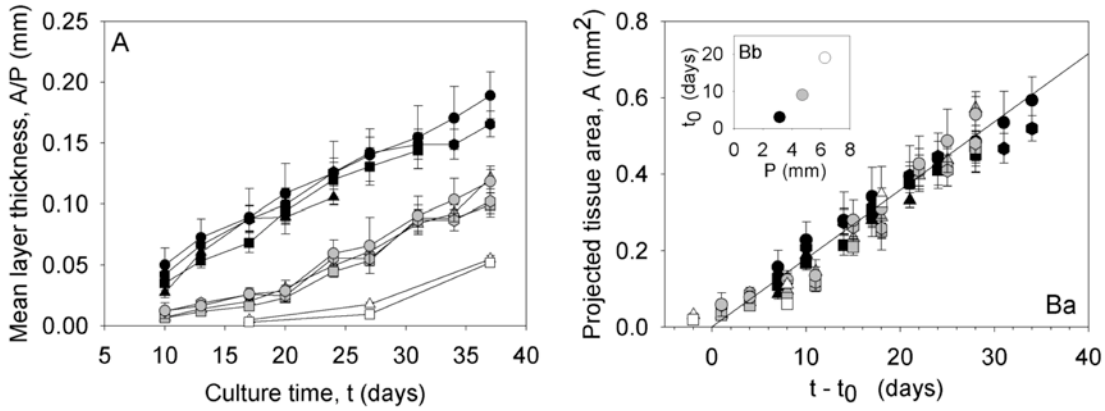

Figure 4. Quantitative tissue formation and kinetics. (A) Mean tissue layer thickness (calculated by the normalisation of the projected tissue area to the perimeter) as a function of culture time in different shapes (illustrated by the appropriate symbols) and different channel perimeters P = 3.14 mm (black), 4.71 mm (grey) and 6.28 mm (white). Data represent the mean value +/- stderr; n=10. (Ba) Projected tissue area as a function of culture time minus lag time, which is the time that is needed until cells start curvature driven growth. (Bb) The lag time is given as a function of initial channel perimeter.

endothelial cells (Schafer et al., 2003). A higher growth rate would therefore be expected in the smaller channels. In order to test this hypothesis, the oxygen content was measured in selected channels throughout the whole culture time. No significant correlation was found between the decrease of the central opening and the relative oxygen concentration value during culture time (Fig. 5) thus excluding the involvement of this mechanistic pathway.

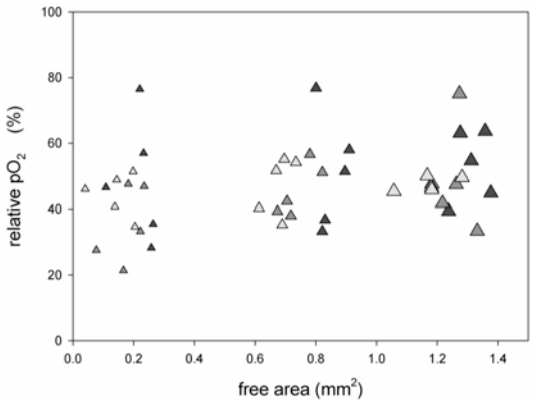

Figure 5. pO_2 measurements. MC3T3-E1 cells were seeded onto the HA and tissue formation was running over a time period of 43 days. At distinct time points, 25d (red symbols), 32d (green symbols) and 43d (yellow symbols), the oxygen concentration inside the central channel was measured in the direct vicinity of the growing tissue. These values, expressed as percentage of air-saturated buffer were, plotted against the free area of the central channel. The size of the triangle indicates the hole size (small: P = 3.14 mm, middle: P= 4.71 mm and large: P=6.28 mm); n=5

The sub-cellular organization of the tissue-like network in the corners suggests another mechanism behind the geometric control of tissue growth. The orientation of the actin stress fibres within cells neighbouring the tissue border shows a strong parallel alignment to the tissue-fluid interface (Fig. 6A). This is contrasted with the situation on the top of the HA plates outside the channels, where actin stress fibres in the cells show a completely random orientation within the multicellular network (Fig. 6B). It is known that amongst other factors, internal and/or external forces can trigger the assembly of filamentous stress fibres (Nelson et al., 2005, Putnam et al., 1998). This might hint towards a mechanism, in which mechanical forces arise in cells predominantly in regions of high curvature i.e. the corners, which in turn stimulates tissue growth.

As a general rule physical systems containing interfaces for which surface tension is important, evolve in such a way that the local motion of the interface is controlled by the local curvature (Pimpinelli and Villain, 1999). The main driving force behind this is the minimisation of interfacial energy via the minimisation of interfacial area. A simple two dimensional mathematical formulation of this assumes that any position on the tissue surface moves normal to it by a distance ds during a time step dt, according to $ds/dt = -\lambda\kappa$, where κ is the local curvature and λ a constant of proportionality. Fig. 1 (lower images) shows the numerical solution of this differential equation for the different channel geometries studied. Despite its simplicity, growth is controlled by only one parameter and one proportionality constant, the model gives exactly the results obtained from cell culture experiments shown in the upper images in Fig. 1. In particular, the corners are rounded first (because they have the largest curvature) and the diameter of the central opening then reduces. In the latter stages of tissue growth, the holes become circular, meaning the growth rate can be expressed as $dR/dt = -\lambda/R$, where R is the radius of the opening. This implies that the mean tissue thickness A/P will increase linearly with time as $A/P = 2\pi\lambda t/P$. The growth rate is larger for small perimeters, which is in agreement with the experimental observations (Fig. 4A). The model also predicts that the total tissue area should increase linearly with time at a rate $2\pi\lambda$ which is independent of the starting perimeter. For comparison A is plotted as a function of time for all the experiments (Fig. 4B). However, the experimental data will only superimpose as suggested by the theory, if a lag-time, t_0 is introduced and the tissue area A is plotted versus $(t - t_0)$. This means that in the cell culture experiments the area increases as $A = 2\pi\lambda(t - t_0)$ for $t \geq t_0$ (Fig. 4B inset). t_0 is an increasing function of

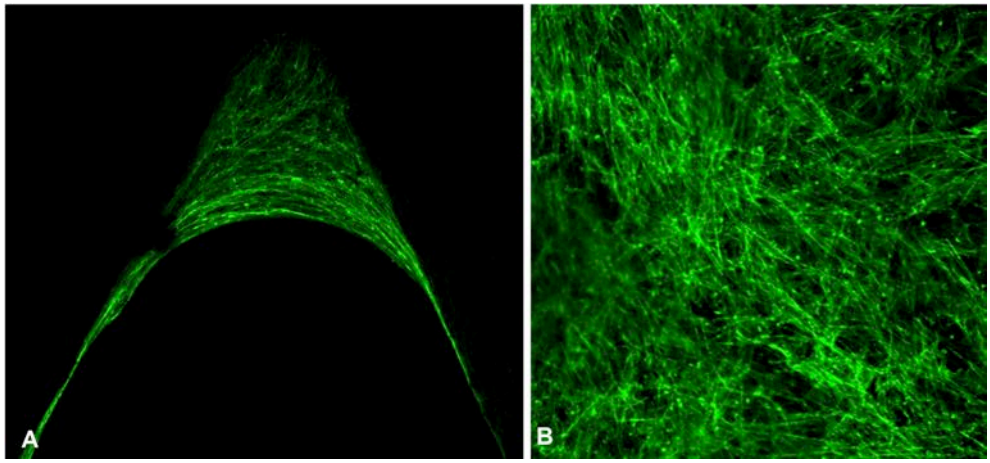

Figure 6. Fluorescence microscopic images of the stained cytoskeletal stress fibres within the new formed tissue. (A) A zoom into the corner of a triangular HA channel shows show a strong orientation of the stress fibres parallel to the tissue surface. (B) An image of the cell network on the external flat surface at regions in-between the channels show a completely random orientation

the initial perimeter (Fig. 5B inset). This lag-time can be understood as the time taken for cells to coat most of the inner channel surface integrating as a coherent network. This happens faster for smaller channel perimeters, corresponding to smaller inner channel surfaces.

4. Discussion

Murine osteoblasts are shown to proliferate and form a tissue-like network into the depth of the HA channels, as verified by confocal laser scanning microscopy. Quantitative analysis of tissue growth within different well-defined channel geometries allowed the evaluation of the effect of geometrical features (channel size and channel shape) on the tissue formation rate. The total quantity amount of new tissue formed in artificial three-dimensional substrates in vitro is surprisingly independent of the shape. It is dependent rather on the channel perimeter with the result, that the shorter the perimeter, the more tissue is formed at any time point. Measurements of the oxygen concentration taken over the course of the tissue growth periods illustrate that differences in oxygen deficiency between the channels is not a major factor. As the tissue thickness A/P is a value that is normalised by the perimeter this implies that other geometrical factors control tissue growth.

The simple model for curvature driven growth can describe the experimentally observed growth behaviour remarkably well, considering it uses just one known, geometric variable (the surface curvature) and one unknown parameter of the growth rate (Fig. 1). Tissue growth always started in the corners of the channels (large local negative curvature), while cells on the channel faces (zero curvature) produced tissue only when their neighbourhood became curved from tissue growing outward from the corners. Curvature driven tissue growth is also consistent with the experimentally measured independence of the average tissue thickness to the channel shape at constant perimeter length. If the assumption that the local growth rate is proportional to local curvature is correct, then the rate of change of average tissue thickness will be proportional to the average curvature. Following Fenchel's theorem (Fenchel, 1929), the average curvature, K ,of any closed convex plane curve is $2\pi/P$ where, P , is the perimeter. All the shapes investigated can be described in two dimensions by closed convex plane curves, meaning at fixed perimeter the average tissue thickness should be the same, as observed experimentally. In addition this also implies that smaller channels, which have higher average curvatures, will have a higher tissue thickness, as is observed. The preceding discussion clearly shows that curvature driven growth corresponds well with the experimental results. The physics behind curvature driven growth is well understood for membrane mechanics, crystal growth, and phase transformations. The driving force in these physical systems is the surface tension, which tends to reduce the surface (and therefore its curvature) as much as possible for a given volume. It is not obvious how to link this to the behaviour of cells and their cytoskeletons, but the observation of stress fibres provides a hint. The strong alignment of the stress fibres with the tissue interface, as well as their high concentration in the corners, suggests that mechanical forces may develop within in the tissue. If there is tensile cell-cell interaction between neighbouring cells in the tissue growth front, this could simulate a physical surface tension as in the physico-chemical systems mentioned above. Of course, this idea is still quite speculative, and requires further work to be ascertained.

Curvature driven growth is a process which leads to self organisation, in that tissue amplification creates a local change in curvature which then in turn feeds back to the cells themselves. As a consequence, curvature driven growth will cause channels or holes to be filled which has implications in many areas of bone biology and medicine. This effect may be the driving force of the filling mechanism of resorption lacunae by osteoblasts after osteoclastic bone resorption by reducing the curvature of the lacunae to zero (Robling et al., 2006, Seeman and Delmas, 2006). The size dependence of the lag-time in the tissue growth process, as well as the size dependence of curvature, points towards a critical size above which closure of the gap would take too long to occur on a physiological timescale. For example, the channels with a diameter of two millimetres showed a strongly reduced tissue growth within five weeks. This is

reminiscent of the existence of a critical defect size in bone above which defect healing no longer occurs (Goldstein, 2000, Weinkamer et al., 2004).

Another aspect of our results is that single cells with a size in the order of a few tens of microns can "feel" radii of curvature on the scale of millimetres. Where cells were stained for actin, it becomes apparent that cells interact through their cytoskeleton. Actin stress-fibres between neighbouring cells in the tissue border are aligned parallel to the tissue-fluid interface in such a way as they appear as a single ring-like structure (Fig. 6A). However, on the top of the HA plates outside the channels, actin stress fibres are randomly oriented (Fig. 6B), suggesting the absence of directed mechanical forces. Even before the ring-like structure is formed, actin stress fibres aligned parallel to the inner tissue surface can be seen in the channel corners. The high concentration of stress fibres in the surface layer as well as their well defined orientation suggests a relation to the development of mechanical forces within the tissue itself allowing curvature driven growth. Such stress fibres indicate that neighbouring cells interact via mechanical forces (Chen et al., 2004, Kaunas et al., 2005). A growing body of evidence suggests that mechanical events, in addition to molecular biological and chemical ones, play a central role in the process where cells explore and react to their neighbourhood. Even in 2-dimensional multicellular systems local mechanical forces appear in defined regions where cell proliferation is also increased compared to the neighbourhood (Nelson et al., 2005, Stegemann and Nerem, 2003). Following this mechanism, cells lying on the faces of the channels start proliferating only when they get a mechanical stimulus from being integrated into the tissue network growing out from the corners. In addition, the dihedral corners may not only be spatially optimised for force generation, as it is known that cells more closely mimic the in vivo environment when they are able to develop focal adhesion sites in three-dimensions as opposed to flat substrates (Beningo et al., 2004, Cukierman et al., 2001, Cukierman et al., 2002, Geiger, 2001). Mechanical equilibrium requires that stress fibres are either attached to the wall (corners) or form closed loops (as observed in the ring-like structures). These rings are also reminiscent of the "purse strings" reported in embryonic tissue healing, in the form of actin bundles aligned with the wound margin (Bement et al., 1993). Thus the wound is closed partially by active mechanical contraction (Jacinto et al., 2001, Martin and Lewis, 1992). It seems that connective tissues may use a highly conserved set of signals and cytoskeletal-based mechanisms to close holes in artificial systems.

5. Conclusion

In this paper quantitative measurements were made of the growth kinetics of collagenous tissue in an osteoblast culture for different three-dimensional channel geometries. Parameters describing channel geometry, namely the channel surface area (related to perimeter) and local curvature have been shown to strongly influence the tissue growth rate. Simple two dimensional simulations support the idea of curvature driven tissue growth, that is, the amount of tissue deposited is proportional to the local curvature. The awareness that a basic geometrical parameter, namely channel curvature, affects tissue formation kinetics in a 3-dimensional environment has far reaching implications in the understanding of bone remodelling and defect healing as well as for scaffold design in bone tissue engineering.

Acknowledgements

JD was funded by the Alexander von Humboldt Foundation.

References

Balaban, N. Q., Schwarz, U. S., Riveline, D., Goichberg, P., Tzur, G., Sabanay, I., Mahalu, D., Safran, S., Bershadsky, A. & Geiger, B. (2001) Force and focal adhesion assembly: a close relationship studied using micropatterned substrates. Nat. Cell Biol., 3, 466-472.

Bement, W. M., Forscher, P. & Mooseker, M. S. (1993) A novel cytoskeletal structure involved in purse string wound closure and cell polarity maintenance. J. Cell Biol., 121, 565-578.

Beningo, K. A., Dembo, M. & Wang, Y. L. (2004) Responses of fibroblasts to anchorage of dorsal extracellular matrix receptors. Proc. Natl Acad. Sci. USA, 101, 18024-18029.

Bischofs, I. B. & Schwarz, U. S. (2003) Cell organization in soft media due to active mechanosensing. Proc. Natl Acad. Sci. USA, 100, 9274-9279.

Cavalcanti-Adam, E. A., Volberg, T., Micoulet, A., Kessler, H., Geiger, B. & Spatz, J. P. (2007) Cell spreading and focal adhesion dynamics are regulated by spacing of integrin ligands. Biophys. J., 92, 2964-2974.

Chen, C. S., Mrksich, M., Huang, S., Whitesides, G. M. & Ingber, D. E. (1997) Geometric control of cell life and death. Science, 276, 1425-1428.

Chen, C. S., Tan, J. & Tien, J. (2004) Mechanotransduction at cell-matrix and cell-cell contacts. Annu. Rev. Biomed. Eng., 6, 275-302.

Choi, J. Y., Lee, B. H., Song, K. B., Park, R. W., Kim, I. S., Sohn, K. Y., Jo, J. S. & Ryoo, H. M. (1996) Expression patterns of bone-related proteins during osteoblastic differentiation in MC3T3-E1 cells. J. Cell Biochem., 61, 609-618.

Cukierman, E., Pankov, R., Stevens, D. R. & Yamada, K. M. (2001) Taking cell-matrix adhesions to the third dimension. Science, 294, 1708-1712.

Cukierman, E., Pankov, R. & Yamada, K. M. (2002) Cell interactions with three-dimensional matrices. Curr. Opin. Cell Biol., 14, 633-639.

Discher, D. E., Janmey, P. & Wang, Y.-L. (2005) Tissue cells feel and respond to the stiffness of their substrate. Science, 310, 1139-1143.

Engler, A. J., Sen, S., Lee Sweeney, H. & Discher, D. E. (2006) Matrix elasticity directs stem cell lineage specification. Cell, 126, 677-689.

Fenchel, W. (1929) Uber Krümmung und Windung geschlossener Raumkurven. Math. Annalen, 101, 1432-1807.

Geiger, B. (2001) Cell biology. Encounters in space. Science, 294, 1661-1663.

Geiger, B. & Bershadsky, A. (2002) Exploring the neighborhood: adhesion-coupled cell mechanosensors. Cell, 110, 139-142.

Geiger, B., Bershadsky, A., Pankov, R. & Yamada, K. M. (2001) Transmembrane crosstalk between the extracellular matrix--cytoskeleton crosstalk. Nat. Rev. Mol. Cell Biol., 2, 793-805.

Goldstein, S. A. (2000) In vivo nonviral delivery factors to enhance bone repair. Clin. Orthop. Relat. Res., 379S, S113-S119.
Habibovic, P., Yuan, H., Van Der Valk, C. M., Meijer, G., Van Blitterswijk, C. A. & De Groot, K. (2005) 3D microenvironment as essential element for osteoinduction by biomaterials. Biomaterials, 26, 3565-3575.
Jacinto, A., Martinez-Arias, A. & Martin, P. (2001) Mechanisms of epithelial fusion and repair. Nat. Cell Biol., 3, E117-23.
Jin, Q. M., Takita, H., Kohgo, T., Atsumi, K., Itoh, H. & Kuboki, Y. (2000) Effects of geometry of hydroxyapatite as a cell substratum in BMP-induced ectopic bone formation. J. Biomed. Mater. Res., 51, 491-499.
Kaunas, R., Nguyen, P., Usami, S. & Chien, S. (2005) Cooperative effects of Rho and mechanical stretch on stress fiber organization. Proc. Natl Acad. Sci. USA, 102, 15895-15900.
Kuboki, Y., Takita, H., Kobayashi, D., Tsuruga, E., Inoue, M., Murata, M., Nagai, N., Dohi, Y. & Ohgushi, H. (1998) BMP-induced osteogenesis on the surface of hydroxyapatite with geometrically feasible and nonfeasible structures: topology of osteogenesis. J. Biomed. Mater. Res., 39, 190-199.
Manjubala, I., Woesz, A., Pilz, C., Rumpler, M., Fratzl-Zelman, N., Roschger, P., Stampfl, J. & Fratzl, P. (2005) Biomimetic mineral-organic composite scaffolds with controlled internal architecture. J. Mater. Sci. Mater. Med., 16, 1111-1119.
Martin, P. & Lewis, J. (1992) Actin cables and epidermal movement in embryonic wound healing. Nature, 360, 179-183.
Nelson, C. M., Jean, R. P., Tan, J. L., Liu, W. F., Sniadecki, N. J., Spector, A. A. & Chen, C. S. (2005) Emergent patterns of growth controlled by multicellular form and mechanics. Proc. Natl Acad. Sci. USA, 102, 11594-11599.
O'brien, F. J., Harley, B. A., Yannas, I. V. & Gibson, L. J. (2005) The effect of pore size on cell adhesion in collagen-GAG scaffolds. Biomaterials, 26, 433-441.
Pimpinelli, A. & Villain, J. (1999) Physics of Crystal Growth, Cambridge, Cambridge University Press.
Putnam, A. J., Cunningham, J. J., Dennis, R. G., Linderman, J. J. & Mooney, D. J. (1998) Microtubule assembly is regulated by externally applied strain in cultured smooth muscle cells. J. Cell Sci., 111 (Pt 22), 3379-3387.
Quarles, L. D., Yohay, D. A., Lever, L. W., Caton, R. & Wenstrup, R. J. (1992) Distinct proliferative and differentiated stages of murine MC3T3-E1 cells in culture: an in vitro model of osteoblast development. J. Bone Miner. Res., 7, 683-692.
Robling, A. G., Castillo, A. B. & Turner, C. H. (2006) Biomechanical and molecular regulation of bone remodeling. Annu. Rev. Of Biomed. Eng., 8, 455-498.
Rumpler, M., Woesz, A., Varga, F., Manjubala, I., Klaushofer, K. & Fratzl, P. (2007) Three-dimensional growth behaviour of osteoblasts on biomimetic hydroxylapatite scaffolds. J. Biomed. Mater. Res., 81A, 40-50.
Schafer, M., Ewald, N., Schafer, C., Stapler, A., Piper, H. M. & Noll, T. (2003) Signaling of hypoxia-induced autonomous proliferation of endothelial cells. FASEB J, 17, 449-451.
Seeman, E. & Delmas, P. D. (2006) Bone quality - The material and structural basis of bone strength and fragility. N. Engl. J. Med., 354, 2250-2261.
Stegemann, J. P. & Nerem, R. M. (2003) Phenotype modulation in vascular tissue engineering using biochemical and mechanical stimulation. Ann. Biomed. Eng., 31, 391-402.
Van Dongen, J. T., Schurr, U., Pfister, M. & Geigenberger, P. (2003) Phloem metabolism and function have to cope with low internal oxygen. Plant. Physiol., 131, 1529-43.
Van Eeden, S. P. & Ripamonti, U. (1994) Bone differentiation in porous hydroxyapatite in baboons is regulated by the geometry of the substratum: implications for reconstructive craniofacial surgery. Plast. Reconstr. Surg., 93, 959-966.
Weinkamer, R., Hartmann, M. A., Bréchet, Y. & Fratzl, P. (2004) Stochastic Lattice Model for Bone Remodeling and Aging. Phys. Rev. Lett., 93, 228102.
Woesz, A., Rumpler, M., Stampfl, J., Varga, F., Fratzl-Zelman, N., Roschger, P., Klaushofer, K. & Fratzl, P. (2005) Towards bone replacement materials from calcium phosphates via rapid prototyping and ceramic gelcasting. Mater. Sci. Eng. C, 25, 181-186.

7.2 [TG2] Two stages in three-dimensional in vitro growth of tissue generated by osteoblast-like cells

Kommareddy, K. P., Lange, C., Rumpler, M., Dunlop, J. W. C., Manjubala, I., Cui, J., Kratz, K., Lendlein, A., Fratzl, P.

*Published in **Biointerphases**, 2010, 5, 45-52.*
doi: 10.1116/1.3431524

Reprinted with permission Open Access Publication

Abstract: Bone regeneration is controlled by a variety of biochemical, biomechanical, cellular, and hormonal mechanisms. In particular, physical properties of the substrate such as stiffness and architecture highly influence the proliferation and differentiation of cells. The aim of this work is to understand the influence of scaffold stiffness and cell seeding densities on the formation of tissue by osteoblast cells within polyether urethane scaffolds containing pores of different sizes. MC3T3-E1 preosteoblast cells were seeded on the scaffold, and the amount of tissue formed within the pores was analyzed for culture times up to 49 days by phase contrast microscopy. The authors show that the kinetics of three-dimensional tissue growth in these scaffolds follows two stages and can be described by a universal growth law. The first stage is dominated by cell-material interactions with cell adherence and differentiation being strongly dependent on the polymer material. After a delay time of a few weeks, cells begin to grow within their own matrix, the delay being strongly dependent on substrate stiffness and seeding protocols. In this later stage of growth, three-dimensional tissue amplification is controlled rather by the pore geometry than the scaffold material properties. This emphasizes how geometric constraints may guide tissue formation *in vitro* and shows that optimizing scaffold architectures may improve tissue formation independent of the scaffold material used.

I. Introduction

Porous three-dimensional scaffolds with interconnected pore channels are used extensively in the field of bone tissue engineering[1,2]. The interconnected pore channel network and pore architecture allows cells to penetrate into the scaffold and be supplied with nutrients, enhancing new tissue growth by the cells[3,4]. Previous reports have shown that a variety of physical parameters of the scaffold influences the behaviour of osteoblast cells, specifically the local surface chemistry[5,6], physical characteristics such as material topography[7-9], roughness[10,11] as well as stiffness[12-14]. The mechanical properties of the substrate, namely stiffness, influence cell differentiation and proliferation[12]. Mesenchymal stem cells for example were shown to differentiate into neurogenic lineages on soft substrates (0.1-1 kPa), myogenic lineages on stiffer substrates (8-17 kPa) and osteogenic lineages on relatively rigid substrates (25-40 kPa)[15]. It has also been demonstrated that cell adhesion depends on roughness and the nanostructure of the surface[16-20] with a higher differentiation potential and lower proliferation rate being observed on rougher surfaces[16]. In addition to geometric features at the nanoscale, the topology of the local environment, at length scales larger than the cell size, also affects the behaviour of cells[9]. These larger length scales, such as the pore size of scaffolds significantly influences cell adhesion, migration and growth[21-23], but the extent of tissue formation by the cells in these pore channels has been rarely studied.

In our earlier study, we designed a simple model system to investigate the effect of pore shape and size within hydroxyapatite (HA) scaffolds (stiffness in GPa range) on the tissue formation by murine pre-osteoblast cells[24]. In the initial phase of tissue formation in the scaffold, cells migrate, adhere and proliferate within the pore structure, a process which is strongly influenced by the material properties and later with ongoing culture time, cells synthesize sufficient amounts of matrix to proliferate inside their own extracellular tissue[25,26]. In the present study polyether urethane (PU) polymers, which exhibited good cell compatibility in in vitro tests [27,28] and biocompatibility in in vivo studies as artificial heart valve and wound dressings[29] or as a potential dialysis catheter[30], with stiffnesses lower than HA, were selected to produce scaffolds with different pore sizes and shapes. The scaffold stiffnesses were controlled by modifying the multiblock copolymer segment ratio of the PU[31,32]. Cell culture experiments were performed on the scaffolds using MC3T3-E1 pre-osteoblast cells, a well established cell line for bone biology studies[33-35] known for lineage differentiation into mature osteoblasts. These experiments enabled the influence of stiffness and different cell seeding protocols on the kinetics of tissue formation to be investigated and compared to the results from the earlier HA scaffolds[24].

II. Materials and methods

A. Materials

Aliphatic polyether urethanes (PU) supplied by Noveon (Wilmington, MA) with the trade name Tecoflex®, were used directly without further purification. The mechanical properties of the polymer sheets were determined from tensile tests at ambient temperature and at 37 °C in water. Tensile tests were carried out on a Z005 tensile tester (Zwick, Ulm, Germany) at ambient temperature and on a Z1.0 tensile tester equipped with a temperature controlled liquid chamber at 37 °C in water, with a strain rate of 5 mm/min. For each PU composition 5 measurements were conducted. The selected polymer samples are named PU75, PU120 and PU310 according to their elastic modulus (E-Modulus) determined at ambient temperature.

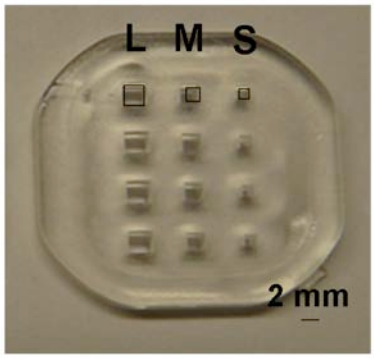

Figure 1. Representative image of PU120 scaffolds with round and square pores of different perimeters (p). S: p = 3.14 mm, M: p = 4.71 mm, L: p = 6.28 mm. The thickness of the scaffolds is 2 mm.

B. Scaffold processing

HAAKE Minijet-Micro injection moulding machine (Thermo Electron GmbH, Karlsruhe, Germany) was applied to prepare 2 mm thick polymer scaffolds with square-shaped pores. The mould temperature was maintained at 25 °C with a pressure of 8 bar. The extrusion cylinder temperature was 190 °C for PU75, 200 °C for PU120 and 210 °C for PU310. The round pores were drilled mechanically into the injection moulded chips. Three different pore sizes were produced in the scaffolds. The perimeter of the small, middle and large pores was 3.14 mm, 4.71 mm and 6.28 mm respectively (Fig. 1).

C. Cell culture experiments

The pre-osteoblastic mouse calvariae MC3T3-E1 cell line (generous gift from Dr. F. Varga, Ludwig Boltzmann Institute of Osteology, Vienna, Austria) was used for in vitro experiments. For seeding on scaffolds, near confluent cells during fourth passage treated with Pronase (Roche diagnostics GmbH, Mannheim, Germany) and EDTA (Sigma-Aldrich, St. Louis, MO) were used. These cells were suspended in a culture medium of α-MEM (Sigma-Aldrich, St. Louis, MO) supplemented with 10% foetal calf serum (FCS) (PAA laboratories, Austria), 50 µg/ml ascorbic acid (Sigma-Aldrich, St. Louis, MO) and 30 µg/ml gentamicin (Sigma-Aldrich, Steinheim, Germany). The cell seeded scaffolds were incubated in a humidified atmosphere with 5% CO_2 at 37 °C up to 49 days, while changing the medium twice a week. Three different cell seeding protocols were followed in cell culture experiments. In the first protocol, $1x10^5$ cells/cm^2 were suspended in 3 ml of medium and poured on the scaffolds with round pores. In the second protocol, $3x10^5$ cells/cm^2 were suspended in 3 ml of medium and poured on the scaffolds with square pores. In both protocols, the cells initially attach on the surface of the scaffold and then migrate into the pores. In the third protocol, $8x10^4$ cells/cm^2 were suspended in a minimal amount of medium and dropped on surface of the scaffold with square pores, leading to aspiration of cell suspension by the pores, which enables complete covering of pores with cells from the very beginning. All the experiments were performed twice under identical conditions.

D. DAPI staining and visualization of cell shape

Sample	E-Modulus at RT [MPA]	E-Modulus at 37°C [MPA]
PU310	312 ± 53	208 ± 29
PU120	120 ± 27	7 ± 2
PU75	74 ± 7	6 ± 3

Table 1. Mechanical properties of polyether urethane (PU) polymer materials determined by tensile tests.

To analyse the initial cell attachment on the surface of PU scaffolds, about $1x10^5$ cells/cm^2 were suspended in medium and seeded on the scaffolds. Initial cell attachment and distribution on the surface, after 6 h of incubation, were studied by DAPI staining (4',6-diamidine-2'-phenylindole dihydrochloride, Roche diagnostics GmbH, Mannheim, Germany). Briefly, after 6 h the cell-culture medium was removed and the cells were washed with DAPI-methanol solution (1 μ g/ml) and incubated in fresh DAPI-methanol solution for 15 min at 37 °C. The staining solution was removed and the samples were washed in phosphate buffered saline (PBS) and observed under fluorescence microscope (Leica DM RB, Germany).

The cell shapes were visualized using DAPI-flourescent iso-thiocyanate (FITC) staining. After 6h cells were briefly washed twice with PBS, and fixed in a 4% paraformaldehyde (PFA, Fluka, Steinheim, Germany) solution for 15 min at room temperature. Unreacted PFA was washed off with PBS. Cells were then permeabilized with 0.1% Triton-X100 (Sigma-Aldrich, Steinheim, Germany) for 2 min, PBS washed and stained with phalloidin-FITC (Invitrogen, Oregon, USA) for 1h. Later samples were washed several times with PBS and stained with DAPI for 15 min at 37 °C. Finally the samples were washed in PBS and observed using a fluorescence microscope (Leica DM RXA2, Germany) with an oil immersion objective and appropriate filters.

E. Alkaline phosphatase staining

The MC3T3-E1 osteoblast-like cells have the potential to undergo differentiation into mature osteoblasts[33]. Alkaline phosphatase (ALP) activity is an early differentiation marker of pre-osteoblastic cells to mature osteoblasts. After 21 days of culture, localization of ALP activity was qualitatively performed with the azo-dye method[36]. The cells were fixed in 4% PFA in PBS for 10 min, intensively rinsed with PBS and then with 0.9% w/v NaCl (Roth, Karlsruhe, Germany). Afterwards the cells were incubated at 37 °C with napthol AS-MX phosphate disodium salt (Sigma-Aldrich, St. Louis, MO) and fast blue RR salt (Sigma-Aldrich, Steinheim, Germany) in 5% sodium tetra borate (Sigma-Aldrich, Steinheim, Germany) buffer containing 0.9% NaCl and MgSO4 (Sigma-Aldrich, Steinheim, Germany). Later the samples were placed in PBS and observed under an optical microscope in transmission mode (Leica DM RXA2, Germany).

F. Confocal microscopy

The alignment of the cells and actin cytoskeleton in the newly formed three-dimensional tissue network was investigated with a confocal laser scanning

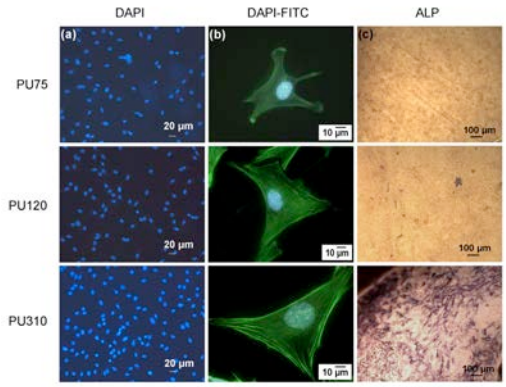

Figure 2. (a) DAPI staining of cells (nuclei) seeded at 10^5 cells/cm^2, 6h after cell seeding (Scale 20µm). (b) FITC-DAPI staining of MC3T3-E1 cells showing the spreading of cytoskeleton on PU75, PU120 and PU310 respectively. (Scale 10µm). (c) Alkaline phosphatase enzyme staining of PU75, PU120 and PU310 respectively after 21 days of culture (Scale 100µm).

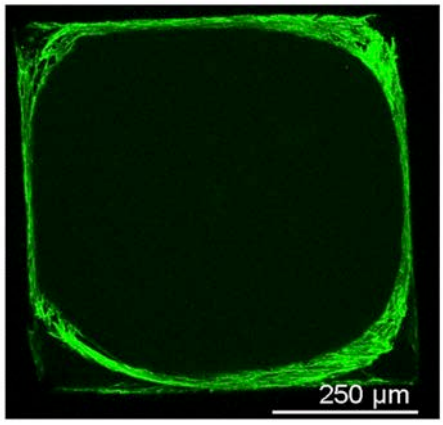

Figure 3. Two dimensional stack projections of FITC-Phalloidin staining of actin filaments in (a) small round pore (z-stack projection is 76µm thick consisting of 10 sections with a 8µm step size) (b) small square pore of PU120 scaffolds after 49 days of culture (z-stack projection is 100µm thick consisting of 100 sections with a 1µm step size).

microscope (Leica TCS SP, Germany), 488 nm laser excitation was used and emission measured at 514 nm. Cells were fixed in 4% PFA in PBS for 10 min; permeabilized with 0.1% Triton-X100 (Sigma-Aldrich, Steinheim, Germany) and later stained with FITC-conjugated-phalloidin ($4x10^{-6}$ M, Sigma-Aldrich, Steinheim, Germany) for 30 min at 4 °C.

G. Phase contrast microscopy and analysis of tissue formation

An inverted phase contrast microscope (Nikon Eclipse TS100 F, Germany) was used to monitor the cell distribution and tissue formation within the pores. Images were captured at least once a week over the culture period of 49 days. The amount of tissue formed within the pores by the cells was estimated from the projected tissue area as seen in the phase contrast images[24]. This projected tissue area was calculated from the area between the inner tissue-medium boundary and the original pore boundary imaged at the start of the experiment. This calculation was performed using Image J software (NIH Image analysis software, USA).

H. Statistical analysis

The delay times (t_0) of tissue formation in all the experiments were analysed for statistical significance using three way ANOVA, performed to compare the interdependency of pore size, material and seeding methods. All pair-wise multiple comparison was done by Holm-Sidak method and p values of less than 0.05 were considered significant.

III. Results

A. Scaffold properties

The PU polymers used were aliphatic multiblock copolymers synthesized from methylene bis(p-cyclohexyl isocyanate) (H_{12}MDI), poly(tetramethylene glycol) (PTMEG, Mn = 1000 g·mol^{-1}) and 1,4-butanediol (1,4-BD)[31,32]. The thermal and mechanical properties of these PU polymers can be adjusted by variation of H_{12}MDI / 1,4-BD to H_{12}MDI / PTMEG segment ratio. The composition, i.e., H_{12}MDI / 1,4-BD to H_{12}MDI / PTMEG segment ratio analyzed by ^{1}H-NMR spectroscopy showed that for PU310 a H_{12}MDI / 1,4-BD segment content was about 58 wt% while the values for the PU120 and PU75 were around 45 wt%[32]. Mechanical properties of the PU materials were investigated by tensile tests at ambient temperature, as well as under physiological conditions at 37 °C in water (Table 1). The elastic modulus was found to increase with increasing content of H_{12}MDI / 1,4-BD segment from 75 MPa to 310 MPa at ambient temperature. In addition, the mechanical properties explored under physiological conditions showed that all PU samples are significantly softer than at ambient temperature. For PU310 an elastic modulus of 208 MPa was observed, while PU120 and PU75 exhibited lower values around 6 MPa to 7 MPa. The softening of the PU samples in water at 37 °C can be explained by approaching the temperature of the glass transition associated to the mixed phase in combination with a softening effect induced by a water uptake of 2 wt%.

B. Cell adhesion and cell shape

Adhesion of MC3T3-E1 pre-osteoblast cells on the surface of polyurethane scaffolds was studied in terms of adhered number of cells and cell shape. On the polymer scaffold made from PU75, the softest polymer substrate used, a smaller number of cells were seen to adhere compared with PU120 and PU310 (Fig. 2a). The individual cells observed by FITC staining showed many broad lamellipodia structures with less actin organization on PU75 with a smaller cell size (Fig. 2b). Whereas on PU310 scaffolds, the stiffest polymer substrate used, the cells developed highly directional lamellipodia with more actin organization, formation of stress fibres and cells were stretched more.

C. Alkaline phosphatase enzyme activity

Alkaline phosphatase is an early marker for differentiation of pre-osteoblasts to mature osteoblasts. The ALP activity of the cells was observed on the surface of the scaffolds, positive cells showed a violet coloration. By comparing the ALP pattern on the three substrate, cells on PU310 exhibit a strong staining for ALP, whereas cells on the other two polymers, PU120 and PU75, were negative (Fig. 2C). This suggests that the stiffer polymer substrate supports differentiation of osteoblast precursor cells.

D. Confocal microscopy

The confocal microscope images of the pores after 49 days of culture showed that cells adhered to the surface of the scaffold after seeding and migration into the pores. Within the pores they proliferated and formed a tissue-like network. In the square pores cells predominantly started to proliferate in corner regions, as shown in Fig. 3 whereas in the circular pores tissue proliferation occurred uniformly across the surface. Within this tissue-like network cells built multilayers and actin-stress fibres of the cells in the tissue were aligned parallel to the internal tissue-medium border.

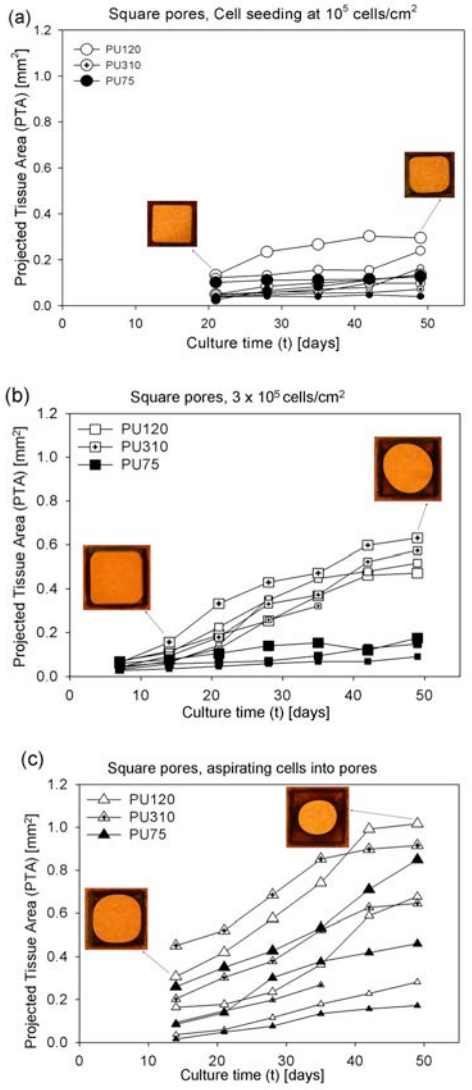

Figure 4. Exemplary data of measured projected tissue area formed as a function of time tissue growth experiment made using different cell seeding protocols (a) 10^5 cells/cm^2, (b) 3 x 10^5 cells/cm^2, and (c) aspiration of cells into pores. The symbols indicate the polyurethane polymer used, PU75 (Black), PU120 (White) and PU310 (Crossed) and the size of the symbol indicates pore size. The inset images are micrographs of the pores at example time points illustrated by arrows in the graphs.

E. Tissue formation

The amount of tissue formed in the pores was analyzed from phase contrast microscopy images. At a seeding concentration of 10^5 cells/cm^2, the tissue growth started earlier on PU310 compared to PU120 and then PU75 (in order of decreasing stiffness) as seen from Fig. 4a. This difference in the early stage of tissue formation can be related to the active reaction of cells to the mechanical properties of the PU substrates (Fig. 2). Further we found that tissue growth started earlier in smaller pores compared to middle and larger pores and were the first to be filled with tissue (images not shown). At a seeding density of 3x10^5 cells/cm^2, where the cells are confluent on the scaffolds after the initial cell attachment phase, the tissue growth rate was independent of channel size, however tissue growth begins earlier for the highest scaffold stiffnesses (Fig. 4b). For the experiments, in which cells are aspirated into the channels (8x10^4 cells/cm^2), neither the substrate nor channel size influenced the start of tissue growth although larger amounts of tissue was formed in the large pores compared to the smaller pores (Fig. 4c).

F. Tissue growth kinetics

The tissue growth kinetics were analysed using the same procedure reported for tissue growth on HA scaffolds, by determining the projected tissue area as a function of time within each pore[24]. The tissue growth in terms of projected tissue area, A, can be described in the form:

$$A = K\left(t - t_0\right) \qquad (1)$$

where K is the growth rate in the later stages and t_0 a delay time needed to reach this stage of tissue growth. The delay time (t_0) was determined empirically by shifting the tissue area data (initially plotted as a function of culture time t) along the horizontal axis until the graphs nearly coincided as shown in Fig. 5a. Fig. 5b summarizes all the data obtained with the PU samples for the projected tissue area plotted as a function of ($t - t_0$). Altogether 54 data sets are superimposed obtained from six experiments with three seeding procedures, each repeated twice, and where each experiment had simultaneously three pore sizes and three materials in the culture medium. The Fig. 5(c-e) give the delay times (t_0) for the three types of seeding procedures respectively, as a function of the pore size.

IV. Discussion

This paper investigates the growth kinetics of three-dimensional tissue formation within the pore channel of polymeric scaffolds. The influence of mechanical properties (stiffness) of the polymer scaffold with square and circular pore channels and different cell seeding densities on the kinetics of tissue growth was observed and compared to a previous study on HA scaffolds[24].

The cell culture experiment on these PU scaffolds were carried out using three different cell seeding protocols. The first protocol, being similar to that previously reported on HA scaffolds[24], showed a low proliferation rate of cells on the polymers (Fig. 4a). Therefore, the seeding density was increased in two ways. First, the same protocol was conserved but the cell density was increased by a factor 3. Using this seeding protocol the cells adhere to the surface of the scaffold after seeding. Afterwards cells proliferate and actively migrate into the pores, followed by tissue

formation. Secondly, $8x10^4$ cells/cm^2 were initially dispersed into a small amount of medium and dropped onto the scaffolds. The consequence was that the medium highly enriched with cells was sucked by capillary forces into the pores and cells attach to the inner wall of the pores from the beginning.

During the initial period of cell culture on the surface of the scaffold, fewer cells were observed on PU120 and PU75 compared to PU310. This shows that substrate stiffness has an impact on cell adhesion, cell spreading and cell proliferation (Fig. 2a, b). Furthermore, differentiation of osteoblast precursor cells seems to be accelerated by a stiffer substrate, as observed in case of PU310 (Fig. 2c). This is consistent with the known influence of substrate stiffness on cell behaviour and differentiation known from other cell types [12-14].

Cells seeded on the scaffolds adhered initially to the surface of the pore channel, then started to proliferate and produce extracellular matrix forming a tissue layer. Cells at the corner of the square pores showed higher proliferation rates and by this behaviour formed a network leaving a round central canal open, regardless of the original pore shape. Due to culture time, this central canal decreased in diameter, but kept its shape until complete closure. There is no initial specificity of the cell location in the circular pores (Fig. 3a), and this resembles the fourth stage of new tissue formation by osteoblast-like cells described as an "osteon-like" structure by Frosch et al[37].

Several remarkable observations can be made based on Fig. 5.

1. The raw data (Fig. 4a-c) obtained from the microscopy observations during the culture period agree remarkably well after the time scales are shifted by an empirical delay time t_0 (Fig. 5a).
2. The late stage growth is linear and the slope agrees perfectly with what was found for tissue growth on HA. This slope is independent of the seeding procedure and of the material, indicating that the late stage tissue growth kinetics is universal for the type of cells considered (Fig. 5b).
3. The delay time before this universal growth behaviour is reached can be substantial (in the order of a month) and varies strongly with material type and with cell seeding density.
4. For all PU materials, the delay time (at similar cell seeding conditions) is larger than for HA (Fig. 5c).
5. There are only small differences between the PU materials. Only with the softest material PU75 there is somewhat longer delay time (full symbols) at all cell seeding densities.
6. The cell seeding density has a dramatic effect on the delay time before the onset of universal three-dimensional growth. Indeed, at normal seeding densities, the delay time slightly increases with pore perimeter (Fig. 5c), at higher densities there is virtually no dependence on pore perimeter (Fig. 5d), and when the cells are sucked directly into the pores the delay time decreases substantially with pore perimeter (Fig. 5e).

The progression of new tissue formation shows a time dependent development and follows two main steps, which can be described as an early and a late stage in growth. Firstly, cell-material interactions play a crucial role at the very beginning and determine cell attachment and proliferation. This is seen clearly in

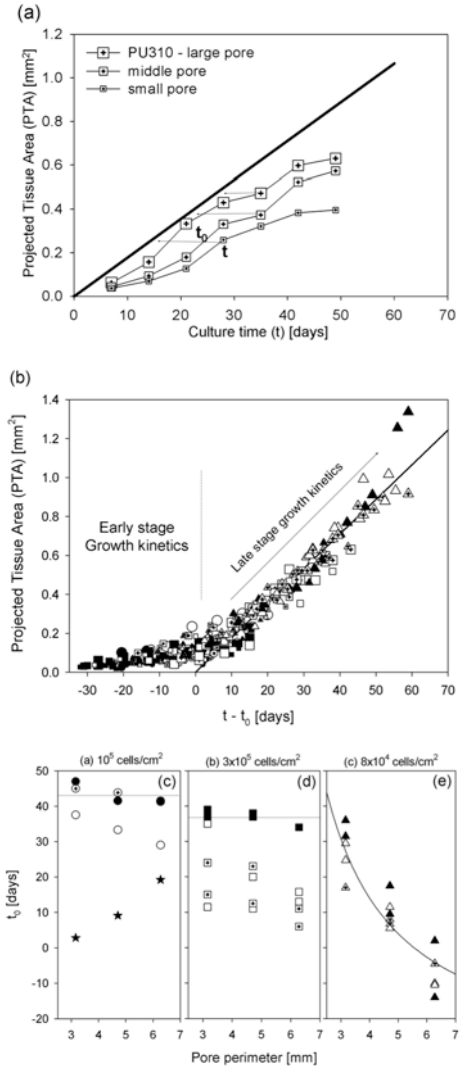

Figure 5. a) Description of the delay time (t_0) determination in one of the experiments performed with PU310 with square shaped pore channels. Projected tissue area was moved horizontally along the X-axis (time) so that they coincide with data of HA. The shift gives empirically the delay time (t_0). (b) All data (three different seeding protocols performed twice, each with three pore sizes and three material types) plotted on top of each other. The full line is the late stage growth kinetics obtained earlier on hydroxyapatite (HA) scaffolds. (Symbols represent the different seeding methods: ○ - 10^5 cells/cm^2, □ - $3x10^5$ cells/cm^2 and △ - aspirating cells $8x10^4$ cells/cm^2 into the pores and the black, white and crossed symbols represent PU75, PU120 and PU310 materials respectively). The three graphs (c-e) show the delay time (t_0) for three cell seeding procedures as a function of the pore perimeter. The colours of symbols indicate the type of PU material. The stars in 'c' shows the values obtained in previous tissue growth experiments on HA for comparison. The values of t_0 significantly varies due to the effect of pore size and seeding method ($P<0.001$) and there is no difference between PU120 and PU75 (softer material) compared to PU310 (harder material).
Note: Circular data points represent the round pores and the square and triangular data points represent the square pores.

the strong dependence of the delay time t_0 on the type of material with the delay time being longer for tissue growth on PU than on HA. This difference can amount to several weeks, which is crucial from a tissue engineering point of view. The critical initial step, cell attachment to the scaffold, involves the formation of focal adhesions, those mediate cell anchoring by physically coupling integrin receptors to the contractile actin cytoskeleton. The pattern of focal adhesions expressed is highly dependent on surface properties, such as chemistry and topographical features[17,20,38]. HA and PU materials provide differences in surface chemistry. This may result in the creation of different focal adhesion molecules. It is known that patterns of vinculin and focal adhesion kinase expression differ strongly when osteoblasts are seeded either onto HA or onto titanium or glass surfaces[39,40]. We speculate that cell adhesion is more efficient on HA than on PU, which gives a higher initial cell number on HA after seeding, confluence is reached sooner and multilayer tissue formation starts earlier in HA.

Cells were seeded using three protocols allowing for the formation of a confluent cell layer between one or three days. The cell seeding density has a dramatic effect on the delay time. This is not unexpected as the cell seeding density influences the time until a confluent cell layer is formed on top of the material and growth into the third dimension can start[41]. With the lowest cell seeding density, cells need time to proliferate before they can migrate from the flat substrate surface into the pores perpendicular to it. Given that the larger pores have larger surface areas, it takes longer for the larger pores to form a confluent cell layer, hence a longer delay time (Fig. 5c). When the cell seeding density is increased by 3 fold, cells take a very short time to reach confluence and the migration can start much earlier resulting in little dependence of the delay time on pore perimeter is seen (Fig. 5d). When a concentrated cell suspension is sucked into the pores (as for Fig. 5e), many more cells end up in larger pores than in smaller ones. In fact, the number of cells in a pore scales with the square of its radius, while the pore surface is only proportional to the radius. This would explain why the delay time is much shorter in the larger pores (Fig. 5e), since the number of cells per unit surface increases with the radius.

In late stages of tissue formation by the osteoblast-like cells, attachment and proliferation was followed by the autonomous synthesis of a collagen matrix. Once sufficient tissue is formed cell-scaffold interactions become irrelevant and the multilayer network of the extracellular matrix (ECM) overtakes the part of the scaffold material as the main controller of cell response. Ongoing three-dimensional amplification of the new tissue now follows new rules and boundary conditions, namely pliability of the extra cellular matrix, the development of forces within the matrix and the local geometry (curvature) of the tissue surface itself[24,42]. The late stage growth kinetics in the PU scaffolds were observed to be exactly the same that of HA and the growth kinetics is again consistent with a growth law in which the local growth rate is proportional to the local curvature of the tissue layer previously produced by the cells, as shown in HA[24]. The fact that the slope of the late growth curve does not depend on cell seeding density nor on the type of material and is even the same for polymer and HA (observations 1 and 2) indicates that at these late stages of tissue growth the supporting material plays little role. At this stage, the extracellular tissue layer is thick enough to support the cells independent of the scaffold and the growth kinetics depends only on the interaction between the cells and their own ECM. This is not unexpected but demonstrates the importance of the millimetre-size architecture of the scaffold because this is what determines the shape of the tissue layer and, hence, the late stage growth kinetics. In summary, the architecture of the scaffold is more important than its chemical nature for supporting the late stages of tissue growth.

V. Conclusions

In this paper, a model scaffold with round and square pore channels made of polyether urethane (PU) with different stiffness (in the MPa range) was used to investigate the tissue formation by osteoblast cells inside the channels. We showed that three-dimensional tissue growth by MC3T3-E1 pre-osteoblast cells in the polymer scaffolds can be roughly divided into two stages. In the early stage, cells form a confluent layer on top of the scaffold where cell-material interactions, such as cell adhesion which is dependent on the stiffness of the three dimensional scaffolds and inner surface roughness of the pores, have a strong influence on the growth kinetics. In the late stage, cells grow within their own matrix and further three-dimensional tissue amplification depends only on geometry but not on the scaffold material. A universal growth law identical to what was found on HA scaffolds was found which depends on scaffold architecture only. The delay time (t_0) to reach the late stage is strongly dependent on the seeding protocol and can become so long (month or longer) in unfavourable cases that the system never reaches the late stage of three-dimensional growth. This systematic analysis provides insights into how geometric constraints may guide tissue formation in vitro and shows that optimizing scaffold architectures may improve tissue formation independently of the scaffold material.

Acknowledgements

The authors are grateful to Deutsche Forschungsgemeinschaft (DFG) for financial support under grant of collaborative research centre scheme (SFB) 760, part Project B3.

References

1 - D. W. Hutmacher, J. Biomater. Sci. Polymer Ed. 12 (1), 107 (2001).

2 - R. Langer, L. G. Cima, J. A. Tamada et al., Biomaterials 11 (9), 738 (1990).

3 - A. S. P. Lin, T. H. Barrows, S. H. Cartmell et al., Biomaterials 24 (3), 481 (2003).

4 - T. M. G. Chu, D. G. Orton, S. J. Hollister et al., Biomaterials 23 (5), 1283 (2002).

5 - D. G. Castner and B. D. Ratner, Surf. Sci. 500 (1-3), 28 (2002).

6 - N. Faucheux, R. Schweiss, K. Lutzow et al., Biomaterials 25 (14), 2721 (2004).

7 - A. S. G. Curtis and C. D. Wilkinson, J. Biomater. Sci. Polymer Ed. 9 (12), 1313 (1998).

8 - J. Park, S. Bauer, K. A. Schlegel et al., Small 5 (6), 666 (2009).

9 - O. Zinger, G. Zhao, Z. Schwartz et al., Biomaterials 26 (14), 1837 (2005).
10 - B. D. Boyan, V. L. Sylvia, Y. H. Liu et al., Biomaterials 20 (23-24), 2305 (1999).
11 - P. Linez-Bataillon, F. Monchau, M. Bigerelle et al., Biomol. Eng. 19 (2-6), 133 (2002).
12 - D. E. Discher, P. Janmey, and Y. L. Wang, Science 310 (5751), 1139 (2005).
13 - H. J. Kong, T. R. Polte, E. Alsberg et al., Proc. Natl. Acad. Sci. U.S.A. 102 (12), 4300 (2005).
14 - C. M. Lo, H. B. Wang, M. Dembo et al., Biophys. J. 79 (1), 144 (2000).
15 - A. J. Engler, S. Sen, H. L. Sweeney et al., Cell 126 (4), 677 (2006).
16 - K. Anselme, M. Bigerelle, B. Noel et al., J. Biomed. Mater. Res. 49 (2), 155 (2000).
17 - C. S. Chen, M. Mrksich, S. Huang et al., Science 276 (5317), 1425 (1997).
18 - S. V. Graeter, J. H. Huang, N. Perschmann et al., Nano Lett. 7 (5), 1413 (2007).
19 - J. Park, S. Bauer, K. von der Mark et al., Nano Lett. 7 (6), 1686 (2007).
20 - J. P. Spatz and B. Geiger, in Cell Mechanics - Methods in Cell Biology, edited by Y. L. Wang and D. E. Discher (Elsevier Press, 2007), Vol. 83, pp. 89.
21 - F. J. O'Brien, B. A. Harley, I. V. Yannas et al., Biomaterials 26 (4), 433 (2005).
22 - E. Charriere, J. Lemaitre, and P. Zysset, Biomaterials 24 (5), 809 (2003).
23 - J. Zeltinger, J. K. Sherwood, D. A. Graham et al., Tissue Eng. 7 (5), 557 (2001).
24 - M. Rumpler, A. Woesz, J. W. C. Dunlop et al., J. Roy. Soc. Int. 5 (27), 1173 (2008).
25 - J. E. Davies, Anat. Rec. 245 (2), 426 (1996).
26 - T. A. Owen, M. Aronow, V. Shalhoub et al., J. Cell. Physiol. 143 (3), 420 (1990).
27 - V. Thomas, T. V. Kumari, and M. Jayabalan, Biomacromolecules 2 (2), 588 (2001).
28 - K. P. Kommareddy, C. Lange, M. Rumpler et al., in Bone (2009), Vol. 44, pp. S261.
29 - N. M. K. Lamba, K. A. Woodhouse, and S. L. Cooper, Polyurethanes in Biomedical Applications. (CRC, Boca Raton, FL, 1998).
30 - John Crabtree, H., Am. Soc. Artif. Intern. Org. 49 (3), 290 (2003).
31 - J. Cui, K. Kratz, and A. Lendlein, Mater. Res. Soc. Symp. Proc. 1190, DOI: 10.1557/PROC (2009).
32 - R. Mohr, K. Kratz, T. Weigel et al., Proc. Natl. Acad. Sci. U.S.A. 103 (10), 3540 (2006).
33 - L. D. Quarles, D. A. Yohay, L. W. Lever et al., J. Bone. Miner. Res. 7 (6), 683 (1992).
34 - J. Y. Choi, B. H. Lee, K. B. Song et al., J. Cell. Biochem. 61 (4), 609 (1996).
35 - M. Rumpler, A. Woesz, F. Varga et al., J. Biomed. Mater. Res. A. 81A (1), 40 (2007).
36 - N. Fratzl-Zelman, H. Horandner, E. Luegmayr et al., Bone 20 (3), 225 (1997).
37 - K. H. Frosch, F. Barvencik, C. H. Lohmann et al., Cell. Tiss. Org. 170 (4), 214 (2002).
38 - V. G. Brunton, I. R. J. MacPherson, and M. C. Frame, Biochim. Biophys. Acta 1692 (2-3), 121 (2004).
39 - A. Okumura, M. Goto, T. Goto et al., Biomaterials 22 (16), 2263 (2001).
40 - M. A. Woodruff, P. Jones, D. Farrar et al., J. Mol. Hist. 38 (5), 491 (2007).
41 - G . Cheng, B. B. Youssef, P. Markenscoff et al., Biophys. J. 90 (3), 713 (2006).
42 - B. Geiger, Science 294 (5547), 1661 (2001).

7.3 [TG3] Geometry as a Factor for Tissue Growth: Towards Shape Optimization of Tissue Engineering Scaffolds.

Bidan, C. M., Kommareddy, K. P., Rumpler, M., Kollmannsberger, P., Fratzl, P., Dunlop, J. W. C

*Published in **Advanced Healthcare Materials**, 2013, 2, 186–194.*
DOI: 10.1002/adhm.201200159

Reprinted with permission from John Wiley and Sons

Abstract: Scaffolds for tissue engineering are usually designed to support cell viability with large adhesion surfaces and high permeability to nutrients and oxygen. Recent experiments support the idea that – in addition to surface roughness, elasticity and chemistry – the macroscopic geometry of the substrate also contributes towards the control of tissue deposition. In this study, we use a previously proposed model for the behavior of osteoblasts on curved surfaces to predict the growth of bone matrix tissue in pores of different shapes. These predictions are compared to in-vitro experiments with MC3T3-E1 pre-osteoblast cells cultivated in two-millimeter thick hydroxyapatite plates containing prismatic pores with square- or cross-shaped sections. The amount and shape of the tissue formed in the pores measured by phase contrast microscopy confirms the predictions of the model. In cross-shaped pores, the initial overall tissue deposition is two times faster than in square shaped pores. These results suggest that the optimization of pore shape may improve the speed of ingrowth of bone tissue into porous scaffolds.

Introduction

Three-dimensional scaffolds are needed for tissue engineering applications and may also help to study the effect of the physical environment on tissue growth in-vitro. The material used,[1] the fabrication process[2] and the architecture of the scaffold[3, 4] are known to influence the biological interactions with the host organism. Although all these parameters are difficult to decouple, quantifying their effects in-vitro is necessary to understand the nature of cell and tissue responses and to design optimal scaffolds for in-vivo experiments and applications.

Cells are known to adapt to the physical properties of their surroundings by integrating the mechanical equilibrium established at their adhesion sites.[5] The resulting mechanical cue is translated into a biochemical signal that triggers biological decisions of the cells.[6] As cells are mechanically attached to each other, either directly or via their extracellular matrix, they are able to synchronize their response on a larger scale. For example, patterning in cell differentiation arises as a response to stiffness[7] or strain[8] patterns, and the distribution of proliferation activity also correlates with the stress distribution in a layer of cells.[9]

Cell fate has also been investigated in three-dimensional artificial scaffolds. Adhesion, proliferation, differentiation and mineralization of cells and tissues have been compared in several scaffolds with varying structures.[10, 11] Recently, Kumar et al[12] showed that the effect of the structural properties of a substrate on gene expression, and thus cell differentiation, can overcome those induced by its composition. Furthermore, pore size and porosity need to satisfy the compromise between a high permeability that enables cell migration and nutrient diffusion within the scaffold, and a large surface area for cell adhesion and extracellular matrix production.[3] Many fabrication processes produce structures with random pores in a large range of sizes

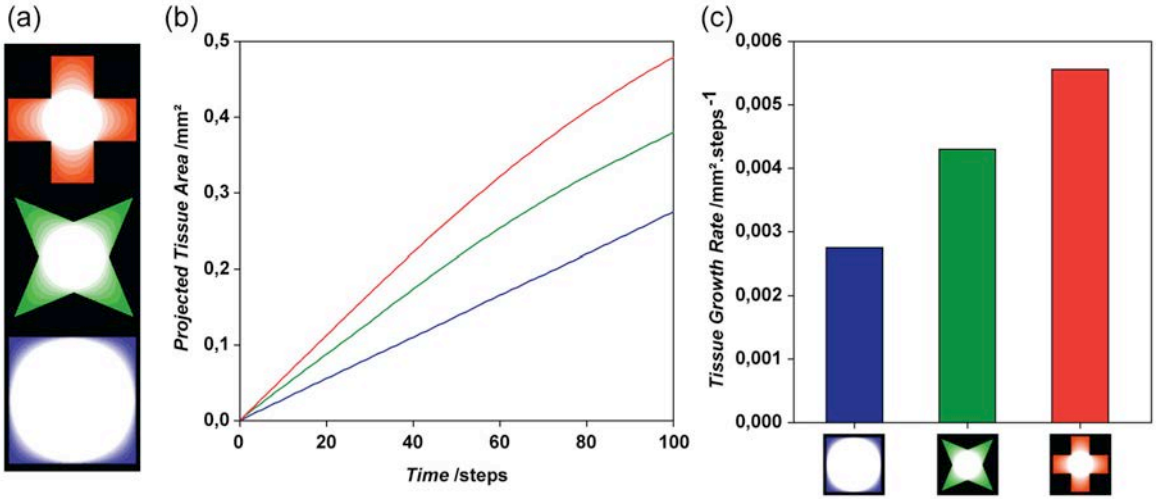

Figure 1. The computational simulation of curvature-driven growth was run on artificial images representing square-, star- and cross- shaped pores of medium size ($P_{medium} = 4.71mm$). (a) The interface tissue/medium evolves toward a circular shape (b) Initial kinetics of growth are significantly affected by the geometry of the pore section before reaching a circular interface (c) Initial growth rates calculated on the 40 first steps of the simulation suggest that a two fold increase in tissue deposition can be expected in cross-shaped pores compared to square-shaped pores. (Adapted from Bidan et al[29].)

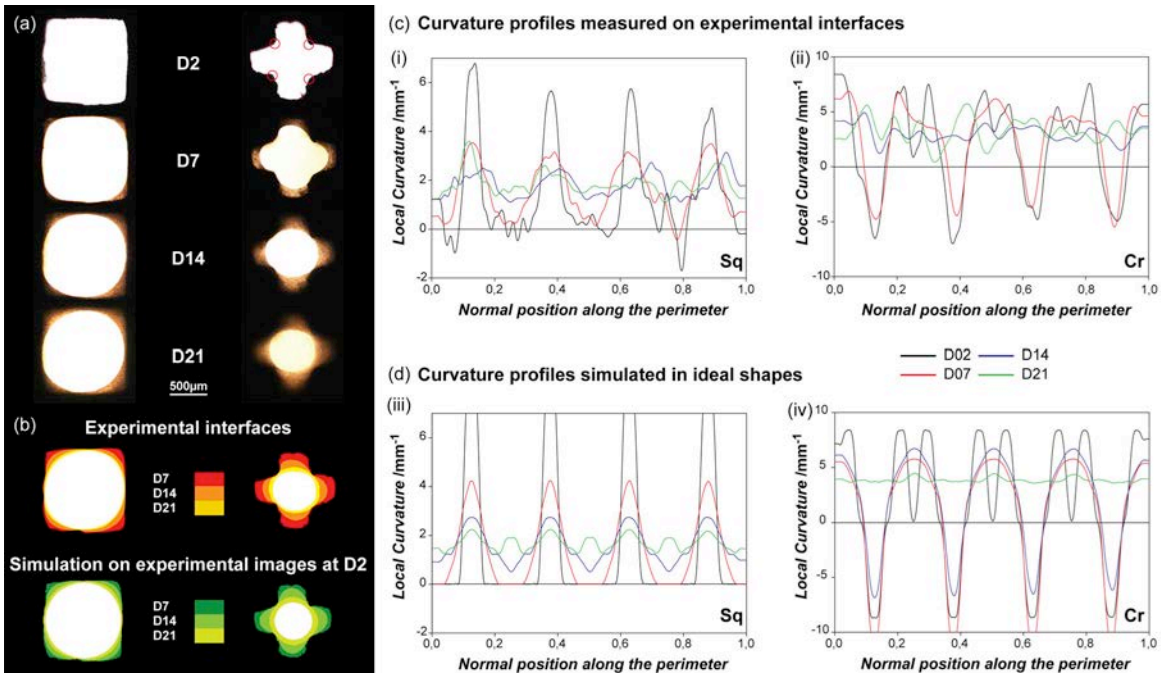

Figure 2. Tissue growth in square- and cross-shaped pores. (a) Phase contrast images of the pore taken 2, 7, 14 and 21 days after seeding the MC3T3-E1 on the scaffolds. (b) The superposition of the interfaces obtained experimentally is compared with the predictions of the curvature-driven growth simulation applied to the actual geometry of the experimental pore at D2. 7, 14 and 21 days of experiments are obtained with 36, 120 and 204 steps of simulation with $r = 8.5\,pxl$, $\alpha = 12\,steps$, $t_0 = 4d$. (c) Curvature profiles of the interface tissue-medium measured at D2, D7, D14 and D21 in a square- (i) and a cross-shaped pore (ii). (d) Curvature profiles are measured on the interfaces predicted by the curvature-driven growth model after 7, 14 and 21 days of culture in ideal square- (iii) and cross-shaped pores (iv). The curvature measurements were smoothed using a mask size of $r = 14.5\,pxl$.

and interconnectivities which are difficult to control. Rapid prototyping techniques are much more accurate in that respect.[13] By printing the scaffold, the architecture and thus many mechanical properties of the structure can be carefully controlled.

Rumpler et al[14] used rapid prototyping to build artificial macro-pores of different controlled geometries and showed that cells locally respond to high curvature by producing tissue. Their hypothesis that the local tissue growth rate was proportional to curvature was confirmed experimentally, not only in pores but also on open surfaces[15], however with the additional observation that tissue does not grow on convexities. The interfacial evolution derived from a two-dimensional curvature-driven tissue growth model matched the experimental observations as well as the in-vivo expectations when comparing with the typical geometries involved in bone remodeling (osteonal and hemi-osteonal lacunae).[16] An interesting consequence of curvature-driven growth was also observed by Rumpler et al[14]. Despite seeing local differences in growth rates in prismatic pores with different convex sections (circlular, square and triangular) but identical surface areas, the total tissue growth rate was found to be independent of shape. This could be understood using Fenchel's law[17], which states that the average curvature in a convex shape, is inversely proportional to the perimeter. This would imply the average growth rate, if curvature controlled, would also be the same.

In previous work[15], we proposed a biological explanation for the geometry dependence of tissue growth. The tissue is built by contractile cells which, after adhesion to a curved substrate, span convex parts of the surface in a way similar to a chord . A model of tensile elements deposited as layers on a surface was shown to give rise to a curvature dependent growth of the tissue. This simple geometrical construction not only justifies the patterns and kinetics of growth observed during the experiments but also the orientation of the collagen fibrils produced by the cells.

This paper aims at understanding how tissue production can be enhanced simply by controlling the geometry of the surface by exploring non-convex pore geometries. The model of curvature-driven growth as implemented in a previous work[15] was first used to predict growth in pores with cross-, star- (non-convex) and square- (convex) shaped sections. The simulations predict higher initial growth rates in non-convex shapes and even a two fold increase in growth rate for a cross-shaped pore compared to a square-shaped one.

To verify the predictions of the two-dimensional model, scaffolds with straight sided pores with cross- and square-shaped sections were produced in hydroxyapatite and incubated with MC3T3-E1 pre-osteoblast cells for in-vitro tissue culture. Not only the motion of the tissue-medium interfaces and the evolution of their curvature profiles compare well to the model, but the quantitative analysis of tissue production also matches the outcomes from the curvature-controlled growth model. Moreover, analyzing the internal structure of the tissue produced provides an additional support to the chord model presented in [15] and constitutes a further step in the understanding of the mechanisms involved in the curvature dependent behavior. Such knowledge is of high interest for developing tools to design scaffolds with the optimal geometry and meeting the

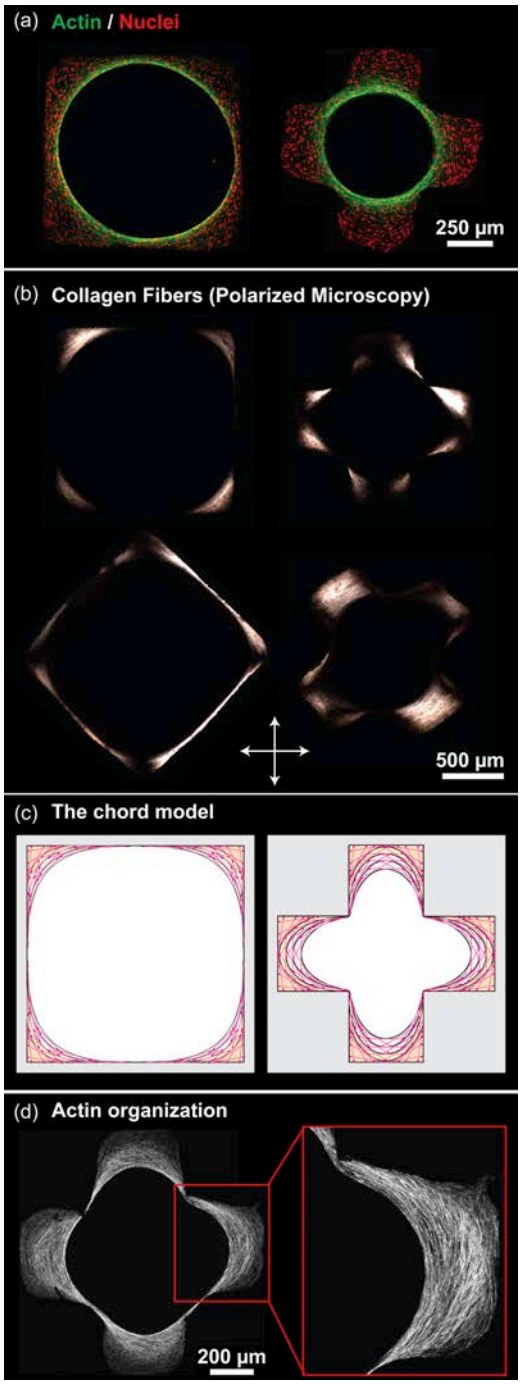

Figure 3. (a) Whatever the geometry of the pore, cells are homogeneously distributed in the tissue (nuclei in red) but actin concentration is much higher at the interface which tends to be circular. (b) Polarized microscopy reveals collagen fibers having the same orientation as the cells, i.e. parallel to the interface tissue/medium. (c) The geometrical construction that considers tissue as an assembly of tensile elements representing contractile cells[15] applies to convex and non-convex geometries. (d) Tissue stained for actin fibers reveals stretched cells organized along the interface as predicted by the chord model.

numerous criteria for tissue engineering and clinical applications.

Results

As a first step, we applied the previously proposed model of curvature-controlled growth to non-convex geometries. The idea was to predict potential changes of growth behavior in comparison to the simple shapes used up to now.[14, 15] Figure 1 shows the growth behavior expected in square-, star- and cross-shaped pores normalized with respect to the perimeter ($P_{medium} = 4.71mm$) of their section. Although the interface between tissue and medium tends to adopt a circular shape in all cases (Figure 1(a)), the initial kinetics of growth is expected to be significantly affected by the geometry of the section of the straight sided pore (Figure 1(b)). For example, tissue is predicted to grow twice as fast in a cross-shaped pore compared to a square-shaped pore or any other convex shape (Figure 1(c)). In order to verify these predictions, tissue was cultured in 2 mm thick hydroxyapatite (HA) plates containing straight sided pores of square (convex) and cross (non-convex) shaped sections. The size of the pores was chosen so that they all had the same initial surface available for cells to adhere to (i.e. the same perimeter for prismatic pores). Once seeded on the top of the scaffolds, the MC3T3-E1 pre-osteoblasts proliferate, migrate and start to produce collagenous extracellular matrix (ECM). Tissue deposition was followed in each pore by phase contrast microscopy over 28 days and quantified in terms of projected tissue area (PTA). As the pores are designed with straight walls, i.e. no difference in curvature along the vertical direction, the PTA is considered to be a relevant proxy to quantify the amount of tissue produced in the pores. Three sets of 5 pores of each size ($P_{medium} = 4.71mm$, $P_{large} = 6.28mm$) and each shape (Sq stand for square and Cr for cross) were independently seeded and showed similar results. As an example, Figure 2(a) shows phase contrast images of the same pore taken at 4 different time points during culture (D2, D7, D14 and D21). As already observed by Rumpler et al in convex shapes[14], tissue deposition starts in the corners whereas no growth occurs on flat surfaces until the surrounding tissue deposition modifies the local geometry. In cross shaped pores, the concave regions of the branches are also quickly filled with tissue. However, the 4 convex points (indicated by red circles on the figure) seem to act as flat surfaces since no growth occurs until the local curvature becomes positive through the global interfacial evolution. This effect of the sign of curvature has already been pointed out in previous studies.[15] In both cases, the interface tissue/medium evolves toward a circle, as predicted by the model of curvature-driven growth applied to the actual geometry of the pore, derived from the experimental images (Figure 2(b)).

The evolution of the geometry in the projection plane was quantified in terms of curvature. Figures 2(c) presents the curvature profiles measured on experimental images taken at different time points. Their behavior compares well with the interfacial curvature profiles measured on images obtained with the curvature-driven growth model applied to ideal square and cross shapes (Figures 2(d)). The 4 peaks of curvature characterizing the corners of a square-shaped pore vanish as the tissue grows; the curvature profile of the interface flattens and becomes characteristic of a circle. In a cross-shaped pore, 8 peaks correspond to the 8 concave corners and 4 regions of highly negative curvature are related to the 4 convex corners. As in the square, all the peaks –

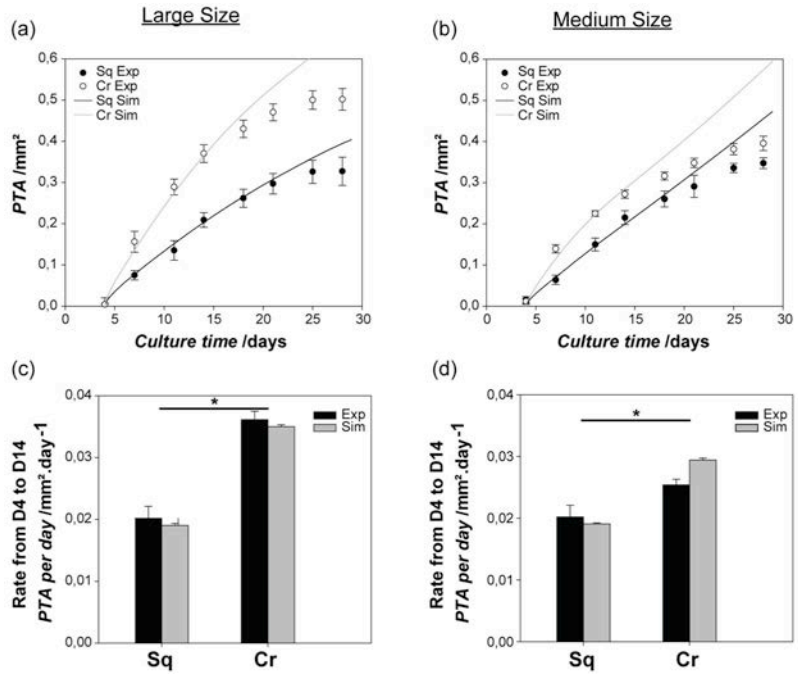

Figure 4. Growth kinetics measured in square- and cross-shaped pores of large (a) and medium (b) size. Experimental and simulated growths are reported in terms of projected tissue area (PTA) ($\alpha = 12 steps$, $t_0 = 4d$). Growth rates are calculated between D4 and D14 with experimental and simulated data in large (c) and medium (d) pores. ANOVA analysis shows no significant differences between the methods used (Exp, Sim) but a significant difference in the tissue growth rates achieved in square and cross ($p < 0.05$). Dots and error bars represent mean values and standard errors respectively ($n = 5$).

whatever their sign – tend to vanish and curvature profiles become smooth as tissue is deposited. Note that differences in curvature values are due to the imperfections of the HA scaffolds, and that the final profiles are not totally smooth due to the discrete character of the binarized images.

To obtain a systematic classification of the effect of non-convex shapes on tissue growth, we approximate the local growth rate in non-convex-shaped pores as following:

$$\frac{ds}{dt} = \begin{cases} \lambda \kappa^{+} & , \kappa > 0 \\ 0 & , \kappa \le 0 \end{cases} \qquad (1)$$

This gives rise to a simple global growth law in terms of projected tissue area:

$$\frac{dPTA_{pore}}{dt} = 2\pi\lambda\kappa^{+*} \qquad (2)$$

with κ^{+*} a constant dimensionless value characteristic of the "non-convexity" of the shape. $\kappa^{+*} = 1$ for convex shapes and $\kappa^{+*} > 1$ for non-convex shapes (Figure 3(a)). Details of the derivation and precise definitions can be found in the supporting information. In cross-shaped pores, the curvature is negative in 4 points, positive in the 8 right angle corners and null elsewhere. In squares, the curvature is positive in the 4 right angle corners and null elsewhere. If the negative curvature plays no role in the growth rate, then the positive curvature averaged on the perimeter in the cross ($\kappa^{+*} = 2$) is twice the one of a square ($\kappa^{+*} = 1$) and growth should be twice as fast. Both simulation and experiments meet this prediction.

The organization of the cells and collagen fibers within the newly formed tissue was investigated qualitatively using immunofluorescence methods. On Figure 4(a), nuclei staining (red) reveals the homogeneous distribution of cells within the tissue as well as a similar density of cells in both the square and cross shaped pores whereas actin fibers (green) are mostly concentrated and highly oriented along the interface tissue/medium.
In larger pores, polarized microscopy enables to image the preferential orientation of the fibrous extracellular matrix deposited by the cells. As shown on Figure 4(b), collagen fibers deep in the tissue are oriented parallel to the substrate, whereas those at the interface have a direction similar to the cells.

The kinetics of new tissue formation within the pores of the scaffolds was followed in the in-vitro system by measuring the projected tissue area (PTA) on phase contrast images taken twice a week. As predicted by the model of curvature-driven growth in ideal shapes (Figure 1), Figures 5(a) and 5(b) reveal that after any time of culture, more tissue has been produced in the cross- than in the square-shaped pores, and this for two different pore sizes ($P_{large} = 6.28mm$ and $P_{medium} = 4.71mm$ respectively). Reporting tissue growth rates calculated between D4 and D14 (Figure 5(c) and 5(d)) also confirms that initial growth rates are almost twice as fast in cross- than in square-shaped pores, independent of the size. Additionally, Figure 5 shows that the model of curvature-driven growth applied to the actual geometry of the pores, also predicts quantitatively the growth behavior for the first two weeks of cell culture. The model is fitted with a single parameter which sets the time scale of the simulation and is calculated with the experimental tissue growth rate in a square-shaped pore. For this set of experiments, 12 steps of simulation represent 1

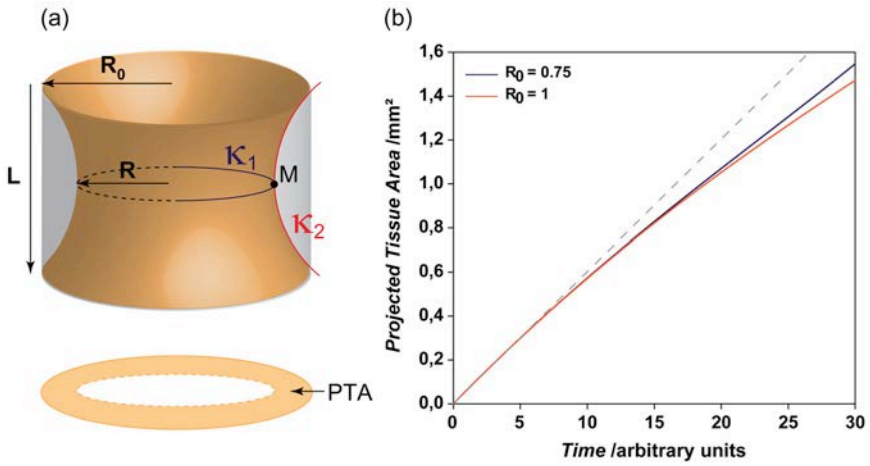

Figure 5. The effect of the curvature in the third dimension may be partly responsible for the slowdown of growth observed experimentally. (a) Schematic representation of tissue repartition in the pore with the associated geometrical descriptors. (b) A numerical derivation was done with $\lambda = 0.01 mm^2 .s^{-1}$, $h = 2mm$ in pores of medium and large sizes. The dashed line indicates a linear growth.

day of culture ($\alpha = 12 steps$). A lag time $t_0 = 4d$ accounting for the time that cells need to settle was incorporated to overlap the curves.

As the predictions on influencing growth kinetics are confirmed by the experiments in single pores, the analytical investigations are extended to scaffolds with multiple pores. One has now to consider that geometry also determines the number of pores which fit in a scaffold with defined size A_{scaff} and porosity φ. The circularity is the dimensionless shape factor (independent on the size) used to characterize the ratio perimeter to area:

$$C = 4\pi \frac{A}{P^2} \qquad (3)$$

which relates to the (maximum) number of pores in the scaffold. As mentioned above, Figure 3(a) classifies pore shapes with respect to their "non-convexity" and their "circularity", two geometrical parameters that influence respectively tissue growth rate in an individual pore and the global porosity of a scaffold made of those pores. The global tissue growth rate can then be expressed as a function of the scaffold and the pore characteristics:

$$\frac{dPTA_{tot}}{dt} = 8\pi^2 \lambda \left(\varphi A_{scaff}\right)\left(\frac{1}{P^2}\right)\left(\frac{\kappa^{**}}{C}\right) \qquad (4)$$

Equation (4) shows that the global tissue growth rate in the scaffold is a product of independent terms characterizing i) cell activity, ii) scaffold properties, iii) pore size and iv) pore geometry. The details of its derivation are available in the supporting information. Figure 4(b) shows how the total tissue growth rate depends on the size and the geometry of the pores. The initial tissue growth rate is considered, i.e. the growth rate achieved until the interface becomes convex. In a plate-like scaffold of a given area (20 mm^2) and given porosity (0.9), small and non-convex pores give rise to higher growth rates (white areas on the bottom right).

Discussion

In this study, a curvature-driven growth model[14, 15] was applied to different (non-convex) geometries. The growth behaviors obtained by computational simulations were verified experimentally using an in-vitro tissue culture system that offers the possibility to vary the geometry of a substrate in a controlled way, independently of the chemistry. Not only the qualitative and quantitative geometrical evolution of the interface tissue/medium, but also the faster tissue generation by MC3T3-E1 cells in non-convex shaped pores (cross) could be derived from the simple hypothesis that the local growth rate is locally proportional to the curvature (if it is positive).

Despite a well-defined experimental protocol, some limitations remain. The hydroxyapatite scaffolds produced by casting and sintering present the expected geometry on the millimeter scale, but the roughness of the surfaces is difficult to control, especially in non-convex shapes. This drawback also justifies the necessity of a computational tool able to quantify the geometry in terms of curvature profile and apply the curvature-controlled growth model directly on experimental images, and therefore take into account the interfacial defects.

The patterns obtained with the curvature-controlled growth model and the ones observed in the experiments can also be derived from the simple geometrical construction using tensile elements presented previously.[15] In essence, this model represents a cell by its internal actin filaments (stress fibers) connecting adhesion sites of the cell. This "chord model" explains intrinsically not only the absence of growth on convexities but also the faster tissue growth and the higher tissue organization in non-convex shapes (Figure 3(a)). This approach is further supported by actin stained tissues showing cells locally oriented parallel to the interface tissue-medium (Figure 3(a) and 3(d)). Considering that this preferential organization is also followed by the collagen fibers synthesized by the cells during tissue growth (Figure 3(b)), one could transfer the geometrical construction to the tissue level in a similar way to the cable model of Bischof et al.[18]

Some other mechanisms involved in tissue growth might also be geometry dependent. For example, cell

migration is known to be faster on curved surfaces than on flat surfaces[19]. Such contact guidance would result in a higher number of cells reaching the corners compared to the flat surfaces. Although this could be a possible mechanism for the tissue response to geometry, previous work suggests that this would only affect the early stages of growth up until a tissue mono-layer is formed[20]. Growth rates later than this early stage were shown to be independent of substrate properties as well as the seeding method, both of which would affect migration. Moreover, the concept of contact guidance into the depth of the pore does not provide any clear explanation for the presence of cells but absence of growth on convex and flat surfaces.

An accumulation of nutrients in confined regions of the pores (close to the concave surfaces) could also be suggested to explain the local dependence of cell proliferation on the curvature, which results in the homogeneous distribution of nuclei throughout the tissue (Figure 3) as already showed in [15]. However, in such pores of millimeter size, diffusion is expected to be sufficient to result in homogeneous composition of the medium. For example, oxygen potential has been shown to be independent of the size of the pore.[14, 15] On the other hand, the ECM proteins secreted by the cells might be more likely to accumulate in the cell network build in the corners due to spatial diffusion constraints and be incorporated into ECM fibers, as opposed to flat of convex surfaces where cells are more exposed to the medium. In that case, the pattern of growth and the organization of the tissue produced would still be a consequence of the spatial arrangement of the chord like contractile cells and be responsive to the substrate curvature.

The curvature-driven growth model predicts a decrease in tissue growth rate in cross shaped pores as soon as the interface tissue-medium becomes convex. However, as already observed in similar experiments, the tissue growth slows down after 18 days of culture, independently of the shape of the pore. Three main hypotheses have been proposed to explain this phenomenon.[15] i) Ageing and differentiation affect the proliferative activity of the cells and thus their ability to produce tissue. ii) Not only cells mature, but also the ECM they produce. With maturing collagen cross-links the matrix could become locally denser, which may be implemented into the model as a gradual reduction of growth rates. iii) Considering the projected tissue area to quantify growth supposes that tissue grows homogeneously all along the height of the three-dimensional pore, which is unlikely. Therefore, one needs two principal curvatures to describe the geometry of the interface along the vertical axis, and they are likely to be of opposite sign. To discuss this last point further, one can analytically estimate the impact of the convexity appearing in the third dimension in a cylinder of radius R_0. As depicted Figure 6(a), if the inward curvature is approximated by a circle (red), the two principal curvatures at the point M are:

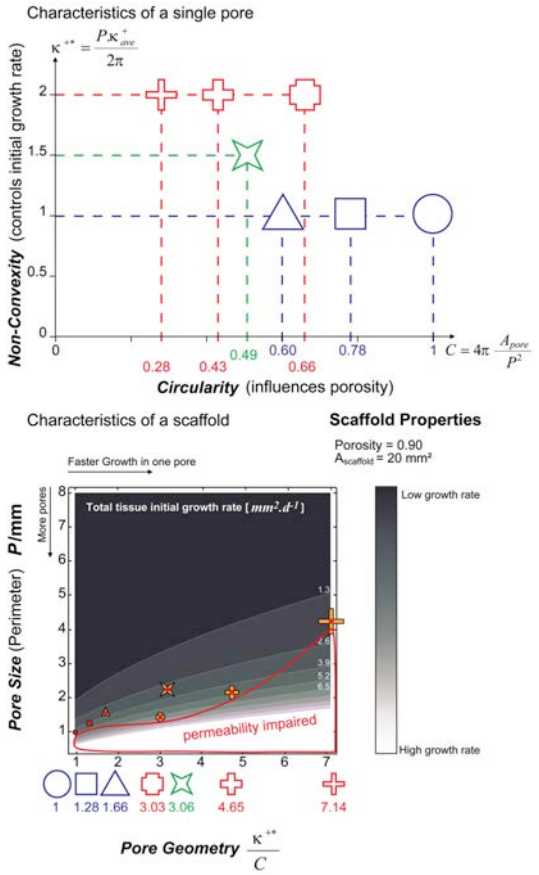

Figure 6. (a) Pore shapes can be classified using the "non-convexity" which determines tissue growth rate in the pore and the "circularity" which influences the number of pores fitting in a scaffold. (b) Contour plot representing the influence of pore geometry and pore size on the total tissue growth rate in a 20 mm² scaffold with a porosity of 0.9. Grey level decreases with the growth rate. For each shape, the dot shows the perimeter corresponding to an inner radius of 150 µm (considered as the limit for good permeability properties). In that respect, smaller perimeters are not relevant for tissue engineering purposes.

$$\begin{cases} \kappa_1 = \dfrac{1}{R} > 0 \\ \kappa_2 = -\dfrac{2\left(R_0 - R\right)}{\left(R_0 - R\right)^2 + \dfrac{L^2}{4}} < 0 \end{cases} \qquad (5)$$

where R is the radius of the pore at time t and L is the depth of tissue deposition. Mean curvatures $H = \dfrac{\kappa_1 + \kappa_2}{2}$ in each point of the interface are lower than the one measured on the projection (κ_1) and, therefore,

$$\frac{dPTA_{pore}}{dt} = -\pi \frac{dR^2}{dt} = 2\pi R.\lambda.H(R) = 2\pi\lambda.\left(1 - \frac{2\left(R_0 - R\right)R}{\left(R_0 - R\right)^2 + \dfrac{L^2}{4}}\right) \qquad (6)$$

$PTA(t)$ can be then derived numerically from Equation (6). Some results presented in Figure 6(b) show, indeed, a slowing down of the growth that is not predicted by the two dimensional model but appears in experiments.

Although the observations and calculations proposed in this paper are simple, they have important consequences for the design of tissue engineering scaffolds. For example, the results suggest that for purely convex channels, the rate of new tissue growth in a single pore is independent of size and geometry. This implies that pore shape can be modified to satisfy other criteria (e.g. strength, fatigue resistance, permeability, etc)[21] without changing the rate of tissue ingress. Moreover, introducing non-convexities into the pore shapes can greatly increase the growth rate (by a factor of 2 in the case of cross-like pores) giving a new opportunity to optimize the architecture of scaffolds for tissue repair.

Integrating an implant in a host organism often implies to produce as much tissue as possible in a short time. In that respect, a lot of highly non-convex pores would be useful. However, having small pores filling fast and completely with agglomerates of cells is also not desired. Indeed, diffusion of nutrients would be impaired and cell viability affected. Moreover, cells also need space to migrate and lay down extracellular matrix. Pores should then be large enough to guarantee a good permeability and leave room for the formation of new tissue and for angiogenesis.[22]
As shown in this study, the geometry of individual pores not only influences density, permeability and the amount of tissue produced in the scaffold, but also the speed and repartition of tissue deposition. In the cross-shaped pore, for example, tissue is generated with a high rate in the branches in a first stage, which could help anchoring the scaffold faster in the host organism. As the interface smoothens and becomes circular (convex), the growth rate slows down, leaving time and space for exchanges through the pore. Experimentally, the slowdown occurs a bit earlier for the reasons discussed above.

A common concern in tissue engineering is the permeability of the scaffold to guarantee cell migration as well as nutrient and waste diffusion necessary for cells to survive. Tissue engineering literature suggests that pores should be at least 300 µm large to ensure a good permeability of the scaffold.[23] For each shape, the size of the inner circle is taken as a limitation for pore size. An inner radius of 150 µm leads to the minimum relevant perimeter. Maximum realistic initial growth rates are estimated for each shape (small shapes on Figure 4(b)). Considering this aspect, the fastest initial growth rate can be obtained using regular crosses with thick branches. The circular interface being quickly reached, the amount of tissue produced at that high rate is however low. The remaining space and the slower growth from this time point could be profitable for angiogenesis and facilitate diffusion as the pore is closing.

All these calculations assume that the totality of the scaffold area can be covered by assembling pores of the same shape. This statement is true for squares, triangles and regular crosses with $k = 0.33$ (see Supporting information). However, it is known that the maximum density achieved by packing circles in a hexagonal arrangement on a surface is 0.90 and star shapes are also not likely to be packed in an optimal arrangement. It is therefore relevant to envisage scaffolds containing pores of different geometries and sizes. Few large highly non-convex shapes can promote the anchoring of the scaffold at the early time points and facilitate diffusion as growth progresses, whereas smaller (mainly convex) pores fitted in between can provide additional surfaces for cells to deposit tissue with a slower rate, but that will also support integration of the implant in the host body. The total initial tissue growth rate obtained in such a scaffold can be estimated by adapting equation (4):

$$\frac{dPTA_{tot}}{dt} = 8\pi^2 \lambda A_{scaff} \sum_i \varphi_i \left(\frac{1}{P_i^2} \right) \left(\frac{\kappa_i^{+*}}{C_i} \right) \qquad (7)$$

with φ_i the contribution of the shape i to the global density.

Conclusion

This work lays stress on the determining role of the geometry of a substrate on the kinetics of tissue deposition. We show that tissue growth can be promoted simply by tuning the curvature of the surfaces where cells deposit their extracellular matrix. A simple geometrical model based on the tensile behavior of the cells, which leads to curvature-controlled growth, can predict both the kinetics achieved and the distribution of tissue deposition. As such simple principles could be of high interest for tissue engineering, we propose some methods to optimize pore design when considering a porous scaffold intended for tissue repair.

Experimental Section

Curvature-driven growth simulation

A model for curvature-driven tissue growth was proposed by Rumpler et al[14] and implemented by Bidan et al[15] in a Matlab (Matlab 7.8.0 R2009a, MathWorks, Natick, MA) code based on a method for measuring curvature on digital images.[24]
This computational simulation is run on binarized images of the pores in which the scaffold is black and the medium is white. In the first step of the simulations the effective curvature is measured at each pixel of the image by convoluting a circular mask with the image. This curvature represents what cells sense from the geometry of the surface. The second step involves turning the white pixels that have a positive effective curvature to black thus representing tissue deposition in concave regions. The process is then repeated iteratively to simulate curvature-controlled growth. To make a quantitative comparison with the experimental results, this simple model only requires the input of a single parameter accounting for the number of iterations needed to simulate one day of culture. This value is calculated using the experimental growth rate measured in a convex shape, the square in this study.
As demonstrated previously [15], this computational model is equivalent to the layering of tensile chords on a surface if the radius of the mask is $\sqrt{3}/2$ times the size of a cell (about $50\mu m$ for an elongated

osteoblast). In the simulations the mask radius is set to $r = 8.5\,pxl$.

Production of the hydroxyapatite (HA) scaffolds

2mm thick HA scaffolds containing straight sided pores are produced by slurry casting as mentioned in previous studies[14, 15]. Pore sections represent squares or crosses and are normalized with respect to their perimeter ($P_{medium} = 4.71mm$, $P_{large} = 6.28mm$).

Molds are designed using the computer-aided design (CAD) software Alibre Design (Alibre Inc., Richardson, TX) and produced with a three-dimensional wax printer, Model Maker II (Solidscape Inc., Merrimack, NH) as described by Manjubala et al[25]. The molds are then filled with a HA slurry made of methacrylamide (MAM) monomers (15g), N-N'-Methylenebisacrylamide (BMAM) (5 g), water (75 g), Dextran (12.5 g) and HA powder (300 g), and cross-linked with ammonium persulfate and N,N,N',N'-Tetramethylethylenediamine (TEMED). The structures are slowly air dried by heating the samples to 50 °C at a rate of 5 °C per day and then holding this temperature for one day. The dried samples are then pre-sintered at 600 °C for 48 h to remove the wax molds and are finally sintered at 1100 °C for 24 h.[26]

Cell culture

Murine pre-osteoblastic cells MC3T3-E1 (provided by the Ludwig Boltzmann Institute of Osteology, Vienna, Austria) are seeded with a density of 105 cells/cm^2 on the surface of the HA scaffolds and cultured for 28 days in α-MEM (Sigma-Aldrich, St. Louis, MO) supplemented with foetal calf serum (PAA laboratories, Linz, Austria) (10 %), ascorbic acid (Sigma-Aldrich, St. Louis, MO) (0.1 %) and gentamicin (Sigma-Aldrich, Steinheim, Germany) (0.1 %) in a humidified atmosphere with CO2 (5 %) at 37 °C.

Imaging

Each pore is imaged every 3 to 4 days using a phase contrast microscope (Nikon Eclipse TS100, Japan) equipped with a digital camera (Nikon Digital sight DS 2Mv). All pictures are taken with a 4x objective, yielding a final image resolution of 205 pixels per mm.

Image analysis

The digital phase contrast images are semi-automatically binarized using ImageJ (National Institutes of Health, Bethesda[27]). The contrast in the images is sufficient to enable scaffold and tissue (represented in black in the binarized images) to be distinguished from the medium (represented in white).

Measurement of tissue growth

Tissue growth in the pores is quantified by determining the projected tissue area (PTA) formed in the pores. As this measurement is two-dimensional, it is only a proxy for quantifying the volume of growth into the depth of the pore. The free section of a pore, corresponding to the white regions in the binarized images, decreases with time. The PTA is then calculated by subtracting the binarized image at an initial time point from the image at the time of interest, and then calculating the remaining area. As cells need time to settle on the scaffold and start tissue deposition, the initial pore section is taken on the second day after seeding (D2).

Curvature measurement

The curvature profile of the interface between the tissue and the medium on each binarized image is calculated using Frette's algorithm[24, 28] implemented in a custom made Matlab code (Matlab 7.8.0 R2009a, MathWorks, Natick, MA) as described in [15]. Briefly, the algorithm first locates the pixels on the tissue-medium interface in the binarized image and the local curvature κ associated with an interface pixel is then estimated from the ratio of the number of black to white pixels lying within a given radius from the interface with the formula:

$$\kappa = \frac{3\pi}{r}\left(\frac{A}{A_{tot}} - \frac{1}{2}\right) \qquad (1)$$

where A is the number of pixels in the mask and on the outer side of the interface, A_{tot} is the number of pixels in the mask and r is the mask radius. The calculation is made for all pixels on the interface on each side of the border. The local curvature in one position of the interface is taken as the mean value of the curvatures measured on the outer pixel and the inner pixel. In the limit of a perfectly smooth interface and an infinitely small radius, this ratio corresponds to the local curvature. In the context of this paper, concave surfaces have a positive curvature.

To quantify interfacial geometry at different time points, the local curvature is given as a function of the position along the interface normalized with respect to its perimeter. In order to reduce the noise induced on the curvature profiles by both the roughness of the experimental interfaces and the digitalization, the mask radius r of the computational tool is set to $r = 14.5\,pxl$ and the resulting profile is then smoothed using a running average algorithm with a sampling proportion of 5% of the total length of the perimeter.

Immunofluorescence staining

Scaffolds are washed with phosphate buffered saline (PBS), fixed with 4 % paraformaldehyde for 5 min and permeabilized overnight with 1 % Triton-X100 (Sigma-Aldrich, Steinheim, Germany) at room temperature. Once washed in PBS, the tissue is stained for actin stress fibers by incubating with Alexa-Fluor 488–phalloidin (Invitrogen, Molecular Probes) (3 x 10-7 M) for 90 min. Nuclei are then stained with TO-PRO 3 692-661 (Invitrogen, Molecular Probes) (3 x 10-6 M) for 5 min. Fluorescent images of the stress fibers are obtained using a confocal laser scanning microscope (Leica TCS SP5).

Acknowledgements

We acknowledge funding from the Leibniz prize of PF running under DFG contract number FR2190/4-1. CB is a member of the Berlin-Brandenburg School for Regenerative Therapies (GSC 203).

References

[1] J. S. Temenoff, A. G. Mikos, Biomaterials, 2000, 21, 2405.

[2] A. G. Mikos, A. J. Thorsten, L. A. Czerwonka, Y. Bao, R. Langer, Polymer, 1994, 35, 1068.

[3] V. J. Chen, L. A. Smith, P. X. Ma, Biomaterials, 2006, 27, 3973.

[4] D. W. Hutmacher, Biomaterials, 2000, 21, 2529.

[5] P. Kollmannsberger, C. M. Bidan, J. W. C. Dunlop, P. Fratzl, Soft Matter, 2011.

[6] V. Vogel, M. P. Sheetz, Current Opinion in Cell Biology, 2009, 21, 38.

[7] A. J. Engler, S. Sen, H. L. Sweeney, D. E. Discher, Cell, 2006, 126, 677.

[8] R. A. Marklein, J. A. Burdick, Advanced Materials, 2010, 22, 175.
[9] C. M. Nelson, R. P. Jean, J. L. Tan, W. F. Liu, N. J. Sniadecki, A. A. Spector, C. S. Chen, Proceedings of the National Academy of Sciences of the United States of America, 2005, 102, 11594.
[10] J. Zeltinger, J. K. Sherwood, D. A. Graham, R. Mueller, L. G. Griffith, Tissue Engineering, 2001, 7, 557.
[11] J. P. St-Pierre, M. Gauthier, L. P. Lefebvre, M. Tabrizian, Biomaterials, 2005, 26, 7319.
[12] G. Kumar, C. K. Tison, K. Chatterjee, P. S. Pine, J. H. McDaniel, M. L. Salit, M. F. Young, C. G. Simon Jr, Biomaterials, 2011.
[13] D. W. Hutmacher, M. Sittinger, M. V. Risbud, Trends in Biotechnology, 2004, 22, 354.
[14] M. Rumpler, A. Woesz, J. W. C. Dunlop, J. T. van Dongen, P. Fratzl, Journal of The Royal Society Interface, 2008, 5, 1173.
[15] C. M. Bidan, K. P. Kommareddy, M. Rumpler, P. Kollmannsberger, Y. J. M. Bréchet, P. Fratzl, J. W. C. Dunlop, PLoS ONE, 2012, 7, e36336.
[16] A. M. Parfitt, Journal of Cellular Biochemistry, 1994, 55, 273.
[17] A. Aeppli, The American Mathematical Monthly, 1965, 72, 283.
[18] I. B. Bischofs, F. Klein, D. Lehnert, M. Bastmeyer, U. S. Schwarz, Biophysical Journal, 2008, 95, 3488.
[19] C. G. Rolli, T. Seufferlein, R. Kemkemer, J. P. Spatz, PLoS ONE, 2010, 5, e8726.
[20] K. P. Kommareddy, C. Lange, M. Rumpler, J. W. C. Dunlop, I. Manjubala, J. Cui, K. Kratz, A. Lendlein, P. Fratzl, Biointerphases, 2010, 5, 45.
[21] L. J. Gibson, Journal of Biomechanics, 2005, 38, 377.
[22] F. P. W. Melchels, B. Tonnarelli, A. L. Olivares, I. Martin, D. Lacroix, J. Feijen, D. J. Wendt, D. W. Grijpma, Biomaterials, 2011.
[23] D. W. Hutmacher, J. T. Schantz, C. X. F. Lam, K. C. Tan, T. C. Lim, Journal of Tissue Engineering and Regenerative Medicine, 2007, 1, 245.
[24] O. I. Frette, G. Virnovsky, D. Silin, Computational Materials Science, 2009, 44, 867.
[25] I. Manjubala, A. Woesz, C. Pilz, M. Rumpler, N. Fratzl-Zelman, P. Roschger, J. Stampfl, P. Fratzl, Journal of Materials Science: Materials in Medicine, 2005, 16, 1111.
[26] A. Woesz, M. Rumpler, J. Stampfl, F. Varga, N. Fratzl-Zelman, P. Roschger, K. Klaushofer, P. Fratzl, Materials Science & Engineering C, 2005, 25, 181.
[27] W. S. Rasband, National Institutes of Health, 2008.
[28] J. W. Bullard, E. J. Garboczi, W. C. Carter, E. R. Fuller Jr, Computational Materials Science, 1995, 4, 103.
[29] C. M. Bidan, P. Kollmannsberger, K. P. Kommareddy, M. Rumpler, Y. J. M. Bréchet, P. Fratzl, J. W. C. Dunlop, CMBBE, 2012.

7.4 [TG4] How Linear Tension Converts to Curvature: Geometric Control of Bone Tissue Growth.

Bidan, C. M., Kommareddy, K. P., Rumpler, M., Kollmannsberger, P., Bréchet, Y. J. M., Fratzl, P., Dunlop, J. W. C.

*Published in **PLoS ONE**, 2012, 7(5), e36336.*
doi:10.1371/journal.pone.0036336

Reprinted from PlosOne Creative Commons Open Access Licence

Abstract: This study investigated how substrate geometry influences in-vitro tissue formation at length scales much larger than a single cell. Two-millimetre thick hydroxyapatite plates containing circular pores and semi-circular channels of 0.5 mm radius, mimicking osteons and hemi-osteons respectively, were incubated with MC3T3-E1 cells for 4 weeks. The amount and shape of the tissue formed in the pores, as measured using phase contrast microscopy, depended on the substrate geometry. It was further demonstrated, using a simple geometric model, that the observed curvature-controlled growth can be derived from the assembly of tensile elements on a curved substrate. These tensile elements are cells anchored on distant points of the curved surface, thus creating an actin "chord" by generating tension between the adhesion sites. Such a chord model was used to link the shape of the substrate to cell organisation and tissue patterning. In a pore with a circular cross-section, tissue growth increases the average curvature of the surface, whereas a semi-circular channel tends to be flattened out. Thereby, a single mechanism could describe new tissue growth in both cortical and trabecular bone after resorption due to remodelling. These similarities between in-vitro and in-vivo patterns suggest geometry as an important signal for bone remodelling.

Introduction

Cells are not only sensitive to biochemical signals [1], but also to the mechanical properties [2] and the geometry [3] of their environment. They detect and respond to these physical characteristics at different length scales. On the sub-cellular level, cells sense and integrate mechanical information via their Focal Adhesions (FAs). These complexes of proteins link the extracellular environment to the cytoskeleton and enable cells to both apply and "feel" forces [4]. The internal cytoskeletal stress is constantly tuned by actin fibre remodelling and acto-myosin contractility [5], giving rise to a mechanical homeostasis in the cell [6]. This in turn enables the geometrical [7,8] and physical [2] properties of the underlying extracellular matrix (ECM) or substrate to be sensed. The information is then transmitted to the nuclei [9] allowing cells to adapt proliferation [10], differentiation [11], apoptosis [12], spreading [13], migration [14], ECM production [15], and orientation during mitosis [16]. As cells are linked directly via cell/cell contacts or indirectly via the ECM, they can mechanically communicate with each other [17] and synchronise their individual decisions to act in a collective way giving rise to cell patterning [10,18] and ECM organisation [19,20] during morphogenesis for example [21].

At the tissue level, the influence and emergence of mechanical properties have been investigated in the context of cancer research [22], cardio-vascular disease [23] and tissue engineering [24]. While a lot of studies on porous scaffolds also revealed an effect of porosity and pore size on cell adhesion, proliferation and matrix deposition (see e.g. [25,26]), relatively few focused on quantifying the role of scaffold architecture on tissue growth kinetics [27,28]. In one study, Ripamonti and co-workers compared tissue growth in natural bone structures and artificial hydroxyapatite scaffolds implanted in vivo [29], and showed preferential tissue production in concave areas of the scaffolds, as also observed in vitro [30]. The kinetics of in vitro bone tissue growth was also measured in pores of controlled geometries in another study [27]. In their study, they showed that the thickness of tissue produced by osteoblasts depended on the local surface curvature. This led to the description of tissue development in terms of curvature-controlled tissue growth (CCTG), which gave good predictions of the tissue shape. Since this description is purely geometric, additional studies are required to elucidate the potential effects of mechanical and biological processes involved in the interfacial motion of tissue (e.g. cell proliferation and ECM production).

A classic example of the interaction between geometry and tissue growth can be found in the process of bone remodelling [31] which allows bone to renew and to adapt to slowly changing mechanical environments. During bone remodelling, three cell types are involved: osteocytes sense mechanical loads in existing bone [32,33,34]and forward the signal to osteoclasts which resorb old or damaged bone, and to osteoblasts which produce new collagenous tissue called osteoid. By definition, resorption and deposition are two processes that locally change the surface geometry of the bone tissue. In cortical bone remodelling, osteoclasts resorb bone, leaving cylindrical pores called osteons [35]. These are then refilled by osteoidal tissue with a central blood vessel, the Haversian canal [36]. During the remodelling of trabecular bone however, osteoclasts dig out small semi-circular channels or grooves called resorption pits or trails which can be seen as hemi-osteons, that are later refilled with osteoid by the osteoblasts [35]. Despite the continually changing local geometry, the mean curvature of the trabecular bone surface is tightly controlled [37]. Indeed, the signals responsible for such a precise spatial orchestration of the cells on the millimetre scale are still unclear. For instance, it is not clear why osteoblasts stop tissue production once a hemi-osteonal lacuna is filled. This provides a strong motivation to understand the influence of geometry

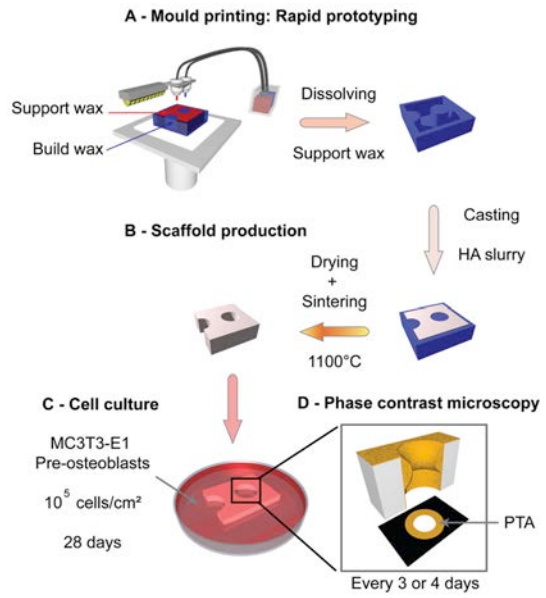

FIGURE 1. Experimental protocol
A - Moulds are produced by rapid prototyping. A build wax (blue) is used to print the mould in 3D. A support wax (red) is added to reinforce the object while printing, and then removed by dissolution. B - Hydroxyapatite slurry is cast into the moulds, slowly dried and sintered. C - Pre-osteoblast cells are seeded (10^5 cells/cm^2) on the scaffolds and cultured for 28 days. D - Tissue growth is quantified by phase contrast microscopy twice a week by measuring the projected tissue area (PTA) in each pore.

on tissue deposition during bone remodelling – the goal of this paper.

Besides the quantitative description of tissue deposition on bone-like substrates, the present study proposes a new physical explanation of how the organisation of contractile cells leads to CCTG, as observed by Rumpler et al. [27]. Circular pores and semi-circular surfaces were designed in hydroxyapatite scaffolds to mimic osteons and osteoclastic resorption pits (hemi-osteons), respectively, and the scaffolds were incubated with MC3T3-E1 pre-osteoblast cells. In order to quantify geometry evolution on experimental images, a computational tool based on the approach of Frette et al. [38] was used to measure the curvature profiles and integrated into an algorithm for CCTG. In this paper, CCTG is shown to be equivalent to a simple geometrical construction representing the organisation of individual tensile elements and called the chord model. This new approach enables curvature-controlled tissue growth to be interpreted as the result of the superposition of linear elements such as stretched cells and collagen fibres. By comparing a simple geometrical model to experiments, this paper also highlights that the sum of mechanical and biological processes responsible for tissue growth responds to simple geometrical rules giving rise to the patterns observed in vitro. This suggests geometry as a key regulatory element for the tight control of tissue deposition during bone remodelling.

Material and methods

Production of the hydroxyapatite (HA) plates

HA plates (2mm thick) containing circular pores and semi-circular vertical channels (nominal diameter 1mm) were made by slurry casting. The moulds were designed using the computer-aided design (CAD) software Alibre Design (Alibre Inc., Richardson, TX) and produced with a three-dimensional (3D) wax printer, Model Maker II (Solidscape Inc., Merrimack, NH) as described in [39] (Fig.1A). The moulds were filled with a HA slurry made of 15g of methacrylamide monomers (MAM), 5g of N-N'-Methylenebisacrylamide (BMAM), 75g of water and 12.5g of Dextran for 300g of HA powder, and crosslinked with ammonium persulfate and N,N,N',N'-Tetramethylethylenediamine (TEMED). The structures were slowly air dried, pre-sintered and finally sintered as done in [40] (Fig.1B).

Cell culture

Murine pre-osteoblastic cells MC3T3-E1 (provided by the Ludwig Boltzmann Institute of Osteology, Vienna, Austria) were seeded with a density of 105 cells/cm^2 on the surface of the HA scaffolds and cultured for 28 days in α-MEM (Sigma-Aldrich, St. Louis, MO) supplemented with 10% foetal calf serum (PAA laboratories, Linz, Austria), 0,1% ascorbic acid (Sigma-Aldrich, St. Louis, MO) and 0,1% gentamicin (Sigma-Aldrich, Steinheim, Germany) in a humidified atmosphere with 5% CO_2 at 37°C (Fig.1C).

Imaging and analysis

Each pore was imaged every 3 to 4 days using a phase contrast microscope (Nikon Eclipse TS100, Japan) equipped with a digital camera (Nikon Digital sight DS 2Mv) (Fig.1D). All pictures were taken with a 4x objective, yielding the final image resolution $1mm = 205\,pxl$.

The digital images were semi-automatically binarised using ImageJ (National Institutes of Health, Bethesda [41]). The contrast in the images enabled scaffold and tissue (black in the binarised images) to be distinguished from the medium (white).

Measurement of the tissue production

Tissue production in the pores was quantified by determining the projected tissue area (PTA) formed in the pores (Fig.1D). As this measurement is two-dimensional, it is only a proxy for quantifying the volume of growth into the depth of the pore. The free section of a pore, corresponding to the white regions in the binarised images, decreases with time. The PTA was then calculated by subtracting the binarised image at an initial time point from the image at the time of interest. As cells needed time to settle and start tissue deposition, the initial pore section was taken on the fourth day after seeding (D4).

The experiments presented here included 6 pores for each shape: circular pores (CIR) and semi-circular channels (SC). Two other sets of experiments repeated in the same conditions showed similar results (data not shown).

Immunofluorescence staining

Some scaffolds were washed with phosphate buffered saline (PBS), fixed with 4% paraformaldehyde and permeabilized with 0.1% Triton-X100 (Sigma-Aldrich, Steinheim, Germany). After 15min blocking in 10% blocking reagent (Roche, Germany), the samples were incubated for 1h in a 1:200 solution of myosin IIb antibody (Cell Signaling Technology, Beverly, MA) and 1h in a 1:200 solution of anti-Rabbit IgG AF 488 (Cell Signaling Technology, Beverly, MA). Once washed in

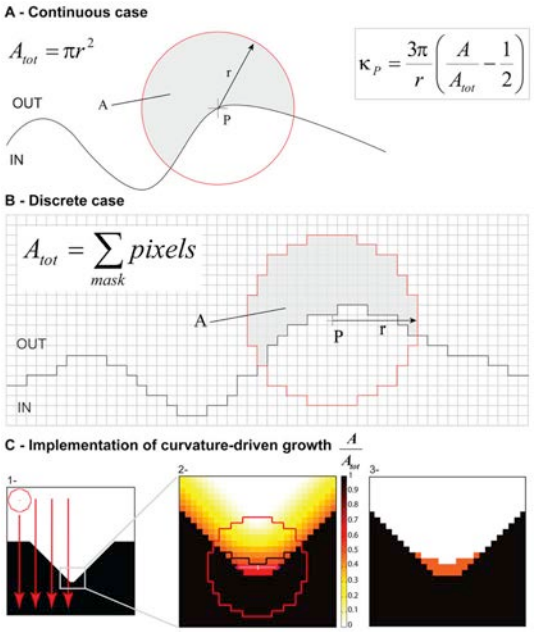

FIGURE 2. Computational methods

A-B - Principle of curvature measurement on continuous (A) and discrete (B) interfaces (adapted from [38]). The grey area represents the contributing area A in equation 1 where $r = 8.5\,pxl$ is the radius of the mask, $A_{tot} = \pi r^2$ in A and $A_{tot} = \sum_{mask} pixels$ in B. C - Implementation of CCTG. The whole image is scanned with the mask (1-) and the ratio $\frac{A}{A_{tot}}$ is attributed to each pixel (2-). A threshold of 0.5, corresponding to $\kappa = 0$, is applied: free pixels where $\kappa > 0$ are filled with tissue (3-). The interface is then updated and the entire procedure is repeated.

PBS, the tissue was stained for actin stress fibers by incubating with TRITC-Phalloidin 4 x 10-8M (Sigma-Aldrich, Steinheim, Germany) for 40min. After fixation, some of the samples were permeabilized as mentioned above and stained for nuclei with a 1:300 solution of TO-PRO3 (Invitrogen, Oregon, USA) for 5min. Images of stress fibres, myosin and nuclei were obtained using a confocal laser scanning microscope (Leica, Germany).

Curvature measurement

The curvature profile of the interface between the tissue and the medium on each binarised image was calculated using Frette's algorithm [38,42] implemented in a custom made Matlab code (Matlab 7.8.0 R2009a, MathWorks, Natick, MA). This method has an advantage over other curvature measurements based on spline fitting [43], in that it can be applied directly to digital images coming from the phase contrast measurements. The algorithm first located the pixels on the tissue-medium interface in the binarised image. The local curvature $\kappa = \frac{1}{R}$ associated with an interface pixel was then estimated from the ratio of the number of black to white pixels lying within a given radius from the interface:

$$\kappa = \frac{3\pi}{r}\left(\frac{A}{A_{tot}} - \frac{1}{2}\right) \qquad \text{(Eq.1)}$$

where A is the number of pixels in the mask and on the outer side of the interface, A_{tot} is the number of pixels in the mask and r is the mask radius (Fig.2A and B).The calculation was made for all pixels on the interface on each side of the border. The local curvature in one position of the interface was taken as the mean value of the curvatures measured on the outer pixel and the inner pixel. In the limit of a perfectly smooth interface and an infinitely small radius, this ratio corresponds to the local curvature. In this paper, a positive curvature is defined as a concave surface (Fig.3). Average curvatures κ_{ave} were determined along the perimeter of the pore for circles, and along a portion of the interface in semi-circles. The precision of the measurements are discussed in Text S1.

Curvature-controlled tissue growth

An equivalent of the CCTG model presented by Rumpler et al. [27] was implemented by incorporating the curvature estimation of Frette et al. [38]. The technique to estimate interfacial curvature on a binary image was extended towards a description of growth by scanning the mask over the entire image, giving "effective curvature" values for all pixels (Fig.2C). Assuming that growth occurs only in concave regions, each white pixel where the effective curvature is positive was changed to black, representing tissue deposition. The process was then iterated to describe CCTG. This method has the advantage that growth can be directly compared with the experimental pore geometries.

In the approximation $R >> r$, the local thickness of tissue produced in one step is proportional to the local curvature (for a proof see Text S1) and compares with the description of CCTG proposed in [27]:

$$\delta_{Comp} = \frac{r^2}{6}\kappa \qquad \text{(Eq.2)}$$

Results

Tissue deposition was observed in each pore by phase contrast microscopy over a period of 28 days. Fig.3A presents images taken at different times during the culture (D4, D7, D14 and D21) and is compared with the CCTG description in Fig.3B. In circular pores, tissue deposition occured homogeneously along the interface, leading to a uniform concentric closing of the cylinder. On semi-circular channels, no tissue formed on the convex corners of the channel neither on the external flat surfaces. Growth is therefore pinned within the channel, resulting in different amounts of tissue as a function of position in the lacuna. In contrast to circular pores, the interface of semi-circular channels flattened with time.

The evolution of tissue shape reveals the determining role of the boundary conditions in the interfacial motion between 4 and 28 days. The average curvature measured on the experimental images increased with ongoing tissue growth in circular pores, whereas curvature slowly decreased on a semi-circular channel (Fig.3A and 4A).

On the growth curves in Fig.4B, the PTA was normalised by the area of the pore (PA) measured on the fourth day of culture. In semi-circular channels, PA was taken to be the free area under the scaffold surface (dashed line in Fig.5). A direct comparison of the fraction of available space filled with tissue was then possible. The experimental data displayed a linear increase of the amount of tissue produced in circular pores up to day 14 in agreement with previous results [27]. Afterwards, tissue amplification

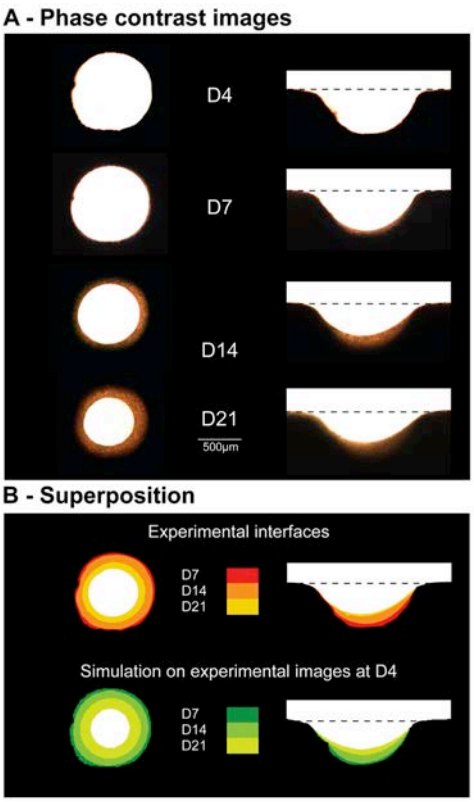

FIGURE 3. Qualitative results: evolution of the geometry

A - Evolution of the tissue interface in a circular pore and on a semi-circular surface. Images taken at different culture times (D4, D7, D14 and D21) during in vitro experiments show behaviours comparable to those observed in osteons and hemi-osteons during bone remodelling. B - The superposition of the interfaces obtained experimentally (top) compares to the one derived from CCTG applied to the actual geometry of the experimental pores at D4 (bottom). 7, 14 and 21 days of culture are simulated by 51; 170 and 289 steps for the circle and 34; 153 and 272 steps for the semi-circle respectively ($r = 8.5\,pxl$, $\alpha = 17.0\,step/day$).

slowed down. Comparison of the early growth behaviour in circular and semi-circular channels, calculated between day 4 and day 14, revealed that tissue growth was significantly higher in the circles compared to semi-circular surfaces (Fig. 4C).

Although the local curvature was supposed to be the same on each point of the surface, the initial growth rates (between D4 and D14) in a circular pore and on a semi-circular surface are different (Fig.4C). A two-way analysis of variance ANOVA showed a statistical difference between the shapes (CIR vs SC) and no significant influence of the methods used (Experiment vs Simulation on experimental shapes vs Simulation on ideal shape). All pair-wise multiple comparisons were done following the Holm-Sidak method and values of less than were considered significant. The geometry of the substrate influenced the speed of tissue production by the cells. The CCTG description correctly predicted that the average curvature diverges as the circular pore filled whereas it should converge toward zero (flat surface) in semi-circular channels (Fig.4A).

In order to compare predictions and in vitro results, a time scale parameter α in $step.day^{-1}$ was derived from the ratio between simulated and experimental growth rates measured in circular pores in $mm^2.step^{-1}$ and $mm^2.day^{-1}$ respectively. The tissue growth rate was derived from the simulations performed on experimental images with $r = 8.5\,pxl$, $\left.\frac{\Delta PTA}{\Delta \tau}\right|_{sim} = 0.00167\,mm^2.step^{-1}$ and experimentally measured on the early stage (D7 to D14) and is considered constant: $\left.\frac{dPTA}{dt}\right|_{\exp} = 0.0284\,mm^2.day^{-1}$. The time scale used in the following is thus $\alpha = 17.0\,step.day^{-1}$.

Quantitative results predicted by application of CCTG on experimental images at D4 are reported in Fig.4B. The simulated projected tissue areas (PTA) were normalised by the area of the respective pores at D4 (PA) and averaged ($n = 6$). An additional lag time was used to overlap simulated and experimental data: $t_{0\_CIR} = 4day$ and $t_{0\_SC} = 5day$. t_0 represents the time cells need to spread and colonize the scaffold before starting growth and is known to depend on the geometry of the pore [44]. Once the single free parameter of the calculations is fitted on the experimental growth in circular pores ($\alpha = 17.0\,step.day^{-1}$), CCTG also correctly described the initial growth behaviour on semi-circular channels (Fig 4A, B and C). However, it did not explain the notable slowdown observed experimentally in both geometries from D14.

A "chord model" to explain curvature-controlled tissue growth

Although CCTG can predict both the geometry and the linear kinetics of tissue formation, it contains no intrinsic time scale and provides no mechanistic explanation of the curvature sensing of cells and tissue.

In the following, tissue is considered as a collection of stretched cells and fibrous ECM, and growth is described as occurring via the assembly of such tensile elements (chords) on a surface. In this section, it is demonstrated that CCTG is a direct consequence of this simple geometric construction. Besides giving a mechanistic interpretation of the CCTG on the cellular level, the chord model also motivates the interaction range (mask size) chosen for measuring curvature and thereby justifies the time scale of the computational implementation.

As cells are the tissue manufacturers, a geometrical description of single cells settled on a surface (Fig.5) provides hints to the local dependence of tissue organisation on the geometry. Once attached to the substrate, cells contract their cytoskeleton thus defining a new interface between the FAs [45]. If the surface is flat or convex, cytoskeletal contraction results in a downward motion of the cell towards the substrate (Fig.5A). However, if the surface is concave, the contracting cell is stretched between the FAs and locally forms a flat interface (Fig.5B).

The chord model presented here consists of a tensile element of length l that connects two points on a surface (Fig.5C) and locally defines a new interface. The effect induced in the perpendicular direction can be described using the largest distance δ_{Chord} between the chord and the substrate. Simple geometrical

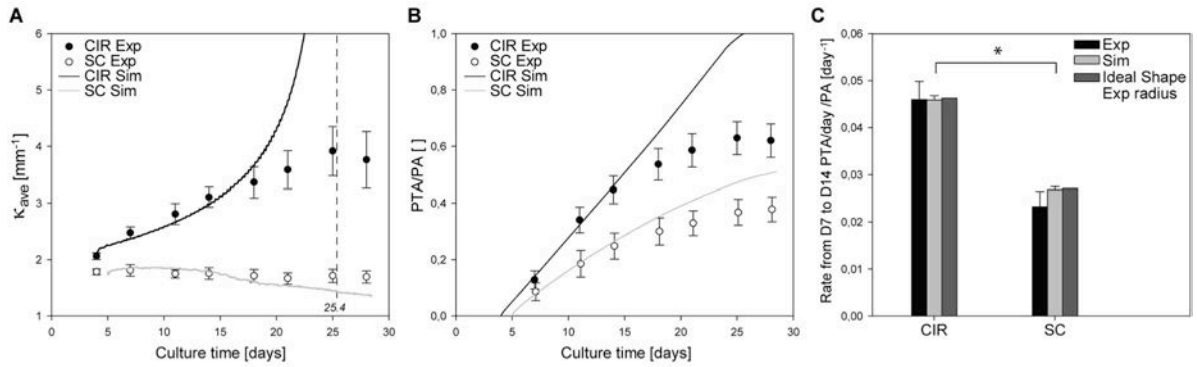

FIGURE 4. Quantitative results: curvature profile and growth rate

Quantitative analysis of tissue growth in circular pores (*CIR*) and on semi-circular channels (*SC*) of 1 mm diameter. A - The average curvature along the perimeter of the circular pore and on a given portion of the semi-circular surfaces is measured on experimental images at different culture times. As $\kappa_{0\_CIR} = 2.047 mm^{-1}$, theoretically circular pores should be filled in about 432 steps or 25.4 days. B - The projected tissue area (PTA) is normalised by the area of the pore (PA) at D4 (reference) and reported as a function of culture time. In A and B, the full lines correspond to the prediction given by CCTG ($r = 8.5 pxl$; $\alpha = 17.0 step/day$). A lag time is used to overlap simulated and experimental data ($t_{0\_CIR} = 4 day$ and $t_{0\_SC} = 5 day$). C - Growth rates are calculated between D7 and D14 with the experimental and the simulated data as well as data simulated on ideal geometries with a radius derived from the experimental images. ANOVA analysis shows no significant differences between the methods used but a statistical difference in the tissue growth rates achieved in CIR and SC ($p < 0.05$). Dots and error bars represent mean values and standard errors, respectively ($n = 6$).

relations (detailed in Text S1 and Figures S1 and S2) demonstrate that the local interfacial motion induced by the deposition of a single chord δ_{Chord} is proportional to the local curvature $\kappa = \frac{1}{R}$ with the hypothesis $R >> l$:

$$\delta_{Chord} = \frac{l^2}{8}\kappa \qquad \text{(Eq.3)}$$

Combining this effect for all possible positions of the chord on the substrate predicts the location of the interface once a collection of tensile elements has been laid down (Fig.5D). Additional layers can then settle iteratively on the surface.

Equations 2 and 3 demonstrate that the superposition of tensile elements on a curved surface generates an interfacial motion equivalent to the CCTG evolution presented earlier (Fig.2 and [27]). Using $r = \frac{\sqrt{3}}{2} l$ as the radius of the mask in the computational method leads to full quantitative consistency between the chord model and the CCTG description: $\delta = \delta_{Chord} = \delta_{Comp} = \frac{l^2}{8}\kappa$. Mathematical details are provided in the Text S1. Moreover, Fig.5D reveals that geometries derived from the chord model also compared well with the experimental observations (Fig.3).

Considering cells as tensile elements, the chord model can describe tissue growth and its curvature-driven behaviour. Additional support comes from the observation of actin fibres that indicate stresses produced by interacting cells. These stress fibres formed rings inside circular channels (Fig.6B), as previously observed [27], which are reminiscent of contractile actin –myosin rings found in wound healing for other cell types [46,47,48]. Actin fibres co-localizing with myosin are shown in concave regions on Fig.6A. These fibres have an arrangement very similar to the chords in Fig.5B, supporting the idea that cells in the tissue collectively exert tensile stress as they adhere to matrix and substrate. On convex surfaces however, Fig.6A clearly shows a much lower density of contractile chords, also in agreement with the model in Fig.5. A convex surface (Fig. 6D) was also tested and interestingly only a mono-layer of tissue was observed even up to late growth stages.

Staining tissue for cell nuclei reveals a homogeneous cell density all over the projected tissue area (Fig.6C). This showed that cell density is independent of curvature. Note that the global geometry of the new interface was independent of the number of chords, i.e. cell density, in one layer. Moreover, the geometry of a substrate is known to influence cell proliferation by determining the stress distribution in the contractile cell layer [10]. Although no proliferation study was performed here, the constant cell density suggests that cell proliferation adapts as the curvature increases and the adhesion surface decreases during tissue growth, leading to the overall constant cell density.

In the computational description presented earlier, the radius of the mask defined the interaction range around a given point and influences the precision of curvature estimation. The equivalence between the CCTG and the chord model together with the cellular approach proposed above motivated us to scale this range to the approximate length of a cell: $r = \frac{\sqrt{3}}{2} l$.

For an elongated osteoblast, $l \approx 50 \mu m$ but with $r = 8.5 pxl$ and $1mm = 205 pxl$, the actual cell length considered here is $l \approx 47 \mu m$. Thereby, the effective curvature values derived in the computational implementation of CCTG represent what cells "feel" from the geometrical features of the surface.

In terms of PTA, the simulated growth rate in $mm^2.step^{-1}$ in an ideal circular pore is constant:

$$\left.\frac{\Delta PTA}{\Delta \tau}\right|_{id} (\tau) = 2\pi R(\tau)\delta(\tau) = \frac{\pi l^2}{4} = \frac{\pi r^2}{3} \qquad \text{(Eq.4)}$$

This constant rate derived in closed convex shapes (circles) confirms the equivalence between the chord

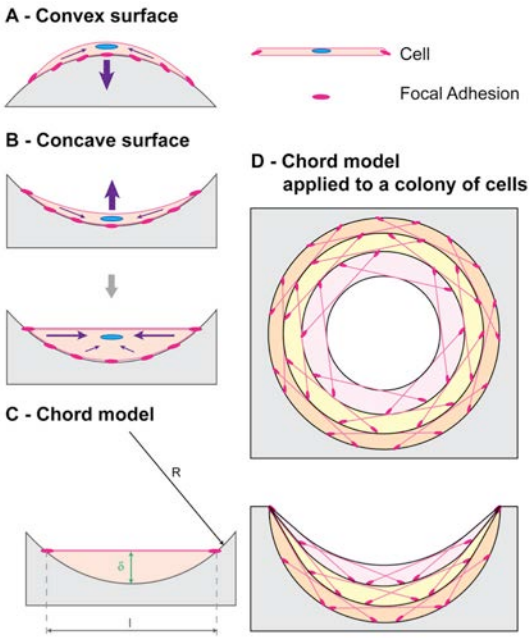

FIGURE 5. A chord model to describe tissue growth
After adhering on a substrate (pink dots), a cell contracts its cytoskeleton (purple arrows) to reach a stable tensile state. A - On a convex surface, the cell remains bent and exerts pressure on the substrate. B - On a concave surface, cell contraction stretches the membrane and results in a local flattening of the surface. C - A chord representing a static stretched cell defines an element of tissue, which thickness δ is proportional to the local curvature of the surface. D - A collection of stretched cells sitting on a concave surface can be seen as an assembly of segments

model and the CCTG description proposed by Rumpler et al. [27], see also Fig S3.

According to equation 4, the simulated growth rate and thus the time scale of the model depend on the interaction range chosen. The simplest approach to determine this time scale is to assume that the experimental growth rate is also proportional to curvature. This requires the definition of one parameter $\alpha(l)$ that fits the time τ of simulated growth in steps to the time t of experimental tissue growth in days, which leads to:

$$\left.\frac{dPTA}{dt}\right|_{exp} = \alpha(l)\frac{\pi l^2}{4} = \alpha(r)\frac{\pi r^2}{3} \qquad \text{(Eq.5)}$$

Equations 4 and 5 show that $\alpha(l)$ scales with the inverse of the square of the interaction range chosen in the model and can always be derived by comparing simulated and measured tissue growth rates in the experimental pores. The interaction range being fixed to $l = 47\mu m$, α is a constant accounting for the kinetics of all the biological phenomena contributing to tissue deposition (cell migration, proliferation, ECM synthesis, etc.).

τ and t being proportional, the interfacial motion derived from the model can be described as a continuous function of time $t = \frac{\tau}{\alpha}$. To quantify kinetics, the evolution of the distance between tissue interface and the substrate (in $mm.step^{-1}$) was derived in an ideal pore by integrating equation 3:

$$\delta(t) = \alpha\frac{l^2}{8R(t)} = -\frac{dR(t)}{dt} \qquad \text{(Eq.6)}$$

This gives a solution in terms of curvature:

$$\kappa(t) = \frac{1}{R(t)} = \frac{\kappa_0}{\sqrt{1-\frac{l^2\kappa_0^2}{4}\alpha t}} \qquad \text{(Eq.7)}$$

The time needed for an ideal circle to be filled was determined for a radius equal to zero and an infinite curvature:

$$t_{fill} = \frac{4}{l^2\kappa_0^2\alpha} \qquad \text{(Eq.8)}$$

Discussion

The amount and the shape of the tissue produced by MC3T3-E1 cells cultured in pores of controlled geometries were quantified in terms of PTA and curvature on phase contrast images taken over a period of 28 days. The chord model not only agrees with the computational implementation of CCTG as described in Fig.2, but it also provides a relevant interpretation on the cellular scale of the equivalent behaviour observed during tissue growth (Fig.3). Moreover, the works of Théry et al. [13] about the shape and the stress state of a cell after spreading and contraction, support the approach sketched on Fig.5.

As described earlier, one step of the computational implementation of CCTG represents roughly the contribution of one layer of cells to the tissue thickness. In agreement with the hypothesis of CCTG, the simulation predicts a constant tissue growth rate (in $mm^2.step^{-1}$) in an ideal circle [27]. This rate only depends on the cell size, arbitrarily set to $47\mu m$ (Eq.7). Measuring the initial experimental rate (in $mm^2.day^{-1}$) in circular pores enabled us to fit the model of growth with a unique parameter that introduces a linear time scale by giving the number of steps needed to represent one day of experiment: $\alpha = 17.0 step.day^{-1}$. Although this parameter should theoretically represent the number of cell layers deposited in one day of culture, the high value suggests that some assumptions are too simple. For example, stretched osteoblasts in culture are probably not homogeneous in size l and are likely to be larger than $47\mu m$. Moreover, a chord model only based on cells implies that the contribution of the ECM is neglected although Fig.6B reveals the presence of collagen fibres aligned with the interface, just as actin fibres in stretched cells. Considering larger cells and/or adding collagen fibres in the definition of the tensile elements would increase the simulated growth rate and decrease α toward more realistic values. Importantly, α does not interfere with the geometrical behaviour of the interface but just rescales the evolution in time.

The circular pores and semi-circular surfaces produced in the experiments were chosen with the same radius, i.e. the same local curvature, along the interface. Although CCTG supposes a local growth rate proportional to the local curvature, Fig.4C shows a significant difference in the normalised global growth rates (PTA/PA) on circular pores and semi-circular surfaces. The qualitative results (Fig.3) as well as the evolution of the average curvature (Fig.4A) suggest the importance of the boundary conditions for the

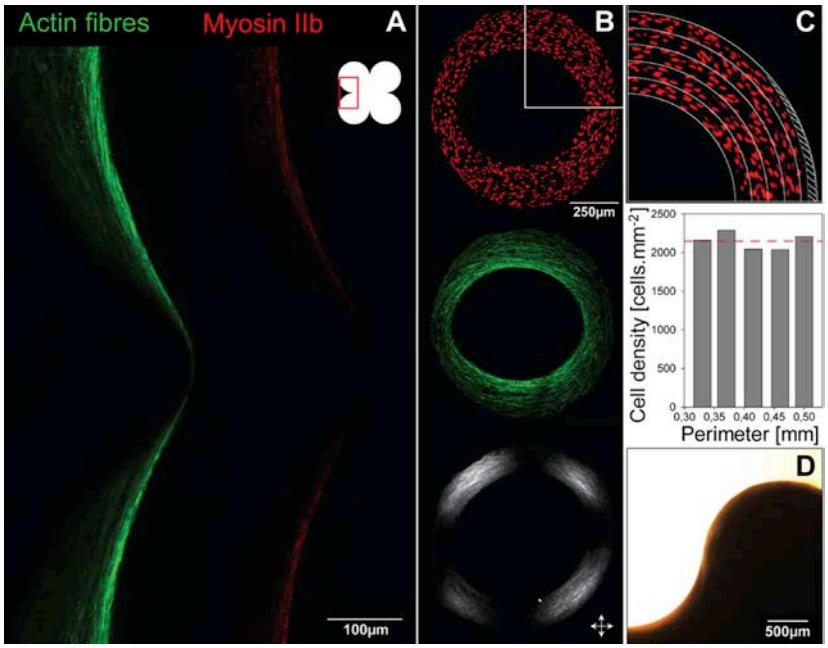

FIGURE 6. Tissue organisation

A - Tissue produced in a pore made of 4 adjacent circles and stained for actin stress fibres and myosin IIb. Actin fibres colocalised with myosin IIb are present on the whole surface but their higher density on concave interfaces suggests a local higher stress state of the cells. B - Tissue is made of cells and collagen. Nuclei (*red*), actin stress fibres (*green*) and collagen fibres (*visualized by polarized microscopy*) are oriented parallel to the interface. The white arrows show polarisation direction. C - The homogeneous distribution of nuclei shows that cell density is independent of geometry and suggests a local dependence of cell proliferation on the local curvature. D - An example of a convex HA surface (D35) on which only a mono-layer of tissue was formed.

pattern of tissue deposition. As no growth occurs on the convexities (Fig.6D), the tissue laid down within concavities flattens the surface in semi-circular channels, i.e. decreases the average curvature. In circular pores however, the concentric growth increases curvature.

To underline the determining role of the convex corners as seen in Fig.6, CCTG was simulated on artificial images (Fig.7A-F). All geometries were based on a semi-circle ($R = 0.5mm$) that is differently linked to the surrounding flat surfaces. Fig.7 shows that although the local curvature is the same on a given portion, tissue deposition (in time and space) depends strongly on the geometry of the surroundings. As the tissue grows, changes in the curvature profile of the interface affect both local and global growth rates. Although the phenomenon is slightly exaggerated due to the discrete character of the computational method (Fig.7A and B), it is interesting to note the slowdown of growth when tissue reaches the convex corners. This suggests geometry as a potential signal for osteoblasts to decrease and eventually stop tissue production when a hemi-osteonal lacuna is filled.

Fig.4B reveals a slowdown of the experimental tissue growth after 18 days of cell culture that is not predicted by the chord model fitted with a linear time scale. However, more complex scaling laws could be used to depict the non-linearities induced as cells slow down proliferation and ECM synthesis when they differentiate and mature [49]. For example, pre-osteoblasts differentiate towards osteoblasts during culture and begin to synthesise alkaline phosphatase (ALP). As the plateau often appears after 14 days of culture or later, which approximately corresponds to the beginning of ALP synthesis by such cells [50], the influence of the differentiation could be a possible explanation for the decrease in tissue production. In parallel, the ECM synthesized by the osteoblasts also undergoes maturation, whereby cross-link formation in the collagen matrix increases with culture time [51,52]. This could implement a denser packing of the tissue and explain the plateau in PTA. As the CCTG description is intrinsically a geometrical description, adapting the time scale would be a simple way to take the effects of cell and matrix maturation into account. For a given interaction range, the number of steps representing one day of culture $\alpha(t)$ would then decrease with time, and the scaling law would require an additional time characteristic representing the slowdown of cell activity with ageing.

Alternatively, the plateau in tissue production observed after two weeks of culture may have a geometrical origin. In the experiments, tissue is grown in 2mm thick scaffolds with straight sided pores, and only the projected tissue area is measured on phase contrast images. Using PTA as a proxy to quantify the amount of tissue produced in the pore implies that the local tissue thickness is homogeneous along the third axis, which is unlikely. Indeed, cells need time to migrate and therefore can not build the same thickness of tissue simultaneously throughout the depth of the channel. Moreover, the extremities of the pore present convex corners in 3D and such boundary conditions are expected to affect the growth pattern along the z-axis. As a consequence, pores are unlikely to remain straight during growth, and a second principal curvature (different from zero) should then complete the geometrical characterisation of the interface in 3D. Although this second principal curvature is expected to play a role, the approaches proposed in this study assume that only one principal curvature (in the image plane) changes during growth whereas the other remains constant and zero (straight sided pores). The slowdown of tissue growth

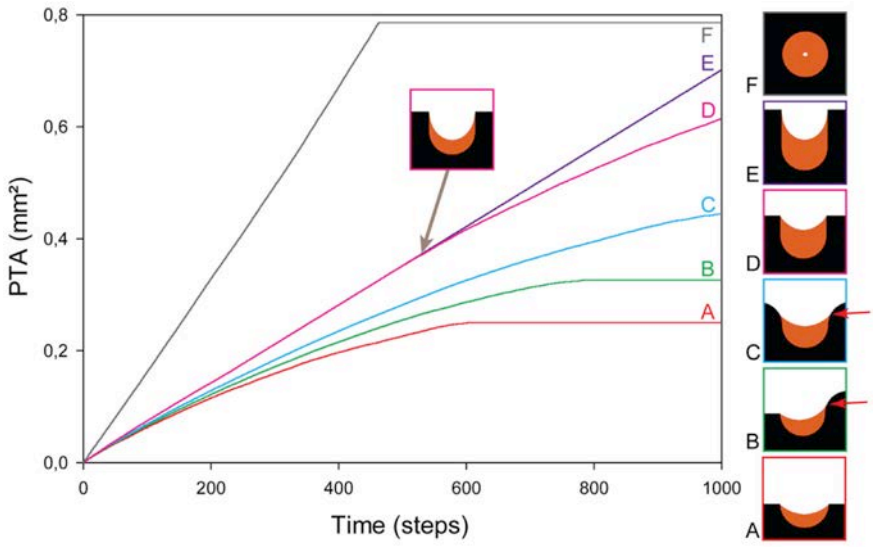

FIGURE 7. Importance of boundary conditions
Tissue growth (orange) is simulated on different artificial images using the CCTG description (A to F). The predicted PTA is reported as a function of iteration steps. Each initial interface (black) contains a semi-circle with a radius of 0.5 mm. The different boundary conditions show the influence expected on tissue growth rate and organisation. On A, B and C, the model predicts that the sharper the convex corners, the slower the growth. Tissue is eventually deposited on convex surfaces after the surroundings have been filled and the interface has locally become concave (red arrows). Comparing A, D and E reveals that shifting the convex corners upward prolongs the duration of a constant growth rate which is half of the one obtained in a full circle (F). Tissue deposition can expand on the walls until it reaches the convex corners. From this time point (inset), the surface joining the pinning points is minimised, which decreases the curvature and slows the growth.

observed in terms of PTA could then be explained by the emergence of a convexity (negative second principal curvature) in the z-direction that is not taken into account in the previous calculations. Extending the CCTG description to 3D would be of great interest to understand which combination of the two principal curvatures is relevant for tissue growth: mean curvature, Gaussian curvature, maximal curvature, etc. As such models predict interface evolution toward surfaces of minimal energy, this 3D mean curvature would then decrease and tend towards zero, much akin to what is observed in trabecular bone [37].

Interestingly, curvature-controlled growth is well known in physics and material sciences and has been used to describe electrochemical coating [53][54], solidification [55], and grain growth [56], for example. Such processes come about in systems with high surface tensions, in which surface energy is linked to curvature through the Laplace equation, as commonly seen in wetting problems [57]. Surface tension has also been shown to be a determining factor in biology, mainly in the context of the Differential Adhesion Hypothesis [58]. This interfacial characteristic is not only responsible for self sorting on the cell level during gastrulation [59] and tumour invasion [60] but also for tissue organisation [28].

While it was known that tissue-producing cells respond to geometry [29] following a principle of CCTG on a millimetre scale [27], the present study shows that the patterns of growth obtained in circular pores and on semi-circular channels are analytically equivalent to those derived from a simple construction based on tensile elements representing stretched cells. No direct geometry sensing is necessary to explain the resulting curvature-controlled growth. The shape of the surface affects the spatial distribution of FAs and thereby the shape of the contractile cells [13] as well as the forces they sense [8] and produce [10]. Adding a time scale enables the model to predict the kinetics of tissue deposition: faster growth occurs in circular pores compared to semi-circular surfaces.

The chord model was able to explain the shape-dependence of growth solely in terms of tension and curvature, without any biological mechanisms such as stress-dependent proliferation or migration. Although such mechanisms are involved on the cellular level and need to be taken into account in a physiological context, our results show that the interplay of contractility and geometry alone can coordinate growth in scaffolds. This reveals a generic physical control mechanism for biological growth processes in bone, independent of specific functional aspects and signalling pathways, that may also be relevant to other tissue types.

The interfacial motion predicted by the model and supported by the experiments is similar to the one occurring in osteons and osteoclastic resorption lacunae during bone remodelling: while circular pores are filled in a concentric way, semi-circular channels are filled layer by layer until the interface becomes flat i.e. the curvature of the surface becomes zero. This implies that osteoblasts do not need a specific signal to stop matrix production when the resorption pit is filled, but the gradual flattening of the bone surface during the filling process are sufficient as a cue. Interestingly the observation that semi-circular pores fill at a slower rate than circular ones is also observed in trabecular and cortical bone, with the filling of hemi-osteons being slower than for osteons (see e.g. [61,62,63]). These results strongly suggest that surface geometry is an important signal for controlling bone remodelling. In this respect the model may also have implications for tissue engineering and of course may be interesting to use it in the design of scaffold materials for implants [64,65,66]. One major difficulty in testing the model

in-vivo is the limited amount of kinetics data available in which local growth rates within a scaffold have been measured. It is possible that recent developments in in-vivo CT may provide suitable data that enables a comparison with the model [67].
The chord model presented in this paper makes the link between the macroscopic curvature-controlled tissue growth observed in vitro and in vivo, and the assembly of stretched cells and other fibrous elements making up the tissue.

Acknowledgements
We thank Fred Vermolen for instructive discussions. CB is a member of the Berlin-Brandenburg School for Regenerative Therapies (GSC 203).

References
1. Ben-Shlomo I, Yu Hsu S, Rauch R, Kowalski HW, Hsueh AJW (2003) Signaling Receptome: A Genomic and Evolutionary Perspective of Plasma Membrane Receptors Involved in Signal Transduction. Science's STKE 2003: 1-9.
2. Discher DE, Janmey P, Wang Y (2005) Tissue cells feel and respond to the stiffness of their substrate. Science 310: 1139-1139.
3. Nelson CM, VanDuijn MM, Inman JL, Fletcher DA, Bissell MJ (2006) Tissue Geometry Determines Sites of Mammary Branching Morphogenesis in Organotypic Cultures. Science 314: 298-300.
4. Bershadsky AD, Balaban NQ, Geiger B (2003) Adhesion-dependent cell mechanosensitivity. Annual review of cell and developmental biology 19: 677-695.
5. Pellegrin S, Mellor H (2007) Actin stress fibres. Journal of Cell Science 120: 3491-3499.
6. Schwarz U, Erdmann T, Bischofs I (2006) Focal adhesions as mechanosensors: The two-spring model. Biosystems 83: 225-232.
7. Spatz JP, Geiger B (2007) Molecular engineering of cellular environments: Cell adhesion to nano-digital surfaces. Cell Mechanics 83: 89-111.
8. Vogel V, Sheetz M (2006) Local force and geometry sensing regulate cell functions. Nature Reviews Molecular Cell Biology 7: 265-275.
9. Wang N, Suo Z (2005) Long-distance propagation of forces in a cell. Biochemical and Biophysical Research Communications 328: 1133-1138.
10. Nelson CM, Jean RP, Tan JL, Liu WF, Sniadecki NJ, et al. (2005) Emergent patterns of growth controlled by multicellular form and mechanics. Proceedings of the National Academy of Sciences of the United States of America 102: 11594-11599.
11. Engler A, Sen S, Sweeney H, Discher D (2006) Matrix Elasticity Directs Stem Cell Lineage Specification. Cell 126: 677-689.
12. Chen CS, Mrksich M, Huang S, Whitesides GM, Ingber DE (1997) Geometric control of cell life and death. Science 276: 1425-1428.
13. Théry M, Pépin A, Dressaire E, Chen Y, Bornens M (2006) Cell distribution of stress fibres in response to the geometry of the adhesive environment. Cell Motility and the Cytoskeleton 63: 341-355.
14. Harland B, Walcott S, Sun SX (2011) Adhesion dynamics and durotaxis in migrating cells. Physical Biology 8: 015011-015011.
15. Brock A, Chang E, Ho CC, LeDuc P, Jiang XY, et al. (2003) Geometric determinants of directional cell motility revealed using microcontact printing. Langmuir 19: 1611-1617.
16. Théry M, Jiménez-Dalmaroni A, Racine V, Bornens M, Jülicher F (2007) Experimental and theoretical study of mitotic spindle orientation. Nature 447: 493-496.
17. Cai YF, Sheetz MP (2009) Force propagation across cells: mechanical coherence of dynamic cytoskeletons. Current Opinion in Cell Biology 21: 47-50.
18. Ruiz SA, Chen CS (2008) Emergence of Patterned Stem Cell Differentiation Within Multicellular Structures. Stem Cells 26: 2921-2927.
19. Latimer A, Jessen JR (2010) Extracellular matrix assembly and organization during zebrafish gastrulation. Matrix Biology 29: 89-96.
20. Kollmannsberger P, Bidan CM, Dunlop J, Fratzl P (2011) The physics of tissue patterning and extracellular matrix organisation: how cells join forces. Soft Matter.
21. Patwari P, Lee RT (2008) Mechanical control of tissue morphogenesis. Circulation Research 103: 234-243.
22. Paszek MJ, Zahir N, Johnson KR, Lakins JN, Rozenberg GI, et al. (2005) Tensional homeostasis and the malignant phenotype. Cancer cell 8: 241-254.
23. Peyton SR, Ghajar CM, Khatiwala CB, Putnam AJ (2007) The emergence of ECM mechanics and cytoskeletal tension as important regulators of cell function. Cell Biochemistry and Biophysics 47: 300-320.
24. Freed LE, Engelmayr GC, Borenstein JT, Moutos FT, Guilak F (2009) Advanced Material Strategies for Tissue Engineering Scaffolds. Advanced Materials 21: 3410-3418.
25. St-Pierre JP, Gauthier M, Lefebvre LP, Tabrizian M (2005) Three-dimensional growth of differentiating MC3T3-E1 pre-osteoblasts on porous titanium scaffolds. Biomaterials 26: 7319-7328.
26. Zeltinger J, Sherwood JK, Graham DA, Mueller R, Griffith LG (2001) Effect of pore size and void fraction on cellular adhesion, proliferation, and matrix deposition. Tissue Engineering 7: 557-572.
27. Rumpler M, Woesz A, Dunlop J, van Dongen J, Fratzl P (2008) The effect of geometry on three-dimensional tissue growth. Journal of the Royal Society Interface 5: 1173-1180.
28. Bischofs IB, Klein F, Lehnert D, Bastmeyer M, Schwarz US (2008) Filamentous network mechanics and active contractility determine cell and tissue shape. Biophysical Journal 95: 3488-3496.
29. Ripamonti U (2009) Biomimetism, biomimetic matrices and the induction of bone formation. Journal of Cellular and Molecular Medicine 13: 2953-2972.
30. Graziano A, d'Aquino R, Cusella-De Angelis MG, Laino G, Piattelli A, et al. (2007) Concave Pit-Containing Scaffold Surfaces Improve Stem Cell-Derived Osteoblast Performance and Lead to Significant Bone Tissue Formation. PLoS ONE 2: e496.
31. Robling AG, Castillo AB, Turner CH (2006) Biomechanical and molecular regulation of bone remodeling. Annual Review of Biomedical Engineering 8: 455-498.
32. Bonewald LF, Johnson ML (2008) Osteocytes, mechanosensing and Wnt signaling. Bone 42: 606-615.

33. Nicolella DP, Moravits DE, Gale AM, Bonewald LF, Lankford J (2006) Osteocyte lacunae tissue strain in cortical bone. Journal of Biomechanics 39: 1735-1743.
34. Owan I, Burr DB, Turner CH, Qiu J, Tu Y, et al. (1997) Mechanotransduction in bone: osteoblasts are more responsive to fluid forces than mechanical strain. American Journal of Physiology-Cell Physiology 273: C810–C815-C810–C815.
35. Parfitt AM (1994) Osteonal and Hemi-Osteonal Remodeling: The Spatial and Temporal Framework for Signal Traffic in Adult Human Bone. Journal of Cellular Biochemistry 55: 273-286.
36. Kerschnitzki M, Wagermaier W, Roschger P, Seto J, Shahar R, et al. (2010) The organization of the osteocyte network mirrors the extracellular matrix orientation in bone. Journal of Structural Biology 173: 303-311.
37. Jinnai H, Watashiba H, Kajihara T, Nishikawa Y, Takahashi M, et al. (2002) Surface curvatures of trabecular bone microarchitecture. Bone 30: 191-194.
38. Frette OI, Virnovsky G, Silin D (2009) Estimation of the curvature of an interface from a digital 2D image. Computational Materials Science 44: 867-875.
39. Manjubala I, Woesz A, Pilz C, Rumpler M, Fratzl-Zelman N, et al. (2005) Biomimetic mineral-organic composite scaffolds with controlled internal architecture. Journal of Materials Science: Materials in Medicine 16: 1111–1119.
40. Woesz A, Rumpler M, Stampfl J, Varga F, Fratzl-Zelman N, et al. (2005) Towards bone replacement materials from calcium phosphates via rapid prototyping and ceramic gelcasting. Materials Science & Engineering C 25: 181-186.
41. Rasband WS (2008) ImageJ. National Institutes of Health.
42. Bullard JW, Garboczi EJ, Carter WC, Fuller Jr ER (1995) Numerical methods for computing interfacial mean curvature. Computational Materials Science 4: 103-116.
43. Worring M, Smeulders AWM (1993) Digital Curvature Estimation. 58: 366-382.
44. Kommareddy KP, Lange C, Rumpler M, Dunlop JWC, Manjubala I, et al. (2010) Two stages in three-dimensional in vitro growth of tissue generated by osteoblastlike cells. Biointerphases 5: 45-52.
45. Geiger B, Spatz JP, Bershadsky AD (2009) Environmental sensing through focal adhesions. Nat Rev Mol Cell Biol 10: 21–33.
46. Bement WM (2002) Actomyosin rings: The riddle of the sphincter. Current Biology 12: R12-R14.
47. Martin P, Parkhurst SM (2004) Parallels between tissue repair and embryo morphogenesis. Development 131: 3021-3034.
48. Salbreux G, Prost J, Joanny JF (2009) Hydrodynamics of Cellular Cortical Flows and the Formation of Contractile Rings. Physical Review Letters 103.
49. Stein GS, Lian JB (1993) Molecular Mechanisms Mediating Proliferation Differentiation Interrelationships during Progressive Development of the Osteoblast Phenotype. Endocrine Reviews 14: 424-442.
50. Quarles LD, Yohay DA, Lever LW, Caton R, Wenstrup RJ (1992) Distinct Proliferative and Differentiated Stages of Murine MC3T3-El Cells in Culture: An In Vitro Model of Osteoblast Development. Journal of Bone and Mineral Research 7: 683-692.
51. Gerstenfeld LC, Riva A, Hodgens K, Eyre DR, Landis WJ (1993) Post-translational control of collagen fibrillogenesis in mineralizing cultures of chick osteoblasts. Journal of bone and mineral research : the official journal of the American Society for Bone and Mineral Research 8: 1031-1043.
52. Saito M, Fujii K, Tanaka T, Soshi S (2004) Effect of low- and high-intensity pulsed ultrasound on collagen post-translational modifications in MC3T3-E1 osteoblasts. Calcified Tissue International 75: 384-395.
53. Sethian JA, Shan Y (2008) Solving partial differential equations on irregular domains with moving interfaces, with applications to superconformal electrodeposition in semiconductor manufacturing. Journal of Computational Physics.
54. Wheeler D, Josell D, Moffat TP (2003) Modeling Superconformal Electrodeposition Using The Level Set Method. Journal of The Electrochemical Society 150: C302-C302.
55. Zhu MF, Kim JM, Hong CP (2001) Modeling of Globular and Dendritic Structure Evolution in Solidification of an Al–7mass% Si Alloy. ISIJ international 41: 992-998.
56. Radhakrishnan B, Zacharia T (1995) Simulation of curvature-driven grain-growth by using a modified Monte-Carlo algorithm. Metallurgical and Materials Transactions a-Physical Metallurgy and Materials Science 26: 167-180.
57. Quere D (2008) Wetting and roughness. Annual Review of Materials Research 38: 71-99.
58. Foty RA, Steinberg MS (2005) The differential adhesion hypothesis: a direct evaluation. Developmental Biology 278: 255-263.
59. Schötz EM, Burdine RD, Jülicher F, Steinberg MS, Heisenberg CP, et al. (2008) Quantitative differences in tissue surface tension influence zebrafish germ layer positioning.
60. Travasso R, Castro M, Oliveira J (2011) The phase-field model in tumor growth. Philosophical Magazine 91: 183-206.
61. Eriksen EF (2010) Cellular mechanisms of bone remodeling. Reviews in Endocrine and Metabolic Disorders 11: 219-227.
62. Parfitt AM (1984) The cellular basis of bone remodeling: the quantum concept reexamined in light of recent advances in the cell biology of bone. Calcified Tissue International 36: 37-45.
63. Agerbaek MO, Eriksen EF, Kragstrup J, Mosekilde L, Melsen F (1991) A reconstruction of the remodelling cycle in normal human cortical iliac bone. Bone and Mineral 12: 101-112.
64. Hollister SJ (2005) Porous scaffold design for tissue engineering. Nature Materials 4: 518-524.
65. Hutmacher DW (2001) Scaffold design and fabrication technologies for engineering tissues - state of the art and future perspectives. Journal of Biomaterials Science-Polymer Edition 12: 107-124.
66. Stevens MM, George JH (2005) Exploring and engineering the cell surface interface. Science 310: 1135-1138.
67. Schulte FA, Lambers FM, Webster DJ, Kuhn G, Müller R (2011) In vivo validation of a computational bone adaptation model using open-loop control and time-lapsed micro-computed tomography. Bone

7.5 [TG5] A theoretical model for tissue growth in confined geometries.

Dunlop, J. W. C., Fischer, F. D., Gamsjäger, E., Fratzl, P.
*Published in **Journal of the Mechanics and Physics of Solids**, 2010, 58(8), 1073–1087.*
doi:10.1016/j.jmps.2010.04.008

Reprinted with permission from Elsevier

Abstract: It is known that cells proliferate and produce extracellular matrix in response to biochemical and mechanical stimuli. Constitutive models considering these phenomena are needed to quantitatively describe the process of tissue growth in the context of tissue engineering and regenerative medicine. In this paper we re-examine the theoretical framework provided by (Ambrosi and Guana, 2007; Ambrosi and Guillou, 2007). We show how a volumetric growth rate term can be obtained (both in a large and small strain setting), which is consistent with the laws of thermodynamics and then apply the model to a simple geometry of tissue growth within a circular pore. The model, despite its simplicity, is comparable with experimental measurements of tissue growth and highlights the contribution of the mechanical stresses produced during tissue growth on the growth rate itself.

1 Introduction

Understanding the kinetics of tissue growth is of major importance for many biological processes, including wound healing (Martin, 1997), tumour growth (Mantzaris, et al., 2004), and bone remodelling (Taylor, et al., 2007). The development of good predictive models is not only fundamental to understanding the progression of disease (Mantzaris, et al., 2004) and healing (Martin, 1997) but also in the design of optimized scaffolds for tissue engineering (Hollister, 2005; Mitragotri and Lahann, 2009; Sengers, et al., 2007). Mesenchymal cells responsible for tissue growth (e.g. connective tissue, bone, cartilage, etc.) are known to integrate physical signals into their growth behaviour (Geiger, et al., 2009). For example, in addition to biochemical growth factors (such as bone morphogenic proteins, etc.) (Hartung, et al., 2006; Place, et al., 2009) and substrate chemistry (Castner and Ratner, 2002; Faucheux, et al., 2004; Tabata, 2009), cell behaviour can be modified by mechanical stimuli (Chen, 2008; Geiger and Bershadsky, 2002), and is strongly influenced by the stiffness (Discher, et al., 2005; Kong, et al., 2005; Lo, et al., 2000), topography (Curtis and Wilkinson, 1998; Zinger, et al., 2005), and surface roughness (Boyan, et al., 1999; Linez-Bataillon, et al., 2002) of the substrate. As an example, Fig.1 shows bone-like tissue growth formed in-vitro by MC3T3-E1 pre-osteoblast cells, within millimetre sized hydroxylapatite channels of different size and shape (Rumpler, et al., 2008). Under these conditions, new tissue forms preferentially in the corners of the channels and is initially quiescent on the faces. This leads to strongly inhomogeneous growth behaviour which seems to depend on the stress state of cells, as indicated by the formation of actin stress fibres (or actin filaments) oriented tangential to the inner surface of the growing tissue (Nelson, et al., 2005; Pathak, et al., 2008). These observations were interpreted using a simple growth law in which the growth rate is taken to be proportional to the local surface curvature (Fig. 1 lower row). In contrast to (Rumpler, et al., 2008), the theory of tissue growth outlined in this current paper is developed based on well known thermodynamic arguments (see e.g. (Martyushev and Seleznev, 2006; Onsager, 1931)) using the approach of Ambrosi and Guana (2007) and Ambrosi and Guillou (2007), respectively. The resulting growth laws are applicable to both, large and small strain settings. The growth kinetics and the evolution of the radial and circumferential stress component of a tissue layer at the inner wall of a cylindrical body are calculated numerically by incrementally applying small strains, and the numerical results are discussed in the context of the experimental findings of Rumpler et al. (2008).

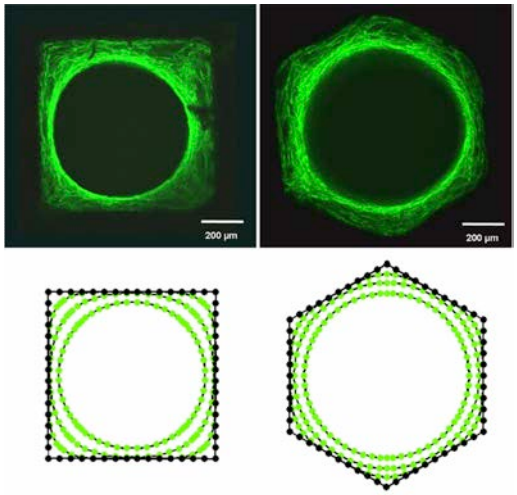

Figure. 1 – After Rumpler et al. (2008), Tissue imaged by actin staining (upper row) and tissue growth described by a simple model (growth-rate proportional to local curvature of the surface) (lower row).

2 Theoretical Framework

Modelling of tissue and/or bone growth has been a research topic in continuum mechanics and later in biomechanics for many years (see for example the review by Taber, (1995)). One of the principal goals of such models is to introduce or derive the experimentally observed coupling between the growth of new material and the local deformation or stress state. Much work has been done in this direction for example in the field of bone remodelling (see e.g. (Dunlop, et al., 2009; Frost, 1987; Huiskes, et al., 2000; Turner, 1991; Weinkamer, et al., 2004)) and tumour growth (Ambrosi and Preziosi, 2002; 2009; Ehlers, et al., 2009). With respect to bone remodelling, the models often consist of a phenomenological rule, introduced ad-hoc, describing how the tissue grows (or is absorbed) as a function of the mechanical state of the tissue. They typically consider growth or absorption not as a growth eigenstrain, but rather by simply removing (or adding) volume elements to the surface or by modifying the local materials properties. Cowin and Hegedus for example proposed an adaptive elasticity concept, in which a phenomenological solid volume change is introduced that depends on the strain tensor (Cowin and Hegedus, 1976; Hegedus and Cowin, 1976). This volume change is implemented as a change in porosity which in turn affects the elastic behaviour; a growth eigenstrain rate is not established however. Later Taber and co-workers (1996; 2001) formulated the growth process in the framework of finite deformations and suggested growth strain ratios, whose material derivatives are proportional to the principle stresses. Garikipati et al. presented an extensive continuum mechanical treatment of the growth process, using a finite deformation setting including inertia terms (Garikipati, et al., 2004). This concept is widely applicable, but not related to a special growth eigenstrain. However, it is referred to a framework consistent with the 2nd law of thermodynamics. This concept was applied by Humer (2008) for a spherical configuration with a Blatz-Ko material and an explicitly given growth term. Volokh (2006) introduced an evolving growth eigenstrain term, based on a mass flux of the tissue or bone matter itself. This term is transferred to an eigenstress term and considered within thermo-elasticity. This promising concept motivated the authors to develop a growth eigenstrain term, which can be handled within elasticity, consistent with the 2nd law of thermodynamics. A well established method to describe both the development of a microstructure by an eigenstrain and the rules of continuum mechanics and thermodynamics is the concept of material (or configurational) forces, which has been widely applied in continuum mechanics and has promoted the understanding of the kinetics of phase transformation in solids. Very important for our purpose, the volumetric growth of a body can be considered as a specific case. A rigorous treatment of this approach was presented by Maugin and coworkers, see e.g. (Epstein and Maugin, 2000). The gradient of the so-called "energy momentum tensor" (or the Eshelby tensor (Eshelby, 1975)) plays here a central role. Kirchner and Lazar recently used this concept to describe bone and arguing that terms quadratic in the stress (the elastic strain energy) may outweigh the remaining terms (Kirchner and Lazar, 2008). The concepts of porous continua has also been applied to swelling media most recently by Ehlers et al. (2009) also using the relations by Ambrosi and co-workers for the constitutive equations. Finally the reader is referred to a recent review on growth in the context of continuum mechanics and thermodynamics by Garakipati (2009). We rather exploit the concept of thermodynamics, studying the dissipation inequality as in the work by Maugin and coworkers, e.g. (Epstein and Maugin, 2000), and follow the path paved by Ambrosi and coworkers (Ambrosi and Guana, 2007; Ambrosi and Guillou, 2007). This current work is focused on the growth of soft tissues. The growth process occurs simultaneously in the whole region as nutrient can be assumed to be supplied simultaneously to each subregion and can be understood as a swelling process. The volumetric growth rate can be obtained (both in a large and small strain setting), whose constitutive law meets the supply of matter by a diffusing nutrient and guarantees a positive entropy production. The following three sections outline the derivation of the thermodynamically consistent growth law. The first describes the mass balance relations which are implemented in the second section, into the dissipation inequality arising from the 2nd law of thermodynamics. The third section describes the biological interpretation of the growth model.

2.1 Kinematics and balance relations

In order to develop a consistent theoretical description of tissue growth some continuum mechanical concepts are required. An appropriate frame of reference for the problem has to be chosen, in which a mass balance relation is defined, which is in turn obeyed during the growth process. Tissue growth could be investigated in two different frames of reference; the reference configuration and the actual configuration. In the reference configuration, any quantity depends on the material coordinates assigned to the material body at a fixed time $t = 0$. This configuration has the advantage that the boundary conditions do not move during growth, making calculations somewhat simpler. An alternative viewpoint is to assign the material coordinates to the (deformed) body at the actual time t. This placement is called actual configuration and the quantity is then measured relative to the deformed body. This system has the advantage that it is observable. Both configurations can be connected to the same spatially fixed coordinate system and readily converted from one to the other via the deformation gradient tensor, $\mathbf{F}$. Following Rodriguez et al (1994) and Ambrosi and Guillou (2007) the deformation gradient can be multiplicatively decomposed in a deformation gradient tensor $\mathbf{F}_e$ due to elastic deformation and a deformation gradient tensor $\mathbf{G}$ related to the growth process,

$$\mathbf{F} = \mathbf{F}_e\mathbf{G} \ . \tag{2.1}$$

The density ρ_a in the actual configuration is related to the density ρ_0 in the reference configuration using the determinant $\mathrm{Det}\,\mathbf{F} > 0$:

$$\rho_0 = \rho_a \mathrm{Det}\,\mathbf{F} \ . \tag{2.2}$$

Following Ambrosi and Guillou (2007) the rate of of the density $\dot{\rho}_0$ in the reference configuration reads

$$\dot{\rho}_0 = \rho_0 \left(\mathbf{I} : \dot{\mathbf{G}}\mathbf{G}^{-1} \right) \tag{2.3}$$

based on the assumption that a pure elastic deformation does not lead to a change of the mass.

A nutrient with the mass fraction c, $[c]=1$, flows as an interstitial fluid through the solid with a flux vector $\boldsymbol{m}$ (mass per area and time), obeying the mass balance

$$Div\,\boldsymbol{m} = -\dot{c}\rho_0 - c\dot{\rho}_0 + \rho_0 \mathbf{E}_0 : \dot{\mathbf{G}}\mathbf{G}^{-1}, \qquad (2.4a)$$

where the second term on the right hand side of Eq. (2.4a) was missed in (Ambrosi and Guillou, 2007). The last term is a source term introduced by Ambrosi and Guillou (2007), which takes into account that nutrient has to be provided during tissue growth. A non-isotropic absorption rate can be described by the tensor $\mathbf{E}_0$. In the special case that the absorption rate is isotropic, $\mathbf{E}_0 = e_0\mathbf{I}$, the mass balance (2.4a) can be rewritten as

$$Div\,\boldsymbol{m} = -\dot{c}\rho_0 + \rho_0(e_0 - c)\left(\mathbf{I} : \dot{\mathbf{G}}\mathbf{G}^{-1}\right). \qquad (2.4b)$$

2.2 Energetics

The chemical free energy per unit The chemical free energy per unit mass ψ_{chem} can be expressed by the chemical potentials of the (growing) tissue μ_s and of the nutrient μ_n giving

$$\psi_{chem} = c\mu_n + (1-c)\mu_s = c(\mu_n - \mu_s) + \mu_s. \qquad (2.5a)$$

Substituting $\mu_n - \mu_s = \mu$ and by setting the chemical potential μ_s to zero in an arbitrary manner (only differences in energies can be measured) one obtains

$$\psi_{chem} = c\mu = c\mu_n. \qquad (2.5b)$$

The total free energy per unit mass ψ consists of the elastic strain energy per unit mass, ψ_{mech}, and the chemically stored free energy per unit mass ψ_{chem},

$$\psi = \psi_{mech} + \psi_{chem} = \psi_{mech} + c\mu. \qquad (2.6)$$

By assuming that neither ψ_{mech} nor m depend explicitly on the nutrient mass fraction c, the partial derivative $\partial\psi/\partial c$ equals m. As a mechanism of conversion of nutrient to tissue, we follow as a possible model, the concept of phase transformations, so that the conversion process is accompanied by an energy change $\Delta\mu$ per unit mass. Note that $\Delta\mu$ includes both the change in the energy per unit mass of the transforming phase and a transformation barrier energy. For an isothermal process the free energy per unit mass ψ therefore, depends on the deformation gradient $\mathbf{F}_e$ and on an internal variable, the mass fraction, c. The rate of $\psi = \psi(\mathbf{F}_e, c)$ is given by

$$\dot{\psi} = \frac{\partial\psi}{\partial\mathbf{F}_e} : \dot{\mathbf{F}}_e + \frac{\partial\psi}{\partial c}\dot{c}. \qquad (2.7)$$

We express now the work rate (the power) $\dot{W}$ provided from outside to a unit mass as

$$\dot{W} = \mathbf{P} : \dot{\mathbf{F}} - Div(\mu_n \mathbf{m}) + \mu_n \rho_0 \mathbf{E}_0 : \dot{\mathbf{G}}\mathbf{G}^{-1}. \qquad (2.8a)$$

$\mathbf{P}$ is the 1st Piola-Kirchhoff stress tensor, and $\mathbf{P} : \dot{\mathbf{F}}$ represents the mechanical energy contribution, - Div$(\mu_n \boldsymbol{m})$ is the outward flux of chemical energy of the nutrient, and the last term in (2.8a) is the volumetric source term or the rate of chemical energy of the nutrient provided to the unit mass.

The internal change of the microstructure is represented by the energy rate $\dot{E}$ consisting of the free energy rate $d(\rho_0\psi)/dt$ and the change of energy due to a conversion of the provided rate (source term) of nutrient to tissue yielding

$$\dot{E} = d(\rho_0\psi)/dt + \Delta\mu\rho_0 \mathbf{E}_0 : \dot{\mathbf{G}}\mathbf{G}^{-1}. \qquad (2.8b)$$

The dissipation, D, is the difference between the rate at which work is done on the system, $\dot{W}$, and the rate of change of energy, $\dot{E}$ (see e.g. Simha, et al. (2008)). The 2nd law of thermodynamics asserts that the dissipation is non-negative for every sub-region of the material body:

$$D = \dot{W} - \dot{E} \geq 0. \qquad (2.8c)$$

Thus the 2nd law of thermodynamics can be formulated as

$$\mathbf{P}:\left(\dot{\mathbf{F}}_e\mathbf{G} + \mathbf{F}_e\dot{\mathbf{G}}\right) - \mu_n \mathrm{Div}\mathbf{m} - \mathbf{m}\cdot\mathrm{Grad}\mu_n - \dot{\rho}_0\psi - \rho_0\dot{\psi} + (\mu_n - \Delta\mu)\rho_0\mathbf{E}_0 : \dot{\mathbf{G}}\mathbf{G}^{-1} \geq 0. \qquad (2.9a)$$

The inequality (2.9a) is equivalent to that derived by Ambrosi and Guillou ((2007), Eq. 3.3), however without the last term on the left side concerning the energy contributions due to the source term of the nutrient. According to Ambrosi and Guillou (2007) we reformulate the inequality (2.9a) and eventually obtain a dissipation inequality

$$\left[\mathbf{F}_e^T\mathbf{P}\mathbf{G}^T - \rho_0(\psi - c\mu)\mathbf{I} - \Delta\mu\rho_0\mathbf{E}_0\right] : \dot{\mathbf{G}}\mathbf{G}^{-1} - \mathbf{m}\cdot\mathrm{Grad}\mu \geq 0. \qquad (2.9b)$$

Note that due to $\mu_n = \mu$ both according source terms go out of the balance (2.9b). The quantity ($\psi - c\mu$), is replaced by the term ψ_{mech} that accounts for the elastically stored energy (per mass), see Eq. (2.6). By rearranging Eq.2.9b, introducing the elastic energy density (per volume) $\varphi_{mech} = \rho_a\psi_{mech}$ and assuming an isotropic absorption rate the dissipation inequality reads as

$$-\left[\mathrm{Det}\mathbf{F}\,\varphi_{mech}\mathbf{I} - \mathbf{F}^T\mathbf{P} + \Delta\mu\rho_0 e_0\mathbf{I}\right] : \mathbf{G}^{-1}\dot{\mathbf{G}} - \mathbf{m}\cdot\mathrm{Grad}\mu \geq 0. \qquad (2.9c)$$

This equation contains two terms, each of which consists of a configurational force multiplied by a flux. Within the square brackets of the first term, the Eshelby energy-momentum tensor $\mathbf{C} = \mathrm{Det}\mathbf{F}\varphi_{mech}\mathbf{I} - \mathbf{F}^T\mathbf{P}$ can be recognized, however it is modified by an additional chemical configurational force, $\Delta\mu\rho_0 e_0\mathbf{I}$. This configurational force is multiplied by a generalised flux namely the growth rate, $\mathbf{G}^{-1}\dot{\mathbf{G}}$. The second term consists of the diffusive flux, multiplied by its conjugate force, namely the gradient in chemical potential. The term $\left(-\mathbf{m}\cdot\mathrm{Grad}\mu\right)$ gives a positive contribution, if the flux $\boldsymbol{m}$ is proportional to $-\mathrm{Grad}\mu$ which is a standard assumption for a diffusive process. Finally the dissipation inequality (2.9c) is always fulfilled, if we introduce a positive parameter $f\left(c\right) > 0$ and set up a linear relation:

$$\mathbf{G}^{-1}\dot{\mathbf{G}} = -f\left(c\right)\left[\left(\mathrm{Det}\mathbf{F}\varphi_{mech} + \Delta\mu\rho_0 e_0\right)\mathbf{I} - \mathbf{F}^T\mathbf{P}\right]. \qquad (2.10)$$

This equation is the simplest form of the tissue growth rate, $\mathbf{G}^{-1}\dot{\mathbf{G}}$, in terms of the deformation gradient tensor (in the large strain setting), which is thermodynamically consistent. From the point of view of thermodynamics, the thermodynamic forces are parallel to the fluxes. This is in accordance with the principle of maximum dissipation, first exploited by Onsager (1931); for references see (Svoboda, et al., 2005). Here we would like to refer to a recently published paper (Vignes and Papadopoulos, 2010), where a so called surface concept with several activation surfaces is followed to ensure positive dissipation similar to multi-surface plasticity. The concept at hand is however much simpler.

An evolution equation can be obtained by reformulating Eq. (2.10) so that it fits within the framework of a small strain setting. The deformation gradient F can be replaced by the unity tensor I. The growth tensor G is converted to the volume changing eigenstrain g. The 1st Piola-Kirchhoff stress tensor P becomes the Cauchy stress tensor σ. Furthermore, we transform $\mathbf{G}^{-1}\dot{\mathbf{G}}$ to the growth eigenstrain rate

$$\dot{\mathbf{g}} = f\left(c\right)\left(\sigma - \varphi_{mech}\mathbf{I} - \bar{\mu}e_0\mathbf{I}\right), \qquad (2.11a)$$

with $\bar{\mu} = \rho_0\Delta\mu$. Since $\varphi_{mech} = \left(\sigma : \mathbb{C}\sigma\right)/2$, with $\mathbb{C}$ being the (4^{th} order) elastic compliance tensor, is usually much smaller compared to the values of the individual components of σ, the φ_{mech}-term can be often neglected,, contrarily to the statement of its role in (Kirchner and Lazar, 2008), giving finally:

$$\dot{\mathbf{g}} = f\left(c\right)\left(\sigma - \bar{\mu}e_0\mathbf{I}\right). \qquad (2.11b)$$

In case that nutrient transforms to tissue $\bar{\mu} < 0$ is required since the nutrient converts to the energetically more favourable phase tissue; this can be viewed as similar to the process of the transformation of an amorphous phase to a crystalline phase, for example. The stress state σ depends on both the boundary conditions and the loading process. Here we refer again to (Taber and Eggers, 1996; Taber and Humphrey, 2001), who suggest a growth rate term as (2.11a) or (2.11b), however neglecting the role of $-\bar{\mu}e_0\mathbf{I}$.

2.3 Biological interpretation of equation 2.11b

Equation 2.11b is an equation for growth (written in terms of an eigenstrain rate) which is thermodynamically admissible, or rather needs to be of this form in order to be consistent with linear non-equilibrium thermodynamics. The principle assumptions behind the rigorous thermodynamic derivation are:

- If there are no constraints to matter transport, or in other words if the diffusion of nutrients is much faster than the growth process, the diffusion equations need not be considered. This is reasonable in most cases for biological systems (except for some notable cases like the cartilage in joints (Hall, 2005)) where the transport of nutrients occurs through blood vessels and capillaries.
- The system evolves/changes in order to maximise dissipation in the sense formulated by Onsager (1931), (see also (Martyushev and Seleznev, 2006) for applications in biology). This just means that the biological system has to act in concordance with the laws of physics (thermodynamics, in particular), but does not imply any limitation with respect to the possibility that various signals (biochemical or mechanical) may influence cell proliferation and tissue growth.

The resulting growth law as given by Eq. (2.11b) then has a number of features:

- The stress term, σ, comes directly from the dissipation term in the derivation and gives an explicit stress dependence. This just means that the occurrence of internal stresses in the tissue has a direct influence on the volume change of the growing tissue, regardless of whether the cells are directly influenced by stress in their activity.
- The second term in the parenthesis is $\bar{\mu}e_0\mathbf{I}$ representing the energy change analogous to the chemical potential change in a chemical reaction (that would transform nutrients into tissue). In this sense, the cells (e.g. fibroblasts, osteoblasts, ...) are considered as thermodynamic machines driven by a chemical potential.
- The pre-factor in Eq. (2.11b),), $f\left(c\right)$, represents a kinetic term and describes the activity of the system. It can be viewed as a term which describes how fast cells react and produce new matrix. Indeed, the parameter describes the growth rate of the tissue in relation to the interplay between mechanical stress state and the energy input $\left(\sigma - \bar{\mu}e_0\mathbf{I}\right)$. Less effective (e.g. old or diseased) cells could be imagined to have less activity and, therefore, a smaller $f\left(c\right)$. Similarly, biochemical growth factors activate the cells and, therefore, would increase $f\left(c\right)$ within the present theoretical description. In principle, $f\left(c\right)$ may therefore depend on various extrinsic parameters, both systemic (such as age or disease) and local (such as local physical or chemical stimuli to the cells).

3 Solution of the model for a simple geometry

In the following we chose the simplest of cases and take both the activity parameter $f(c)$ and the energy term $\bar{\mu}e_0$ as being constants and investigate what can be derived for a simple geometry of tissue growing inside a circular pore.

3.1 The geometrical and mechanical setting

We consider a layer of tissue growing (in the actual configuration) within an undeformable hollow cylinder with an outer radius, R, and the inner tissue radius r_i (Fig 2). Since the closing of an initial hole by growth of tissue is studied, it could be viewed as consisting of large deformations. However, we consider the growth process rather than any large deformation process expressed in an incremental form. In order to model the growth process we study the deformation state of an actual configuration with the inner radius r_i at the starting time t_i and select the time interval $t_{i+1} - t_i$ in such a way that only small deformations and stresses can be expected. In this case the use of a small strain setting is justified, and we assume the system to behave as linear elastic. The growth process is then replaced by an according eigenstrain, given by the product of the growth rate $\dot{\mathbf{g}}$, Equation (2.11b), and the time increment $t_{i+1} - t_i$. The deformation state due to this eigenstrain delivers the changed configuration at time t_{i+1} by adding the displacements to the starting configuration at time t_i. Linear elasticity (Hooke's law) allows also for a superposition of the stresses. Finally, the equations of elasticity are solved in rate form, and the actual topology and stress rate are found by time integration, for details see section 3.2. The tissue is assumed to be isotropically elastic with a Young's modulus *E* and Poisson's ratio *n*. We ignore any variation in the axial direction and, therefore, work within a plane stress setting of a disk with unit thickness.

The strain components, ε_r and ε_ϑ, are related to the radial displacement *u,* by standard kinematics as:

$$\varepsilon_r = \frac{du}{dr} = u', \quad \varepsilon_\vartheta = \frac{u}{r}. \tag{3.1}$$

The quantity *r* is the radial coordinate, $r_i \le r \le R$.

Due to the cylindrical symmetry of the problem and the boundary conditions, we observe a stress state, σ, with only two non-zero principal stress components; σ_r in the radial and σ_ϑ in the circumferential direction. We assume for a loading increment a small strain setting and, therefore, an additive decomposition of the strain tensor ε into an

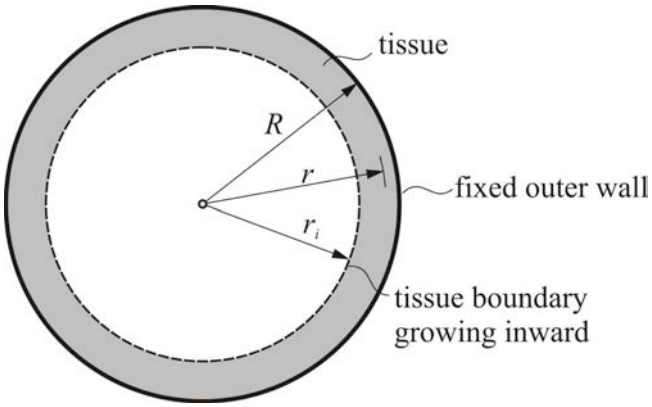

Figure 1. Sketch of the pore geometry

elastic contribution, $\varepsilon_{\mathbf{el}}$, and a contribution from the growth eigenstrain $\mathbf{g}$, i.e. $\varepsilon = \varepsilon_{\mathbf{el}} + \mathbf{g}$. Hooke's law ($\sigma = \mathbb{C}^{-1} : \varepsilon_{\mathbf{el}}$) yields in this case with $\tilde{E} = E/(1-\nu^2)$

$$\sigma_r = \tilde{E}(\varepsilon_r + \nu\varepsilon_\vartheta) - \tilde{E}(g_r + \nu g_\vartheta), \tag{3.2a}$$

and

$$\sigma_\vartheta = \tilde{E}(\nu\varepsilon_r + \varepsilon_\vartheta) - \tilde{E}(\nu g_r + g_\vartheta). \tag{3.2b}$$

The stress components must obey the equilibrium condition

$$\frac{\mathrm{d}}{\mathrm{d}r}(r\sigma_r) - \sigma_\vartheta = 0. \tag{3.3}$$

For the strain components ε_r and ε_ϑ in (3.2 a-b) the relations expressed in Eqs. (3.1) are used. Then the following differential equation is obtained by inserting the stress components σ_r and σ_ϑ into the equilibrium condition (3.3), with $u'' = d(u')/dr$ as

$$ru'' + u' - \frac{u}{r} = \frac{d}{dr}\left[r(g_r + \nu g_\vartheta)\right] - (\nu g_r + g_\vartheta). \tag{3.4}$$

3.2 Evolution equations for the growth process

Since only the rate $\dot{\mathbf{g}}$ of $\mathbf{g}$ is known, (2.11a-b), the relations, Eqs. (3.1-3.4) can be reformulated in rate form by replacing u and $\mathbf{g}$ by their time derivatives. Of course, the radial coordinate r is unaffected by this operation; however, r_i becomes now a time-dependent function $r_i(t)$. A solution of the time derivative of (3.4) follows as

$$\dot{u} = Ar + \frac{B}{r} + \dot{u}_p(r). \tag{3.5}$$

The quantities A and B are integration constants, $\dot{u}_p(r)$ is a particular solution corresponding to the right side of the time derivative of Eq. (3.4). The integration constants A and B are derived using the boundary conditions ($r = R$: $\dot{u} = 0$ and $r = r_i$: $\sigma_r = 0$). Details can be found in Appendix A.

The first step to the solution is now to find the particular solution $\dot{u}_p$ according to the components $\dot{g}_r$, $\dot{g}_\vartheta$ instead of g_r, g_ϑ. The components of the growth eigenstrain rate are related to the components of the stresses σ_r, σ_ϑ by the constitutive equations (2.11b) yielding, after some analysis using the equilibrium equation (3.3),

$$r\dot{u}_p'' + \dot{u}_p' - \frac{\dot{u}_p}{r} = \nu f(c)\left[\left(r\sigma_\vartheta\right)' - \sigma_r\right] = S(r). \tag{3.6a}$$

The right side of (3.6a) can be reformulated by applying again the equilibrium condition (3.3) as,

$$S(r) = \nu f(c) r\left[3\sigma_r' + r\sigma_r''\right]. \tag{3.6b}$$

After applying the method of "Variation of the Constants", one can find the particular solution $\dot{u}_p(r)$ as

$$\dot{u}_p(r) = -\frac{1}{2}\left[r\int_r^R \frac{S(\bar{r})}{\bar{r}}\,d\bar{r} - \frac{1}{r}\int_r^R \bar{r}S(\bar{r})\,d\bar{r}\right] \tag{3.7a}$$

by use of the relation $d\left(\int_r^R h(\bar{r})\,d\bar{r}\right)\Big/dr = -h(r)$.

Insertion of $S(r)$ from (3.6b) yields after some analysis,

$$\dot{u}_p(r) = \nu f(c) r\sigma_r(r). \tag{3.7b}$$

This surprisingly simple result can directly be checked by evaluating the left side of (3.6a) and comparing it with (3.6b). Solution (3.5) can be rewritten by using the particular solution (3.7b) as

$$\dot{u} = Ar + \frac{B}{r} + \nu f(c) r\sigma_r. \tag{3.7c}$$

Inserting the coefficients A and B (Appendix A) into (3.7c) gives the rate of displacement $\dot{u}(r)$, as

$$\dot{u}(r) = -\frac{f(c)r_i^2R^2r}{(1+\nu)r_i^2 + (1-\nu)R^2}\left\{\begin{array}{l}\left(\dfrac{(1-\nu)}{r_i^2} + \dfrac{(1+\nu)}{r^2}\right)\nu\sigma_r(R) \\ -(1+\nu)\left(\dfrac{1}{r^2} - \dfrac{1}{R^2}\right)\bar{\mu}e_0\end{array}\right\} + \nu f(c) r\sigma_r(r). \tag{3.7d}$$

The rates of the stress components $\dot{\sigma}_r$ and $\dot{\sigma}_\vartheta$ are obtained by introducing the displacement rate $\dot{u}(r)$ and the components of the eigenstrain rate $\dot{\mathbf{g}}$ into the rate form of Hooke's law, Eqns (3.2 a-b), yielding:

$$\frac{\dot{\sigma}_r}{\tilde{E}} = \dot{u}' + \nu\frac{\dot{u}}{r} - f(c)\left(\sigma_r + \nu\sigma_\vartheta\right) + (1+\nu) f(c)\bar{\mu}e_0, \tag{3.8a}$$

$$\frac{\dot{\sigma}_\vartheta}{\tilde{E}} = \nu\dot{u}' + \frac{\dot{u}}{r} - f(c)\left(\nu\sigma_r + \sigma_\vartheta\right) + (1+\nu) f(c)\bar{\mu}e_0. \tag{3.8b}$$

The solution for $\dot{u}(r)$ as given in Eq. (3.7d) is inserted into Eqs. (3.8a) and (3.8b), and with the equilibrium condition (3.3) one obtains the rates of the components of the stresses $\dot{\sigma}_r$ and $\dot{\sigma}_\vartheta$ as follows

$$\begin{aligned}\frac{\dot{\sigma}_r}{\tilde{E}} = &-\frac{f(c)r_i^2R^2}{(1+\nu)r_i^2 + (1-\nu)R^2}\left\{\nu(1-\nu^2)\left(\frac{1}{r_i^2} - \frac{1}{r^2}\right)\sigma_r(R)\right. \\ &\left. + \left[\frac{(1-\nu^2)}{r^2} + \frac{(1+\nu)^2}{R^2}\right]\bar{\mu}e_0\right\} - (1-\nu^2) f(c)\sigma_r + (1+\nu) f(c)\bar{\mu}e_0\end{aligned}, \tag{3.9a}$$

$$\begin{aligned}\frac{\dot{\sigma}_\vartheta}{\tilde{E}} = &-\frac{f(c)r_i^2R^2}{(1+\nu)r_i^2 + (1-\nu)R^2}\left\{\nu(1-\nu^2)\left(\frac{1}{r_i^2} + \frac{1}{r^2}\right)\sigma_r(R)\right. \\ &\left. - \left[\frac{(1-\nu^2)}{r^2} - \frac{(1+\nu)^2}{R^2}\right]\bar{\mu}e_0\right\} - (1-\nu^2) f(c)\sigma_\vartheta + (1+\nu) f(c)\bar{\mu}e_0\end{aligned}. \tag{3.9b}$$

It is worth mentioning that (3.9a) fulfils the boundary condition $\dot{\sigma}_r\big|_{r_i} = \dot{\sigma}_r(r_i) \equiv 0$.

The equations above can be rearranged as

$$\frac{\dot{\sigma}_r}{\tilde{E}} + \left(1-\nu^2\right) f(c)\sigma_r = \frac{\left(1-\nu^2\right) f(c) R^2}{\left(1+\nu\right) r_i^2 + \left(1-\nu\right) R^2}\left(\nu\sigma_r(R) - \bar{\mu} e_0\right)\left(-1+\frac{r_i^2}{r^2}\right), \tag{3.10a}$$

$$\frac{\dot{\sigma}_\vartheta}{\tilde{E}} + \left(1-\nu^2\right) f(c)\sigma_\vartheta = \frac{\left(1-\nu^2\right) f(c) R^2}{\left(1+\nu\right) r_i^2 + \left(1-\nu\right) R^2}\left(\nu\sigma_r(R) - \bar{\mu} e_0\right)\left(-1-\frac{r_i^2}{r^2}\right). \tag{3.10b}$$

In the following the rate of the displacement $\dot{u}$, and the rate of the components of the stresses $\dot{\sigma}_r$ and $\dot{\sigma}_\vartheta$ are expressed in a normalized, i. e. dimension-free form. Therefore, it is advantageous to introduce the dimension-free quantities; the dimension-free time $\tau = \frac{t}{t_0}$ with $t_0 = \frac{1}{\left|\bar{\mu} e_0 f(c)\right|}$, the dimension free radius $\tilde{r} = r/R$ and $\tilde{r}_i = r_i/R$, respectively, and the dimension free stress components $\tilde{\sigma}_r = \sigma_r(\tilde{r})/\sigma_0$ and $\tilde{\sigma}_\vartheta = \sigma_\vartheta(\tilde{r})/\sigma_0$ where $\sigma_0 = \left|\bar{\mu} e_0\right|$ and $\tilde{\mu} = \frac{\left|\bar{\mu} e_0\right|}{\tilde{E}}$; note that $\bar{\mu}$ is assumed, as usual, to be a negative quantity.

The following expressions for the normalized quantities are obtained after inserting $\tau, \tilde{r}, \tilde{r}_i, \tilde{\sigma}_r, \tilde{\sigma}_\vartheta, \tilde{\mu}$ into Eq. (3.7d) and Eqs. (3.10a-b) and using the auxiliary function $F = \frac{\left(1-\nu^2\right)\left(\nu\tilde{\sigma}_r(1)+1\right)}{\left(1-\nu\right)+\left(1+\nu\right)\tilde{r}_i^2}$:

$$\frac{\mathrm{d}u}{\mathrm{d}\tau} = -\frac{\tilde{r}_i^2 \cdot \tilde{r}}{\left(1+\nu\right)\tilde{r}_i^2 + \left(1-\nu\right)}\left\{\begin{array}{l}\left(\frac{\left(1-\nu\right)}{\tilde{r}_i^2} + \frac{\left(1+\nu\right)}{\tilde{r}^2}\right)\nu\tilde{\sigma}_r(1) \\ +\left(1+\nu\right)\left(\frac{1}{\tilde{r}^2}-1\right)\end{array}\right\} + \nu\tilde{r}\tilde{\sigma}_r(\tilde{r}), \tag{3.11a}$$

$$\frac{\mathrm{d}\tilde{\sigma}_r}{\mathrm{d}\tau} = -\frac{1}{\tilde{\mu}}\left[F\cdot\left(1-\frac{\tilde{r}_i^2}{\tilde{r}^2}\right) + \left(1-\nu^2\right)\tilde{\sigma}_r\right], \tag{3.11b}$$

$$\frac{\mathrm{d}\tilde{\sigma}_\vartheta}{\mathrm{d}\tau} = -\frac{1}{\tilde{\mu}}\left[F\cdot\left(1+\frac{\tilde{r}_i^2}{\tilde{r}^2}\right) + \left(1-\nu^2\right)\tilde{\sigma}_\vartheta\right]. \tag{3.11c}$$

Eqs. (3.11a-c) give together with the boundary conditions ($\tilde{r}=1$: $\dot{u}=0$ and $\tilde{r}=\tilde{r}_i$: $\sigma_r = 0$) and the initial conditions ($\tau = 0: \tilde{r}_i = 1-\delta,\ \tilde{\sigma}_r(1) = 0$) the general solution for the displacement $u(\tilde{r},\tau)$ and the stresses $\tilde{\sigma}_r(\tilde{r},\tau)$ and $\tilde{\sigma}_\vartheta(\tilde{r},\tau)$ as functions of radial position and time. As both $\mathrm{d}\tilde{\sigma}_r(1)/\mathrm{d}\tau$ and $\left(\mathrm{d}u/\mathrm{d}\tau\right)\big|_{\tilde{r}=\tilde{r}_i} = \mathrm{d}\tilde{r}_i/\mathrm{d}\tau$ are zero for $\tilde{r}_i = 1\pi$ a very small normalized initial tissue thickness, $\delta = 10^{-4}$, is introduced. Alternatively one can calculate from $\left(\mathrm{d}u/\mathrm{d}\tau\right)\big|_{\tilde{r}=\tilde{r}_i} = \mathrm{d}\tilde{r}_i/\mathrm{d}\tau$ and $\left(\mathrm{d}\tilde{\sigma}_r/\mathrm{d}\tau\right)\big|_{\tilde{r}=1}$ the unknown quantities $\tilde{r}_i$ and $\tilde{\sigma}_r(1)$ first, which evolve according to

$$\frac{\mathrm{d}\tilde{r}_i}{\mathrm{d}\tau} = -\frac{2\nu\tilde{r}_i\tilde{\sigma}_r(1) + \left(1+\nu\right)\left(\tilde{r}_i - \tilde{r}_i^3\right)}{\left(1-\nu\right)+\left(1+\nu\right)\tilde{r}_i^2}, \tag{3.12}$$

and

$$\frac{\mathrm{d}\tilde{\sigma}_r(1)}{\mathrm{d}\tau}\cdot\tilde{\mu} = -\frac{\left(1-\nu^2\right)\left[\left(1+\tilde{r}_i^2\right)\tilde{\sigma}_r(1) + \left(1-\tilde{r}_i^2\right)\right]}{\left(1-\nu\right)+\left(1+\nu\right)\tilde{r}_i^2}, \tag{3.13}$$

where Eqs. (3.12) and (3.13) can be found as special cases of Eqs. (3.11a-b). Together with the initial conditions $\tau = 0: \tilde{r}_i = 1-\delta,\ \tilde{\sigma}_r(1) = 0$ Eqs. (3.12) and (3.13) form an initial value problem. Then, the solutions $\tilde{r}_i$ and $\tilde{\sigma}_r(1)$ can be inserted into Eqs. (3.11a-c). An additional derivation of the rates, Eqs. (3.12) and (3.13) can be found in Appendix B.

It is also worthwhile expressing the growth equation (2.11b) in terms of the dimension free parameters giving the following simple equation:

$$\frac{\mathrm{d}\mathbf{g}}{\mathrm{d}\tau} = \tilde{\sigma} + \mathbf{I} \tag{3.14}$$

3.5 Numerical solutions to the evolution equations

The coupled equations for the evolution of the pore radius, Eq. (3.12), and the radial stress at the pore wall, Eq. (3.13), were integrated numerically for different values of $\tilde{\mu}$ and ν. Solutions of Eqs. (3.11a-c) for growth in a cylindrical pore, for different values of $\tilde{\mu}$ and ν, are presented in Fig. 3. The calculated tissue area fraction, $A = 1-\tilde{r}_i^2$, is plotted as a function of time in Fig. 3a. All curves coincide on an approximate "master curve" being roughly independent of $\tilde{\mu}$ and ν, although the curves overlap exactly only when the Poisson's ratio is 0 (as appropriate to describe a fibrous

network). The simulated growth behaviour is roughly sigmoidal in shape and has three main stages, namely a slow initial portion increasing exponentially to a roughly linear region, finally slowing down as the pore is filled. Although the experimental data given in (Rumpler, et al., 2008) do not extend to times when the pore becomes completely filled, there is still remarkable similarity between the simulated growth rate and the data at early times. When $\nu = 0$, equation (3.12) can be solved analytically (For details see Appendix C). For early times, $\tau \ll 1$, the growth rate is exponential:

$$A(\tau) = 1 - \tilde{r}_i^2 \sim \exp(\tau - \tau_0) \qquad (3.15)$$

with $\tau_0 = \alpha \ln 10$ being a delay time corresponding to the time taken for the first layer of tissue to nucleate. An increase in the Poisson's ratio, ν, or the normalised change in the chemical potential, $|\tilde{\mu}|$ for $\nu \neq 0$, results in only a small increase in the growth rate. As the time (Fig 3a) is given in units of $|\bar{\mu} e_0 f(c)|$ a stronger change in the chemical potential for growth, and a higher cell activity will result in a faster growth rate, as expected.

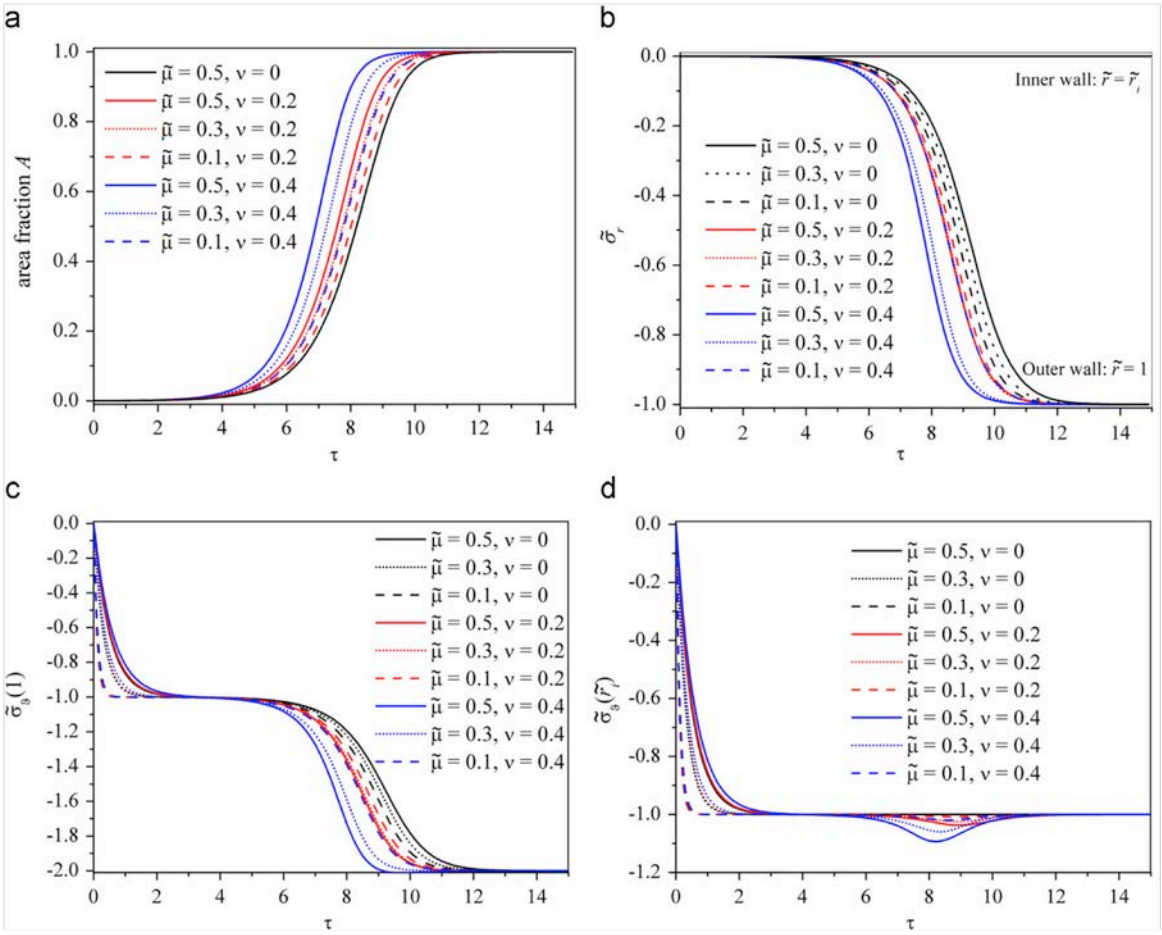

Figure 3a) Normalized area fraction of transformed tissue, $A = 1 - \tilde{r}_i(\tau)^2$ as a function of τ. **b)** Radial stress at the outer wall, $\tilde{\sigma}_r(1)$ as a function of normalized time τ. The radial stress $\tilde{\sigma}_r(\tilde{r}_i)$ at the inner wall is zero. **c)** Circumferential stress at the outer wall, $\tilde{\sigma}_\vartheta(1)$ as a function of normalized time τ. **d)** Circumferential stress at the inner wall, $\tilde{\sigma}_\vartheta(\tilde{r}_i)$ as a function of normalized time τ.

The radial stress on the outer pore wall (Eq. 3.13) can also be calculated, and the numerical solutions are plotted in Figure 3b. As the inner boundary is a free surface, the radial stress is zero. As with the area fraction, when the appropriate units of stress are used (here we plot in units of the change in chemical potential $|\bar{\mu} e_0|$) all curves fall onto a master curve with only small variations with $\tilde{\mu}$ and ν. An increase in both the Poisson's ratio and the change in chemical potential increases the speed at which the stress saturates. The saturation radial stress, however, if expressed in units of $|\bar{\mu} e_0|$, is independent of $\tilde{\mu}$ and ν being compressive with a value of -1.

The circumferential stresses at both the inner and outer boundaries are also calculated from Eq. 3.11 and the solutions to the pore radius, Eq. (3.12), and the radial stress at the wall, Eq. (3.13), and plotted on Figure 3c. The behaviour is quite different to the evolution of the radial stress at the outer pore wall. The stress drops very quickly to a value of -1 (compressive stress) and, as at this stage the initial tissue layer is thin (compare Fig. 3c and Fig. 3d), the stresses at both the inner and outer boundaries are almost the same. The radial growth only starts occurring when the circumferential stress in the initial tissue layer reaches a stress value of -1. However as soon as tissue starts to

grow more rapidly, around $\tau \sim 4$, the circumferential stresses at the inner and outer boundaries become markedly different. While the stress in the outer pore wall, $\tilde{r} = 1$, decreases to a value of -2, the circumferential stress in the inner wall $\tilde{r} = \tilde{r}_i$ remains constant, apart from a small perturbation. This perturbation is due to a coupling between the radial and the circumferential stresses described by the Poisson coefficient and is, of course, not seen for $\nu = 0$.

Summarising the behaviour in Fig. 3, the initial quiescent stage corresponds to the fast increase of compressive circumferential stress in the initial tissue layer. Only when this (normalized) stress reaches a value of -1 does the exponential growth and the fast development of compressive radial stresses at the outer wall set in. At this stage a large stress gradient in the circumferential stresses forms between the inner and outer layers (it must be kept in mind that the radial stress is also zero on the inner boundary also giving rise to a stress gradient).
When Eqs. (3.11a-c) are simultaneously solved by considering the initial and the boundary conditions the distributions in circumferential and radial stresses across the grown tissue as a function of time are obtained. From the point of view of continuum mechanics the integration can be described as following: A material point is generated at a distinct radius $\tilde{r} = \hat{\tilde{r}}$ at the time $\tau_c\left(\hat{\tilde{r}}\right)$ belonging to $\tilde{r}_i\left(\tau_c\right) = \hat{\tilde{r}}$. Then the material point keeps its position $\tilde{r} = \hat{\tilde{r}}$, which means that it does not move along the radius, except to small deformations. Therefore, the quantities $\tilde{\sigma}_r\left(\hat{\tilde{r}}\right), \tilde{\sigma}_\theta\left(\hat{\tilde{r}}\right)$ follow by integration of (3.11b) and (3.11c) with constant $\tilde{r} = \hat{\tilde{r}}$ for $\tau > \tau_c\left(\hat{\tilde{r}}\right)$.
The circumferential and radial stress distributions as a function of radius $\tilde{r}$ for various times, τ, are depicted in Figure 4 ($\tilde{\mu} = 0.5$ and $\nu = 0$). As can be concluded also from Figs 3a and 3b the radial stress is close to zero at $\tau \leq 4$. Even at $\tau = 7$ the radial stresses in the tissue are still small (Fig. 4a). Once the circumferential stress reaches this level of -1, growth starts accelerating and the radial stress starts building up (Fig. 4a). The spatial gradient $\mathrm{d}\tilde{\sigma}_r / \mathrm{d}\tilde{r}$ at $\tilde{r} = \tilde{r}_i$ follows from the equilibrium condition (Eq. 3.3) with the boundary condition ($\tilde{\sigma}_r(\tilde{r}_i) = 0$). The according tangents are depicted in Fig. 4a. As a consequence of the radial growth in the confined pore, the circumferential stress becomes even more compressive at the inner pore wall tending towards values of -2 at pore closure (Fig. 4b). These high compressive circumferential stresses relax in the rest of the grown tissue back to a value of -1 (e.g see $\tau = 11$ in Fig 4b)

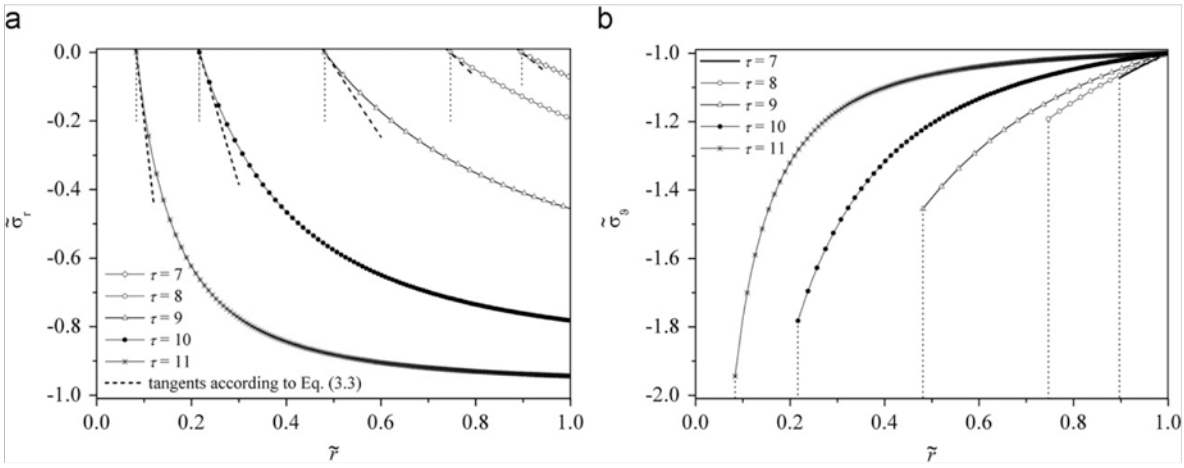

Figure 4a) Radial stress $\tilde{\sigma}_r\left(\tilde{r}\right)$ distributions across the grown tissue as a function of radius, $\tilde{r}$ for $\tilde{\mu} = 0.5, \nu = 0$. Tissue grows into the centre of the pore $\tilde{r} = 0$ from right to left. Dashed lines indicate the gradients $\left(\mathrm{d}\sigma_r / \mathrm{d}t\right)\Big|_{\tilde{r}=\tilde{r}_i}$ following the equilibrium condition Eq. (3.3). Dotted lines indicate position of inner pore boundary for the different times. **b)** Circumferential stress $\tilde{\sigma}_\vartheta\left(\tilde{r}\right)$ distributions across the grown tissue as a function of radius, $\tilde{r}$ for $\tilde{\mu} = 0.5, \nu = 0$. Tissue grows into the centre of the pore $\tilde{r} = 0$ from right $\tilde{r} = 1 - \delta$ to left. Dotted lines indicate position of inner pore boundary for the different times ($\tilde{\tau} = 7,\ 8,\ 9,\ 10,\ 11$).

4 Discussion and Outlook

The development of a gradient in circumferential stresses, with the largest magnitude being close to the inner surface of the pore (Fig 4b), matches at least qualitatively the occurrence of circumferential tensile stress fibres seen in the tissue growth experiments of Rumpler et al. (2008) (Fig. 1). At first glance it may appear somewhat counterintuitive to compare the predicted compressive tissue stresses to the tensile actin stress fibres observed experimentally. However, the underlying assumption behind the model is that cells, although not modelled explicitly, are evenly distributed everywhere throughout the tissue and synthesize extracellular matrix according to their local stress state according to $\dot{\mathbf{g}} = f\left(\sigma - \bar{\mu} e_0 \mathbf{I}\right)$. That is, the model rather reflects the response of the continuum (tissue) to new tissue formation by the cells. In order for this new tissue to be accommodated, space must be made by compressing the surrounding tissue which in turn alters the local stress state experienced by the cells. The cells can compress their surroundings in two different ways; they either actively contract by creating tensile forces in their cytoskeleton

(Geiger, et al., 2009), or they just produce new matrix resulting in an effective swelling inside the confinement of the pore. The net result in both cases is the same. There is, however, a limit to the compressive stress that cells can attain represented by a negative term in the growth eigenstrain rate. This means that the tissue will grow in such a way as to reach a uniform stress within the tissue growing inside the pore. The application of the above equation to tissue growth on convex surfaces however would predict tensile stresses to develop. This would lead to an accelerating growth rate (this can be modelled by applying the eigenstrain rate equation to growth outwards from a cylinder similar to section 3), which is not observed experimentally (unpublished data). Therefore future research will also be directed in this aspect, especially studying the role of a surface stress. In the current model, the parameters $f(c)$ and $\bar{\mu} e_0 \mathbf{I}$, representing the cell activity and the change of energy during tissue growth respectively, are taken to be constant. In principle these parameters could also include a dependence on stress, and further work is being done to address this.

5 Conclusions

In this paper we derive and investigate a thermodynamically based model for tissue growth. The model was applied to the simple geometry of tissue growing within a cylindrical pore. Remarkably the growth kinetics and the calculated stress distributions are similar to experimental results from tissue cultures (Rumpler, et al., 2008). These similarities are very interesting, keeping in mind that the description of the biological system (with $f(c)$ and $\bar{\mu} e_0 \mathbf{I}$ being constant) is the simplest possible. Nevertheless, the treatment shows that internal stresses (which cells can sense) develop inevitably during tissue growth, which supports the idea that the regulation of tissue growth is to a large extent stress-driven.

Acknowledgements

We appreciate the intensive correspondence with and the comments from Prof. D. Ambrosi, Italy. P.F. and E.G. are grateful for support by the Alexander von Humboldt Foundation and the Max Planck Society in the framework of the Max Planck Research Award funded by the Federal Ministry of Education and Research. The authors are grateful to the Deutsche Forschungsgemeinschaft (DFG) for partial financial support under the grant of collaborative research centre scheme (SFB) 760.

References

Ambrosi, D., Guana, A., 2007. Stress-modulated growth. Math Mech Sol 12, 319-342.

Ambrosi, D., Guillou, A., 2007. Growth and dissipation in biological tissues. Cont Mech Thermo 19, 245-251.

Ambrosi, D., Preziosi, L., 2002. On the closure of mass balance models for tumor growth. Math Mod Meth Appl Sci 12 (5), 737-754.

Ambrosi, D., Preziosi, L., 2009. Cell adhesion mechanisms and stress relaxation in the mechanics of tumours. Biomechanics and Modeling in Mechanobiology 8 (5), 397-413.

Boyan, B.D., Sylvia, V.L., Liu, Y.H., Sagun, R., Cochran, D.L., Lohmann, C.H., Dean, D.D., Schwartz, Z., 1999. Surface roughness mediates its effects on osteoblasts via protein kinase A and phospholipase A(2). Biomaterials 20 (23-24), 2305-2310.

Castner, D.G., Ratner, B.D., 2002. Biomedical surface science: Foundations to frontiers. Surf Sci 500 (1-3), 28-60.

Chen, C.S., 2008. Mechanotransduction - a field pulling together? J Cell Sci 121 (20), 3285-3292.

Cowin, S.C., Hegedus, D.H., 1976. Bone remodeling I. theory of adaptive elasticity. J Elasticity 6 (3), 313-326.

Curtis, A.S.G., Wilkinson, C.D., 1998. Reactions of cells to topography. J Biomat Sci Polym Ed 9 (12), 1313-1329.

Discher, D.E., Janmey, P., Wang, Y.-L., 2005. Tissue cells feel and respond to the stiffness of their substrate. Science 310, 1139-1143.

Dunlop, J.W.C., Hartmann, M.A., Brechet, Y.J., Fratzl, P., Weinkamer, R., 2009. New Suggestions for the Mechanical Control of Bone Remodeling. Calcif Tiss Int 85 (1), 45-54.

Ehlers, W., Markert, B., Röhrle, O., 2009. Computational Continuum Biomechanics with Application to Swelling Media and Growth Phenomena. GAMM Mitt 32, 135-156.

Epstein, M., Maugin, G.A., 2000. Thermomechanics of volumetric growth in uniform bodies. Int J Plasticity 16, 951-978.

Eshelby, J.D., 1975. The elastic energy-momentum tensor. J Elasticity 5, 321-335.

Faucheux, N., Schweiss, R., Lutzow, K., Werner, C., Groth, T., 2004. Self-assembled monolayers with different terminating groups as model substrates for cell adhesion studies. Biomaterials 25 (14), 2721-2730.

Frost, H.M., 1987. Bone Mass and the Mechanostat - a Proposal. Anat Rec 219 (1), 1-9.

Garikipati, K., 2009. The Kinematics of Biological Growth. ASME Appl Mech Rev 62 (3), 030801.

Garikipati, K., Arruda, E.M., Grosh, K., Narayanan, H., Calve, S., 2004. A continuum treatment of growth in biological tissue: the coupling of mass transport and mechanics. J Mech Phys Solids 52 (7), 1595-1625.

Geiger, B., Bershadsky, A., 2002. Exploring the neighborhood adhesion-coupled cell mechanosensors. Cell 110 (2), 139-142.

Geiger, B., Spatz, J.P., Bershadsky, A.D., 2009. Environmental sensing through focal adhesions. Nat Rev Mol Cell Biol 10 (1), 21-33.

Hall, B., 2005. Bones and Cartilage: Developmental and Evolutionary Skeletal Biology. Elsevier, San Diego.

Hartung, A., Sieber, C., Knaus, P., 2006. Yin and Yang in BMP signaling: Impact on the pathology of diseases and potential for tissue regeneration. Signal Transduction 6 (5), 314-328.

Hegedus, D.H., Cowin, S.C., 1976. Bone remodeling II. small strain adaptive elasticity. J Elasticity 6 (4), 337-352.

Hollister, S.J., 2005. Porous scaffold design for tissue engineering. Nat Mater 4 (7), 518-524.

Huiskes, R., Ruimerman, R., van Lenthe, G.H., Janssen, J.D., 2000. Effects of mechanical forces on maintenance and adaptation of form in trabecular bone. Nature 405, 704-706.
Humer, A., 2008. On the modeling of growth: A continuum mechanics approach for problems with volume distributed production terms of mass and linear momentum. JK University, Linz, Austria.
Kirchner, H., Lazar, M., 2008. The thermodynamic driving force for bone growth and remodelling: a hypothesis. J Roy Soc Int 5, 183-193.
Kong, H.J., Polte, T.R., Alsberg, E., Mooney, D.J., 2005. FRET measurements of cell-traction forces and nano-scale clustering of adhesion ligands varied by substrate stiffness. Proc Nat Acad Sci USA 102 (12), 4300-4305.
Linez-Bataillon, P., Monchau, F., Bigerelle, M., Hildebrand, H.F., 2002. In vitro MC3T3 osteoblast adhesion with respect to surface roughness of Ti6A14V substrates. Biomol Eng 19 (2-6), 133-141.
Lo, C.-M., Wang, H.-B., Dembo, M., Wang, Y.-L., 2000. Cell movement is guided by the rigidity of the substrate. Biophys J 79, 144-152.
Mantzaris, N.V., Webb, S., Othmer, H.G., 2004. Mathematical modeling of tumor-induced angiogenesis. J Math Biol 49 (2), 111-187.
Martin, P., 1997. Wound Healing - Aiming for Perfect Skin Regeneration. Science 276 (5309), 75-81.
Martyushev, L.M., Seleznev, V.D., 2006. Maximum entropy production principle in physics, chemistry and biology. Phys Rep 426 (1), 1-45.
Mitragotri, S., Lahann, J., 2009. Physical approaches to biomaterial design. Nat Mater 8 (1), 15-23.
Nelson, C.M., Jean, R.P., Tan, J.L., Liu, W.F., Sniadecki, N.J., Spector, A.A., Chen, C.S., 2005. Emergent patterns of growth controlled by multicellular form and mechanics. Proc Nat Acad Sci USA 102 (33), 11594-11599.
Onsager, L., 1931. Reciprocal Relations in Irreversible Processes. I. Phys Rev 37 (4), 405-405.
Pathak, A., Deshpande, V.S., McMeeking, R.M., Evans, A.G., 2008. The simulation of stress fibre and focal adhesion development in cells on patterned substrates. J Roy Soc Int 5 (22), 507-524.
Place, E.S., Evans, N.D., Stevens, M.M., 2009. Complexity in biomaterials for tissue engineering. Nat Mater 8 (6), 457-470.
Rodriguez, E.K., Hoger, A., Mcculloch, A.D., 1994. Stress-Dependent Finite Growth in Soft Elastic Tissues. J Biomech 27 (4), 455-467.
Rumpler, M., Woesz, A., Dunlop, J., van Dongen, J., Fratzl, P., 2008. The effect of geometry on three-dimensional tissue growth. J Roy Soc Int 5, 1173-1180.
Sengers, B.G., Taylor, M., Please, C.P., Oreffo, R.O.C., 2007. Computational modelling of cell spreading and tissue regeneration in porous scaffolds. Biomaterials 28 (10), 1926-1940.
Simha, N.K., Fischer, F.D., Shan, G.X., Chen, C.R., Kolednik, O., 2008. J-integral and crack driving force in elastic-plastic materials. J Mech Phys Solids 56 (9), 2876-2895.
Svoboda, J., Turek, I., Fischer, F.D., 2005. Application of the thermodynamic extremal principle to modeling of thermodynamic processes in material sciences. Phil Mag 85 (31), 3699-3707.
Tabata, Y., 2009. Biomaterial technology for tissue engineering applications. J Roy Soc Int 6 (Suppl_3), 311-324.
Taber, L.A., 1995. Biomechanics of growth, remodeling, and morphogenesis. ASMEJ Appl Mech Rev 48, 487-545.
Taber, L.A., Eggers, D.W., 1996. Theoretical study of stress-modulated growth in the aorta. J Theor Biol 180 (4), 343-357.
Taber, L.A., Humphrey, J.D., 2001. Stress-modulated growth, residual stress, and vascular heterogeneity. ASME Biomech Eng 123 (6), 528-535.
Taylor, D., Hazenberg, J.G., Lee, T.C., 2007. Living with cracks: damage and repair in living bone. Nat Mater 6, 263-268.
Turner, C.H., 1991. Homeostatic control of bone structure: An application of feedback theory. Bone 12, 203-217.
Vignes, C., Papadopoulos, P., 2010. Material growth in thermoelastic continua: theory, algorithmics and simulation. Comput Methods Appl Mech Engrg 199, 979-996.
Volokh, K.Y., 2006. Stresses in soft tissues. Acta Biomater 2, 493-504.
Weinkamer, R., Hartmann, M.A., Bréchet, Y., Fratzl, P., 2004. Stochastic lattice model for bone remodeling and aging. Phys Rev Lett 93, 228102.
Zinger, O., Zhao, G., Schwartz, Z., Simpson, J., Wieland, M., Landolt, D., Boyan, B., 2005. Differential regulation of osteoblasts by substrate microstructural features. Biomaterials 26 (14), 1837-1847.

7.6 [TG6] Modelling the role of surface stress on the kinetics of tissue growth in confined geometries.

Gamsjäger, E., Bidan, C. M., Fischer, F. D., Fratzl, P., Dunlop, J. W. C.
*Published in **Acta Biomaterialia**, 2013, 9, 5531–5543.*
DOI:/10.1016/j.actbio.2012.10.020

Reprinted with permission from Elsevier

Abstract: In a previous paper we presented a theoretical framework to describe tissue growth in confined geometries based on the work of Ambrosi et al. A thermodynamically consistent eigenstrain rate for growth was derived using the concept of configurational forces and used to investigate growth in holes of cylindrical geometries. Tissue growing from concave surfaces can be described by a model based on this theory. However, an apparently asymmetric behaviour between growth from convex and concave surfaces has been observed experimentally, but is not predicted by this model. This contradiction is likely to be due to the presence of contractile tensile stresses produced by cells near the tissue surface. In this contribution we extend the model in order to couple tissue growth to the presence of a surface stress. This refined growth model is solved for two geometries, within a cylindrical hole and on the outer surface of a cylinder, thus demonstrating how surface stress may indeed inhibit growth on convex substrates.

1. Introduction

Evidence is accumulating that, in addition to biochemical factors, the physical environment in contact with cells and tissues modifies and controls cells' behaviour. Individual cells can sense the stiffness of a substrate, for example, with stem cells being able to differentiate along different pathways depending on the elastic properties of the substrate [1-4]. The surface roughness has also been demonstrated to influence cell adhesion and proliferation of several different cell types [5]. Similarly, the geometry of the sites available for cell adhesion, determined by features such as the density of ligands [6, 7], as well as the size [8] and the shape of adhesive areas [9, 10], plays a role in cell spreading, apoptosis and differentiation. Finally, cells behave differently depending on whether they are completely surrounded by a matrix in three dimensions or are just sitting on a flat surface in two dimensions [11]. Such geometric effects are also seen at the multicellular or the tissue level [12], where an imposed shape gives rise to boundary constraints on the contractile behaviour of tissue, in turn controlling proliferation and further growth [13]. The collective behaviour of cells, such as MC3T3-E1 pre-osteoblasts cultured within three-dimensional holes, is influenced by the shape of the holes' cross-sections, and may be described by a simple model of curvature controlled growth [14]. This model is consistent with the idea that cells, and extracellular matrix they organise, act as tensile elements within the tissue and predicts the differing growth rates observed experimentally in osteons and hemi-osteons [15]. Furthermore, it has also been shown that after the initial stages of cell spreading, the rate of growth was found to be independent of the substrate material [16], highlighting the crucial role played by geometry. In order to understand such behaviour, it is important to develop suitable theoretical models for tissue growth. One such approach was presented in a previous paper by the authors [17], where tissue growth was described by an eigenstrain (as resulting from cell divisions and synthesis of extracellular matrix by the cells) which depends on the local stress in the tissue. While very encouraging results were obtained with this model, it could not predict experimentally observed asymmetry between tissue growing on convex and concave surfaces [15, 18, 19]. It is the goal of this paper to remedy this by introducing the additional action of surface stress, as observed to occur in tissue cultures.

2. Motivation

2.1 Experimental motivation

From an experimental standpoint surprisingly few quantitative studies have investigated the role of geometry on tissue formation, although much work has been done on how geometric features control the behaviour of single cells (see e.g. [6-10]). Observations of bone tissue growth in-vivo show that there is a significantly higher amount of bone tissue formed in concavities as opposed to convex (or planar) surfaces (see for example [18, 19] and reference contained therein). The geometry of artificial bone defects in turn influences the lamellar arrangement of new bone [20], and also appears to control lamellar bone formation during bone fracture healing [21]. This has of course practical consequences, for instance in periodontal treatment, where it is also observed that the presence of 'bony walls', which create local concavities on which new tissue can grow, assists the regeneration of new bone [22]. Finally, evaluations of computed tomography measurements of trabecular bone show that trabecular bone has close to zero mean surface curvature. This implies that, also in-vivo, there is indeed a strong control of (and response to) tissue geometry by the bone cells themselves [23].

Quantification of the tissue response to substrate geometry was studied in-vitro by observing growth in simplified scaffolds containing only a few straight-sided pores with controlled cross-sections [14, 15]. In the initial study by Rumpler et al [14] pores containing only concave surfaces were produced in hydroxyapatite using rapid prototyping and tested in culture with MC3T3-E1 murine pre-osteoblast cells. It was shown for these shapes that tissue growth occurred only on concave surface, with growth occurring on flat surfaces only when the local tissue surface curvature changed due to tissue ingrowth from the surroundings. Bidan et al [15] extended this work by looking at the response of the same cells to semi-circular channels produced on the surface of the

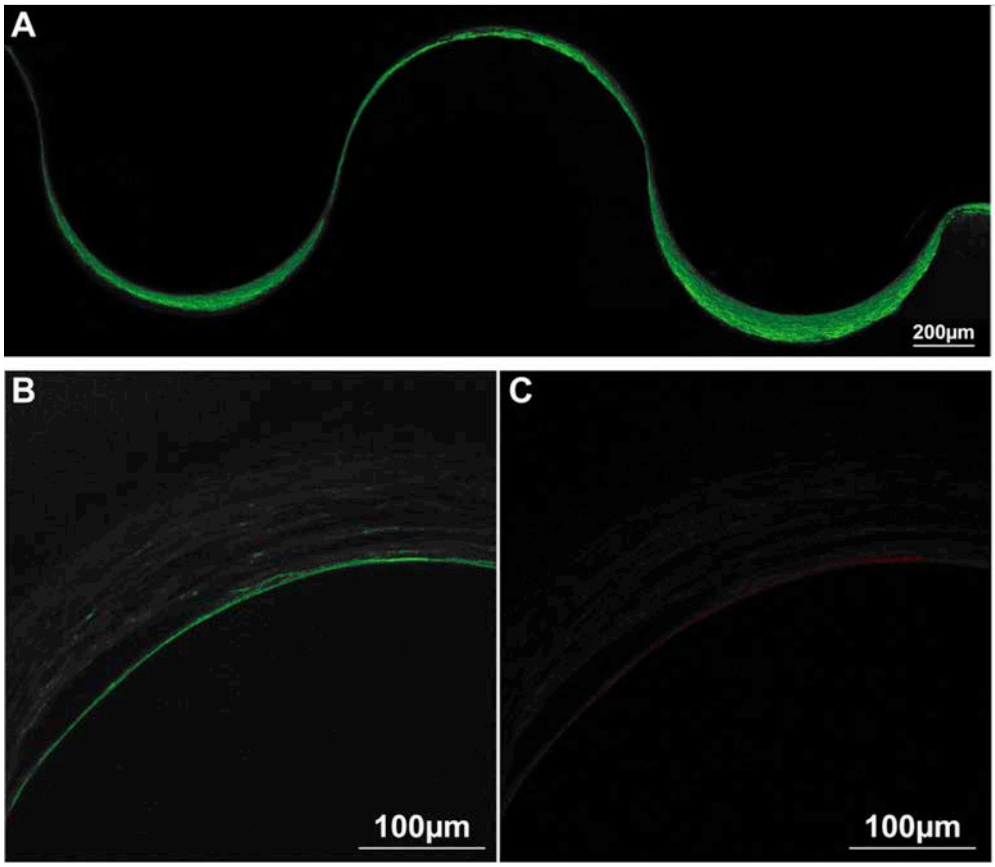

Fig. 1: Experimental evidence for the asymmetry between growth on convex and concave surfaces. a) A stack of confocal images of tissue stained for actin (green) on a wave like substrate with the scaffold below and medium above. b,c) a stack of 3 slices deep in the tissue showing the high concentration of actin (b, green) and myosin (c, red) at the tissue medium interface.

scaffolds. Growth was observed to be 'pinned' on the corners of the channels, with only a thin layer of tissue being produced, indicating that tissue growth in-vitro is sensitive to the local sign of curvature.

To further investigate this curvature sensitivity, a 'wave-like' surface was produced in hydroxyapatite using rapid-prototyping with repeating concave channels and convex ridges. The scaffold synthesis and cell culture experiments were performed identically to the experiments described in [14, 15], for more details see Appendix A.

A typical tissue configuration is depicted in Figure 1a) which shows a confocal image stack of the tissue formed on the wave-like surface. The lower dark region in the image is the scaffold, (opaque) and the upper dark region is the media (no signal), actin stress fibres (present in the tissue) appear at the interface in green. More tissue is formed on the concave surfaces compared to the convex one, again supporting the idea that there is a dependency of 'bone-like' tissue growth on the sign of curvature. A potential reason for this sign dependence of growth could come from the high contractility of the cells themselves that develops primarily on the tissue-medium interface as indicated by the colocalisation of actin and myosin at the interface (Fig. 1b). A tensile surface stress has a different effect on underlying cells depending on whether the surface is convex or concave. This provides an experimental motivation behind the main goal of this paper, to examine tissue growth from a theoretical perspective in simplified concave and convex scaffolds and to test the role of surface stress on growth.

2.2 Theoretical motivation

In a preceding paper [17] a thermodynamically consistent rate $\dot{\mathbf{g}}$ of a growth tensor $\mathbf{g}$ being an eigenstrain tensor to represent tissue growth (later denominated as eigenstrain rate in a small strain setting) was derived, based on work by Ambrosi and co-workers [24, 25], see also the recent review article by Ambrosi et al. [26]. The provision of matter occurs by the diffusion of a nutrient which is converted by cells into tissue. The concept of material or configurational forces is followed as it is often applied to describe the kinetics of phase transformations [see e.g. 27]. The basic idea is to incorporate within the concept of configurational forces the dissipation inequality, mass and energy balance relations for the conversion of nutrient into tissue. This equation can then be used to derive a growth rate in which positive entropy production is guaranteed in accordance with the principle of maximal dissipation [28, 29]. The eigenstrain rate $\dot{\mathbf{g}}$ for tissue growth derived in [17] is given as

$$\dot{\mathbf{g}} = f\left(\sigma - \bar{\mu} e_0 \mathbf{I}\right) \quad . \qquad (1)$$

The quantity $f > 0$ can be considered as a mobility factor (a kinetic term describing how fast cells react and produce new matrix), $\bar{\mu} e_0$ is the (usually negative) change in Helmholtz energy during formation of the solid tissue phase from a diffusing nutrient; $\boldsymbol{\sigma}$ is the stress tensor (small strain setting)

and $\mathbf{I}$ the unit tensor. Therefore, two thermodynamic quantities drive growth, namely the stress state $\boldsymbol{\sigma}$ and the (chemical) Helmholtz energy term $-\bar{\mu}e_0\mathbf{I}$. Recently Ganghoffer [30] has published a similar concept and extended it also with a surface (interface) growth term. A derivation of the eigenstrain rate $\dot{\mathbf{g}}$ based on the normality concept, using a "homeostatic" surface, was also recently introduced, in which only a stress-driven growth rate was derived including no chemical term such as $\bar{\mu}e_0$, see Loret et al. [31]. Finally a small strain setting has been shown to be acceptable and sufficient to describe growth when written in an incremental form. This means that the growth process in the time interval $\left[t, t+\mathrm{d}t\right]$ is represented by the eigenstrain increment $\dot{\mathbf{g}}dt$. According to Hodge and Papadopoulos [32] the actual configuration at time t can be considered as an evolving reference configuration. Thus, the total strain increment defined within a small strain setting $\dot{\varepsilon}dt = \left(\dot{\varepsilon}_{el} + \dot{\mathbf{g}}\right)dt$, where $\dot{\varepsilon}_{el}$ is the elastic strain rate, defines the change of the geometrical configuration in the above mentioned time interval due to growth. The eigenstrain rate $\dot{\mathbf{g}}$ enforces the elastic strain rate $\dot{\varepsilon}_{el}$ to obtain a physically admissible (i. e. compatible) deformation state. The eigenstress rate $\dot{\sigma}$ is a direct consequence of the elastic strain rate $\dot{\varepsilon}_{el}$. This means that the eigenstress state σ corresponds directly to the eigenstrain $\mathbf{g}$. In case that there are no external forces (e.g. surface stresses or body forces) present, the eigenstress state σ is equivalent to the total stress state and the eigenstress rate $\dot{\sigma}$ directly corresponds to the eigenstrain rate $\dot{\varepsilon}_{el}$ as described in [17] Of course, the stress state σ acts in the solid phase, which is assumed to be an assembly of cells together with the formed extracellular matrix.

Equation (1) was implemented to describe a layer of tissue growing within a cylindrical hole of outer radius, R [17]. Solving the mechanical equations of equilibrium in cylindrical coordinates leads to two sets of coupled differential equations which give the change of inner radius r_i, at the tissue-medium boundary, and the radial stress at the outer radius R, as well as the stress state in the interior of the tissue as a function of position r, $r_i \le r \le R$. The growth kinetics predicted by the model were in good qualitative agreement with the experiments performed for closing cylindrical holes [14]. The calculated stress distribution, with high compressive circumferential stresses predicted at the internal tissue-medium boundary, also corresponds well to the higher concentrations of actin stress-fibres observed experimentally at the tissue boundary. Although this seems somewhat counterintuitive, the presence of actin stress-fibres indicates tensile rather than compressive loading, the model shows the (compressive) response of the tissue to the (tensile) action of the cells themselves.

The model can also be readily applied to describe tissue growth outwards from the convex surface of a cylindrical scaffold. Uniform growth on a convex surface results in higher tensile stresses leading to ever increasing growth rates through Eq. (1). The

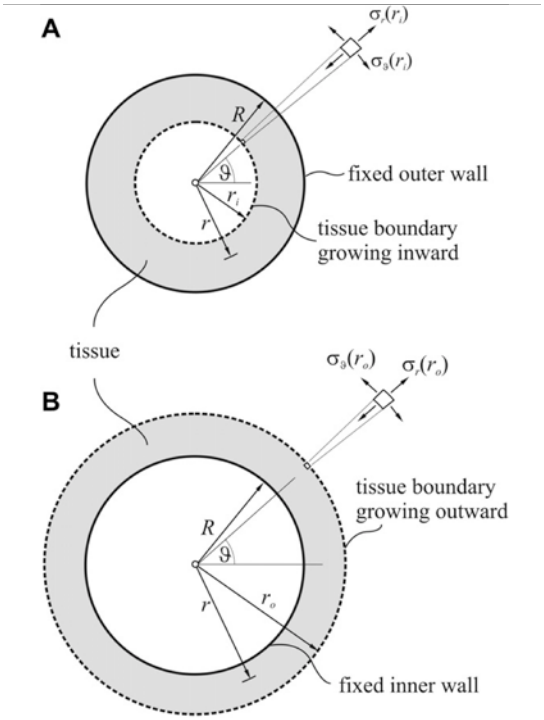

Fig. 2: Schematic sketch of tissue growth starting from a cylindrical wall at position R, the radial coordinate is r; a) Radial growth from the inner wall of the cylinder to its centre, r_i is the position of the inner boundary, b) Radial growth from the outer wall of the cylinder to the outside, r_o is the position of the outer boundary.

predicted exponential growth on convex surfaces is in contrast to experimental results where no growth, apart from the formation of a thin monolayer of cells, is observed on convex surfaces ([15, 19] and Fig. 1a). In fact growth can and does occur on convex surfaces but only after tissue has grown sufficiently from surrounding concavities to make the local tissue surface concave. This effect of the sign of curvature does not appear explicitly in Eq. (1) and is required for a correct description and prediction of tissue growth. Asymmetry can be introduced into $\dot{\mathbf{g}}$, if, in addition to the eigenstress state due to growth, an effective "surface stress" is also included. This idea is inspired by the experimental results of Rumpler et al. [14] and Bidan et al [15], where tissue growth was described by a simple model for "curvature-driven" growth. This is also consistent with the review by Lecuit and Lenne [33], which discusses the hypothesis that tissues, as collections of adhesive and contractile cells, may display an "effective surface stress", of cell aggregates which arises simply when cells adhere to each other and pull through their cytoskeleton (see also the stained stress fibres in Rumpler et al. [14] and the co-localisation of actin and myosin in [15] and Fig. 1b). This surface stress is surface curvature dependent and, therefore, may lead to different growth behaviour on concave vs convex surfaces. Such ideas have already been successfully implemented within an extended Potts model, and simulations have demonstrated the important role that an effective tissue surface stress plays in cell sorting [34], and morphogenesis [35, 36]. In addition to surface tension (understood as surface energy) due

to positive adhesive interactions, there is also the additional surface stress, produced by the contractile behaviour of cells lying on the tissue surface itself. This has been shown to play an important role for example in the prediction of cell shapes within a tissue [37] but is difficult to separate completely from the surface stress produced via adhesion between cells. It is therefore clear that a tissue surface stress needs to be included as a further thermodynamic quantity within the theoretical framework of [17]. This means that σ in Eq. (1) has not only to include the eigenstress state, but also the stress state due to a "surface stress".

The role of surface energy (surface tension) and surface stress in Materials Science has significantly increased in recent times, since smaller and smaller objects are being studied experimentally. It is worth mentioning that clear definitions with respect to the terms "surface energy, surface tension and surface stress" are necessary, the reader is referred to [38-40]. The effective surface stress developed during tissue growth is somewhat different however from the usual understanding of surface stress in Materials Science. Here, active cells situated at the surface of a cylinder, develop a surface tensile stress state in the circumferential direction of the hole. In the notation of continuum mechanics, the activity of cells on the surface, i.e. the surface stress, can be described by a positive membrane γ in a (virtual) thin layer mounted onto the surface of the growing tissue. The membrane force γ has the dimension of force per length or, in other words, of energy per area, which is the same dimension as that for surface energy (surface tension) and sometimes the reason for confusion. For a cylindrical arrangement this membrane force is actually the force per unit height of the cylinder acting in the circumferential direction. The layer of contractile cells is assumed to be attached to the tissue-medium interface of tissue growing inside a cylindrical hole. Local equilibrium of an element of the (virtual) layer requires that a positive radial stress γ/r_i must therefore act outwards onto the tissue, since no surface pressure is active on the inner surface of the layer. This is also an outcome of the so-called "Laplace–Young equation" in Surface Science, see e.g. sect 1-2 of [39]. This finally means that the tissue feels a radial tensile stress $\sigma_r = \gamma/r_i$ at its inner (hole) surface, $r = r_i$. In other words, the cells, responsible for the membrane force γ, tend to close the hole. The opposite effect takes place, if the contractile layer (the cells) is attached to the outer surface of a cylinder, $R \le r \le r_o$. Then the cells – and the according (virtual) membrane force – produce a radial compressive stress $-\gamma/r_o$ on the outer surface of the (possibly) growing object at $r = r_o$. The cells work now against the growth of the outer object intending to reduce the outer radius r_o. One can easily imagine that outside growth is not possible for zero (chemical) change in Helmholtz energy. This argumentation is also supported by experimental observations. The goal of this paper is now to implement the membrane force γ, which is called the "surface stress" in accordance with the notation in Materials Science, into the growth concept at hand. This is done by adding a new geometry dependent boundary condition into the original model. The outcome of the model is then compared with the current concept of "curvature-driven" growth.

For sake of clarity, it should be noted again that the denomination surface tension is used in materials science for the surface energy per unit area (which goes back to Gibbs) as well as the surface stress. The surface tension is precisely defined as the change in Helmholtz energy per unit extension of the interfacial area at constant temperature and constant volumes of both phases involved ([41]). Both, surface energy per unit area and surface stress (reversible work per unit area needed to elastically stretch a pre-existing surface), have the same dimensions (as mentioned above) and obtain the same value in the case of liquids. In the case of solids both physical entities may have different values, as the surface energy (per unit area) usually depends on the strain state. To avoid any confusion we will use the term "surface stress" in the following.

3. Modelling

3.1 General aspects

In this section the model developed in [17] is extended to include the surface stress. This is done by combining the constitutive law for growth (Eq. (1)) with Hooke's Law and the appropriate boundary conditions allowing for the geometry dependent surface stress. The following facts must be met by the model:

- The actual geometry is controlled by both the elastic deformation state and growth state; the rate of the latter depends on the total stress state σ via Eq. (1).
- The total stress state σ includes σ^{ss}, the surface stress state.
- The surface stress state σ^{ss}, i.e. stress state in the specimen due to the surface stress, depends on the actual geometry via r_i or r_o.
- Consequently, the surface stress state σ is coupled with the growth process due to the actual geometry, yielding a coupling stress state σ^c.
- Finally, three concurrent processes are active and contribute to the total stress state σ by a
  - o growth stress state σ^g,
  - o surface stress state σ^{ss},
  - o coupling stress state σ^c.

3.2 Kinematical and mechanical setting

As in the previous paper [17] we consider a cylindrical disc of unit height, subjected to plane stress during confined growth. The tissue, consisting of both cells and extracellular matrix, is taken to be linear-elastic, with Young's modulus E, and Poisson's ratio ν; both are assumed to be constant in space. In the following context $\tilde{E} = E/\left(1-\nu^2\right)$ is used.

We assume a small strain setting and additively decompose the strain tensor ε into two contributions, namely $\mathbf{g}$, the growth eigenstrain and ε_{el}, the elastic strain. Combining this with Hooke's law gives the radial and circumferential stresses, respectively, as a function of the strain components, i.e. $\sigma_r = \tilde{E}\left(\varepsilon_r + \nu\varepsilon_\vartheta\right) - \tilde{E}\left(g_r + \nu g_\vartheta\right)$ and

$\sigma_\vartheta = \tilde{E}\left(\varepsilon_\vartheta + \nu\varepsilon_r\right) - \tilde{E}\left(g_\vartheta + \nu g_r\right)$. The position in the cylindrical coordinate system is described by the radial distance r. Growth starts from the position $r = R$, with a starting tissue thickness δ small compared to R, at time t = 0. Two geometries are studied corresponding either to growth inside a cylindrical hole $\left(0 \le r_i \le r \le R\right)$ (Fig. 2a) or growth outside of a cylinder $\left(R \le r \le r_o\right)$ (Fig. 2b).

A radial stress $\sigma_r\left(r_i\right) = \gamma / r_i$ or $\sigma_r\left(r_o\right) = -\gamma / r_o$ is assumed acting on the inner or outer surface in this new model.

Due to the symmetry of growth in this setting no shear stress components occur. Standard kinematic relations apply giving the radial and circumferential strain components (ε_r and ε_ϑ, resp.) in cylindrical coordinates as functions of radial displacement u as

$$\varepsilon_r = \frac{du}{dr} = u', \ \varepsilon_\vartheta = \frac{u}{r} .. \qquad (3.1)$$

The prime indicates spatial derivatives with respect to the radial position r.

The following normalised parameters are used: $\tilde{r} = r / R$, $\tilde{r}_i = r_i / R, \tilde{r}_o = r_o / R$,

$\tilde{u} = u / R$, $\tilde{\mu} = \left|\bar{\mu} e_0\right| / \tilde{E}$ (3.2a)

which are identical to those in the previous paper [17].

Due to the introduction of γ and meeting the possibility of $\bar{\mu} = 0$, the following normalised parameters are different to those in the previous paper [17], except to the normalisation of γ which was not dealt with there:

$$\tilde{\gamma} = \frac{\gamma}{\tilde{E} R}, \tilde{\sigma}_r = \sigma_r / \tilde{E}, \tilde{\sigma}_\vartheta = \sigma_\vartheta / \tilde{E}, \qquad (3.2b)$$

$$\tau = \tilde{E} f t , \qquad (3.2c)$$

f is the parameter in Eq. (1), t time.

3.3 The role of growth

Some results from the previous paper [17] are repeated here. A tissue layer is assumed to develop inwards from the fixed wall of a cylindrical hole due to a growth process, or in other words, due to a stress-dependent eigenstrain rate. No surface stress is active.

Two quantities were calculated, namely the normalized rates of inner radius $\tilde{r}_i^g$ and the normalized radial stress $\tilde{\sigma}_r^g\left(1\right)$ at the fixed wall, $r = R$ or $\tilde{r} = 1$. The superscript "g" is set to refer to growth only. Details of the calculation can be found in the previous paper and are summarized in the Appendix B. The results are

$$\frac{d\tilde{r}_i^g}{d\tau} = -\frac{\left[2\nu\tilde{r}_i\tilde{\sigma}_r\left(1\right) + \left(1+\nu\right)\tilde{\mu}\left(\tilde{r}_i - \tilde{r}_i^3\right)\right]}{\left(1+\nu\right)\tilde{r}_i^2 + \left(1-\nu\right)}, \qquad (3.3)$$

$$\frac{d\tilde{\sigma}_r^{\,g}\left(1\right)}{d\tau} = -\frac{\left(1-\nu^2\right)\left[\left(1+\tilde{r}_i^2\right)\tilde{\sigma}_r\left(1\right) + \tilde{\mu}\left(1-\tilde{r}_i^2\right)\right]}{\left(1+\nu\right)\tilde{r}_i^2 + \left(1-\nu\right)} \qquad (3.4)$$

3.4 The role of surface stress

In this section the role of the surface stress only is treated; consequently no eigenstrain is considered. The quantities to be calculated are the normalized stress components $\tilde{\sigma}_r^{ss}\left(\tilde{r}\right)$ and $\tilde{\sigma}_\vartheta^{ss}\left(\tilde{r}\right)$. The superscript "ss" is set to refer to surface stress only. Since all calculations run along standard elasticity, details of the calculations can be found in the Appendix C. The results are

$$\tilde{\sigma}_r^{\,ss}\left(\tilde{r}\right) = \tilde{\gamma}\frac{\tilde{r}_i}{\left(1+\nu\right)\tilde{r}_i^2 + \left(1-\nu\right)}\left[\left(1+\nu\right) + \frac{\left(1-\nu\right)}{\tilde{r}^2}\right], \qquad (3.5a)$$

$$\tilde{\sigma}_\vartheta^{\,ss}\left(\tilde{r}\right) = \tilde{\gamma}\frac{\tilde{r}_i}{\left(1+\nu\right)\tilde{r}_i^2 + \left(1-\nu\right)}\left[\left(1+\nu\right) - \frac{\left(1-\nu\right)}{\tilde{r}^2}\right]. \qquad (3.5b)$$

The normalised radial stress $\tilde{\sigma}_r^{\,ss}\left(1\right)$ at the fixed wall, $r = R$ or $\tilde{r} = 1$, follows from (3.5a) as

$$\tilde{\sigma}_r^{ss}\left(1\right) = \tilde{\gamma}\frac{2\tilde{r}_i}{\left(1+\nu\right)\tilde{r}_i^2 + \left(1-\nu\right)} a . \qquad (3.6a)$$

Its derivative with respect to normalised time τ reads as

$$\frac{d\tilde{\sigma}_r^{ss}\left(1\right)}{d\tau} = \tilde{\gamma}\frac{2\left[\left(1-\nu\right) - \left(1+\nu\right)\tilde{r}_i^2\right]}{\left[\left(1+\nu\right)\tilde{r}_i^2 + \left(1-\nu\right)\right]^2}\cdot\frac{d\tilde{r}_i}{d\tau} . \qquad (3.6b)$$

3.5 Coupling between the roles of growth and surface stress state

As outlined in Section 2, the surface stress state exerted by the cells is represented by an external radial tensile stress γ / r_i at the inner hole contour and an external radial stress with the value $-\gamma / r_o$ at the outer contour. Obviously, the actual radii r_i and r_o determine the values of the radial stress on the inner and outer contours, and these radii themselves change with growth. Since growth depends also on the local stress state in the specimen, the external radii are affected by the actual stress state, which itself depends explicitly on the external radii via the contribution of the external radial stresses γ / r_i and $-\gamma / r_o$. Concluding, growth is immediately coupled to geometry via the surface stress state. The change of the geometry occurs due to growth, driven simultaneously by a chemical supply and the stress state, which itself depends explicitly on the geometry.

We describe the evolution of the geometry by virtually splitting each time increment into two virtual sub-increments. In each of the two sub-increments a different step of evolution process occurs. Due to the elastic material behaviour and a small strain setting a superposition of both these steps is possible.

The <u>first step</u> is addressed to the change of the system due to growth only with the role of surface stress kept constant, $\sigma_r\left(r_i\right) = \gamma / r_i$, $\sigma_r\left(r_0\right) = -\gamma / r_0$ and r_i, r_0 set equal to the starting radius in this time increment. In the <u>second step</u> the role of surface stress due to the change of the inner radius r_i and outer radius r_0 is adapted elastically only according to Sect. 3.4.

Since all calculations again use standard elasticity theory, they are outlined in Appendix D. The two quantities of interest are still the normalized rates of inner radius $\tilde{r}_i$ and the radial stress $\tilde{\sigma}_r\left(1\right)$ consisting of three contributions. The first two contributions, denoted as $d\tilde{r}_i^* / d\tau$ and $d\tilde{\sigma}_r^*\left(1\right) / d\tau$, refer to the

growth process and due the coupling with the surface stress state as

$$\frac{d\tilde{r}_i^*}{d\tau} = -\frac{2\nu\tilde{r}_i\tilde{\sigma}_r(1)+(1+\nu)\tilde{\mu}\left(\tilde{r}_i-\tilde{r}_i^3\right)}{(1+\nu)\tilde{r}_i^2+(1-\nu)} + \tilde{\gamma}\frac{\tilde{r}_i^2(1+\nu)-(1-\nu)}{(1+\nu)\tilde{r}_i^2+(1-\nu)}, \quad (3.7a)$$

$$\frac{d\tilde{\sigma}_i^*}{d\tau} = -\frac{\left(1-\nu^2\right)\left[\left(1+\tilde{r}_i^2\right)\tilde{\sigma}_r(1)+\tilde{\mu}\left(1-\tilde{r}_i^2\right)\right]}{(1+\nu)\tilde{r}_i^2+(1-\nu)} + \tilde{\gamma}\frac{2\left(1-\nu^2\right)\tilde{r}_i^2}{(1+\nu)\tilde{r}_i^2+(1-\nu)}. \quad (3.7b)$$

The third contribution is that due to surface stress only, see Sect. 3.4., and Eqs. (D.8), (D.9). Adding up those three terms yields

$$\frac{d\tilde{r}_i}{d\tau} = \frac{d\tilde{r}_i^*}{d\tau}\left[1-\tilde{\gamma}\frac{4\tilde{r}_i}{\left[(1+\nu)\tilde{r}_i^2+(1-\nu)\right]^2}\right]^{-1}, \quad (3.8a)$$

$$\frac{d\tilde{\sigma}_r(1)}{d\tau} = \frac{d\tilde{\sigma}_r^*(1)}{d\tau} + \tilde{\gamma}\frac{2\left[(1-\nu)-(1+\nu)\tilde{r}_i^2\right]}{\left[(1+\nu)\tilde{r}_i^2+(1-\nu)\right]^2}\cdot\frac{d\tilde{r}_i}{d\tau}. \quad (3.8b)$$

Insertion of Eqs. (3.7a-b) into Eqs. (3.8a-b) forms a system of two coupled differential equations for the two quantities $\tilde{r}_i$, $\tilde{\sigma}_r(1)$ with the initial conditions $\tau=0:\tilde{r}_i=1-\delta,\tilde{\sigma}_r(1)=\tilde{\gamma}$ with $\delta \ll 1$ being a small perturbation.

3.6 Evolution equations for the stress state $\tilde{\sigma}_r(\tilde{r}),\tilde{\sigma}_\vartheta(\tilde{r})$

Both stress terms are decomposed into three contributions, namely those due to growth, $\tilde{\sigma}_r^g(\tilde{r}),\tilde{\sigma}_\vartheta^g(\tilde{r})$, those due to coupling via the growth eigenstrain rate, Eq. (1), $\tilde{\sigma}_r^c(\tilde{r}),\tilde{\sigma}_\vartheta^c(\tilde{r})$, and those due to the surface stress $\tilde{\sigma}_r^{ss}(\tilde{r})$ and $\tilde{\sigma}_\vartheta^{ss}(\tilde{r})$. The first two contributions exist only in rate form. Therefore, only the rates of the total stress terms can be calculated and are derived as the sum of the rates of three contributions.

The rates due to growth follow from [17, Eqs (3.9 a-b)] as

$$\frac{d\tilde{\sigma}_r^g}{d\tau} = -\frac{\nu\left(1-\nu^2\right)\left[1-\tilde{r}_i^2/\tilde{r}^2\right]\tilde{\sigma}_r(1)-\begin{bmatrix}\left(1-\nu^2\right)\tilde{r}_i^2/\tilde{r}^2\\+(1+\nu)^2\tilde{r}_i^2\end{bmatrix}\tilde{\mu}}{(1+\nu)\tilde{r}_i^2+(1-\nu)} - \left(1-\nu^2\right)\tilde{\sigma}_r(\tilde{r})-(1+\nu)\tilde{\mu}, \quad (3.9a)$$

$$\frac{d\tilde{\sigma}_\vartheta^g}{d\tau} = -\frac{\nu\left(1-\nu^2\right)\left[1+\tilde{r}_i^2/\tilde{r}^2\right]\tilde{\sigma}_r(1)-\begin{bmatrix}\left(1-\nu^2\right)\tilde{r}_i^2/\tilde{r}^2\\-(1+\nu)^2\tilde{r}_i^2\end{bmatrix}\tilde{\mu}}{(1+\nu)\tilde{r}_i^2+(1-\nu)} - \left(1-\nu^2\right)\tilde{\sigma}_\vartheta(\tilde{r})-(1+\nu)\tilde{\mu}. \quad (3.9b)$$

Since both rates due to growth, Eqs. (3.9a-b), involve the total stress terms $\tilde{\sigma}_r(\tilde{r}),\tilde{\sigma}_\vartheta(\tilde{r})$ on their r.h.s., both coupling stress terms are derived from $\dot{u}+\nu\dot{u}'/r$ with respect to σ_r^c and $\nu\dot{u}+\dot{u}'/r$ with respect to σ_ϑ^c , using only the contribution $A_c r+B_c/r$ to $\dot{u}$ and not any stress terms, see (B.1), (B.2), (D.2.b), as

$$\frac{d\tilde{\sigma}_r^c}{d\tau} = \tilde{\gamma}\frac{\left(1-\nu^2\right)\tilde{r}_i}{(1+\nu)\tilde{r}_i^2+(1-\nu)}\cdot\left[(1+\nu)+\frac{(1-\nu)}{\tilde{r}^2}\right], \quad (3.10a)$$

$$\frac{d\tilde{\sigma}_\vartheta^c}{d\tau} = \tilde{\gamma}\frac{\left(1-\nu^2\right)\tilde{r}_i}{(1+\nu)\tilde{r}_i^2+(1-\nu)}\cdot\left[(1+\nu)-\frac{(1-\nu)}{\tilde{r}^2}\right]. \quad (3.10b)$$

The stress rates due to surface stress follow from the derivatives of $\tilde{\sigma}_r^{ss}(\tilde{r})$, $\tilde{\sigma}_r^{ss}(\tilde{r})$, Eqs. (3.5a-b), with respect to τ and include, therefore, the rate $d\tilde{r}_i/d\tau$ as

$$\frac{d\tilde{\sigma}_r^{ss}}{d\tau} = -\tilde{\gamma}\frac{(1+\nu)\tilde{r}_i^2-(1-\nu)}{\left[(1+\nu)\tilde{r}_i^2+(1-\nu)\right]^2}\left[(1+\nu)+\frac{(1-\nu)}{\tilde{r}^2}\right]\cdot\frac{d\tilde{r}_i}{d\tau}, \quad (3.11a)$$

$$\frac{d\tilde{\sigma}_\vartheta^{ss}}{d\tau} = -\tilde{\gamma}\frac{(1+\nu)\tilde{r}_i^2-(1-\nu)}{\left[(1+\nu)\tilde{r}_i^2+(1-\nu)\right]^2}\left[(1+\nu)-\frac{(1-\nu)}{\tilde{r}^2}\right]\cdot\frac{d\tilde{r}_i}{d\tau}. \quad (3.11b)$$

Adding now the three contributions together yields finally the initial value problems

$$\frac{d\tilde{\sigma}_r}{d\tau}+\left(1-\nu^2\right)\tilde{\sigma}_r(\tilde{r}) = RHS_r\left(\tilde{r}_i,\tilde{\sigma}_r(1),\frac{d\tilde{r}_i}{d\tau};\tilde{r}\right) \quad (3.12a)$$

$$\frac{d\tilde{\sigma}_\vartheta}{d\tau}+\left(1-\nu^2\right)\tilde{\sigma}_\vartheta(\tilde{r}) = RHS_\vartheta\left(\tilde{r}_i,\tilde{\sigma}_r(1);\frac{d\tilde{r}_i}{d\tau};\tilde{r}\right). \quad (3.12b)$$

The abbreviations RHS_r, RHS_ϑ represent the r.h.s. of the according differential equations, stemming from the sums of r.h.s. of the three contributions, see Eqs. (3.9a-b), (3.10a-b), (3.11a-b), excluding the terms with $\tilde{\sigma}_r(\tilde{r}),\tilde{\sigma}_\vartheta(\tilde{r})$ in Eqs. (3.9a) and (3.9b), resp. The radial distance $\tilde{r}$ can be considered as a parameter. The initial conditions follow as $\tau=0:\tilde{r}_i=1-\delta$, $\tilde{\sigma}_r(\tilde{r}_i)=\tilde{\gamma}$, $\tilde{\sigma}_\vartheta(\tilde{r}_i)=\nu\tilde{\gamma}$ according to Eq. (3.5b).

Remark: The model can also be used to study the case of growth on the outer surface of a cylinder. Since the effect of the surface stress is a compressive radial stress outside, $\tilde{\gamma}$ must be replaced by $-\tilde{\gamma}$ and $\tilde{r}_i$ by $\tilde{r}_o$ everywhere in all the equations of sect. 3.6.

4. Solutions of the evolution equations

4.1 Analytical results and discussion

A significant simplification of the evolution equations can be obtained, if ν is set to 0. This step is followed for both inward and outward growth. The analytic results are also checked by numerical results, for details see sect. 4.2.

4.1.1 Inward Growth

First we deal with the case that $\tilde{\mu}$ (the normalized Helmholtz energy when tissue is formed from nutrient) is set to zero. Eq. (3.7a) then becomes

$$\frac{d\tilde{r}_i^*}{d\tau} = \tilde{\gamma}\frac{\tilde{r}_i^2 - 1}{\tilde{r}_i^2 + 1}. \tag{4.1}$$

Eq. (3.8a) can be written as

$$\frac{d\tilde{r}_i}{d\tau} = \tilde{\gamma}\frac{\tilde{r}_i^2 - 1}{\tilde{r}_i^2 + 1}\left(1 - \tilde{\gamma}\frac{4\tilde{r}_i}{\left(1+\tilde{r}_i^2\right)^2}\right)^{-1}. \tag{4.2}$$

For $\tilde{\gamma} << 1$ and $\tilde{r}_i \le 1$ one can use

$$\left(1 - \tilde{\gamma}\frac{4\tilde{r}_i}{\left(1+\tilde{r}_i^2\right)^2}\right)^{-1} \approx 1 + \tilde{\gamma}\frac{4\tilde{r}_i}{\left(1+\tilde{r}_i^2\right)^2} \approx 1.$$

Then the evolution of the inner radius, described by $\frac{d\tilde{r}_i}{d\tau}$, can be approximated by

$$\frac{d\tilde{r}_i}{d\tau} \approx -\tilde{\gamma}\frac{1-\tilde{r}_i^2}{1+\tilde{r}_i^2}. \tag{4.3}$$

An approximation for the rate of the normalized radial stress follows from (3.7b) and (3.8b) and skipping the $-\tilde{\gamma}^2$ term as

$$\frac{\mathrm{d}\tilde{\sigma}_r(1)}{\mathrm{d}\tau} + \tilde{\sigma}_r(1) \approx \tilde{\gamma}\frac{2\tilde{r}_i}{1+\tilde{r}_i^2}. \tag{4.4}$$

The set of differential equations (4.3), (4.4) can be solved analytically with the initial conditions ($\tau = 0 : \tilde{r}_i = 1-\delta,\ \tilde{\sigma}_r(1) = \tilde{\gamma}$), where $\delta << 1$ is some small perturbation in thickness. For $\tilde{r}_i(\tau)$ one finds by direct integration

$$\tilde{\gamma}\tau = \tilde{r}_i - 1 + \delta + \ln\frac{(1-\tilde{r}_i)}{(1+\tilde{r}_i)} + \ln\frac{(2-\delta)}{\delta}. \tag{4.5}$$

Consequently, $\tilde{\sigma}_r(1)$ can be found also by direct integration using (4.5) in inverted form as

$$\tilde{\sigma}_r(1) = \tilde{\gamma}e^{-\tau}\left(1 + \int_0^{\tau}\frac{2\tilde{r}_i(\tilde{\tau})}{1+\tilde{r}_i^2(\tilde{\tau})}\cdot e^{\tilde{\tau}}\,d\tilde{\tau}\right). \tag{4.6}$$

From Eq. (4.6) one can immediately see that $\tilde{\sigma}_r(1)$ is a positive quantity, $0 \le \tilde{\sigma}_r(1)/\tilde{\gamma} \le 1$. The process stops, when $\tilde{r}_i$ becomes 0 at time τ_f. The upper limit of $\tilde{\sigma}_r(1) = \tilde{\gamma}$ can easily be found by assuming $\tilde{r}_i(\tilde{\tau}) = 1$ in the integrand of (4.6). In addition one can estimate the value of $\tilde{\sigma}_r(1)$ at time τ_f by approximating the rational function $f(\tilde{r}_i) = 2\tilde{r}_i/(1+\tilde{r}_i^2)$ in the integrand of (4.6) by a function $1-(\tilde{\tau}/\tau_f)^m$ with m being a positive exponent. Then one can show, after performing the integration in Eq. (4.6) and some analysis, that $\tilde{\sigma}_r(1)/\tilde{\gamma}$ at

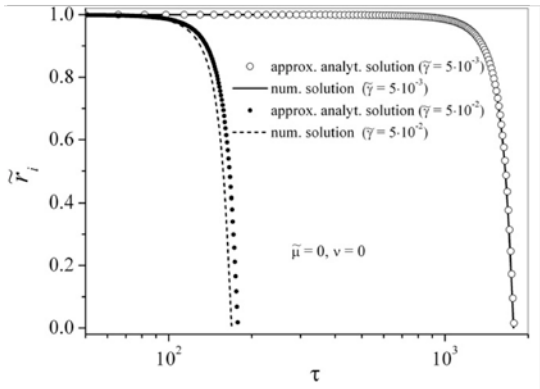

Fig. 3: Comparison of the analytical and the numerical solution. Normalised inner hole radius $\tilde{r}_i(\tau)$ as function of τ for two different values of $\tilde{\gamma}$ with $\tilde{\mu} = 0$ and $\nu = 0$. The initial thickness of the layer is $\delta = 1.10^{-4}$.

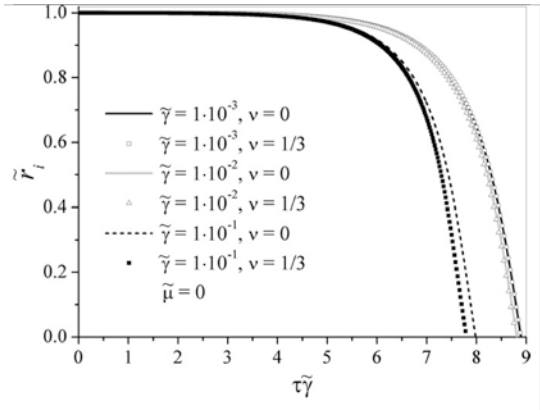

Fig. 4: Normalized inner hole radius $\tilde{r}_i(\tau)$ as function of $\tau\tilde{\gamma}$ for different values of $\tilde{\gamma}$ with $\tilde{\mu} = 0$ and with Poisson's ratio $\nu = 0$, $\nu = 1/3$. The initial thickness of the layer is $\delta = 1\cdot10^{-4}$.

$\tau_f >> 1$ is of the order of magnitude of m/τ_f. This means that $\tilde{\sigma}_r(1)/\tilde{\gamma}$ obtains at time τ_f a rather small value tending to 0 for τ_f tending towards ∞.

Studying the case $\tilde{\mu} \neq 0$, the role of the surface stress term $\tilde{\gamma}$ can be considered as a contribution to the Helmholtz energy term $\tilde{\mu}$, if one checks Eq. (3.7a) together with (3.8a) and skips the terms with $\tilde{\gamma}^2$, yielding

$$\frac{d\tilde{r}_i}{d\tau} = -\left(\tilde{r}_i\tilde{\mu} + \tilde{\gamma}\right)\frac{\left(1-\tilde{r}_i^2\right)}{\left(1+\tilde{r}_i^2\right)}. \tag{4.7}$$

In the starting period of the hole closing process $\tilde{r}_i$ is near 1, and we have $\tilde{\mu} + \tilde{\gamma}$ as driving forces; in the final period we have only $\tilde{\gamma}$. A further consequence is that we have for $\tilde{\mu} = 0$ a growth process, if $\tilde{\gamma}$ is present. The analytical solution and the numerical

solution are almost identical for small values of $\tilde{\gamma}$ as can be seen from Fig. 3.

Finally, one can deduce from the differential equations (4.4) and (4.7) that some scaling parameters control the development of the system:

- If we introduce the time parameter $\tau\tilde{\gamma}$ in (4.7), only the scaling parameter $\tilde{\mu}/\tilde{\gamma}$ controls the evolution of $\tilde{r}_i$ with respect to $\tau\tilde{\gamma}$.
- If we introduce the stress parameter $\tilde{\sigma}_r(1)/\tilde{\gamma}$, then, according to (3.7b) and (3.8b), again only the scaling parameters $\tilde{\mu}/\tilde{\gamma}$ controls the evolution of $\tilde{\sigma}_r(1)/\tilde{\gamma}$ with respect to τ . Of course, a preposition for such a scaling is $\tilde{\gamma} \neq 0$.
- If $\tilde{\mu} = 0$, one may conclude that no scaling exists. However, one should keep in mind that Poisson's ratio ν still plays a role in the case that it is not set to zero as considered above.

4.1.2 Outward growth

The structure of the evolution equations for $\tilde{r}_i$ and $\tilde{r}_0$ is demonstrated best by the simplified situation that $\tilde{\mu}$ (the normalized Helmholtz energy when tissue is formed from nutrient) is set to zero. Furthermore, $\tilde{\gamma}$ must be replaced by $-\tilde{\gamma}$ for the case of outward growth. The differential equation (4.7) shows clearly the asymmetry of the problem solution and is repeated for

the inner growth $\frac{d\tilde{r}_i}{d\tau} = -\tilde{\gamma}\frac{1-\tilde{r}_i^2}{1+\tilde{r}_i^2}$, (4.8a)

the outer growth $\frac{d\tilde{r}_o}{d\tau} = -\tilde{\gamma}\frac{\tilde{r}_o^2-1}{\tilde{r}_o^2+1}$. (4.8b)

In both cases the rates $d\tilde{r}_i/d\tau$, $d\tilde{r}_o/d\tau$ are negative, meaning no outer growth is possible. Eq. (4.7) teaches immediately that for $d\tilde{r}_o/d\tau > 1$ the quantity $\tilde{\mu}$ must be greater than $\tilde{\gamma}, \tilde{\mu} \geq \tilde{\gamma}$, to allow for an outside growth process at $\tilde{r}_o = 1$. Therefore, one needs as additional driving force the modified chemical potential $\tilde{\mu} > |\tilde{\gamma}|$ in the case of outside growth!

4.2 Numerical results and discussion

The coupled equations for the evolution of the hole radius $\tilde{r}_i$, Eq. (3.8a), and the radial stress at the outer wall $\tilde{\sigma}_r(1)$, Eq. (3.8b), were integrated numerically for different values of $\tilde{\gamma}$.

According to the discussion on scaling parameters in Sect. 4.1.1 the radial position of the (inner) tissue-medium boundary $\tilde{r}_i(\tau)$ is plotted in Fig. 4 against

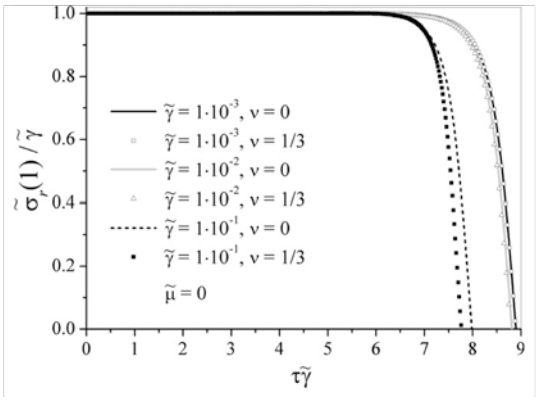

Fig. 5: Normalized outer radial stress $\tilde{\sigma}_r(1)/\tilde{\gamma}$ as function of $\tau\tilde{\gamma}$ for different values of $\tilde{\gamma}$ and $\tilde{\mu} = 0$ with a Poisson's ratio $\nu = 0$, $\nu = 1/3$. The initial thickness of the layer is $\delta = 1\cdot10^{-4}$.

$\tau\tilde{\gamma}$ for $\tilde{\mu} = 0, \nu = 0$ and $1/3$, and various values of $\tilde{\gamma}$. The curves to $\nu = 0$ and $\nu = 1/3$ nearly coincide for a certain $\tilde{\gamma}$ value.

A corresponding study is performed for the radial stress $\tilde{\sigma}_r(1)$ as a diagram of $\tilde{\sigma}_r(1)/\tilde{\gamma}$ versus $\tau\tilde{\gamma}$. Here we use a common time-axis $(\tau\tilde{\gamma})$, so that the plots for $\tilde{r}_i$ and $\tilde{\sigma}_r(1)$ can directly be compared with respect to the time parameter. Again two nearly coinciding curves to $\nu = 0$ and $\nu = 1/3$ for certain $\tilde{\gamma}$ values can be observed in Fig. 5.

From the experimental point of view, the circumferential stress component $\tilde{\sigma}_\vartheta$ is the quantity, which is easiest to be compared with experimental data as it is related to the concentration of actin stress-fibres in the tissue. Since the inner radius r_i or $\tilde{r}_i$ in dimension-free form is that position, where the surface stress is acting, the value of $\tilde{\sigma}_\vartheta(\tilde{r}_i)$ is provided. For $\tilde{\mu} = 0$ and $\nu = 0$ it is possible to use Eq. (4.3) in combination with Eq. (3.12b) for inward growth. This fact allows for an easy integration of Eq. (3.12b). Fig. 6 demonstrates $\tilde{\sigma}_\vartheta(\tilde{r}_i)/\tilde{\gamma}$ as a function of $\tilde{r}_i$. In addition the circumferential stress component $\tilde{\sigma}_\vartheta^{ss}(\tilde{r}_i)$ only due to the surface stress is depicted, see Eq. (3.5b) for $\nu = 0$. One can report the following facts:

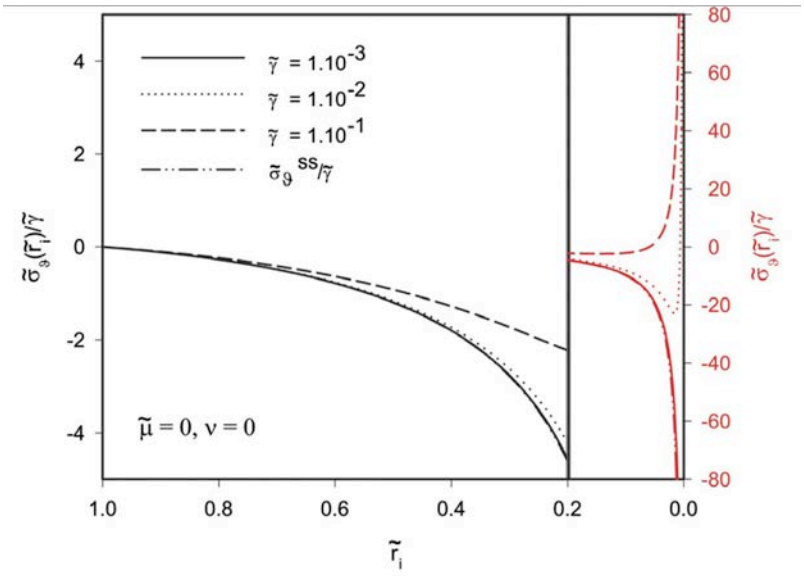

Fig. 6: Circumferential stress $\tilde{\sigma}_\vartheta(\tilde{r}_i)/\tilde{\gamma}$ at the inner hole radius as function of the normalised inner hole radius $\tilde{r}_i$ for different values of $\tilde{\gamma}$ with $\tilde{\mu}=0$, $\nu=0$. The curve $\tilde{\sigma}_\vartheta^{ss}/\tilde{\gamma}$ demonstrates the role of surface stress only. The right hand side of the graph is shown in red at a different scale. The initial thickness of the layer was $\delta = 1\cdot 10^{-4}$.

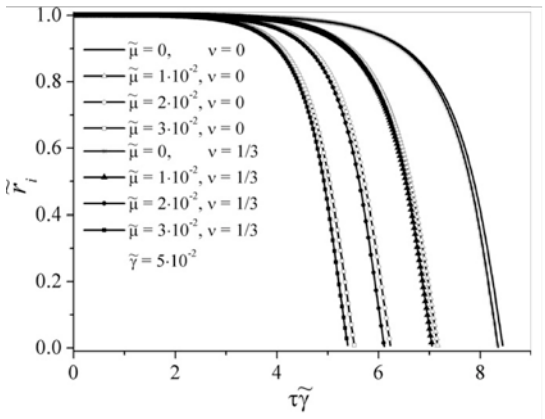

Fig. 7: Normalised inner hole radius $\tilde{r}_i(\tau)$ as a function of $\tau\tilde{\gamma}$ for a fixed value of $\tilde{\gamma}$ and with different values of $\tilde{\mu}$ and with Poisson's ratio $\nu = 0, \nu = 1/3$. The initial thickness of the layer is $\delta = 1\cdot 10^{-4}$.

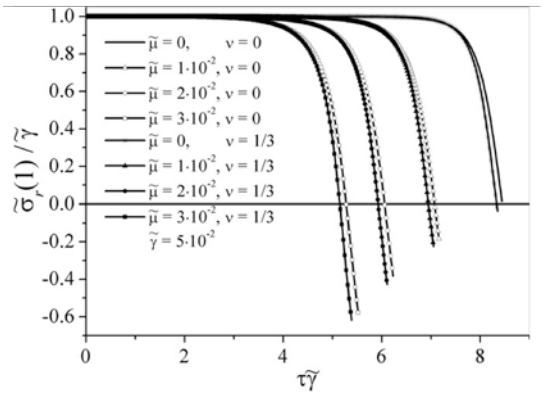

Fig. 8: Normalised outer radial stress $\tilde{\sigma}_r(1)/\tilde{\gamma}$ as a function of $\tau\tilde{\gamma}$ for different values of $\tilde{\mu}$ and with Poisson's ratio $\nu = 0, \nu = 1/3$. The initial thickness of the layer is $\delta = 1\cdot 10^{-4}$.

- Over a wide range of $\tilde{r}_i$ $\left(\tilde{r}_i > 0.2\right)$ the circumferential stress $\tilde{\sigma}_\vartheta\left(\tilde{r}_i\right)$ is mainly controlled by the surface stress. For small values of $\tilde{\gamma}$ (i.e. $\tilde{\gamma} = 1\cdot 10^{-3}$) the surface stress only is responsible for $\tilde{\sigma}_\vartheta\left(\tilde{r}_i\right)$ over the whole range of $\tilde{r}_i$. An order of magnitude estimate for $\tilde{\gamma}$ is obtained by the following reasoning. By using literature data (for murine sarcoma cell aggregates as published in Guevorkian et al [42]) we can get an estimate for the range of surface energies measured in culture. These authors measured a surface tension of $6\cdot 10^{-3}\,\mathrm{Nm}^{-1}$, which when (normalised according to our notation) by the stiffness (~ 100 Pa) and the actual pore radius (~ 1 mm in our experiments) gives a normalised value $\tilde{\gamma} \approx 6\times 10^{-2}$. Of course it must be kept in mind that these values could differ considerably as the stiffness alone would depend on the maturity of the tissue produced. Currently it is not possible to measure the tissue stiffness inside the small pores used in the experiments.
- For low values of $\tilde{r}_i$, say $\tilde{r}_i < 0.2$, the interaction of the surface stress with the growth process becomes more and more relevant, see the right part of Fig. 6, and even may turn the circumferential stress $\tilde{\sigma}_\vartheta\left(\tilde{r}_i\right)$ into the tension regime. However, the closing of a rather small hole $\left(\tilde{r}_i < 0.2\right)$

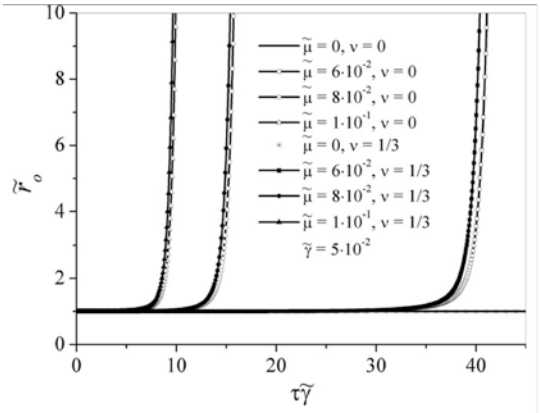

Fig. 9: Growth starting from the outer surface of the cylinder. Normalized outer cylinder radius $\tilde{r}_o(\tau)$ as function of $\tau\tilde{\gamma}$ for different values of $\tilde{\mu}$ and with Poisson's ratio $\nu = 0$, $\nu = 1/3$. The initial thickness of the layer is $\delta = 1 \cdot 10^{-4}$.

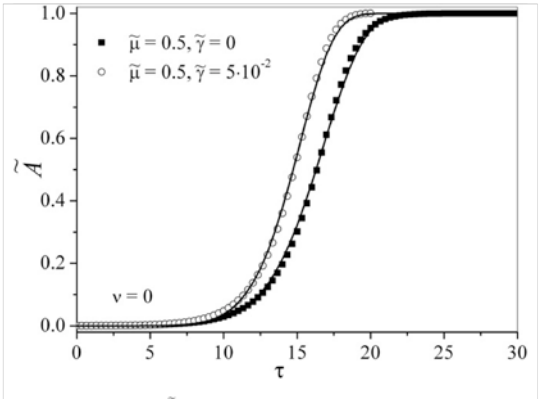

Fig. 11: Normalized area $\tilde{A}$ versus normalized time τ for $\tilde{\mu} = 0.5$. The surface stress $\tilde{\gamma}$ is set to 0 and 0.5, resp.; $\nu = 0$. The initial thickness of the layer is $\delta = 1 \cdot 10^{-4}$.

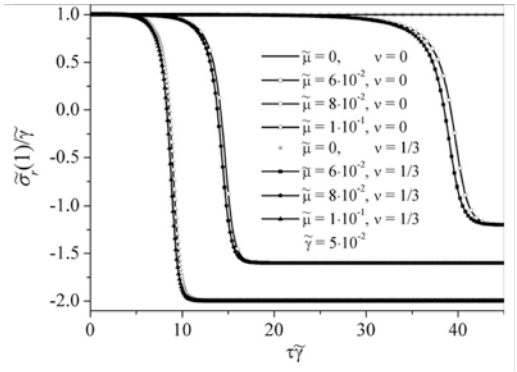

Fig. 10: Growth starting from the outer surface of the cylinder. Normalized radial stress, $\tilde{\sigma}_r(1)/\tilde{\gamma}$ as function of $\tau\tilde{\gamma}$ for different values of $\tilde{\mu}$ and with Poisson's ratio $\nu = 0$, $\nu = 1/3$. The initial thickness of the layer is $\delta = 1 \cdot 10^{-4}$.

occurs extremely fast, see Fig. 4, so that some other effects may appear which overtake the "closing process".

Figures 7 to 10 demonstrate the influence of the scaling parameter $\tilde{\mu}/\tilde{\gamma}$ for one fixed value of $\tilde{\gamma}$. Four values are considered for $\tilde{\mu}/\tilde{\gamma}$, namely 0, 0.2, 0.4, 0.6. Furthermore, two sets of curves are presented, one for $\nu = 0$ and the other one for $\nu = 1/3$. Fig. 7 and Fig. 9 demonstrate the growth of the inner radius $\tilde{r}_i$ and outer radius $\tilde{r}_o$, resp., versus $\tau\tilde{\gamma}$. Fig. 8 and Fig. 10 demonstrate the development of $\tilde{\sigma}_r(1)/\tilde{\gamma}$ for inner and outer growth, resp., versus $\tau\tilde{\gamma}$.

5. Conclusions and Remarks

5.1 Area growth

Experimentalists may also be interested in the evolution of the grown area, represented by the dimension-free quantity $\tilde{A} = 1 - \tilde{r}_i^2$ (or for outside growth $\tilde{r}_o^2 - 1$). Then Eq. (4.3) can be converted to the form

$$\frac{d\tilde{A}}{d\tau} = 2\tilde{\gamma}\frac{\tilde{A}\sqrt{1-\tilde{A}}}{2-\tilde{A}} \quad . \tag{5.1}$$

Plotting the normalised area $\tilde{A}$ versus normalised time τ shows sigmoidal-shaped (trans)formation curves. These curves can be fitted by the Johnson-Mehl-Avrami (JMA) equation as

$$\tilde{A} = 1 - \exp(-k\tau^n) \tag{5.2}$$

with k and n being fitting parameters.

The normalised area $\tilde{A}$ for inner growth is plotted versus time τ for two cases in Fig. 11, one with surface stress $\tilde{\gamma} = 0.5$ (calculated points are represented by open circles) and one without surface stress $\tilde{\gamma} = 0$ (calculated points are represented by full squares). The normalised chemical potential $\tilde{\mu}$ is set to 0.5 in both cases. The lines are the JMA-fitting curves. In case of zero surface stress, $\tilde{\gamma} = 0$, the fitting parameters $k = 2.28 \cdot 10^{-9}$ and $n = 7$ are calculated; for $\tilde{\gamma} = 0.5$ an appropriate fit can be found by $k = 1.20 \cdot 10^{-9}$ and a slightly higher value of $n = 7.5$. One may argue that the relevance of these parameters k and n is limited with respect to the physics behind. However, it is interesting to note that the kinetics of tissue growth can be described by two parameters, which can be determined in case of underlying experimental data.

The time dependence of the (trans)formed volume fraction, when investigating the kinetics of diffusive phase transformations in solids, is frequently also captured by JMA-fits. Thus, a method used in metallurgy since many decades could also be helpful describing the kinetics of tissue growth. The numerical exponent n varies from 1 to 4 in case of diffusive phase transformations of metals as can be found in [43]. If the kinetics of tissue growth is

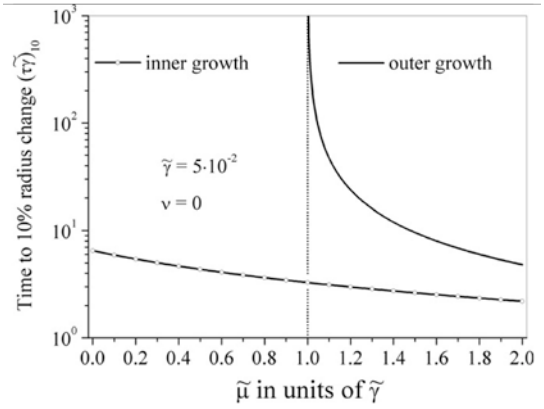

Fig. 12. Time to 10% radius change as function of $\tilde{\mu}$ in units of $\tilde{\gamma}$ for $\tilde{\gamma} = 5 \cdot 10^{-2}$, and $\nu = 0$, for tissue growth on the inner surface of a cylinder (inner growth) and on the outer surface of a cylinder (outer growth), which is only possible for $\tilde{\mu}/\tilde{\gamma} \geq 1$.

described by JMA equations, the exponent n appears to be significantly higher. Here a value of 7 is obtained in case of zero surface stress, and this value becomes even higher in case of surface stress considered. As tissue growth not only depends on the difference of the chemical potentials of nutrient and tissue but is to a large extent stress-driven, the higher values of n can be, at least, understood qualitatively. The main reason for this difference may have its origin in the totally different mechanisms of growth in both compared cases. In the case of relatively thin layers of tissue, diffusion of nutrient will play only a limited role and growth will rather controlled by the amount of surface stress and the cell activity. At early time points the nature of the substrate may play a role in cell colonisation [16], although this is not addressed in the current model.

Concerning inward growth one may be interested in how the growth process proceeds after the hole has closed. We have then a disk without a hole and a residual stress state $\tilde{\sigma}_r = \tilde{\sigma}_r^0, \tilde{\sigma}_\vartheta = \tilde{\sigma}_\vartheta^0$ at the dimensionless time $\tilde{\tau} = 0$, which is counted from the time period after hole closure. We deal now with a full disk, which is fixed at the outer radius $\tilde{r} = 1$. The further derivations are based on Sect. 3.3 with $B = 0$ in (3.3) and outlined in detail in the Appendix E. Below one finds a collection of the must important relations, which are formulated for $\nu = 0$ as

$$\tilde{\sigma}_r + \tilde{\mu} = \left(\tilde{\sigma}_r^0 + \tilde{\mu}\right)\exp\left(-\tilde{\tau}\right), \qquad (5.3a)$$

$$\tilde{\sigma}_\vartheta + \tilde{\mu} = \left(\tilde{\sigma}_\vartheta^0 + \tilde{\mu}\right)\exp\left(-\tilde{\tau}\right). \qquad (5.3b)$$

The growth strains $\tilde{g}_r$, $\tilde{g}_\vartheta$ (- both quantities are the components of the vector **g** in Eq. (1)-) after hole closing read

$$\tilde{g}_r = \left(\tilde{\sigma}_r^0 + \tilde{\mu}\right)\left(1 - \exp\left(-\tilde{\tau}\right)\right), \qquad (5.4a)$$

$$\tilde{g}_\vartheta = \left(\tilde{\sigma}_\vartheta^0 + \tilde{\mu}\right)\left(1 - \exp\left(-\tilde{\tau}\right)\right). \qquad (5.4b)$$

The total strain ε_r, ε_ϑ, as sum of the growth strain and the elastic strain, yields the area strain

$$\varepsilon_A = \tilde{\varepsilon}_r + \tilde{\varepsilon}_\vartheta = \sigma_r^0 + \sigma_\vartheta^0. \qquad (5.5)$$

Note that all quantities above are functions of $\tilde{r}$ except the quantity $\tilde{\mu}$.

Obviously the area strain (5.5) for $\nu = 0$ remains unchanged and keeps to its value immediately after hole closure, although the stress state and consequently the growth strain state rearrange themselves during further growth. In other words, for $\nu = 0$ the area strain remains unchanged after the hole is closed. For $\nu \neq 0$ Eq. (E7.2) yields an area strain varying in time but in the same order of magnitude as Eq. (5.5).

5.2 Control of growth

The analysis, described in Section 4 and depicted in Figures 7 to 10, demonstrates that growth is controlled by the ratio $\tilde{\mu}/\tilde{\gamma}$. The asymmetry between inner and outer growth becomes clearer in Figure 12 which depicts the time taken (in units $\tau\tilde{\gamma}$) for growth to result in a 10% radius change as a function of $\tilde{\mu}$ in units of $\tilde{\gamma}$. This diagram can be viewed as a proxy for growth speed as a function of the control parameter $\tilde{\mu}/\tilde{\gamma}$. Changing $\tilde{\gamma}$ leads to no qualitative changes in the curves (data not shown). For inner growth at a fixed value of $\tilde{\gamma} = 5 \cdot 10^{-2}$ the growth speed slowly increases (or the time for growth decreases) with increasing driving force $\tilde{\mu}$. In this case, the surface stress acts in the same direction as the driving force which accelerates growth. For outer growth, however, the driving force for growth acts against the surface stress. This leads to a divergence in the time for 10% radial change at $\tilde{\mu}/\tilde{\gamma} = 1$. For control parameters below this ratio no growth is observed. Approaching tissue growth as a competition between a driving force for cell proliferation and extracellular matrix production versus an effective surface stress induced by contractile cells may well be a useful approach. In principle these parameters can be varied experimentally, for example by inhibiting actomyosin contractility in the cells as done by Bischofs et al. [44] or by varying nutrient availability.

5.3 Some final remarks

We want to emphasize that we do not use an extra surface growth term by an according eigenstrain rate as e.g. [30]. However, we "reflect" the role of surface by a surface stress, which is directly transferred by the cells acting on and near the surface. The radial stress σ_r at the positions r_i or r_o, namely $\sigma_r = \gamma / r_i$ or $-\gamma / r_o$, is the conjugate mechanical quantity to the physical and biologically reality of cells acting as "contractile elements". We consider this point of view as directly related to and motivated by the experimental observation.

The presence of a compressive stress component (e.g. the circumferential stress component, see Fig. 6) may give rise to the question if a structural instability may occur, e.g. the formation of a wavy hole contour. Since such a phenomenon has not yet been observed for an axisymmetrical geometrical setting, we leave this topic to a future study. However, it should be mentioned that most recently three studies concerning growth and structural stability have been published, [45-47]. In these studies, the situation is insofar simplified, as a constant growth eigenstrain

and not an eigenstrain rate, depending on the chemistry and the stress state as Eq. (1), is used.

Acknowledgements

P.F. and E.G. are grateful for support by the Alexander von Humboldt Foundation and the Max Planck Society in the framework of the Max Planck Research Award funded by the Federal Ministry of Education and Research. F.D.F. acknowledges support made possible through the Humboldt Research Award. C. B. is a member of the Berlin-Brandenburg School for Regenerative Therapies (GSC 203).

References

[1] Engler AJ, Sen S, Sweeney HL, Discher DE. Matrix elasticity directs stem cell lineage specification. Cell 2006;126:677-89.

[2] Discher DE, Janmey P, Wang YL. Tissue cells feel and respond to the stiffness of their substrate. Science 2005;310:1139-43.

[3] Huebsch N, et al. Harnessing traction-mediated manipulation of the cell/matrix interface to control stem-cell fate. Nat Mater 2010;9:518-26.

[4] Gilbert PM, et al. Substrate elasticity regulates skeletal muscle stem cell self-renewal in culture. Science 2010;329:1078-81.

[5] Gentile F, et al. Cells preferentially grow on rough substrates. Biomaterials 2010;31:7205-12.

[6] Arnold M, et al. Cell interactions with hierarchically structured nano-patterned adhesive surfaces. Soft Matter 2009;5:72-7.

[7] Cavalcanti-Adam EA, Volberg T, Micoulet A, Kessler H, Geiger B, Spatz JP. Cell spreading and focal adhesion dynamics are regulated by spacing of integrin ligands. Biophys J 2007;92:2964-74.

[8] Chen CS, Mrksich M, Huang S, Whitesides GM, Ingber DE. Geometric control of cell life and death. Science 1997;276:1425-8.

[9] Kilian KA, Bugarija B, Lahn BT, Mrksich M. Geometric cues for directing the differentiation of mesenchymal stem cells. Proc Natl Acad Sci USA 2010;107:4872-7.

[10] Thery M, Pepin A, Dressaire E, Chen Y, Bornens M. Cell distribution of stress fibres in response to the geometry of the adhesive environment. Cell Motil Cytoskeleton 2006;63:341-55.

[11] Cukierman E, Pankov R, Stevens DR, Yamada KM. Taking cell-matrix adhesions to the third dimension. Science 2001;294:1708-12.

[12] Kollmannsberger P, Bidan CM, Dunlop JWC, Fratzl P. The physics of tissue patterning and extracellular matrix organisation: how cells join forces. Soft Matter 2011;7:9549-60.

[13] Nelson CM, et al. Emergent patterns of growth controlled by multicellular form and mechanics. Proc Natl Acad Sci USA 2005;102:11594-9.

[14] Rumpler M, Woesz A, Dunlop JWC, van Dongen JT, Fratzl P. The effect of geometry on three-dimensional tissue growth. J Roy Soc Int 2008;5:1173-80.

[15] Bidan CM, et al. How linear tension converts to curvature: geometric control of bone tissue growth. Plos One 2012;7:e36336.

[16] Kommareddy KP, et al. Two stages in three-dimensional in vitro growth of tissue generated by osteoblastlike cells. Biointerphases 2010;5:45-52.

[17] Dunlop JWC, Fischer FD, Gamsjäger E, Fratzl P. A theoretical model for tissue growth in confined geometries. J Mech Phys Sol 2010;58:1073-87.

[18] Ripamonti U, Roden L. Biomimetics for the induction of bone formation. Expert Rev Med Devic 2010;7:469-79.

[19] Ripamonti U, Roden LC, Renton LF. Osteoinductive hydroxyapatite-coated titanium implants. Biomaterials 2012;33:3813-23.

[20] Shapiro F. Bone development and its relation to fracture repair. The role of mesenchymal osteoblasts and surface osteoblasts. Eur Cells Mater 2008;15:53-76.

[21] Kerschnitzki M, Wagermaier W, Liu YF, Roschger P, Duda GN, Fratzl P. Poorly Ordered Bone as an Endogenous Scaffold for the Deposition of Highly Oriented Lamellar Tissue in Rapidly Growing Ovine Bone. Cells Tissues Organs 2011;194:119-23.

[22] Schuckert KH, Osadnik M. Bone tissue engineering in oral surgery: a new method of bone development in periodontal surgery. Tissue Eng Part C Methods 2011;17:1179-87.

[23] Jinnai H, Watashiba H, Kajihara T, Nishikawa Y, Takahashi M, Ito M. Surface curvatures of trabecular bone microarchitecture. Bone 2002;30:191-4.

[24] Ambrosi D, Guana F. Stress-modulated growth. Math Mech Sol 2007;12:319-42.

[25] Ambrosi D, Guillou A. Growth and dissipation in biological tissues. Cont Mech Thermodyn 2007;19:245-51.

[26] Ambrosi D, et al. Perspectives on biological growth and remodeling. J Mech Phys Sol 2011;59:863-83.

[27] Epstein M, Maugin GA. Thermomechanics of volumetric growth in uniform bodies. Int J Plast 2000;16:951-78.

[28] Onsager L. Reciprocal relations in irreversible processes. I. Phys Rev 1931;37:405-26.

[29] Svoboda J, Turek I, Fischer FD. Application of the thermodynamic extremal principle to modeling of thermodynamic processes in material sciences. Philos Mag 2005;85:3699-707.

[30] Ganghoffer J-F. Mechanical modeling of growth considering domain variation—Part II: Volumetric and surface growth involving Eshelby tensors. J Mech Phys Sol 2010;58:1434-59.

[31] Loret B, Simoes FMF. Elastic-growing tissues: A growth rate law that satisfies the dissipation inequality. Mech Mater 2010;42:782-96.

[32] Hodge N, Papadopoulos P. A continuum theory of surface growth. Proc Roy Soc A 2010;466:3135-52.

[33] Lecuit T, Lenne PF. Cell surface mechanics and the control of cell shape, tissue patterns and morphogenesis. Nat Rev Mol Cell Biol 2007;8:633-44.

[34] Graner F, Glazier JA. Simulation of biological cell sorting using a 2-dimensional extended Potts-model. Phys Rev Lett 1992;69:2013-6.

[35] Maree AFM, Hogeweg P. How amoeboids self-organize into a fruiting body: Multicellular coordination in Dictyostelium discoideum. Proc Natl Acad Sci USA 2001;98:3879-83.

[36] Krieg M, et al. Tensile forces govern germ-layer organization in zebrafish. Nat Cell Biol 2008;10:429-U122.

[37] Käfer J, Hayashi T, Marée AFM, Carthew RW, Graner F. Cell adhesion and cortex contractility

determine cell patterning in the Drosophilaretina. Proc Natl Acad Sci USA 2007;104:18549-54.
[38] Cammarata RC. Surface and Interface Stress Effects in Thin-Films. Prog Surf Sci 1994;46:1-38.
[39] Fischer FD, Waitz T, Vollath D, Simha NK. On the role of surface energy and surface stress in phase-transforming nanoparticles. Prog Mater Sci 2008;53:481-527.
[40] Hecquet P. Stability of vicinal surfaces and role of the surface stress. Surf Sci 2010;604:834-52.
[41] Kondepudi D, Prigogine I. Modern thermodynamics. From heat engines to dissipative structures. Chichester: John Wiley and Sons; 1998.
[42] Guevorkian K, Colbert MJ, Durth M, Dufour S, Brochard-Wyart F. Aspiration of Biological Viscoelastic Drops. Phys Rev Lett 2010;104:218101.
[43] Porter DA, Easterling KE, Sherif MY. Transformations in Metals and Alloys. 3rd Edition ed. Boca Raton: CRC Press, Taylor and Francis; 2009.
[44] Bischofs I, Klein F, Lehnert D, Bastmeyer M, Schwarz U. Filamentous Network Mechanics and Active Contractility Determine Cell and Tissue Shape. Biophys J 2008;95:3488-96.
[45] Moulton DE, Goriely A. Circumferential buckling instability of a growing cylindrical tube. J Mech Phys Sol 2011;59:525-37.
[46] Dervaux J, Ben Amar M. Buckling condensation in constrained growth. J Mech Phys Sol 2011;59:538-60.
[47] Li B, Cao YP, Feng XJ, Gao JJ. Surface wrinkling of mucosa induced by volumetric growth: Theory, simulation and experiment. J Mech Phys Sol 2011;59:758-74.

7.7 [TG7] Tissue growth controlled by geometric boundary conditions: a simple model recapitulating aspects of callus formation and bone healing

Fischer, F. D., Zickler, G., Dunlop, J. W. C., Fratzl, P.

*Published in **Journal of the Royal Society Interface**, 2015, 12, 20150108.*
Doi: 10.1098/rsif.2015.0108

Reprinted with permission from the Royal Society

Abstract: The shape of tissues arises from a subtle interplay between biochemical driving forces, leading to cell growth, division and extracellular matrix formation, and the physical constraints of the surrounding environment, giving rise to mechanical signals for the cells. Despite the inherent complexity of such systems, much can still be learnt by treating tissues which constantly remodel, as simple fluids. In this approach remodeling relaxes all internal stresses except for the pressure which is counterbalanced by the surface stress. Our model is used to investigate how wettable substrates influence the stability of tissue nodules. It turns out for a growing tissue nodule in free space, the model predicts only two states: either the tissue shrinks and disappear, or it keeps growing indefinitely. However as soon as the tissue wets a substrate, stable equilibrium configurations become possible. Furthermore by investigating more complex substrate geometries, such as tissue growing at the end of a hollow cylinder, we see features reminiscent of healing processes in long bones, such as the existence of a critical gap size above which healing does not occur. Despite its simplicity, the model may be useful in describing various aspects related to tissue growth, including biofilm formation and cancer metastases.

Introduction

Morphogenesis is controlled via the complex interaction between biochemical and mechanical signals arising from cell generated tensions (1, 2). Such signaling is mediated through the presence of boundaries, whose shapes determine the formation of morphogen gradients (3) and the local stress state, which in turn controls cell proliferation (4), differentiation (5) and apoptosis (6, 7). Depending on the physical environment, these boundaries may either be static, as is the case for solid substrates, or they may move as new tissue is formed (8). One important simplification that can be made to help understand this problem, is based on the observation that tissues, or at least cell agglomerates, can behave like viscous fluids with measureable surface tensions when observed for sufficiently long time scales (9-12). If one describes tissues as fluids, then the equilibrium shape of their boundaries will be determined on one hand by the wettability of any substrates upon which they are sitting (13) and on the other hand by the Laplace-Young equation giving a link between interfacial curvature and tissue pressure (14). Interestingly, it has been shown that even simple shapes of wettable regions on flat substrates display a rich variety of equilibrium liquid droplet morphologies at constant volume when surface tension plays an important role in the energy of the system (15-17). This suggests the possibility of a similar richness for fluid-like tissues growing under the influence of large surface tensions. As the stress state of cells is coupled to growth (18, 19) an exploration of the consequence of geometric boundary conditions on surface tension mediated growth may help explain the observed influence of shape on tissue growth in-vitro (20, 21) and in-vivo (22, 23), the goal of this paper.

Many physical models for tissue growth have been studied previously (see, e.g. (8, 24, 25)) and they often use rather subtle material models, including second gradient approaches, see e.g. (26, 27) and (28) for a recent overview. To simplify our model however we simplify the material behavior to that of an ideal fluid (i.e. constant pressure), which relaxes local stress concentrations by viscous flow at a rate much faster than the growth which causes them. Since in our case growth dominates over elastic deformations we can also avoid treating potential coupling between the two (see, e.g., (29-31)). We start with a simple approach fully compatible with thermodynamics (32-36) which considers both a biochemical driving force (in the form of a chemical potential) and a mechanical one (including volume stresses as well as surface stresses). Then we assume that local tissue remodeling is sufficiently rapid compared to the growth rate, so that the tissue can essentially be regarded as an ideal fluid on the time-scale of growth. By local tissue remodeling we describe the processes by which cells can rearrange their orientation and position with respect to each as well as to move, reorient and degrade the extracellular matrix in which they are sitting. The driving force for remodeling has its origin in the thermodynamics of the irreversible process controlled by the dissipation; for details we refer to (36) and the contributions by Ambrosi et al., e.g. (24, 33, 34). With these assumptions, we show that the problem reduces to a single free parameter interpreted as a critical curvature for tissue growth. This critical curvature is given by the ratio of the chemical potential, describing the tendency of the tissue to grow as a result of biochemical signals (e.g. growth factors), and the surface energy, which leads to a tissue pressure that may inhibit or accelerate growth. The appearance of surface energy in the critical curvature means that geometric boundary conditions may play an important role on growth, a major focus of this paper. For the following we assume that the tissue fully wets a given surface and explore the role of surface shape on the resultant growth. Our problem is thus related to the evolution of droplets interacting with partially wettable surfaces (15-17), where growth corresponds to an increase of the droplet volume. We first investigate the growth of an unsupported volume of

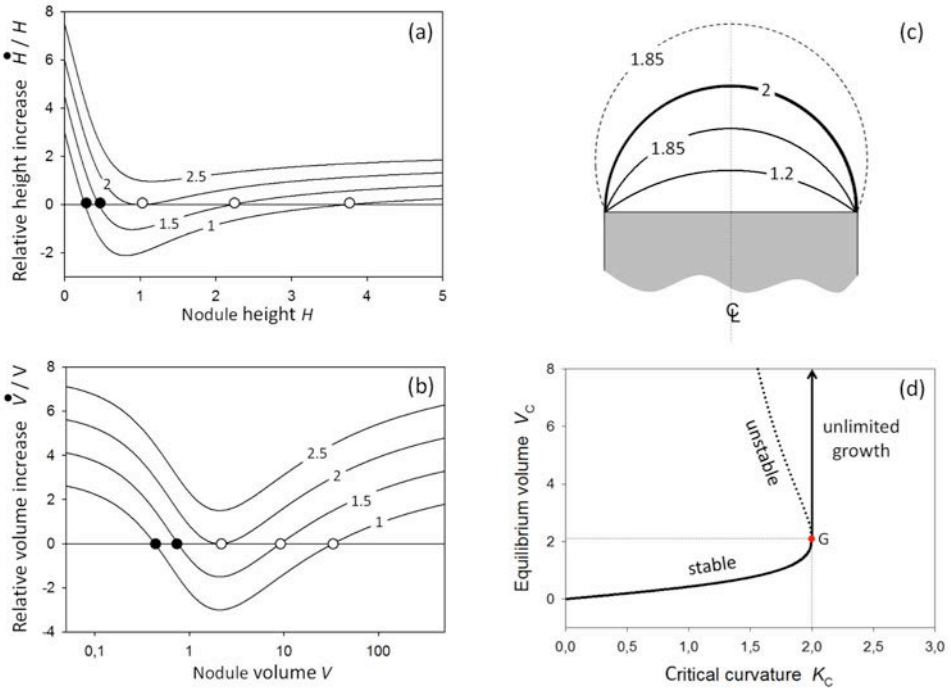

Figure 1: The relative rates of the increase in (a) height (Eq. (7)), and (b) volume (Eq. (5)), for spherical nodules sitting on top of a full cylinder. Numbers indicate the value critical curvature K_C used to calculate each curve. (c) Spherical nodules sitting on top of a full cylinder for several cross sections marked by the values of their curvature K. When $K = 2$, the height of the nodule, H, is equal to the cylinder radius, R_O. Note that for every curvature, there are two possible configurations, smaller or larger than the half sphere corresponding to $K = 2$ (as shown for the example with $K = 1.85$). (d) Graph of the equilibrium volume V_C of a nodule sitting on top of a full cylinder of radius 1, as a function of the biochemical driving force (i.e. the critical curvature) K_C. The point G is the limit for stable growth where unlimited growth starts. The branch corresponding to unstable equilibria (open circles in (a,b)) is shown by a broken line.

tissue (or nodule) and then its growth upon a circular disk, this analysis is then extended to tissue growth on a circular ring. Despite the simplicity of the geometries analyzed, tissues grow into shapes with exquisite complexity with many aspects emulating what can be observed in callus formation and evolution during bone healing. We compare some of the predictions of the model to the kinetics of bone healing in various mammalian species and to the existence of a critical defect size above which healing is prevented. The surprising level of coincidence suggest that during bone healing cells might indeed behave like liquids and thus profit from the self-organization capacities of wetting and surface tension.

Formulation of the model hypotheses

We use the formalism for growth outlined in (35, 36) but assume that the growing body behaves like an ideal fluid, with a defined surface stress γ, for details see (14). This relies on the assumption that there are three separable time scales, that of growth, remodeling and elasticity. The typical time for growth is taken to be much longer than the relaxation of stresses by tissue remodeling processes. If the body behaves like an ideal fluid (at long time scales), and is subjected to a constant surface stress, then the shape of the body will have a constant surface mean curvature when in mechanical equilibrium. This is formulated by the Laplace-Young equation, $p = \gamma K$, where p is the pressure acting in the body, γ is the surface stress (assumed to have the same value as the surface energy) and K is the surface curvature (defined as the absolute value of the trace of the curvature tensor or twice the surface mean curvature); for details see, e.g., (14). For simple geometric boundary conditions the equilibrium fluid shape can be calculated analytically, giving curves that relate pressure (or curvature) to volume, for more complex geometries numerical solutions such as "Surface Evolver" (37) can be used.

Once the relation between pressure (or surface curvature) and volume is known for a given tissue geometry in mechanical equilibrium, then we can analyze its stability under the conditions of growth. We do this in the following using the equation of growth $\dot{\mathbf{g}} = f\left(\boldsymbol{\sigma} - \bar{\mu} e_0 \mathbf{I}\right)$ from (35). Here $\mathbf{g}$ is the growth eigenstrain tensor, $\boldsymbol{\sigma}$ the stress tensor which is given as $-p\mathbf{I}$, where $\mathbf{I}$ is the unity tensor, $-\bar{\mu} e_0 \mathbf{I}$ the chemical potential tensor and f a mobility coefficient. The chemical driving force for growth is a "chemical potential" $\mu = -\bar{\mu} e_0$, with a sign chosen such that μ is generally positive. The growth equation may be simplified with these assumptions to an equation depending on a chemical driving force $\mu \geq 0$,

$$\frac{\dot{V}}{V} = 3f\left(-p + \mu\right), \quad (1)$$

where we have defined V as the volume and $\dot{V}$ as its time rate. Note that the convention is that tensile stresses are positive, while the pressure p is taken positive when compressive (thus the inversion of the

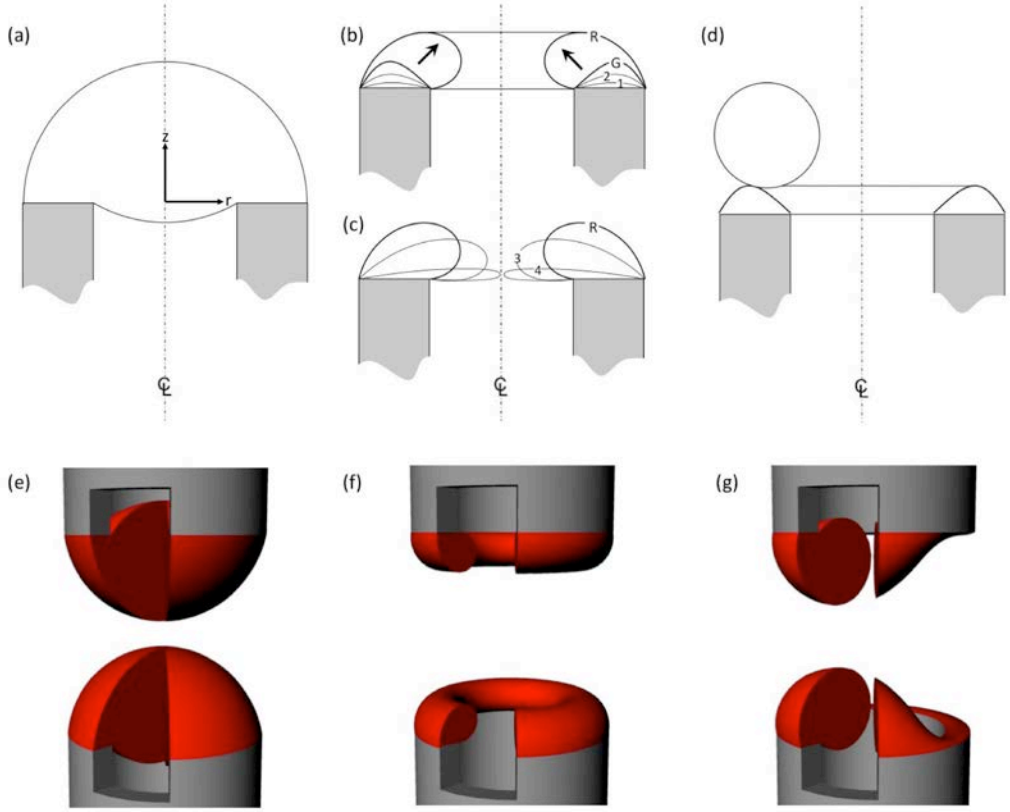

Figure 2: Topologically possible configurations with constant curvature sitting on the top of an open thick-walled cylinder. (a) A complete cap based on spherical calottes on the top and in the inner cylinder (both with same radius of curvature). These correspond to the stable branch S_3 in Fig. 3. (b) Nodoids partially covering the cylinder gap; nodoids labeled 1, 2 and G are on the stable branch S_1 in Fig. 3; nodoids between G and R (arrows) corresponds to the unstable branch U_1. (c) Further nodoids (labeled 3,4, R) corresponding to the stable branch S_2 in Fig. 3. Such nodoids have the same curvature as those in (b) but a larger volume. (d) Nodoid with a spherical bulge (modeled by an adjacent droplet of identical mean curvature);nodoids with a spherical bulge correspond to the unstable branches U_2 and U_3 in Fig. 4. Figs (e-g) are 3D-renderings of numerical simulations performed in Surface Evolver, for the topologies in (a) (b) and (d). Note that the sketch in (d) is just an approximation of the real configuration shown in (g), neglecting the connecting zone between the spherical bulge and nodoid.

signs in (1)). Using the Laplace-Young relation, Eq.(1) can be rewritten as

$$\frac{\dot{V}}{V} = -3f\gamma\left(K - K_c\right). \qquad (2)$$

It is clear from this equation that the tissue nodule will grow whenever its surface curvature K is smaller than a critical curvature $K_c = \mu/\gamma$. This critical value depends on the ratio of chemical potential for growth (generated by biochemical signals such as growth factors) and on the surface stress on the outer boundaries of the nodule and is interpreted as a kinetic control parameter for growth.

Growth of an unsupported tissue nodule

As a first and most simple case, we consider an unsupported tissue nodule growing in suspension. Local mechanical equilibrium implies that the nodule must be spherical with radius $R = 2/K$. Under these conditions, Eq. (2) can be rewritten in a form reminiscent of a nucleation problem, see, e.g., (38).

$$\begin{aligned}\dot{R} &= -2f\gamma\left(1 - R/R_c\right) \\ &= -2f\gamma\left(\left(1 - K_c/K\right)\right),\end{aligned} \qquad (3)$$

where $R_c = 2/K_c = 2\gamma/\mu$ is the critical radius. From this equation, the tissue nodule will be in equilibrium when $\dot{R} = 0$, i.e. $R = R_c$. Whether this is stable or not, depends on how $\dot{R}$ changes for small variations in R close to R_c . As $\dot{R} > 0$ for $R > R_c$ and $\dot{R} < 0$ for $R < R_c$, the unsupported nodule will keep on growing when larger than the critical radius (at least as long as the supply of nutrients and therefore the critical curvature K_c is maintained at the same level) but will disappear when it is smaller than R_c , meaning the equilibrium configuration is indeed unstable.

Growth of a tissue nodule perfectly wetting a disk

We now consider a nodule that perfectly wets the circular cap on top of a full cylinder for which the walls are not wettable (Fig. 1c). We suppose that there is a constant contribution of the surface stress at the contact between the support (light grey in Fig. 1c) and the nodule (perfect wetting). For this boundary condition the nodule will satisfy mechanical equilibrium when it is a segment of a sphere or calotte with a radius $R = 2/K$. Fig. 1c shows several examples for spherical nodules sitting on top of a full cylinder. Calling H the height of the calotte, measured from the surface of the support, the volume of the nodule is given as

$$\begin{aligned}V &= \pi H^2\left(R - H/3\right) \\ &= \pi H\left(3R_0^{\,2} + H^2\right)/6,\end{aligned} \qquad (4)$$

where R_0 is the outer radius of the circular support. From now one we express all linear dimensions are expressed in units of the outer radius, with $R_0 = 1$, but keep to the same symbols for the sake of simplicity. Time t is also renormalized by introducing $\tau = f\gamma t / R_0$. Inserting this into Eq. (2) yields

$$\frac{\dot{V}}{V} = -3\left(K - K_C\right), \qquad (5)$$

where the dot now indicates the derivation with respect to normalized time τ. In addition to Eq. (5), we can also write a relation between volume V and H as well as H and the surface curvature K as

$$V = \pi H\left(3 + H^2\right)/6, \qquad K = 4H/\left(1 + H^2\right), \qquad (6)$$

which allows K to be expressed as a function of V. Insertion of this expression into Eq. (5) yields the rate of increase of volume as a function of the nodule volume. A similar approach also gives the rate of increase of the nodule height as a function of its current height, expressed analytically as

$$\frac{\dot{H}}{H} = \frac{3 + H^2}{\left(1 + H^2\right)^2} K_C \left(H^2 - 4\frac{H}{K_C} + 1 \right). \qquad (7)$$

Eqs. (5) and (7) predict now two equilibrium states for H, when $\dot{H} = 0$ (and $\dot{V} = 0$), provided that $K_C < 2$. The stability of these states can be visualized with the help of Fig. 1a,b which shows plots of Eqs. (5) and (7) for different values of K_C. Here a short remark concerning the term "stable" may be useful. We consider a kinetic process and a kinetic stability criterion. We observe a stable behaviour of the system, if a small increase of $H\left(V\right)$ from a starting position leads to negative values of $\dot{H}/H\left(\dot{V}/V\right)$ and consequently a tendency of the system to move back to the starting position – and vice/versa for a small decrease of $H\left(V\right)$ and positive values of $\dot{H}/H\left(\dot{V}/V\right)$. Such stable configurations are highlighted by full circles in Fig. 1a,b. The situation is exactly opposite for the unstable equilibria (open circles). Stable equilibria correspond to nodules smaller than a half-sphere (full lines in Fig. 1c), while nodules larger than a half-sphere are in unstable equilibria (broken line in Fig. 1c). Hence, for a given biochemical driving force expressed by the critical curvature K_C, there are stable nodule configurations described by the corresponding curves in Fig. 1c and with characteristic volumes and heights as given by Fig. 1a,b.

Fig. 1a,b shows that growth of the nodule will not stop when the critical curvature K_C exceeds the value of 2. Interestingly (and in contrast to the unsupported nodule discussed in the previous section), the unstable equilibrium nodule (open circles in Fig. 1a,b) does not disappear, when its curvature is smaller than K_C. It runs for $K_C < 2$ along the curves in Fig. 1a,b from the unstable (open circles) to the stable state (full circles). In this sense, the nodule at equilibrium is dormant, but can reach a state of unconstrained growth as soon as the critical curvature K_C driving force increases for some reason beyond 2 (for example by a burst of growth factors). This is summarized in Fig. 1d, where V_C, the nodule volume corresponding to K_C, is plotted as a function of K_C. Portions of the curve with positive slope correspond to stable branches. Conversely, negative slopes correspond to unstable branches. Indeed, if a decrease in thermodynamic driving force (corresponding to a decrease in critical curvature) would lead to an increase in volume, the configuration cannot be stable.

Growth of a tissue nodule perfectly wetting an annulus

We now consider the growth of tissue pinned to the top of an open thick-walled cylinder (that is a flat circular ring, or annulus). We again normalize the linear space dimensions such that the outer radius of the open thick-walled cylinder is $R_0 = 1$, and assume the walls of the cylinder are non-wetting. The dimension of the inner radius is kept as a parameter R_I.

The analysis is done in a completely analogous way to the previous sections. Outside the contact to the annulus (the top of the open thick-walled cylinder), the nodule will have a surface with constant curvature. Such surfaces are in general nodoids (39). To describe this axisymmetric surface, we introduce a radial coordinate r, such that $R_I \le r \le R_0 = 1$, and an axial coordinate z parallel to the cylinder axis of the support. The function linking z with r in the nodoid depends on two parameters, the (constant) surface curvature K and the position R_H $\left(R_I < R_H < R_0\right)$ where there is a horizontal tangent to the profile (that is, the position of the maximum of the nodoid, sitting on top of the open thick-walled cylinder), and can be written as

$$z(r,K,R_H)=\pm\left\{\begin{array}{l}\dfrac{\left[\cos(\theta_I)-\cos(\theta)\right]}{K}\\ +R_H\left[\mathrm{E}\left(\theta,\dfrac{-1}{(R_HK)^2}\right)-\mathrm{E}\left(\theta_I,\dfrac{-1}{(R_HK)^2}\right)\right]\\ -R_H\left[\mathrm{F}\left(\theta,\dfrac{-1}{(R_HK)^2}\right)-\mathrm{F}\left(\theta_I,\dfrac{-1}{(R_HK)^2}\right)\right]\end{array}\right\} \quad (8)$$

with

$$\theta=\arcsin\left(K\left(r^2-R_H^2\right)/2r\right). \quad (9)$$

The quantity θ represents the polar angle as parameterization with the starting value $\theta_I \le \theta$. The current formulation ensures that $z(\theta_I)=0$. The functions E and F are the incomplete elliptic integrals of the first and the second kind. Both signs in front of the bracket point to the fact that z may describe both the contour and its mirror image with respect to the plane $z=0$. For details, see Supplementary Material and the references therein.

It is interesting to note that several topologically different shapes (as previously described by (15,17,40)) may fulfill the requirements of constant mean curvature and of meeting the boundary condition (pinning) on the top of the open thick-walled cylinder. These are sketched in Fig. 2. The first topology (Fig. 2a) is a spherical cap covering the central channel, the second topology (Figs 2b,c) corresponds to various nodoids and the third (Fig. 2d) is a nodoid with a spherical droplet of identical curvature attached to it. This last (much simplified) configuration was considered here, because Lipowsky and co-workers (15,17,40) showed that nodoidal objects could bifurcate into conformations with a significant spherical bulge. Figs 2 e-g were calculated using Brakke's "Surface-Evolver" software (37), for details see the Supplementary Material.

Fig. 3 shows relations between volume and curvature for all these cases and for three values of the inner radius (i.e. the ratios of the inner radius R_I and the outer radius R_0) of the support cylinder. For relatively thick-walled cylinders (Fig. 3a,b), there are three stable branches (labeled S), two of which correspond to nodoids and there are three unstable branches (labeled U). Branch S_1 corresponds to a wetting of the ring-like cylinder top and the gradual development of a nodoid with increasing volume (at increasing critical curvature K_C, shapes 1, 2 and G in Fig. 2b). Beyond some value of the critical curvature K_C (close to 2.2 and to 4 in Fig. 3a and b, respectively), the branch ends and growth becomes unstable, see branch U_1. At the end of this branch, denoted by R in Fig. 3c another stable branch S_2 is reached, where a further increase of the volume is not possible. This is the largest possible nodoid that satisfies the boundary conditions. Nodoids along S, will respond to a decrease in critical curvature by following path S_2 (with shapes of the type shown in Fig. 2c). Interestingly, branch S_2 is tangent (and nearly identical at small volumes) to another stable branch S_3 that corresponds to a closed spherical cap (Fig. 3a) as a second possible topology. Hence, bifurcation from

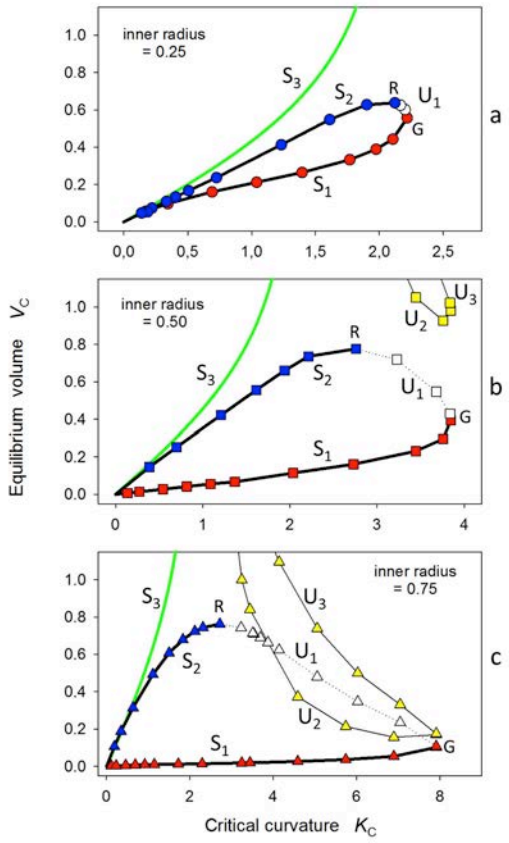

Figure 3: Relation between the equilibrium volume V_C and critical curvature K_C for nodules growing on the top of an open thick-walled cylinder, with different ratios of inner to outer radius: 0.25 (a), 0.5 (b) and 0.75 (b). Both volume and curvature have units given as fractions of the outer wall radius $R_0 = 1$. Curve branches with positive slope are stable, while those with negative slope are unstable with respect to the growth equation (Eq. (5). Labels S_1 to S_3 and U_1 to U_3 correspond to configurations described in Fig. 2. Labels G and R denote nodoids with the largest curvature and the largest volume, respectively.

the topology shown in Fig. 2c to 2a is possible and very likely. When calculating the volume-curvature relations for the third topology (Fig. 2d), the corresponding branches (U_2 and U_3) are barely visible in the upper right corner of Fig. 3b and completely outside the field of view in Fig. 3a. The situation is rather different for relatively thin-walled cylinders (Fig. 3c). It turns out that the curves for nodoids of type shown in Figs 2b and 2c, with a drop-like spherical bulge (U_2 and U_3) are actually in the same range as the ones for nodoids and bifurcations are possible. Most notably, the curves cross at a value of the critical curvature close to 8, where it is possible that the nodoid (of the type depicted in Fig. 2c) bifurcates to another topology (of the type depicted in Fig. 2d). This consists of a nodoid (of the type depicted in Fig. 2b) of smaller volume but with the same curvature by generating an additional spherical bulge with exactly this curvature taking up the extra volume. After this bifurcation, growth of the spherical bulge becomes unstable (branch U_2 in Fig. 3c), in a manner equivalent to the unstable branch in Fig. 1d. The curves shown in Fig. 3 were also verified with numerical calculations using "Surface Evolver" (37) that also showed a bulging bifurcation (Fig. 2g). Despite the strong simplification of the analytical

model (as shown in Fig. 2d), there is excellent qualitative agreement between the analytical and

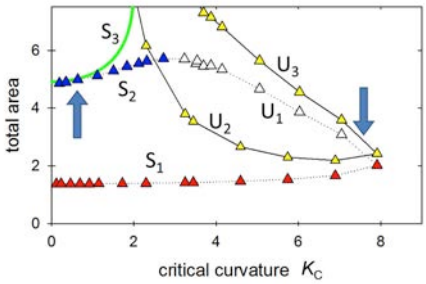

Figure 4: Total area of the newly formed tissue on top of an open thick-walled cylinder for an internal radius of 0.75. The symbols are the same as in Fig. 3c. The two arrows indicate positions where the overlap of two branches in Fig. 3c suggests to possibility of bifurcations.

numerical solutions.

This analysis of potential bifurcations merits a more thorough analysis. For this, we plot the total free surface area of the tissue nodule as a function of critical curvature for the relatively thin-walled cylinder with an inner radius of 0.75 (Fig. 4). Given that surface energy governs the development of shape, the total area, which is proportional to total surface energy, will tend to be minimal. A bifurcation from one topology to another is only possible without a jump in volume and at given curvature. Indeed, curvature is imposed on the system by the biochemical driving force expressed by K_c and changes in volume require the synthesis of additional tissue and can, therefore, not be instantaneous. In Fig. 4, two possible bifurcations can be observed, namely one between the paths U_1 and U_2 crossing close to a critical curvature of $K_c = 8$ and the other one between the paths S_2 and S_3 approaching asymptotically for small curvatures. These two points are marked by arrows in Fig. 4. It turns out that configurations due to S_2 and S_3 have nearly the same surface area at small curvatures, which means that a bifurcation is likely but not necessary. However, if biochemical driving forces increase the critical curvature K_c again, it is more likely that the system follows the path S_2, which has the lower surface area and consequently surface energy at equal critical curvature. The bifurcation between the paths U_1 and U_2 is of a totally different nature. When curvature increases along the path S_1 and exceeds the maximum value at G, so that further growth becomes unstable along the path U_1, the formation of a spherical bulge significantly lowers the surface energy, so that a bifurcation from path U_1 to path U_2 becomes highly probable. The bulge itself is unstable, and will continue to grow in a similar way to the unstable branch of the calotte (Fig. 1d). It should be mentioned again that for thicker cylinder walls, U_1 and U_2 do not intersect (Fig. 3a,b) so that the bifurcation towards uncontrolled growth is not expected above a certain wall thickness. Without the bifurcation towards a spherical bulge (which is the case for inner radii significantly smaller than 75% of the outer radius), the configurations labeled G and R in Fig. 3 correspond to those with the largest curvature and the largest volume, respectively. Quantitative data for these two configurations are given in Table 1.

Comparison to callus formation and bone healing

The model described above has only one free parameter, the critical curvature K_c, and is based on three main biological hypotheses. To recap, the model relies on the following conditions:

1) Tissue is remodeled on a time scale much shorter than growth, which justifies the description of the tissue as an effective ideal fluid (on the time-scale of months) (10).
2) There is a surface stress, which results in a surface curvature-dependent internal pressure inside the tissue (9,11,12,21,41).
3) Growth of a tissue, by cell proliferation and extracellular matrix formation, depends on its pressure through the growth equation. Such a dependency on pressure is known from the growth of tumor spheroids (18,42), and in principle can be controlled by the organism (e.g., via growth factors).

Despite the simplicity of the above model, the coupling of growth with the external surface geometry via the internal pressure leads to surprisingly complex behaviour as a function of the boundary conditions. Interestingly this behaviour is reminiscent of many features seen in biological tissues. While an unsupported nodule is unstable (disappearing at small driving forces and showing unlimited growth at large driving forces), there are equilibrium sizes for the nodule when adhering to a substrate. The stabilizing effect of substrates on growing tissues has been observed in cancer metastases (18,43) and clearly plays an important role in biofilm formation (44).

Our model shows that growth of a tissue is also dependent on the shape of the surface upon which it adheres. When the tissue grows on top of a hollow cylinder, which is the same geometry as the free ends of bone in the simulated fracture gap after an osteotomy (45), there is a maximum height the tissue will grow to, for a given value of critical curvature. Assuming that similar growth occurs from both sides of the fracture gap in an osteotomy, our model thus predicts the existence of a maximum bridgeable gap size. This is reminiscent of the so-called "critical defect size" known from bone healing (46). Such calculations of course assume no wetting of the external bone surface which may occur during bone fracture-healing due to damage or removal of the periosteum (e.g. (47)).The prediction of the model is that the critical gap size is 70%, 78% and 61% of the outer diameter of the cylindrical tube, when the inner diameter is 75%, 50% and 25% of the outer diameter, respectively (Table 1). Most land mammals have a ratio of inner to outer diameter lower than 75% (48), and typically have critical defect sizes of 1 to 2 times the outer bone diameter (49). For example, the ratios of critical defect sizes to bone diameters are reported to be: 1.3-1.5 times in feline tibias (49), 1.5-2 times in dog ulnas (49), and 2-2.5 times in sheep tibias (46). These ratios are of a similar order of magnitude as the model predictions. For thin walled cylinders (wall thickness less than 25% of the radius), the model predicts a bifurcation towards uncontrolled growth of spherical bulges, which could have implications in the

fracture healing of thin walled bones such as those found in birds. Our theory predicts that if the fracture gap is too large and then tissue starts to resorb, a cap will form that will gradually close the tubes at each side of the gap (Fig. 2e). Remarkably, such closure is observed in pseudarthrosis or non-union of bone fractures e.g. (50). In our theory, this arises due to a kinetic instability of the growth process, which is described by the evolution equation of the shape of the actual configuration leading to different paths for resorption and growth (Fig. 3).

In conclusion, if the above conditions 1 to 3 are fulfilled in a growing tissue, then the organism needs to control only one parameter, namely the proliferation rate (that leads to the growth pressure or the critical curvature as used in our model), in order to achieve a complex sequence of structures surprisingly similar to in-vivo observations. In addition to bone fracture healing our model may be interesting for biofilm formation and cancer research as it shows how the presence of tissue surface tension, and liquid like properties can lead to radically different behaviors of tissues on surfaces.

Author Contributions:

PF, FDF designed the study and developed the analytical model, GZ solved the nodoid equations and JD performed the numerical growth simulations. PF, FDF and JD wrote the manuscript and all authors gave final approval for publication.

Acknowledgements:

The authors wish to thank Ron Shahar and Reinhard Lipowsky for stimulating discussions.

Funding:

We acknowledge the Alexander von Humboldt foundation for supporting the visit of F.D.F to the Max Planck Institute of Colloids and Interfaces through the Humboldt Award.

References:

1. Lecuit T, Le Goff L. Orchestrating size and shape during morphogenesis. Nature. 2007;450(7167):189-92.
2. Mammoto T, Ingber DE. Mechanical control of tissue and organ development. Development. 2010;137(9):1407-20.
3. Nelson CM, VanDuijn MM, Inman JL, Fletcher DA, Bissell MJ. Tissue Geometry Determines Sites of Mammary Branching Morphogenesis in Organotypic Cultures. Science. 2006;314(5797):298-300.
4. Nelson CM, Jean RP, Tan JL, Liu WF, Sniadecki NJ, Spector AA, et al. Emergent patterns of growth controlled by multicellular form and mechanics. Proc. Natl. Acad. Sci. USA. 2005;102(33):11594-9.
5. Wan LQ, Kang SM, Eng G, Grayson WL, Lu XL, Huo B, et al. Geometric control of human stem cell morphology and differentiation. Integr. Biol. 2010;2(7-8):346.
6. Helmlinger G, Netti PA, Lichtenbeld H, Melder RJ, Jain RK. Solid stress inhibits the growth of multicellular tumor spheroids. Nat. Biotechnol. 1997;15(8):778-83.
7. Montel F, Delarue M, Elgeti J, Malaquin L, Basan M, Risler T, et al. Stress Clamp Experiments on Multicellular Tumor Spheroids. Phys. Rev. Lett. 2011;107(18):188102.
8. Kollmannsberger P, Bidan CM, Dunlop JWC, Fratzl P. The physics of tissue patterning and extracellular matrix organisation: how cells join forces. Soft Matter. 2011;7:9549–60.
9. Foty RA, Steinberg MS. The differential adhesion hypothesis: a direct evaluation. Dev. Biol. 2005;278(1):255-63.
10. Lecuit T, Lenne P-F. Cell surface mechanics and the control of cell shape, tissue patterns and morphogenesis. Nat. Rev. Mol. Cell. Biol. 2007;8(8):633-44.
11. Krieg M, Arboleda-Estudillo Y, Puech P-H, Käfer J, Graner F, Müller DJ, et al. Tensile forces govern germ-layer organization in zebrafish. Nat. Cell Biol. 2008;10(4):429-36.
12. Manning ML, Foty RA, Steinberg MS, Schoetz E-M. Coaction of intercellular adhesion and cortical tension specifies tissue surface tension. Proc. Natl. Acad. Sci. USA. 2010;107(28):12517-22.
13. Douezan S, Guevorkian K, Naouar R, Dufour S, Cuvelier D, Brochard-Wyart F. Spreading dynamics and wetting transition of cellular aggregates. Proc. Natl. Acad. Sci. USA. 2011;108(18):7315-20.
14. Fischer FD, Waitz T, Vollath D, Simha NK. On the role of surface energy and surface stress in phase-transforming nanoparticles. Prog. Mater. Sci. 2008;53(3):481-527.
15. Lenz P, Fenzl W, Lipowsky R. Wetting of ring-shaped surface domains. Europhys. Lett. 2001;53(5):618-24.
16. Gau H, Herminghaus S, Lenz P, Lipowsky R. Liquid morphologies on structured surfaces: From microchannels to microchips. Science. 1999;283(5398):46-9.
17. Schäfle C, Brinkmann M, Bechinger C, Leiderer P, Lipowsky R. Morphological Wetting Transitions at Ring-Shaped Surface Domains. Langmuir. 2010;26(14):11878-85.
18. Basan M, Risler T, Joanny J-F, Sastre Garau X, Prost J. Homeostatic competition drives tumor growth and metastasis nucleation. HFSP J. 2009;3(4):265-72.
19. Shraiman BI. Mechanical feedback as a possible regulator of tissue growth. Proc. Natl. Acad. Sci. USA. 2005;102(9):3318-23.
20. Bidan CM, Kommareddy KP, Rumpler M, Kollmannsberger P, Fratzl P, Dunlop JWC. Geometry as a Factor for Tissue Growth: Towards Shape Optimization of Tissue Engineering Scaffolds. Adv. Healthc. Mater. 2013;2:186-94.
21. Rumpler M, Woesz A, Dunlop JWC, van Dongen JT, Fratzl P. The effect of geometry on three-dimensional tissue growth. J. Roy. Soc. Interface. 2008;5(27):1173-80.
22. Ripamonti U, Roden LC, Renton LF. Osteoinductive hydroxyapatite-coated titanium implants. Biomaterials. 2012;33(15):3813-23.
23. Shapiro F. Cortical Bone Repair - the Relationship of the Lacunar-Canalicular System and Intercellular Gap-Junctions to the Repair Process. J. Bone Joint. Surg. Am. 1988;70A(7):1067-81.
24. Ambrosi D, Ateshian GA, Arruda EM, Cowin SC, Dumais J, Goriely A, et al. Perspectives on biological growth and remodeling. J. Mech. Phys. Solids. 2011;59(4):863-83.
25. Schwarz US, Safran SA. Physics of adherent cells. Rev. Mod. Phys. 2013;85(3):1327-81.
26. Madeo A, George D, Lekszycki T, Nierenberger M, Remond Y. A second gradient continuum model accounting for some effects of

micro-structure on reconstructed bone remodelling. C.R. Mecanique. 2012;340(8):575-89.
27. Madeo A, Lekszycki T, Dell'Isola F. A continuum model for the bio-mechanical interactions between living tissue and bio-resorbable graft after bone reconstructive surgery. C.R. Mecanique. 2011;339(10):625-40.
28. Del Vescovo D, Giorgio I. Dynamic problems for metamaterials: Review of existing models and ideas for further research. Int. J. Eng. Sci. 2014;80:153-72.
29. Ganghoffer JF, Plotnikov PI, Sokolowski J. Mathematical Modeling of Volumetric Material Growth in Thermoelasticity. J. Elast. 2014;117(1):111-38.
30. Ganghoffer JF. Mechanical modeling of growth considering domain variation-Part II: Volumetric and surface growth involving Eshelby tensors. J. Mech. Phys. Solids. 2010;58(9):1434-59.
31. Ganghoffer JF. A contribution to the mechanics and thermodynamics of surface growth. Application to bone external remodeling. Int. J. Eng. Sci. 2012;50(1):166-91.
32. Ambrosi D, Mollica F. The role of stress in the growth of a multicell spheroid. J. Math. Biol. 2004;48(5):477-99.
33. Ambrosi D, Preziosi L. On the closure of mass balance models for tumor growth. Math. Models Methods Appl. Sci. 2002;12(5):737-54.
34. Ambrosi D, Preziosi L, Vitale G. The interplay between stress and growth in solid tumors. Mech. Res. Commun. 2012;42:87-91.
35. Gamsjäger E, Bidan CM, Fischer FD, Fratzl P, Dunlop JWC. Modelling the role of surface stress on the kinetics of tissue growth in confined geometries. Acta Biomater. 2013;9:5531-43.
36. Dunlop JWC, Fischer FD, Gamsjäger E, Fratzl P. A theoretical model for tissue growth in confined geometries. J. Mech. Phys. Solids. 2010;58(8):1073-87.
37. Brakke KA. The surface evolver. Exper. Math. 1992;1(2):141-65.
38. Kalikmanov VI. Nucleation Theory. Dordrecht: Springer; 2013.
39. Delaunnay C. Sur la surface de révolution dont la courbure moyenne est constante. J. Math. Pures. Appl. 1841;6:309-14.
40. Lenz P. Wetting phenomena on structured surfaces. Adv. Mater. 1999;11(18):1531-4.
41. Foty RA, Pfleger CM, Forgacs G, Steinberg MS. Surface tensions of embryonic tissues predict their mutual envelopment behavior. Development. 1996;122(5):1611-20.
42. Alessandri K, Sarangi BR, Gurchenkov VV, Sinha B, Kiessling TR, Fetler L, et al. Cellular capsules as a tool for multicellular spheroid production and for investigating the mechanics of tumor progression in vitro. Proc. Natl. Acad. Sci. USA. 2013;110(37):14843-8.
43. Cameron MD, Schmidt EE, Kerkvliet N, Nadkarni KV, Morris VL, Groom AC, et al. Temporal progression of metastasis in lung: Cell survival, dormancy, and location dependence of metastatic inefficiency. Cancer Res. 2000;60(9):2541-6.
44. Hall-Stoodley L, Costerton JW, Stoodley P. Bacterial biofilms: From the natural environment to infectious diseases. Nat. Rev. Microbiol. 2004;2(2):95-108.
45. Epari DR, Schell H, Bail HJ, Duda GN. Instability prolongs the chondral phase during bone healing in sheep. Bone. 2006;38(6):864-70.
46. Reichert JC, Saifzadeh S, Wullschleger ME, Epari DR, Schutz MA, Duda GN, et al. The challenge of establishing preclinical models for segmental bone defect research. Biomaterials. 2009;30(12):2149-63.
47. Liu YF, Manjubala I, Schell H, Epari DR, Roschger P, Duda GN, et al. Size and Habit of Mineral Particles in Bone and Mineralized Callus During Bone Healing in Sheep. J. Bone Miner. Res. 2010;25(9):2029-38.
48. Currey JD, Alexander RM. The Thickness of the Walls of Tubular Bones. J. Zool. 1985;206(Aug):453-68.
49. Hollinger JO, Kleinschmidt JC. The critical size defect as an experimental model to test bone repair materials. J. Craniofac. Surg. 1990;1(1):60-8.
50. Harrison LJ, Cunningham JL, Stromberg L, Goodship AE. Controlled induction of a pseudarthrosis: A study using a rodent model. J. Orthop. Trauma. 2003;17(1):11-21.

7.8 [AC1] An excursion into the design space of biomimetic architectured biphasic actuators.

Turcaud, S., Guiducci, L., Bréchet, Y. J. M., Fratzl, P., Dunlop, J. W. C.

*Published in **International Journal of Materials Research**, 2011, 102, 607–612.*
doi: 10.3139/146.110517

Reprinted with permission © Carl Hanser Verlag, Muenchen

Abstract: Natural hygromorph actuators, such as those found in the pine cone or in the awns of wheat and the storksbill, achieve a large variety of motions by controlling the distribution of swellable tissues inside their geometries. Such natural systems provide inspiration for the design of artificial actuators where swelling is triggered by any external expansion field. One way to achieve differential swelling inside a structure is to consider two elastic phases with different expansion properties and to apply a uniform expansion field. The resultant motion depends on the geometric distribution of the two phases and the cross section of the structure. This paper uses the finite element method to explore how the geometry and symmetry of the initial structure controls the range of motion available.

1 Introduction

The recent increase in investigations of structure-function relationships in biological systems by material scientists (Fratzl 2007; Bhushan 2009) opens a large range of potentially interesting design principles that can be translated from Nature to the engineering world (Dunlop and Brechet 2009). Passive actuated plant systems are particularly well-suited for a biomimetic approach to the development of artificial actuators, as they do not require active transport of ATP to supply chemical energy to cells. Actuation in these systems is rather controlled by the architectural arrangement of dead tissues which swell to differing degrees upon hydration (Burgert and Fratzl 2009; Fratzl and Barth 2009; Martone et al. 2010). An additional advantage for bioinspired robotics shared by many simple natural actuating systems is their properties of decentralization and embodiment (Pfeifer et al. 2007). By this it is meant their ability to integrate sensing and actuating functions at the material level so as to avoid central control of the system, which typically needs a complex information pathway (sensors to central control unit to actuator). Hygrophilic swelling of dead plant tissues although somewhat simple in concept, still leads to complex macroscopic movements like bending, twisting and helical actuation dependent on the underlying tissue architecture. This article is based on a top-down approach, where hygrophilic plant tissues are modelled as thermo-mechanical continua in order to explore the relation between the architectural distribution of expanding properties inside a given geometry and the resulting movement for a given stimulus.

Nature provides several examples of nastic actuated systems in which plant organs move or generate stresses due to differential swelling of their constituent tissues. This is nicely illustrated by seed dispersal units like wheat awns and the pine cone. Wheat is propelled on and into the ground by daily humidity cycles that give rise to reversible planar bending of the awns (Elbaum et al. 2007; Elbaum et al. 2008) while ratchets account for unidirectional movement (Kulic et al. 2009) and closed wet pines cones open while drying thus releasing the seeds (Dawson et al. 1997). In both cases, the orientation of stiff cellulose microfibrils embedded in the hygroscopic hemicellulose matrix of the secondary cell walls is responsible for the differential swelling properties of the seed dispersal units, as the shrinkage upon drying will primarily occur transversally to the fibres. Such a multi-cellular bilayer with one region's fibres oriented parallel to the cell axis and the other region's fibres with random or perpendicular orientations will give rise to planar bending and can inspire simple biomimetic systems (Reyssat and Mahadevan 2009). More generally, swelling can also generate either compressive or tensile growth stresses in so-called "reaction wood", depending on the average angle of the cellulose microfibrils to the main cell axis (Burgert et al. 2007). General mechanisms of multi-cellular stiff cellulose architecture inside a soft swellable matrix have been reviewed for plant actuation systems in (Fratzl et al. 2008) and mechanosensing (Fratzl and Barth 2009). In poplar tension wood for example (Goswami et al. 2008), an additional G-layer of parallel cellulose microfibrils, also found in the tissue of contractile roots (Schreiber et al. 2010), is responsible for the generation of high tensile stresses. Design limits between fast movements in which active driving forces or instabilities are at play, as in the buckling of the Venus flytrap (Forterre et al. 2005) or the explosive fracture of seed expulsions (Witztum and Schulgasser 1995), and slow movements where passive dead tissue is at work, on which we focus here, can be made based on mechanical and hydraulic considerations (Skotheim and Mahadevan 2005). Symmetry considerations (Curie's principle) of the geometry and material distribution can predict the planar bending of the aforementioned plant systems (wheat awn, pine cone). A large number of reversible motions or stresses can be powered by choosing a clever couple of the distribution of material properties inside the geometry and an appropriate expansion/contraction field.

Although nature is able to "design" its materials at each hierarchical length-scale, this is difficult to achieve for artificial materials, due to limitations in common manufacturing techniques. As in the pine cones, many artificial devices have been produced based on the bending of a bilayer made up of two materials, each showing a different volume change in response to a changing external field. Well established

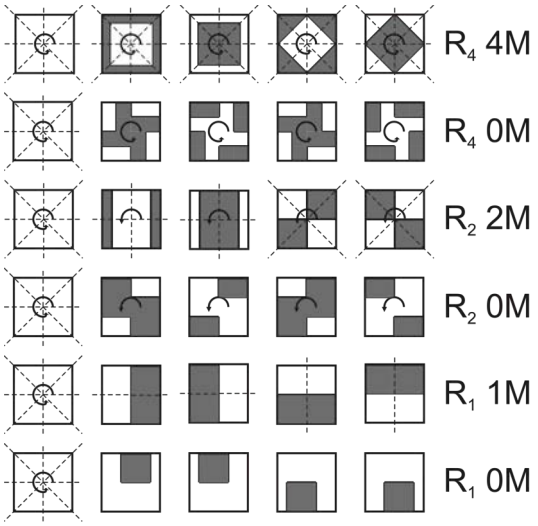

Figure 1: Non-exhaustive examples of material-distributions reducing the number of symmetries of a square profile. Breaking mirror symmetries while preserving rotational ones allows twisting to occur (rows 2 and 4). When only one mirror plane remains bending can occur (row 5). When two many symmetries remains, symmetry locking takes place (rows 1 and 3). When no symmetry elements is present,, actuation is apparently unpredictable (row 6).

manufacturing techniques such as μ-stereolithography can be used to produce bilayers of photocurable polymers that bend upon changing humidity (Lee et al. 2008). Other examples include Cu/Cr bilayers that change curvature reversibly upon oxidation/reduction cycles (Randhawa et al. 2010). Shape-memory materials have also awakened a great interest in the design of artificial actuators. Actively foldable origami-like structures have been designed in which simple bending motion of shape-memory joints is coupled with a crease pattern of a planar sheet in order to obtain several programmable shapes (Hawkes et al. 2010). Shape-memory polymers can in particular be tuned to respond not only to temperature changes but also to electrical fields, light intensity, humidity fields (Behl et al. 2010) or a combination of these (Sellinger et al. 2010). Magnetic shape-memory foams are also becoming intriguing for tomorrow's applications since significant induced strains have been shown and some manufacturing drawbacks have been overcome (Acet 2009). Even if such systems show the feasibility of bioinspired actuation, the majority of them are based on bilayers bending in a single plane, with different materials distributed only along one transverse direction.

The goal of this paper is to explore the complexity of movements of one body shape (straight slender element) made of two elastic phases with different expansion coefficients distributed along the two transverse directions. The role of symmetry in sampling the space of allowable movements is addressed firstly in the next section. Examples of two different families of biphasic actuators are then simulated in the sections following using the finite element method in order to determine their actuation patterns.

2 Symmetry Considerations

2.1 Curie's Principle

As we consider invariant architectures along the length of the body (uniform cross-sections), symmetry elements reduce to mirror symmetries ($n*M$) and rotation symmetries (R_n), where n is respectively the number of mirror planes and the multiplicity of the rotation (the angle of rotation is $360/n$). In the plane, the inversion centre is equivalent to R_2. Multiple mirror symmetries imply rotation symmetries, but the inverse statement doesn't hold in general ($n*M \Rightarrow R_n$).If symmetry exists in the base configuration it is kept in the deformed configuration as stated by Curie's principle: "Effects have at least the symmetries of their causes" (Curie 1894). In general, this means that mirror symmetries only allow planar bending to occur in the mirror plane, whereas rotation symmetries only allow the structure to twist around its rotation axis. If multiple symmetries exist in the initial configuration, they all remain in the deformed configuration. As a result, overlapping symmetries result in no deformation (symmetrical locking). For example, the presence of both a mirror plane and a rotation axis implies no bending and no twisting as both movements would break one of the symmetries. Such preliminary consideration enables to make predictions on the allowable actuation patterns based on the symmetry of the undeformed actuator.

2.2. Materials Distribution Restricts Symmetries of Geometrical Shape

Profiles can be anything from asymmetric to multiply symmetric. Examples of the latter are regular n-sided polygons, possessing n symmetry planes (mirrors) which imply n-fold rotational symmetries. Moreover n-sided polygons will also posses all p-fold rotational symmetries, where p is a product of a subset of primary numbers present in the decomposition of n ($n = p_1 * p_2 * \ldots * p_m$ and $p = p_{i1} * p_{i2} * \ldots * p_{ik}$, where ($i1 \ldots ik$) is a subset of ($1 \ldots m$)). Distribution of two material phases inside the profile can only maintain or decrease the number of the symmetry elements of the geometrical shape. The final symmetry elements of the body are thus equal to the symmetry elements of the geometry reduced by the choice of the material distribution.

2.3 Repetitive Unit Cell

A systematic way of designing complex material distribution inside a given geometrical shape is to look at the smallest portion of the profile, which if mirrored/rotated along a defined number of symmetry elements of the profile builds up the whole cross-section. The design of this portion, or repetitive unit cell (RUC) will produce different patterns. The symmetry of the patterns can be larger than the symmetry elements used for its generation.

3 Setting the FE Model

In general, the spatial distribution of the material properties (elastic modulus and expansion coefficient) within a given geometry determines the deformation of the object subjected to a uniform expansion field (humidity, temperature, chemical, magnetic or electric field) and thus its overall movement. All the architectures are based on a straight slender beam with a square profile which can

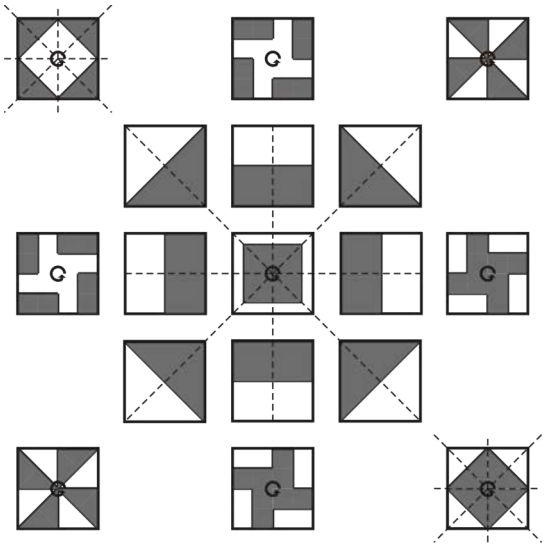

Figure 2: The squared profile possesses 4 mirror planes and a 4-fold rotational axis (4*M, R4). For a constant passive/active area ratio of 50:50, those symmetry elements can either be maintained by the material distribution (centre, upper left and downer right corner), decreased to a single mirror plane (inner contour) or to one 4-fold rotational axis (outer contour). The inner contour is used as RUC for the outer contour showing that the 4-fold patterned cross-section can still possess 4 mirror planes if the RUC possess a mirror plane passing through the centre of rotation.

be mapped to any geometrical form in the plane (Janichen and Perner 2006).

3.1 Implementation

Analytical solutions are known for the special case of thermal bilayers, where thermal expansion coefficients vary in one plane of the cross-section leading to a planar bending of the bilayer in this plane (Timoshenko 1925). However, the general case of an arbitrary distribution of materials is difficult to address analytically. This motivates a solution using the finite element method implemented parametrically in Abaqus 6.9 (www.simulia.com) through an appropriate script written in Python. All the architectures are based on a cubic lattice defined by adjustable length and partitioning parameters. The lattice is filled with two different material phases, active and passive, having the same elastic properties (elastic modulus and Poisson's ratio) and different expansion properties (longitudinal coefficient of thermal expansion). Additionally, a void phase made of a very soft extensible material enables to make mechanical holes in the system. A uniform constant expansion field is applied to the structure and the static equilibrium configuration is computed taking non-linear geometrical effects into account. An adaptive meshing technique (ALE) is used in order to reduce distortion effects of the elements which are simple 8-node linear brick elements (C3D8). No boundary condition is needed as the thermal load induces an auto-equilibrated eigenstrain. The aim of the calculation is to qualitatively predict actuation patterns and to explore the space of allowable movements.

3.2. Simplifying Assumptions

The reversibility of natural actuation processes translates into elasticity in the context of continuum mechanics and the differential swelling expansion of the actuating material is analogous to thermal expansion with spatially varying thermal expansion coefficients. In the calculation the assumption of linear thermo-elasticity is made, and, thus, does not consider potential changes in elastic and swelling properties with the intensity of the expansion field. Also, the focus on biphasic materials and constant cross-section does not enable to model continuously varying properties as in functionally graded materials (FGM). Nevertheless, the context of linear elasticity seems well suited to reproduce slowly actuated movements and to reflect, at least qualitatively, the symmetry effects.

4 Results and Discussion

In the context of elastic materials, the actuation process is reversible, as observed in many natural actuators. Thus, it is possible to go from a straight element to a curved or twisted one, and to reverse the transformation. In the absence of buckling phenomena, this transformation will be continuous, fully reversible, and with no hysteresis. Complex movements can be achieved by combining basic patterns. This combination, however, is not linear, as there is a coupling between bending and twisting. Indeed , if stresses are additives, the strain energy is quadratic, and the cross terms will give the coupling between the different deformation modes. It appears to be more difficult to bend a twisted shape or vice-versa. Depending on whether the aim is to generate displacement or force, the stiffness must be respectively small or large. Slender elements will enable large displacements with small deformations and stresses through geometrical amplification. A classification of actuators could further emphasize the ambivalence between displacement and force generation (Zupan et al. 2002).

4.1. Actuation Patterns

All the symmetry elements of the initial object are preserved in the deformed state, which delimits the space of allowable movements. In the absence of symmetry locking, one mirror plane or rotational axis allows for planar bending and twisting respectively. The actual actuation pattern inside the space of allowable movements for a given object appears to depend on several geometrical properties of the cross-section.

4.2. Bending

Bending is straightforward as the presence of a mirror plane implies planar bending (figure 3 (a)). Analytical formulas for curvature are known for simple bilayers (Timoshenko 1925) and can be generalised to other geometries. It is also possible to control the local curvature of the straight element by rotating the mirror plane of the cross section along the length of the object. Helical actuation can be achieved this way. The second moment of inertia of the cross-section is inversely proportional to the radius of curvature leading to large displacements in the case of small inertia. Geometrical effect like opened cross-sections can amplify the global displacements.

4.3. Twisting

Twisting seems more sensitive to other geometrical factors. In the case of a compact cross-section (figure 3 (b)), no actual twisting is observed despite the 4-

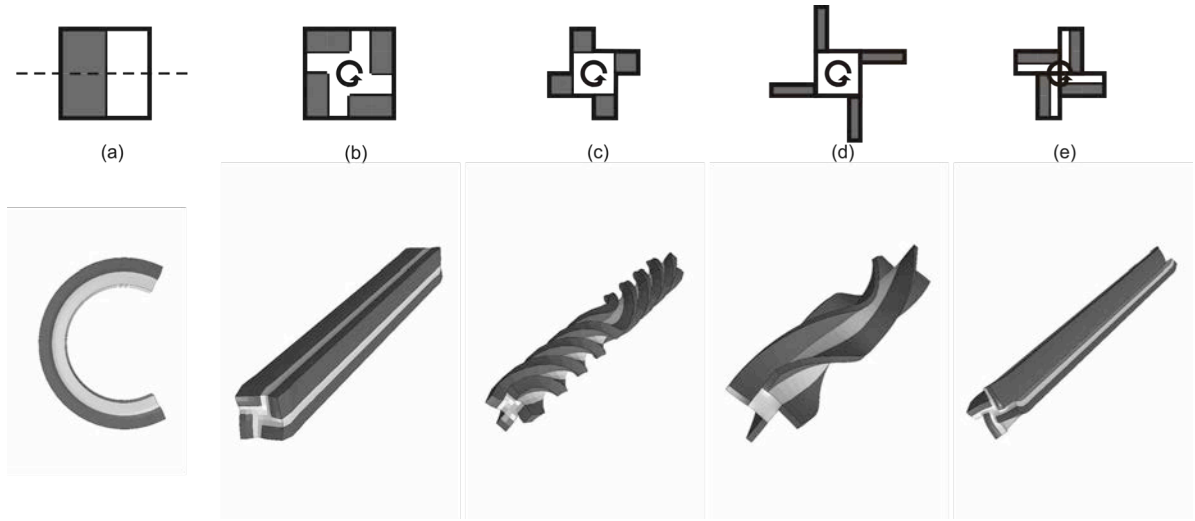

Figure 3 actuation patterns for several cross-sections with passive/active area ratio of 50:50: (from left to right) (a) Classical bilayer bending in its mirror plane; (b) Closed 4-fold cross-section with bilayer RUC remains straight; (c) Opened 4-fold cross-section with bilayer RUC shows huge twisting; (d) Opened 4-fold cross-section with bigger moment of inertia shows less twisting than (c). (e) Opened 4-fold cross-section with differently oriented bilayer RUC remains straight.

fold rotational symmetry axis. However, the augmentation of free-borders with the volume ratio of the two phases staying equal seems to trigger twisting (figure 3 (c)). The moment of inertia of the cross-section seems to relate inversely to the amount of twisting (figure 3 (d)). The eccentricity of the expanding region relative to the geometric centre of the cross-section is proportional to the degree of twisting.

4.4. Geometrical Parameters

Empirical definitions of geometrical parameters that control actual actuation can be proposed. These empirical definitions arise from the observed actuation patterns. The next step (not attempted here) would be to try correlating quantitative measures of movements (radius of curvature, twisting angle) to these geometrical parameters.

A general parameter is the phase fraction, corresponding to the ratio between the volume of the active and passive domains. For a constant cross-section, the area ratio is equal to the volume ratio. Topological considerations such as the connectivity of the phase regions also play a role for the control of the actuation patterns.

In the case of twisting, other geometrical parameters are necessary to distinguish between the observed actuation patterns. On of them is compactness, defined as the ratio between the area of the cross-section and the area of the n-sided regular polygon (with the smallest possible n value) containing the cross-section. All other parameters being equal, a compact cross-section will not twist, whereas an open cross-section will. Concavity defined as the ratio between the perimeter of the shape and the perimeter of the smallest convex contour containing the shape also plays a role similar to geometrical amplification. Compactness and concavity are truly disjoined concepts as there are cross-sections with equal compactness but different concavity and vice-versa. Eccentricity defined as the distance between the centres of the active regions to the geometrical centre of the shape controls the twisting rate of the section. These are only qualitative consideration based on the results of the finite element calculations, without the attempt of a complete classification of all possible shapes.

Conclusion

In this contribution, the effects of material distribution and overall architecture on the actuation patterns of a composite made of swellable and non-swellable materials constituent have been investigated. The space of possible actuation patterns can be restricted by symmetry considerations regarding the initial shape. For constant cross-sections, it is possible to achieve planar bending or twisting when the material distribution breaks some of the symmetry elements of the initial shape, preserving one mirror plane or one rotational axis. The observed actuation behaviour seems to depend on several geometrical parameters, which can be described empirically as phase ratio, topology, compactness and concavity of the cross-section as well as eccentricity. This bioinspired approach towards actuation enables the design space of biphasic actuators to be explored. Besides geometrical considerations, energies and internal stresses could also play a role and it would be interesting to look at the stress repartition inside the cross-section or to optimize the stored strain energy, which has nor been attempted in the present work. The questions whether asymmetric shapes can be decomposed into a set of symmetric shapes in order to predict their actuation patterns remain open, as well as the influences of defects on the material. This paper has been restricted to investigating only variations in architecture and material distribution within the 2D cross section of a simple beam. Despite this extreme simplification, it has been found that the space of allowed movements is quite rich, including bending, twisting and curling. The study reported in this paper is clearly preliminary and much more remains to be investigated. Foe example, more complex material distributions (in 3D) and shapes could enable further unexplored actuation movements. Moreover, it is not clear what the effect would be, if the discrete multiphase materials would be replaced by graded material properties. It is quite likely, that material optimisation methods could be of use for this problem

(Torquato 2010). Finally, it is important to stress that such systems need to be manufactured to be useful, which imposes further restrictions on the design space. But this initial study already shows that this simple bio-inspired approach may enable the design of artificial actuated materials with a wide span of potential applications.

Acknowledgements
The authors would like to thank Yael Abraham, Thomas Antretter, Rivka Elbaum, Matt Harrington, Davide Ruffoni and especially Ingo Burgert for stimulating discussions on actuation in plant systems.

References:

Acet, M. (2009). "Magnetic Shape Memory Magnetoelastic Sponges." Nature Materials 8(11): 854-855.

Behl, M., Razzaq, M. Y. and Lendlein, A. (2010). "Multifunctional Shape-Memory Polymers." Advanced Materials 22(31): 3388-3410.

Bhushan, B. (2009). "Biomimetics: lessons from nature - an overview." Philosophical Transactions of the Royal Society a-Mathematical Physical and Engineering Sciences 367(1893): 1445-1486.

Burgert, I., Eder, M., Gierlinger, N. and Fratzl, P. (2007). "Tensile and compressive stresses in tracheids are induced by swelling based on geometrical constraints of the wood cell." Planta 226(4): 981-987.

Burgert, I. and Fratzl, P. (2009). "Actuation systems in plants as prototypes for bioinspired devices." Philosophical Transactions of the Royal Society A: Mathematical, Physical and Engineering Sciences 367(1893): 1541-1557.

Curie, P. (1894). "Sur la symétrie dans les phénomènes physiques, symétrie d'un champ électrique et d'un champ magnétique." Journal de physique théorique et appliquée 3(1): 393-415.

Dawson, C., Vincent, J. F. V. and Rocca, A.-M. (1997). "How pine cones open." Nature 390(6661): 668-668.

Dunlop, J. W. C. and Brechet, Y. J. M. (2009). "Architectured Structural Materials: A Parallel Between Nature and Engineering." Architectured Multifunctional Materials 1188: 15-25
241.

Elbaum, R., Gorb, S. and Fratzl, P. (2008). "Structures in the cell wall that enable hygroscopic movement of wheat awns." Journal of Structural Biology 164(1): 101-107.

Elbaum, R., Zaltzman, L., Burgert, I. and Fratzl, P. (2007). "The role of wheat awns in the seed dispersal unit." Science 316(5826): 884-886.

Embury, D. and Bouaziz, O. (2010). "Steel-Based Composites: Driving Forces and Classifications." Annual Review of Materials Research, Vol 40 40: 213-241.

Forterre, Y., Skotheim, J. M., Dumais, J. and Mahadevan, L. (2005). "How the Venus flytrap snaps." Nature 433(7024): 421-425.

Fratzl, P. (2007). "Biomimetic materials research: what can we really learn from nature's structural materials?" Journal of the Royal Society Interface 4(15): 637-642.

Fratzl, P. and Barth, F. G. (2009). "Biomaterial systems for mechanosensing and actuation." Nature 462(7272): 442-448.

Fratzl, P., Elbaum, R. and Burgert, I. (2008). "Cellulose fibrils direct plant organ movements." Faraday Discussions 139: 275-282.

Goswami, L., Dunlop, J. W. C., Jungnikl, K., Eder, M., Gierlinger, N., Coutand, C., Jeronimidis, G., Fratzl, P. and Burgert, I. (2008). "Stress generation in the tension wood of poplar is based on the lateral swelling power of the G-layer." The Plant Journal 56: 531-538.

Hawkes, E., An, B., Benbernou, N. M., Tanaka, H., Kim, S., Demaine, E. D., Rus, D. and Wood, R. J. (2010). "Programmable matter by folding." Proceedings of the National Academy of Sciences of the United States of America 107(28): 12441-12445.

Janichen, S. and Perner, P. (2006). "Aligning concave and convex shapes." Structural, Syntactic, and Statistical Pattern Recognition, Proceedings 4109: 243-251.

Kulic, I. M., Mani, M., Mohrbach, H., Thaokar, R. and Mahadevan, L. (2009). "Botanical ratchets." Proceedings of the Royal Society B-Biological Sciences 276(1665): 2243-2247.

Lee, H., Xia, C. and Fang, N. X. (2008). "Biomimetic microactuator powered by polymer swelling " Proceedings of the ASME 13: 765-769.

Martone, P. T., Boller, M., Burgert, I., Dumais, J., Edwards, J., Mach, K., Rowe, N., Rueggeberg, M., Seidel, R. and Speck, T. (2010). "Mechanics without Muscle: Biomechanical Inspiration from the Plant World." Integrative and Comparative Biology.

Pfeifer, R., Lungarella, M. and Iida, F. (2007). "Self-organization, embodiment, and biologically inspired robotics." Science 318(5853): 1088-1093.

Randhawa, J. S., Keung, M. D., Tyagi, P. and Gracias, D. H. (2010). "Reversible Actuation of Microstructures by Surface-Chemical Modification of Thin-Film Bilayers." Advanced Materials 22(3): 407-+.

Reyssat, E. and Mahadevan, L. (2009). "Hygromorphs: from pine cones to biomimetic bilayers." Journal of The Royal Society Interface.

Schreiber, N., Gierlinger, N., Putz, N., Fratzl, P., Neinhuis, C. and Burgert, I. (2010). "G-fibres in storage roots of Trifolium pratense (Fabaceae): tensile stress generators for contraction." Plant Journal 61(5): 854-861.

Sellinger, A. T., Wang, D. H., Tan, L. S. and Vaia, R. A. (2010). "Electrothermal Polymer Nanocomposite Actuators." Advanced Materials 22(31): 3430-+.

Skotheim, J. M. and Mahadevan, L. (2005). "Physical Limits and Design Principles for Plant and Fungal Movements." Science 308(5726): 1308-1310.

Timoshenko, S. (1925). "Analysis of bi-metal thermostats." Journal of the Optical Society of America and Review of Scientific Instruments 11(3): 233-255.

Torquato, S. (2010). "Optimal Design of Heterogeneous Materials." Annual Review of Materials Research, Vol 40 40: 101-129.

Witztum, A. and Schulgasser, K. (1995). "The Mechanics of Seed Expulsion in Acanthaceae." Journal of Theoretical Biology 176(4): 531-542.

Zupan, M., Ashby, M. F. and Fleck, N. A. (2002). "Actuator classification and selection - The development of a database." Advanced Engineering Materials 4(12): 933-940.

7.9 [AC2] Shape-Programmed Folding of Stimuli-Responsive Polymer Bilayers.

Stoychev, G., Zakharchenko, S., Turcaud, S., Dunlop, J. W. C., Ionov, L
*Published in **ACS Nano**, 2012, 6(5), 3925–3934.*
Doi: 10.1021/nn300079f

Reprinted with permission from the American Chemical Society

ABSTRACT. We investigated the folding of rectangular stimuli-responsive hydrogel-based polymer bilayers with different aspect ratios and relative thicknesses placed on a substrate. It was found that long-side rolling dominates at high aspect ratios (ratio of length to width) when the width is comparable to the circumference of the formed tubes, which corresponds to a small actuation strain. Rolling from all sides occurs for higher actuation, namely when the width and length considerably exceed the deformed circumference. In the case of moderate actuation, when the width and length are comparable to the deformed circumference, diagonal rolling is observed. Short-side rolling was observed very rarely and in combination with diagonal rolling. Based on experimental observations, finite-element modeling as well as energetic considerations, we argued that bilayers placed on a substrate start to roll from corners due to quicker diffusion of water. Rolling from the long-side starts later but dominates at high aspect ratios in agreement with energetic considerations. We have showed experimentally and by modeling that the main reasons causing a variety of rolling scenarios are (i) non-homogenous swelling due to the presence of the substrate and (ii) adhesion of the polymer to the substrate.

Introduction. Design of hollow 3D objects such as capsules and tubes is highly demanded for cell encapsulation, drug delivery, design of self-healing materials [1]. Most approaches for fabrication of capsules are based on the use of particles or fibers as templates, which are covered by functional materials. Hollow functional structures are, thus, formed after the removal of the core. Recently, the use of self-folding films – thin films, which are able to form different 3D structures, was suggested as a template-free alternative to the traditional template-based approaches [2]. The main advantage of self-folding films is the possibility to transfer a pattern, created on the surface of the unfolded film, into the inner and outer walls of the folded 3D structure [3].

Inorganic and polymer-based bilayers are examples of self-folding films, which fold due to relaxation of internal stresses originated from dissimilar properties of the two layers, such as lattice mismatch, thermal expansion or swellability. Inorganic-based self-folding films are promising for a variety of fields ranging including transport [4], nanooptics [5] , energy storage elements [6], photovoltaic power applications [7], optics [8], engineering of scaffolds [9] as well as being suitable to investigate the role of confinement on cell behavior [10]. Polymer based self-folding films, on the other hand, are particularly promising for biotechnological application such as encapsulation of cells [11] and design of biomaterials [12]. These and other applications require precise control of the folding for fabrication of 3D objects with a defined shape. In particular, it was demonstrated that the resulting shape of the folded 3D object can be controlled by the shape of the original bilayer. For example, rectangular bilayers form tubes [11a] while star-like bilayers are able to form envelope-like capsules[11b].

Generally, the rolling of a rectangular bilayer may occur according to three different scenarios: long-side, short-side and diagonal rolling (see Figure 1). The effects of film shape on the character of folding were experimentally investigated on examples of purely inorganic and composite polyaniline-inorganic bilayers. Smela et al showed that short-side rolling was preferred in the case of free homogeneous actuation and that this preference increased with aspect ratio (ratio of length to width of rectangular pattern)[13]. Li et al experimentally demonstrated the opposite scenario [14], namely a preference for long-side rolling, in the case where bilayers are progressively etched from a substrate. They observed that when the tube circumference was much larger than the width, or the aspect ratio of the rectangle was high, rolling always occurred from the long side. When the tube circumference was much smaller than the width and the aspect ratio of the membrane pattern was not very high, the rolling resulted in a mixed yield of long- and short-side rolling, as well as a "dead-locked turnover" shape. Short-side rolling occurred at small aspect ratios when the deformed circumference is close to the width. In these self-rolling systems, the active component undergoes relatively small volume changes or actuation strains, which are nearly homogenous over the whole sample. Hydrogels films, which are also able to fold, demonstrate considerably different properties [15]. First, hydrogels undergo large volume changes (up to 10 times) upon swelling and contraction. Second, the swelling of a hydrogel is often kinetically limited: due to slow diffusion of water through hydrogel, the parts which are closer to the edges swell first while the parts which are closer to the center of the films swell later. Thus, the actuation profile inside the active layer is heterogeneous. In this paper we investigate the effects of shape, size and rolling curvature on the direction of folding of rectangular polymer bilayers placed on a substrate, where the bottom component is a stimuli-responsive hydrogel.

Experimental Observations

Experimental preparation. Two families of polymeric bilayers, made of an active and a passive layer, are studied. The passive component is either hydrophobic polycaprolactone (PCL) or random copolymer poly(methylmethacrylate-co-benzophenone acrylate) (P(MMA-BA)). The active component is a thermoresponsive hydrogel formed either by photoscrosslinked poly(N-isopropylacrylamide-co-acrylic acid-co-benzophenone acrylate) (P(NIPAM-AA-BA)) or by

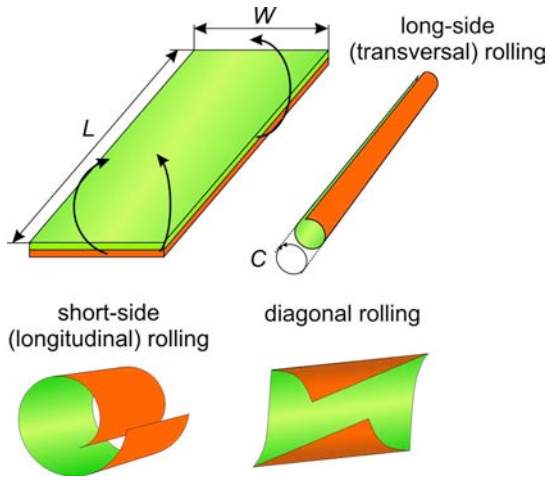

Figure 1. Scheme of rolling of a polymer bilayer according to different scenario: short-side, long-side and diagonal rolling.

poly(N-isopropylacrylamide-co-benzophenone acrylate) (P(NIPAM-BA)). Thermoresponsive hydrogels swell and shrink at reduced and elevated temperature, respectively. The passive hydrophobic P(MMA-BA) and PCL layers restrict swelling of the active hydrogel. As a result, the bilayer made of these polymers does not uniformly expand/shrink but folds and unfolds due to swelling and collapse of the hydrogel layer, respectively.

P(NIPAM-AA-BA)/(P(MMA-BA) and P(NIPAM-BA)/PCL bilayers were prepared using photolithography as described earlier [11a]. First, we prepared two sets of patterned bilayers of P(NIPAM-AA-BA)/(P(MMA-BA), which differ in thickness (H) of the P(MMA-BA) layer that results in different rolling curvature. One set formed narrow tubes with the diameter d = 20 µm ($H_{P(MMA-BA)}$ = 500 nm; $H_{P(NIPAM-AA-BA)}$ = 1200 nm), while the second set forms wider tubes with diameters in the range d = 70-90 µm ($H_{P(MMA-BA)}$ = 1200 nm; $H_{P(NIPAM-AA-BA)}$ = 1200 nm). The rectangular bilayers of different lengths (L = 100 - 1000 µm) and aspect ratios (ratio of length (L) to width (W), A = L/W = 1 - 8) were fabricated using specially designed photomasks. After removal of the non-crosslinked polymer, the patterned bilayers were exposed to PBS solution (pH = 7.4) at room temperature. As a result, photocrosslinked P(NIPAM-AA-BA) swelled leading to rolling of the bilayer and formation of tubes. The folded films formed by each set of bilayers were then mapped by optical microscopy in order to assess the rolling radius as well as the deformation pattern (see Figure 2 and 3).

Experimental results. It was found that the final diameter of the tube is independent of the size of the bilayer (L,W), but everything else being equal (Young Modulus of active and passive layer as well as activation strain), it is solely controlled by the relative thickness of the active and passive layers[16], and thus is (almost) constant for each set of experiments. The direction of rolling strongly depends on the size and shape of the films as well as on the thickness of the active and passive layer (see Figure 4). We distinguished four general types of rolling: long-side rolling, diagonal rolling, short-side rolling as well as mixed all-side rolling, which is a combination of the three first types. The character of preferential rolling is plotted as a function of the absolute values of width, length and aspect ratio, as well as normalized values, which are obtained by dividing the length or width by the typical circumference of the rolled tube (C = π x d, Figure 1).

Three types of rolling were observed when narrow tubes (d = 20 µm) are formed: long-side, diagonal and all-side rolling (see Figure 4a). It must be noted that no short-side rolling was observed. The all-side rolling (see Figure 2 a1-3, b1-2) occurs when the width of the films considerably exceeds circumference of rolling for aspect ratios of one or two. Decrease of the width for an aspect ratio of 2 or more results in preferential long-side rolling (see Figure 2 b3, c1-3, d1-3), when the normalized length is more than 2. Depending on the ratio of width (W) to circumference (C) incompletely rolled tubes (W/C < 1), completely rolled tubes (W/C ~ 1) or doubled tubes (W/C ≥ 2) are formed. Further decrease of the length leads to a mixture between long-side and diagonal or all-side rolling (see Figure 2 a4, b4, c4 and d4). The most promising parametric window for potential applications, such as microfluidics [15c] and cells encapsulation [11a], is thus bilayers with aspect ratio of 4 or more.

Different rolling behavior is observed when wide tubes (d = 70 - 90 µm) are formed (see Figure 4b). First, the films with the highest aspect ratio slightly bend and almost do not roll because of the large circumference (see Figure 3 d1-4). Second, other bilayers roll either according to diagonal or all-side rolling scenarios. Diagonal rolling is observed in the cases of square films (L/W = 1) when two opposite corners bend to each other (see Figure 3 a1-a4). "Tick or check mark-like" structures (see for example Figure 3 c1, the film in the middle) in a combination with diagonal rolling are observed in almost all cases at L/W > 1 when either adjacent or opposite corners bend to each other, respectively. Bending from short sides was observed in combination with diagonal rolling only in one case (see Figure 3 b4).

The results obtained for narrow (Figure 2 and 4a) and wide (Figure 3 and 4b) tubes plotted as a function of normalized length and width are not fully identical. Figure 4b is shifted to larger values of L/C. The reason of this effect is not completely clear and could be due to effects related to heterogeneities in the swelling behavior, which are hard to be fully considered. On the other hand, there is a clear correlation between the results given in Figure 4a and b which is qualitatively summed up in Figure 4c. For example, all-side rolling is observed when both length and width considerably exceed the deformed circumference. Diagonal rolling is observed when L = W and both are comparable to the circumference. In this case, short diagonally-rolled tubes are formed. Mixtures of diagonal rolling and the formation of "tick or check mark-like" structures (tube in the middle of Figure 3c1) is observed when L > W and both L and W are comparable to the circumference. The long-side rolling takes place when the length considerably exceeds the deformed circumference (L/C > 4) and aspect ratio is larger than 4. As result long tubes are formed, at least in the case of narrow tubes (d = 20 µm). In order to test the hypothesis that long tubes are formed when L/C > 4 and W ≈ C also in the case of wide tubes (d = 70 - 90 µm), we investigated rolling of 1800 µm x 300 µm large bilayers tubes ($H_{P(MMA-BA)}$ =

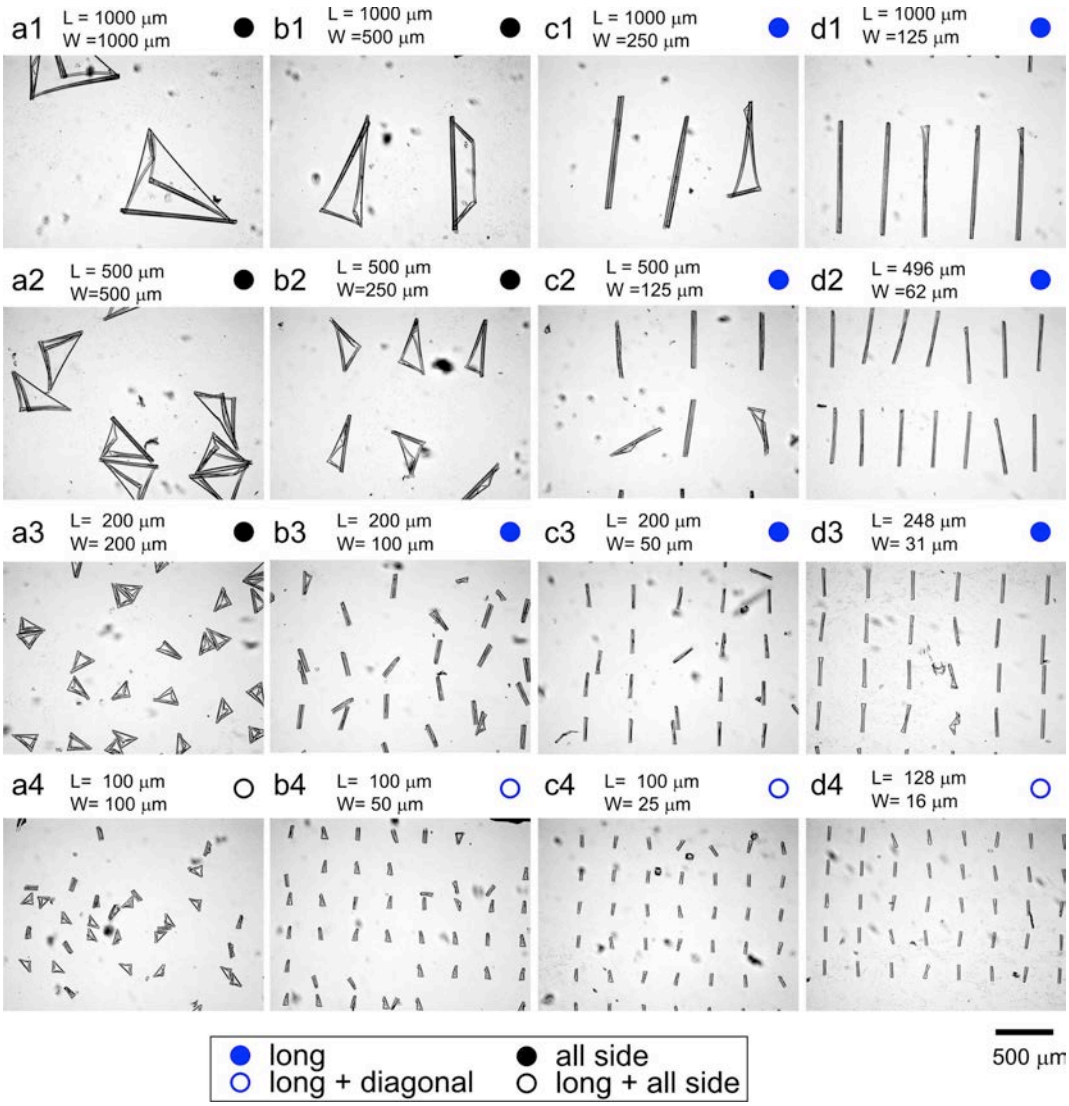

Figure 2. Microscopy snapshots of folded P(NIPAM-AA-BA) - P(MMA-BA) bilayers of different length (L) and width (W) which form narrow tubes of diameter d = 20 μm, $H_{P(MMA-BA)}$ = 500 nm; $H_{P(NIPAM-AA-BA)}$ = 1200 nm.

1200 nm, $H_{P(NIPAM-AA-BA)}$ = 1200 nm, W/C = 1.2; L/C = 7.5). Indeed, rolling resulted in preferential formation of longitudinal tubes (see Figure 4d) is in agreement with our predictions.

Mechanism of rolling. In order to clarify the variety of observed rolling scenarios, we experimentally investigated swelling and rolling of the bilayers. Rolling was investigated first using members of the second family of patterned bilayers formed by poly(N isopropylacrylamide – co – benzophenone acrylate) (P(NIPAM-BA)) and polycaprolactone (PCL) with high aspect ratio (L/W = 6, H_{PCL} = 300 nm, $H_{P(NIPAM-BA)}$ = 750 nm) [11a]. Initially, the polymer films were immersed in warm water where the active P(NIPAM-BA) hydrogel monolayer shrinks. The temperature was gradually decreased and rolling was observed. Diagonal rolling started from corners and stopped when two rolling fronts met each other (Figure 5a). Long-side rolling started later (Figure 5b) but eventually dominated leading to a switching of the diagonally-rolled corners to long-side rolled (Figure 5c,d). The formed double tubes were unrolled at elevated temperature (Supplementary Materials, Movie S1). The central part of the rolled bilayer, which has a shape of a line (Figure 5e), is still adhered to the substrate after rolling because the bilayer remains almost undeformed there. This adhesion area directs long-side rolling during second circle of temperature decrease and prevents short-side rolling. The second rolling, thus, proceeded similar to the first one: rolling starts from the corners and then switched to long-side rolling.

In order to explain the fact that rolling starts from the corners we experimentally investigated the swelling process. This was performed in qualitative manner by observing changes in the interference pattern of white light with the bilayer during swelling. In order to avoid bending and folding of the bilayer during swelling, a very thin P(NIPAM-AA-BA) layer (H = 35 nm) under a thick P(MMA-BA) layer (H = 400 nm) was used. Due to effect of interference of the light, which is mirrored from top and bottom surfaces of the bilayer, the changes of colors (see Figure 6) reflect changes in the film thickness. It is observed that color of the films start to change at the corners first, which confirms the assumption that the inhomogeneous activation profile in the active layer due to slow water diffusion into the hydrogels is at the origin of the experimentally observed fact that rolling starts at corners. Thus, based on the observations of rolling

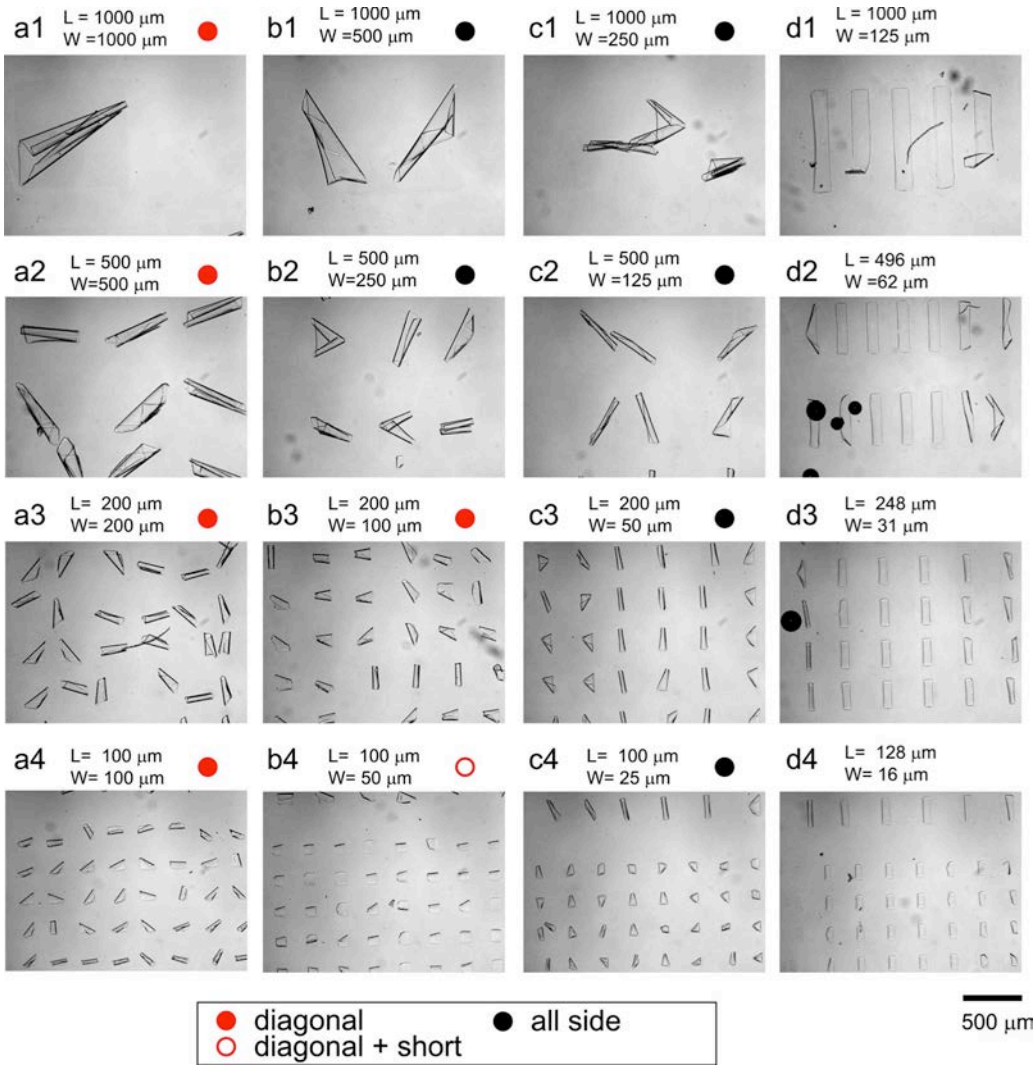

Figure 3. Microscopy snapshots of folded P(NIPAM-AA-BA)- P(MMA-BA) bilayers with different length (L) and width (W) which form wide tubes of diameter d = 70 – 90 µm, $H_{P(MMA-BA)}$ = 1200 nm; $H_{P(NIPAM-AA-BA)}$ = 1200 nm.

and swelling mechanisms we can argue that diffusion determines folding in first moments of folding while adhesion seems to play a decisive role at later stages of folding.

Theoretical considerations

Diffusion driven actuation. The observed long-side folding of rectangular bilayers for some specific shape parameters contradicts the bending of bilayer actuators, which occurs along short side [13,16]. However, this holds under the assumption that the active layer is homogeneously activated and that there is no interaction with a substrate. It is the case of a freely floating bilayer where diffusion of water inside the hydrogel layer is not restricted by any substrate. It was confirmed that such freely-floating bilayers undergo short side rolling that is similar to the behavior of standard actuators (Figure 7a). As the studied bilayers are placed on a substrate, it is reasonable to assume that diffusion of water inside the active monolayer upon activation (T<T_0) occurs primarily through its lateral sides. Additionally, not only does the substrate confine diffusion, it also exerts adhesion forces to the bottom surface of the bilayer that impede actuation until a certain threshold of delimitation forces is reached. This means that bending, which requires detachment of the substrate, only occurs for a sufficient activation strain. In particular, non-swollen areas do not bend.

Finite-element simulations

The diffusion pattern is assumed to obey a classical diffusion law (Fick's law) with a constant imposed boundary condition on the lateral sides of the active monolayer. Well known in one dimension, the two-dimensional diffusion pattern was obtained through a finite-element simulation using ABAQUS at different time points for different monolayer shapes (aspect ratio). Diffusion of water inside a hydrogel can be described as a first approximation by steady-state heat diffusion inside a medium with constant diffusivity. We used linear three-dimensional diffusion elements (DC3D8), in order to be able to apply the resulting activation field to actuate bilayers subsequently, and applied a constant boundary condition on the lateral surfaces. The solvent diffusion, however, is a very complex process which is quite difficult to fully describe because the boundary conditions of diffusion change as the film deforms and detaches from the substrate. We aimed to discuss diffusion in the very first moments of swelling, when the film starts to deform, as we believe that subsequent deformation of the film are largely

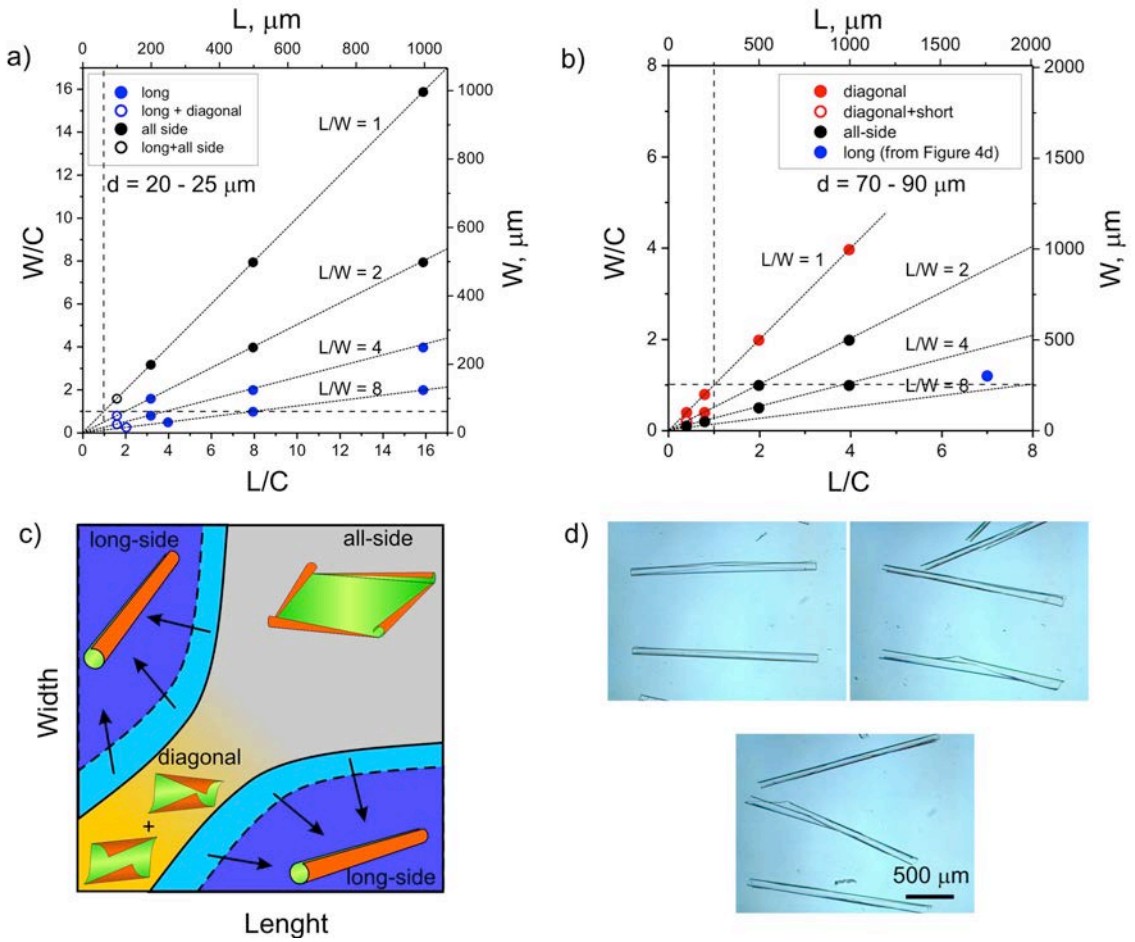

Figure 4. Dependence of preferential rolling direction of P(NIPAM-AA-BA) - P(MMA-BA) bilayers on the size and shape of the films when a) narrow (d = 20 µm, $H_{P(MMA-BA)}$ = 500 nm; $H_{P(NIPAM-AA-BA)}$ = 1200 nm) and b) wide (d = 70 - 90µm, $H_{P(MMA-BA)}$ = 1200 nm; $H_{P(NIPAM-AA-BA)}$ = 1200 nm) tubes are formed. Dashed lines correspond to L/C = 1 and W/C = 1 (L and W are length and width of the film, respectively; C is the circumference of the rolled tube); c) Schematic diagram of rolling scenario as a function of length and width, arrows indicate how the diagram changes when circumference (C) increases; d) Examples of wide tubes (d= 80 µm, $H_{P(MMA-BA)}$ = 1200 nm; $H_{P(NIPAM-AA-BA)}$ = 1200 nm) formed by rolling of 1800 µm x 300 µm large bilayers (corresponds to the blue point in Figure 4b).

determined by its starting deformation. The simulation allowed us to predict an inhomogeneous two-dimensional diffusion pattern that eventually becomes homogeneous after a sufficient time (see figure 6a-b).

Subsequently, we applied the obtained thermal field at different time points to a bilayer of same aspect ratio. Both layers of the bilayer are made of a linear elastic material with normalized Young modulus of 1 and a Poisson ratio of 0.3. This crude simplification relies on the fact that the stiffness contrast between the active and the passive layer does not significantly affect the rolling radius of a bilayer [16]. The bottom-layer possesses in-plane thermal expansion coefficients equal to 1, whereas the top-layer is thermally inactive. In order to understand the influence of substrate adhesion, we imposed a fixed kinematical boundary condition at an internal rectangular bottom surface, scaled from the external shape. We used a fine mesh of first-order eight-node elements with reduced-integration (C3D8R), which are able to follow the large displacements at reasonable cost. The deformed shape corresponding to an edge-activation of the bilayer at a given time point in the diffusion process, was calculated in a static step taking non-linear geometric effects into account. Adaptive meshing techniques were used to avoid large distortions in mesh elements upon actuation. We compared the obtained results with the one obtained using Riks method and found no discrepancy between the predicted deformed shapes. Surprisingly, convergence using a combination of adaptive meshing techniques on a fine mesh with a static non-linear geometric step proved to be better than using Riks method. This simple uncoupled model already shows that sharp activation strains near the edges combined with an internal constraint of the bottom layer produces interesting deformation patterns for different aspect ratios. In particular, the model predicts that short and long side rolling is more favorable at L/W < 4 and L/W > 4, respectively (see Figure 7 b).

The appearance of all-side and diagonal rolling in experiments at smaller aspect ratios accounts for the fact that no preferential direction appears for bending deformations. Also, imperfections of the material properties of the polymer film and substrate can be responsible for the observed symmetry-breaking.

Energetic considerations

The fact that edge activation of a constrained bilayer

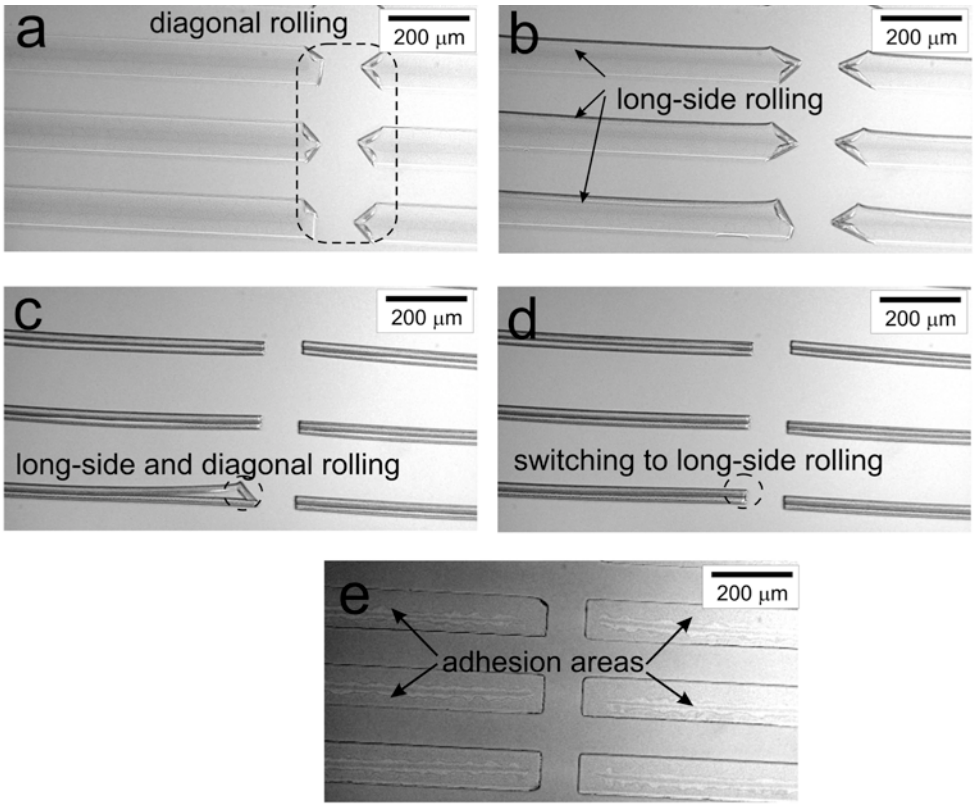

Figure 5. Time-resolved rolling of P(NIPAM-BA) - PCL bilayer (H_{PCL} = 300 nm, $H_{P(NIPAM-BA)}$ = 750 nm, 930µm x 90µm), diameter of the tube d = 41 µm (a-e, Supplementary movie S1)

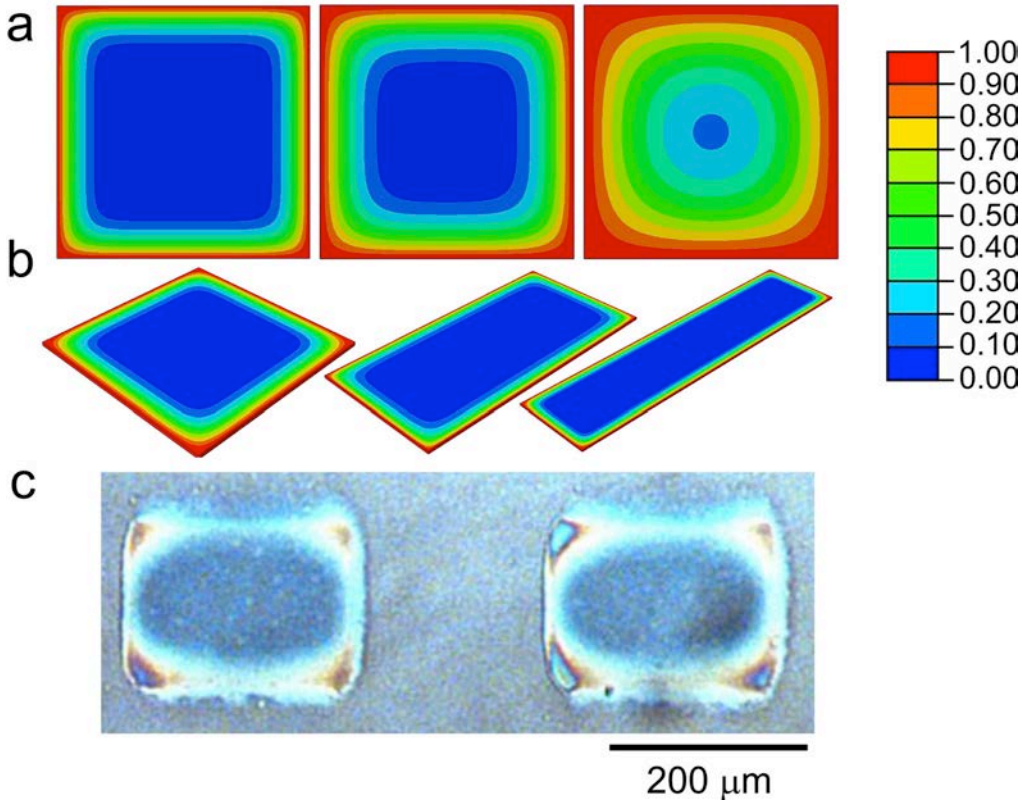

Figure 6. Color map of the calculated swelling (from 0 to 1) controlled by water diffusion in the active monolayer with a lateral constant boundary condition (blue is non swollen) dependent on time (a) and shape (b) obtained by finite element simulations as well as experimentally obtained microscopy snap-shot of swollen P(NIPAM-BA) - PMMA bilayer ($H_{P(MMA-BA)}$ = 400 nm; $H_{P(NIPAM-AA-BA)}$ = 35 nm) after few seconds of swelling (c).

leads to long-side rolling, is also suggested by plate theory. The elastic energy of plate-like objects can be decomposed into a stretching and a bending term according to Föppl von Kármán plate theory [17], in which the in-plane strains are integrated over the thickness taking into account the edge-activation. This

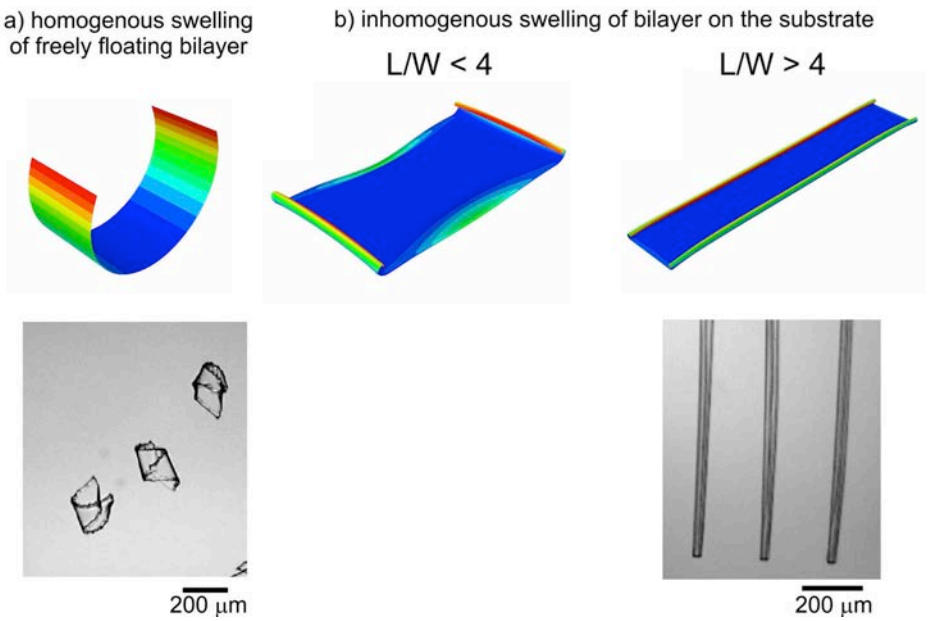

Figure 7. Simulation and experimentally observed folding of rectangular bilayers at different conditions: (a) freely floating rectangular bilayer (homogenous swelling, Supplementary movie S2) (b) rectangular bilayer on substrate (inhomogeneous swelling, Supplementary movie S1)

formulation describes accurately the elastic energy of a bilayer plate upon edge-activation and can be solved numerically (this will be done in a subsequent paper). Another approach, which is less subtle, but that also leads to accurate results, is a finite-element method solving the 3D mechanical problem by finite-element method. Essentially the problem can be described in the following way: we make an additive decomposition of the total strain in the active layer into an Eigen (or swelling strain) and an elastic strain $\varepsilon_{kl}^{T} = \varepsilon_{kl}^{eig} + \varepsilon_{kl}^{el}$. The Eigen strain is given as $\varepsilon_{ij}^{eig} = \alpha\delta_{ij}$ where δ_{ij} is the Kronecker delta, isotropic swelling is assumed in the current model. The amount of swelling depends on the swelling coefficient α which in turn can vary spatially according to the solution of the diffusion equation. As the active layer is constrained by the passive layer, incompatibilities result in elastic strains and thus stresses through Hooke's law $\sigma_{ij} = E_{ijkl}\varepsilon_{kl}^{el}$. The final shape of the structure upon changes the spatial distribution and magnitude of α are calculated by minimizing the elastic energy of the system. For further details of the finite element method see e.g [18]. The stretching term being linear in thickness, while the bending term is cubic, bending deformations are favored when the plate is sufficiently thin. Unlike in a beam-like bilayer, actuation triggers a biaxial expansion field inside the plate, which creates internal stresses in the long and in the short direction of the plate. Relaxation of internal stresses perpendicular to the edge of the bilayer will lead to bending, whereas relaxation of internal stresses parallel to the edge of the bilayer will produce stretching that will eventually lead to wrinkling as in the edge of long leaves [19]. Because of the presence of the substrate, internal stresses perpendicular to the edge of the bilayer are more easily relaxed, leading to simple bending, while internal stresses parallel to the edge of the bilayer produce simple stretching. As the aspect ratio increases, it is thus less costly to relax stresses into bending on the long side than on the short side. This explains qualitatively why long-side rolling is observed as the aspect ratio increases.

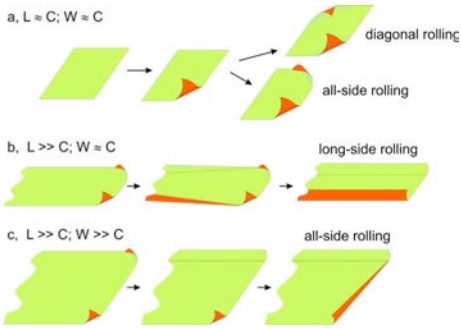

Figure 8. Schematic of rolling leading to in diagonal rolling, long-side rolling and all-side rolling.

Finite-element modeling and energetically considerations show that the experimentally observed appearance of long tubes for large aspect ratios and high activation strains are due to: (i) non-homogenous swelling due to slow lateral diffusion, as well as (ii) adhesion of the bilayer to the substrate constraining the deformations. Both these factors are caused by the specific geometry of the experiment: (i) polymer bilayer is deposited on the substrate and (ii) active polymer is the bottom layer.

Rolling scenario. Finally, by considering modeling and experimental results, the following scenario of rolling of hydrogel-based polymer bilayer laying on a substrate is assigned. The rolling starts from the edges due to faster diffusion of water from the lateral surfaces, which then are able to detach from the substrate and to bend. Rolling can start either from two adjacent (for example Figure 3 d2 right lower

polymer film or Figure 3 b2 left upper film) or opposite edges (almost all polymer films in Figure 2 a2) or from all corners simultaneously, which is less probable if the bilayer is small due to the presence of imperfections and becomes energetically unfavorable once a sufficient actuation strain is reached. Rolling is almost immediately finished if the films are small and if the deformed circumference is comparable to the size of the bilayer. As a result, diagonally-rolled tubes are formed if rolling starts from two opposite corners (Figure 8a) or "tick or check mark-like" structures (for example Figure 3 c1, the film in the middle) are formed if rolling starts from two adjacent corners.

A more complicated scenario is observed when the width of the films is small and the length is considerably larger than the deformed circumference. Rolling starts at the corners first like before, but. long-side rolling starts later (Figure 8b and Figure 5) and is energetically favored. Rolling along the short side is unfavorable because it implies more stored stretching energy along the long side. Further long-side rolling makes diagonally rolled corners unfavorable and leads to the switching of bent corners to a "long-side rolling" scenario. Depending on the width of the film compared to the deformed circumference, either an incompletely rolled tube is formed, or the two long-side rolling fronts collide into a completely rolled or doubled tube.

If the deformed circumference is considerably smaller than the width and length of the films (which implies a high activation strain), then rolling starts first from corners and then continues along all sides (Figure 8c). The rolling fronts do not collide until several revolutions are made, which were shown to be almost irreversible [11a]. As a result, already rolled fronts are unable to unroll and irreversible all-side rolling is observed.

Conclusions. We investigated in detail folding of rectangular stimuli-responsive hydrogel-based polymer bilayers located on a substrate with different lengths, widths and thicknesses. It was found that long-side rolling dominates at high aspect ratios (ratio of length to width) when the width is comparable to the circumference of the formed tubes. Rolling from all sides occurs when the width and length considerably exceed this circumference. Diagonal or all-side rolling is observed when the width and length are comparable to the circumference. Short-side rolling was observed very rarely and in combination with diagonal rolling. Based on both experimental observations and theoretical assumptions, we argued that bilayers placed on a substrate start to roll from corners due to quicker diffusion of water. Rolling from long-side starts later but dominates at high aspect ratio due to energetic considerations. We have showed experimentally and by finite-element modeling confirmed by theoretical considerations, that the main reasons causing a variety of rolling scenarios are (i) non-homogenous swelling due to slow diffusion of water in hydrogels and (ii) adhesion of polymer to a substrate until a certain threshold. Moreover, non-homogenous swelling determines folding in first moments while adhesion player decisive role at later stages of folding.

The films which we investigated are fabricated on the micro scale. On the other hand, the knowledge obtained in this work is applicable to thinner films to direct their folding in order to form tubes with diameter in the nano range. We believe that the obtained knowledge can be particularly helpful for design of self-folding objects with highly complex shapes.

Acknowledgement. The authors are grateful to DFG (Grant IO 68/1-1) and IPF for financial support. We also thank Yves Bréchet for discussions about the FE simulations.

References

(1) Esser-Kahn, A. P.; Odom, S. A.; Sottos, N. R.; White, S. R.; Moore, J. S. Macromolecules 2011, 44, 5539.

(2) (a) Ionov, L. Soft Matter 2011, 7, 6786(b) Leong, T. G.; Zarafshar, A. M.; Gracias, D. H. Small 2010, 6, 792.

(3) (a) Randhawa, J. S.; Kanu, L. N.; Singh, G.; Gracias, D. H. Langmuir 2010, 26, 12534(b) Luchnikov, V.; Sydorenko, O.; Stamm, M. Adv. Mater. 2005, 17, 1177(c) Cho, J. H.; Gracias, D. H. Nano Lett. 2009, 9, 4049.

(4) Solovev, A. A.; Sanchez, S.; Pumera, M.; Mei, Y. F.; Schmidt, O. G. Adv. Funct. Mater. 2010, 20, 2430.

(5) Smith, E. J.; Liu, Z.; Mei, Y. F.; Schmidt, O. G. Appl Phys Lett 2009, 95.

(6) Bof Bufon, C. C. s.; Cojal González, J. D.; Thurmer, D. J.; Grimm, D.; Bauer, M.; Schmidt, O. G. Nano Lett. 2010, 10, 2506.

(7) Guo, X. Y.; Li, H.; Ahn, B. Y.; Duoss, E. B.; Hsia, K. J.; Lewis, J. A.; Nuzzo, R. G. Proc. Natl. Acad. Sci. U. S. A. 2009, 106, 20149.

(8) Schwaiger, S.; Broll, M.; Krohn, A.; Stemmann, A.; Heyn, C.; Stark, Y.; Stickler, D.; Heitmann, D.; Mendach, S. Phys Rev Lett 2009, 102.

(9) (a) Gracias, D. H.; Tien, J.; Breen, T. L.; Hsu, C.; Whitesides, G. M. Science 2000, 289, 1170(b) Leong, T.; Gu, Z. Y.; Koh, T.; Gracias, D. H. J. Am. Chem. Soc. 2006, 128, 11336(c) Randall, C. L.; Kalinin, Y. V.; Jamal, M.; Manohar, T.; Gracias, D. H. Lab Chip 2011, 11, 127(d) Jamal, M.; Bassik, N.; Cho, J. H.; Randall, C. L.; Gracias, D. H. Biomaterials 2010, 31, 1683.

(10) Huang, G. S.; Mei, Y. F.; Thurmer, D. J.; Coric, E.; Schmidt, O. G. Lab Chip 2009, 9, 263.

(11) (a) Zakharchenko, S.; Puretskiy, N.; Stoychev, G.; Stamm, M.; Ionov, L. Soft Matter 2010, 6, 2633(b) Stoychev, G.; Puretskiy, N.; Ionov, L. Soft Matter 2011, 7, 3277.

(12) Zakharchenko, S.; Sperling, E.; Ionov, L. Biomacromolecules 2011, 12, 2211.

(13) Alben, S.; Balakrisnan, B.; Smela, E. Nano Lett. 2011, 11, 2280.

(14) Chun, I. S.; Challa, A.; Derickson, B.; Hsia, K. J.; Li, X. Nano Lett. 2010, 10, 3927.

(15) (a) Stuart, M. A. C.; Huck, W. T. S.; Genzer, J.; Muller, M.; Ober, C.; Stamm, M.; Sukhorukov, G. B.; Szleifer, I.; Tsukruk, V. V.; Urban, M.; Winnik, F.; Zauscher, S.; Luzinov, I.; Minko, S. Nat Mater 2010, 9, 101(b) Singamaneni, S.; McConney, M. E.; Tsukruk, V. V. ACS Nano 2010, 4, 2327(c) Jamal, M.; Zarafshar, A. M.; Gracias, D. H. Nature Communications 2011, 2.

(16) Timoshenko, S. J. Opt. Soc. Am. Rev. Sci. Instrum. 1925, 11, 233.

(17) Audoly, B.; Pomeau, Y. Elasticity and geometry : from hair curls to the non-linear response

of shells; Oxford University Press: Oxford; New York, 2010.
(18) Zienkiewicz, O. C.; Taylor, R. L.; Elsevier.
(19) Liang, H. Y.; Mahadevan, L. Proc. Natl. Acad. Sci. U. S. A. 2011, 108, 5516.

7.10 [AC3] Hierarchical Multi - Step Folding of Polymer Bilayers.

Stoychev, G., Turcaud, S., Dunlop, J. W. C., Ionov, L.
*Published in **Advanced Functional Materials**, 2013 23, 2295–2300.*
DOI: 10.1002/adfm.201203245

Reprinted with permission from John Wiley and Sons

Abstract: A highly complex multi-step folding of isotropic stimuli-responsive polymer bilayers resulting in a variety of 2D and 3D structures is reported. Experimental observations allow determination of empirical rules, which can be used to direct the folding of polymer films in a predictable manner. In particular, it is demonstrated that these rules can be used for the design of a 3D pyramid. The understanding and know-how attained in this study allow the very simple design of highly complex, self-folding 3D objects and open new horizons for 3D patterning, important for the design of microfluidic devices, biomaterials, and soft electronics.

1 Introduction

Nature offers an enormous arsenal of ideas for the design of novel materials with superior properties and interesting behavior. In particular, self-assembly and self-organization, which are fundamental to structure formation in nature, attract significant interest as promising concepts for the design of intelligent materials.[1] Self-folding stimuli-responsive polymer films are exemplary biomimetic materials[2] and can be viewed as model systems for bioinspired actuation. Such films, on one hand, mimic movement mechanisms in certain plant organs[3,4] and, on the other hand, are able to self-organize and form complex 3D structures.[5] These self- folding films consist of two polymers with different properties. Because of the nonequal expansion of the two polymers, these films are able to form tubes,[6,7] capsules[8] or more complex structures.[9] Similar to origami, the self-folding polymeric films provide unique possibilities for the straightforward fabrication of highly complex 3D microstructures with patterned inner and outer walls that cannot be achieved using other technologies.

There are two general approaches for the design of self- folding films. The first approach is based on the use of complexly patterned films, where locally deposited active materials form hinges.[10] Homogenous bilayer films are used in the second approach.[11] Because of the isotropy of the mechanical properties of the bilayer, the formed structures are hinge- free and have rounded shapes. Importantly, in all reported cases, folding runs in one step. On the other hand there are reports that folding in nature can have a very complex character, which strongly depends on the geometry and swelling path[12] that may result in multistep folding (development of curvature in different directions).[3] In this contribution, we demonstrate that the shape of isotropic polymer bilayers is able to direct folding in a sophisticated manner leading to even more complex hierarchical folding than in nature. In particular, films can undergo sequential folding steps by forming various 3D shapes with sharp hinges. By analyzing the folding patterns we elucidated empirical rules, cross-checked by analytical considerations and backed up with finite-element simulations, which allow the folding to be directed, leading to the design of specific 3D shapes. We also highlight the importance of path-dependency in the activation of the actuator, which enables to lock it in a local energy minimum, which can differ from the global one.

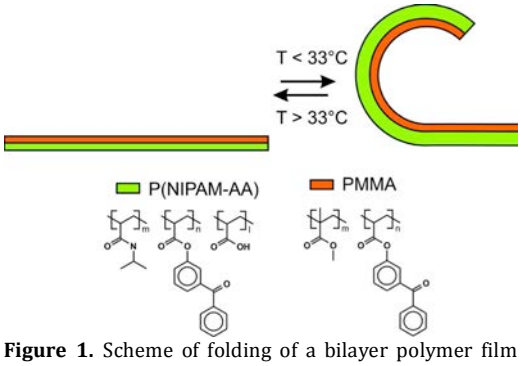

Figure 1. Scheme of folding of a bilayer polymer film consisting of two polymers: hydrophobic PMMA and thermoresponsive hydrogel P(NIPAM-AA).

2 Results and Discussions

For the experiments we used polymer films consisting of two layers of photo-crosslinked polymers: the active layer being a random thermoresponsive copolymer poly(N-isopropylacrylamide-co-acrylic acid) (P(NIPAM-AA) and the passive layer being poly-(methylmethycrylate) (PMMA) (**Figure 1**). The bilayer, prepared as described elsewhere,[7] is located on a silica wafer in such a way that the active and passive polymers are the bottom and top layers, respectively. The bilayer is undeformed in PBS 0.1 M pH = 7.4 environment at T > 70 ° C and folding occurs after cooling below 70 ° C (Figure 1).

Due to the relatively slow diffusion rate of water inside the P(NIPAM-AA) layer, actuation is driven by the progression of the diffusion front, along which the hydrogel starts to swell. This induces a path-dependency in the folding pattern as the bilayer is not homogeneously activated, but progressively swells as water diffuses from the lateral sides. The investigation of swelling was performed in a qualitative manner by observing the color change of the films which, due to light interference, reflects the change in optical path length (OPL) (**Figure 2**). The OPL varies as a function of the film thickness and refractive index, which in turn depends on the swelling degree.[13] The nonswollen elliptical and star-like films have a homogenous blue (Figure 2a) and reddish (Figure 2d) color, respectively. The difference in the color of both films is caused by their different starting thicknesses (Figure 2). The color of the films starts to change immediately after immersion in water at 25 ° C, with

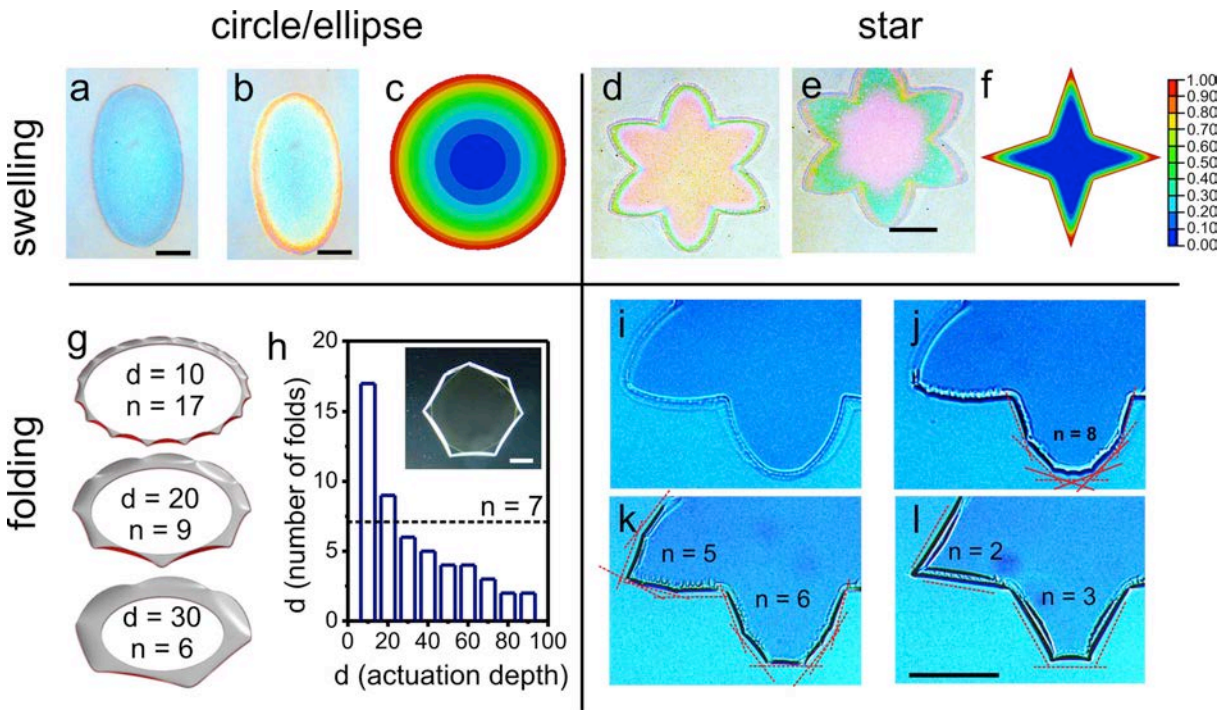

Figure 2. Swelling (upper panels) and first step of folding (lower panels) of circular/elliptical (left panels) and star-like (right panels) bilayer polymer films. a,b,d,e) Microscopy snapshots of swelling elliptical and star-like P(NIPAM-AA)/PMMA bilayers immediately after immersion in water (a,d) and after ca. 60 s incubation (b,e); c,f) Color map of the calculated swelling (from 0 to 1) controlled by water diffusion in the active monolayer with a lateral constant boundary condition (blue is non swollen) dependent on shape obtained by finite element simulations; g) Finite element simulations of wrinkling of a bilayer crown representing the activated edge in case of a circular shape; h) The number of wrinkles is inversely proportional to the actuation depth. Dashed line corresponds to the experimental observation of heptahedrons (inset) when folding is typically stopped in the case of circular shapes. The red line corresponds to n = 170/d. i–l) Two rays of six-ray star during wrinkling, decrease of number of wrinkles is observed. a, b) HPNIPAM = 35 nm, HPMMA = 400 nm; d,e) HPNIPAM = 35 nm, HPMMA = 500 nm; i–l) H(PNIPAM-AA) = 1200 nm, HPMMA = 400 nm, scale bar is 200 μm.

the elliptical film becoming redder while the star-like film becomes green (Figure 2b,e). The changes of color in both cases start from the outer periphery of the bilayer film. As the active layer is confined between a water-impermeable silicon wafer and hydrophobic PMMA, this suggests that water can only penetrate inside the layer from the lateral sides.[14] The depth of water penetration along the perimeter of the film (activation depth) is uniform in both cases in the first moments of swelling. The differences in the swelling behavior between the two shapes appear after several seconds of incubation in water. The activation pattern depends on the external shape of the bilayers, with the position of the diffusion front (the activation depth) depending on the distance to the tissue border. This can been seen clearly in the differences of the activation pat- terns in the convex shapes like ellipse (Figure 2b), and concave ones like star (Figure 2d). For the star-like bilayers, the tips of the triangular-like arms swell faster than their base and their polygonal central part. This can be explained by the fact that after a certain time the diffusion fronts on either side of the arms intersect resulting in faster swelling. The experimental results show that the swelling starts from the periphery of the films and that the activation profile strongly depends on the shape of the film as con- firmed by simple finite element simulations (see Figure 2c,f).

We next modeled and experimentally investigated the folding of circular/elliptical and star-like films. Modeling predicts that multiple wrinkles are formed along the perimeter of folding bilayer when it is edge-activated (Figure 2g). The spatial wavelength of the wrinkles is proportional to the activation depth (d) as observed in the wrinkles of leafs due to excessive radial edge-growth[15] and solved analytically in the context of geometrically nonlinear elasticity.[16] As the activation depth increases, the number of wrinkles decreases as P/d, where P is the perimeter of the shape (Figure 2h). The fact that there is both a gradient in radial- (edge-activation) and transversal direction (bilayer), results in a combination of wrinkling and bending, respectively (Figure 2g,h). In full agreement with the modeling predictions, experimental results show that the number of wrinkles decreases during folding (Figure 2i-l). Due to the transversal bending effect, the wrinkles actually evolve into local partial tubes as the activation depth increases. We observed that, at some point, the wrinkles stop to merge and their number remains constant. The probability of merging of two tubes depends on the angle (β, Figure 2h) between them. Experimentally, we found that the critical value of β below which merging of folded tubes was not observed is ca. 120–150°, which corresponds to 6–8 wrinkles when starting with a circular shape (inset in Figure 2h and Figure S3 in the Supporting Information). Based on these experimental observations we derived the first folding rule: "*Bilayer polymer films placed on a substrate start to fold from their periphery and the number of formed wrinkles/ tubes decreases until the angle between adjacent wrinkles/tubes approaches 130°*".

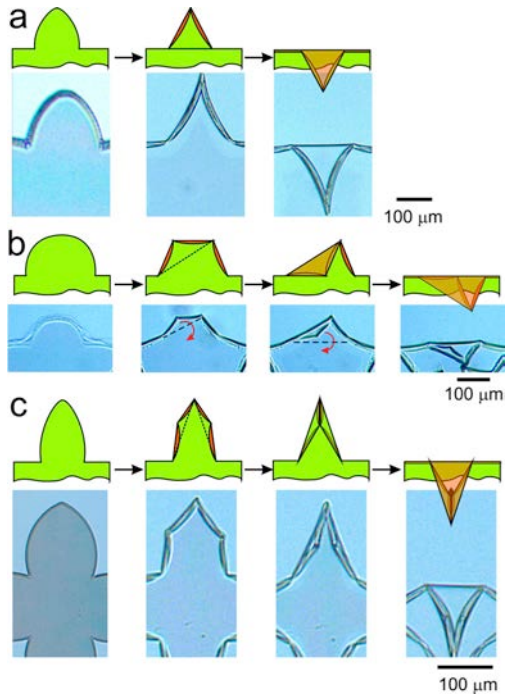

Figure 3. Seconds step of folding of elliptical arms depending on their shape. (a) $H_{(PNIPAM-AA)}$ = 1200 nm, H_{PMMA} = 170 nm; (b) ($H_{(PNIPAM-AA)}$ = 1200 nm, H_{PMMA} = 400 nm; (c) $H_{(PNIPAM-AA)}$ = 900 nm, H_{PMMA} = 170 nm.

After the number of wrinkles/tubes along the perimeter of the bilayer film stopped to change the bilayers are locked for some time until the subsequent folding step occurs. For example, the wrinkled semi-ellipse bends towards its base (**Figure 3**a). To explain the origin of the second step of folding we considered the geometry of the film after the first folding step. As mentioned, wrinkling of a bilayer leads to the formation of tubes along the perimeter of the film. Considering the fact that the rigidity of the tubes is higher than that of the undeformed films, the polygonal shapes are stiffened by this tube formation, and therefore possess a number of weak points located at the intersection of the tubes, i.e., at the vertices. These points act like hinges and folding is only observed along the lines connecting them (dashed line in Figure 3a). The formation of hinges during folding of isotropic bilayers, which to our knowledge has not been reported in the literature, is induced by the progressive activation from the lateral sides and the folded shapes are controlled by the initial shapes of the bilayers. This leads to the second rule of the folding: *"After the wrinkles along the perimeter of the film form tubes, further folding proceeds along the lines connecting the vertexes of the folded film".*

In case there are more than two hinges in the film, a question arises: upon which connecting line will the folding occur? The number of hinges is largely determined by the shape of the semi-ellipses. The regular semi-ellipse, which has a triangular shape after the first step of folding, simply bends toward the base along the line connecting the two bottom vertexes (dashed line in Figure 3a). If the semi-ellipse is more rounded, it forms a trapezoid after the first-step of folding (Figure 3b). In the second step of folding, the trapezoid bends along one of the lines connecting the opposite top and bottom vertexes

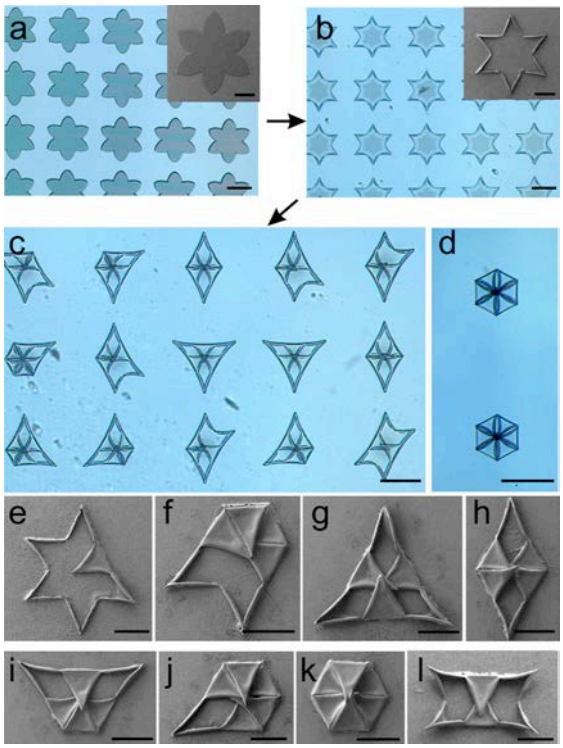

Figure 4. Examples of structures obtained by progressive edge-activation of six-ray star- like bilayers. a) Patterned bilayers; b) First step of actuation: wrinkles collapse into tubes; c–l) Second step of actuation: rays fold leading to several configurations depending on the order of folding. Scale bars are 200 µm, H(PNIPAM-AA) = 1200 nm, HPMMA = 260 nm.

(dashed line in the second image from the left in Figure 3b). Next, the formed triangle bends towards its base along the line connecting the two bottom vertexes. The elongated semi-ellipse forms four folds after the first step of folding (Figure 3c). Interestingly, the semi- ellipse folds further along the lines connecting the vertexes at the base and the top vertex and no folding along the lines connecting neither the vertexes of the middle nor the ones at the base is observed. Looking at the evolution of the activation pattern through time (diffusion profile see Figure 2), we observe that the lines connecting the hinges can only be used if they are within the activated pattern (red). Thus, the third rule of the folding states: "*the folding goes along the lines which are closer to the periphery of the films*".

Six-ray stars demonstrate the formation of very complex structures (**Figure 4**). Notably simultaneous folding of all rays is observed very rarely and in most cases tri- angles (Figure 4g) were formed. We investigated the folding in a time-resolved manner in order to explain the formation of the tri- angles (**Figure 5**). Similar to the experiment demonstrated in Figure 2, wrinkles get longer and bend transversally into tubes (Figure 5b) thus increasing the rigidity of the ray. Next, one of the rays folds towards the center of the star (II in Figure 5c). Folding of this ray leads to the formation of a rigid semi-rolled tube, which is formed by the folded ray and the tubular shoulders of the adjacent rays (Figure 5c). The angle between the base of the folded ray and the shoulders of the neighboring arms is close to 180° (Figure 5c). In this configuration, the weak points located at the

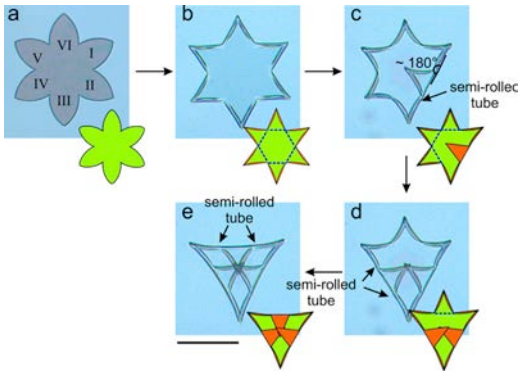

Figure 5. Microscopy snap-shots illustrating the mechanism of formation of triangles during actuation of a six-ray stars. Scale bar is 200 μm, H(PNIPAM-AA) = 1200 nm, HPMMA = 170 nm.

intersection between I–II and II–III has disappeared and rays I and III (Figure 5c) cannot bend anymore. As a result, only three remaining rays (IV, V, VI) can bend. If ray V folds, no additional rays can bend (Figure 4l).

If ray IV folds (Figure 5d) ray V is blocked. Finally, ray VI can fold leading to the formation of a triangle (Figure 5e). The discussed principle can be easily applied to understand the formation of the other observed figures (Figure 4c–l, Supporting Information Figure S2 and Figure S3). In fact, several factors can be held responsible for the observed symmetry breaking (rays do not fold at the same time) such as inhomogeneities in the films and shape imperfections resulting in small deviations from the symmetric diffusion profile. Based on these experimental observations, one can derive the fourth folding rule:*"Folding of the rays may result in blocking of the neighboring rays if the angle between the base of the folded ray and the shoulders of the neighboring rays is close to 180° ".*

Finally, we applied the derived rules for the design of truly 3D structures–pyramids. In fact, the reason why six-ray star formed flattened folded structures is their short arms and the hindering of folding of rays. Therefore, in order to fabricate pyramids we

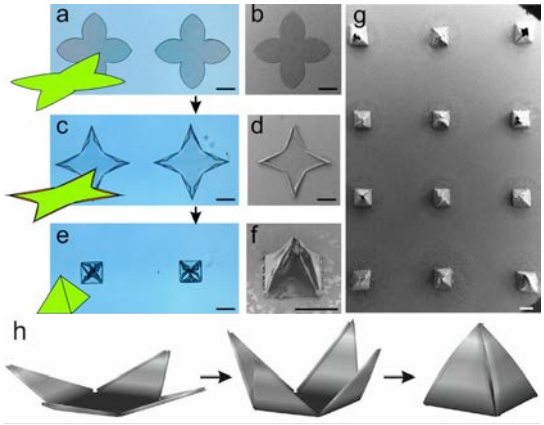

Figure 6. Sequential actuation of four-ray stars leads to the formation of pyramids. a,b) unac- tivated film; c,d) after wrinkling of the ray periphery into tubes, arrows indicate four wrinkles formed on each arm during first step of folding; e–g) after folding of rays leading to the forma- tion of pyramids. Scale bar is 200 μm, H(PNIPAM-

increased the relative length of the rays and changed the angle between them by decreasing their number (**Figure 6**a,b). The rays of the fabricated four-ray stars first wrinkle along their perimeter (Figure 6c, d). Four tubes are formed along the perimeter of each ray (first rule, Figure 6c), which then collapse two by two and form triangles (second rule, Figure 6d). Since the angle between the folds located on the shoulders of each ray is considerably smaller than 180° , the folding of rays is not self- interfering (forth rule) and all rays fold in the direction of the center of the star (third rule) thus forming a hollow pyramid (Figure 6e–g) that is supported by simulations (Figure 6h). In fact these rules are also applicable to other shapes such as rectangles. As an example we included two-step folding of rectangles (Supporting Information Figure S4).

We observed that, in general, folding rules are applicable to all thickness (we performed many experiments with different thicknesses). The difference between the thin and thick films are in minor. For example, we observe that when star-like thin fold than all six arms (Figure 4d,k) can fold inside because rigidity of the film is not that high. In the case of thick films, we typically observed folding of 3–4 arms (Figure 4g,l).

3 Conclusions

In conclusion, we investigated the actuation of patterned bilayers placed on a substrate. Due to the edge-activation of the bilayers, the observed deformed shapes differ from the classical ones obtained by homogeneous activation. We found that films can demonstrate several kinds of actuation behavior such as wrinkling, bending and folding that result in a variety of shapes. It was demonstrated that one can introduce hinges into the folded structure by proper design of the bilayer's external shape through diffusion without having to use site selective deposition of active polymers. Experimental observations lead us to derive four empirical rules backed up by theoretical understanding as well as simulations. We then demonstrated how those rules can be used to direct the folding of edge-activated polymer bilayers through a concrete example–the design of a 3D pyramid. We believe that the derived understanding and know-how will allow very simple design of highly complex, self-folding 3D objects and will open new horizons for 3D patterning which is highly important for the design of microfluidic devices, biomaterials, soft electronics, etc.

4 Experimental Section

Materials: *N*-isopropylacrylamide (NIPAM, Aldrich), 4-hydroxybenzophenone (Fluka), polycaprolactone (*M*n = 70 000–90 000 Da, Aldrich), benzophenone (Aldrich) and acryloyl chloride (Fluka) were used as received. Methyl methacrylate (MMA, Aldrich) and acrylic acid were purified by filtration through Al2O3 column before polymerization.

Synthesis of 4-Acryloylbenzophenone (BA): 4-Hydroxybenzophenone (20 g, 0.1009 mol), diisopropylethylamine (19.3 mL, 0.1110 mol) and 80 mL of methylene chloride were added into 200 mL three-necked round-bottom flask fitted with an overhead stirrer, a thermometer, and an addition funnel with acroloyl chloride (9.02 mL, 0.1110 mol) solution in 20 mL of methylene chloride. The acroloyl chloride solution was added dropwise into the flask

under cooling (0–5 ° C) for ca 3 h. The methylene chloride was removed by rotary evaporation. The residue was washed with 80 mL of 20% HCl, 80 mL of saturated solution of sodium hydrocarbonate and dried over sodium sulphate. The solution was passed through a silica gel column with chloroform as the eluent. Chloroform was removed by rotary evaporator. Finally, 24.44 g (95%) of ABP was obtained. 1H NMR (CDCl3, 500 MHz): 6.05 (dd, J1 = 10.40, J2 = 1.26, 1H), 6.34 (dd, J1 = 10.40, J3 = 17.34, 1H), 6.64 (dd, J3 = 17.34, J2 = 1.26, 1H), 7.27 (m, 2H), 7.49 (m, 2H), 7.59 (m, 1H), 7.80 (m, 2H), 7.86 (m, 2H).

Synthesis of P(NIPAM-AA-BA): BA (0.28 g, 1,12 mmol); NIPAM (6 g, 51.57 mmol), AA (0.2556 g, 3.36 mmol), AIBN (0.01632 g, 0.38 mmol) were added in 50 mL flask. Components were dissolved in 30 mL ethanol and degassed with nitrogen for 30 min. The mixture was purged with nitrogen for 30 min. The polymerization was carried at 70 ° C under nitrogen atmosphere with mechanical stirring overnight. After cooling, the mixture was poured in 750 mL diethyl ether, the precipitate was filtered and dried in vacuum at 40 ° C. *Synthesis of P(MMA-BA)*: 6.3 g MMA (62.7 mmol), 0.24 g BA (0.96 mmol) and 0.05 g AIBN (0.31 mmol) were dissolved in 30 mL of toluene. The mixture was purged with nitrogen for 30 min. The polymerization was carried at 70 ° C under nitrogen atmosphere with mechanical stirring overnight. After cooling, the mixture was poured in 750 mL diethyl ether, the precipitate was filtered and dried in vacuum at 40 ° C. *Preparation of Polymer Bilayers*: In a typical experiment, poly-(NIPAN-BA) was dip-coated from its ethanol solution on silica wafer substrate. P(MMA-BA) was dip-coated from toluene solution on the poly-(NIPAM-BA) film. The bilayer film was illuminated through a photomask (Toppan Photomasks inc.) by halogen lamp for 40 min to crosslink the polymers. The illuminated film was rinsed in chloroform in order to remove the polymers from non-irradiated areas. The prepared bilayers were then dried again in air before experiment and contained no water. The observation of bilayer was performed by Axiovert Zeiss Microscope using 5× and 10× air objectives.

Numerical Simulations: Simulations were performed in Abaqus v6.11 using the standard finite-element method. In order to simulate the diffusion process in the active layer we performed a 2D heat transfer analysis with imposed temperature on the free perimeter of the shapes (circle, semi-ellipsoid) and constant diffusive properties This resulted in a time-dependent temperature distribution that mimics the swelling process The resulting nodal temperatures at an early point in time were then applied to the corresponding 3D bilayer shapes having a mismatch in expansion properties (passive layer has 0 thermal expansion, while the active layer has in-plane expansion coefficients of 1). Due to symmetries only the relevant part of the bilayers were simulated in order to reduce computational costs. The resultant actuated shape was obtained through a geometrically nonlinear static step. For more detailed information see ref. [14]. Doing this, we assumed that diffusion-driven actuation follows a quasistatic process in which the timescales of diffusion and actuation are clearly separated. The progression of the diffusion front is slow (s) while the resultant mechanical actuation is fast (ms). This enabled us to consider the two phenomena separately thereby neglecting potential couplings between swelling and mechanical properties. Results are only qualitative, as the actual material characteristics of the hydrogels were not measured. However, the actuation pattern, and thus the number of wrinkles, only depends on the depth of the differential edge-activation named “activation depth” in this paper. This enabled us to predict and confirm the experimental actuation patterns with simple normalized properties.

Acknowledgements

The authors are grateful to DFG (Grant IO 68/1-1) and IPF for financial support. The authors are grateful to K.-J. Eichhorn and R. Schulze (IPF) for assistance with ellipsometry.

References

[1] a) A. Terfort, N. Bowden, G. M. Whitesides, *Nature* **1997**, *386*, 162; b) G. M. Whitesides, B. Grzybowski, *Science* **2002**, *295*, 2418.

[2] a) T. G. Leong, A. M. Zarafshar, D. H. Gracias, *Small* **2010**, *6*, 792; b) L. Ionov, *Soft Matter* **2011**, *7*, 6786.

[3] M. J. Harrington, K. Razghandi, F. Ditsch, L. Guiducci, M. Rueggeberg, J. W. C. Dunlop, P. Fratzl, C. Neinhuis, I. Burgert, *Nat. Commun.* **2011**, *2*, 337.

[4] a) J. W. C. Dunlop, R. Weinkamer, P. Fratzl, *Mater. Today* **2011**, *14*, 70; b) J. M. Skotheim, L. Mahadevan, *Science* **2005**, *308*, 1308; c) L. Mahadevan, S. Rica, *Science* **2005**, *307*, 1740.

[5] M. Jamal, A. M. Zarafshar, D. H. Gracias, *Nat. Commun.* **2011**, *2*, 527.

[6] S. Zakharchenko, E. Sperling, L. Ionov, *Biomacromolecules* **2011**, *12*, 2211.

[7] S. Zakharchenko, N. Puretskiy, G. Stoychev, M. Stamm, L. Ionov, *Soft Matter* **2010**, *6*, 2633.

[8] G. Stoychev, N. Puretskiy, L. Ionov, *Soft Matter* **2011**, *7*, 3277.

[9] A. Azam, K. Laflin, M. Jamal, R. Fernandes, D. Gracias, *Biomed. Microdevices* **2011**, *1*, 51.

[10] D. H. Gracias, V. Kavthekar, J. C. Love, K. E. Paul, G. M. Whitesides, *Adv. Mater.* **2002**, *14*, 235.

[11] G. S. Huang, Y. F. Mei, D. J. Thurmer, E. Coric, O. G. Schmidt, *Lab Chip* **2009**, *9*, 263.

[12] a) H. Y. Liang, L. Mahadevan, *Proc. Natl. Acad. Sci. USA* **2011**, *108*, 5516; b) H. Liang, L. Mahadevan, *Proc. Natl. Acad. Sci. USA* **2009**, *106*, 22049.

[13] a) I. Jung, J. S. Rhyee, J. Y. Son, R. S. Ruoff, K. Y. Rhee, *Nano- technology* **2012**, *23*, 025708; b) J. Henrie, S. Kellis, S. M. Schultz, A. Hawkins, *Opt. Express* **2004**, *12*, 1464.

[14] G. Stoychev, S. Zakharchenko, S. Turcaud, J. W. C. Dunlop, L. Ionov, *ACS Nano* **2012**, *6*, 3925.

[15] M. Marder, E. Sharon, S. Smith, B. Roman, *Europhys. Lett.* **2003**, *62*,

[16] B. Audoly, A. Boudaoud, *C. R. Acad. Sci., Ser. IIb: Mec.* **2002**, *330*,
831 .

7.11 [AC4] An instant multi-responsive porous polymer actuator driven by solvent molecule sorption.

Zhao, Q., Dunlop, J. W. C., Qiu, X., Huang, F., Zhang, Z., Heyda, J., Dzubiella, J., Antonietti, M., Yuan, J.

*Published in **Nature Communications**, 5, 4293.*
DOI: 10.1038/ncomms5293

Reprinted with permission from Nature Publishing Group

Abstract: Fast actuation speed, large shape deformation and robust responsiveness are critical to synthetic soft actuators. Despite this a simultaneous optimization of all these aspects without trade-offs remains unresolved. Here we describe porous polymer actuators which bend in response to acetone vapor (24 kPa, 20 °C) at a speed of an order of magnitude faster than the state-of-the-art, coupled with a large-scale locomotion. They are meanwhile multi-responsive toward a variety of organic vapors in both the dry and wet states, distinctive from the traditional gel actuation systems that become inactive when dried. The actuator is easy-to-make and survives even after hydrothermal processing (200 °C, 24 h) and pressing-pressure (100 MPa) treatments. In addition, the beneficial responsiveness is transferable, being able to turn "inert" objects into actuators via surface coating. This advanced responsiveness arises from the combination of porous morphology and the "poly(ionic liquid) ~ solvent" interaction mediated by the counter anions.

Adaptive soft matter, such as responsive gels, elastomers, shape memory and electro-active polymers, are attracting burgeoning interest in material science, engineering, medicine and biology[1-16]. Fast and robust responsiveness coupled with large scale displacement are eagerly sought after[17], which have been the defining feature of biological actuators but missing from synthetic counterparts[18-23]. For example, Sea cucumbers can alter the stiffness of their dermis within seconds to obtain survival advantages[18]; the Venus flytrap can close their leaves in a second for efficient prey capture[19]. On the other hand, the hygroscopic movements of pine cones[23] and ice plant seed capsules[21], though slower, can function even when the host organisms are dead. Recently, enormous efforts have been paid to these bio-prototypes, with progresses being made on responsive nanocomposites and surfaces[3], energy generators and transducers[24,25], programmable origami[26], soft robotics[27-29], smart gels[30-32], and artificial muscles[33-35]. Yet, most of the polymer actuators suffer from the relatively slow and small scale movements; furthermore, they are susceptible to severe circumstances and involve complex preparation such as multistep lithographic processes[20,36]. In this scenario, actuators bearing rapid responsiveness and strong tolerance toward aggressive milieus are highly desirable for promptly and reliably converting external stimuli to mechanical movement. In addition, multi-responsive actuators viable in both the swollen and dry states remain a challenge, e.g., hydrogel actuators become inactive when dried.

To address these requirements, we engineered a novel structural model fostering the ultrafast and robust actuation movement through the solvent molecules adsorption mechanism (Fig. 1a). Two features are essential to this model. First, the major component of the actuator membrane is a cationic poly(ionic liquid) polymer which possesses bulk organic counter anions (e.g. bis(trifuoromethanesulfonyl)imide, Tf2N) that can preferably interact with a variety of organic solvent vapors as will be demonstrated below. Second, the actuator membrane represents a unique synergy of an electrostatic complexation gradient and a porous architecture through the membrane. In this design, the electrostatic complexation provides ionic cross-linking network and structural robustness; the porous structures give rise to a fast responsiveness by accelerating the internal mass transport and large scale actuation arising from high compressibility. As such, the mechanic actuation can be instantly triggered by variation of solvent vapor and humidity; the structure also survives very harsh processing steps to prove their wide operation window in various environments.

Results

Preparation and characterizations of the porous membrane. The porous actuator membrane was prepared from a mixture solution of a cationic poly(ionic liquid), poly(3-cyanomethyl-1-vinylimidazolium bis(trifuoromethanesulfonyl)imide) (abbreviated as "PILTf2N", Tf2N denotes the counter anion) and a carboxylic acid-substituted pillar[5]arene (C-pillar[5]arene) that bears ten acid groups (COOH) (Supplementary Fig. S1). PILTf2N and C-pillar[5]arene were first dissolved in dimethyl sulfoxide (DMSO) in a 1:1 molar ratio of the imidazolium cation ring (on PILTf2N) to COOH groups (on C-pillar[5]arene). Subsequently the solution was cast on a glass plate and dried at 80 °C for 1 h (Please note: the membrane surfaces facing the air and the glass plate are defined as TOP and BOTTOM surfaces, respectively). Then the membrane was soaked in aqueous ammonia (Fig. 1a, left scheme); after 2 h a free-standing membrane with a scalable size was peeled off from the glass plate and denoted as PILTf2N/C-pillar[5]arene (Supplementary Fig. S2 ~ Fig. S4). During the soaking step the ammonia will diffuse into the membrane from top to bottom, deprotonate the COOH into COO-NH4+ groups and simultaneously trigger the electrostatic complexation between the negatively charged C-pillar[5]arene with the anionic PILTf2N chains (Supplementary Fig. S2). As such, a gradient in the degree of electrostatic

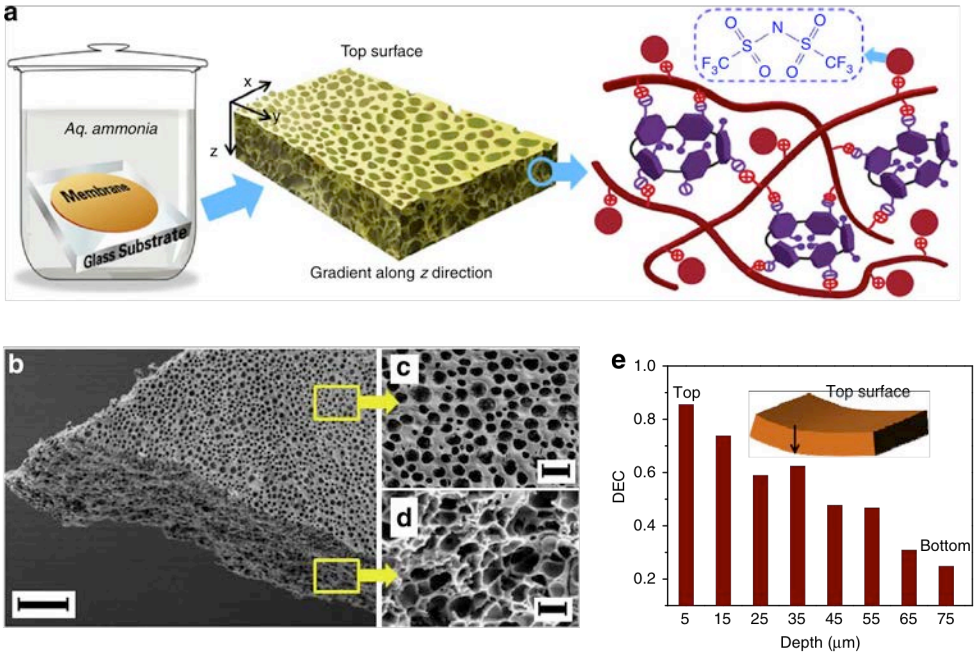

Figure 1 | Design concept and structure characterizations of the membrane actuator. (a) A scheme illustrating the preparation route (left), porous morphology (middle) and the chemical structure (right) of the PILTf2N/C-pillar[5]arene membrane actuator. On the right: the red line and purple ring represent PILTf2N polymer chains and C-pillar[5]arene molecules, respectively; this cartoon schematises the electrostatic complexation between the imidazolium cations on PILTf2N and the carboxylate anions on C-pillar[5]arene molecules. (b–d) SEMmorphologies of the membrane actuator: general view (b, scale bar (black), 30 mm); top surface (c, scale bar, 3 mm); and cross-section (d, scale bar: 1 mm); (e) the structural gradient of the DEC along the membrane cross-section (top–down direction). The DEC of the membrane is defined as the ratio of the imidazolium units that have electrostatically complexed with COO- groups (on C-pillar[5]arene) to the overall amount of imidazolium units (Supplementary Fig. 3). Experimentally, DEC values at different locations of the membrane are determined by the sulphur content at different locations of the membrane cross-section (Supplementary Fig. 4).

complexation (DEC) along the membrane cross-section (z direction in Fig. 1a) forms, because the complexation is coupled to the top-down diffusion of ammonia into the membrane. While the complexation between PILTf2N and C-pillar[5]arene is quantitatively accompanied by the release of Tf2N counter anions into solution, the DEC is inversely proportional to the Tf2N residue in the membrane. Because sulfur exists only in Tf2N, its content is a quantitative measure of Tf2N. In detail, the Tf2N content was found increase along the TOP-DOWN direction (Supplementary Fig. S4) and vice versa for the DEC (Fig. 1c), i.e., the top surface has a lower Tf2N content and thus a higher DEC than the bottom.

The membrane network is shown to be very stable in common organic solvents because electrostatic complexation is characteristic for its exceptional stability in organic solvents.[37] As a supporting proof, the weight of the membrane remains stable after being soaking in solvents for 24 h (Supplementary Fig. S5). In addition, the as-prepared membranes also feature an interconnected porous architecture, with macropores (200 nm ~ 3 μm) across the membrane (Fig. 1b). The pore formation is basically related to the electrostatic complexation between PILTf2N and C-pillar[5]arene, a mechanism we have discovered recently for creation of porous polyelectrolyte networks from a PILTf2N-poly(acrylic acid) system.[38]

Superfast actuation of the membrane. The PILTf2N/C-pillar[5]arene membrane exhibits an unprecedented fast actuation speed in response to acetone stimulus. When placed in acetone vapor (24 kPa, 20 °C), the flat membrane bent quickly into a closed loop in ~ 0.1 s with the top surface inward, and further into a multiply wound coil in 0.4 s (Fig. 2a, Supplementary Movie S1). Upon exposure back in air, the membrane recovered its original shape rapidly in ~ 3 s; this process is reversible and repeatable (Supplementary Fig. S6). The kinetics of the bending and unbending movements is assessed by plotting the curvature of the membrane against time (Fig. 2b), resulting in a bending curvature of 1.33 mm^{-1} in 0.4 s, i.e., the membrane actuator bent one complete circle in about every 0.1 s. We compared the actuation speed of the membrane actuator with previously reported polymeric actuators in the literature (Fig. 2c). As curvature of bending scales inversely with membrane thickness 39, we plot 'curvature × membrane thickness' versus time, and the lines of constant actuation speed. The fastest actuators are found in the top left of this diagram (red, solid circle). It is seen that our membrane actuator outperforms conventional polymer actuators in terms of the response rate and the amplitude of movement—allowing for the simultaneous combination of ultra-fast actuation and large scale deformation that existing soft actuators do not exhibit (Supplementary Movie S1).

Next, we quantified the mechanical force generated by the membrane bending. As depicted in Fig. 2d, a flat membrane piece was located 2 mm above a cylinder on an electronic balance. When an acetone atmosphere was applied, the membrane bent down towards the cylinder, simultaneously imposed a force on the balance; by cutting off the acetone vapor flow, the original shape was resumed, accompanied by a decrease in the force exerted on the balance. The force was read out directly from the balance in the form of

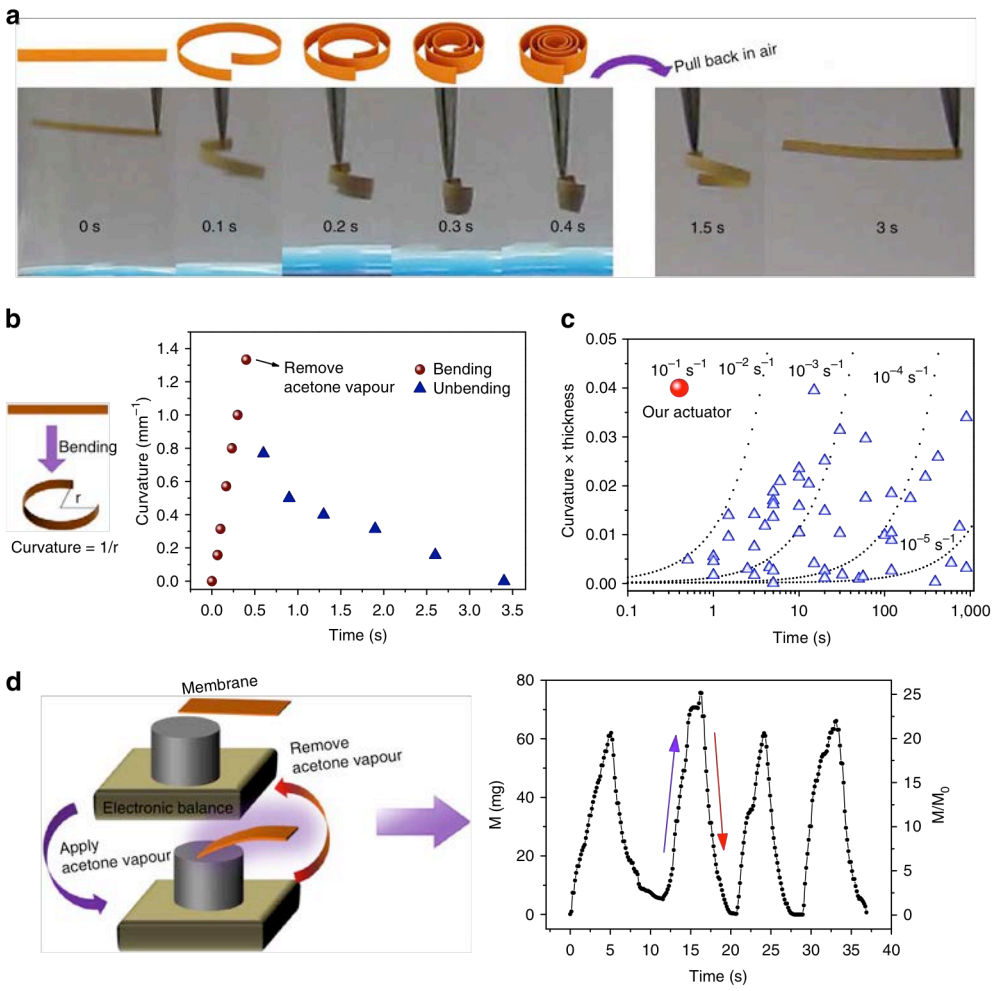

Figure 2 | Actuation of the membrane actuator. (a) Adaptive movement of a PILTf2N/C-pillar[5]arene membrane (1 mm x 20 mm x 30 mm) placed in acetone vapour (24 kPa, 20 °C, left) and then back in air (right). Note: acetone solvent is stained in blue. (b) Plot of curvature against time for the membrane actuator in (a); on the left: a schematic of how the curvature is calculated. (c) Plot of 'curvature x thickness' against time for the membrane actuator in (a) and from literature results (blue triangle) compared with lines of constant actuation speed (Supplementary Fig. 11 and Supplementary Table 1). (d) Plot of the force generated by membrane actuator in (a) against time when the membrane was exposed to acetone vapour (24 kPa, 20 °C) and air alternatively; M is the force that the actuator exerted on the balance; M0 is the weight of the actuator membrane. On the left: schematic illustration of the experimental force measurement set-up.

weight (experimental error: 2 mg); it increased and declined rapidly in ca. 2 s and 5 s (Fig. 2d), which is coupled to the bending and stretching movements of the membrane actuator towards the on/off state of the acetone vapor. The maximum force detected here (0.75 mN, 75 mg) is already 25 times of the actuator weight (3 mg). In a control experiment without the membrane actuator, only negligible forces can be observed (< 1 mg, Supplementary Fig. S7).

Robust and multiple responsiveness of the actuator. In addition to operating under normal conditions, the actuator survives very harsh treatments. After storage in liquid nitrogen (~ -190 °C, 2 h) followed by annealing (150 °C, 24 h) and high pressure pressing (100 MPa, 24 h), the actuator remained active; it bent into a semicircle in ~ 0.5 s (Fig. 3a), slower than the original form but still significantly faster in comparison with most common polymer actuators (Fig. 2c). Morphological examination by SEM and porosity analysis by mercury intrusion confirm that pore compaction occurs as a result of the high pressing pressure, which blocks a part of the pore channels and leads to a slower response rate (Supplementary Fig. S9). Even after a hydrothermal processing (200 °C, 24 h, Supplementary Fig. S10), the actuator remained viable (Fig. 3b). Moreover, the membrane actuator was found to be active in liquid acetone solvent at -50 °C (Supplementary Fig. S11), a temperature well below the glass transition of even most rubbers in which gel based actuators no-longer operate. Aside from this exceptional robustness, the smart responsiveness can be rendered to even cylindrical objects by coating the membrane onto them, which is easy to implement due to the high polarizability and interfacial activity of poly(ionic liquid)s.[38] This possibility is exemplified here by a human hair, which after constructing an asymmetrical coating of the responsive porous membrane onto its surface "dances" in acetone vapor (Fig. 3c, Supplementary Movie S2 and Fig. S12). In addition, the membrane actuator also features multi-responsive properties as it readily exhibits hygroscopic actuation. When shaped as a star, the hygroscopic actuator can mimic an "artificial flower" that blossoms and closes in response to humidity changes, indicative of an ability

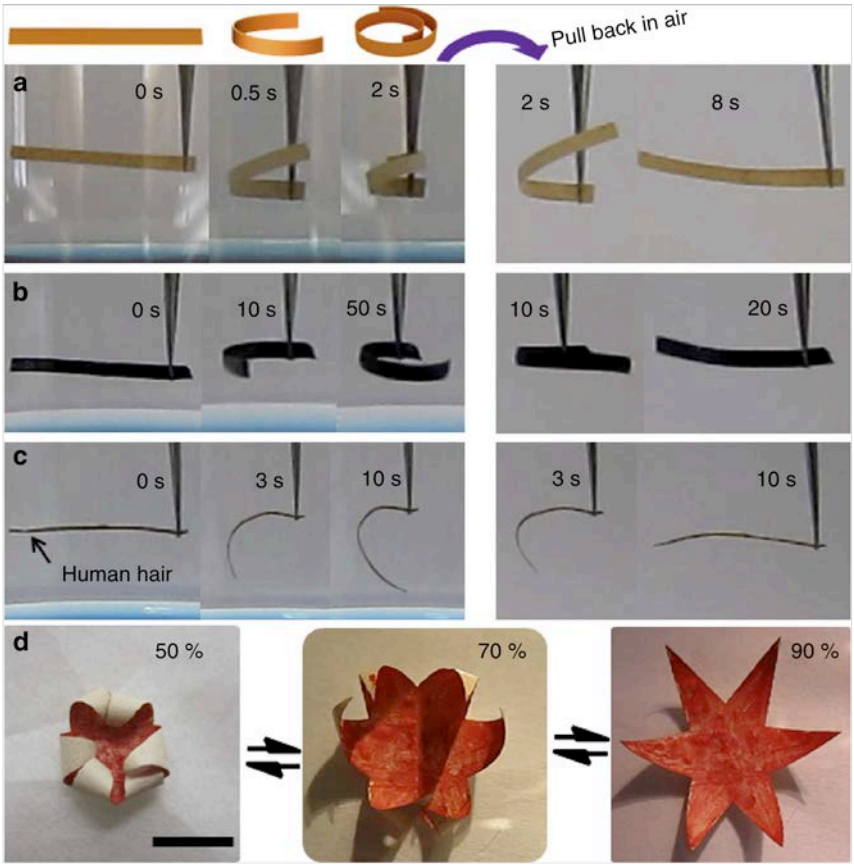

Figure 3 | Robustness and multiple responsiveness of the actuator. (a) Adaptive movement of a PILTf2N/C-pillar[5]arene membrane (1 mm x 20 mm x 30 mm) placed in acetone vapour (24 kPa, 20 °C, left) and then back in air (right); the membrane was immersed in liquid nitrogen (2 h), followed by annealing (150 °C, 24 h) and high-pressure pressing at 100 MPa for 24 h. (b) The same actuation experiment after hydrothermal processing the membrane in water (200 °C, 24 h). Here the membrane is black owing to its partly carbonaceous nature. (c) Motion of a membrane-coated human hair in acetone vapour and then back in air. (d) The reversible closing and opening of a star-shaped membrane actuator 'flower' upon switching the humidity between 50 and 90% at 20 °C; here the top surface of the membrane was stained red while the bottom surface retains the original light yellow colour; inserted number is the relative humidity; scale bar, 1 cm.

of cooperative actuation to "enwrap" objects (Fig. 3d). As such, the actuation spans from both the dry state to wet state, which is beneficial because traditional gels usually become inactive when dried (Supplementary Fig. S13 and Fig. S14).

Actuation mechanism. The mechanism for this unique actuation is addressed at two levels: why the membrane could bend in response to acetone vapor, and what is the key structure responsible for the superfast bending kinetics (Fig. 4). First, from a purely geometric perspective the curvature C=1/r can be approximated as

$$C \sim \frac{1}{h}\left(\varepsilon_b - \varepsilon_t\right) \qquad (1)$$

Where ε_t and ε_b are the swelling strains due to solvent - PILTf2N/C-pillar[5]arene interactions, in the top and bottom regions of the membrane respectively, and h is the membrane thickness . Any stimulus that can drive the actuator must be able to impact ε_t and ε_b unequally.

In line with the definition of DEC (Fig. 1c, Supplementary Fig. S4), a part of imidazolium units from PILTf2N undergo complexation with C-pillar[5]arene and provide a stable network because C-pillar[5]arene is insoluble in acetone and the electrostatic complexation bonding features high stability in organic solvent (Supplementary Fig. S5).[37] Meanwhile, the rest of PILTf2N are not involved in complexation and exist as "imidazolium~Tf2N" ion pairs, shown by the chemical structures in Fig. 4a. The existence and density of the "imidazolium~Tf2N" ion pairs are confirmed by monitoring the sulfur content along the cross-section. In this context it is important to note that strong interactions exist between acetone solvent molecules and the "imidazolium~Tf2N" ion pair, because the acetone solvent can easily dissolve PILTf2N. Indeed our atomistically-resolved molecular dynamics (MD) computer simulations of the "imidazolium~Tf2N" pair in water-acetone mixture reveal that the acetone adsorbs stronger to the ion pair than water (Supplementary Fig. S16 ~ Fig. S18, part 15). In particular, a large number of water molecules are preferentially replaced by acetone molecules around the rather hydrophobic fluorine groups of the Tf2N anion, see the MD snapshot on the right hand side of Fig. 4a and the analysis in the SI.

When the membrane is placed in acetone vapor, the solvent molecules diffuse rather rapidly into the membrane from both the top and bottom surfaces, as indicated by the blue track "A" schemed in Fig. 4a. The acetone molecules will adsorb to the "imidazolium ~ Tf2N" ion pair (red dots, Fig. 4a) owing to their preferential interaction with the anion. Given the

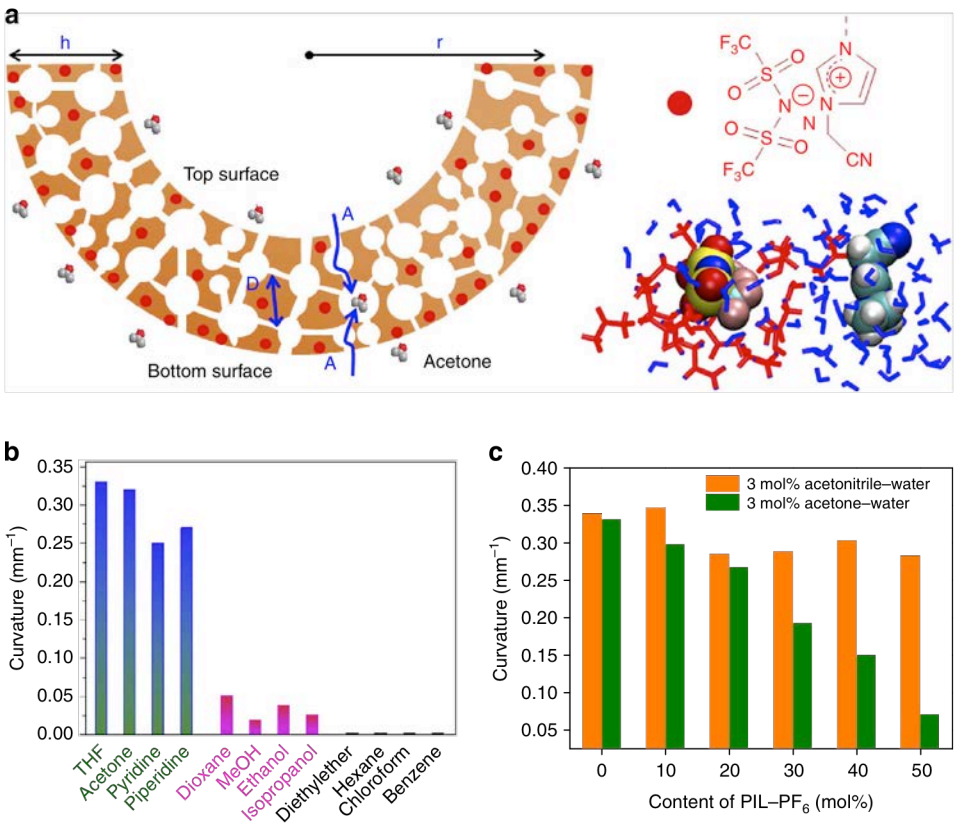

Figure 4 | Actuation mechanism via solvent molecule sorption. (a) A scheme of the porous membrane actuator (left, not to scale), definition of variables: h, thickness of the membrane; r, radius of the bended membrane arch; D, thickness of the pore wall; A, the diffusion track of acetone molecules from outside to the surface of pore walls inside the membrane; (top right) chemical structure of the 'imidazoliumBTf2N' pair; (lower right) the representative snapshot of solvent redistribution around the 'imidazolium B Tf2N' ion pair: water molecules (blue) are partially displaced by acetone molecules (red), which adsorb more to the Tf2N anion on the left of the snapshot. (b) Curvatures of PILTf2N/C-pillar[5]arene membrane actuator in vapour of different solvents (2 kPa, 20 °C). (c) Effect of PF6 anion content on curvature of PIL(Tf2N þ PF6)/C-pillar[5]arene membrane actuator in 3 mol% acetonitrile–water and 3 mol% acetone–water mixture, respectively.

gradient of DEC along the cross-section (i.e., the top surface region has less "imidazolium~Tf2N" ion pairs owing to the higher DEC, Fig. 1c), understandably the bottom surface region is more solvated by acetone compared to the top. As such, the local solvent osmotic pressure increase leads to more swelling[40] of the bottom part, such that $\varepsilon_t < \varepsilon_b$ and the membrane bends with the top surface inward according to equation (1). Moreover, equation (1) suggests that only small swelling strain differences of around 4% would account for the maximum curvature reached of C=1.34 mm-1. This is in good agreement with the observation that at the maximum bending, the porous morphology of the membrane actuator shows little-to-no detectable change via SEM characterization when the experimental error is considered (Supplementary Fig. S19).

As another support to this mechanism, it is found that the amplitude of actuation in general is specific and proportional to the "solvent~PILTf2N" interaction, if various solvents are compared. For example, the solvents that can dissolve PILTf2N polymer, i.e. strong "solvent~PILTf2N" interaction (acetone, THF, piperidine and pyridine, Supplementary Table S3) triggers the strongest actuation; solvents that cannot dissolve but can swell the PILTf2N polymer (dioxane, methanol, ethanol and isopropanol) can only drive the actuator with slower kinetics and weaker bending (Fig. 4b). On the contrary, solvents that can neither dissolve nor swell the PILTf2N polymer (diethyl ether, benzene, cyclohexane and chloroform), fail to drive the actuator, i.e. the polymer membrane does not bend at all in the vapor of these solvents. Further evidence is given by the anion effect: we exchanged the Tf2N anion with PF6 which has a weak interaction with acetone but strong interaction with acetonitrile (PILPF6 is insoluble in acetone but soluble in acetonitrile). By exchanging Tf2N stepwise with PF6 anions, the actuation curvature of PIL(Tf2N+PF6)/C-pillar[5]arene membrane in aqueous acetone solution gradually decreases while the actuation curvature in aqueous acetonitrile basically remains the same. As such, both Fig. 4b and Fig. 4c clearly confirm that the stronger "PILTf2N - solvent" interaction on a molecular level produces stronger actuation, which agrees well with the solvent adsorption mechanism. Regarding the gradient structures, we prepared a control membrane which has a similar porous morphology but a symmetrical DEC distribution across the membrane (Supplementary Fig. S20). Now, the membrane only slightly bends when placed in acetone vapor, because the actuation stress now on both surfaces largely offsets each other.

With respect to the fast bending kinetics, swelling is a diffusion-determined process in which the rate-determining step is that the solvent molecules have to diffuse through the dense polymer network to reach their final adsorption sites. The standard diffusion law is expressed in equation (2), where $\langle x^2 \rangle$ is the mean

squared distance travelled in a time t and γ is the diffusion constant.

$$\langle x^2 \rangle = 2\gamma t \qquad (2)$$

For a nonporous material, the solvent has to travel a mean distance on the order of the membrane thickness, $\sqrt{}$<x2>~h, to solvate the whole membrane. For our porous membrane with submicron scale interconnected pore channels, the solvent vapor molecules can almost instantaneously travel to the pore surfaces via the unhindered (percolating) micron-sized pore channel accesses (blue track "A" schemed in Fig. 4a). Then, the acetone molecules only have to diffuse through a distance of roughly $\sqrt{}$ <x²>~D, which is the average thickness of the pore wall, to solvate the whole polymer matrix. From cross-sectional SEM image in Fig. 1b, the average D is estimated to be < 1 μm, which is much smaller than the overall membrane thickness, h=30 μm. Using the diffusion law in equation 2, the diffusion rate ratio for porous materials (t_p) and nonporous materials (t_{np}) can now be expressed by

$$\frac{t_p}{t_{np}} = \left(\frac{D}{h}\right)^2 \qquad (3)$$

which indicates that the diffusion rate in the porous membrane is improved by almost three orders of magnitude. Thus, the porous architecture accelerates the actuation speed by providing an instant access to the pore walls throughout the membrane, and reducing the rate-limiting diffusion distance (D ~ 1 μm compared to h ~ 30 μm). As a comparison, we prepared another nonporous control membrane that retains the linear gradient (Supplementary Fig. S21); understandably the membrane shows slower responsiveness and smaller bending toward acetone stimulus. We further found that the pore compaction resulted from too high pressing pressure (100 MPa) also reduced the actuation kinetics, since the denser the porous structure is, the slower the diffusion is (Fig. 3a).

Discussion

Traditionally, the swelling of the polymer networks is the dominant mechanism to modulate hydrogel and ion gel actuators, but it is a relative slow process limited by the retarded diffusion in a wet state. In our actuator design, a gradient structure was introduced into an electrostatically cross-linked porous membrane, whereas the adsorption of the solvent vapor molecules at the pore surface results in a local volume change giving rise to actuation movements. Importantly, due to the pore-accelerated mass transport, the surface adsorption can take place instantaneously in contact with solvent vapor molecules, at a speed of several orders of magnitude faster than bulk swelling. As such, the PILTf2N/C-pillar[5]arene actuator features an instant, robust, and multiple responsiveness spanning both the swelling and dry modes. Not only the actuator gives a record actuation speed among all synthetic polymer actuators so far, the combination of multiple advantages in one single actuator set it apart from previous soft actuators. For example, in line with the actuation mechanism and owing to the actuator's versatile responsiveness to a variety of organic solvents, the membrane appeared responsive even toward vapors from perfume or tea tree oil (both contain a considerable amount of ethanol, Supplementary Movie S3), verifying its actuation ability to bio-benign stimuli. More significantly, the membrane actuator can distinguish 13 types of aqueous miscible solvents through two sets of actuation experiments (Supplementary Fig. S22). We regard this implication as substantial because it renders the actuation available for facile and quantitative analysis of solvent quality without the need of sophisticated or expensive instruments. By further modulating the "PIL ~ solvent" interactions and the porous morphologies, exciting opportunities may arise as it may foster high throughput analysis with improved resolution and capacity, which is now ongoing in our lab.

This conceptual methodology is virtually applicable to a wide range of polymers and small molecules with complementary interactions, opening new avenues for adaptive soft matters with fast response rate and complex movements. In addition, given the ionic nature of the constituent polymers and solution based processing, the underlying principles seamlessly interface with more fabrication technologies, such as spinning and patterning, holding great promise for micro-actuation devices of high complexity, and smart ionics spanning multiple length-scales.

Methods

Materials. Both the carboxylic acid-substituted pillar[5]arene (C-pillar[5]arene) and poly(3-cyanomethyl-1-vinylimidazolium bis(trifuoromethanesulfonyl)imide), PILTf2N, were synthesized and characterized (Supplementary Fig. S1). The apparent molecular weight and polydispersity index of PCMVImTf2N polymer was 1.15 × 105 g/mol and 2.95, respectively. All the solvents used in this study were of analytic grades.

Preparation and characterization of membrane actuators. Typically, 1.0 g of PILTf2N polymer and 0.27 g of C-pillar[5]arene were dissolved in 10 mL of DMSO solvent to form a homogeneous solution. Then the solution was cast onto a clean glass plate, dried at 80 °C for 1 h, and soaked in 0.2 wt% aqueous ammonia (2 h, 20 °C), giving rise to free-standing membranes with thickness ~ 30 μm. Note that membrane actuators can be modulated by tailoring the concentration of ammonia (0.02 ~ 0.2 wt%) and the soaking time (2 ~ 48 h). Morphologies of the membranes were examined by scanning electron microscopy performed on a GEMINI LEO 1550 microscope at 3 kV; samples were coated with a thin layer of gold before examination. The chemical compositions and electrostatic complexation structures of the membrane were characterized by Fourier Transform Infrared Spectrometer and energy dispersive x-ray spectroscopy (Supplementary Fig. S2 ~ Fig. S4).

Solvent vapor stimulus actuation. Organic solvents were put in a glass beaker at 20 °C. Then a piece of membrane strip (20 mm × 1 mm × 30 μm) was placed ~ 5 mm above the liquid phase of the solvent; the solvent vapor will trigger the fast bending movement. Afterward, the membrane was pulled back into air to accomplish the shape recovery. This process was repeated for 50 times to confirm the good durability

of the actuation function. For the perfume triggered actuation, perfume (COCO MADEMOISELLE, CHANEL) was used instead of organic solvents. Please note: in all cases, the membrane actuator was NOT in contact with the liquid body of both the solvents and perfume. All the actuation movements were recorded by a digital camera (Canon IXUS130, frames per second 30). For hygroscopic actuation (Fig. 3d), the star shaped membrane (30 μm thick) was placed in a test chamber (model WKL 34, Weiss Technik), whereby the temperature was kept 20 °C and the humidity was modulated from 50% ~ 90%, during which the membrane open and closed reversibly.

Acknowledgements

Authors would like to thank the Max Planck Society for financial support. J.Y. thanked Simon Prescher for the polymer synthesis, Mr. Matthias Kollosche for mechanical tests. J.D. and J.H. acknowledge financial support from the Alexander von Humboldt Foundation and the Deutsche Forschungsgemeinschaft (DFG).

Author contributions

Q.Z., J.Y. and M.A. conceived the research. Q.Z. and X.Q. performed the hygroscopic actuation experiments. Z.Z. and F.H. synthesized the pillar[5]arene molecules. J.D. and J. H. performed simulations and analysis. Q.Z. carried out all the rest experiments. Q.Z., J.Y. J.W.D. and M.A. analysed data and wrote the paper. All authors read and revised the paper.

References

1 Stuart, M. A. C. et al. Emerging applications of stimuli-responsive polymer materials. Nat. Mater. 9, 101-113 (2010).

2 Ma, M., Guo, L., Anderson, D. G. & Langer, R. Bio-inspired polymer composite actuator and generator driven by water gradients. Science 339, 186-189 (2013).

3 Sidorenko, A., Krupenkin, T., Taylor, A., Fratzl, P. & Aizenberg, J. Reversible switching of hydrogel-actuated nanostructures into complex micropatterns. Science 315, 487-490 (2007).

4 Lendlein, A., Jiang, H. Y., Junger, O. & Langer, R. Light-induced shape-memory polymers. Nature 434, 879-882 (2005).

5 Kim, J., Hanna, J. A., Byun, M., Santangelo, C. D. & Hayward, R. C. Designing responsive buckled surfaces by halftone gel lithography. Science 335, 1201-1205 (2012).

6 Lee, K. J. et al. Spontaneous shape reconfigurations in multicompartmental microcylinders. Proc. Natl. Acad. Sci. U. S. A. 109, 16057-16062 (2012).

7 Keplinger, C. et al. Stretchable, transparent, ionic conductors. Science 341, 984-987 (2013).

8 Kim, J. et al. Programming magnetic anisotropy in polymeric microactuators. Nat. Mater. 10, 747-752 (2011).

9 Yu, Y. L., Nakano, M. & Ikeda, T. Directed bending of a polymer film by light - miniaturizing a simple photomechanical system could expand its range of applications. Nature 425, 145-145 (2003).

10 van Oosten, C. L., Bastiaansen, C. W. M. & Broer, D. J. Printed artificial cilia from liquid-crystal network actuators modularly driven by light. Nat. Mater. 8, 677-682 (2009).

11 Wu, Z. L. et al. Three-dimensional shape transformations of hydrogel sheets induced by small-scale modulation of internal stresses. Nat. Commun. 4, 1586 (2013).

12 Kim, O., Shin, T. J. & Park, M. J. Fast low-voltage electroactive actuators using nanostructured polymer electrolytes. Nat. Commun. 4, 2208 (2013).

13 Jager, E. W. H., Smela, E. & Inganas, O. Microfabricating conjugated polymer actuators. Science 290, 1540-1545 (2000).

14 Zhou, Y. et al. High-temperature gating of solid-state nanopores with thermo-responsive macromolecular nanoactuators in ionic liquids. Adv. Mater. 24, 962-967 (2012).

15 Ahir, S. V. & Terentjev, E. M. Photomechanical actuation in polymer-nanotube composites. Nat. Mater. 4, 491-495 (2005).

16 Aida, T., Meijer, E. W. & Stupp, S. I. Functional supramolecular polymers. Science 335, 813-817 (2012).

17 Baker, C. O. et al. Monolithic actuators from flash-welded polyaniline nanofibers. Adv. Mater. 20, 155-158 (2008).

18 Capadona, J. R., Shanmuganathan, K., Tyler, D. J., Rowan, S. J. & Weder, C. Stimuli-responsive polymer nanocomposites inspired by the sea cucumber dermis. Science 319, 1370-1374 (2008).

19 Forterre, Y., Skotheim, J. M., Dumais, J. & Mahadevan, L. How the venus flytrap snaps. Nature 433, 421-425 (2005).

20 Erb, R. M., Sander, J. S., Grisch, R. & Studart, A. R. Self-shaping composites with programmable bioinspired microstructures. Nat. Commun. 4, 1712 (2013).

21 Harrington, M. J. et al. Origami-like unfolding of hydro-actuated ice plant seed capsules. Nat. Commun. 2, 337 (2011).

22 Armon, S., Efrati, E., Kupferman, R. & Sharon, E. Geometry and mechanics in the opening of chiral seed pods. Science 333, 1726-1730 (2011).

23 Harlow, W. M., Cote, W. A. & Day, A. C. The opening mechanism of pine cone scales. J Forest 62, 538-540 (1964).

24 Kobatake, S., Takami, S., Muto, H., Ishikawa, T. & Irie, M. Rapid and reversible shape changes of molecular crystals on photoirradiation. Nature 446, 778-781 (2007).

25 Shepherd, H. J. et al. Molecular actuators driven by cooperative spin-state switching. Nat. Commun. 4, 2607 (2013).

26 Stoychev, G., Turcaud, S., Dunlop, J. W. C. & Ionov, L. Hierarchical multi-step folding of polymer bilayers. Adv. Funct. Mater. 23, 2295-2300 (2013).

27 Morin, S. A. et al. Camouflage and display for soft machines. Science 337, 828-832 (2012).

28 Leong, T. G. et al. Tetherless thermobiochemically actuated microgrippers. Proc. Natl. Acad. Sci. U. S. A. 106, 703-708 (2009).

29 Palleau, E., Morales, D., Dickey, M. D. & Velev, O. D. Reversible patterning and actuation of hydrogels by electrically assisted ionoprinting. Nat. Commun. 4, 2257 (2013).

30 Burdick, J. A. & Murphy, W. L. Moving from static to dynamic complexity in hydrogel design. Nat. Commun. 3, 1269 (2012).

31 Qiu, X. et al. Selective separation of similarly sized proteins with tunable nanoporous block copolymer membranes. Acs Nano 7, 768-776 (2013).
32 Eun Chul, C., Jin-Woong, K., Fernandez-Nieves, A. & Weitz, D. A. Highly responsive hydrogel scaffolds formed by three-dimensional organization of microgel nanoparticles. Nano Lett. 8, 168-172 (2008).
33 Foroughi, J. et al. Torsional carbon nanotube artificial muscles. Science 334, 494-497 (2011).
34 Takashima, Y. et al. Expansion–contraction of photoresponsive artificial muscle regulated by host–guest interactions. Nat. Commun. 3, 1270 (2012).
35 Steven, E. et al. Carbon nanotubes on a spider silk scaffold. Nat. Commun. 4, 2435 (2013).
36 Stellacci, F. Towards industrial-scale molecular nanolithography. Adv. Funct. Mater. 16, 15-16 (2006).
37 Thunemann, A. F., Muller, M., Dautzenberg, H., Joanny, J. F. O. & Lowen, H. in Polyelectrolytes with defined molecular architecture ii Vol. 166 Advances in polymer science (ed M. Schmidt) 113-171 (2004).
38 Zhao, Q. et al. Hierarchically structured nanoporous poly(ionic liquid) membranes: Facile preparation and application in fiber-optic ph sensing. J. Am. Chem. Soc. 135, 5549-5552 (2013).
39 Timoshenko, S. Analysis of bi-metal thermostats. Journal of the Optical Society of America and Review of Scientific Instruments 11, 233-255 (1925).
40 De gennes, p. G. Scaling concepts in polymer physics. Cornell University Press: Ithaca, NY, (1979).

7.12 [AC5] Porous poly(ionic liquid) actuator with ultra-high sensitivity to solvents

Zhao, Q., Heyda, J., Dzubiella, J., Täuber, T., Dunlop, J. W. C., Yuan, J.
*Published in **Advanced Materials**, 2015, 27, 2913-2917.*
DOI: 10.1002/adma.201500533

Reprinted with permission from John Wiley and Sons

Currently, synthetic polymer actuators are being actively pursued owing to their importance in artificial muscles, molecular motors, soft robotics, programmable origami, and energy generators.[1] These smart materials are capable of adaptive motion, and/or reversible shape variation responding to external stimuli.[2] Among various aspects of actuators, it is necessary to develop higher sensitivity in actuating setups to realize signaling output at a rather early stage of external trigger, which is important for both fundamental research and practical applications. In this regard biological actuators are compelling models possessing the defining ability to sense and respond to subtle alterations in environmental conditions such as humidity and forces.[3] For example, wheat awns can propel their seeds on and into the ground in response to humidity changes.[3d] The study on such biological actuators demonstrates the important role of material architecture (pore-size, fiber orientation, etc.) on actuation and highlights its potential in the design of artificial actuators. Recently, enormous efforts are being paid to make synthetic polymer actuators more sensitive, such as reducing the electric voltage for driving polymer electrolyte actuators,[4] decreasing the energy consumption for light-responsive actuators,[5] and improving the humidity sensitivity of hygroscopic actuators.[6] Despite much success achieved so far, there is still plenty of potential to improve the sensitivity of synthetic polymer actuators.

Solvent stimulus polymer actuators (SSPAs) represent an important mechanism encompassing a significant breadth of utility including responsive gels,[7] grippers,[8] nano-robotics,[9] and solvent stimulus shape memory polymers.[10] For SSPAs usually the solvent diffusion into actuators results in heterogeneous volume changes giving rise to macroscopic shape changes and/or adaptive movements. In some cases, solvents may not trigger the actuation directly; instead, the real stimuli (e.g., pH, electrolytes, etc.) are coupled to solvent systems and reach the site of action through the diffusion of solvents and swelling in the polymer matrix.[11] Yet like most polymer actuators, SSPAs suffer from a relatively low sensitivity—usually a substantial amount of secondary solvents is required to mix with the primary solvent in order to produce noticeable shape deformation or displacement.[12] In some cases SSPAs were even shuttled between two different solvents to acquire the response, because a large gradient in solvent concentration is a necessity for promoting the solvent diffusion into bulk polymers.[12a] Thus large-scale actuation triggered by a low portion of solvent stimulus (e.g., < 0.5 mol%) remains an elusive challenge.

Here we report a porous poly(ionic liquid) (PIL) membrane actuator exhibiting exceptional sensitivity to low organic solvent concentrations. The membrane preparation follows a similar method we recently invented for porous polymer actuators in gas phase.[13] Since solution phase actuation is more general for polymer actuators, our interest was directed to construct new SSPAs with high sensitivity. The actuator readily bends to an arc (curvature 0.076 mm^{-1}) upon adding as low as 0.25 mol% acetone molecules (1 acetone per 400 water molecules). To make a quantitative comparison, we define the actuator's sensitivity to organic solvents concentration as the amount of curvature change triggered by adding 1 mol% of the solvents. Thus our membrane is found to be at least one order of magnitude more sensitive than other state-of-the-art SSPAs.

The membrane chemically consists of two polyelectrolytes, a cationic PIL, poly[3-cyanomethyl-1-vinylimidazolium bis(trifuoromethanesulfonyl)imide] (denoted as PCMVImTf2N), and poly(acrylic acid) (denoted as PAA, molecular weight 2 000 Da, a commercial product from Sigma Aldrich). Specifically speaking, PILs are polymerization products of ionic liquid monomers. The high density packing of ionic liquid species in PILs gives rise to distinctive properties, e.g., tunable solubility in organic media, surface activities, broad glass transition temperature, etc.[14] Recently there is huge attention on applying PILs as innovative polyelectrolytes to build up advanced materials and (multi)functional devices.[15] The PCMVImTf2N used in this research was synthesized according to our previous report (Figure S1, supporting information).[16]

To prepare the porous membrane, PCMVImTf2N and PAA were dissolved in dimethylformamide, solution-cast on a glass plate, dried (80 °C, 2 h), and subsequently soaked in aqueous ammonia (0.2 wt%, 20 °C, 2 h). Afterwards a free-standing membrane (denoted as PCMVImTf2N-PAA) was easily peeled off from the glass plate. Note that the surfaces facing aqueous ammonia and the glass plate are denoted as TOP and BOTTOM surfaces, respectively (Figure S2, supporting information). During the soaking step, water and ammonia molecules diffused into the film from the top surface and triggered the electrostatic complexation between PCMVImTf2N and PAA, a novel self-assembly mechanism we discovered recently for fabricating nanoporous membranes.[13a] As-prepared PCMVImTf2N-PAA membranes feature a combination of porous morphology (Figure S3, supporting information) and a gradient in electrostatic complexation (Figure S4 ~ S5, supporting information) between cationic

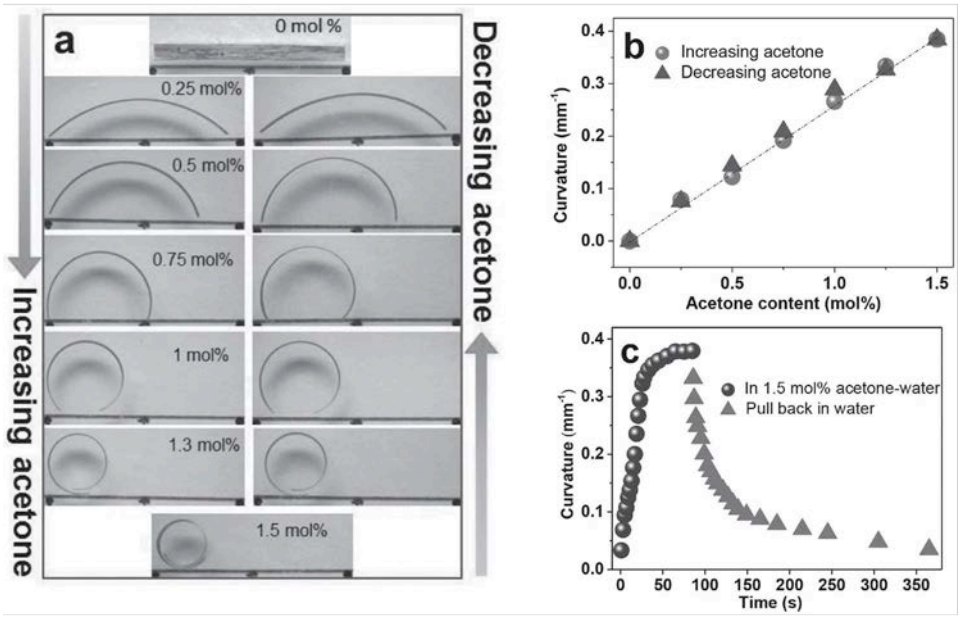

Figure 1. (a) shape deformation of a PCMVImTf2N-PAA membrane (1 mm × 20 mm × 30 μm) in response to the molar amount of acetone molecules in a water-acetone mixture at 20 °C (left column: increasing acetone content, right column: decreasing acetone content); note: inserted numbers are the acetone content; the membrane was kept for 5 mins to reach bending equilibrium at each acetone concentrations; the membrane (originally yellowish) was painted in red color for better visibility: the color painting does not affect the actuation; the thick blue bar is a 20 mm scale bar (please see Figure S9, supporting information for the experimental setup), (b) plot of curvature (mm^{-1}) of the membrane actuator against acetone content (mol%); (c) plot of curvature (mm^{-1}) of the membrane actuator against time when placing it in a 1.5 mol% acetone-water mixture and back in water.

PCMVImTf2N and the anionic PAA (neutralized by ammonia) from top to bottom.

The PCMVImTf2N-PAA membrane actuator is straight and flat in water (Figure 1a, top), and its top surface steadily bends inward (curvature = 0.076 mm^{-1}, Figure S6) upon adding acetone up to 0.25 mol% relative to water. By increasing acetone content to 1.5 mol%, the membrane arch bends continuously and ends up with a closed loop (Figure 1a, left column). By decreasing the acetone concentration, the membrane actuator gradually reverts to the original shapes with high accuracy (Figure 1a, right column). Figure 1b quantitatively shows that the curvature of the actuator appears linearly proportional to acetone content, plus being highly reversible. This bending-stretching cycle can be repeated at least 20 times with high accuracy (Figure S7, supporting information). Furthermore the bending kinetics were studied (Figure 1c). Transferring the membrane directly from water into a 1.5 mol% acetone-water mixture, its curvature increases rapidly versus time, then levels off and reaches a plateau after 50 s. Pulling back in water, the recovery of the membrane curvature is slower, which is understandable given the slower rate of acetone releasing from the membrane due to the solvent-polymer attractive interaction. In addition, the temperature influence on the bending actuation was also observed but rather as a secondary effect (Figure S8, supporting information). As both mechanical properties and the ionic bonding in solution are affected by temperature, it remains yet unclear which dominates the temperature effect in the shape deformation of the porous actuators.

Moreover, we found that the actuator can also respond to other solvents such as tetrahydrofuran, 1,4-dioxane, and ethanol with similarly high sensitivity (Figure S10, supporting information). In the literature, a variety of SSPAs can respond to solvents exchange, but with much lower sensitivity. Here the PCMVImTf2N-PAA actuator is at least one order of magnitude more sensitive than systems recently reported (Table S1, supporting information). For example, 50 mol% acetone is required for a phenol-formaldehyde bi-layer film bending to a curvature of 0.35 mm^{-1},[12d] whereas the PCMVImTf2N-PAA actuator bends to a similar curvature (0.38 mm^{-1}) requiring only 1.5 mol% acetone. Because it is known that bending actuation is inversely proportional to membrane thickness (Figure S11, supporting information), we also plot "normalized sensitivity" (curvature multiplied by thickness) as well as the apparent sensitivity to compare our membrane's sensitivity with other data reported recently in literature (Table S1, supporting information).

The "stimulus ~ actuator" interaction is commonly recognized as a precondition for SSPAs. In this context a strong "acetone ~ PCMVImTf2N" interaction indeed exists, as hinted by the fact that PCMVImTf2N is soluble in acetone but not in water. Moreover, the membrane possesses a gradient in complexion degree through its cross-section (Figure S4 ~ S5, supporting information), with highest polarity and minimal cross-linking density at the bottom of the membrane. The resultant acetone absorption gradient leads to a swelling gradient across the membrane, decreasing from bottom to top, which in turn drives the bending of the membrane.[13b] The gradient in cross-linking is also likely to produce a gradient in the elastic modulus through the membrane, however this modulus gradient is unlikely to have a strong effect on bending compared to the role of the swelling gradient, as known from the classical analysis of bi-metal thermostats.[17] One potential advantage of a graded membrane as opposed to classical bi-layers is the reduction in interfacial stresses that are produced in a

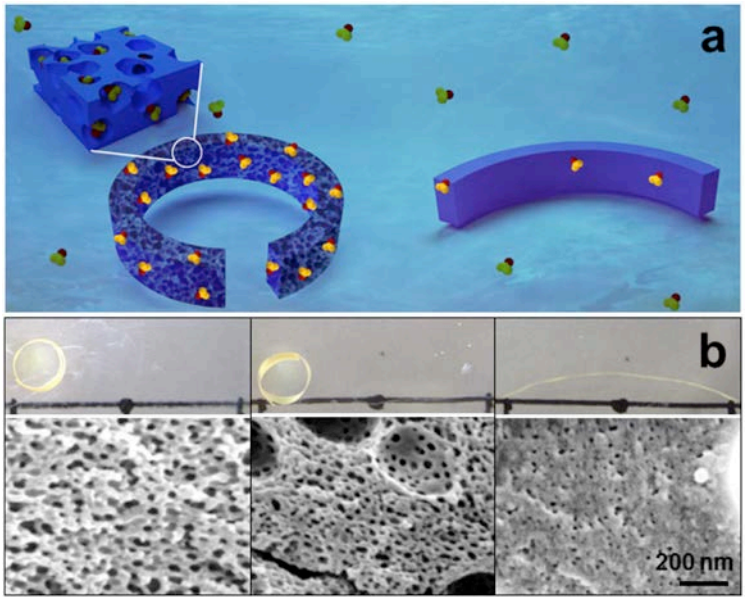

Figure 2. (a) A schematic mechanism of the sensitive actuation of a porous membrane actuator (on the left) compared to dense one (right), (b) effect of PAA's molecular weight on the bending actuation of three PCMVImTf2N-PAA membranes (1 mm × 20 mm × 30 μm) placing in 1.5 mol % acetone-water mixture at 20 °C for 10 mins (top panel, NOT painted in red color), and their corresponding porous architectures (bottom panel, SEM pictures of membrane cross-sections). Note: the three membranes were made in the same procedure, except that the molecular weight of PAA from the left to right is 2 000, 5 000, and 100 000 Da, respectively.

bi-layer. Such stress concentrations are unwanted as they may increase the likelihood of delamination and failure in a bi-layer, but also represent stored elastic energy (coming from the energy of the solvent) that serves no actuation function. By creating appropriate gradients in swellability one may improve efficiency giving actuation at lower acetone concentrations.

In addition, the PCMVImTf2N-PAA actuator membrane is nanoporous (30-100 nm in pore size), in stark contrast to common SSPAs that are dense.[12] The pore channels not only accelerate mass transport of solvents into the membrane, but also weakens the overall bending rigidity, since part of its solid bulk (where the pores stay) is replaced by mobile liquids (Figure 2a). Put another way, pore structures circumvent the need for a high acetone concentration normally required for driving the molecular diffusion and penetration in dense materials, thus leading to a higher sensitivity to solvent concentration.

Reference experiments support our mechanistic views. First, the physical blend of PCMVImTf2N and PAA as control membranes without electrostatic complexation and pore structure show negligible response to acetone solvent (Figure S12, supporting information), verifying that the combination of electrostatic complexation and porous architecture are prerequisites for sensitive actuation. Additionally, by modulating the molecular weight of PAA, the membranes were tailored from highly nanoporous to less porous and finally non-porous states (Figure 2b, bottom panel). Consequently, the less porous actuator (Figure 2b, sample on the right) shows much smaller bending in a 1.5 mol% acetone-water mixture than porous films. Given the same chemical nature of the three membranes, unambiguously the pores are playing critical roles improving their sensitivity. However, because the membrane's bending actuation is affected by a multiple of pore structural parameters, future study is needed to engineer these structure features, such as pore size, pore size distribution and pore shape, for task-specific actuation.

The actuator's high sensitivity allows for functionality unattainable with common SSPAs, such as discriminating solvent quality even including isomers. In butanol isomer-water mixtures it shows different bending curvatures (red bars in Figure 3a and inset pictures). To the best of our knowledge this represents the first trial of "reading" solvent isomers, i.e. subtle solvent quality, by SSPAs. We conducted molecular dynamics (MD) simulations to shed more light on the molecular interactions and adsorption processes between the polymer membrane and the butanol isomers. Since the preferential adsorption of solvent to the ionic-liquid-like (IL) groups is responsible for the outstanding membrane properties (sensitivity and selectivity), we simulated the solvation of one PIL-ion pair in the presence of different solvent compositions (see section 3, supporting information). We indeed find an excess adsorption (over water) to the PIL-ion-pair for all three butanol isomers. We have quantified the adsorption with the common adsorption coefficient Γ which has positive values if the butanol is in excess over water; see the blue bars in Figure 3a. Hence, all butanol isomers solvate the PIL-ion-pair better than water and will lead to a larger swelling (and bending) of the membrane due to an enhanced osmotic pressure. Moreover, we see in Figure 3a that the butanol isomers feature an increasing adsorption in the order 1-butanol > 2-butanol > isobutanol. Our mechanistic view is fully supported by the experimental fact that the curvature of the actuator follows exactly the same trend if solvated by these isomers. From the MD simulations we find that on a microscopic level the adsorption trend is related to subtle changes of the detailed interaction of the isomers (with varying hydrophobicity) to the PIL-ion pairs, see Figure 3b for representative simulations snapshots and cartoons depicting the molecular

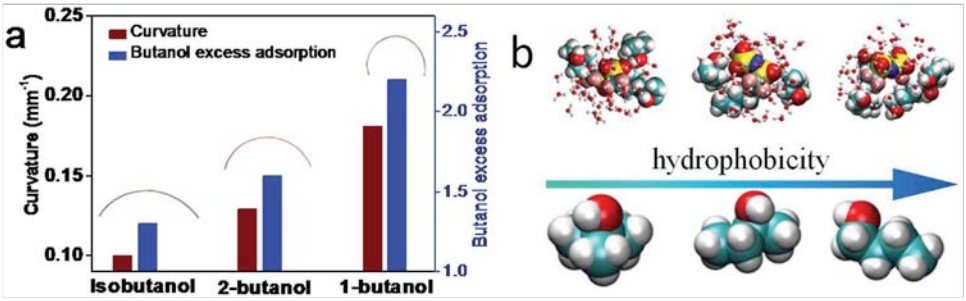

Figure 3. (a) Red column: curvature of PCMVImTf2N-PAA actuator membrane in water containing 1.25 mol% butanol isomers (isobutanol, 2-butanol, and 1-butanol) at 20 oC. Blue column: excess absorption of butanol isomers to the PIL-ion pair calculated by all-atom molecular dynamics computer simulations. The inserts are photographs of the bent membrane arch (top view); (b) representative scheme showing the composition of the 1st solvation layer of PIL-ion pair for the three isomers (top panel) and the growing hydrophobicity (and decreasing solubility) of the respective butanol isomers (bottom panel, isobutanol, 2-butanol, and 1-butanol from left to right).

structure. More details to the simulation results can be found in the supporting information (Figure S13 ~ S18).

In addition the actuator is combined with other beneficial functionalities such as cooperative actuation, i.e., a group of individual actuators could work cooperatively to accomplish more complicated tasks. This feature is viable even at a relatively small signal input owing to the actuator's high sensitivity. For example, 30 pieces of PCMVImTf2N-PAA membranes were put in a 5 mol% acetone-water mixture, which simultaneously bent and interpenetrated into each other, forming a compact "membrane coil" comprised of entangled and interlocked membrane stripes (Figure 4, Figure S19, supporting information). Put back into water, the "membrane coil" deaggregates into the original individual membrane shapes (Figure 4a). Here the actuator's high sensitivity is required, otherwise the interpenetration and entangling of different membranes is not effective enough to lock the compact "membrane coil". Given that disentangling this "membrane coil" by hand only ends up with membrane rupture, the cooperative actuation hints to microdevices capable of multistep manipulation

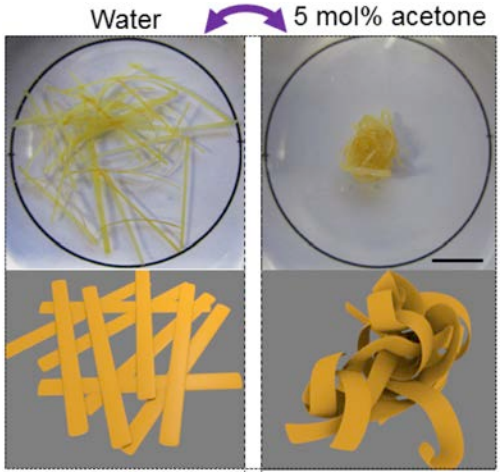

Figure 4. Cooperative actuation of 30 PCMVImTf2N-PAA membranes (1 mm × 25 mm × 30 μm) shuttled between water (left) and a 5 mol% acetone-water mixture (right); pictures were taken at a top view; the schemes (bottom panel) illustrate the entangling-unentangling of membrane stripes. The scale bar is 1 cm.

and/or fabrications.

In summary, we introduced a new concept for fabricating solvent stimulus polymer actuators with unprecedented sensitivity and accuracy. This was accomplished by integrating porous architectures and electrostatic complexation gradients in a poly(ionic liquid) membrane that bears ionic liquid species for solvent sorption. In contact with 1.5 mol% of acetone molecules in water, the actuator membrane (1 mm × 20 mm × 30 μm) bent into a closed loop. While the interaction between solvents and the polymer drives the actuation, the continuous gradient in complexation degree combined with the porous architecture optimizes the actuation, giving it a high sensitivity and even the ability to discriminate butanol solvent isomers. The membrane is also capable of cooperative actuation. The design concept is easy to implement and applicable to other polyelectrolyte systems, which substantially underpins their potentials in smart and sensitive signaling microrobotics/devices.

Supporting information

Supporting Information (materials characterization, actuation, and molecular dynamic simulations) is available from the Wiley Online Library or from the author.

Acknowledgements

QZ, KT and JY would like to thank the Max Planck Society for financial support. JH and JD thank the Alexander-von-Humboldt (AvH) Stiftung, Germany, for financial support.

References

[1] a) M. M. Ma, L. Guo, D. G. Anderson, R. Langer, Science 2013, 339, 186-189; b) C. Keplinger, J.-Y. Sun, C. C. Foo, P. Rothemund, G. M. Whitesides, Z. Suo, Science 2013, 341, 984-987; c) C. O. Baker, B. Shedd, P. C. Innis, P. G. Whitten, G. M. Spinks, G. G. Wallace, R. B. Kaner, Adv. Mater. 2008, 20, 155-158; d) G. Stoychev, S. Turcaud, J. W. C. Dunlop, L. Ionov, Adv. Funct. Mater. 2013, 23, 2295-2300; e) H. Thérien-Aubin, Z. L. Wu, Z. Nie, E. Kumacheva, J. Am. Chem. Soc. 2013, 135, 4834-4839; f) M. Behl, K. Kratz, U. Noechel, T. Sauter, A. Lendlein, Proc. Natl. Acad. Sci. U. S. A. 2013, 110, 12555-12559; g) A. Sidorenko, T. Krupenkin, A. Taylor, P. Fratzl, J. Aizenberg, Science

2007, 315, 487-490; h) R. R. Kohlmeyer, J. Chen, Angew. Chem. Int. Ed. 2013, 52, 9234-9237; i) Z. Q. Pei, Y. Yang, Q. M. Chen, E. M. Terentjev, Y. Wei, Y. Ji, Nat. Mater. 2014, 13, 36-41; j) E. W. H. Jager, E. Smela, O. Inganas, Science 2000, 290, 1540-1545.
[2] a) M. A. C. Stuart, W. T. S. Huck, J. Genzer, M. Mueller, C. Ober, M. Stamm, G. B. Sukhorukov, I. Szleifer, V. V. Tsukruk, M. Urban, F. Winnik, S. Zauscher, I. Luzinov, S. Minko, Nat. Mater. 2010, 9, 101-113; b) T. Aida, E. W. Meijer, S. I. Stupp, Science 2012, 335, 813-817; c) X. Yan, F. Wang, B. Zheng, F. Huang, Chem. Soc. Rev. 2012, 41, 6042-6065; d) L. Dongbo, W. F. Paxton, R. H. Baughman, T. J. Huang, J. F. Stoddart, P. S. Weiss, MRS Bull. 2009, 34, 671-681; e) X. M. Sun, W. Wang, L. B. Qiu, W. H. Guo, Y. L. Yu, H. S. Peng, Angew. Chem. Int. Ed. 2012, 51, 8520-8524; f) B. P. Lee, S. Konst, Adv. Mater. 2014, 26, 3415-3419.
[3] a) J. R. Capadona, K. Shanmuganathan, D. J. Tyler, S. J. Rowan, C. Weder, Science 2008, 319, 1370-1374; b) P. Fratzl, F. G. Barth, Nature 2009, 462, 442-448; c) R. M. Erb, J. S. Sander, R. Grisch, A. R. Studart, Nat. Commun. 2013, 4; d) R. Elbaum, L. Zaltzman, I. Burgert, P. Fratzl, Science 2007, 316, 884-886.
[4] a) O. Kim, T. J. Shin, M. J. Park, Nat. Commun. 2013, 4, 2208; b) J. Biggs, K. Danielmeier, J. Hitzbleck, J. Krause, T. Kridl, S. Nowak, E. Orselli, X. Quan, D. Schapeler, W. Sutherland, J. Wagner, Angew. Chem. Int. Ed. 2013, 52, 9409-9421; c) K. Mukai, K. Asaka, T. Sugino, K. Kiyohora, I. Takeuchi, N. Terasawo, D. N. Futoba, K. Hata, T. Fukushima, T. Aida, Adv. Mater. 2009, 21, 1582-1585; d) L. R. Kong, W. Chen, Adv. Mater. 2014, 26, 1025-1043.
[5] a) Z. Jiang, M. Xu, F. Li, Y. Yu, J. Am. Chem. Soc. 2013, 135, 16446-16453; b) O. S. Bushuyev, T. A. Singleton, C. J. Barrett, Adv. Mater. 2013, 25, 1796-1800.
[6] a) L. T. de Haan, J. M. N. Verjans, D. J. Broer, C. W. M. Bastiaansen, A. P. H. J. Schenning, J. Am. Chem. Soc. 2014, 136, 10585-10588; b) Y. Ma, Y. Zhang, B. Wu, W. Sun, Z. Li, J. Sun, Angew. Chem. Int. Ed. 2011, 50, 6254-6257.
[7] a) M. R. Islam, X. Li, K. Smyth, M. J. Serpe, Angew. Chem. Int. Ed. 2013, 52, 10330-10333; b) E. Palleau, D. Morales, M. D. Dickey, O. D. Velev, Nat. Commun. 2013, 4, 2257; c) M. Nakahata, Y. Takashima, A. Hashidzume, A. Harada, Angew. Chem. Int. Ed. 2013, 52, 5731-5735; d) Z. L. Wu, M. Moshe, J. Greener, H. Therien-Aubin, Z. H. Nie, E. Sharon, E. Kumacheva, Nat. Commun. 2013, 4.
[8] a) T. G. Leong, C. L. Randall, B. R. Benson, N. Bassik, G. M. Stern, D. H. Gracias, Proc. Natl. Acad. Sci. U. S. A. 2009, 106, 703-708; b) J. S. Randhawa, T. G. Leong, N. Bassik, B. R. Benson, M. T. Jochmans, D. H. Gracias, J. Am. Chem. Soc. 2008, 130, 17238-17239.
[9] a) Y. Zhou, W. Guo, J. Cheng, Y. Liu, J. Li, L. Jiang, Adv. Mater. 2012, 24, 962-967; b) J. Kim, J. A. Hanna, M. Byun, C. D. Santangelo, R. C. Hayward, Science 2012, 335, 1201-1205.
[10] a) D. Quitmann, N. Gushterov, G. Sadowski, F. Katzenberg, J. C. Tiller, ACS Appl. Mater. Interfaces 2013, 5, 3504-3507; b) R. Xiao, T. D. Nguyen, Soft Matter 2013, 9, 9455-9464; c) J. Mendez, P. K. Annamalai, S. J. Eichhorn, R. Rusli, S. J. Rowan, E. J. Foster, C. Weder, Macromolecules 2011, 44, 6827-6835.
[11] a) Y. Zou, A. Lam, D. E. Brooks, A. S. Phani, J. N. Kizhakkedathu, Angew. Chem. Int. Ed. 2011, 50, 5116-5119; b) C. X. Ma, T. F. Li, Q. Zhao, X. X. Yang, J. J. Wu, Y. W. Luo, T. Xie, Adv. Mater. 2014, 26, 5665-5669.
[12] a) K. J. Lee, J. Yoon, S. Rahmani, S. Hwang, S. Bhaskar, S. Mitragotri, J. Lahann, Proc. Natl. Acad. Sci. U. S. A. 2012, 109, 16057-16062; b) K. D. Harris, C. W. M. Bastiaansen, D. J. Broer, Macromol. Rapid Commun. 2006, 27, 1323-1329; c) W.-E. Lee, Y.-J. Jin, L.-S. Park, G. Kwak, Adv. Mater. 2012, 24, 5604-5609; d) M. K. Khan, W. Y. Hamad, M. J. MacLachlan, Adv. Mater. 2014, 26, 2323-2328.
[13] a) Q. Zhao, M. Yin, A. P. Zhang, S. Prescher, M. Antonietti, J. Yuan, J. Am. Chem. Soc. 2013, 135, 5549-5552; b) Q. Zhao, J. W. C. Dunlop, X. L. Qiu, F. H. Huang, Z. B. Zhang, J. Heyda, J. Dzubiella, M. Antonietti, J. Y. Yuan, Nat. Commun. 2014, 5, 4293.
[14] a) J. Yuan, D. Mecerreyes, M. Antonietti, Prog. Polym. Sci. 2013, 38, 1009-1036; b) D. Mecerreyes, Prog. Polym. Sci. 2011, 36, 1629-1648; c) M. D. Green, T. E. Long, Polym. Rev. 2009, 49, 291-314; d) J. Lu, F. Yan, J. Texter, Prog. Polym. Sci. 2009, 34, 431-448.
[15] a) K. H. Zhang, X. L. Feng, X. F. Sui, M. A. Hempenius, G. J. Vancso, Angew. Chem. Int. Ed. 2014, 53, 13789-13793; b) F. Schuler, B. Kerscher, F. Beckert, R. Thomann, R. Mulhaupt, Angew. Chem. Int. Ed. 2013, 52, 455-458; c) Q. Zhao, P. Zhang, M. Antonietti, J. Yuan, J. Am. Chem. Soc. 2012, 134, 11852-11855; d) J. C. Cui, W. Zhu, N. Gao, J. Li, H. W. Yang, Y. Jiang, P. Seidel, B. J. Ravoo, G. T. Li, Angew. Chem. Int. Ed. 2014, 53, 3844-3848; e) X. F. Sui, M. A. Hempenius, G. J. Vancso, J. Am. Chem. Soc. 2012, 134, 4023-4025; f) R. L. Gao, D. Wang, J. R. Heflin, T. E. Long, J. Mater. Chem. 2012, 22, 13473-13476.
[16] J. Y. Yuan, C. Giordano, M. Antonietti, Chem. Mater. 2010, 22, 5003-5012.
[17] S. Timoshenko, J. Opt. Soc. Am. 1925, 343, 233-255.

7.13 [AC6] Pressurized honeycombs as soft-actuators: a theoretical study.

Guiducci, L., Fratzl, P., Bréchet, Y. J. M., Dunlop, J. W. C.
*Published in **Journal of the Royal Society Interface**, 2014, 20140458.*
Doi: 10.1098/rsif.2014.0458

Reprinted with permission from the Royal Society

(Note: Fig 8 has been corrected see Errata on Royal Society web-site)

Abstract: The seed capsule of Delosperma nakurense is a remarkable example of a natural hygromorph, which unfolds its protecting valves upon wetting to expose its seeds. This beautiful mechanism responsible for this motion is generated by a specialised organ based on an anisotropic cellular tissue filled with a highly swelling material. Inspired by this system we study the mechanics of a diamond honeycomb internally pressurised by a fluid phase. Numerical homogenization by means of iterative finite element simulations is adapted to the case of cellular materials filled with a variable pressure fluid phase. Like its biological counterpart, it is shown that the material architecture controls and guides the otherwise unspecific isotropic expansion of the fluid. Deformations up to twice the original dimensions can be achieved by simply setting the value of input pressure. In turn, these deformations cause a marked change of the honeycomb geometry and hence promote a stiffening of the material along the weak direction. To understand the mechanism further we also developed a micromechanical model based on the Born model for crystal elasticity to find an explicit relation between honeycomb geometry, swelling eigenstrains and elastic properties. The micromechanical model is in good qualitative agreement with the finite element simulations. Moreover, we also provide the force-stroke characteristics of a soft actuator based on the pressurised anisotropic honeycomb, and show how the internal pressure has a non-linear effect which can result into negative values of the in-plane Poisson's ratio. As nature shows in the case of the Delosperma nakurense seed capsule, cellular materials can be used not only as low-weight structural material, but also as simple but convenient actuating materials.

1 Introduction

Natural hygromorphs are biological systems that can generate a specific actuation (ie displacement or force) as a response a change in humidity occurring for example between day and night [1, 2]. They are interesting examples for bio-inspired materials design, as they typically operate without metabolic energy meaning that actuation is achieved through the arrangement or architecture of the underlying constituent materials (cellulose fibrils, hemicellulose and lignin etc) [3, 4]. In other words, the materials-architecture of the actuating tissue controls and guides the otherwise unspecific isotropic swelling of the single components [5-7].

Natural hygromorphs can be found for example in the seed dispersal units of wild wheat awns [1], or in the scales of the pine-cone [8, 9]. In each of these systems, the actuating organ is structured in a similar way to a bilayer, where two materials with different swelling properties are juxtaposed. These differences in swellabilities are a consequence of the microstructural organization of the reinforcing cellulose fibrils in the secondary cell-wall. When water is absorbed into the swellable matrix polymers, volumetric expansion occurs mainly perpendicular to the stiff crystalline cellulose fibrils: the microfibril angle of the cellulose fibrils thus directs the swelling deformation of the cell [10, 11]. At the macroscopic level of the bilayer, wetting/drying cycles correspond to an alternate bending/straightening motion, as predicted by the Timoshenko model of a two-material plate undergoing thermal deformations [11]. Another natural passive actuator exploiting the microscopic architecture of the cellulose fibrils is the awn of the stork's bill [12]. The macroscopic coiling movement appears to originate from a mechanically uniform cell layer made up of intrinsically coiling cells, rather than a spatial distribution of differently swelling materials [13]. In each cell the cellulose helix is tilted with respect to the cell main axis: in a fully swollen state the matrix exerts a pressure on the helix, which uncoils and aligns to the cell main axis; while drying, the helix tilts and tightens, thereby causing a macroscopic spiralling movement.

Cellulose microfibril orientation also controls the extent of forces generated during swelling. In the roots and xylem of higher plants, specialised tissues have evolved that are able to generate a contraction force (tensile stresses) on the surrounding tissues [14-16]. In these tissues the cells possess thick walls with a lignified secondary cell-wall having high microfibril angles (about 36 degrees) and an innermost gelatinous-layer (G-layer) consisting of axially oriented cellulose fibrils. One explanation for the development of tensile stresses comes from the idea that lateral swelling from the G-layer puts the cell walls under pressure. Due to the high microfibril angle, these walls, translate the hoop stress into a longitudinal tensile stress [17].

The shape of the cells in the swelling tissue also plays an important role in hygroscopic actuation systems. This was shown in a recent study on the hydro-actuated unfolding of the ice plant (Delosperma nakurense) seed capsule [18]. The seed capsule contains five seed chambers, separated by septa (Fig. 1). In the dry state (Fig. 1a), five valves close the chambers to prevent accidental seed dispersion, with the centre of each valve pushed against a corresponding septum. As liquid water comes into the tissues, the valves unfold (Fig. 1c), moving away from the septa, spanning an angular trajectory of about 150 degrees. The specialised organ promoting this movement is the hygroscopic keel (highlighted in red in Fig. 1c), a prominent tissue attached to the centre of the inner valve surface, consisting of two halves which, in the dry state, pack onto the septum.

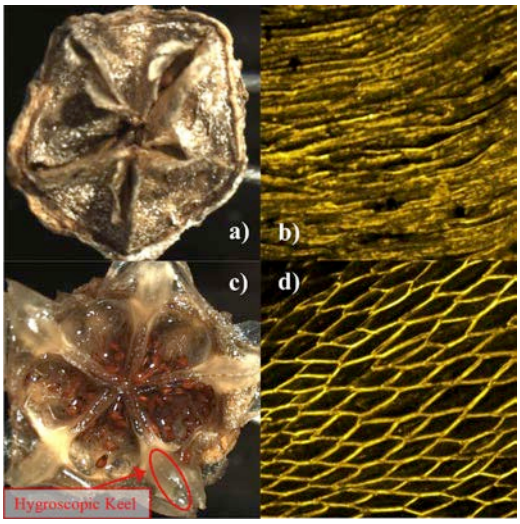

Figure 1 | Anatomy and material architecture of the hydro-actuated Delosperma nakurense seed capsule. The seed capsule of the Delosperma nakurense is a natural example of passive actuation driven by water adsorption. The dry seed capsule (a) opens upon water absorption c) due to the expansion of the hydroscopic keel. One of the five keels is highlighted in red in c). The anisotropic architecture and differential composition of the keels tissue (as seen in b) in the dry state and d) in the wet state) enables a huge localised swelling which translates in the opening of the valves that protect the seeds (images provided courtesy of K. Razghandi, b,d are modified from Ref [18] with permission).

Structural and chemical characterization of the keels tissue revealed a highly anisotropic honeycomb structure, with elliptical shaped cells. The cell walls were lignified and lined with a "cellulosic inner layer" (CIL) consisting of as-yet unidentified hygroscopic polysaccharides. In the dry state the cells appear collapsed and closely packed together. During swelling the CIL absorbs large amounts of water. The resultant volume expansion occurs mainly along the cells cross-sectional short axis, with a net deformation of up to 4 times the original cell width. Hence, the swollen CIL exerts a pressure on the cells' walls, giving rise to an overall shape change of the keel tissue (Figs 1 b and d). Although this tissue was analysed experimentally, little is known about the role of cell-architecture and cell shape on the swellability of honeycombs. The goal of this paper is to develop a suitable theoretical model to describe such systems and use it to explore the design space of swellable honeycomb actuators.

Many studies have been conducted on the mechanical behaviour of regular cellular materials, see e.g. [19-23]. These models estimate the macroscopic "continuum" mechanical properties of a regular cellular material from microscopic parameters like nodal connectivity, cell shape, relative density, and mechanical properties of the cell-wall material [20, 24-26]. Moreover, the influence of cell-size distribution, irregularity and point defects on the elastic and failure properties of honeycombs and foams has also been extensively studied [27-29]. In these studies, the mechanical properties of the cellular material are discussed by simulating "simple" boundary value problems (uniaxial, biaxial or pure shearing loading). Despite the large amount of work being done on the mechanics of honeycombs, surprisingly, no systematic study has been conducted on internal loading conditions like hydrostatic pressurization on the honeycomb inner surface, relevant to understanding the actuation of the ice-plants, has been conducted. One study, by Niklas, that goes in this direction, provided a theoretical description of the effect of a turgid protoplast pressurizing a thick walled plant cell on its effective stiffness [30]. Here the cell was considered cylindrical and isolated, and no collective effect at the tissue level or cell shape influence was considered. Other studies [31, 32] are concerned with the effect of a turgor pressure on the effective stiffness of foam solids like the parenchyma tissue, but their scope limits to isotropically shaped cells in the stretching dominated regime. Some studies have investigated the influence of cell shape on the overall expansion of honeycombs, however these considered only a small orthotropic expansion of the honeycomb walls rather than an internal pressurisation [33]. No explicit investigation of microscopic swelling deformation at less than fully turgid pressures has been provided.

Internal pressurisation in hollow structures has also awakened the interest of applied research fields such as soft robotics. In a recent study, Martinez et al. [34] combine elastomers with flexible inextensible paper reinforcements to produce a new class of soft pneumatic actuators. Here, the driving force for actuation comes from an external source of pneumatic pressure, while the desired actuation is controlled by the crease pattern and spatial arrangement of paper sheets embedded in an elastomer. Another study by Pagitz et al. [35] presents a novel concept for pressure-actuated cellular structures that is inspired by the nastic movement of plants. They consider a composite plate-like cantilever formed by a two arrays of prismatic cells with identical pentagonal and hexagonal cross sections. Differences in internal pressures for each array of cells, corresponds to an equilibrium configuration that resembles a circular arc. By changing the initial shape of the cells, also non circular arc shapes can be achieved.

In the following we will present a theoretical model for the assessment of the performance of a swellable honeycomb. This should be of some relevance for understanding the mechanical aspects related to the hygroscopic actuation in the ice plant seed capsules. Nonetheless, the model should be also general enough to give an insight about the applicability of anisotropic honeycombs as possible candidates for pressure driven actuators. The pressure may be generated from a swelling process (as in the keel's tissue of the ice plant), or an external source (as in pneumatic soft robots). In both cases, notwithstanding the necessary simplifications introduced in the model, our aim is to give a deeper understanding of the mechanical performance of pressurised anisotropic honeycombs.

The actuation performance of the honeycomb will be investigated in terms of three complementary responses: the eigenstrains developed by the honeycomb upon a certain internal pressure (i.e. the magnitude of accessible motion), the forces generated at a given stroke, and its effective stiffness in a given pressurised configuration. In the following we somewhat abuse the term eigenstrains since the effect of a pressure on a hollow structure as the honeycomb

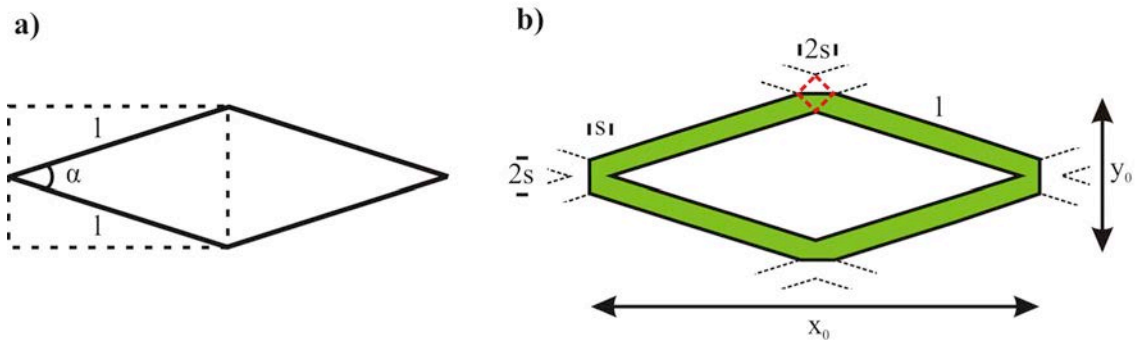

Figure 2 | Diamond honeycomb geometry. Diamond honeycomb geometry results from periodic repetition of the unit cell (dashed box) along lattice vectors at an angle +-α/2 to the horizontal so that each joint connects four inclined members (a). This geometry has been imported in the finite element model unit cell as a fluid-filled honeycomb with finite thickness walls (b). The FE honeycomb has slender walls (t=3, l=41) and strong anisotropy (X0/Y0 = 4:1). The joints (red dotted) are built as squares of side $\sqrt{2}$ s (s=2.5).

will generally cause an elastic stress in its walls, and hence is not a stress free transformation strain [36]. This notwithstanding, if one considers the pressurising agent as part of the investigated system (as in our contribution here), then the net elastic stresses are null and the macroscopic strain of the structure is stress-free in an averaged sense.

As a test case we will consider a bi-dimensional anisotropic honeycomb consisting of diamond shaped cells, inspired by the tissue of the ice-plant keels. Our modelling approach, described in the methods section, is based on a finite element (FE) model comprising all relevant geometrical and mechanical parameters of the honeycomb. To calculate the quantities we are aiming at (eigenstrains, exerted forces and stiffness) we first simulate a hydrostatic pressurisation, and get an equilibrated pressurised configuration characterised by its eigenstrains. From this configuration, we perform basic loading conditions of the structure such as uniaxial stretching and in-plane shearing, to get the full stiffness tensor of the pressurised honeycomb. These simulations are repeated in a parametric study where the effect of cell wall stiffness and swelling pressure on the model´s behaviour is addressed. In the discussion section, we will show how these results can be interpreted in terms of an analytical micromechanical model, and critically evaluate the prediction ability of our modelling strategy. In the final section we will provide some conclusions and outlook for future work.

2 Numerical Model

2.1 Shape of the unit cell and mechanical properties

Geometry of the investigated system

The honeycomb considered here is a diamond shaped honeycomb resembling the ice-plant keels tissue. The unit cell consists of two inclined beams, joined at an angle α=28°. The regular lattice is obtained by shifting the unit cell along two lattice vectors at an angle +-α/2 to the horizontal. In contrast to a hexagonal honeycomb, each joint of the infinite lattice connects 4 inclined members (Fig. 2a).

Finite Element Model

In the dry state the ice plant keels´ tissue is completely collapsed, with barely no cell lumens observable. In the swollen state the cells´ walls are pushed apart by the swelling of the CIL inside the lumens (Fig. 1). Based on the volumetric expansion that it undergoes, in the swollen state the material in the lumen can contain up to 95% water. Although direct mechanical measurements of the CIL have proven unpractical, it can be inferred that the lumen´s elastic modulus is negligible, when compared to the much stiffer lignified walls.

Following this abstraction (Fig. 2b), the unit cell of the finite element model measures X_0=80 mm by Y_0= 20 mm and comprises a structural domain coinciding with one full diamond-shaped honeycomb cell and a fluid domain occupying the remaining space; to be close to the keels' geometry, the walls are modelled as slender beams of length l=41 mm and thickness t=3 mm so that l/t>10. The resulting honeycomb angle measures 28° degrees; with such an anisotropic shape care has been taken to avoid excessive bulkiness of the joints. These are built as squares of side $\sqrt{2}$ s (s=2.5 mm) (red dotted area) in order to make their rigidity independent from the direction of the loading. The walls are considered to be linearly elastic with a Young modulus (1GPa) and Poisson´s ratio (0.3), according to values reported for cell wall transverse modulus of spruce wood in moist conditions [6]. The lumen is modelled as a fluid cavity subjected to a constant pressure p. The geometry, material constitutive equation, boundary conditions and discretization have been implemented in the commercial finite element software ABAQUS 6.12 ® (Dassault Systémes Simulia Corp.). In particular, the structural domain was discretised with 1040 linear, two dimensional, plane stress, reduced integration continuum elements (ABAQUS 6.12 element library: CPS4R), with four elements across the wall´s thickness to precisely capture the stress gradient. The "enhanced hourglass control" option has been used to avoid deformation artefacts at the fluid-structure boundary. Mesh size independence has been verified by using a superfine 16704 elements mesh (16 elements across the wall thickness), resulting in predictions of honeycomb expansion deviating by less than 1%.

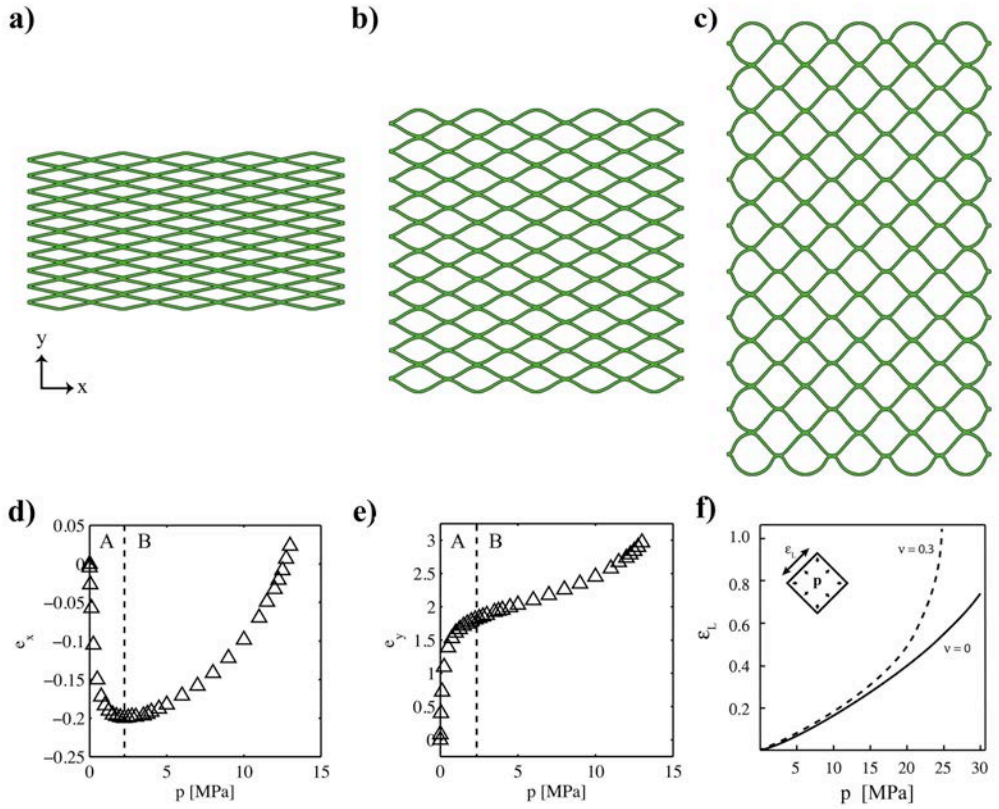

Figure 3 | Deformation of an anisotropic honeycomb with isotropic linear elastic walls (E=1 GPa, υ=0.3) under internal pressure. (a) Initial configuration at zero pressure. (b) At lower pressure (p=0.3 MPa) the cells volume is maximized by bending deformation of the walls and localized distortion of the joints with an increase of the honeycomb angle (bending regime). (c) As the internal pressure increases (p=7.5 MPa) the further volume increase can be accommodated only by stretching the walls (stretching regime). Swelling eigenstrains, (d) in the x-direction, and (e) in the y-direction as a function of inner pressure. The swelling eigenstrains change rapidly at low pressures, where the honeycomb deforms mainly by bending and joint opening. Along the y direction there is up to a 3-fold expansion, while the x dimension shrinks. The dotted line (p-2.25 MPa) highlights the transition from a bending dominated (A) to a stretching dominated (B) regime. At higher pressures (p>10) the loading of the honeycomb becomes unstable and the strains diverge. The reason for this is highlighted in (f) which shows the influence of internal pressure on wall stretching in a square vessel using a modified Laplace law that includes the effect of the Poisson's ratio of the cell-walls. At low pressures the walls stretch linearly with the pressure, however as the pressure increases, a non-zero Poisson's ratio leads to wall thinning. The pressure has a positive feedback on the strain in the walls and at a certain (finite) pressure the load is unbalanced and the strain diverges. As a comparison, a material with zero Poisson's ratio, doesn't experience this type of unbalanced loading at least for reasonable values of strains.

2.2 Eigenstrains in a finite sized honeycomb

To assess the tissue strain as a function of swelling pressure, a system of 5-by-10 cells has been considered. Here, the fluid elements have been subjected to a hydrostatic pressure, leaving the external boundaries free, and symmetry conditions were applied to avoid rigid body motion. Upon pressurization, the system undergoes an anisotropic deformation (Figs. 3 a-c). Along the y direction, which is the soft direction of the honeycomb, the system expands greatly, even at very low pressure. On the other hand, in the x direction the system first shrinks slightly, and then expands again at higher pressures. Looking at the single cells the deformation is characterised by two regimes. At lower pressure the honeycomb walls deform mostly in bending: their deformed shape is sigmoidal, with localised rotation at the joints that causes an opening of the honeycomb angle and a net increase of the fluid volume. As the pressure increases the honeycomb angle approaches its maximum value of 90°, while the walls get stretched. At very high pressure any further volume increase happens at the expense of significant wall stretching.

2.3 Eigenstrains in an equivalent periodic system

The specimen size, relative to the cell size, is known to influence the assessment of mechanical properties like stiffness and strength. Such scale effects depend on the loading type (shear, uniaxial), but usually become negligible in specimens larger than 5 repetitions of the unit cell [37]. In order to calculate the eigenstrains and properties of the homogeneous honeycomb, we investigated the system of a single unit with periodic boundary conditions. We start with the diamond structure (Fig. 2) and add a constant fluid pressure p into the lumina, whereby the problem is treated in 2D. X_0 and Y_0 are the horizontal and vertical dimensions of the diamond before deformation and X and Y after some deformation. Periodic boundary conditions imply that X and Y are fixed and only some deformation of the walls may occur due to compressibility of walls' material (ν<0.5). Hence, for each value of X and Y, a finite element simulation can be used to determine the equilibrium shape of the diamond and the associated

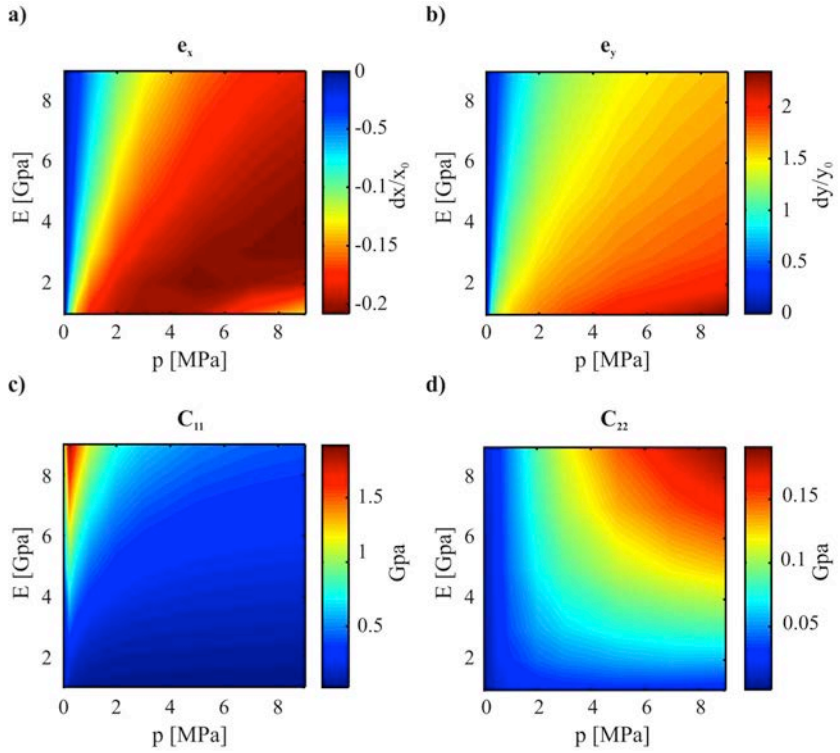

Figure 4 | Eigenstrains and effective stiffness maps. Swelling eigenstrains (a,b) and principal stiffness (c,d) along the honeycomb weak (right) and strong (left) directions, as function of internal pressure (in MPa) and wall's Young modulus (in GPa). Stiffness colour bar in GPa. Swelling eigenstrains generally increase going from stiff honeycomb walls and low internal pressure to high pressure and soft walls. The effect of pressure on stiffness is twofold, since it stiffens the weak direction and softens the strong direction, as a possible consequence of the pressure-related shape change of the honeycomb.

elastic energy $E_{el}(X,Y)$. For symmetry reasons, we do not expect shear to occur spontaneously in the system (at least not with positive internal pressures). Therefore, the total energy change of the system due to deformation is:

$$E_{tot} = E_{el}(X,Y) - \frac{1}{2} p\,(XY - X_0 Y_0) \quad (1)$$

The first term is the elastic energy stored in the walls which is counteracted by second term, the work done by the internal pressure. Minimizing this expression for X and Y should give the shape corresponding to the mechanical equilibrium. In practical terms, this means numerical calculation of E_{el} for a range of (X, Y)-values and then searching for the one that minimises E_{total}. The swelling strain referred in the following as the eigenstrain is then simply:

$$\bar{\mathbf{e}} = \begin{pmatrix} \frac{\bar{X}}{X_0} - 1 & 0 \\ 0 & \frac{\bar{Y}}{Y_0} - 1 \end{pmatrix} \quad (2)$$

Where both $\bar{X}$ and $\bar{Y}$ are the values of X and Y that minimise the total energy, which are thus functions of the internal pressure p (see supplementary material).

2.4 FE homogenization and parametric study

The effective elastic properties of the pressurised honeycomb in its equilibrium shape can be calculated via a numerical homogenization. A bidimensional, 2-plane symmetric, plane stress system as the anisotropic honeycomb considered here will generally show orthotropic elastic properties described by a stiffness tensor of the kind:

$$\mathbf{C} = \begin{bmatrix} C_{11} & C_{12} & 0 \\ C_{12} & C_{22} & 0 \\ 0 & 0 & C_{66} \end{bmatrix} \quad (3)$$

Basic loading states were simulated deforming the relaxed system (in equilibrium with the fluid pressure) with uniaxial stretching/shrinking in direction 1 and 2 and an in-plane 12 shearing. Then the corresponding effective stiffness component are calculated as the ratio between the average stress on the boundary and the applied probing strain [38]. Pressure equilibration and subsequent elastic properties homogenization were repeated in a parametric study spanning several values of p (from 0 to 9 MPa) and E (from 1 to 9 GPa).

3. Results

3.1 Baseline FE model

As for a square lattice, the diamond honeycomb considered here is a bending dominated lattice, meaning that the main deformation modes and hence the apparent stiffness depends on the bending rigidity of the beams. In the baseline model the wall stiffness is set to 1 GPa and the inner pressure varies up to 13 MPa. As a consequence, already at pressures lower than 1 MPa the honeycomb is able to double its original dimension along the y direction (Fig. 3 d,e). This is due to the bending dominated deformation and localised deformation at the joints already described for the finite size system (Fig. 3). At the same time the

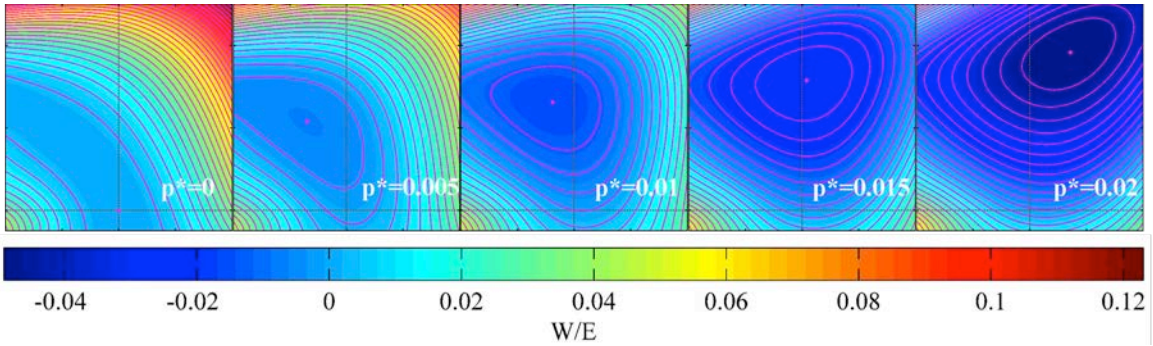

Figure 5 | Lattice energy evolution for increasing pressure calculated using the Born Model. Colour maps of the lattice strain energy density normalized by the walls modulus E for input strains εx=[-0.5, 0.5], εy=[-0.5, 5], as the pressure increases (left to right). The black dotted lines are the axes εy=0 and εx=0. In each box, isolines are spaced by a value 4*E-3. For p=0, the steepest direction corresponds to a volumetric deformation of the lattice, while the shallowest (narrow valley) to a deviatoric one. The direction of the shallowest path correlates well with a pure transversal deformation of the wall.

structure shrinks only slightly along the x direction. Around p=2.25 MPa the horizontal strain shows a minimum and the vertical one an inflection point. From this point onwards, as pressure increases, we observe that both eigenstrains increase, although with a reduced slope. Here the joints are already completely opened and any further increase of the fluid volume must be accommodated by stretching of the honeycomb walls. At very high pressures (p>10 MPa) the eigenstrains increase more than linearly and diverge. The reason for this divergence is due to the properties of the cell-wall material rather than the structure, and can be understood by the following simplified example.

In the stretching dominated regime all cells are fully expanded and have a square shape (Fig. 3c). Since the cells are all equal and the internal pressure is the same, we can study only one cell with side length l and wall thickness $t/2$ (where l and t are the length and thickness of the honeycomb beams). This cell is a pressure vessel; for a cylindrical pressure vessel, the longitudinal stress in the wall is given by the Laplace law:

$$\sigma_L = p\frac{R}{T} \qquad (4)$$

Here R is the radius of the vessel and T is the wall thickness. In our case, as the pressure increases, the cells' volume increases while the walls become thinner according to our choice of material Poisson's ratio (ν=0.3). Eq. 4 can be expressed in terms of ε_L assuming plane stress and using the constitutive relations, $\sigma_L = \frac{E}{1-\nu^2}\left(\varepsilon_L + \nu\varepsilon_T\right)$, $\sigma_T = \frac{E}{1-\nu^2}\left(\varepsilon_T + \nu\varepsilon_L\right)$. Assuming $\sigma_T = p << \sigma_L$, we can substitute $\sigma_T = 0$; also, given the square geometry of the cell, in the pressurised state $R = \frac{l}{\sqrt{2}}\left(1+\varepsilon_L\right)$ and $T = \frac{t}{2}\left(1+\varepsilon_T\right)$. With these assumptions Eq. 4 can be rearranged to become:

$$E\varepsilon_L = p\sqrt{2}\frac{l\left(1+\varepsilon_L\right)}{t\left(1-\nu\varepsilon_L\right)} \qquad (5)$$

Which states that the walls stretching in the pressurised state depends on the walls' aspect ratio, the material properties and on the internal pressure. Since in our honeycomb $l/r = 10$, we can solve Eq. 5 as a function of the pressure. It is straightforward to verify that the wall strain increases linearly at low pressures and diverges at a finite value of pressure (Fig. 3f). This is exactly what we observe in our FE simulations at the transition from the stretching dominated regime to even higher pressures. In such cases it was not possible to find a stable equilibrium configuration (in FE) past a certain value of pressure. Materials with ν=0 do not experience this instability (at least for reasonable walls strains), which means that the third regime is material (rather than structure) dependent and has to be considered in real applications.

Hence we can describe the swelling or actuation behaviour of the structure as being characterised by a bending dominated regime where the structure expands more sensitively to fluid pressure and a stretching dominated regime, where the structure is less sensitive. The maximum expansion and the relative importance of the two regimes depend on the geometry of the honeycomb: the more anisotropic the cells making up the honeycomb, the larger the maximum expansion, with a narrower bending regime and high pressure-stroke sensitivity. Conversely, a pressurised regular square lattice, would show no bending dominated regime, small expansion and poor sensitivity.

3.2 Parametric study

The results from the parametric study on the FE model are summarised in Fig. 4 in the form of eigenstrains and effective stiffness maps along the stiff (e_x, C_{11}) and soft axes (e_y, C_{22}) of the honeycomb as a function of pressure (0<p<9 Mpa) and wall Young modulus (1<E<9 GPa), whereas the initial geometry of the model is preserved (walls aspect ratio l/t and honeycomb angle α_0 stay constant). At this level of pressure, e_x is always negative and small (some percentage shrinkage) while e_y is everywhere positive and very large (up to three-fold expansion). Both the e_x and e_y maps (Fig. 4, a,b) show a similar distribution across the parameter space: their absolute value increases from the top-left corner (stiff honeycomb walls, low internal pressure) to the bottom-right corner (high pressure and soft walls). Nonetheless,

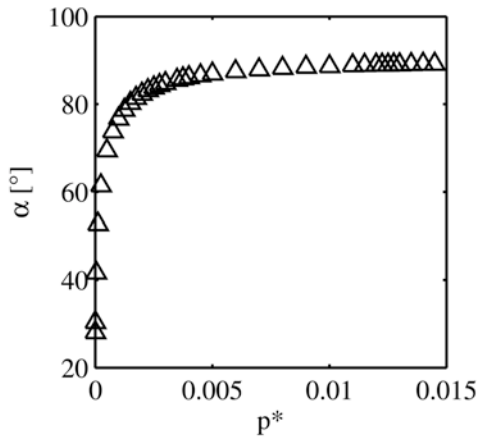

Figure 6 | Lattice angle α for increasing pressure p* for the Born Model. Normalized parameters describing deformation (α) and loading (p*) of the pressurised lattice clearly show the bending dominated (p*<0.002) and stretching dominated (p*>0.002) regimes observed in the FE model (Fig. 4). Note p* is the pressure normalised by the wall

while the e_y is monotonic throughout the whole parameter space, the e_x map shows a peak that doesn't coincide with the bottom-right corner. Here, at low wall stiffnesses (~1 GPa) and high inner pressures (p 5 to 9 MPa) e_x increases again. This behaviour derives from the deformation mechanism of the walls which is a combination of large bending at low pressures and smaller amounts of stretching at high pressures. Shifting from soft to stiffer walls allows the effect of the inner pressure to be tuned: at low wall stiffnesses (E=1-2 GPa), only a small pressure jump (from 0 to 2 MPa) suffices to increase the eigenstrains abruptly, whereas for higher walls moduli, this effect is much more gradual.

As for the effective stiffness (that is, the apparent elastic modulus of the honeycomb when subjected to a load, where subscripts 1, 2 refer to loading directions *x, y*), there is a monotonic (although non-linear) proportionality between the walls modulus and C_{11}, C_{22} (Fig. 4 c,d). Somewhat counter-intuitively, a pressure increase stiffens the weak direction (C_{22} increases towards the right Fig. 4 d) but also softens the strong one (C_{11} increases towards the left, Fig. 4 c). Generally, pressure acting inside the cells would be expected to stiffen the structure, in contrast to what is observed here for C_{11}. It is likely that this softening effect is geometry-related. As pressure deforms the honeycomb, almost axially oriented walls are rotated away from the x axis, which places them in bending thus reducing the overall structural stiffness in the x direction.

To investigate this idea we try to understand this evidence in terms of a simpler analytical model governed by explicit geometrical parameters that fully characterise the honeycomb.

3.3 Born lattice model

A simpler equivalent mechanical model of the diamond honeycomb is an oblique two-dimensional lattice with centres sitting in the honeycomb joints. The deformation state of this lattice is fully identified by the value of the lattice angle α and the point-to-point strain ε, so that the lattice strains e_x, e_y along the principal directions are obtained by a simple projection. Following other researchers [39,40], we describe the lattice elasticity by means of the Born model. Here each material point is connected only to its nearest neighbours by two kinds of springs: a longitudinal spring K_l and a transverse one K_t. The non-zero transverse stiffness K_t is needed to avoid the so called uniconstant elasticity theory governed by 'Cauchy relations'. For an isotropic medium, the Cauchy relations imply a Poisson's ratio of 1/4 for all materials described by the model [41], As already pointed out by Fratzl and Penrose [42] this is a consequence of considering just central forces for a crystal, which clearly doesn´t hold for real crystals or general lattice materials. Since the lattice geometry replicates the continuum model used in the FE simulations, we assign to the longitudinal and transverse spring constants a value reflecting their axial and bending rigidity, which changes as a function of the angle at which they are loaded (see supplementary material).

$$K_l = E\frac{t}{l}c_1(\alpha)$$
$$K_t = E\left(\frac{t}{l}\right)^3 c_2(\alpha) \qquad (4)$$

The fluid related term is simply written as the work done by the fluid from the undeformed normalised volume $V_0 = \frac{1}{2}\sin(\alpha_0)$ to a generic deformed one $V = \frac{1}{2}(1+2\varepsilon)\sin(\alpha)$. The pressure in general is not restricted to a specific form, but following the FE study, we choose a constant value (isobaric) which is independent of the volume of the single cell. In passing we also note that different forms of pressure terms could also be implemented in the model to capture its potentially different physical origins. For example, an osmotic pressure could be included, and will be in general dependent on the volume of the solute-solvent mixture, while a fluid confined to the cells will undergo an isothermal transformation.

For such a system we can write the internal potential:

$$W = W_{stretching} + W_{bending} + W_{pressure} \qquad (5)$$

Where:

$$W_{stretching} = K_l(\alpha)\frac{(\varepsilon-\varepsilon_r)^2}{\sin(\alpha_r)}$$
$$W_{bending} = K_t(\alpha)\frac{\sin\left(\frac{\alpha-\alpha_r}{2}\right)^2}{\sin(\alpha_r)}$$
$$W_{pressure} = -p\frac{V-V_r}{V_r} \qquad (6)$$

where lattice angle α_r , wall strain ε_r and lumen volume V_r refer to a reference configuration. Clearly, the swelling eigenstrains are the coordinates of the energy minimum (Fig 5) when the reference is set to the undeformed configuration ($\alpha_r=\alpha_0$, $\varepsilon_r=0$). Eigenstrains and stiffness can be found from Eq 5) and the following geometric relationship between the eigenstrains and the lattice angle and wall strain:

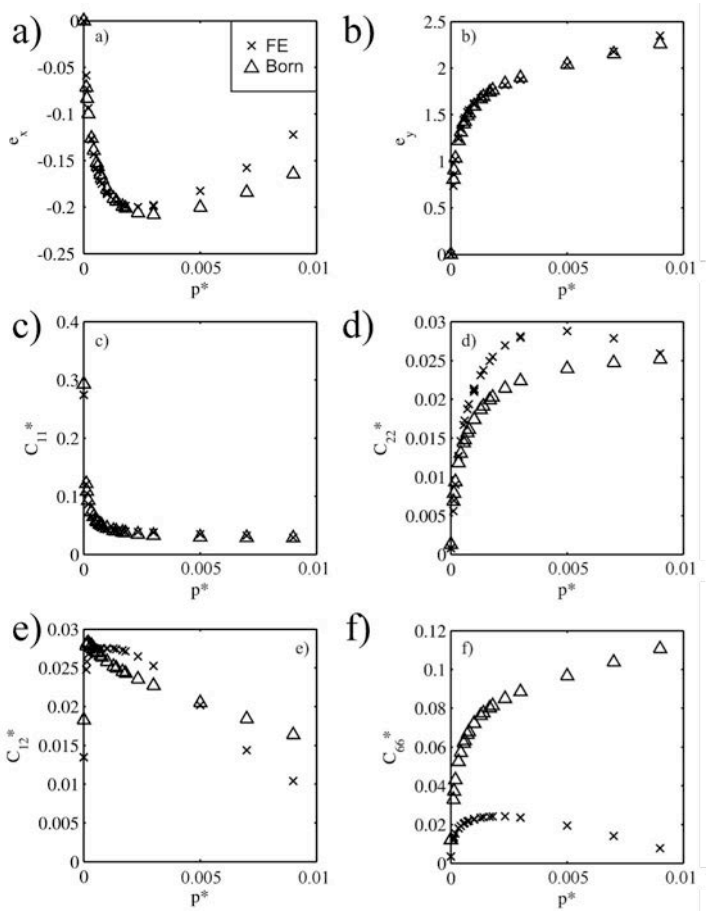

Figure 7 | Eigenstrains (a,b) and stiffness (c-f) master curves: comparison between the FE and Born lattice model. Swelling eigenstrains and effective stiffness as a function of reduced pressure p^*. Stiffness components are normalized by modulus E. The components of the apparent stiffness tensor vary according to the two stage behaviour. In particular the honeycomb becomes softer along the x direction and stiffer along the y direction as a result of the change in geometry occurring upon pressurization. Also, it can be seen that Born model follows very well the FE simulations, with a major exception in the case of C_{66} where localized joint rotations become more important.

$$\varepsilon_x = (1+\varepsilon_r)\frac{\cos\left(\frac{\alpha_r}{2}\right)}{\cos\left(\frac{\alpha_0}{2}\right)} - 1$$
$$\varepsilon_y = (1+\varepsilon_r)\frac{\sin\left(\frac{\alpha_r}{2}\right)}{\sin\left(\frac{\alpha_0}{2}\right)} - 1 \qquad (7)$$

For E=1 GPa, $d\varepsilon_x/dp=0$ falls at p=3.03 MPa which, although not being exactly the same, is still quite close to the value observed in the FE simulations (p=2.25 MPa), considering the relatively broad minimum observed for both simulations (see Fig. 3d as well as 7a for a direct comparison).

The effective stiffness tensor components instead are found via the following:

$$C_{11} = \frac{\partial^2 W}{\partial \varepsilon_x^2}, \quad C_{22} = \frac{\partial^2 W}{\partial \varepsilon_y^2},$$
$$C_{12} = \frac{\partial^2 W}{\partial \varepsilon_x \partial \varepsilon_y}, \quad C_{66} = \frac{\partial^2 W}{\partial \gamma_{xy}^2} \qquad (8)$$

The reference configuration in this case is the honeycomb's pressurised state where $\alpha_r=\alpha_p$, $\varepsilon_r=\varepsilon_p$.

3.4 Deformation modes of a Born lattice under pressure

The internal potential is described by the strain energy density of the mechanical lattice-fluid system. In Fig. 5 the energy density "landscape" of the lattice is reported as a function of the principal lattice strains ε_x, ε_y, (mapping (α, ε) -> (ε_x, ε_y)), where the internal pressure is set to zero (for convenience, the energy density value is normalised by the value of wall stiffness E). The y-strain spans a broader range than the x-strain since this is the weaker direction. As expected, the steepest path runs across the first and third quadrant where a biaxial deformation ((ε_x>0, ε_y>0) and (ε_x<0, ε_y<0)) causes the lattice beams to deform axially, corresponding to a volumetric deformation of the lattice. Conversely, the lowest isolines are found for (ε_x<0, ε_y>0) a pure deviatoric deformation of the lattice. In this narrow valley the energy minimum is found (for ε_x=0, ε_y=0).

Upon pressurizing the system the landscape changes considerably. In Fig. 5 the normalised energy contours are reported for increasing values of the normalised internal pressure p^* ($p^*=p/E$).

There are two effects that can be observed. Firstly, the energy minimum migrates from the left area (ε_x<0, ε_y>0) to the upper right area (ε_x>0, ε_y>0) of the deformation space. The location of the minimum in

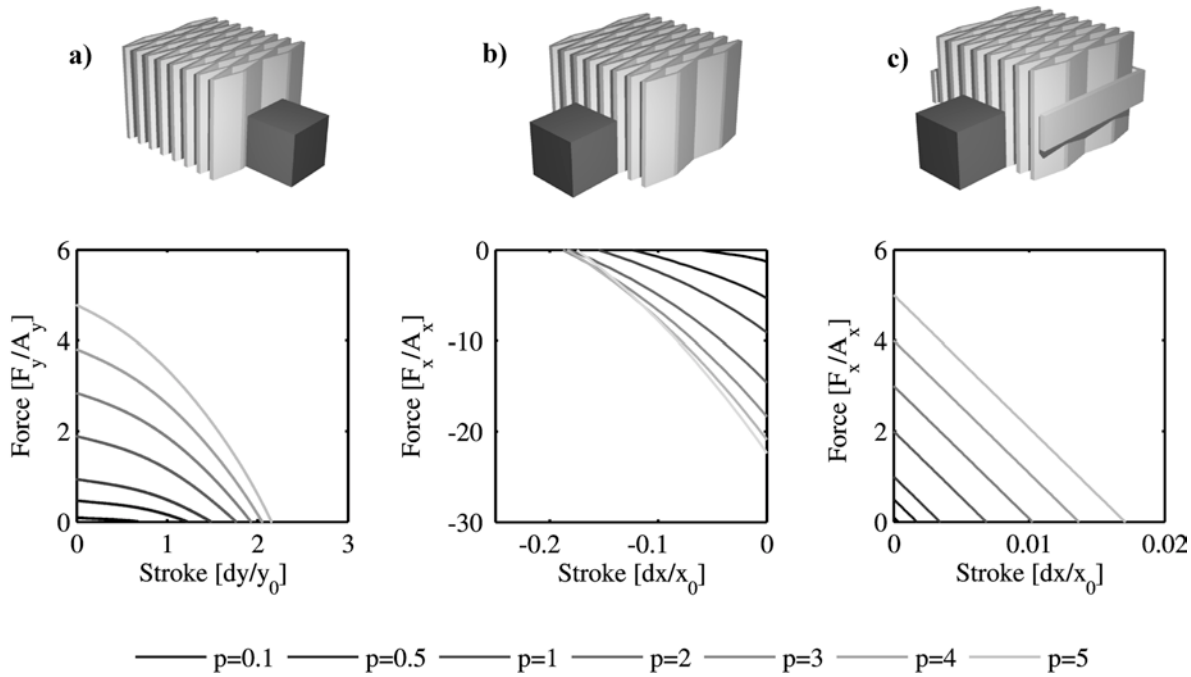

Figure 8 | Working configurations and force developed by a honeycomb actuator. A pressurised honeycomb (grey) can be used as a linear actuator to displace an external load (dark cube). At least three configurations can be thought of: a) applying a moderate pushing force at high strokes; b) applying a high pulling force at low strokes; c) applying a low pushing force at very low strokes. Three graphs (bottom) show the working characteristics for different pressures fed in the honeycomb.

each plot gives the deformation state of the lattice as it goes from the unloaded to the pressurised state. Indeed, the corresponding strains compare well with the swelling eigenstrains in the finite element simulations (Fig. 4). Secondly, the shape of the isolines changes from an arc to a closed rounded one, which is a hint for a structural transformation of the system. This is confirmed by the angular deformation of the lattice for increasing normalised pressures (Fig. 6), where the lattice angle approaches 90° (isotropic geometry).

3.5 FE and Born model comparison

Considering several values of fluid pressure and walls' Young modulus, actuation maps similar to those of Fig. 4 can be created. For clarity, each tensor component is normalised by the material Young modulus E ( ) and presented as function of normalised pressure p* (Fig. 7): by doing this, all data collapse onto a single master curve. Tensorial quantities in Fig. 7 are calculated by evaluating equation (8) with finite differences. Their "true" value is found for an infinitesimal probing strain (εx, εy, γxy). since large (>10%) probing strains will cause the honeycomb geometry to distort, introducing geometric non-linearities [43]. Hence, the stiffness tensor components reported in Fig. 7 are evaluated at the pressurised state (αp,εp) of the Born lattice applying the same probing strain εx=εy=1% used for the FE parametric study. This is important to emphasise, since the strain energy density W depends on the choice of the reference configuration.

From the master curves, there is a good qualitative agreement between the FE and Born models for the whole extent of the parametric space considered (Fig. 7). The direct components C11 and C22 (Fig. 7 c,d) experience respectively a rapid increase/decrease for a slight increase of p* (0 to 0.002). This is due to the process already described: as the pressure increases, the lattice switches rapidly to a more isotropic geometry, strengthening the soft direction y at the expense of the x direction. At higher pressures (p*>0.005) the FE model predicts a softening of C11 and C22 which is not observed in the Born model. A further increase of pressure will not affect the honeycomb geometry (which already approaches a square (Fig. 6)) so that the Born model prediction of these components tend to a constant valueTherefore we conclude that the softening effect observed only in the FE simulations is due to the walls strain divergence at high pressure due to Poisson's effect introduced in section 3.1.

The cross stiffness component C12 (Fig 7 e) is characterised by a fast increase at low pressure (consistent with strong geometry change in the bending dominated regime), but then decreases linearly at higher pressures, which (for the reasons just introduced) cannot be related to geometry change. Moreover, since this behaviour is observed in both the FE and Born models, it cannot be ascribed to the aforementioned Poisson's effect. This peculiar behaviour can be explained if we recall that C12 measures the response of the material transversally to the probing strain direction. The transverse reaction force will be partially compensated by the internal pressure, thereby causing the observed inverse linear dependence.

The C66 component evidences a poor agreement between the two models. This is not too surprising, since the parametrization of the polynomials c1 and c2 implies only relative displacement between the joints (see section 3.3). To improve the prediction for the C66 component one could introduce a localised joint rotation as an additional microstructural parameter. This is equivalent to a move from a classical continuum mechanics theory (where the

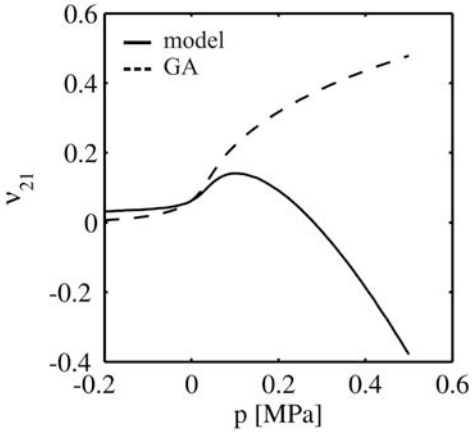

Figure 9 | Poisson´s ratio as function of inner pressure for 1GPa stiff walls. The effect of the pressure on the honeycomb Poisson's ratio is twofold: a pure structural effect due to a varying honeycomb angle (Gibson-Ashby prediction, dotted line) would give υ tending to unity for increasing pressures, whereas a transverse expansion caused by the pressurising fluid soon causes υ to diverge to negative values.

strain state depends only on the displacement from the reference to the deformed configuration) to a Cosserat continuum theory (where the strain state depends also on microscopic rotations) [25].

3.6 Honeycomb based actuator

Fig. 8 shows the performance characteristics of the pressurised honeycomb described earlier (α_0=28°, t/l>10, E=1GPa) when used as an actuator. Reported is the force exerted as function of the stroke (ie actuation stress versus strains) for several values of the pressure fed in the system. Following Zupan [44] we describe the actuator performance in terms of two complementary normalised attributes. The maximum stroke divided by the actuator length parallel to this stroke is the actuator strain (or normalised stroke), and the maximum generated force divided by its cross section perpendicular to the stroke is the actuator stress (or normalised force). In this honeycomb actuator the energy required to produce mechanical work is stored in the fluid. An external compressor is ideally connected to the volume enclosed by the honeycomb walls and a flexible membrane sealing the top and bottom surfaces (not shown). In Figs 8 a, and b two working configurations of the honeycomb actuator are depicted, where it is respectively used to produce force along the y and the x directions. In both cases the transversal direction is free to deform. In the third configuration (Fig. 8 c), the actuator is generating force along the x direction, being constrained along the y direction. Each graph represents a family of curves depicting the output stress at different pressure input: the actuator performance changes drastically at different levels of energy source. As expected, the maximum stroke (where the output curve meets the zero stress axis) coincides with the actuation eigenstrains.

Interestingly, the force output along the weak direction y is non monotonic with the stroke. Obviously it starts from a zero-stroke value close to the set value of the pressure (which measures the amount of energy fed in the system) but, as the stroke increases, it firstly increases to an upper limit and then decreases till eventually it reaches zero. The stress produced is bigger than the pressure input into the system. This is not contradictory, but is a sign that the actuator works in different configurations as the stroke changes. At low strokes ($dy/y_0<1$) the expanding fluid has to overcome just a small energy barrier (walls bending). The pressure is constant but since the fluid volume increases, the total energy available to produce mechanical work increases with the stroke. At higher strokes the honeycomb walls start deforming in stretching, hence the energy cost is higher and the force generated lower, till it eventually reaches zero. In this configuration the system capitalises on the big angular deformation of the walls to produce high strains at moderate stresses.

Conversely, when the actuator is used to produce force along the strong x-direction (Fig 8, b), the stress output is high and the strokes are low. More importantly the stress generated is negative: the actuator "pulls". Moreover, unlike the force output along the weak direction y, increasing the input pressure doesn´t always mean a higher tensile stress. At a certain pressure (p>2 here) the stretching of the walls becomes significant and partially compensates the contraction along the x-direction. Hence the actuator can be fine-tuned, to produce different tensile stresses at several strokes.

Constraining the y direction (Fig 8c), causes the actuator to produce a compressive stress, which is smaller, in absolute terms, than in the unconstrained case: since the honeycomb angle cannot open, the only possible deformation mechanism is due to walls stretching, which is rather energetically costly. Here the actuator works in a low strain - low stress fashion. Such a behaviour is reminiscent of the lever-arm principle used by wood cells to generate tensile or compressive stresses [10]: if the microfibril angle (equivalent to half of the honeycomb angle here) is less then 45° the only way to swell the cell is to shorten it along the longitudinal direction (the strong direction here).

3.7 Tunable Poisson´s ratio material

As seen, the material properties of an anisotropic cellular material vary strongly with the internal pressure it is subjected to. In particular the pressure has two separate effects: the substantial change in material´s geometry (structural effect) and the intrinsic pressure contribution to the load-bearing capacity of the material (fluid-related effect). Fig. 9 shows the dependency of the Poisson´s ratio υ_{21} at several inner pressures. The value predicted by the Gibson-Ashby model [23] (Fig. 9 dotted line) depends only on the actual geometry (α_p is honeycomb angle in the pressurised state) and acts as a reference to disentangle the pure structural from the fluid-related contribution:

$$\upsilon_{21} = \frac{\sin^2\left(\frac{\alpha_p}{2}\right)}{\cos^2\left(\frac{\alpha_p}{2}\right)} \qquad (9)$$

As the pressure increases α_p becomes larger (see Fig 6) and υ_{21} quickly goes to unity. The full line (Fig. 9) shows the prediction given by the pressurised honeycomb model subjected to a strain ε_2=1%.

Obviously the two curves coincide at p=0, and are close for small values of pressure. Our model predicts larger values at negative pressures. At positive pressures however, the pressurised honeycomb prediction diverges to even more negative values. Since the applied probing deformation is positive, the available volume in the honeycomb increases and the fluid (which is kept at constant pressure) expands also in the transverse direction. As a result the sign of the Poisson´s ratio becomes negative. This effect is qualitatively similar to the long-term positive cross-sectional strains that a longitudinally prestretched rubber-like polymer specimen experiences when it is immersed in a fluid [45]. In summary a pressurizing fluid put in the honeycomb can act as a free parameter to drastically change its Poisson's ratio even to negative values. This can be useful in a number of applications, as auxetic materials can show enhanced shear modulus compared to positive Poisson's ratio materials, and can be efficient materials for sandwich cores [46].

4 Conclusions

Cellular materials and honeycombs have long been among smart alternatives to classical bulk-materials, that give tunable materials properties via control of the underlying pore or cell architecture. Although known for improving the range of applications of classical materials with respect to many applications – load bearing, crash energy absorbers, thermal insulators- they could potentially be used also in the field of linear actuators. In the case of honeycombs subjected to inner pressure, we showed how their intrinsic characteristics (anisotropy, material properties, input pressure) could greatly simplify the design process for a linear actuator and the choice of the relevant parameters. The case of *Delosperma nakurense* seed capsule well provides an ideal natural system using this concept, optimised to work in a high stroke, low force configuration. Pressurised honeycombs could prove to be very versatile: similar systems can be implemented with different values of pressure and Young's modulus to scale up and generate bigger forces. In addition, the very same honeycomb can be used in different working configurations to generate either compression or tension.

In this paper we mainly discussed the influence of pressure and wall properties on eigenstrains, generated forces and effective stiffness. The next step would be to apply the same approach (analytical modelling via Born model and validation with FE simulations) to explore the role of material's architecture on their behaviour under pressurization: a more complex material architecture – as for asymmetric, aperiodic frameworks, and non-convex cells- could greatly expand the actuation capabilities upon pressurisation. From a methodological viewpoint, the present work tackles all the relevant mechanical aspects of a pressurised honeycomb, since the simplified lattice spring model predicts the finite element simulations, while being beneficially easier to implement. In addition, a theoretical basis was provided to compare the finite size and the periodic finite element systems. As a future development of the present study, an environmental sensitive pressure source should be considered, as in the case of a superabsorbent hydrogel confined in the honeycomb cells, which is a closer biomimetic embodiment of the natural system. Also, a theoretical description of out of plane effects deriving from frustrated or hindered volumetric expansion or tapering of the honeycomb walls along the cells axis could expand the range of the available motion of this planar symmetric system to the full three dimensional space.

Acknowledgements

The authors thank Luca Bertinetti, Khashayar Razghandi, Matt Harrington and Ingo Burgert for extensive discussions. We acknowledge the Humboldt Foundation for supporting the visit of YB to Potsdam through the Gay-Lussac-Humboldt Award and support through the Leibniz prize of PF running under DFG contract number FR2190/4-1.

References

1. Elbaum, R., S. Gorb, and P. Fratzl, Structures in the cell wall that enable hygroscopic movement of wheat awns. Journal of Structural Biology, 2008. 164(1): p. 101-107.
2. Burgert, I. and P. Fratzl, Actuation systems in plants as prototypes for bioinspired devices. Philosophical Transactions of the Royal Society a-Mathematical Physical and Engineering Sciences, 2009. 367(1893): p. 1541-1557.
3. Fratzl, P. and F.G. Barth, Biomaterial systems for mechanosensing and actuation. Nature, 2009. 462(7272): p. 442-448.
4. Turcaud, S., et al., An excursion into the design space of biomimetic architectured biphasic actuators. International Journal of Materials Research, 2011. 102(6): p. 607-612.
5. Baskin, T.I., Anisotropic expansion of the plant cell wall. Annual Review of Cell and Developmental Biology, 2005. 21: p. 203-222.
6. Salmen, L., Micromechanical understanding of the cell-wall structure. Comptes Rendus Biologies, 2004. 327(9-10): p. 873-880.
7. Marklund, E. and J. Varna, Micromechanical modelling of wood fibre composites. Plastics Rubber and Composites, 2009. 38(2-4): p. 118-123.
8. Dawson, J., J.F.V. Vincent, and A.M. Rocca, How pine cones open. Nature, 1997. 390(6661): p. 668-668.
9. Allen, R. and A.B. Wardrop, The opening and shedding mechanism of the female cones of pinus radiata. Australian Journal of Botany, 1964. 12: p. 125-134.
10. Burgert, I., et al., Tensile and compressive stresses in tracheids are induced by swelling based on geometrical constraints of the wood cell. Planta, 2007. 226(4): p. 981-987.
11. Timoshenko, S., Analysis of bi-metal thermostats. Journal of the Optical Society of America and Review of Scientific Instruments, 1925. 11(3): p. 233-255.
12. Abraham, Y., et al., Tilted cellulose arrangement as a novel mechanism for hygroscopic coiling in the stork's bill awn. Journal of the Royal Society Interface, 2012. 9(69): p. 640-647.
13. Aharoni, H., et al., Emergence of Spontaneous Twist and Curvature in Non-Euclidean Rods:

Application to Erodium Plant Cells. Physical Review Letters, 2012. 108(23).
14. Schreiber, N., et al., G-fibres in storage roots of Trifolium pratense (Fabaceae): tensile stress generators for contraction. Plant Journal, 2010. 61(5): p. 854-861.
15. Goswami, L., et al., Stress generation in the tension wood of poplar is based on the lateral swelling power of the G-layer. Plant Journal, 2008. 56(4): p. 531-538.
16. Mellerowicz, E.J. and T.A. Gorshkova, Tensional stress generation in gelatinous fibres: a review and possible mechanism based on cell-wall structure and composition. Journal of Experimental Botany, 2012. 63(2): p. 551-565.
17. Fratzl, P., R. Elbaum, and I. Burgert, Cellulose fibrils direct plant organ movements. Faraday Discussions, 2008. 139: p. 275-282.
18. Harrington, M.J., et al., Origami-like unfolding of hydro-actuated ice plant seed capsules. Nature Communications, 2011. 2.
19. Gibson, L.J., Modeling the Mechanical-Behavior of Cellular Materials. Materials Science and Engineering a-Structural Materials Properties Microstructure and Processing, 1989. 110: p. 1-36.
20. Gibson, L.J., Biomechanics of cellular solids. Journal of Biomechanics, 2005. 38(3): p. 377-399.
21. Gibson, L.J. and M.F. Ashby, The Mechanics of 3-Dimensional Cellular Materials. Proceedings of the Royal Society of London Series a-Mathematical Physical and Engineering Sciences, 1982. 382(1782): p. 43-&.
22. Gibson, L.J., et al., The Mechanics of Two-Dimensional Cellular Materials. Proceedings of the Royal Society of London Series a-Mathematical Physical and Engineering Sciences, 1982. 382(1782): p. 25-42.
23. Gibson, L.J. and M.F. Ashby, Cellular solids : structure and properties. 2nd ed. ed. 1997, Cambridge: Cambridge University Press.
24. Fleck, N.A., V.S. Deshpande, and M.F. Ashby, Micro-architectured materials: past, present and future. Proceedings of the Royal Society a-Mathematical Physical and Engineering Sciences, 2010. 466(2121): p. 2495-2516.
25. Kumar, R.S. and D.L. McDowell, Generalized continuum modeling of 2-D periodic cellular solids. International Journal of Solids and Structures, 2004. 41(26): p. 7399-7422.
26. Masters, I.G. and K.E. Evans, Models for the elastic deformation of honeycombs. Composite Structures, 1996. 35(4): p. 403-422.
27. Fazekas, A., et al., Effect of microstructural topology upon the stiffness and strength of 2D cellular structures. International Journal of Mechanical Sciences, 2002. 44(10): p. 2047-2066.
28. Ruffoni, D., et al., Effect of minimal defects in periodic cellular solids. Philosophical Magazine, 2010. 90(13): p. 1807-1818.
29. Zhu, H.X., J.R. Hobdell, and A.H. Windle, Effects of cell irregularity on the elastic properties of 2D Voronoi honeycombs. Journal of the Mechanics and Physics of Solids, 2001. 49(4): p. 857-870.
30. Niklas, K.J., Mechanical-Behavior of Plant-Tissues as Inferred from the Theory of Pressurized Cellular Solids. American Journal of Botany, 1989. 76(6): p. 929-937.
31. Gao, Q. and R.E. Pitt, Mechanics of Parenchyma Tissue Based on Cell Orientation and Microstructure. Transactions of the Asae, 1991. 34(1): p. 232-238.
32. Oey, M.L., et al., Effect of turgor on micromechanical and structural properties of apple tissue: A quantitative analysis. Postharvest Biology and Technology, 2007. 44(3): p. 240-247.
33. Rafsanjani, A., et al., Swelling of cellular solids: From conventional to re-entrant honeycombs. Applied Physics Letters, 2013. 102(21).
34. Martinez, R.V.a.F., C.R. and Chen, X. and Whitesides, G.M., Elastomeric Origami: Programmable Paper-Elastomer Composites as Pneumatic Actuators. Advanced Functional Materials, 2012.
35. Pagitz, M., E. Lamacchia, and J.M.A.M. Hol, Pressure-actuated cellular structures. Bioinspiration & Biomimetics, 2012. 7(1).
36. Eshelby, J.D., The Determination of the Elastic Field of an Ellipsoidal Inclusion, and Related Problems. Proceedings of the Royal Society of London Series a-Mathematical and Physical Sciences, 1957. 241(1226): p. 376-396.
37. Onck, P.R., Scale effects in cellular metals. Mrs Bulletin, 2003. 28(4): p. 279-283.
38. Kanit, T., et al., Determination of the size of the representative volume element for random composites: statistical and numerical approach. International Journal of Solids and Structures, 2003. 40(13-14): p. 3647-3679.
39. Buxton, G.A., C.M. Care, and D.J. Cleaver, A lattice spring model of heterogeneous materials with plasticity. Modelling and Simulation in Materials Science and Engineering, 2001. 9(6): p. 485-497.
40. Hassold, G.N. and D.J. Srolovitz, Brittle-Fracture in Materials with Random Defects. Physical Review B, 1989. 39(13): p. 9273-9281.
41. Lakes, R., Deformation Mechanisms in Negative Poisson Ratio Materials - Structural Aspects. Journal of Materials Science, 1991. 26(9): p. 2287-2292.
42. Fratzl, P. and O. Penrose, Ising model for phase separation in alloys with anisotropic elastic interaction .2. A computer experiment. Acta Materialia, 1996. 44(8): p. 3227-3239.
43. Warren, W.E., A.M. Kraynik, and C.M. Stone, A Constitutive Model for Two-Dimensional Nonlinear Elastic Foams. Journal of the Mechanics and Physics of Solids, 1989. 37(6): p. 717-733.
44. Zupan, M., M.F. Ashby, and N.A. Fleck, Actuator classification and selection - The development of a database. Advanced Engineering Materials, 2002. 4(12): p. 933-940.
45. Urayama, K. and T. Takigawa, Volume of polymer gels coupled to deformation. Soft Matter, 2012. 8(31): p. 8017-8029.
46. Dirrenberger, J., S. Forest, and D. Jeulin, Effective elastic properties of auxetic microstructures: anisotropy and structural applications. International Journal of Mechanics and Materials in Design, 2013. 9(1): p. 21-33.

7.14 [AC7] The Geometric Design and Fabrication of Actuating Cellular Structures

Guiducci, L., Weaver, J. C., Bréchet, Y. J. M., Fratzl, P., Dunlop, J. W. C.
*Published in **Advanced Materials Interfaces**, 2015, online DOI: 10.1002/admi.201500011*

Reprinted with permission from John Wiley and Sons

Biological actuators provide a rich source of inspiration for the architectural design of their synthetic analogs [1]. In particular the hygromorphs found in the plant kingdom provide many examples of mechanically actuating systems that don't require a metabolic energy source to function [2]. In these systems, directed, controlled forces/deformations are generated at the material–level, through the introduction of appropriate meso-scaled architectures [3]. As a result, both load bearing and morphing functions can be combined into a single integrated actuating material [4]. From a materials perspective, plant tissues can be viewed as porous composite materials, made up of a honeycomb-like array of cells, whose walls consist of stiff cellulose microfibrils embedded in a softer hygroscopic matrix of lignin, hemi-cellulose and other polysaccharides [5]. The cellulose microfibril angle (MFA) that these reinforcing structures make with the long axis of the plant cell, has a strong influence on both the rigidity and mechanical actuation behavior of plant tissues [2,6,7]. Just by controlling the simple architectural parameter of MFA, plants with the same polymeric building blocks can grow tissues that produce tensile or compressive strains along the plant cell longitudinal axis. Such a configuration is optimal to produce large stresses such as those needed to balance increasing gravitational loads on branches as plants grow[7,8], but are limited in the magnitude of strains that can be produced [9]. Nevertheless, since the mechanical work, the product of force and displacement, cannot exceed the chemical energy gained upon moisture sorption[10], it should be possible to conceive a different actuating tissue architecture where displacements are maximized at the expense of force.

In this regard, a relevant example can be found in the actuating seed capsules of ice plants (family Aizoacea)[11]. The capsules studied consist of five chambers enclosed by five leaflets, which are actuated by highly swellable hygroscopic keels. Upon contact with sufficient liquid water, large directional strains of up to 300% are achieved in the keels, thus opening the capsule and enabling subsequent seed release[12]. This active tissue has a regular, honeycomb-like structure with anisotropically shaped cells, filled with a highly swellable cellulosic inner layer (CIL). A large volume increase of the CIL upon hydration is transformed into large expansions along the honeycomb's soft direction (i.e. in plane). Using a simplified model of this tissue, we recently showed how such a pressurized anisotropic honeycomb could give rise to large directed expansions[13]. In particular, we showed how the magnitude of expansion strains and generated forces depend on the bending and stretching dominated regimes that the honeycomb undergoes as internal pressure increases. In the following, we generalize these concepts beyond one single honeycomb geometry and propose a criterion for the geometric design of periodic honeycombs undergoing a desired, controlled, mechanical actuation. We then test our hypotheses by combining finite element (FE) simulations with swelling experiments on composite honeycomb materials produced using state of the art multi-material 3D printing, and demonstrate how the shape of the structural unit (SU) [1], that makes up a honeycomb actuator, can be used to tailor the onset of bending and stretching, thus inducing any desired state of deformation.

Possible methods for mechanically actuating honeycombs is to inflate the SUs either via pressurization as in typical pneumatic/hydraulic actuators, or via a swellable medium, as in the ice plant seed capsules[11]. If we consider a structural unit of a honeycomb as a framework of beams and joints, there are two possible mechanisms of expansion of the SU. Either (1) the SUs keep their shape and increase their perimeter or (2) they keep their perimeter length and change the shape. Typically for beams and rigid joints, the energy required for stretching a beam, W_s is greater than that for bending it, W_b, i.e. ($W_s \approx t/l >> W_b \approx (t/l)^3$), where l/t is the aspect ratio of the beam. This means that except for triangular honeycombs, where any shape change involves stretching, all polygons will preferably expand as a result of joint bending, unless they have reached the maximum area for a fixed perimeter or the highest convexity. This idea is illustrated in the left column of **Figure 1** which shows the mechanisms by which n-sided polygons can change area and equivalently, how prismatic structural units could change volume. From a simplified perspective, we can look at a cell's SUs expansion as a purely geometric one involving no mechanics – with the goal of identifying the most convex polygon for a given set of rigid sides. To the best of our knowledge, the first record of this approach dates back to A. M. Legendre [14], who, in the early 1800s, demonstrated that in the Euclidean 2D space, the cyclic polygon –that is a polygon inscribed in a circle- is the most convex form, implying that it has the greatest area at constant perimeter[14]. The cyclic polygon is unique for any given set of sides[15] and it can be found by calculating the radius of the enclosing circle through the following relation:

[1] To avoid confusion with the biological term, cell, we use the term structural unit (SU) or tile interchangeably to describe the elementary "cell" that makes up a honeycomb.

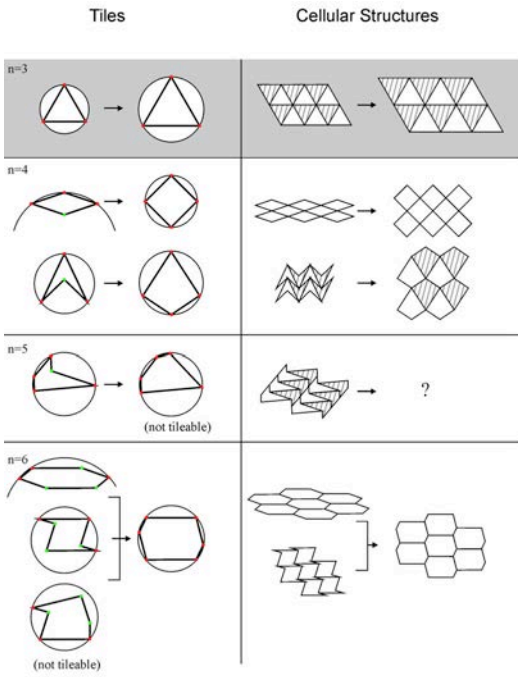

Figure 1. Left column. The highest expansion of an isoperimetrical n-sided polygon is achieved in the cyclic configuration, that is, when all polygon vertexes lie on the circumscribed circle (red dots). Subjected to inflation, polygons with n>3 morph into the cyclic configuration by changing the internal angles while keeping the side lengths fixed (white boxes). Stretching the polygon's sides (as for triangles and all other cyclic polygons) is always a possible mechanism of expansion, actuating cellular structure. During its morphing, a tile can acquire a non-tessellating shape (here, for n=5) which further limits the choice of actuating tiles.

$$f(R):\sum_{i=1}^{n} ArcSin\left(\frac{l_i}{2R}\right)=\pi \qquad (1)$$

where n is the number of sides and l_i are the unfolded (node-to-node) lengths of the sides. Despite its simplicity, this relationship can also be used to predict the actuation capacity of honeycombs based on different shapes of their structural units. If we do not allow for stretching of the perimeter, a cyclic polygon cannot increase its area. Conversely, any other polygon will experience the maximum expansion when it reaches the cyclic configuration with the same side lengths l_i.

Once a potential polygon shape that may change area (volume) upon bending is chosen, the next question is whether it tiles the 2D space (Figure 1, right side). A periodic tiling can be generated by applying one of the five 2D Bravais translations to the polygonal unit of choice, given that the angles meeting at a node sum up to 2π. For this to occur, however, the polygon must be a parallelogram or par-hexagon (ie polygons of 4 or 6 sides, with opposite sides equal and parallel) (Figure 1)[16]. More general periodical tilings can be created if the tile complies with the so-called Conway rules [17]. These state that a polygon of up to 6 sides tiles the plane if two of its sides are related by translational symmetry (that is, equal and parallel) and the rest of the sides are centrosymmetric (each side has a C2 centre). Then the tiling is built by 180° rotations of the polygon around each C2 center (Figure 1, blank-dashed tilings). In addition, 4-sided polygons with just centrosymmetric sides tile the plane as well (the spear-shaped one in Figure 1).

By these rules, it is also possible to check whether the inflated SU will tile the plane or not (Figure 1, n=5). Indeed the tessellation can introduce a constraint onto the SU expansion, preventing the cyclic configuration from being achieved. Therefore, SUs best suited for actuation are those that respect the tessellation condition in the initial, fully inflated and all intermediate states in between.

In the following, we apply these concepts to design two-dimensional actuating honeycomb materials with a wide range of different architectures. As building blocks, we chose a non-convex tile or structural unit shaped like the letter "L" and another shaped like one of the Tetris® tiles (in the following L- and T-cells). The presence of re-entrant 90° corners in these SUs makes it possible to assemble them into several 2D tilings (L1-L7 and T1-T11 honeycombs; see **Figure SI 1**), generating honeycombs of different topological classes (with three-fold or four-fold nodes). The proposed honeycombs were studied by means of finite element (FE) simulations and physical swelling experiments in terms of their actuation behavior (achieved expansions/forces) in response to a source of inflation. In our FE simulations, the source of inflation is a static pressure applied inside each SU, as in real pneumatic actuators, with a resultant deformation depending only on the honeycomb architecture, the material properties of its walls, and the magnitude of pressure. In this way, we could directly test whether the geometric arguments introduced previously would still be valid in a scenario where the mechanical properties of the honeycomb material are also accounted for.

The volume expansion of the honeycomb upon pressurization was similar to our previous results obtained from diamond-shaped honeycombs[13] (**Figure 2**). Large volume changes occur at low pressures, followed by smaller rates of volume increase at higher pressures (Figure 2B) [13]. Both the real and simulation experiments, confirm our assumption that the nodes and 90° kinks on the SU's perimeter act as concentration points for the deformation (Figure 2A), so that they function as rotation hinges for the walls, resulting in a low-pressure, large volume increase (Figure 2B).

When the walls deformations resemble freely rotating rigid bars, as in this case, tessellations can show auxetic behavior. Moreover these can undergo multiple deformation pathways (mechanisms) when subjected to a uniaxial probing strain. Consequently, specific ones can be selected depending on which symmetries are broken during the deformation, resulting in different Poisson's ratio for the same tessellation (Mitschke). Although no specific symmetries were enforced during the pressurization, our simulations show unique deformation pathways. We believe that this effect results from an energy minimization requirement: at each level of pressure, the SUs acquire the most expanded state (lowest energy), thus tracing a unique pathway. Nonetheless, when the walls are unfolded, the SUs acquire their cyclic configuration (Figure 2A, p=1.5 MPa) as predicted by our geometrical argument. From this point on the SUs shape stays practically unchanged

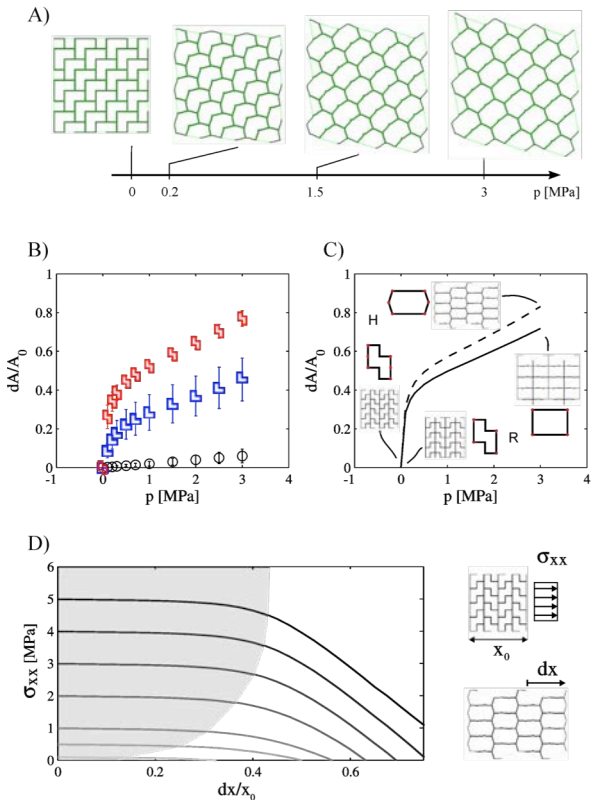

Figure 2. A) Expansion of an inflated non-convex honeycomb, as predicted by FE simulations. B) Average inflation curves of all T- (in red) and L-honeycombs (in blue), showing the area strain as a function of internal pressure (with standard deviation). Black circles represent the average inflation of regular triangular, square and hexagonal honeycombs with cells of same area. C) Influence of topology on volume expansion in hexagonal (H) and rectangular (R) honeycombs based on same T-tile D) Performance (output stress σ_{xx} exerted at given strain dx/x_0) of a pressurized re-entrant hexagonal honeycomb for several input pressure values (p=0.1, 0.5, 1, 2, 3, 4, 5). The grey-shaded area highlights the space where the actuator expresses more than 90% of the input pressure.

while the walls deform by stretching, resulting in a slower volume increase upon further inflation. This inherent non-linear mechanical response arises from the transition from bending to stretching dominated behavior, which depends on the starting SU geometry. Averaging all of the inflation curves relative to the type of SU (Figure 2B) reveals two well separated curves, with the L-honeycombs lying below the less convex T-honeycombs. This result can be traced back to the number of 90° kinks on the cell´s perimeter: having 4 kinks on the SU's perimeter, T-honeycombs "hide" a larger expansion potential than L-honeycombs, which only have 2.

When the inflation curves of two honeycombs with the same SU geometries (Figure 2C) but different topologies are compared, a larger volume expansion is observed for the honeycomb with 3-fold nodes (whose cells morph into hexagons) than the 4-fold one (whose cells morph into rectangles). Since the initial SU perimeter is the same, this difference is ascribed to the honeycomb topology: indeed the number and length of the SU's sides is different (a hexagon with sides of length *l,l,3l,l,l,3l* and a rectangle with sides *2l,3l,2l,3l*) which results in the hexagon having a larger area than the rectangle in the inflated state. Even at high pressures, in all the honeycombs studied we don't observe any topological coarsening (eg. rectangular to hexagonal honeycomb, as in Figure 2C), which is typical in soap froths microstructure evolution: since our choice of material is linear elastic, no plastic "flowing" of the nodes can take place. As the pressure increases, the stretching of the SU's walls is not negligible. In the limit of very high pressures, we expect the honeycombs should tend asymptotically to the best space filling configuration, according to their topology: that is a regular tiling by equilateral hexagons (for 3-fold nodes) or squares (for 4-fold nodes). Instead, this configuration could not be reached due to a singularity in the honeycomb expansion (for $p \rightarrow 7\ MPa$) arising from our choice of the material properties of the walls (see Supporting Information). Although not exhaustive, our simulations show that purely geometric parameters determine the available range of deformations. The effect of non-geometric parameters, such as the rigidity of the honeycomb walls, is to scale these curves (volume expansion scales with p/E, as we showed in our previous paper[13]), which implies that such an actuating honeycomb can be built from any solid with a sufficient elastic range.

The large expansions produced upon pressurization are translated into directed strain/stress by the specific architectures of each honeycomb. Uniaxial, biaxial, equi-biaxial or shearing expansions (see, respectively, honeycombs: L5; T1-T7, T11; L6, L7; L1, T8-T10 in Figure SI 1) can be "coded" in the tiling pattern using the same cells. For example, the overall volume expansion can be very anisotropic, and the honeycomb elongating mainly along one direction. This yields a linear actuator with a characteristic stress-strain (σ_{xx}-dx/x_0) output (honeycomb T4 in Figure 2D). Remarkably, as the actuator deploys, the output stress stays almost equal in magnitude to the input pressure: the grey-shaded area highlights the space where the actuator expresses more than 90% of the input pressure. This result reveals how the actuator can function practically with negligible output force loss for much of the accessible stroke range, since the work of deformation required to bend the walls at the hinge points is minimal.

To experimentally verify our theoretical predictions, we used state of the art multimaterial 3D printing to fabricate physical models of non-convex honeycombs which were capable of actuation via solvent swelling (**Figure 3**). These models consisted of stiff, non-swelling walls (E_{Mat1}=530 MPa, ε_{Mat1}=3.3E-3) lined by swellable soft inclusions (E_{Mat2}=404 kPa, ε_{Mat2}=0.363). In these experiments, the swellability was controlled by increasing or decreasing the polymer cross-linking density, without significantly altering its bulk chemistry, thus resulting in excellent interfacial adhesion between the two constituent phases. Since the solvent was absorbed by the inclusions and not the walls, we could control the three dimensional distribution of swelling inside the structural units, in a similar manner to the so-called 4D printing of shape memory composites[18]. The resulting deformation of the 3D printed honeycombs matches the predictions of the FE simulations (Figure 3), although compared to the pressurized simulations, smaller total strains were achieved due to the limited free swelling expansion of the soft material (ε_{Mat2}=0.363). In our

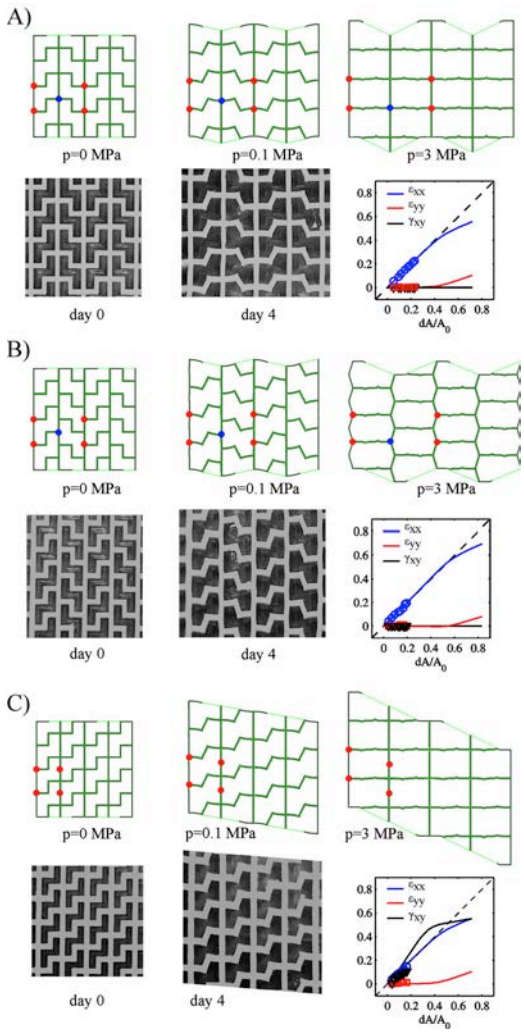

Figure 3. Deformations in inflating (FE) and swelling (rapid prototyped models) T- honeycombs with different architectures providing: A, B) macroscopic biaxial expansion; C) macroscopic biaxial and shearing expansion. Although smaller, the honeycomb strains measured in the swelling experiments (empty markers) are consistent with the FE simulations prediction (solid lines), thus illustrating how the honeycombs' expansion is primarily dictated by their architecture.

simulations, we also observed (see **Figure SI 3**) that the use of a more swellable material (such as a hydrogel) might achieve even larger expansions comparable with those observed in the pressurized structures. This confirms the importance of geometric material design regardless of the physical principle that generates volume expansion in the SUs (whether pressurization- or swelling-based). When volume expansion is based on swelling or, more generally, a diffusion process, a large scale actuator suffers from slow activation times, since diffusion time is proportional to the square of the characteristic length. Indeed, efficient diffusion based osmotic actuators profit from low frequency, high force, low stroke applications[19]. Nevertheless, these issues can be addressed using microporous swelling polymers, where capillary transport and a reduced characteristic length of the diffusive process accelerate the activation speed [20].

The interplay between mechanics, geometry and topology was recently recognized to determine the actuation of cellular structures triggered by an external compressive load[21]. In this paper, we have demonstrated a novel concept of controlling the actuation of cellular materials subjected to positive internal pressure through the geometric design of the shape and tiling of the constituent structural units. Careful control of the SU architecture can lead to a variety of actuation behaviors. This could be especially interesting for soft-robotics, a new branch of engineering[22], which aims to achieve typical robotic tasks like actuation or locomotion using structures made of elastomers, optionally paired with inextensible reinforcements. Similar to elastomeric soft actuators, a pneumatic actuator based on a cellular structure will possess a very low specific weight, regardless of the material used in its construction, and can be conveniently actuated remotely by a connected pneumatic source as demonstrated by Shepard et al [25]. Furthermore, it is also possible that actuators of this kind would benefit from the damping properties of the inflating gas in applications such as object manipulation and walking where absorbing shocks and preventing vibrations are essential. Despite the apparent complexity of such cellular solids, with recent progress in advanced multi-material 3D printing technologies, it is now possible to fabricate them, as we have demonstrated. As such technologies further develop, they will allow researchers more and more freedom to explore the role of geometry on functional materials at multiple length scales.

Experimental Section

Preparation of Models: Virtual 3D models of non-convex honeycombs were created with Rhinoceros® 4 (Robert McNeel & Associates). The T SUs short/long sides measured 5/10 mm, respectively. The walls and inclusions were 2 mm and 1.3 mm thick, respectively, leaving a 0.4 mm thick slit in the cells' center (see Figure 3). The 3D models were obtained by extruding a trimmed 6-by-6 SUs square patch of the honeycomb with resulting dimensions of 60x60x5 mm and were exported as stereolithography (STL) files for 3D printing.

Rapid prototyping: All samples were constructed with an Objet® Connex500 multi-material 3D printer. During the fabrication process, a photosensitive liquid precursor (the 3D printer ink) is deposited in a voxel-by-voxel fashion. Several precursors are used to print multiple materials with different properties and the resulting modulus can be tuned by varying the concentration of photo-initiator. A UV light lamp cross-links the liquid precursors in a layer-by-layer fashion and this process is repeated until the full 3D model is built. In our models, the walls and inclusions are printed from a mixture of precursors resulting respectively in stiff duroplastic (Mat1) and soft rubber-like (Mat2) materials that we characterized experimentally (see next section).

Experimental Characterization of 3D Printed Materials: Young's modulus, *E*, of Mat1 and Mat2 materials in their cured state was assessed by tensile-testing 3D-printed flat dog-bone specimens in a Roell-Zwick testing apparatus according to the ASTM D 638 standard (Pre-load: 0.05 MPa, Test speed: 1 mm/min). Measured values were: E_{Mat1}=530 MPa, E_{Mat2}=404 kPa. The linear expansion due to swelling was measured with a ruler after soaking 50 mm long

3D-printed bar specimens in isopropanol (iso-propan-2-ol) for 7 days and the measured values were: ε_{Mat1}=3.3E-3, ε_{Mat2}=0.363. The materials' Young moduli in their swollen state were measured in compression mode on 3D-printed cylindrical specimens in the same Roell-Zwick testing apparatus, using a custom made stage with a solvent chamber and a flat plunger (Mat1: E=65.85 MPa, ν=0.49; Mat2: E=0.48 MPa, ν =0.25; we estimated the values of ν as suggested in [23]).

Model Swelling Experiments: The 3D printed samples were soaked in isopropanol in glass Petri dishes, covered with a glass lid and sealed with an O-ring. The swelling process was recorded with a digital camera by taking snapshots every 20 minutes until a stable configuration was obtained (4 to 5 days). Swelling deformations were measured in the central field of the sample with the aid of image analysis software (ImageJ [24]).

Finite Element Simulations: All honeycomb geometries, domain discretization and finite element (FE) analysis were performed with the commercial finite element software ABAQUS 6.12® (Dassault Systémes Simulia Corp.). We studied the honeycombs' in-plane deformations as the result of both an internal pressurization and the swelling (anelastic expansion) of a material filling the SUs. Both cases were treated as static, plane stress, and large displacement (i.e. the Green-Lagrange nonlinear strain tensor defined on the current configuration is used).

Simulations of internally pressurized honeycombs. To avoid boundary effects, we studied a 6x6 SU square patch with periodic boundary conditions (details in Supporting Information). The T/L cells' short and long sides measured 5/5.774 mm and 10/11.548 mm, respectively. T/L honeycombs had a wall thickness of 0.5/0.5774 mm and were discretized using 4-node bilinear plane stress quadrilateral, reduced integration elements (CPS4R) with mesh sizes of ≈12500 elements. The walls had a Hookean constitutive law with E=1GPa, ν=0.3. Iterative FE simulations were performed to calculate each honeycomb's equilibrated configuration at a given pressure *p* applied in the cells.

Simulations of swelling honeycombs: Swelling of 6x6 cells honeycombs with stiff walls and soft cells was simulated for honeycombs T1, T4, T8 (details in Supporting Information). Walls and SUs were considered linear elastic with mechanical and expansion properties as measured for Mat1 and Mat2 materials respectively.

Supporting Information

Supporting Information is available from the Wiley Online Library or from the author.

Acknowledgements

The authors acknowledge the Humboldt Foundation for supporting the visit of Yves Bréchet to Potsdam through the Gay-Lussac-Humboldt Award and support through the Leibniz prize of PF running under DFG contract number FR2190/4-1.

References

[1] a) J. W. C. Dunlop, P. Fratzl, Scr. Mater. 2013, 68, 8; b) P. Fratzl, F. G. Barth, Nature 2009, 462, 442; c) S. Armon, E. Efrati, R. Kupferman, E. Sharon, Science 2011, 333, 1726; d) E. Reyssat, L. Mahadevan, J. R. Soc. Interface 2009, 6, 951; e) A. R. Studart, R. M. Erb, Soft Matter 2014, 10, 1284.

[2] I. Burgert, P. Fratzl, Phys. Eng. Sci. 2009, 367, 1541.

[3] M. F. Ashby, Y. J. M. Brechet, Acta Mater. 2003, 51, 5801.

[4] M. Pagitz, E. Lamacchia, J. M. A. M. Hol, Bioinspir. Biomim. 2012,
7, 016007.

[5] T. Speck, I. Burgert, Annu. Rev. Mater. Res. 2011, 41, 169.

[6] J. Keckes, I. Burgert, K. Frühmann, M. Müller, K. Kölln,
M. Hamilton, M. Burghammer, S. V. Roth, S. E. Stanzl-Tschegg,
P. Fratzl, Nat. Mater. 2003, 2, 810.

[7] a) I. Burgert, M. Eder, N. Gierlinger, P. Fratzl, Planta 2007, 226, 981;
b) L. Goswami, J. W. C. Dunlop, K. Jungnikl, M. Eder, N. Gierlinger,
C. Coutand, G. Jeronimidis, P. Fratzl, I. Burgert, Plant J. 2008, 56, 531. [8] N. Schreiber, N. Gierlinger, N. Putz, P. Fratzl, C. Neinhuis,
I. Burgert, Plant J. 2010, 61, 854.

[9] P. Fratzl, R. Elbaum, I. Burgert, Faraday Discuss. 2008, 139, 275.

[10] L. Bertinetti, F. D. Fischer, P. Fratzl, Phys. Rev. Lett. 2013, 111, 238001.

[11] M. J. Harrington, K. Razghandi, F. Ditsch, L. Guiducci, M. Rueggeberg, J. W. C. Dunlop, P. Fratzl, C. Neinhuis, I. Burgert, Nat. Commun. 2011, 2, 337.

[12] K. Razghandi, L. Guiducci, J. W. C. Dunlop, P. Fratzl, C. Neinhuis, I. Burgert, Bioinspired, Biomim. Nanobiomater. J. 2014, 3, 169.

[13] L. Guiducci, P. Fratzl, Y. J. M. Brechet, J. W. C. Dunlop, J. R. Soc. Interface 2014, 11, 20140458.

[14] To avoid confusion with the biological term, cell, we use the term structural unit (SU) or tile interchangeably to describe the elemen- tary "cell" that makes up a honeycomb.

[15] A. M. Legendre, D. C. T. Brewster, Elements of Geometry and Trigo- nometry: With Notes, Oliver & Boyd, Edinburgh 1824.

[16] I. Pinelis, J. Geom. 2005, 82, 156.

[17] A. L. Loeb, Concepts & Images: Visual Mathematics, Birkhauser,
Boston, MA 1993, 14.

[18] D. Schattschneider, Math. Mag. 1980, 53, 224.

[19] a) H. Mitschke, V. Robins, K. Mecke, G. E. Schroder-Turk,
P. Roy. Soc. A-Math. Phys. 2013, 469, 20120465; b) H. Mitschke, J. Schwerdtfeger, F. Schury, M. Stingl, C. Korner, R. F. Singer, V. Robins, K. Mecke, G. E. Schroder-Turk, Adv. Mater. 2011, 23, 2669.

[20] Q. Ge, H. J. Qi, M. L. Dunn, Appl. Phys. Lett. 2013, 103, 131901.

[21] a) E. Sinibaldi, A. Argiolas, G. L. Puleo, B. Mazzolai, Plos One 2014, 9, e102461; b) E. Sinibaldi, G. L. Puleo, F. Mattioli, V. Mattoli, F. Di Michele, L. Beccai, F. Tramacere, S. Mancuso, B. Mazzolai, Bioinspir. Biomim. 2013, 8, 025002.

[22] a) B. G. Kabra, S. H. Gehrke, ACS Sym. Ser. 1994, 573, 76; b) Q. Zhao, J. W. C. Dunlop, X. L. Qiu, F. H. Huang, Z. B. Zhang, J. Heyda, J. Dzubiella, M. Antonietti, J. Y. Yuan, Nat. Commun. 2014, 5, 4293.

[23] a) S. Babaee, J. Shim, J. C. Weaver, E. R. Chen, N. Patel, K. Bertoldi, Adv. Mater. 2013, 25, 5044; b) S. H. Kang, S. Shan, A. Kosmrlj, W. L. Noorduin, S. Shian, J. C. Weaver, D. R. Clarke, K. Bertoldi, Phys. Rev. Lett. 2014, 112, 098701; c) J. Shim, S. C. Shan, A. Kosmrlj, S. H. Kang, E. R. Chen, J. C. Weaver, K. Bertoldi, Soft Matter 2013, 9, 8198.
[24] a) L. Margheri, C. Laschi, B. Mazzolai, Bioinspir. Biomim. 2012, 7, 025004; b) R. V. Martinez, J. L. Branch, C. R. Fish, L. H. Jin, R. F. Shepherd, R. M. D. Nunes, Z. G. Suo, G. M. Whitesides, Adv. Mater. 2013, 25, 205; c) B. Mazzolai, L. Margheri, M. Cianchetti, P. Dario, C. Laschi, Bioinspir. Biomim. 2012, 7, 025005; d) E. T. Roche, R. Wohlfarth, J. T. B. Overvelde, N. V. Vasilyev, F. A. Pigula, D. J. Mooney, K. Bertoldi, C. J. Walsh, Adv. Mater. 2014, 26, 1200; e) D. Trivedi, C. D. Rahn, W. M. Kierb, I. D. Walker, Appl. Bionics Biomechanics 2008, 5, 99.
[25] R. F. Shepherd, F. Ilievski, W. Choi, S. A. Morin, A. A. Stokes, A. D. Mazzeo, X. Chen, M. Wang, G. M. Whitesides, Proc. Natl. Acad. Sci. USA 2011, 108, 20400.
[26] R. H. Pritchard, E. M. Terentjev, Polymer 2013, 54, 6954.
[27] C. A. Schneider, W. S. Rasband, K. W. Eliceiri, Nat. Methods 2012, 9, 671.